

# Search for lepton-flavour violating decays of a Higgs-like boson at LHCb

THÈSE N° 8152 (2017)

PRÉSENTÉE LE 1 DÉCEMBRE 2017  
À LA FACULTÉ DES SCIENCES DE BASE  
LABORATOIRE DE PHYSIQUE DES HAUTES ÉNERGIES 1  
PROGRAMME DOCTORAL EN PHYSIQUE

ÉCOLE POLYTECHNIQUE FÉDÉRALE DE LAUSANNE

POUR L'OBTENTION DU GRADE DE DOCTEUR ÈS SCIENCES

PAR

**Chitsanu KHUREWATHANAKUL**

acceptée sur proposition du jury:

Prof. H. M. Rønnow, président du jury  
Prof. A. Bay, directeur de thèse  
Dr Ph. Ilten, rapporteur  
Dr X. C. Vidal, rapporteur  
Prof. J.-P. R. Kneib, rapporteur



ÉCOLE POLYTECHNIQUE  
FÉDÉRALE DE LAUSANNE

Suisse  
2017



~ ARTEM DELECTIONI VITA EST ~







การจะพัฒนาทุกสิ่งทุกอย่างให้เจริญนั้น  
จะต้องสร้างและเสริมขึ้นจากพื้นฐานเดิมที่มีอยู่ก่อนทั้งสิ้น

ถ้าพื้นฐานไม่ดีหรือคลอนแคลนบกพร่องแล้ว  
ที่จะเพิ่มเติมเสริมต่อให้เจริญขึ้นไปอีกนั้น ยากนักที่จะทำได้

จึงควรระเข้าใจให้แจ่มชัดว่า นอกจากจะมุ่งสร้างความเจริญแล้ว  
ยังต้องพยายามรักษาพื้นฐานให้มั่นคง ไม่บกพร่อง พร้อมๆกันไว้

— พระบรมราโชวาท พระบาทสมเด็จพระเจ้าอยู่หัวรัชกาลที่ ๙  
King Bhumibol Adulyadej, 1927 – 2016





# Acknowledgements

It's all about the journey, not the destination: All the care and kindness from people, acknowledged hereinafter or otherwise, helped in the crystallization of this work...

Days and nights, as I knocked on his door accompanied with the news, be it good or bad, turning away from his table and initiating the discussion with a smile is unquestionably the most memorable part of Prof. Aurelio Bay throughout my thesis. Lasting from two minutes to six hours, our discussions showed me his open-minded insight, virtuous patience, and most importantly, the respect and belief, that fueled me through the finishing line...

The conservation of conversation is inapplicable during the moment I spend with Stephane Tourneur, my mentoring postdoc. Not only he could instructively answer any queries of mine, he always bundled them with constructive suggestions, as well as unhesitantly and passionately taking steps back to explain me any remaining confusions until none is left, or it was getting toward the midnight...

It was such a privilege to be working alongside the people of QEE working group. Like a fine Swiss hike, it is challenging, inspirational, down-to-earth, and worthwhile in every step taken. I have learned a lot from them, especially the wisdom from Philip Ilten, Xabier Cid Vidal, William Barter, Wouter Hulsbergen, and Stephen Farry. I'll surely miss that 2pm Vidyo meeting...

The colleagues at the LPHE truly make the environment unique, which wouldn't be possible without Prof. Tatsuya Nakada and Prof. Olivier Schneider at the helm, as well as our sweet secretaries Erika Luthi and Esther Hoffmann who always provide us an assistance to administrative tasks, oftentimes more complicate than our research. The room BSP 616 will be missed, alongside with the laughs, advices, synergy, alleviation, and gratitude I shared with my office mates; Julien Rouvinet and Bastien Muster during the first half, and the umoristico-e-sincero Guido Andreassi in the latter half. Indeed, it's now time to write my entry on that whiteboard...

The community of Thai students has always been an important moral compass and emotional support to me. The original group of ATSS founders, *Succinum Rerum*, as well as each and every new generations joined since then, helped reminding me to what cause all of this hard work are for...

## Acknowledgements

---

I'm grateful to have learned numerous life lessons from P'Meaw which aided me to stand strong and walk tall through the PhD...

Perhaps merely once a year, the faith I get refilled from H'Bright & Chan, and my comrade; Kai, Sia, Bomb, Best, and Choi, is insanely invaluable. May the force be with you...

And who would have imagined? With Aga, we have passed a decade of friendship, keeping each other company and our sanity intact whilst the world revolved chaotically around us...

To Altag and Lesnas who, even in the deep slumber, have never given up on me...

While it may have been a rather bumpy ride, the love from my dear girlfriend Eve remained unfaltering against all odds and distances, and instilled into the fabric of this work. WFFLLL...

At last but not least, without my beloved family, none of this would be possible. The joy of finishing this work becomes minor compare to the moment we are together...

And thus, there is only one thing left to say;  
*Thank you.*

*Lausanne, 1 December 2017*

C. K.

# Abstract

This thesis presents the search for a charged-lepton flavour violation via a model-independent Higgs-like boson decaying to a muon and a tau lepton,  $H \rightarrow \mu\tau$ . The validation of high- $p_T$  tau lepton identification is performed with the measurement of  $Z \rightarrow \tau^+\tau^-$  production cross-section, using  $2\text{ fb}^{-1}$  of integrated luminosity from  $pp$  collisions at  $\sqrt{s} = 8\text{ TeV}$  collected by the LHCb experiment at the LHC in 2012. The tau leptons are reconstructed in both leptonic and hadronic decay channels. The cross-section, restricted to events with both tau leptons having a transverse momentum greater than  $20\text{ GeV}/c$  and a pseudorapidity between 2 and 4.5, and with a tau pair invariant mass between 60 and  $120\text{ GeV}/c^2$ , is measured to be

$$\sigma_{Z \rightarrow \tau^+\tau^-} = 95.20 \pm 2.13 \pm 4.79 \pm 0.17 \pm 1.10\text{ pb}.$$

The uncertainties are statistical, systematic, from the LHC beam energy, and from the integrated luminosity. The results are compatible with the lepton universality hypothesis in  $Z$  decays, and are in agreement with NNLO Standard Model predictions.

Using the validated tau-lepton identification and detection efficiencies, the search for  $H \rightarrow \mu\tau$  covering 99% of tau decay modes found no statistically significant excess. The upper limit on the cross-section times branching fraction,  $\sigma_{gg \rightarrow H \rightarrow \mu\tau}$ , at 95% confidence level is set, ranging from about  $22\text{ pb}$  for  $m_H = 45\text{ GeV}/c^2$  to  $4\text{ pb}$  at  $195\text{ GeV}/c^2$ . Assuming the Standard Model Higgs, the limit on the branching fraction is  $\mathcal{B}(H \rightarrow \mu\tau) < 25.7\%$ , corresponding to a Yukawa coupling of  $\sqrt{|Y_{\mu\tau}|^2 + |Y_{\tau\mu}|^2} < 1.69 \times 10^{-2}$ .

**Keywords:** LHCb, tau lepton,  $Z^0 \rightarrow \tau^+\tau^-$ , lepton universality,  $H \rightarrow \mu^-\tau^+$ , charged-lepton-flavour-violation.



# Résumé

Ce travail de thèse présente la recherche de la violation des saveurs leptoniques chargée par des bosons semblables au boson de Higgs se désintégrant en un muon et un lepton tau,  $H \rightarrow \mu\tau$ . La validation de l'identification du lepton tau à haut  $p_T$  a été obtenue par la mesure de la section efficace de  $Z \rightarrow \tau^+\tau^-$ , en utilisant les données enregistrées par l'expérience LHCb durant l'année 2012 des collision  $pp$  avec une énergie dans le centre de masse de  $\sqrt{s} = 8$  TeV, correspondant à une luminosité intégrée de  $2 \text{ fb}^{-1}$ . Des leptons tau sont reconstruits dans les canaux de désintégration leptoniques et hadroniques. La section efficace pour les événements contenant des leptons tau avec une quantité de mouvement transverse plus grande que  $20 \text{ GeV}/c$ , une pseudorapidité entre 2 et 4.5, et une masse invariante des paires de leptons tau entre 60 et  $120 \text{ GeV}/c^2$ , a été mesurée et vaut :

$$\sigma_{Z \rightarrow \tau^+\tau^-} = 95.20 \pm 2.13 \pm 4.79 \pm 0.17 \pm 1.10 \text{ pb},$$

où les incertitudes sont statistique, systématique, sur l'énergie d'un faisceau, et sur la luminosité. Les résultats sont compatibles avec l'universalité leptonique, et avec les prédictions au niveau NNLO du Modèle Standard.

La recherche de  $H \rightarrow \mu\tau$  en utilisant l'identification et les efficacités de détection des leptons tau ne trouve aucun excès statistique. Les limites supérieures au niveau de confiance de 95% sur les sections efficaces de production,  $\sigma_{gg \rightarrow H \rightarrow \mu\tau}$ , ont été établies à 22 pb pour  $m_H = 45 \text{ GeV}/c^2$ , jusqu'à 4 pb pour  $m_H = 195 \text{ GeV}/c^2$ . Pour le boson de Higgs du Modèle Standard, la limite supérieure sur le facteur de branchement est  $\mathcal{B}(H \rightarrow \mu\tau) < 25.7\%$ , correspondant au couplage de Yukawa  $\sqrt{|Y_{\mu\tau}|^2 + |Y_{\tau\mu}|^2} < 1.69 \times 10^{-2}$ .

**Mots clefs** : LHCb, lepton tau,  $Z^0 \rightarrow \tau^+\tau^-$ , universalité leptonique,  $H \rightarrow \mu^-\tau^+$ , violation des saveurs leptoniques chargée.





## บทคัดย่อ

วิทยานิพนธ์นี้นำเสนอการค้นหาละเมิดเลขรสนของเลปตอนแบบมีประจุในปฏิกิริยา  $H \rightarrow \mu\tau$  ของโบซอนเสมือนฮิกส์แบบไม่จำกัดโมเดลทางทฤษฎีสลายไปสู่มีวอนกับเทาเลปตอน ในการที่จะยืนยันการตรวจจับเทาเลปตอนที่มีโมเมนตัมตัดขวางค่อนข้างสูง ปฏิกิริยา  $Z \rightarrow \tau\tau$  ได้ถูกเลือกใช้ด้วยการวัดภาคตัดขวางการผลิต โดยได้ข้อมูลปริมาณ  $2 \text{ fb}^{-1}$  ของลูมินอซิตีที่สะสมจากการชนกันของโปรตอน-โปรตอนที่  $\sqrt{s} = 8 \text{ TeV}$  จากการเก็บข้อมูลของ LHCb ตลอดปีพ.ศ. ๒๕๕๕ เทาเลปตอนถูกสร้างใหม่ทั้งในช่องทางการสลายแบบเลปตอนและฮาดรอน ภาคตัดขวางการผลิตที่ถูกจำกัดเฉพาะเทาเลปตอนที่มีโมเมนตัมตัดขวางมากกว่า  $20 \text{ GeV}/c$  ความรวดเร็วเหมือนระหว่าง 2 ถึง 4.5 และคู่ของเทาเลปตอนที่มีมวลหนึ่งระหว่าง 60 ถึง  $120 \text{ GeV}/c^2$  ได้ผลการตรวจวัดเท่ากับ

$$\sigma_{Z \rightarrow \tau^+\tau^-} = 95.20 \pm 2.13 \pm 4.79 \pm 0.17 \pm 1.10 \text{ pb}$$

โดยมีค่าความไม่แน่นอนจากทางสถิติ จากทางกระบวนการ จากผลการวัดพลังงานของลำแสงจาก LHC และจากการวัดลูมินอซิตีที่สะสมตามลำดับ ผลลัพธ์นี้สอดคล้องกับสมมติฐานของความเป็นสากลของเลปตอนจากโบซอน Z และกับค่าคาดการณ์จากแบบจำลองมาตรฐาน ณ ระดับ NNLO

ขั้นตอนและค่าสมรรถภาพการตรวจจับเทาเลปตอนที่ได้รับการยืนยันข้างต้น ถูกนำไปประยุกต์ต่อในการค้นหาปฏิกิริยา  $H \rightarrow \mu\tau$  ครอบคลุมมากกว่าร้อยละ 99 ของช่องทางการสลายตัวของเทาเลปตอน โดยมิได้พบสัญญาณอย่างมีนัยยะสำคัญ ซึ่ดจำกัดบน ณ ระดับความเชื่อมั่นร้อยละ 95 ของภาคตัดขวางการผลิตจำเพาะ  $\sigma_{gg \rightarrow H \rightarrow \mu\tau}$  ถูกจำกัดไว้ที่  $22 \text{ pb}$  สำหรับมวล  $m_H = 45 \text{ GeV}/c^2$  เรื่อยไปถึง  $4 \text{ pb}$  สำหรับมวล  $195 \text{ GeV}/c^2$  ในกรณีของฮิกส์โบซอนจากแบบจำลองมาตรฐาน สัดส่วนช่องทางการสลาย  $B(H \rightarrow \mu\tau)$  ถูกจำกัดที่ร้อยละ 25.7 ตรงกับค่าการควมของยูคว่า  $\sqrt{|Y_{\mu\tau}|^2 + |Y_{\tau\mu}|^2} < 1.69 \times 10^{-2}$

**คำสำคัญ:** LHCb เทาเลปตอน  $Z^0 \rightarrow \tau^+\tau^-$  ความเป็นสากลของเลปตอน  $H \rightarrow \mu^-\tau^+$  การละเมิดเลขรสนของเลปตอนแบบมีประจุ



# Contents

<b>Acknowledgements</b>	<b>i</b>
<b>Abstract (English/Français/ ไทย)</b>	<b>iii</b>
<b>1 Introduction</b>	<b>1</b>
<b>I LHC Physics</b>	<b>3</b>
<b>2 Theory</b>	<b>5</b>
2.1 Standard Model (SM)	5
2.2 Beyond the Standard Model	6
2.2.1 Limitation of the Standard Model	6
2.2.2 Proposals of Extension to the Standard Model	8
2.3 Charged Lepton Flavour Violation	10
2.3.1 Lepton Flavour Violation (LFV) and the Standard Model	10
2.3.2 Charged Lepton Flavour Violation (CLFV) and New Physics (NP)	10
2.3.3 Higgs-mediated Charge Lepton Flavour Violation (HCLFV)	11
2.3.4 Status of HCLFV searches & constraints	13
2.4 The Tau Lepton	15
2.4.1 Decays of Tau Lepton	15
2.4.2 Identification of High- $p_T$ Tau Lepton	16
2.4.3 Gateway for New Physics	16
<b>3 Experimental Environment</b>	<b>19</b>
3.1 CERN and Large Hadron Collider (LHC)	19
3.2 The LHCb detector	24
3.3 Event Reconstruction	30
3.4 Analysis Framework	34
3.5 The LHCb Working Groups	34
<b>II Measurement of the Inclusive <math>Z \rightarrow \tau\tau</math> Production Cross-section</b>	<b>37</b>
<b>4 <math>Z \rightarrow \tau\tau</math> at LHCb</b>	<b>39</b>
4.1 Background Processes	40

## Contents

---

4.2	Cross-section Measurement . . . . .	40
4.3	Data Samples . . . . .	41
4.3.1	Real Data . . . . .	41
4.3.2	Simulated Samples . . . . .	41
<b>5</b>	<b>Signal Selection</b> . . . . .	<b>43</b>
5.1	Fiducial Region . . . . .	43
5.2	Acceptance . . . . .	44
5.3	Trigger Requirement . . . . .	45
5.4	Candidate Reconstruction . . . . .	46
5.4.1	Track Quality . . . . .	46
5.4.2	Particle Identification . . . . .	46
5.5	Kinematic Preselection . . . . .	46
5.6	Candidate Selection . . . . .	47
5.6.1	Tau Candidate Selection . . . . .	47
5.6.2	Di-tau Candidate Selection . . . . .	52
5.7	Summary of Selections . . . . .	54
<b>6</b>	<b>Background Estimation</b> . . . . .	<b>57</b>
6.1	Drell-Yan Process . . . . .	57
6.1.1	Channel $\tau_\mu\tau_\mu, \tau_e\tau_e$ . . . . .	57
6.1.2	Channel $\tau_\mu\tau_{h1}, \tau_e\tau_{h1}, \tau_\mu\tau_e$ . . . . .	59
6.2	QCD and $Vj$ Processes . . . . .	61
6.3	$t\bar{t}, WW, WZ, Z \rightarrow b\bar{b}$ . . . . .	64
6.4	$Z \rightarrow \tau\tau$ Cross-feed . . . . .	64
6.5	Summary . . . . .	64
<b>7</b>	<b>Reconstruction Efficiencies</b> . . . . .	<b>71</b>
7.1	Tracking Efficiencies . . . . .	72
7.1.1	Muon Tracking . . . . .	72
7.1.2	Electron Tracking . . . . .	72
7.1.3	Charged Hadron Tracking . . . . .	74
7.2	Efficiencies of the Kinematic Preselection . . . . .	75
7.3	PID Efficiencies . . . . .	75
7.3.1	Muon Identification . . . . .	75
7.3.2	Electron Identification . . . . .	77
7.3.3	Charged Hadron Identification . . . . .	79
7.4	Global Event Cut Efficiency . . . . .	81
7.5	Trigger Efficiencies . . . . .	82
7.5.1	Muon Trigger . . . . .	82
7.5.2	Electron Trigger . . . . .	82
7.6	Summary . . . . .	83
<b>8</b>	<b>“Offline” Selection Efficiencies</b> . . . . .	<b>85</b>
8.1	Transverse Momentum Asymmetry ( $A_{p_T}$ ) . . . . .	86
8.2	Upper Cut on the Di-lepton Invariant Mass . . . . .	86
8.3	Isolation ( $\hat{I}_{p_T}$ ) . . . . .	86
8.4	Impact Parameter (IP) . . . . .	87

8.5	Azimuthal Separation ( $\Delta\phi$ )	88
8.6	Variables for the Di-tau Channels with $\tau_{h3}$	88
<b>9</b>	<b>Uncertainties</b>	<b>91</b>
<b>10</b>	<b>Results</b>	<b>95</b>
10.1	Fiducial Cross-sections	95
10.2	Cross-section Ratios at Different Centre-of-mass Energies	96
10.3	Lepton Universality	97
10.4	Tau Lepton Decay Branching Fraction	97
<b>III</b>	<b>Search for CLFV of a Higgs-like scalar decay <math>H \rightarrow \mu\tau</math></b>	<b>99</b>
<b>11</b>	<b><math>H \rightarrow \mu\tau</math> at LHCb</b>	<b>101</b>
<b>12</b>	<b>Signal Selection</b>	<b>103</b>
12.1	Acceptance	103
12.2	Trigger and Reconstruction Requirements	103
12.3	Offline Selection	104
12.4	Summary of Selections	107
<b>13</b>	<b>Background Estimation</b>	<b>109</b>
13.1	$Z \rightarrow \tau\tau$	109
13.2	Drell-Yan Process	110
13.2.1	Channel $\mu\tau_\mu$	110
13.2.2	Channel $\mu\tau_{h1}, \mu\tau_e$	111
13.3	QCD and $Vj$ Processes	111
13.4	$t\bar{t}, WW, WZ, Z \rightarrow b\bar{b}$	113
13.5	Summary	113
<b>14</b>	<b>Signal Efficiencies</b>	<b>119</b>
14.1	Acceptance, $\mathcal{A}$	119
14.2	Reconstruction Efficiency, $\epsilon_{\text{rec}}$	120
14.3	Selection Efficiency, $\epsilon_{\text{sel}}$	121
<b>15</b>	<b>Uncertainties</b>	<b>123</b>
<b>16</b>	<b>Signal Likelihood</b>	<b>125</b>
16.1	Test Statistics	125
16.2	Likelihood Model	126
16.3	Uncertainties	128
16.4	Correlated Uncertainties	128
16.4.1	System of 4 Correlated Variables	129
16.4.2	System of 2 Correlated Variables	129
16.4.3	System of Fully Correlated Variables	130
16.5	Upper Limit	130
16.6	Validation	131

<b>17 Results</b>	<b>133</b>
17.1 Signal upper limit . . . . .	133
17.2 Future prospect . . . . .	137
<b>Conclusion</b>	<b>141</b>
<b>Appendix</b>	<b>145</b>
<b>A Selection of <math>Z \rightarrow \tau\tau</math></b>	<b>145</b>
A.1 Acceptance . . . . .	145
A.2 Trigger-Stripping Specification . . . . .	148
A.3 Kinematic Preselection . . . . .	152
A.4 Assisted Candidate Selection . . . . .	155
A.4.1 Variables Correlation Matrix . . . . .	155
A.4.2 Variables Ranking . . . . .	158
A.4.3 Suggested Cut-based Selection . . . . .	160
A.5 Tau Candidate Selection . . . . .	165
A.6 Di-tau Candidate Selection . . . . .	169
<b>B Muon Misidentification</b>	<b>171</b>
<b>C Backgrounds of <math>Z \rightarrow \tau\tau</math></b>	<b>173</b>
<b>D Combined Plots of <math>Z \rightarrow \tau\tau</math></b>	<b>181</b>
<b>E Reconstruction Efficiencies</b>	<b>191</b>
E.1 Binned Efficiencies . . . . .	191
E.2 Equivalent Efficiencies . . . . .	195
<b>F <math>Z \rightarrow \tau\tau</math> Cross-section Measurement</b>	<b>199</b>
<b>G Combining Cross-sections with Uncertainties</b>	<b>201</b>
<b>H Generator-level <math>H \rightarrow \mu\tau</math></b>	<b>203</b>
<b>I Selection of <math>H \rightarrow \mu\tau</math></b>	<b>207</b>
<b>J Background estimation of <math>H \rightarrow \mu\tau</math></b>	<b>219</b>
J.1 Estimation from Simulation . . . . .	219
J.2 Combined Plots of $H \rightarrow \mu\tau$ . . . . .	222
<b>K <math>H \rightarrow \mu\tau</math> Efficiencies</b>	<b>229</b>
<b>L Validation of Fit Models</b>	<b>237</b>
L.1 Upper Limit Strategies . . . . .	237
L.2 Selection Regimes . . . . .	239
L.3 Analysis Channels & Simultaneous Fit . . . . .	240
L.4 Uncertainties as Nuisance Parameters . . . . .	241
L.5 Shape Uncertainty . . . . .	243

L.6 RooKeysPdf as Distribution Shape . . . . .	246
<b>M Search for <math>H \rightarrow \mu\tau</math> results</b>	<b>249</b>
M.1 Signal Yield . . . . .	249
M.2 Production Cross-section, $\sigma_{gg \rightarrow H \rightarrow \mu\tau}$ . . . . .	251
M.3 Branching Fraction, $\mathcal{B}_{H \rightarrow \mu\tau}$ . . . . .	254
<b>Bibliography</b>	<b>265</b>
<b>List of figures</b>	<b>267</b>
<b>List of tables</b>	<b>277</b>
<b>Curriculum Vitae</b>	<b>283</b>





# 1 Introduction

**Phy·sics** (noun) /fɪz.ɪks/  
The branch of science concerned  
with the nature and properties of  
matter and energy.

---

Oxford English Dictionary

As a human, we love to identify a pattern. It has been this way since the dawn of the civilization: Looking for an order within a chaos, awaiting for a next sunrise after a sunset, connecting for a language to not being left alone, and striving for a harmonious life with the nature. As recognized by various philosophical schools and religious beliefs, we may merely want to use those patterns to answer where we were from, what matters to us now, and where we shall be.

To physicists, there is probably no greater joy, or “Awakening”, than energetically witnessing an anticipated piece fit accordingly into the pattern: A key that fits into its lock, Gallium that fits into Mendeleev’s periodic table, Gravitational wave that fits into general relativity, and Higgs boson that fits into the Standard Model.

Conversely, nothing is more irritating than unsolved phenomena residing right next to our awakened selves.

As the Standard Model of Particle Physics shines through the scrutiny and established itself as a cornerstone at the end of the 20th century, with so many puzzles left unsolved, its name is no longer befitting. In Part I, the theoretical motivation for a search for New Physics via lepton-flavour-violation will be explored, including constraints from recent experiments, as well as the description of experimental environment at LHCb to pursuit such goal

Choosing  $H \rightarrow \mu\tau$  decay as a search for New Physics, an extensive study on high- $p_T$  tau lepton identification at LHCb is indispensable, which is the subject of Part II. The  $Z \rightarrow \tau\tau$  decay<sup>1</sup> is a perfect control channel for this purpose, where the results can be compared to  $Z \rightarrow \mu\mu$  and  $Z \rightarrow ee$  analyses at LHCb. The establishing performance of tau lepton identification and reconstruction will benefit other searches involving tau lepton in the future.

---

<sup>1</sup>  $Z$  implies  $Z/\gamma^*$ , includes contributions from virtual photon production and its interference with  $Z$  boson production.

## Chapter 1. Introduction

---

The search for  $H \rightarrow \mu\tau$  decay is ultimately presented in Part III, where  $H$  is a model-independent Higgs-like scalar of an unspecified mass within the coverage of this analysis. The signal extraction procedures largely derived from the  $Z \rightarrow \tau\tau$  analysis, benefiting from validated methods and efficiencies. At the end, a hypothesis testing allows an exclusion limit on  $H \rightarrow \mu\tau$  production and leptons Yukawa coupling to be placed.

## Part I

# LHC Physics



# 2 Theory

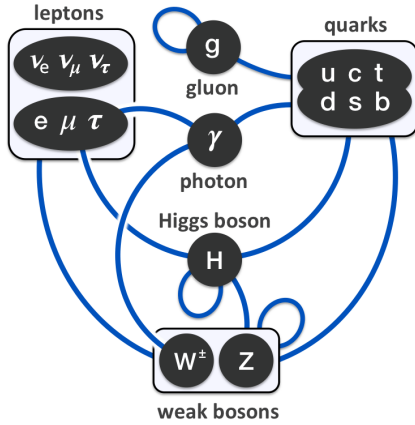
## 2.1 Standard Model (SM)

The *Standard Model of particle physics* (SM) describes three fundamental interactions (electromagnetic (EM), weak, and strong) in a single framework, including a classification of elementary particles, using the *Quantum Field Theory* (QFT) as a theoretical ground. This section briefly provides the overview of the content of SM. More detail treatments can be found in several literature including [1, 2, 3].

“Symmetry” is the key to understanding the principle of laws in nature. In the SM, the interaction between particles can be considered, on one hand, as the interaction mediated by force-carrier *gauge bosons*; and on the other hand, as an operation from a symmetry group leaving the Lagrangian of the system locally invariant. The gauge bosons of the former description are *photons* (EM force), *gluons* (strong force), and  $W^\pm, Z^0$  bosons (weak force). The group structure in the latter description can be written as  $SU(3)_C \otimes SU(2)_L \otimes U(1)_Y$ , governing the conserved color, handedness, and hypercharge respectively. The couplings between gauge bosons and other particles (including themselves) can sufficiently determine the dynamic of the system, which are needed to be measured experimentally. The summary of couplings is shown in Fig. 2.1a.

In contrast to force-carriers, the SM includes *fermions* (particles of spin  $1/2$ , they obey the *Fermi-Dirac statistics*). They can be classified by their couplings with gauge bosons; *quarks* have coupling to gluons, whilst *leptons* do not. The quarks are commonly grouped into “down-type” ( $d, s, b$ ) and “up-type” ( $u, c, t$ ) of electric charge  $-1/3$  and  $+2/3$  respectively. The leptons can be further grouped into *charged leptons* ( $e, \mu, \tau$ ) and *neutrinos* ( $\nu_e, \nu_\mu, \nu_\tau$ ), where the latter can only interact via the weak force. The fermions of SM can alternatively be grouped into 3 *families*, shown in Fig. 2.1b. For each fermion there exists also an *anti-particle* counterpart, having the same mass but opposite internal quantum numbers.

The classical concept of particle mass is considered as an effective result of a coupling to the *Higgs boson*, a sole scalar (spin zero) particle in the SM. It is chronologically the last particle to be discovered in 2012 [6, 7] and completed the prediction of SM particles. The underlying procedure giving  $W^\pm, Z^0$  bosons their masses as observed from experiments is called *Spontaneous symmetry breaking* of  $SU(2) \otimes U(1)$  by the Higgs field, parameterized by mass of Higgs boson,  $m_H$ , and its *vacuum expectation value* (*vev*),  $v$ . Both massive fermions and gauge bosons acquire mass through the *Higgs mechanism*, leaving photons and gluons as massless particles of SM. Quark mass terms in the SM Lagrangian cannot be simultaneously diagonalized with the quark- $W$ -boson coupling terms, leading to separated



(a) Couplings between SM elementary particles [4]

**Standard Model of Elementary Particles**

		three generations of matter (fermions)							
		I		II		III			
QUARKS	mass	=2.4 MeV/c <sup>2</sup>	=1.275 GeV/c <sup>2</sup>	=172.44 GeV/c <sup>2</sup>	0	=125.09 GeV/c <sup>2</sup>			
	charge	2/3	2/3	2/3	0	0			
	spin	1/2	1/2	1/2	0	0			
		u	c	t	g	H			
		up	charm	top	gluon	Higgs			
		d	s	b	γ				
	down	strange	bottom	photon					
LEPTONS	mass	=0.511 MeV/c <sup>2</sup>	=105.67 MeV/c <sup>2</sup>	=1.7768 GeV/c <sup>2</sup>	=91.19 GeV/c <sup>2</sup>				
	charge	-1	-1	-1	0				
	spin	1/2	1/2	1/2	0				
		e	μ	τ	Z				
		electron	muon	tau	Z boson				
		νe	νμ	ντ	W				
	electron neutrino	muon neutrino	tau neutrino	W boson					
		SCALAR BOSONS		GAUGE BOSONS					

(b) Properties of SM elementary particles [5]

Figure 2.1 – Overview of the standard model of physics.

“mass” and “flavour” eigenstates. The *Cabibbo–Kobayashi–Maskawa* (CKM) matrix relates two eigenstates, where the off-diagonal elements signify the degree of *quark mixing* across generations. Due to the absence of right-handed neutrinos, no equivalent mixing is defined for the SM leptons.

The summary of SM Lagrangian can be written in an infamous “coffee mug” version [8] as

$$\mathcal{L} = \underbrace{-\frac{1}{4}F_{\mu\nu}F^{\mu\nu}}_{\text{Gauge bosons couplings}} + \underbrace{i\bar{\psi}\not{D}\psi}_{\text{Fermions dynamic}} + \underbrace{\psi_i y_{ij} \psi_j \phi + h.c.}_{\text{Fermions masses}} + \underbrace{|D_\mu \phi|^2}_{\text{Weak bosons masses}} - \underbrace{V(\phi)}_{\text{Higgs dynamic and mass}}$$

## 2.2 Beyond the Standard Model

### 2.2.1 Limitation of the Standard Model

The SM has been proven a successful theory through the challenges in the previous decades, notably the prediction of particles before their discovery such as the charm quark (1974), *W* and *Z* boson (1983), top quark (1995), and Higgs boson (2012). It is also able to predict precise theoretical values compatible with the experimental measurement, such as the anomalous magnetic dipole moment of an electron. Nevertheless, there remains several limitations that the SM alone cannot explain. These can be considered as unexplained phenomena, unobserved theoretical prediction, and theoretical problems.

**Hierarchy problem (of Higgs boson mass)** The effective mass of Higgs boson (squared) contains loop correction terms summing over all particles coupled to the Higgs, which is expected to large and comparable to the new physics scale, in contradiction with the observed mass of  $\sim 125 \text{ GeV}/c^2$ .

**Strong CP problem** In the Lagrangian describing the SM, there is no mechanism which enforces CP (combined Charge and Parity symmetry) conservation. Given the experimentally observed CP-violation in the weak interaction, why is it not observed

in the strong interaction (QCD)?

**Matter-antimatter asymmetry** With the SM, the Big Bang should produce equal amounts of matter and anti-matter, in contradiction with the current observation. It is possible that physical laws become different between them.

**Gravity and QFT** The gravity as a fundamental force (and thus the theory of general relativity) is not included in the SM, where the major problem lies in the renormalizability of gravity (via its force-carrier: the *graviton*) when the usual treatment of QFT is applied.

**Anomalous magnetic dipole moment of muon** While the prediction from the SM for the anomalous magnetic dipole moment of *electron* is consistent with the experimental value within  $10^9$ , there is currently about  $3.4\sigma$  deviation for the anomalous magnetic dipole moment of the *muon* [9].

**Dark matter and dark energy** Cosmological observation for the existence of dark matter and dark energy, accounting for 95% of energy in the universe, is not explainable by the SM. The distribution is shown in Fig. 2.2.

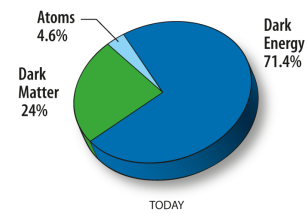


Figure 2.2 – Current known distribution of matter in the observable universe [10].

**Number of parameters** The SM contains a total of 18 parameters (9 fermions masses, 3 gauge couplings, 4 from CKM matrix, 2 for the Higgs field). Assuming massive neutrinos adds 7 more parameters (3 neutrinos masses, 4 from neutrino mixing matrix.) This amount can be considered “unnatural” given that they are all required to be tuned to experimental results. Example of constraining CKM parameters is shown in Fig. 2.3.

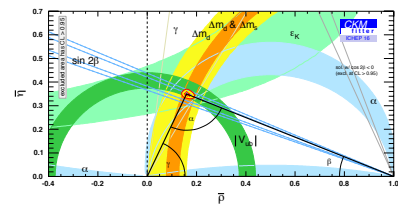


Figure 2.3 – Current constraints on the CKM matrix [11].

**Gauge coupling unification** The coupling parameters of 3 forces in the SM ( $SU(3) \times SU(2) \times U(1)$ ) have the energy scale dependence such that they are found to be nearly intersect near a point at the so-called GUT scale ( $\Lambda_{\text{GUT}} \sim 10^{16}$  GeV). Is this merely a coincidence? Or a particular hint of larger Lie group unifying 3 subgroups?

### 2.2.2 Proposals of Extension to the Standard Model

Given numbers of unsolved problems in physics, it is by nature of physicists to pursuit for possible explanations. Some of these *Physics beyond the Standard Model* (BSM) are described below. It is worth noting that these extensions are not necessary mutually exclusive:

**Grand Unified Theory (GUT)** The GUT proposes the existence of single symmetry comprising the electromagnetic, weak, and strong forces. This is represented by a larger gauge symmetry group with unified coupling constant, for example, in a *Georgi–Glashow model* ( $SU(5) \supset SU(3) \times SU(2) \times U(1)$ ) [12], or  $SO(10)$  model.

**Supersymmetry (SUSY)** The SUSY proposes a new symmetry relating fermions and bosons [13], such that in an unbroken symmetry each fermion-boson pair (*superpartner*) share the same properties except the spin. The SM effectively represents SUSY being fully-broken, leaving particles and their superpartners with different physical properties. The SUSY model (and its variants) gains a significant theoretical motivation as it is able to solve several of the problems listed above, including the hierarchy problem (by virtue of correction from superpartner in the problematic fine-tuning), the gauge coupling unification (Fig. 2.4), and having a superparticle which can play the role of a candidate for dark matter.

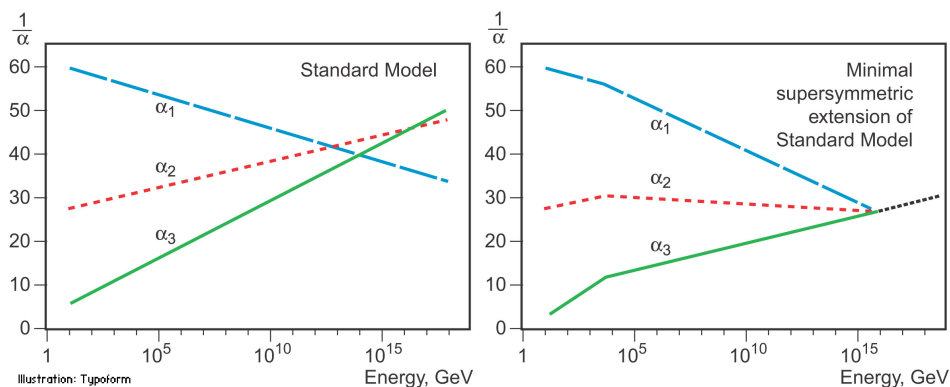


**Figure 2.4** – Changes on the running gauge couplings in the Minimal Supersymmetric SM, where the gauge coupling unification is observed at a higher energy scale, assuming  $SU(5)$  symmetry group [14].

**Axion and Peccei–Quinn (PQ) mechanism** The PQ mechanism [15] aims to solve the Strong-CP problem by proposing an extension to the QCD Lagrangian such that there is an explicit CP-violating term. This consequently leads to the existence of a new particle, the *axion*, expected to be very light, with zero electric charge, and to have a negligible interaction with the weak and strong force. The coupling of the axion to the SM photon can be used for its generation and detection (*cf.*, Fig. 2.5).

**Two-Higgs-doublets model (2HDM)** The 2HDM proposes the Higgs sector to consist of 2 doublets (in contrast with the minimal Higgs model assumed in the SM, which



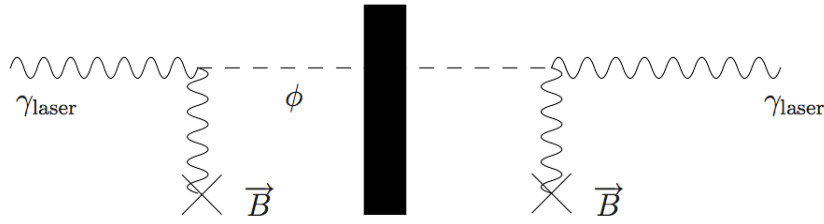


**Figure 2.5** – Coupling of axion and photon can be exploit in the “light-shining-through-wall” experiment [16].

is one doublet). This leads to the existence of 5 physical states of Higgs scalars, as well as bearing 6 free parameters [17]. The 2HDM is motivated by several reasons; MSSM and axion models rely on the existence of 2 doublets Higgs. The model also provides an additional source of CP violation, thus responds to the baryon asymmetry problem in the early universe.

**String theory and Extra dimension** The string theory, in a simple description, replaces point particles by *strings* of length at Planck scale ( $\mathcal{O}(10^{-35})\text{m}$ ), where the string can be either *open* or *closed*, and different vibrational modes of string represents different fundamental particles. Initially there are several variants of string theory, but as suggested by Whitten in 1995, they can be regarded as different limits of a single theory, now referred as *M-theory* (Fig. 2.6). The M-theory requires an existence of ten (or eleven) dimensions (arguing that the SM and observable universe is *embedded* in 4D-brane), as well as SUSY to be consistently formulated [18]. Whilst the mathematical treatment can be challenging, the string theory is able to directly address the unification of gravity and quantum field theory, providing a *quantum gravity* theory.

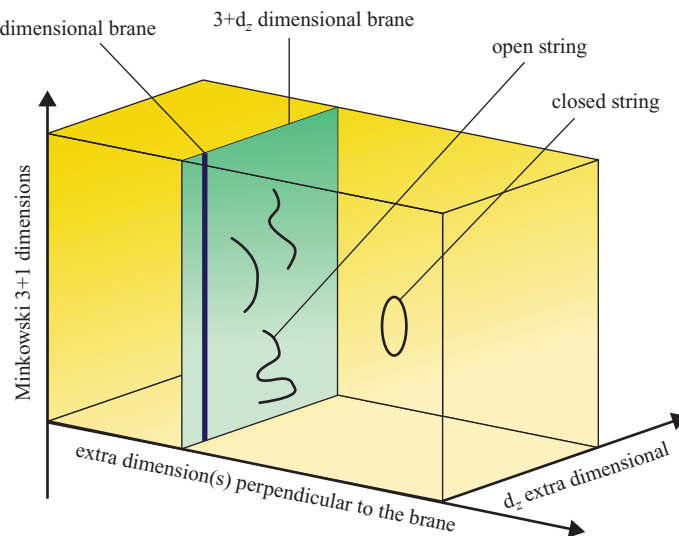


**Figure 2.6** – Illustration of elements in M-theory [19].

## 2.3 Charged Lepton Flavour Violation

Many extensions of the standard model feature the violation of lepton flavour conservation as an experimental observable. This Section will discuss in more details the motivation, framework, and current constraints of this approach.

### 2.3.1 Lepton Flavour Violation (LFV) and the Standard Model

The *conservation of lepton number* is a selection rule in the Standard Model introduced in 1953 [20], such that the total sum of the lepton number is conserved in all elementary particle reactions. Each lepton has the quantum number of +1, the anti-leptons of -1. The conservation restricted to each individual *flavour* ( $L_e, L_\mu, L_\tau$ ) is also observed and considered as a global symmetry.

However, the observation of *neutrino oscillation* is a contradiction to the above flavour conservation law (e.g., Fig. 2.7). The oscillation requires at least one neutrino to be massive, and the mixing matrix can be defined between the mass eigenstates and the flavour (weak interaction) eigenstates [21, 22].

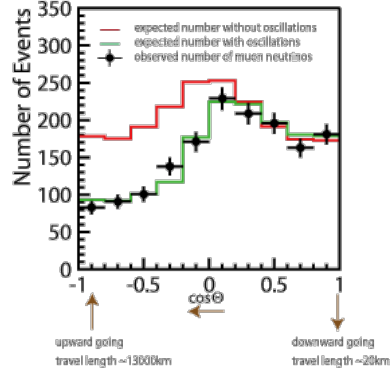


**Figure 2.7** – Observation of atmospheric neutrinos found to be compatible with the neutrino oscillation scenario [23].

### 2.3.2 Charged Lepton Flavour Violation (CLFV) and New Physics (NP)

The lepton flavour violation in the neutrino sector poses the same skepticism in the charged leptons sector. The *charged lepton flavour violation* (CLFV) narrows the focus to processes that violate the individual lepton flavour conservation, does not involve the neutrino, and the total lepton number is conserved. Within the SM, the oscillation of neutrinos allows the LFV process through loops [24], shown in Fig. 2.8. However, it is suppressed by a factor  $(\Delta m_{ij}/M_W)^4$ , where  $\Delta m_{ij}$  is the mass difference between neutrino of the violating flavour, and  $M_W$  is the mass of  $W$  boson. An explicit computation can be made, for example, for the radiative LFV decay [25]:

$$\mathcal{B}(\mu \rightarrow e\gamma) = \frac{3\alpha_{\text{EM}}}{32\pi} \left| \sum_{i=2,3} U_{2i} \frac{\Delta m_{1i}^2}{M_W^2} U_{i1}^\dagger \right|^2 \approx 10^{-54}$$

given the lepton mixing matrix  $U$ . Being almost zero, this branching fraction can be regarded as the origin of an “accidental” charged lepton flavour conservation, given the current experimental sensitivity. **In practice, any detection of CLFV would therefore be a clear sign of New Physics.**

Several NP models provide an enhancement to the LFV suppressed channel. Continuing on the muon-electron flavour violation example, a model-independent effective Lagrangian

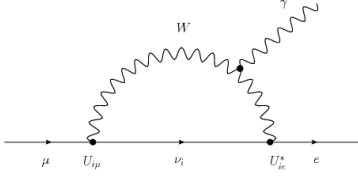


**Figure 2.8** – Highly-suppressed CLFV decay in the SM [26].

can be parameterized as [27]:

$$\begin{aligned} \mathcal{L}_{\text{CLFV}} = & \frac{m_\mu}{(1 + \kappa)\Lambda^2} \bar{\mu}_R \sigma_{\mu\nu} e_L F^{\mu\nu} + h.c. \\ & + \frac{\kappa}{(1 + \kappa)\Lambda^2} \bar{\mu}_L \gamma_\mu e_L (\bar{u}_L \gamma^\mu u_L + \bar{d}_L \gamma^\mu d_L) + h.c. \end{aligned}$$

where the model assumes that CLFV is mediated by an effective operator of dimension five or higher. Other non-dominating interference terms are omitted from this expression. The common variables from the SM electroweak are used, with additional variables ( $\Lambda, \kappa$ ) used to parameterized the new physics effective operators:  $\Lambda$  is the energy scale of new physics, and  $\kappa$  governs the contribution from each term in the Lagrangian. The first term is often referred as the “loop” or “dipole-type” term, and dominates when  $\kappa \ll 1$ , whereas the second term is referred as the “contact” or “four-fermion” term, and dominates when  $\kappa \gg 1$ . Several NP models can be classified in this parameterization [28]. Examples are shown in Fig. 2.9.

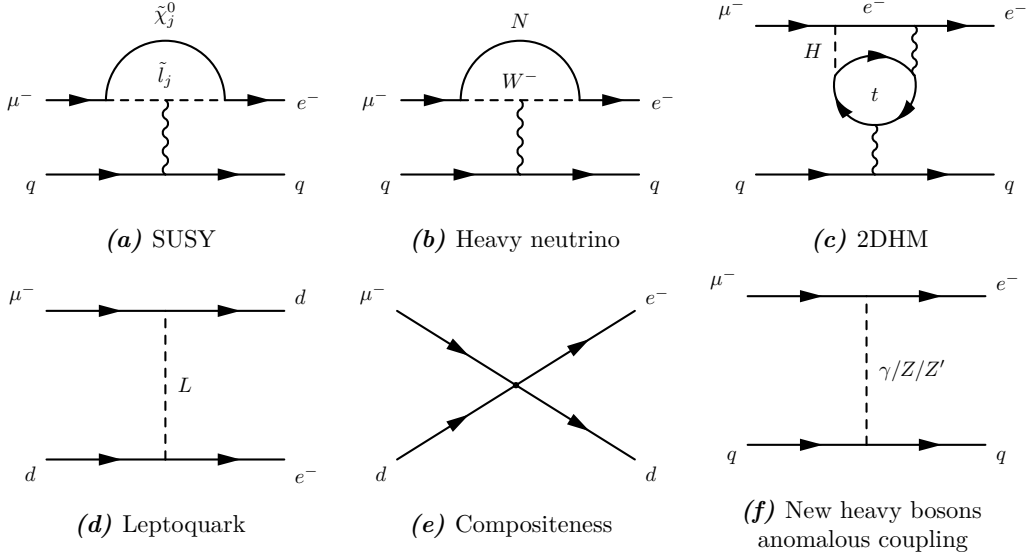


**Figure 2.9** – Possible CLFV from the NP processes. The upper row can be classified as “loop” type, and the lower row as “contact” type. Diagrams adapted from [25, 29].

### 2.3.3 Higgs-mediated Charge Lepton Flavour Violation (HCLFV)

The Yukawa coupling of Higgs-like boson to the charged leptons, be it a Standard Model Higgs or not, provides an interesting gateway to the discovery of CLFV. The *Higgs-mediated charge lepton flavour violation* (HCLFV) is proposed in a multitude of variations including an effective theory with relaxed renormalizability requirements [30], supersymmetric models

[31, 32, 33, 34, 35], composite Higgs models [36, 37], Type-III Two Higgs Doublet Model [38, 39] Randall-Sundrum models [40, 41], flavour symmetries [42], and other models [43, 44, 45, 46, 47, 48, 49, 50].

In the SM, the electroweak symmetry breaking mechanism provides the coupling of Higgs boson to the fermion pairs, where the couplings to 3 generations of charged leptons can be encapsulated as the Yukawa matrix,  $Y_{ij}$ . The relevant Higgs-fermion interaction term in the Lagrangian after electroweak symmetry breaking is

$$\mathcal{L}_Y = -Y_{ij}(\bar{f}_L^i f_R^j)h + h.c. \quad , \quad Y_{ij} = \begin{pmatrix} Y_{ee} & Y_{e\mu} & Y_{e\tau} \\ Y_{\mu e} & Y_{\mu\mu} & Y_{\mu\tau} \\ Y_{\tau e} & Y_{\tau\mu} & Y_{\tau\tau} \end{pmatrix}$$

The coupling matrix is diagonal in the absence of CLFV ( $Y_{ii} = vm_i$ , where  $v$  is the  $vev$  of the Higgs field). Through the modification on this Yukawa matrix by each model, the degree of CLFV can be determined. More specifically, if one assumes the existence of NP with scale  $\Lambda$  in which the dimension-6 operator no longer vanishes, the additional term to the SM Lagrangian coupled to the SM Higgs, assuming no other new particles apart from the existing SM particles, can be written as [30, 47]:

$$\Delta\mathcal{L}_Y = \frac{Y_{ij}^{\text{NP}}}{\Lambda^2}(\bar{f}_L^i f_R^j)h(h^\dagger h) + h.c.$$

with the higher-dimension terms truncated and the derivative terms omitted. The introduced flavour matrix  $Y^{\text{NP}}$  can be *a priori* complex and non-diagonal. The effective Yukawa matrix  $Y_{ij}$  with the effect of additional term included can be written in the lepton mass basis as

$$Y_{ij} = \underbrace{\frac{m_i}{v}\delta_{ij}}_{\text{SM}} + \underbrace{\frac{v^2}{\sqrt{2}\Lambda^2}\hat{Y}_{ij}^{\text{NP}}}_{\text{NP}} \quad (2.1)$$

with  $Y^{\text{NP}}$  being rotated to this basis as  $\hat{Y}^{\text{NP}}$ . The diagonal SM Yukawa matrix  $Y$  is recovered in the limit of  $\Lambda \rightarrow \infty$ . The scale of  $\Lambda$  can be approximated to  $vm_t/m_b \sim \mathcal{O}(1 \text{ TeV})$  [44], making it not too far from the sensitivity of the LHC, as well as interestingly close to the hierarchy-problem scale. The result of eq. 2.1 can be generalized in the presence of additional Higgs in the model by including the summation over all Higgses [30].

The expression in eq. 2.1 can also be recast as a decay width of the Higgs-like boson  $h$  to the chosen LFV channel, as well as the branching fraction [30]:

$$\Gamma(h \rightarrow l_i l_j) = \frac{m_h}{8\pi} (|Y_{ij}|^2 + |Y_{ji}|^2) \quad , \quad \mathcal{B}(h \rightarrow l_i l_j) = \frac{\Gamma(h \rightarrow l_i l_j)}{\Gamma(h \rightarrow l_i l_j) + \Gamma_{\text{SM}}}$$

where  $\Gamma_{\text{SM}}$  is the width of SM Higgs boson. The above expression allows the study in different CLFV channels to be collected and compared in term of the Yukawa coupling matrix, which is discussed in the following section.

### 2.3.4 Status of HCLFV searches & constraints

The status of the HCLFV searches can be summarized in term of the bounds of  $Y_{ij}$  matrix [30] shown in Table 2.1. The results are collected from different measurement channels including the radiative decay  $l_1 \rightarrow l_2\gamma$ , the 3-bodies decay  $l \rightarrow l_1l_2l_3$ ,  $\mu \rightarrow e$  conversion in nuclei, and muonium-antimuonium oscillations. These process are shown in Fig. 2.10.

The summary of bounds in Table 2.1 shows that the current constraints on the Yukawa couplings with  $\tau$  lepton is relatively weak compared to the constraints on the first two generations. This is exploited in recent studies from CMS/ATLAS, providing the limit of SM Higgs decay  $\mathcal{B}(H \rightarrow \mu\tau) < \mathcal{O}(1\%)$ . Moreover, because  $\tau$  leptons couple to Higgs more strongly than other charged leptons, as well as having experimental signatures less challenging than the quark sector (due to QCD modelling, detector response, *etc.*), these reasons make  $\tau$  leptons a very appropriate probe for HCLFV phenomena.

**Table 2.1** – Constraints on HCLFV for a Higgs mass of 125 GeV/ $c^2$ , adapted from [30].

Channel	Coupling	Bound	Reference
$h \rightarrow \mu e$	$\sqrt{ Y_{\mu e} ^2 +  Y_{e\mu} ^2}$	$< 5.4 \times 10^{-4}$	CMS [51]
$h \rightarrow \tau e$	$\sqrt{ Y_{\tau e} ^2 +  Y_{e\tau} ^2}$	$< 2.26 \times 10^{-3}$	CMS [52]
		$< 2.9 \times 10^{-3}$	ATLAS [53]
$h \rightarrow \tau \mu$	$\sqrt{ Y_{\tau \mu} ^2 +  Y_{\mu \tau} ^2}$	$< 1.43 \times 10^{-3}$	CMS [52]
		$< 3.5 \times 10^{-3}$	ATLAS [54]
$\mu \rightarrow e\gamma$	$\sqrt{ Y_{\mu e} ^2 +  Y_{e\mu} ^2}$	$< 3.6 \times 10^{-6}$	PDG [55]
$\tau \rightarrow e\gamma$	$\sqrt{ Y_{\tau e} ^2 +  Y_{e\tau} ^2}$	$< 1.4 \times 10^{-2}$	PDG [55]
$\tau \rightarrow \mu\gamma$	$\sqrt{ Y_{\tau \mu} ^2 +  Y_{\mu \tau} ^2}$	$< 1.6 \times 10^{-2}$	PDG [55]
$\mu \rightarrow 3e$	$\sqrt{ Y_{\mu e} ^2 +  Y_{e\mu} ^2}$	$< 3.1 \times 10^{-5}$	SINDRUM [56]
$\tau \rightarrow 3e$	$\sqrt{ Y_{\tau e} ^2 +  Y_{e\tau} ^2}$	$< 1.2 \times 10^{-1}$	BELLE [57]
$\tau \rightarrow 3\mu$	$\sqrt{ Y_{\tau \mu} ^2 +  Y_{\mu \tau} ^2}$	$< 2.5 \times 10^{-1}$	PDG [58]
$\mu \rightarrow e$ conversion	$\sqrt{ Y_{\mu e} ^2 +  Y_{e\mu} ^2}$	$< 1.2 \times 10^{-5}$	SINDRUM II [59]
$M$ - $\bar{M}$ oscillations	$ Y_{\mu e} + Y_{e\mu}^* $	$< 7.9 \times 10^{-2}$	MACS [60]

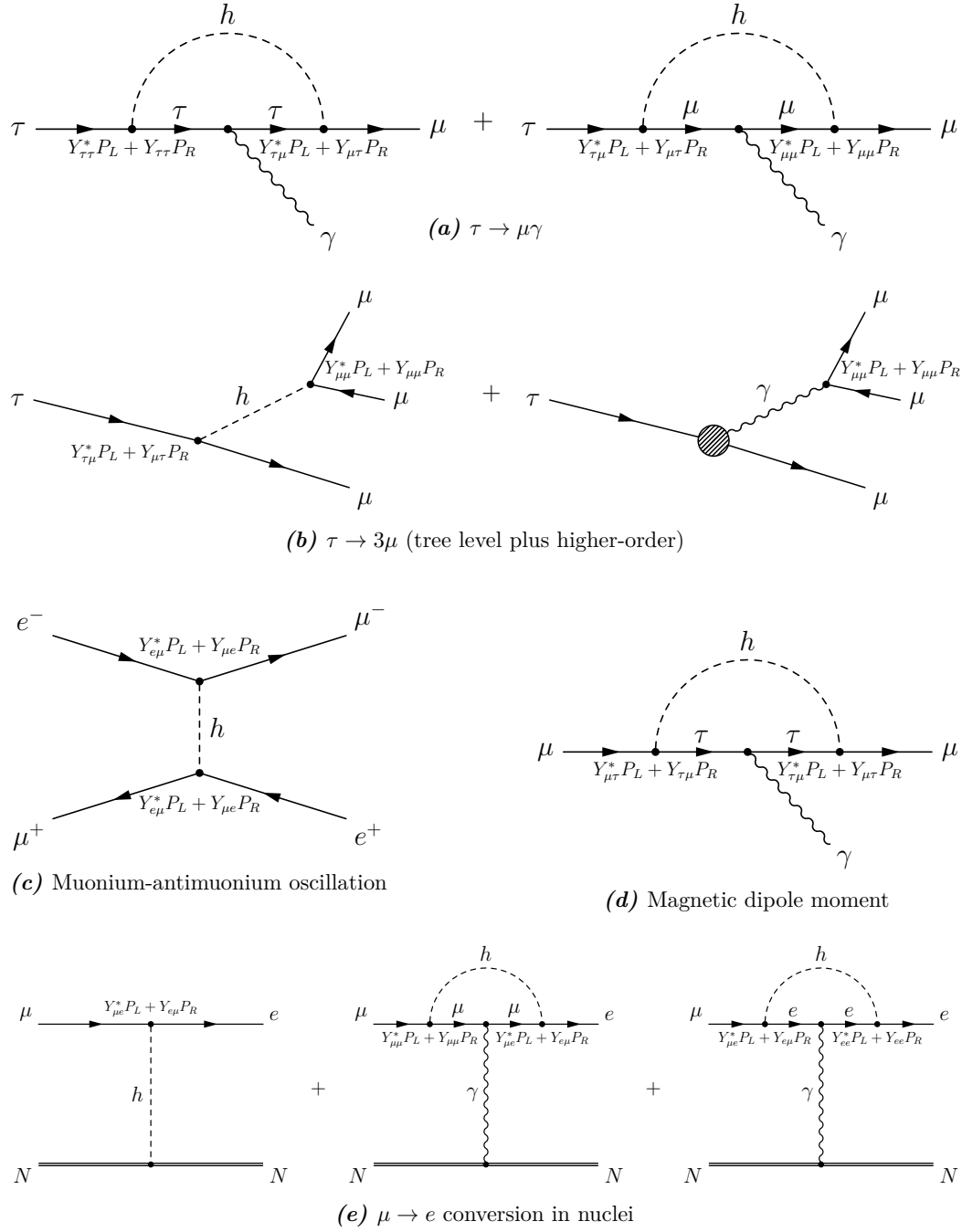


**Figure 2.10** – Various low-energy measurements constraining HCLFV, shown with the relevant Yukawa couplings.

## 2.4 The Tau Lepton

The  $\tau$  lepton is the third generation of the charged lepton family. It was discovered at the SPEAR experiment at SLAC during 1974-1977, earning Martin Perl a Nobel Prize in Physics in 1995 [61]. The properties of the  $\tau$  lepton have been studied extensively [3], establishing a rest mass of  $1776.9 \text{ MeV}/c^2$  (in contrast with  $105.6 \text{ MeV}/c^2$  of the muon, and  $0.511 \text{ MeV}/c^2$  of the electron), and a proper lifetime of 290.3 fs.

### 2.4.1 Decays of Tau Lepton

The most fascinating property of the  $\tau$  lepton is its decay channels. Its large mass is larger than that of the lightest hadron ( $\pi$ ). The  $\tau$  lepton is thus the only lepton which decays via weak charge current to both leptonic and hadronic modes, providing a unique link between the electroweak and QCD theories. In recent years, the  $\tau$  lepton has been used to validate different areas of the SM [62]: testing lepton universality via  $Z \rightarrow ll$  decays, measuring the QCD coupling at low-mass scales, determining the strange quark mass, as well as studying the hadronic contribution to the anomalous magnetic moment of the muon.

The decay channels of  $\tau$  leptons are summarized in Table 2.2, taken from [3]. More details on the of  $\tau$  lepton decay can be found in [63, 64]. At a glance, a  $\tau$  lepton is more likely to decay via hadronic channels than leptonic ones due to three possible quark colours. The ratio between lepton channels,  $\mathcal{B}_{\tau \rightarrow \mu} / \mathcal{B}_{\tau \rightarrow e} = 0.976$ , is also found to be consistent with the SM prediction due to the phase-space.

**Table 2.2** – Branching fraction of each  $\tau$  lepton decay channel, as grouped in this analysis. The conjugated mode is implied. Charged hadronic product represented by  $h^\pm$  stands for  $\pi^\pm$  or  $K^\pm$ . “neutrals” stands for  $\gamma$ 's and/or  $\pi^0$ 's.

Process	$\mathcal{B}$ [%]
$\tau^- \rightarrow \mu^- \bar{\nu}_\mu \nu_\tau$	$17.41 \pm 0.04$
$\tau^- \rightarrow e^- \bar{\nu}_e \nu_\tau$	$17.83 \pm 0.04$
$\tau^- \rightarrow h^- \nu_\tau \geq 0 \text{ neutrals}$	$50.11 \pm 0.09$
$\tau^- \rightarrow h^- h^- h^+ \nu_\tau \geq 0 \text{ neutrals}$	$14.57 \pm 0.07$
(others)	$< 0.08$

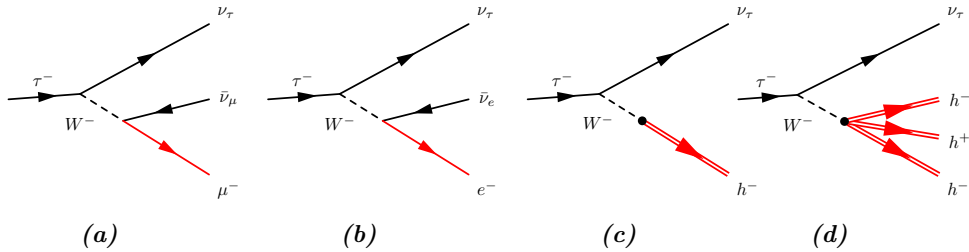


**Figure 2.11** – List of major decay channels of  $\tau$  lepton, grouped into 4 channels in this analysis. Only the charged final state particle(s) marked in red are used for the reconstruction, denoted as (a)  $\tau_\mu$  (b)  $\tau_e$  (c)  $\tau_{h1}$  (d)  $\tau_{h3}$ . The conjugated mode is implied, as well as possible neutral hadrons (omitted from figure) from the hadronic decay of the  $W$ .

### 2.4.2 Identification of High- $p_T$ Tau Lepton

The  $\tau$  lepton has a relatively short lifetime ( $c\tau = 87.03 \mu\text{m}$ ). The reconstruction can only be made from its decay products. The different processes are shown in Fig. 2.11. The  $p_T$  of  $\tau$  lepton before decay influences the kinematic of decay products. A high- $p_T$  lepton is conventionally defined as a lepton with  $p_T \gtrsim 20 \text{ GeV}/c$ , which is appropriate for LHC energies. The following characteristics and limitations should be taken into account for the  $\tau$  identification from its decay products:

**Spin correlation** In a process producing a pair of  $\tau$  leptons, their spin correlation should be taken into account (during the event simulation), as it can influence the phase-space distribution of the  $\tau$  lepton decay products [64]. The computation also depends on the spin of mother particle (*e.g.*,  $Z \rightarrow \tau\tau$  of spin 1,  $H \rightarrow \tau\tau$  of spin 0), where full information of the hard process is required for the mother of non-zero spin.

**Lifetime & Displacement** With a mean lifetime of 290.3 fs, the  $\tau$  lepton is expected to fly a measurable distance inside the detector before it decays. A minimal *flight distance* of the reconstructed candidate can be imposed, or a minimal *impact parameter* for a daughter particle, when the reconstruction of a secondary vertex is not viable.

**Isolation** The decay of a high- $p_T$   $\tau$  lepton is expected to result in a boosted, high- $p_T$ , and isolated charged track, for one prong decays. Idem, considering the combination of the 3 collimated charged tracks, for 3 prongs decays.

**Neutrino loss** With one or two neutrinos produced by its decay, the  $\tau$  lepton can only be reconstructed from partial information, from the sum of its visible decay products. The technique of *missing energy* is also used if applicable.

**Direction** The boost of decay products of high- $p_T$   $\tau$  lepton maintains some degree of collimation.

**Cross-feed** The decay of a  $\tau$  lepton in one channel may incorrectly be reconstructed as the candidate of another channel. This is referred to as “cross-feed”, for example:

- $\tau_e$ : A fake electron can come from a neutral pion decay ( $\pi^0 \rightarrow e^+e^-\gamma$ ) or from bremsstrahlung photons, with subsequent pair-production, or from a misidentified hadron. See also Fig. 2.12.
- $\tau_{h1}$ : A fake single charged-hadron can come from a partially reconstructed  $\tau_{h3}$ , a fragmentation, as well as a misidentified electron.
- $\tau_{h3}$ : Similar to  $\tau_{h1}$ , a fake 3-prongs charged hadron can come from a false combinatorics of  $\tau_{h1}, \tau_{h3}$ , a fragmentation, as well as a misidentified-electron.
- $\tau_\mu$ : A fake single muon can be produced by the decay of heavier hadron (*e.g.*,  $K \rightarrow \mu \dots$ ,  $D_s^+ \rightarrow \mu \dots$ ), or also from misidentified hadrons.

### 2.4.3 Gateway for New Physics

The  $\tau$  lepton plays a special role in many of the proposed NP models, making it a very sensitive NP probe. For example, the coupling in Higgs mechanism has a dependency on



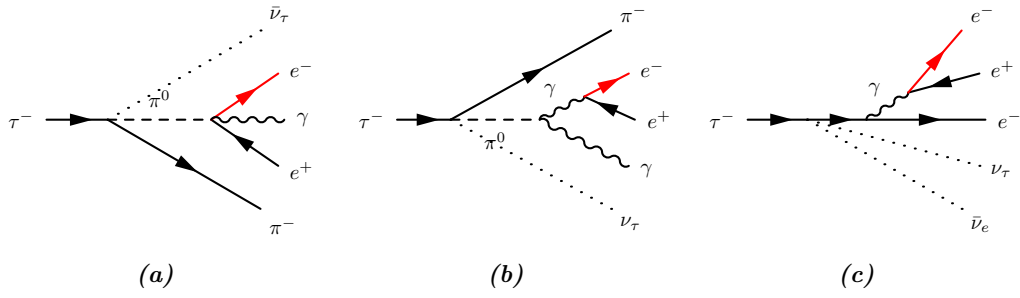


**Figure 2.12** – Some of the possibilities of cross-feed  $\tau_e$  candidate. (a) neutral pion decay in  $\tau_{h1}$ , (b) pair-production from  $\pi^0 \rightarrow \gamma\gamma$  decay, (c) bremsstrahlung to pair-production.

the particle mass, allowing a study for further understanding of the dynamics of mass generation. Recent studies in  $B$ -meson involving a decay to  $\tau$  lepton also challenge the lepton universality [65]. Finally, many HCLFV models have weak constraints in  $\tau$ -related channels, unlike the tightly-constrained  $\mu - e$  channel, and thus becomes the basis upon the work in this thesis pursuits.



# 3 Experimental Environment

## 3.1 CERN and Large Hadron Collider (LHC)

The *European Organisation for Nuclear Research* (CERN) is currently the largest collaboration in the field of experimental high energy physics. It is situated at the Franco-Swiss border near Geneva, and employs more than 2500 people, from over 70 countries and 120 different nationalities [66]. Established by a convention in 1954, the mission of CERN has four strands [67]:

- *Research*: Seeking and finding answers to questions about the universe
- *Technology*: Advancing the frontiers of technology
- *Collaborating*: Bringing nations together through science
- *Education*: Training the scientists of tomorrow

### 3.1.1 Accelerator System

The *Large Hadron Collider* (LHC) is the latest accelerator complex constructed at CERN. It is a synchrotron accelerator, providing counter-rotating hadron beams around its circular 27km ring, situated 100m underground. At nominal performance, the LHC aims to provide two proton beams of energy 6.5 TeV. This is achievable from the series of accelerators in the system which progressively boost the energy of a beam, shown in Fig. 3.1. The chain of accelerators (and its target proton energy boost) [68] are *LINAC2* (50 MeV), *Proton Synchrotron Booster* (PSB; 1.4 GeV), *Proton Synchrotron* (PS; 25 GeV), *Super Proton Synchrotron* (SPS; 450 GeV), and finally the LHC (6.5 TeV).

### 3.1.2 Experiments & Detectors

A range of experiments are housed at CERN, pursuing the question of nature ranging from the microscopic to astronomic scale. The overview of the experiments are shown in Fig. 3.2. Among these experiments, seven of them are classified as the *LHC experiments*: ATLAS, CMS, LHCb, ALICE, TOTEM, LHCf, and MoEDAL. Each detector differs in term of the design purpose, reconstruction technique, as well as the geometrical acceptance. The *pseudorapidity*,  $\eta$ , of the reconstructible particle is often used to compare the coverage

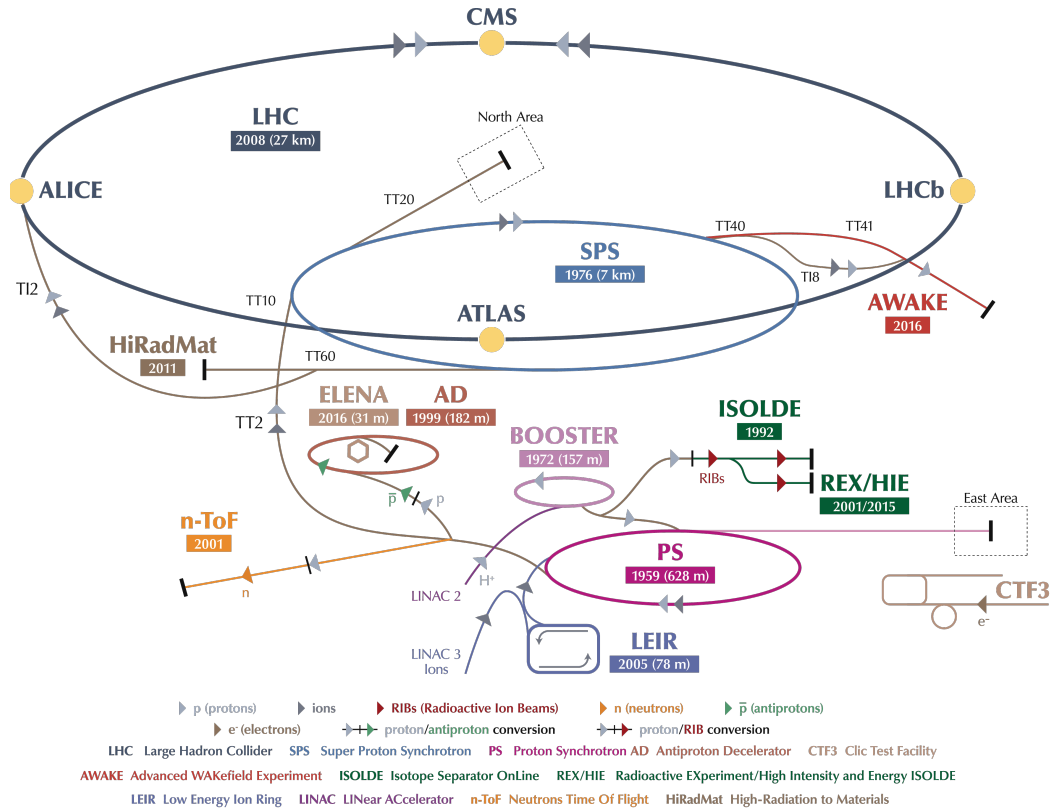


Figure 3.1 – The accelerators complex at CERN [69].

between different detectors. It is defined as

$$\eta = \frac{1}{2} \log \left( \frac{|\vec{p}| + p_z}{|\vec{p}| - p_z} \right) = -\log(\tan(\theta/2))$$

where it can be defined in terms of particle momentum  $\vec{p}$ , or the angle between its trajectory and the beam axis. The comparison of geometrical acceptances from different LHC experiments is shown in Fig. 3.3. This thesis uses the data collected from the LHCb experiment.

### 3.1. CERN and Large Hadron Collider (LHC)



Figure 3.2 – Experiments at CERN[70].

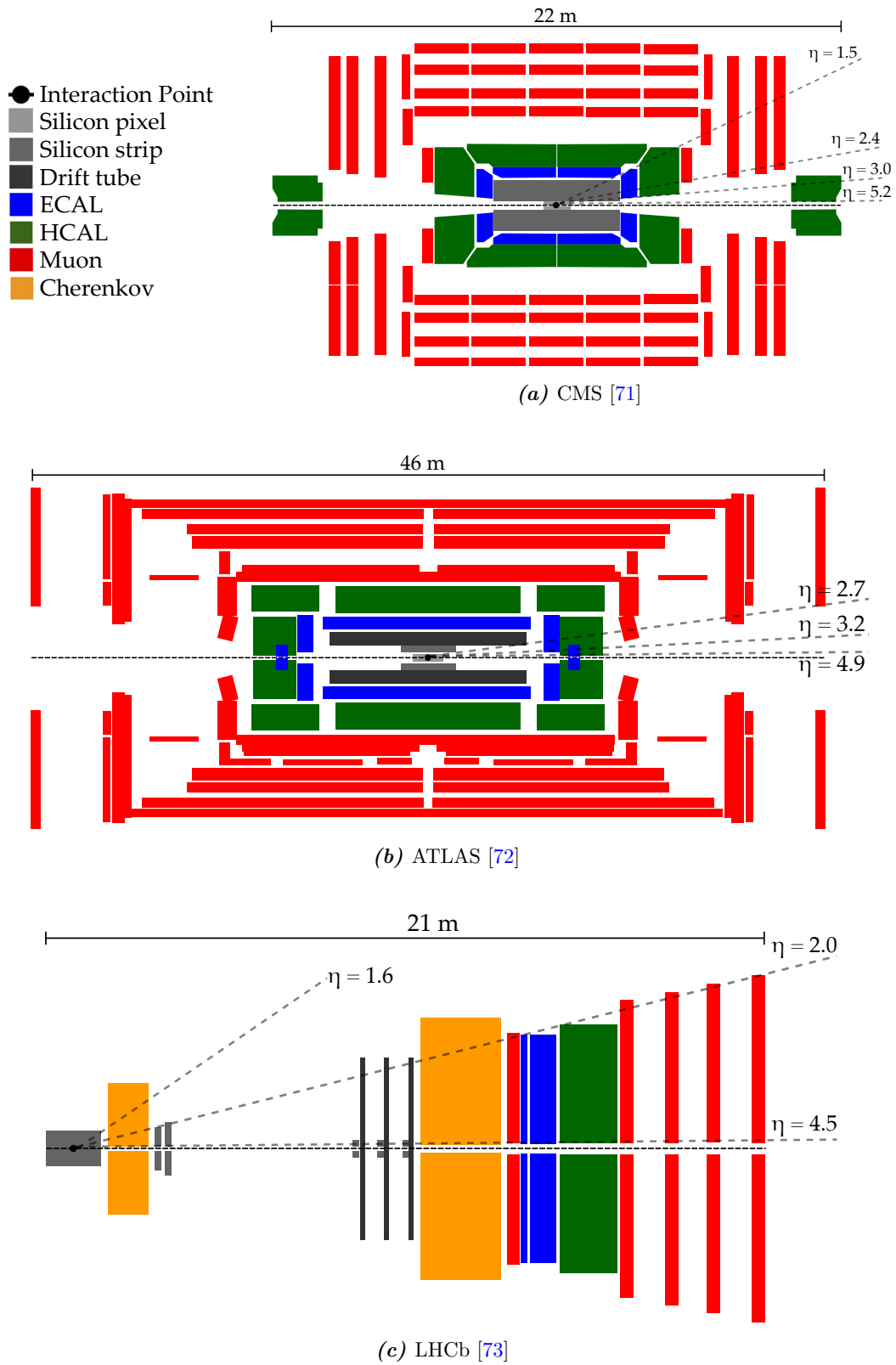


**Figure 3.3** – Comparison of the detector components and their geometrical acceptance found in the major LHC experiments. Illustration from [64].

### 3.1.3 Milestones & Roadmap

The LHC was officially inaugurated on 21 October 2008. Its operational schedule can be divided into several periods of data collection, alternating by the “shutdown” period for maintenance and upgrade. The collision between beams is mainly the proton-proton ( $pp$ ) collision, with other configuration available such as proton-lead, lead-lead, *etc.*. The *Phase 1* spans from 2008 to 2023, which consists of the following periods:

- Run 1 (2010-2013): The LHC began commissioning in 2010, delivered beams for  $pp$  collision at the centre-of-mass energy of  $\sqrt{s} = 7$  TeV. In the following years its limit were explored and pushed for larger performance, resulting in  $pp$  centre-of-mass energy increased to 8 TeV in the year 2012 [74]. The summary of delivered integrated luminosity is shown in Fig. 3.4.

Anecdotally, the commissioning was originally planned to start in 2008. However, the infamous magnet quench incident occurred on 19 September 2008 delayed the operation schedule. A thorough examination and maintenance of the system took place for a year before the commissioning started again in late 2009 [75].

- Run 2 (2015-2018): The LHC in this period delivered beams for  $pp$  collision at  $\sqrt{s} = 13$  TeV, pushing toward its nominal design of 14 TeV.
- Run 3 (2020-2023): The LHC is planned to deliver beams for  $pp$  collision at  $\sqrt{s} = 14$  TeV.

The subsequent *Phase 2* of the LHC, dubbed *High-Luminosity Large Hadron Collider* (HL-LHC), will spans approximately from 2025 until 2035. It will provide an upgrade for a larger number of collisions, allowing the better search sensitivity beyond the design performance of LHC [76].

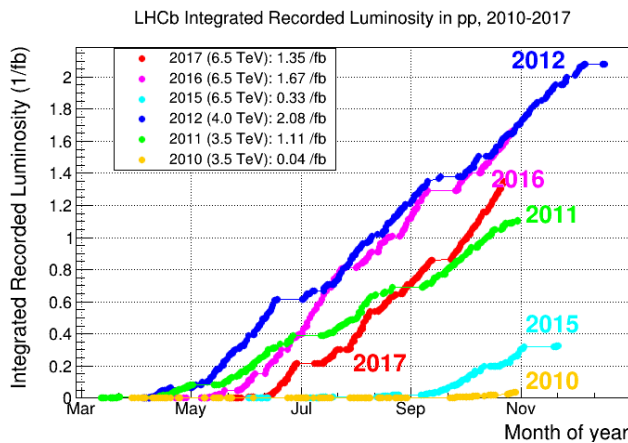


**Figure 3.4** – Integrated luminosity delivered by year collected at the LHCb. One inverse femtobarn ( $\text{fb}^{-1}$ ) is roughly equivalent to 80 million million collisions [77].



### 3.2 The LHCb detector

The LHCb detector is a single-arm spectrometer optimized for the study of  $B$ -physics (interaction involving hadron with  $b$ -quark), which can be considered as a gateway to different physics programmes, such as CP violation, SM rare decay measurement, exotic hadrons, and beyond standard model searches. The focus on forward region ( $2 < \eta < 5$ ) stems from the kinematics of  $b\bar{b}$  production at large centre-of-mass energy, which tends to be highly boosted and results in the decay products along the beam axis.

A distinctive feature at LHCb compared to general-purpose detectors (CMS, ATLAS) is the choice of low *pile-up*, or the average number of inelastic interactions in visible events, achieved by a *luminosity levelling* procedure [78]. The typical value of pile-up at LHCb is  $\sim 2$  (depending on year and run condition), compared to  $\sim 21$  for CMS[79] and ATLAS[80]. The lower number of pile-up may have a disadvantage of having less luminosity being recorded, but several advantages are achieved:

- By having small number of interaction, the event reconstruction has a cleaner topology, and the physics analysis becomes more robust, especially for the heavy-flavor decay.
- More efficient computational performance, as there is less occupancy in the detector.
- The detector ageing is more prolonged, as the irradiation is reduced.

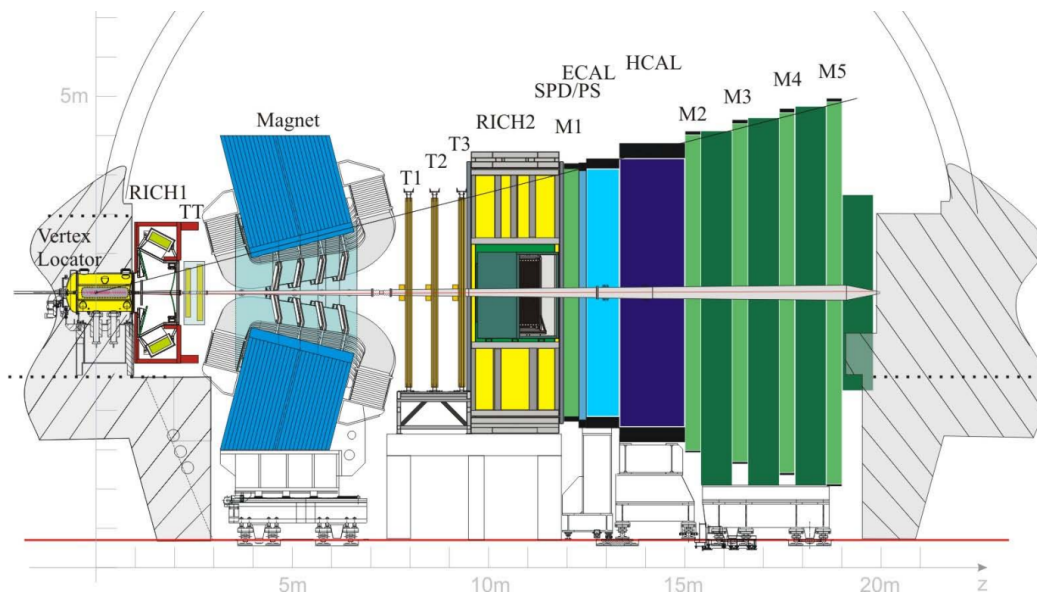


Figure 3.5 – The LHCb detector [81].

The subdetectors of LHCb are shown in Fig. 3.5. They are listed in the following section ordered along the beamline, from the innermost volume of the interaction point outward. This axis is referred as the  $z$ -axis in the coordinate system used in LHCb. The  $y$ -axis is vertical pointing upward, and the  $x$ -axis is horizontal pointing from the interaction point toward the centre of LHC ring. Most subdetectors of LHCb are horizontally-separable into 2 halves, allowing the assembly, maintenance, and access to the beam pipe. The full detector description can be found in [73], and the detector performance in [82].



### 3.2.1 Vertex Locator (VELO)

The VELO is a silicon-strip detector surrounding the interaction region. It aims to provide an accurate track position measurement used for the determination of primary and secondary interaction vertex positions. This is important for  $b,c$ -physics program in LHCb where it relies on the distinctive displaced vertices in the forward region.

The VELO is composed of a series of 42 semi-circular silicon sensors placed along the beam direction, as shown in Fig. 3.6. The two halves together occupy the cylindrical volume of diameter 8.4 cm and length 106.5 cm around the interaction point, which covers the geometrical acceptance of  $1.6 < \eta < 4.9$ . The close VELO aperture is smaller than the injected beam width, so the two halves are retracted away from the beamline outside the data acquisition phase in order to protect the detector from the radiation damage. In each module, the 2 semi-circular halves are responsible for the measurement of the radial and azimuthal coordinates  $(r, \phi)$  of the hits. Together with the  $z$ -coordinate of each module, the complete three-dimensional coordinates can be reconstructed. On the upstream of interaction region, 4 stations are used as a veto module rejecting an event with high pileup.

In terms of performance, the VELO has a signal-to-noise ratio of about 20, and a best hit resolution of  $4 \mu\text{m}$  at the optimal track angle. The impact parameter (IP) and decay time, extensively used for the  $\tau$  lepton identification in this thesis, is crucial upon the precision of the VELO. The impact parameter resolution can be expressed as,

$$\delta_{\text{IP}} = \delta_{\text{HIT}} \oplus \frac{\delta_{\text{MSE}}}{p_{\text{T}}}$$

where the factors governing the resolution expression can be seen: the first contribution is due to the detector resolution, and the second to multiple scattering, with the dependency on the transverse momentum of the particle. The values of  $\delta_{\text{HIT}} = 11.6 \text{ mm}$  and  $\delta_{\text{MSE}} = 23.4 \text{ mm GeV}$  are found from the study of 2012 data [83], as shown in Fig. 3.7a. The resolution is found to be underestimated in the simulation, due to the non-uniform material distribution in the VELO. In the vicinity of  $\phi = \pm\pi/2$ , where the two halves overlap, the increase in the IP resolution can also be seen in Fig. 3.7b.

### 3.2.2 Ring Imaging Cherenkov Detectors (RICH)

The RICH is a photodetector that measures the Cherenkov radiation, emitted from the charged particle passes through a medium at a velocity greater than the phase velocity of light in that medium. Given the angle  $\theta$  between the velocity vector of the particle and the radiated light, the velocity of the particle in natural units,  $\beta$ , can be obtained from the relation  $\beta n = 1/\cos\theta$ , where  $n$  is the refractive index of the chosen medium.

The RICH system is separated into 2 subdetectors; RICH1 is situated after the VELO, using aerogel and  $\text{C}_4\text{F}_{10}$  as a medium. It's optimized for the separation of pions and kaons of momentum from 1 to 60 GeV/ $c$ , and within the pseudorapidity range of  $2.1 < \eta < 4.4$ . The RICH2 is situated after the OT, optimized for the separation of pions and kaons at higher momentum from 15 GeV/ $c$  to beyond 100 GeV/ $c$ . It uses  $\text{CF}_4$  as the medium, and covers the pseudorapidity range of [3.0, 4.9].

### Chapter 3. Experimental Environment

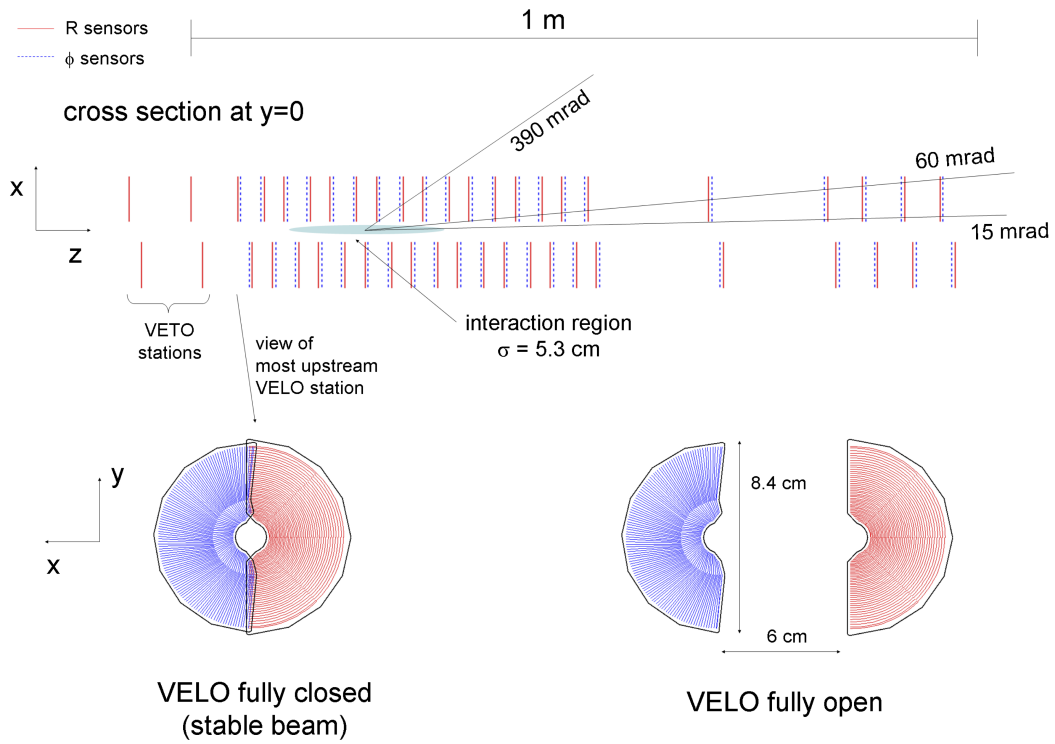


Figure 3.6 – Schematic of the VELO module and sensors [73].

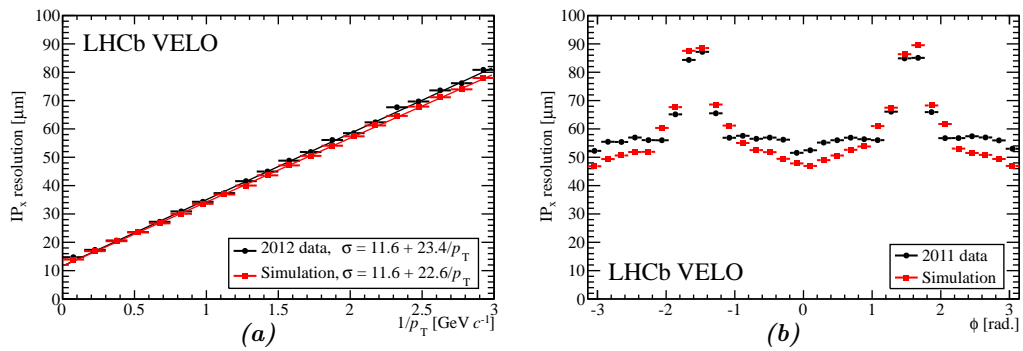


Figure 3.7 – VELO impact parameter resolution dependencies [83].

### 3.2.3 Tracker Turicensis (TT)

The TT is a 4-layer silicon-microstrips tracking station aimed to provide the momentum information of the traversing charged particle. It is located after the RICH1, housed in a tight, 5°C-cooled, thermally and electrically insulated detector volume. It has an active surface area of about 8.4 m<sup>2</sup>, which covers the pseudorapidity range of  $2 < \eta < 4.9$ . Each layer contains the strip modules above and below the  $xz$ -plane, with the second and third layers rotated over a smaller stereo angle, giving an orientation of  $0^\circ, +5^\circ, -5^\circ, 0^\circ$  with respect to the  $yz$ -plane, as shown in Fig. 3.8.

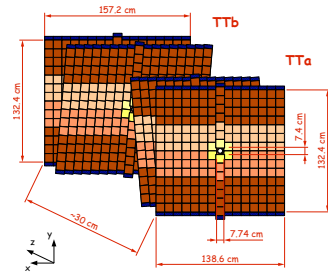


Figure 3.8 – Schematic of 4-layer TT [73].

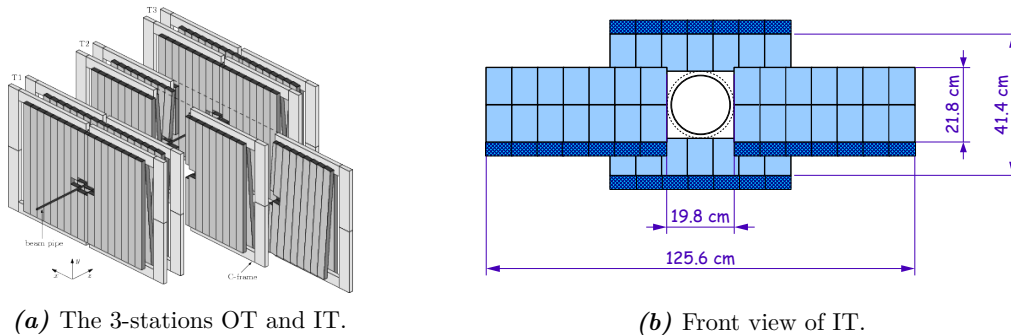
### 3.2.4 Magnet

A warm saddle-shaped dipole magnet is placed after the TT, providing the field which bends the particle trajectory on the  $xz$ -plane, enabling the measurement of particle momentum from the track curvature. The field profile is shown in Fig. 3.13, which provides an integrated magnetic field of 4 Tm for track of 10 m length. Two polarities of the magnet configuration (*up*, *down*) are used in LHCb on approximately the same amount of data during the acquisition, in order to allow the study that depend on the particle electric charge.

### 3.2.5 Inner Tracker (IT) and Outer Tracker (OT)

The IT and OT are pairs of tracking subdetectors, situated at 3 stations marked T1, T2, T3 in the Fig. 3.5. At each station, the IT is built close to the beam, optimized for the large occupancy of charged particles passing through, whereas the OT is built surrounding the IT, optimized for the full LHCb geometrical acceptance. The IT and OT at each station also follows the 4-layer structure as TT, where the middle layers are rotated in stereo angle to form  $(0^\circ, +5^\circ, -5^\circ, 0^\circ)$  structure, as shown in Fig. 3.9.

The IT is a silicon-microstrips tracking of the same technology as TT. Its geometrical acceptance is  $3.4 < \eta < 5$  in the  $xz$ -plane, and  $4.5 < \eta < 4.9$  in the  $yz$ -plane, designed to maximize the resolution in the magnetic bending plane. The OT is a drift-time gaseous-strawtube detector, composed of 70% Argon and 30% CO<sub>2</sub>, allowing the drift time of less than 50 ns. It complements the geometrical acceptance of the IT, providing  $1.8 < \eta < 3.4$  in the  $xz$ -plane, and  $2 < \eta < 4.5$  in the  $yz$ -plane.



(a) The 3-stations OT and IT.

(b) Front view of IT.

Figure 3.9 – Overview of the OT and IT [73].

### 3.2.6 Scintillating Pad Detector (SPD) and Preshower Calorimeter (PS)

The SPD and PS are the scintillator subdetectors designed to provide fast particle identification as well as rejection of background, notably the inelastic  $pp$  collision. Both subdetectors rely on the emitted radiation when a particle traverses the scintillator material being transmitted to the multi-anode photomultiplier tubes via wavelength-shifting fibres. The SPD covers the geometrical acceptance of  $2.1 < \eta < 4.4$ . Its calorimeter surface is 7.6 m wide and 6.2 m high. Four quadrants can be identified, each with 3 lateral segmentations of increasing cell size as further away from the beamline, as shown in Fig. 3.10a. The segmentation is needed as the hit density can vary up to 2 magnitudes over the calorimeter surface. The PS is situated behind the SPD, with thin lead converter in-between. The PS is also built with the same structure as the SPD, providing one-to-one correspondence between cells for optimal reconstruction.

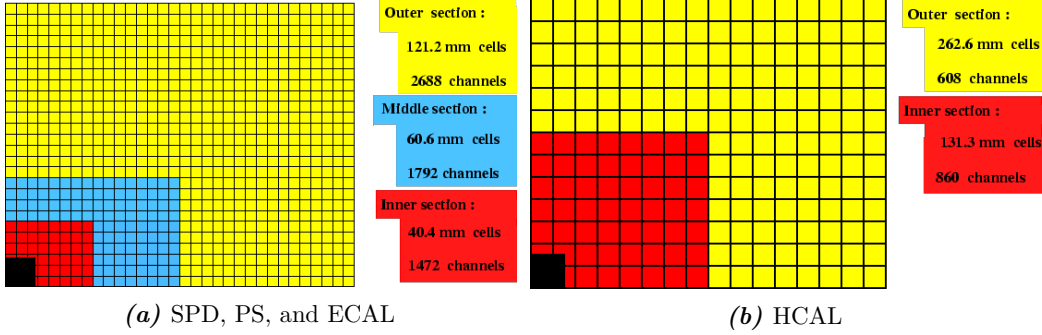


Figure 3.10 – Lateral segmentation of the calorimeters, shown only single quadrant [73].

### 3.2.7 Electromagnetic Calorimeter (ECAL) and Hadronic Calorimeter (HCAL)

The ECAL and HCAL are calorimeters of Shashlik technology, where their layers alternate between scintillating tiles and lead absorbers. They are situated after the SPD/PS, providing the measurement of cluster position and the transverse energy deposited by a particle, which are electrons and photons for ECAL, and hadrons (*e.g.*, protons, neutrons, pions) for HCAL. The ECAL has the same lateral layout and geometrical acceptance as SPD/PS (Fig. 3.10a), whereas the HCAL has an acceptance of  $2.1 < \eta < 4.2$  (Fig. 3.10b). The ECAL and HCAL also differ in the orientation of alternating layers, which is along the  $z$ -axis for ECAL and the  $x$ -axis for HCAL.

The resolution of the energy measurement from both calorimeters can be parameterized as

$$\frac{\sigma_E}{E} = \frac{\sigma_{\text{samp}}}{\sqrt{E}} \oplus \sigma_{\text{calib}} \oplus \frac{\sigma_{\text{noise}}}{E}$$

where  $\sigma_{\text{samp}}$  is due to sampling fluctuation,  $\sigma_{\text{calib}}$  is from calibration uncertainty, and  $\sigma_{\text{noise}}$  is the noise term. The data-driven study found  $\sigma_{\text{samp}} = 9.5 \times 10^{-2} \text{ GeV}^{1/2}$ ,  $\sigma_{\text{calib}} = 0.83\%$  for ECAL [84], and  $\sigma_{\text{samp}} = 0.69 \text{ GeV}^{1/2}$ ,  $\sigma_{\text{calib}} = 9\%$  for HCAL [73], with the noise term negligible.

### 3.2.8 Muon System

The muon system performs the measurement of muon trajectory. It is separated into 5 stations (M1-M5) and situated behind the calorimeters, except the first station (M1) is situated in front, for the precise position measurement before the multiple scattering in the calorimeters. The layout is shown in Fig. 3.11. To cope with a large hit density, the design of M1 station is based on a triple-gas electron multiplier, whereas the other stations are multi-wire proportional chamber, interleaved with 80 cm iron absorber between each station to ensure that only muons pass through to the stations. The muon system covers the acceptance of  $2.0 < \eta < 4.6$ , allowing the detection of muon of  $p > 3 \text{ GeV}/c$  and  $p_T > 0.8 \text{ GeV}/c$ .

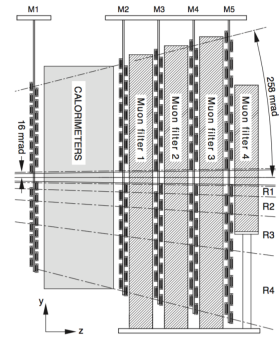


Figure 3.11 – Sideview of muon stations [73].

### 3.2.9 High Rapidity Shower Counters for LHCb (HERSCHEL)

The HERSCHEL is the system of forward shower counters, providing the measurement of particles at large pseudorapidity region  $5 < \eta < 8$ . It is based on plastic scintillation counters, with light guides connected to the photomultipliers. The system consists of 5 stations, with 2 stations situated in the forward region behind the LHCb detector, and 3 stations in the backward region, as shown in Fig. 3.12. Its installation finished in December 2014, making it operational for Run 2. HERSCHEL is largely motivated by diffractive physics, especially the central exclusive production (CEP) programme at LHCb, where it is susceptible to a large inelastic background in the high-pseudorapidity region, [85].

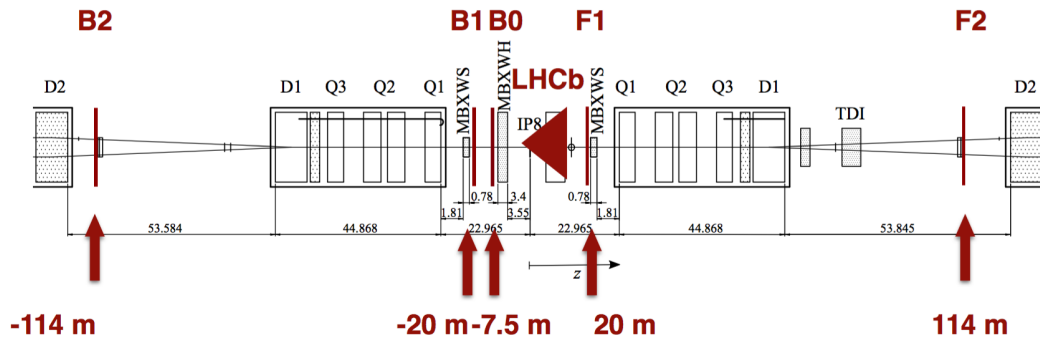


Figure 3.12 – Schematic of HERSCHEL stations around the interaction point at LHCb [85].

### 3.3 Event Reconstruction

For each collision, the LHCb event reconstruction framework utilizes the information from each subdetector to provide a description of the event. This includes the number of particles, their types, trajectories (tracks), charges, energies, and momentum information, as well as vertices composed of parent and children particles. The algorithms in the event reconstruction framework are generally classified into 2 classes:

- *Online*, where a fast description of the event is made (nearly) synchronously with the data acquisition, which is crucial for the trigger system.
- *Offline*, where the detector-wide information are used to provide an accurate description of the event. It is processed asynchronously from the data acquisition, usually on the computing farm, as it requires more computation resources. The offline reconstruction can be improved over time as the reconstruction algorithms are being more refined.

The recent upgrade on reconstruction framework continuously bridges the advantages of both classes, making the *online* reconstruction as accurate as the *offline* version whilst respecting the computation time. This allows the *online* reconstructed event to be fully usable for the physics analysis, and greatly reduces the computation resources in the intermediate stages.

The components of event reconstruction will be discussed in the following sections.

#### 3.3.1 Tracking

The tracking provides the information of trajectory for each particles in the event. It is commonly referred to only the tracks from charged particles, as neutral particles do not directly leave tracks in the tracker subdetectors, so their trajectories are available from calorimeter clusters only. The reconstructed tracks are classified into different types, depending on which subdetector(s) they used information from, as shown in Fig. 3.13:

**VELO** The VELO track is produced where the magnetic field is negligible, so it bears no momentum information. As the VELO also covers the central pseudorapidity region ( $-4.5 < \eta < 4.5$ ), the forward as well as backward tracks can be reconstructed, which is mainly utilized for the vertex reconstruction.

**Upstream = VELO + TT** The upstream track indicates the track of low momentum, which is deflected by the magnetic field before reaching other tracking stations.

**Downstream = TT + (IT/OT)** The downstream track indicates the track from long-lived parent particle decaying outside the VELO.

**Long = VELO + (IT/OT)** The Long track is the most precise and commonly used track, using the information from VELO and T track, and optionally from TT track.

**MuonTT = TT + Muon** The MuonTT track uses only the hits from TT and Muon subdetectors. As this is complementary to the basis of Long track, it can be used to provide a data-driven study of muon tracking efficiency.

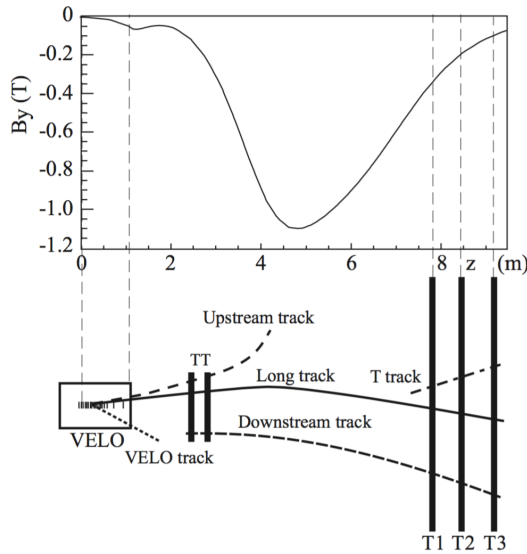


**Figure 3.13** – Different track types classified in the LHCb event reconstruction with the sub-detectors involved, shown with the corresponding  $y$ -component magnetic field long the  $z$ -axis of the LHCb detector. The momentum information can also be determined for the track types that pass through the magnetic field, where the curvature radius is inversely proportional to its momentum [73].

### 3.3.2 Calorimetry

The calorimetry provides the information of energy for each particle in the event, mainly utilizing the information from SPD, PS, ECAL, and HCAL. For each reconstructed track, the trajectory can be extrapolated through the clusters in the calorimeters, where the sum of energies from those clusters can be associated to the track. Inside the reconstruction framework, this reconstructed track with associated calorimeter information is referred as **ProtoParticle**.

Once the particle identification is completed (see the next section), an additional stage of energy recovery from bremsstrahlung is performed which is especially important for electrons. This is achieved by collecting photon candidates with their trajectories compatible with the parent electron, and correct the track momentum and energy correspondingly, as illustrated in Fig. 3.14. The recovery procedure is imperfect in practice, resulting often in the reconstructed electron of less energy than its truth value.

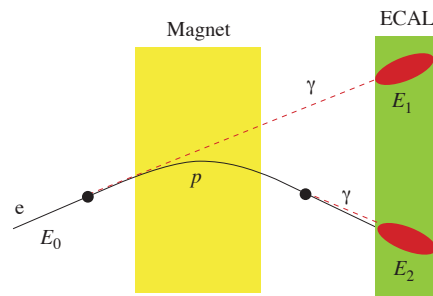


**Figure 3.14** – Schematic illustration of bremsstrahlung correction [73].

### 3.3.3 Particle Identification (PID)

The particle identification determines the types of particles in each event using the information (or lack thereof) from subdetectors, schematically shown in Fig. 3.15a. In the reconstruction framework, the particles are classified as either *Basic particle* or *Intermediate particle*. The intermediate particles (e.g.,  $J/\psi$ ,  $D^0$ ) are composed of the basic particles, or other intermediate particles in a recursive way. For each basic particle, the outline of identification strategies is the following:

### Chapter 3. Experimental Environment

**Muons** The track is identified as muon if it passes minimal a number of muon stations (as a function of track momentum). As the muon deposits no energy in the ECAL and HCAL, it provides a very clean reconstruction signature and becomes a basis for mainstream analyses in LHCb.

**Electrons** The electron is expected to deposit energy in PRS and ECAL clusters. Some charged hadron can fake as an electron, in which the information from PRS, RICH and HCAL can be used to suppress the fake electron.

**Photons** The photon can be identified as ECAL clusters with no associated track, as well as no cluster in the SPD.

**Neutral pions** The neutral pion almost always decays to a pair of photons, where the same identification strategy as photon can be used. The neutral pion is classified in the reconstruction framework as *merged* or *resolved*, whether the pair of photons deposit the energy onto ECAL as single or multiple clusters. This poses a potential case for fake photons, and vice versa.

**Hadrons** The hadrons are mostly identifiable with information from HCAL, where a considerable amount of energy deposit is expected, and from RICH, where different hadrons can be distinguished via their Cherenkov radiation profile, as shown in Fig. 3.15b.

Different identification algorithms relies on the strategies outlined above, in such a way that different analyses may employ different techniques, such as using the detector responses directly (hits, energies), the pattern recognition likelihood (DLL), or the neural-network recognition (ProbNN).

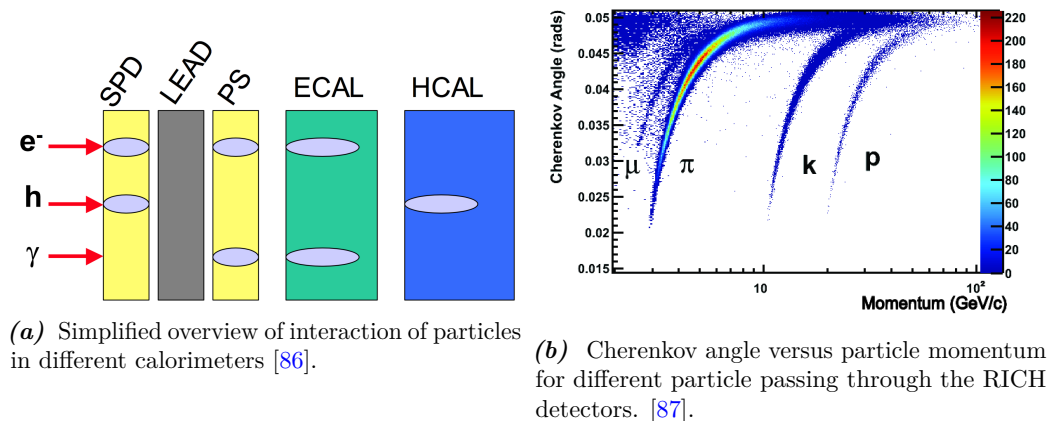


Figure 3.15 – LHCb calorimetry responses.



### 3.3.4 Triggers

The trigger system is essential to data acquisition at LHCb, providing a fast decision of which event to be stored. It aims to maximize the number of events with physics processes of interest while minimizing computation and storage resources. The reconstructed candidates and detector responses of the event passing the trigger system are written to the storage, allowing further processing at later date for physics (or "Offline") analysis.

In 2012, the LHC delivered beams with a bunch crossing rate of 40 MHz, leading to approximately 10 MHz of visible  $pp$  interaction at LHCb. In order to satisfy the persistency requirement at 5 kHz, the LHCb trigger system is divided into 3 levels, scaling in processing time and reconstruction robustness: L0, HLT1, HLT2. The corresponding scheme is shown in Fig. 3.16.

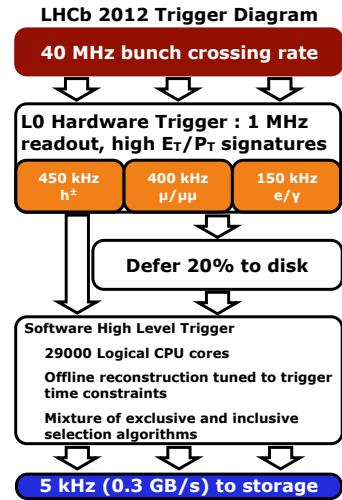


Figure 3.16 – LHCb trigger scheme in 2012 [88].

**L0 (Level 0)** The L0 trigger aims to reduce the readout rate to 1 MHz. It relies on the VELO rejection of events with large number of pileup interaction, on the SPD rejection of events with large number of track multiplicities, and on calorimeters and muon system requiring highest- $p_T, E_T$  candidate in the event to be above the given threshold, as most discardable collisions fail to satisfy these requirements.

**HLT1 (High Level Trigger 1)** The HLT1 aims to further reduce the readout rate to approximately 50 kHz. Given the CPU restriction, the event reconstruction at this level contains partially-reconstructed tracks and the primary vertex information from tracking subdetectors.

**HLT2 (High Level Trigger 2)** The HLT2 aims to finally reduce the readout rate to meet the persistency rate at approximately 5 kHz. The full pattern recognition for all tracks in the event is performed, as well as the reconstruction of secondary vertices, allowing specific decay channels to be selected at this level. The HLT2 is also designed to run asynchronously to the data acquisition, deferring the event reconstruction to the CPU farm during the no-collision window.

### 3.3.5 Luminosity determination

The accurate determination of colliding-beam luminosity is essential for the precise cross-section measurements. For a proton-proton colliding bunch pair, the instantaneous luminosity can be written as [64],

$$L = \frac{\mu N_b f}{\sigma_{\text{inelastic}}}$$

where  $\mu$  is the average number of visible interactions per bunch crossing,  $N_b$  is the number of proton bunches,  $f$  is the revolution frequency, and  $\sigma_{\text{inelastic}}$  is the proton-proton inelastic cross-section.

In order to determine  $L$ , only the values of  $\mu$ , and  $\sigma_{\text{inelastic}}$  are unknown and need to be measured. The  $\mu$  can be determined from observables that are proportional to the interaction rate, which must be measured in every bunch crossing, whereas  $\sigma_{\text{inelastic}}$  is only needed to be measured once. An extensive detail on the luminosity determination procedure can be found in [89]. Using two different techniques to determine  $\sigma_{\text{inelastic}}$ , (Van-de-meer scan, and Beam-gas imaging), the luminosity is determined with a precision of 1.16% for the proton-proton collision at 8 TeV, representing the most precise measurement at a bunched-beam hadron collider.

### 3.4 Analysis Framework

The analysis framework of LHCb is built on top of GAUDI [90] developed between collaborations at CERN. The software stack is organized into a hierarchy of projects as shown in Fig. 3.17, where each project is responsible for different stages of the analysis workflow. The software are written in C++, and interfaced in PYTHON for the run-time configuration. The BRUNEL project [91] is responsible for the offline reconstruction, both from actual collision data and from Monte Carlo (MC) simulation. The user analysis packages are organized under the DAVINCI project [92]. The generation of MC sample relies on the GAUSS project [93], with the BOOLE project [94] responsible for the subdetector responses, and the MOORE project [95] for the emulation of the trigger response.

The data collected at the pit are stored on magnetic tapes (using  $\sim 13.3$  PB in 2012 [96]). Due to the limited accessible bandwidth, only a subset of the data are preselected and available for the user analysis via the STRIPPING framework [97]. The *Worldwide LHC Computing Grid* (WLCG) [98] provides an infrastructure of computing and storage resources. They are organized into 4 *tiers* of different services, shown in Fig. 3.18. The DIRAC framework [99] provides a management layer of data distributed over the WLCG, and GANGA software [100] provides a user interface for analysis job submission to different backends, including the WLCG.

The LHCb analysis framework is being constantly developed in order to improve the performance and robustness alongside the computing community at the time, as well as to prepare for the upcoming physics Run-II and Run-III. The *Task Force on Core Software (TFCS)* [101] was formed to tackle the issues, including the migration of framework version control system from SVN to GIT, the modernization of old C++0x to C++14, the scaling improvement of computing model (“functional framework”). The continuous development means users have to be constantly aware of the current technology and its usages, as well as encourages the contribution to the development from interested users<sup>1</sup>.

### 3.5 The LHCb Working Groups

The LHCb collaboration consists of 1160 personnel (number as of 15 July, 2017 [102]), relatively a small part of CERN. At the top level, the *Collaboration Board* is composed of one representative from each institute and the LHCb management team [103]. From the physics analysis point of view, the collaboration can be branched into different *Physics*

---

<sup>1</sup>This is organized as *hackathon* several times in a year, where the author often participates.

### 3.5. The LHCb Working Groups

*analysis working groups* (PWGs) as listed in Table 3.1 where different physics programs can be specialized and pursued. The *Physics performance working groups* (PPGs) are organized orthogonal to the PWGs, in order to effectively communicate the operational performance to each PWGs and vice-versa<sup>2</sup>. Lastly, the *Technical board* oversees the detector design, construction, budgets, and schedule.

**Table 3.1** – List of the working groups as organized at the LHCb collaboration.

Physics analysis working groups (PWGs)	Physics performance working group (PPGs)
<i>B</i> -decays to Charmonia (B2CC)	Tracking, Alignment & Vertexing
<i>B</i> -decays to Open Charm (B2OC)	Flavour Tagging
<i>B</i> -hadrons and Quarkonia (BandQ)	Luminosity
Charmless <i>b</i> -hadron decays (BnoC)	PID and Calorimeter Objects
Charm Physics (Charm)	Simulation
Ions and fixed target (IFT)	Statistics
QCD, Electroweak & Exotica (QEE)	Stripping
Rare Decays (RD)	
Semileptonic <i>B</i> -decays (SL)	

<sup>2</sup>The author joined QEE working group, and held the position of Stripping liaison during the period of this thesis.

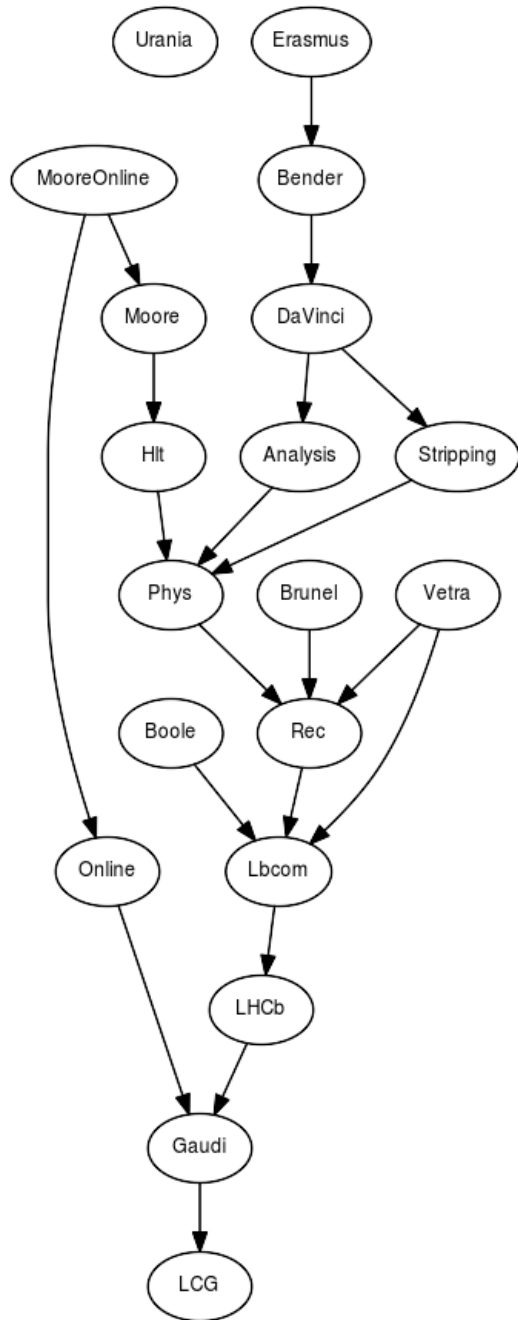


Figure 3.17 – Projects and their dependencies in the LHCb framework.

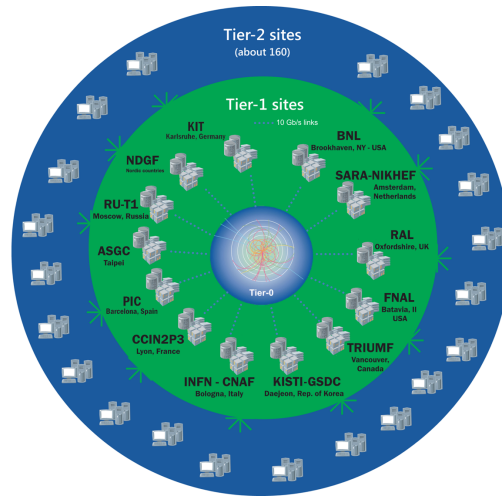
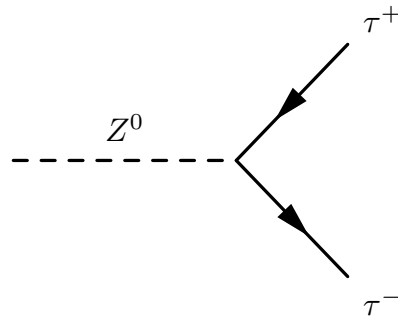


Figure 3.18 – Layers of WLCG Tier-0, Tier-1, and Tier-2 sites as of June 2014 [104].

## Part II

# Measurement of the Inclusive $Z \rightarrow \tau\tau$ Production Cross-section





## 4 $Z \rightarrow \tau\tau$ at LHCb

The measurement of production cross-section  $Z$  boson decaying to  $\tau$ -leptons provides important tests of the SM. It also lays the foundation of BSM searches with  $\tau$ -lepton signatures. Measurements at LHC using  $pp$  collision at  $\sqrt{s}=7$  TeV has been performed by the ATLAS [105], CMS [106], and LHCb [107] experiments. All experiments found a good agreement between measured cross-sections and their theoretical predictions, with LHCb yields the most precise measurement.

In this section, the measurement of the production cross-section of  $Z$  boson in a fiducial phase-space volume of LHCb (called *fiducial region* in the following Section 5.1) is presented, using a decay mode to two  $\tau$  leptons. The analysis procedures are refined from the previous analysis [107] performed in 2011, and completes the trilogy of 2012  $Z \rightarrow ll$  study at LHCb ( $Z \rightarrow \mu\mu$  [108] and  $Z \rightarrow ee$  [109]). This measurement is also an important validation of the  $\tau$  lepton identification and reconstruction at LHCb.

The  $\tau$  lepton decays to 4 major channels as discussed in Section 2.4.1. From the 4 decay channels, the chosen di-tau ( $\tau^+\tau^-$ ) final states are grouped into 10 mutually-exclusive channels, listed in Table 4.1. Among these channels, the pure-hadronic channels ( $\tau_{h1}\tau_{h1}$ ,  $\tau_{h1}\tau_{h3}$ ,  $\tau_{h3}\tau_{h3}$ ) are not included in this analysis due to the high QCD background and the inherent limitation of LHCb trigger specification during Run-I. The  $Z \rightarrow \tau\tau$  candidates are thus reconstructed in the following 7 di-tau channels,  $\tau_\mu\tau_\mu$ ,  $\tau_\mu\tau_{h1}$ ,  $\tau_\mu\tau_{h3}$ ,  $\tau_\mu\tau_e$ ,  $\tau_e\tau_e$ ,  $\tau_e\tau_{h1}$ ,  $\tau_e\tau_{h3}$ , which cover 58% of the total branching fraction. The selection of  $Z \rightarrow \tau\tau$  candidates is discussed in Chapter 5.

**Table 4.1** – Branching fraction of each di-tau decay channel, as considered in this analysis.

$\mathcal{B}$ [%]	$\tau_\mu$	$\tau_e$	$\tau_{h1}$	$\tau_{h3}$
$\tau_\mu$	$3.03 \pm 0.01$	$6.21 \pm 0.02$	$17.45 \pm 0.05$	$5.07 \pm 0.03$
$\tau_e$	—	$3.18 \pm 0.01$	$17.87 \pm 0.05$	$5.20 \pm 0.03$
$\tau_{h1}$	—	—	$25.11 \pm 0.09$	$14.60 \pm 0.08$
$\tau_{h3}$	—	—	—	$2.12 \pm 0.02$

## 4.1 Background Processes

The following background processes are expected in the  $Z \rightarrow \tau\tau$  analysis. Considering a single  $\tau$  lepton, the  $\tau_e, \tau_\mu$  processes can be faked by the leptonic decays of electroweak bosons  $W$ , and  $Z$ , as well as by semileptonic decays of heavy flavors. In the case of hadronically-decaying  $\tau$  ( $\tau_{h1}, \tau_{h3}$ ), QCD or electroweak process with jets of hadrons are the main sources of background. Moreover, the particle misidentification can also contribute to the background, as well as cross-feeds discussed in Section 2.4.2. The list of background processes are illustrated with Feynman diagrams in Fig. 4.1. The estimate of number of background candidates for each process will be treated in Chapter 6.

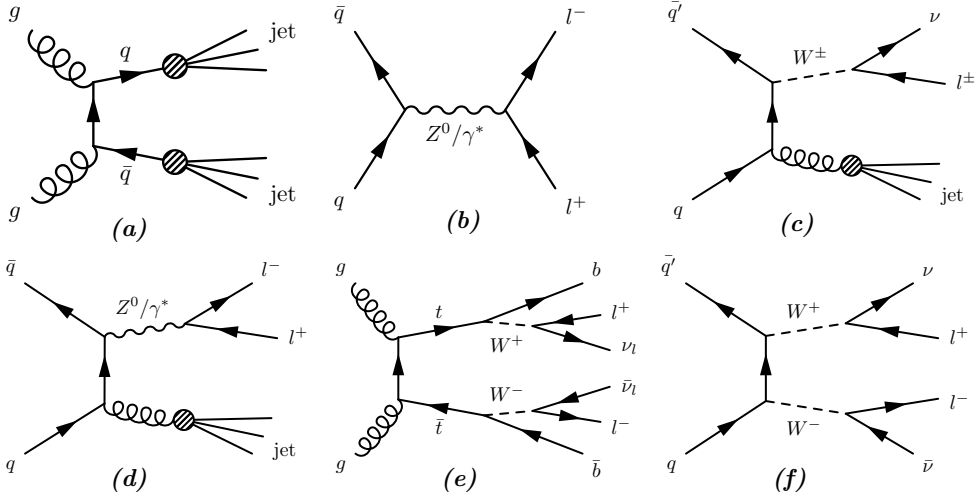


**Figure 4.1** – List of major background processes in this study. (a) QCD from gluon-pair, (b) Drell-Yan, (c)  $W$ +jet, (d)  $Z$ +jet, (e)  $t\bar{t}$ , (f)  $WW$ . Note that the conjugated mode and topologically-equivalent diagrams are implied.

## 4.2 Cross-section Measurement

The production cross-section of  $Z \rightarrow \tau\tau$  at Born level in QED, where  $Z$  is produced within the LHCb fiducial region is measured for each di-tau channel from the formula

$$\sigma = \frac{N_{\text{sig}}}{\mathcal{L} \mathcal{B} \varepsilon_{\text{tot}}} \quad , \quad \varepsilon_{\text{tot}} = \mathcal{A} \varepsilon_{\text{rec}} \varepsilon_{\text{sel}} \quad (4.1)$$

with following definitions:

$\mathcal{L}$ , **integrated luminosity**, will be discussed in Section 4.3, using  $1976.2 \pm 22.9 \text{ pb}^{-1}$  for all channels of analysis.

$\mathcal{B}$ , **di-tau decay branching fraction**, as shown in Table 4.1.

$\mathcal{A}$ , **acceptance**, will be discussed in Section 5.2.

$N_{\text{sig}}$ , **estimated number of signal candidates**, will be discussed in Chapter 6.

$\varepsilon_{\text{rec}}$ , **reconstruction efficiency**, will be discussed in Chapter 7.

$\varepsilon_{\text{sel}}$ , **selection efficiency**, will be discussed in Chapter 8.



## 4.3 Data Samples

### 4.3.1 Real Data

This analysis uses the data collected at  $\sqrt{s} = 8$  TeV during the 2012 Run-I period, corresponding to  $1976.18 \pm 22.92 \text{ pb}^{-1}$  of integrated luminosity after excluding the dataset with anomalous number of candidates per unit of luminosity [110].

### 4.3.2 Simulated Samples

Several simulated samples are used to define the analysis strategy and for calibration. The simulated samples are generated with the detector conditions of 2012. The list of samples are summarized in Table 4.2. The simulated samples are from the LHCb central production, with a few exceptions where they are generated with the Lausanne cluster<sup>1</sup>.

**Table 4.2** – Details of simulated samples used in this analysis, sorted by `decfile-ID` as used in LHCb. The cross-section is at leading-order from PYTHIA 8, unless stated otherwise. Where relevant, the branching ratio is already applied to the cross-section.

Process	ID	Events	$\sigma\mathcal{B}$ [pb]	$\varepsilon_{\text{gen}}$ [%]	Remarks
$t\bar{t}$	41900010	4,042,228	211	3.00	[1]
$WW \rightarrow \ell\dots$	42021000	223,475	34.3	7.78	-
$WZ \rightarrow \ell\dots$	42021001	238,199	12.3	5.55	-
$Z \rightarrow \tau\tau$	42100000	4,046,990	857	37.0	[2]
$Z \rightarrow \tau\tau$	42100003	996,131	866	—	[3]
$Z \rightarrow \mu\mu$	42112011	20,571,464	4466	39.1	-
$Z(\rightarrow\mu\mu) + \text{jet}$	42112022	5,073,236	1239	33.6	-
$Z(\rightarrow\mu\mu) + c$	42112052	2,019,302	572	1.22	-
$Z(\rightarrow\mu\mu) + b$	42112053	2,011,907	571	0.51	-
$Z \rightarrow ee$	42122011	2,369,246	4385	38.3	-
$Z \rightarrow b\bar{b}$	42150000	10,399,697	3848	16.1	[4]
$W(\rightarrow\tau\nu_\tau) + \text{jet}$	42300010	2,576,506	$1.31 \times 10^4$	28.1	-
$W(\rightarrow\mu\nu_\mu) + \text{jet}$	42311011	10,015,768	$1.32 \times 10^4$	23.6	-
$W(\rightarrow\mu\nu_\mu) + \text{jet}(\rightarrow\mu\dots)$	42311012	69,950	$1.32 \times 10^4$	$7.45 \times 10^{-3}$	[5]
$W(\rightarrow e\nu_e) + \text{jet}$	42321010	2,080,560	$1.32 \times 10^4$	27.7	-
Minimum bias	49001000	1,021,185	$4.34 \times 10^8$	$7.79 \times 10^{-1}$	-
$c\bar{c} \rightarrow \mu\dots$	49011004	1,167,321	$1.64 \times 10^6$	$1.78 \times 10^{-2}$	-
$b\bar{b} \rightarrow \mu\dots$	49011005	1,118,554	$1.54 \times 10^6$	$9.44 \times 10^{-2}$	-
$c\bar{c} \rightarrow e\dots$	49021004	1,057,501	$1.64 \times 10^6$	$1.52 \times 10^{-2}$	-
$b\bar{b} \rightarrow e\dots$	49021005	1,033,611	$1.54 \times 10^6$	$8.89 \times 10^{-2}$	-

Remarks

1. Use POWHEG-BOX r2092 [111, 112, 113, 114] as a generator.
2. Central production, no  $\gamma^*$  interference.

<sup>1</sup> A computing farm of 20-nodes Intel(R) Xeon(R) CPU E5-2650 v2 @ 2.60GHz.

3. Local production, with  $\gamma^*$  interference. Has fiducial and acceptance cut, so the  $\varepsilon_{\text{gen}}$  is not uniform but varies across di-tau channel. This sample implements the tau spin correlation and decay via PYTHIA 8.175 as suggested by [115].
4. Use PYTHIA 6 as a generator, no  $\gamma^*$  interference.
5. Local production. Required second muon of  $p_T > 5 \text{ GeV}/c$ ,  $\Delta\phi(\mu_1, \mu_2) > 2.6$ .

# 5 Signal Selection

The analysis is organized into several stages as shown in Fig. 5.1, where criteria at each stage are discussed in detail throughout this section. The full summary of selections in the tabulated form is provided in Section 5.7. In this document, for channels with identical particles,  $\tau_\mu\tau_\mu$  and  $\tau_e\tau_e$ , the two particles are  $p_T$  ordered, the first has the largest  $p_T$ .

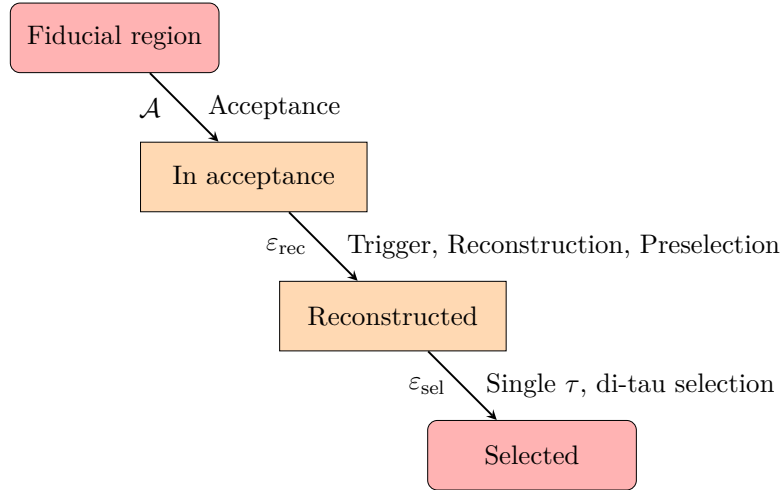


*Figure 5.1* – Schema of  $Z \rightarrow \tau\tau$  candidates selection stages organized in this analysis.

## 5.1 Fiducial Region

The cross-sections computed in this analysis are relative to the fiducial region defined to have  $60 < m(\tau\tau) < 120 \text{ GeV}/c^2$  for the di-tau mass, and each  $\tau$  with  $p_T(\tau) > 20 \text{ GeV}/c$ , and  $2.0 < \eta(\tau) < 4.5$ . This choice of the fiducial volume is the same as in the other LHCb  $Z \rightarrow ll$  analyses [108, 109, 107].

## 5.2 Acceptance

The  $\tau$  lepton is expected to decay inside the LHCb detector and can be (partially) reconstructed from its decay products. The “acceptance” range for the di-tau candidates is defined on its charged daughters  $p_T$ ,  $\eta$ , and the di-tau  $m$ , taking into account the momentum loss due to unmeasured particles (neutrinos and neutrals). In order to keep the compatibility with the previous analyses, as well as aligning with the constraints from trigger (see Section 5.3) and reconstruction efficiency calibration sample (see Chapter 7), the acceptance requirements for each di-tau channel are the following:

$\tau_\mu\tau_\mu$  Requiring one muon with  $p_T > 20 \text{ GeV}/c$ , and a second muon with  $p_T > 5 \text{ GeV}/c$ . Both muons are required to be inside the LHCb geometrical acceptance,  $2.0 < \eta < 4.5$ . The reconstructed invariant mass of the pair must be greater than  $20 \text{ GeV}/c^2$ .

$\tau_\mu\tau_{h1}$  Requiring one muon with  $p_T > 20 \text{ GeV}/c$ , and a single charged hadron with  $p_T > 10 \text{ GeV}/c$ . Both muon and charged hadron must be inside the LHCb geometrical acceptance,  $2.0 < \eta < 4.5$ , and the mass of the pair greater than  $30 \text{ GeV}/c^2$ .

$\tau_\mu\tau_{h3}$  Requiring one muon with  $p_T > 20 \text{ GeV}/c$ , and three charged hadrons all having  $p_T > 1 \text{ GeV}/c$  with at least one of them having  $p_T > 6 \text{ GeV}/c$ . The sum of momenta from the three charged hadrons must have  $p_T > 12 \text{ GeV}/c$ , and the 3-prongs invariant mass within  $700\text{--}1500 \text{ MeV}/c^2$ . Muon and the 3 charged hadrons have  $2.0 < \eta < 4.5$ . The invariant mass calculated from the four-momenta sum of muon and three charged hadrons must be greater than  $30 \text{ GeV}/c^2$ .

$\tau_e\tau_e$ ,  $\tau_e\tau_{h1}$ ,  $\tau_e\tau_{h3}$  The criteria are similar to the ones applied to the  $\tau_\mu\tau_\mu$ ,  $\tau_\mu\tau_{h1}$ ,  $\tau_\mu\tau_{h3}$  channels respectively, with the requirement on muon replaced by the electron.

$\tau_\mu\tau_e$  Requiring one muon and one electron with  $p_T > 5 \text{ GeV}/c$ , and one of them  $p_T > 20 \text{ GeV}/c$ . Both leptons must be inside the geometrical acceptance  $2.0 < \eta < 4.5$ , and the invariant mass of the pair greater than  $20 \text{ GeV}/c^2$ .

The choice of invariant mass cut roughly follows the kinematic relation valid for a 2-body decay back-to-back:

$$m^2 = (E_1 + E_2)^2 - (\vec{p}_1 + \vec{p}_2)^2 \geq m_1^2 + m_2^2 + 2p_1p_2(1 - \cos\theta) \geq 4p_{T1}p_{T2}$$

where  $\theta$  is the angle between the momenta of the two decay products. Given that the transverse boost of the  $Z$  is typically small, the relation is a good approximation for the  $Z \rightarrow \tau\tau$  process.

The selection from the acceptance criteria is visualized by an example in Figs. 5.2 and 5.3, using  $Z \rightarrow \tau\tau$  events generated at the next-to-leading order via POWHEG-BOX r2092 [111, 112, 113, 114] with MSTW08NL090c1 as a PDF set [116] via LHAPDF 6.1.6 [117], and showered with PYTHIA 8.175 [118, 119]. The complete list of figures are available in appendix A.1.

The acceptance factor,  $\mathcal{A}$ , is defined as the number of events with a di-tau candidate after the final state radiation (FSR) and passing the acceptance selection discussed above,

divided by the number of  $Z \rightarrow \tau\tau$  inside the LHCb fiducial region before the FSR. The values of  $\mathcal{A}$  for each di-tau channel is obtained from simulation at next-to-leading order.

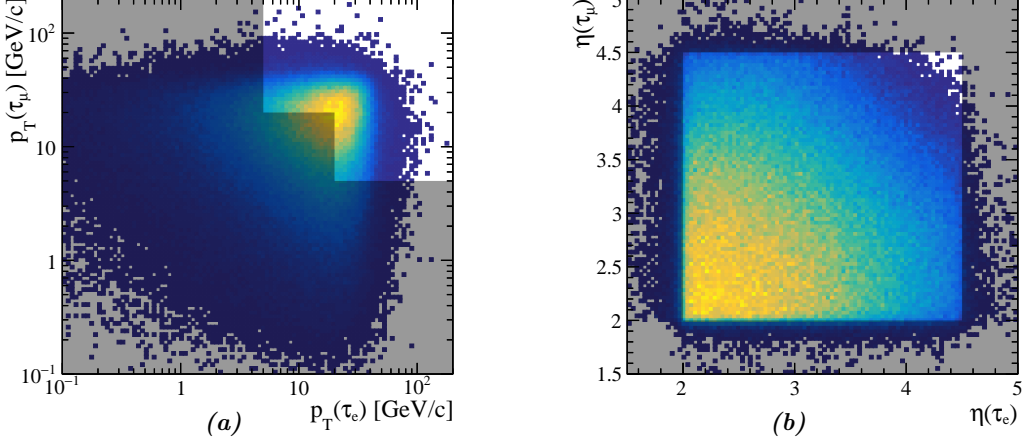


**Figure 5.2** – The selected di-tau acceptance region is shown as the area not covered by the gray mask, for the  $\tau_\mu\tau_e$  channel. The fiducial region requirement was applied. The distributions are shown as a function of (a)  $p_T$  (b)  $\eta$  of  $\tau_e$  (horizontal axis) and  $\tau_\mu$  (vertical axis). The plots are obtained at generator level.

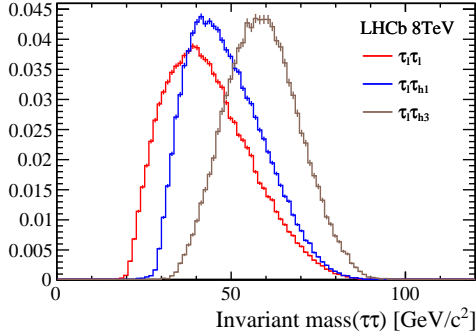


**Figure 5.3** – The invariant mass of di-tau candidates at generator level for  $Z \rightarrow \tau\tau$  in the fiducial region, with all  $p_T$  and  $\eta$  acceptance cuts applied. The  $\tau_e$  and  $\tau_\mu$  candidates are grouped together as  $\tau_l$ . Note that the minimal invariant mass used in this analysis is  $20 \text{ GeV}/c^2$  for  $\tau_l\tau_l$  (black curve), and  $30 \text{ GeV}/c^2$  for both  $\tau_l\tau_{h1}$  (red) and  $\tau_l\tau_{h3}$  (blue).

### 5.3 Trigger Requirement

The online selection is based on muon (*muon-alley*) and electron (*electron-alley*) triggers, as listed in Table 5.1. Depending on the decay channel, the trigger requirement needs the muon in  $\tau_\mu$  to be TOS (triggered-on-signal) by the muon-alley, or the electron in  $\tau_e$  to be TOS by the electron-alley. In the channel with more than one  $\tau_e$  or  $\tau_\mu$ , either of the leptons can be TOS for its respective alley. Details on the trigger requirements can be found in appendix A.2 and [120].

**Table 5.1** – List of triggers defined for each trigger alley.

Muon-alley	Electron-alley
LOMuon	LOElectron
Hlt1SingleMuonHighPT	Hlt1SingleElectronNoIP
Hlt2SingleMuonHighPT	Hlt2SingleTFVHighPtElectron

## 5.4 Candidate Reconstruction

The tau and di-tau candidates are obtained from the reconstructed particles passing the trigger algorithm, track quality cut, and particle identification criteria. In the particular case of the  $\tau_{h3}$  decay, the candidate is reconstructed from the combination of 3 charged hadrons with correct charge combination, *i.e.*,  $\tau^+ \rightarrow h^+h^+h^-$ , and  $\tau^- \rightarrow h^-h^-h^+$ , implying the existence of a measurable secondary vertex. The di-tau is subsequently reconstructed combining two tau candidates of opposite electric charge. A vertex fit is not required in the process as the displacement from both tau candidates is not necessary compatible with the primary vertex.

### 5.4.1 Track Quality

The reconstruction of a tau candidate uses long tracks with probability- $\chi^2 > 0.01$ , identical for every di-tau channel.

### 5.4.2 Particle Identification

The particle identification criteria are applied separately for muons, electrons, and charged hadrons used in the reconstruction of the tau candidate. The criteria are chosen to be mutually exclusive.

**Muons** The reconstructed muons are tracks having at least 2 muon-station-hits for track with  $p_T > 3 \text{ GeV}/c$ , at least 3 station-hits if  $p_T > 6 \text{ GeV}/c$ , and 4 station-hits if  $p_T > 10 \text{ GeV}/c$ .

**Charged hadrons** The reconstructed charged hadrons are tracks assuming mass of a pion. It is required to be in the HCAL acceptance, and deposits an energy of  $E_{\text{HCAL}}/p > 0.05$ , as well as to fail a loose muon ID criterion, defined as having at least 2 muon-station-hits for track with  $p_T > 3 \text{ GeV}/c$ , and at least 3 station-hits if  $p_T > 6 \text{ GeV}/c$ .

**Electrons** The reconstructed electrons are tracks assuming mass of an electron. It is required to fail the loose muon ID. The electron is also required to be in the acceptance of PS, ECAL, HCAL sub-detectors, and deposit a considerable amount of energy in the PS, ECAL, but not in HCAL:  $E_{\text{PS}} > 50 \text{ MeV}$ ,  $E_{\text{ECAL}}/p > 0.1$ , and  $0 \leq E_{\text{HCAL}}/p < 0.05$ , where  $p$  is the momentum of an electron.

## 5.5 Kinematic Preselection

The reconstructed di-tau candidates are required to satisfy the same selections for  $p_T$ ,  $\eta$ ,  $m$ , as at acceptance level (Section 5.2). From simulation, the preselection efficiency at this stage is expected to be close to unity for  $\tau_\mu$ , slightly less for  $\tau_{h1}$ ,  $\tau_{h3}$ , and significantly smaller for  $\tau_e$ . Due to imperfect bremsstrahlung recovery, the electron momentum is smaller than the real value. An illustration of this effect is given in Fig. 5.4, for the  $\tau_\mu\tau_e$  channel. The complete list of figures is available in appendix A.3.

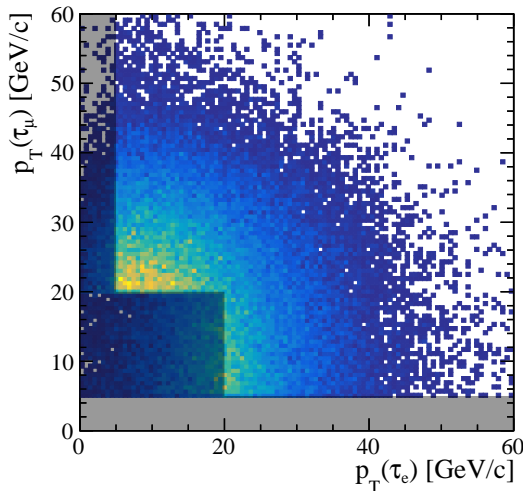


**Figure 5.4** –  $p_T$  of the reconstructed muon vs  $p_T$  of the reconstructed electron, in the  $\tau_\mu\tau_e$  channel, from  $Z \rightarrow \tau\tau$  simulated sample. The kinematic preselection excludes the shaded region. Notice that the reconstructed electrons can populate the region below this cut, because of the bremsstrahlung loss.

In the LHCb analysis framework, the kinematic preselection is applied on top of the stripping selection (using version `Stripping20`). The line `Z02TauTau_MuXLine` is used for the reconstruction of  $\tau_\mu\tau_\mu$ ,  $\tau_\mu\tau_{h1}$ ,  $\tau_\mu\tau_{h3}$  candidates, and `Z02TauTau_EXLine` for  $\tau_e\tau_e$ ,  $\tau_e\tau_{h1}$ ,  $\tau_e\tau_{h3}$  candidates. For a  $\tau_\mu\tau_e$  candidate, an event passing either line is sufficient. The stripping specifications details can also be found in appendix [A.2](#).

## 5.6 Candidate Selection

Selection criteria are applied to the reconstructed tau candidates, which are subsequently combined to form the  $Z$  decay candidates. Cut-based selections are used, applied sequentially. A summary of the criteria, dubbed *offline selection*, is given in Tables [5.8](#) and [5.9](#). The simulated samples listed in Section [4.3.2](#), as well as same-sign candidates from data (di-tau candidates with taus of identical electric charge) are used in the optimization procedure based on the figure of merit (FOM)  $S/\sqrt{S+B}$ , where  $S$  is the number of expected signal obtained from simulation and  $B$  the number of background candidates from simulation or from same-sign samples<sup>1</sup>.

*A priori*, it is possible to have more than one reconstructed di-tau candidate per event. After all selection requirements are applied, the number of di-tau candidates per event is checked; no events are observed with multiple di-tau candidates in either data or simulated samples. In the auxiliary studies (*e.g.*, tag-and-probe study, particle misidentification study), when multiple candidates per event arises, only one is selected at random. The order of the Sections follow the analysis flow.

### 5.6.1 Tau Candidate Selection

This section describes the criteria chosen to purify the  $\tau$  lepton sample. The study of correlation effects and details of the optimization are available in appendix [A.4](#). The complete set of figures is given in appendix [A.5](#). As there are many di-tau channels and variables under study, only some of the distributions are displayed in this section.

<sup>1</sup>The procedure is assisted by the TMVA [\[121\]](#) package cut-based optimization (`TMVA.Types.kCuts`).

5.6.1.1 Combination Quality of  $\tau_{h3}$ 

In the 3-prongs case, a vertex fit is performed on the triplets. A  $\chi^2/\text{ndf} < 20$  from the fit is required. Several triplets can be present in the event. A first selection is based on the topology of the candidate in  $\eta$ - $\phi$  space. The distance in  $\eta$ - $\phi$  between any pair of charged hadrons,  $\Delta R_{\text{max}}$ , is expected to be small for true 3-prongs candidates and becomes smaller as the total  $p_T$  of the three prongs increases. To ensure a well collimated topology, the selection requires  $\Delta R_{\text{max}}/p_T < 0.005 \text{ (GeV}/c)^{-1}$ , where  $p_T$  is the vectorial sum of the transverse momenta of the three prongs. The choice of decorrelation between  $\Delta R_{\text{max}}$  and  $p_T$  is performed similarly to the method adopted by CMS [122]. The two variables and selection thresholds are illustrated in Fig. 5.6.

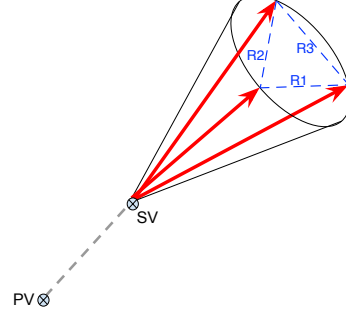


Figure 5.5 – Illustration of  $\tau_{h3}$  cone and distances  $R_i$  between prongs.

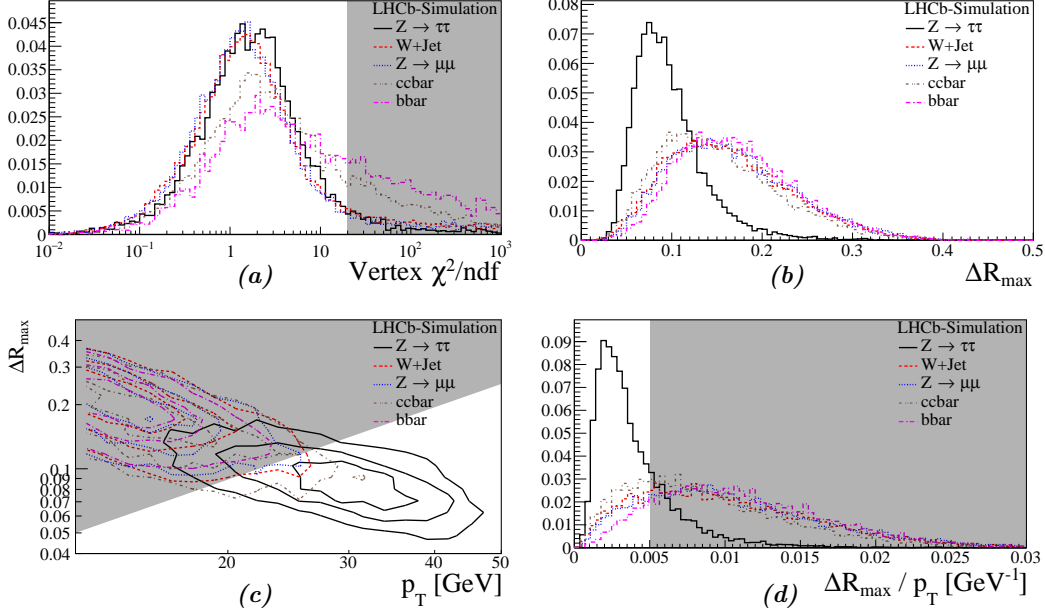


Figure 5.6 – Combination quality variables of  $\tau_{h3}$  from  $\tau_{\mu}\tau_{h3}$  channel: (a) vertex fitting  $\chi^2/\text{ndf}$ , (b)  $\Delta R_{\text{max}}$ , (c)  $\Delta R_{\text{max}}$  and  $p_T$  contours (d)  $\Delta R_{\text{max}}$  between prongs divided by the  $p_T$  of  $\tau_{h3}$ . The  $Z \rightarrow \tau\tau$  signal from simulation (black) is compared against other prominent backgrounds.



## 5.6.1.2 Isolation

This criterion is applied to all tau candidates. The isolation variable for a particle is defined as

$$\hat{I}_{p_T} = \frac{p_T}{(\vec{p} + \vec{p}_{\text{cone}})_T}$$

where  $\vec{p}_{\text{cone}}$  is the sum of momenta from all charged tracks around the given particle within radius  $R_{\eta\phi} = 0.5$ , and the subscript T refers to the transversal component of the momentum. The particle is referred as *fully isolated* if  $\hat{I}_{p_T} \rightarrow 1$ . The tau leptons from  $Z$  decays are expected to be isolated, as illustrated in Fig. 5.8. The selection based on this observable requires  $\hat{I}_{p_T} > 0.9$  for all tau candidates.

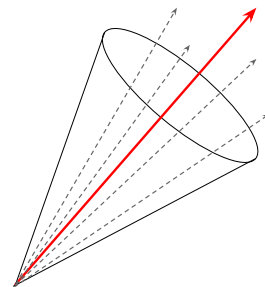


**Figure 5.7** – Illustration of neighbor tracks inside the cone around a tau candidate used to compute the isolation.

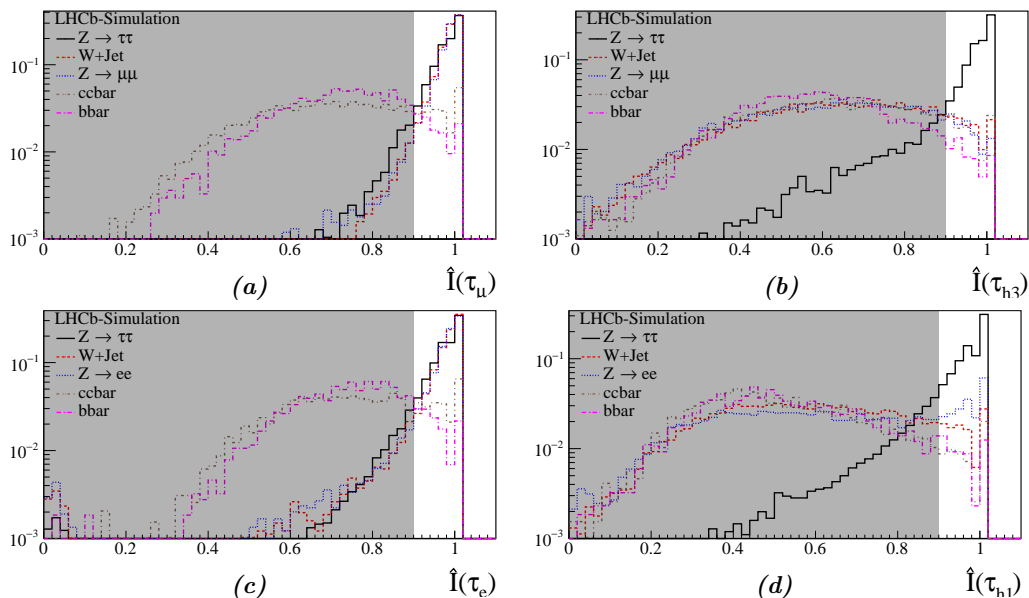


**Figure 5.8** – Isolation variable  $\hat{I}_{p_T}$  for (a)  $\tau_\mu$ , (b)  $\tau_{h3}$  from  $\tau_\mu\tau_{h3}$  channel, and (c)  $\tau_e$ , (d)  $\tau_{h1}$  from  $\tau_e\tau_{h1}$  channel.

5.6.1.3 Decay Time and Corrected Mass of  $\tau_{h3}$ 

The vertex fit for  $\tau_{h3}$  candidate provides a secondary vertex (SV), assumed to be the tau lepton decay position. A refitting of the primary vertex (PV) is performed after removing tracks from the candidate.

The variable named *decay time* is an estimate of the elapsed proper time for the particle traveling from the PV to the SV. The goal is to select candidates compatible with the  $\tau$  lifetime of  $290.3 \pm 0.5$  fs [123]. The decay time is calculated as  $|\vec{d}|m/|\vec{p}|$ , where  $\vec{d}$  is the distance from PV to SV,  $m$  and  $\vec{p}$  are the invariant mass and momentum of  $\tau_{h3}$ . Given the uncertainties on the input variables ( $\vec{d}, m, \vec{p}$ ), the decay chain is fitted (via a Kalman filter) for a better precision on those parameters [124]. The decay time result cannot be exact, due to the missing  $\nu_\tau$ , and other neutrals not included in the  $\tau_{h3}$  reconstruction. This variable is illustrated in Fig. 5.9a. The selection requires  $\tau_{h3}$  to have a decay time  $> 60$  fs.

The *corrected mass*,  $m_{\text{corr}}$ , of the  $\tau_{h3}$  candidate with respect to the PV is defined as

$$m_{\text{corr}} = \sqrt{m^2 + p^2 \sin^2 \theta} + p \sin \theta$$

where  $m$ ,  $p$  is the invariant mass and momentum of  $\tau_{h3}$  candidate, and  $\theta$  is the angle between the momentum and flight direction of the candidate. This quantity defines the minimum mass that the particle can have which is consistent with the direction of flight, recovering part of the momentum component carried by neutrals, transverse to the flight direction of the tau candidate. The selection requires  $m_{\text{corr}} < 3 \text{ GeV}/c^2$ . This variable is illustrated in Fig. 5.9b.

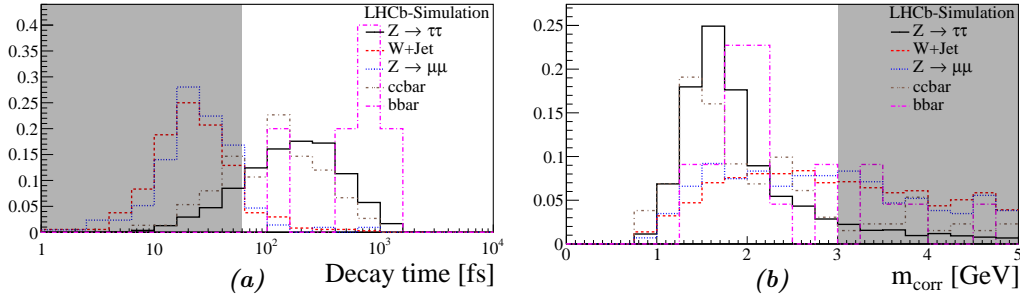


**Figure 5.9** – Variable used for  $\tau_{h3}$  identification based on a secondary vertex, shown with  $\tau_{h3}$  from  $\tau_\mu\tau_{h3}$  candidates: (a) *decay time*, (b) *corrected mass*  $m_{\text{corr}}$ .

## 5.6.1.4 Impact Parameter

For  $\tau_e$ ,  $\tau_\mu$ , and  $\tau_{h1}$ , it is not possible to reconstruct the SV corresponding to the  $\tau$  decay position. Instead, the *impact parameter* (IP) of the track with respect to the best PV is used. A large IP is an indication of a long lifetime. The PV refit procedure is performed after removing the  $\tau$  decay track, as described for  $\tau_{h3}$ . The distribution of IP is given as an example in Fig. 5.11. The selection requires  $IP > 0.03$  mm for  $\tau_{h1}$  in channel  $\tau_\mu\tau_{h1}$ ,  $\tau_e\tau_{h1}$ . It also requires  $IP > 0.05$  mm for the second  $\tau_\mu$  in channel  $\tau_\mu\tau_\mu$ , as well as for the second  $\tau_e$  in channel  $\tau_e\tau_e$ . No IP selection is applied to the  $\tau$  candidate with the largest  $p_T$ , as suggested by the FOM study.

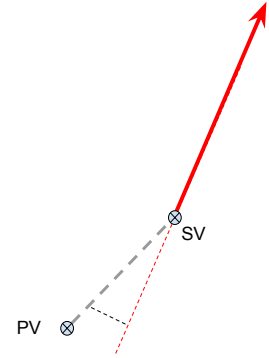


**Figure 5.10** – Illustration of the impact parameter of a tau candidate.

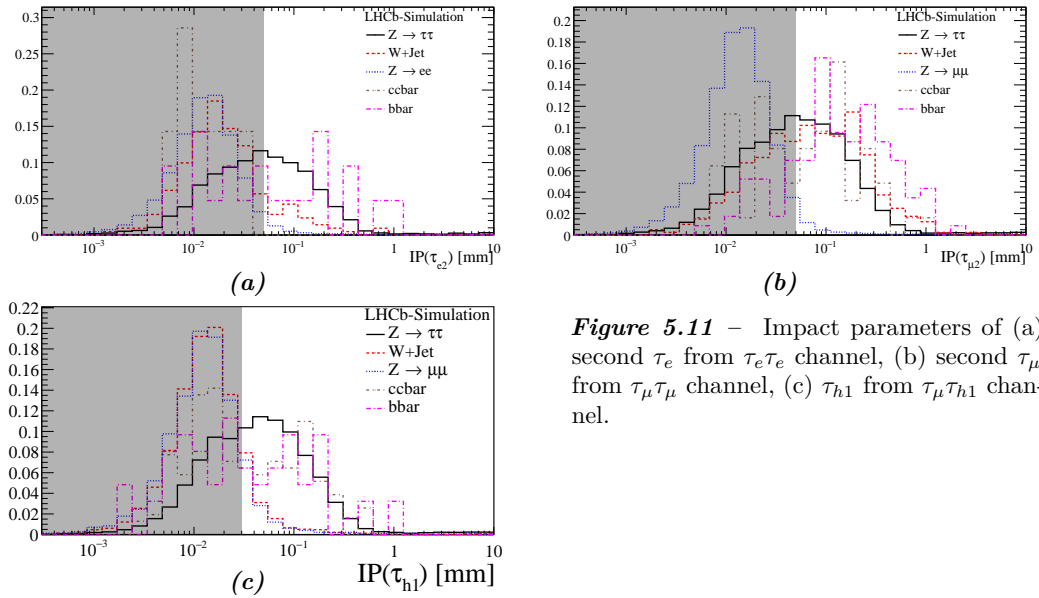


**Figure 5.11** – Impact parameters of (a) second  $\tau_e$  from  $\tau_e\tau_e$  channel, (b) second  $\tau_\mu$  from  $\tau_\mu\tau_\mu$  channel, (c)  $\tau_{h1}$  from  $\tau_\mu\tau_{h1}$  channel.

## 5.6.2 Di-tau Candidate Selection

Further selection variables for a di-tau candidate are exploited. Only a subset of the corresponding distributions are shown, the remaining figures can be found in appendix A.6.

### 5.6.2.1 Invariant Mass

The invariant mass of the di-tau candidates is expected to be reconstructed below the on-shell  $Z$  mass ( $\sim 91 \text{ GeV}/c^2$ ) because of the missing energy from neutral particles not included in the reconstruction. Optimizing for largest  $S/\sqrt{S+B}$  as shown in Fig. 5.12, an upper limit at  $60 \text{ GeV}/c^2$  is placed in  $\tau_\mu\tau_\mu$  and  $\tau_e\tau_e$  channels to remove the  $Z \rightarrow \mu\mu$ ,  $Z \rightarrow ee$  backgrounds. No upper limit is applied to the other channels.

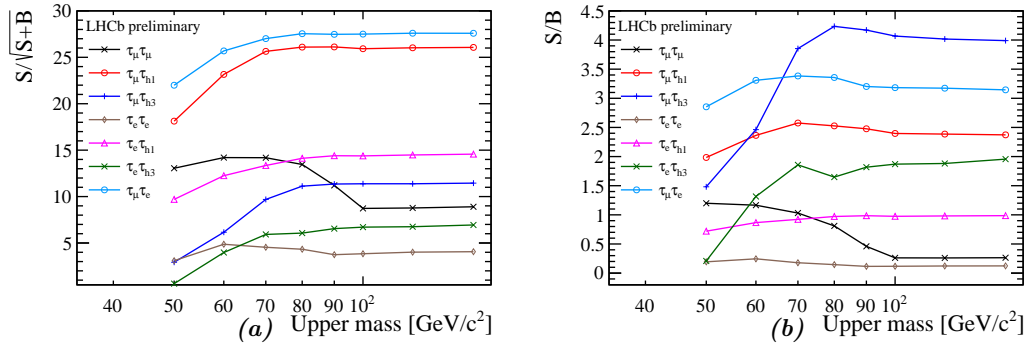


**Figure 5.12** – Figure-of-merits as a function of maximum di-tau invariant mass selection, with all selections applied: (a)  $S/\sqrt{S+B}$ , (b)  $S/B$ . At the right-most bin, no mass cut is applied.

### 5.6.2.2 Azimuthal Separation

The  $\tau$  leptons from a  $Z \rightarrow \tau\tau$  decay are expected to fly back-to-back in the transverse plane, given that the  $Z$  typically has only a small transverse boost. Moreover, because of the boost of the  $\tau$  lepton, the daughter tend to retain the original mother direction. Thus, the back-to-back decay direction is expected to be preserved by the two  $\tau$  candidates. The *azimuthal separation* angle,  $\Delta\phi \in [0, \pi]$ , is defined as the angle between two tau candidates in the transversal plane. The selection requires  $\Delta\phi > 2.7$  for all di-tau channel. Examples of distributions are shown in Fig. 5.14.

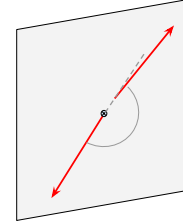


**Figure 5.13** – Illustration of  $\Delta\phi$  between two  $\tau$  candidate.

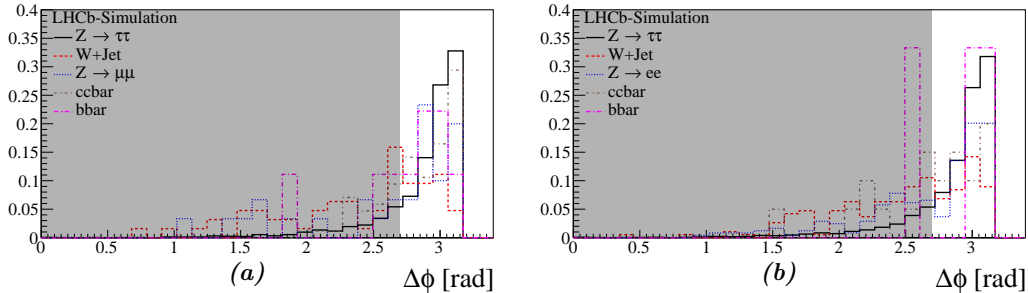


**Figure 5.14** – Azimuthal separation,  $\Delta\phi$ , for (a)  $\tau_\mu\tau_{h3}$ , (b)  $\tau_e\tau_{h1}$  channel.

### 5.6.2.3 Transverse Momentum Asymmetry

The *transverse momentum asymmetry* between two particles is defined as:

$$A_{p_T} := \frac{|p_{T1} - p_{T2}|}{p_{T1} + p_{T2}}$$

In  $Z \rightarrow ll$  process, the distribution of  $A_{p_T}$  for the two leptons peaks at zero. In  $Z \rightarrow \tau\tau$  process, where this quantity is applied to the  $\tau$  decay products (instead of the  $\tau$  lepton), the asymmetry is expected to be larger, because of the missing energy from the undetected neutrals. Other processes such as QCD or  $W$ +jet also display a larger value of  $A_{p_T}$ . The selection requires  $A_{p_T} > 0.1$  in the channels  $\tau_\mu\tau_\mu$  and  $\tau_e\tau_e$ , and  $A_{p_T} < 0.6$  in the channel  $\tau_\mu\tau_e$ . Examples of distributions are shown in Fig. 5.15. The  $A_{p_T}$  criterion is found to be less effective when hadronic decays are involved as a high- $p_T$  selection is already applied, so this cut is not used for the channels involving  $\tau_{h1}$ ,  $\tau_{h3}$ .

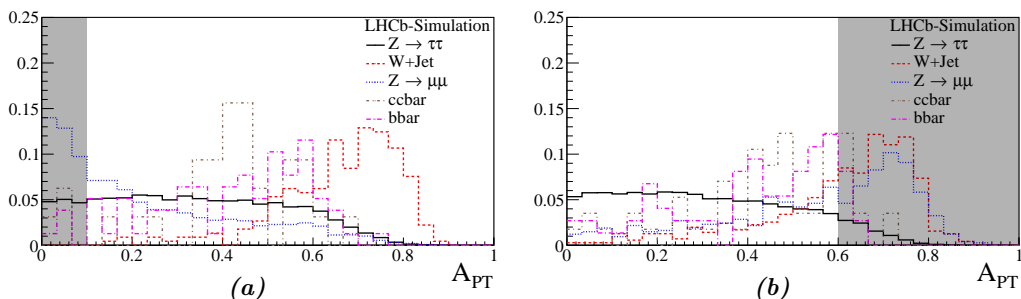


Figure 5.15 – Transverse momentum asymmetry,  $A_{p_T}$ , for (a)  $\tau_\mu\tau_\mu$ , (b)  $\tau_\mu\tau_e$  channel.

### 5.6.2.4 Distance of Closest Approach

The *distance of closest approach* (DOCA) between the decay products of the two  $\tau$  candidates is expected to be large, because of the  $\tau$  lifetime. The same is expected for the decay of couples of  $b$ -hadrons, while the DOCA must be low for prompt decays like  $Z \rightarrow \mu\mu$ , and of the same order of the vertex position resolution.

The  $Z \rightarrow \mu\mu$  simulated sample is compared to data for validation, where the di-muons pass the preselection requirement, with  $p_T > 20 \text{ GeV}/c$ ,  $80 < m_{\mu\mu} < 100 \text{ GeV}/c^2$ , for each muon. The  $\chi_{\text{DOCA}}^2$  distributions in data and simulation are shown in Fig. 5.16. The distribution from  $Z \rightarrow \tau\tau$  is also shown. The data/simulation discrepancy at  $\chi_{\text{DOCA}}^2 \sim 10$ , the potential cut value, has pushed to abandon this variable.

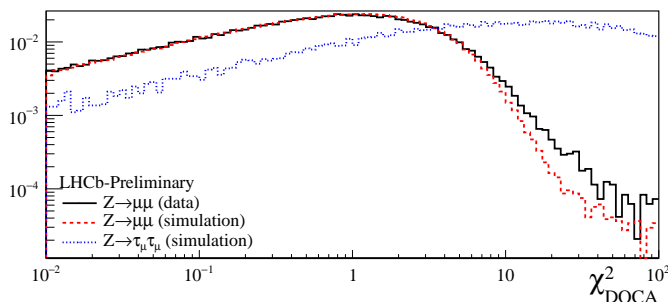


Figure 5.16 – Distribution of  $\chi_{\text{DOCA}}^2$  for  $Z \rightarrow \mu\mu$  from data (black),  $Z \rightarrow \mu\mu$  from simulated sample (red),  $\tau_\mu\tau_\mu$  candidate of  $Z \rightarrow \tau\tau$  from simulated sample (blue). The data-simulation disagreement can be observed in the vicinity of  $\chi_{\text{DOCA}}^2 \sim 10$ .

## 5.7 Summary of Selections

**Table 5.2** – Definition of the LHCb  $Z$ -boson fiducial region.

Variables	Unit	Cut
$m(\tau_1\tau_2)$	GeV/ $c^2$	[60, 120]
$p_T(\tau)$	GeV/ $c$	$> 20$
$\eta(\tau)$	-	[2, 4.5]

**Table 5.3** – Trigger and stripping requirements.

Channel	Trigger requirement	Stripping requirement
$\tau_\mu\tau_\mu$	Muon-alley TOS by (either or both) $\tau_\mu$	Z02TauTau_MuXLine
$\tau_\mu\tau_{h1}$	Muon-alley TOS by $\tau_\mu$	Z02TauTau_MuXLine
$\tau_\mu\tau_{h3}$	Muon-alley TOS by $\tau_\mu$	Z02TauTau_MuXLine
$\tau_e\tau_e$	Electron-alley TOS by (either or both) $\tau_e$	Z02TauTau_EXLine
$\tau_e\tau_{h1}$	Electron-alley TOS by $\tau_e$	Z02TauTau_EXLine
$\tau_e\tau_{h3}$	Electron-alley TOS by $\tau_e$	Z02TauTau_EXLine
$\tau_\mu\tau_e$	Either: (i) Electron-alley TOS by $\tau_e$ (ii) Muon-alley TOS by $\tau_\mu$	Z02TauTau_EXLine Z02TauTau_MuXLine

**Table 5.4** – Acceptance cuts. The subscript 1(2) refers to the  $\tau$  lepton decay product candidate labeled at position 1(2) of the respective di-tau channel. The  $p_T$  cuts in channel  $\tau_\mu\tau_\mu$ ,  $\tau_e\tau_e$ , and  $\tau_\mu\tau_e$  are interchangeable between the two  $\tau$  lepton decay product candidates.

Variables	Unit	$\tau_\mu\tau_\mu$	$\tau_\mu\tau_{h1}$	$\tau_\mu\tau_{h3}$	$\tau_e\tau_e$	$\tau_e\tau_{h1}$	$\tau_e\tau_{h3}$	$\tau_\mu\tau_e$
$m(\tau_1\tau_2)$	GeV/ $c^2$	$> 20$	$> 30$	$> 30$	$> 20$	$> 30$	$> 30$	$> 20$
$p_T(\tau_1)$	GeV/ $c$	$> 20$	$> 20$	$> 20$	$> 20$	$> 20$	$> 20$	$> 20$
$p_T(\tau_2)$	GeV/ $c$	$> 5$	$> 10$	$> 12$	$> 5$	$> 10$	$> 12$	$> 5$
$\eta(\tau_1)$	-	[2, 4.5]	[2, 4.5]	[2, 4.5]	[2, 4.5]	[2, 4.5]	[2, 4.5]	[2, 4.5]
$\eta(\tau_2)$	-	[2, 4.5]	[2, 4.5]	—	[2, 4.5]	[2, 4.5]	—	[2, 4.5]

**Table 5.5** – Additional acceptance cuts for  $\tau_{h3}$  in  $\tau_\mu\tau_{h3}$  and  $\tau_e\tau_{h3}$  channel, where  $h$  denotes a single charged hadron used in the construction of 3-prongs  $\tau_{h3}$ .

Variables	Unit	Cut
$\min(p_T(h))$	GeV/ $c$	$> 1$
$\max(p_T(h))$	GeV/ $c$	$> 6$
$\eta(h)$	-	[2, 4.5]
$m(\tau_{h3})$	MeV/ $c^2$	[700, 1500]

## 5.7. Summary of Selections

**Table 5.6** – Particle identification cuts.

Variables	Unit	Muons	Charged hadrons	Electrons
ISMUON	-	True	-	-
ISMUONLOOSE	-	-	False	False
InAccPrs	-	-	-	True
InAccEcal	-	-	-	True
InAccHcal	-	-	True	True
$E_{PS}$	MeV	-	-	> 50
$E_{ECAL}/p$	-	-	-	> 0.1
$E_{HCAL}/p$	-	-	> 0.05	< 0.05

**Table 5.7** – Tracking selection criteria. They are applied identically to all muons, charged hadrons, and electrons used in the reconstruction of the  $\tau$  candidate.

Variables	Cut
Track type	LONG
Track prob. $\chi^2$	> 0.01

**Table 5.8** – Summary of the criteria for the offline selection. The subscript 1(2) refers to the  $\tau$  lepton decay product candidate labeled at position 1(2) of the respective di-tau channel.

Variables	Unit	$\tau_\mu\tau_\mu$	$\tau_\mu\tau_{h1}$	$\tau_\mu\tau_{h3}$	$\tau_e\tau_e$	$\tau_e\tau_{h1}$	$\tau_e\tau_{h3}$	$\tau_\mu\tau_e$
IP <sub>1</sub>	mm	—	—	—	—	—	—	—
IP <sub>2</sub>	mm	> 0.05	> 0.03	—	> 0.05	> 0.03	—	—
$\hat{I}_{p_T 1,2}$	-	> 0.9	> 0.9	> 0.9	> 0.9	> 0.9	> 0.9	> 0.9
$\Delta\phi$	rad	> 2.7	> 2.7	> 2.7	> 2.7	> 2.7	> 2.7	> 2.7
$A_{p_T}$	-	> 0.1	—	—	> 0.1	—	—	< 0.6
$m(\tau_1\tau_2)$	GeV/ $c^2$	< 60	—	—	< 60	—	—	—

**Table 5.9** – Additional offline selection criteria for  $\tau_{h3}$  in  $\tau_\mu\tau_{h3}$  and  $\tau_e\tau_{h3}$  channels.

Variables	Unit	Cut
Vertex $\chi^2/\text{ndf}$	-	< 20
$\Delta R_{\text{max}}/p_T$	(GeV/ $c$ ) <sup>-1</sup>	< 0.005
$m_{\text{corr}}$	GeV/ $c^2$	< 3.0
Decay time	fs	> 60





# 6 Background Estimation

The estimation of the number of backgrounds for  $Z \rightarrow \tau\tau$  candidates is discussed in this section. The results are summarized in Table 6.5. The techniques used are largely retained from the previous  $Z \rightarrow \tau\tau$  analysis [107]. The background from the different processes are estimated by a data-driven approach when possible. This is the case of the background from the QCD and  $Z \rightarrow ll$  processes, which are the most important.

When the data-driven approach is not possible, the number of candidates is computed with the help of simulated background samples. The number of candidates from process  $x$  for a given di-tau channel is estimated from the corresponding simulated set using the relation

$$N = \mathcal{L} \sigma_x \varepsilon_{\text{gen}} \varepsilon_{\text{total-sel}}$$

where  $\sigma_x$  is the production cross-section of the process,  $\varepsilon_{\text{gen}}$  is the generator-level selection efficiency, and  $\varepsilon_{\text{total-sel}}$  represents the total selection efficiency, obtained by dividing the number of events passing the final selection by the number of events after the generator-level selection. The list of the calculated values is given in Table 6.7. The table includes the predictions for the signals, also inferred from the simulated sets, as well as the predictions for the  $Z \rightarrow ll$ , QCD and  $Vj$  processes, for which the background is subsequently estimated from data. The uncertainties are only statistical, taken from the uncertainties of  $\sigma_x$  and  $\varepsilon_{\text{gen}}$  given by the generator, and for  $\varepsilon_{\text{total-sel}}$  the Clopper-Pearson method [125] at 68.3% confidence level is used.

## 6.1 Drell-Yan Process

The Drell-Yan process,  $Z \rightarrow ll$ , contributes to the background in a way which depends on the di-tau channel. The process  $Z \rightarrow \mu\mu$  affects the  $\tau_\mu\tau_\mu$ ,  $\tau_\mu\tau_{h1}$ , and  $\tau_\mu\tau_e$  channels, and  $Z \rightarrow ee$  the  $\tau_e\tau_e$ ,  $\tau_e\tau_{h1}$ , and  $\tau_\mu\tau_e$  channels. The  $Z \rightarrow ll$  background is irrelevant for  $\tau_\mu\tau_{h3}$  and  $\tau_e\tau_{h3}$  channels. This section considers only the fake candidates originated directly from the  $Z \rightarrow ll$  decay. The contribution from  $Z$ +jet is treated in Section 6.2.

### 6.1.1 Channel $\tau_\mu\tau_\mu$ , $\tau_e\tau_e$

The  $Z \rightarrow \mu\mu$  background distribution for the  $\tau_\mu\tau_\mu$  channel is obtained by scaling the simulated mass distributions in such a way to obtain the same amount of candidates as in data under the  $Z$ -peak,  $80 < m(\tau_\mu\tau_\mu) < 100 \text{ GeV}/c^2$ . The  $Z \rightarrow ee$  background distribution in the  $\tau_e\tau_e$  channel is obtained in a similar fashion, but the region used for normalization is

## Chapter 6. Background Estimation

enlarged to  $70 < m(\tau_\mu\tau_\mu) < 100 \text{ GeV}/c^2$ . In order to account for other kinds of background, the number of same-sign di-electron candidates in the peak region is subtracted from the data distribution, prior to normalization. Note that the presence of genuine  $Z \rightarrow \tau\tau$  inside the normalization region is negligible.

The mass distributions are shown in Fig. 6.1, with the area under the  $Z$ -peak normalized to data. The results are summarized in Table 6.1, with the associated statistical uncertainty.

**Table 6.1** – Determination of the  $Z \rightarrow ll$  background in  $\tau_\mu\tau_\mu$  and  $\tau_e\tau_e$  channels.

Background	$Z \rightarrow \mu\mu$	$Z \rightarrow ee$
Z-peak range for normalization [ $\text{GeV}/c^2$ ]	[80,100]	[70,100]
Number of candidates in data inside Z-peak	$901.0 \pm 30.0$	$437.0 \pm 20.9$
Estimation of the $Z \rightarrow ll$ background in signal region	$249.7 \pm 8.8$	$420.8 \pm 25.3$

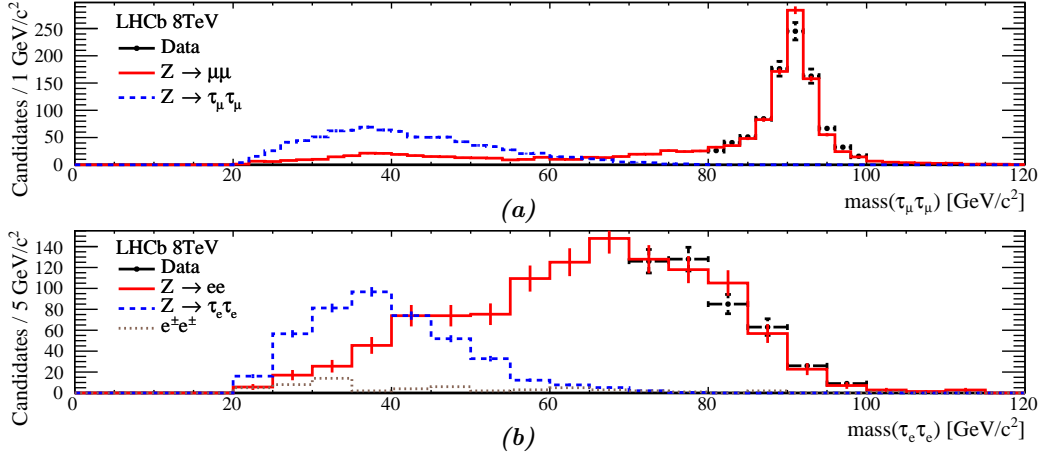


**Figure 6.1** – Mass distribution for (a) the  $Z \rightarrow \mu\mu$  background after the  $\tau_\mu\tau_\mu$  candidate selection, and (b) the  $Z \rightarrow ee$  background in  $\tau_e\tau_e$  candidates. The number of candidates in data (black dot) under the  $Z$  peak is used to normalize the  $Z \rightarrow ll$  background from simulated events (red). The distribution from  $Z \rightarrow \tau\tau$  (blue) is shown for reference with an arbitrary normalization.

### 6.1.2 Channel $\tau_\mu\tau_{h1}$ , $\tau_e\tau_{h1}$ , $\tau_\mu\tau_e$

The  $Z \rightarrow \mu\mu$  process can be a background to the  $\tau_\mu\tau_{h1}$  channel when one of the two muons is misidentified as a charged hadron (denoted as  $\mu \rightarrow h$ ). The estimation technique is to use the number of di-muon in data passing the  $\tau_\mu\tau_{h1}$  selection, subsequently scaled by the muon misidentification rate.

The expected number of fake candidates,  $N_{Z \rightarrow \mu\mu}^{\tau_\mu\tau_{h1}}$ , is calculated from the following expression:

$$N_{Z \rightarrow \mu\mu}^{\tau_\mu\tau_{h1}} = \sum^{\mu^- \mu^+} \epsilon_{\mu \rightarrow h}^{\tau_\mu\tau_{h1}}(l_1, l_2) - \sum^{\mu^\pm \mu^\pm} \epsilon_{\mu \rightarrow h}^{\tau_\mu\tau_{h1}}(l_1, l_2)$$

$$\epsilon_{\mu \rightarrow h}^{\tau_\mu\tau_{h1}}(l_1, l_2) = \epsilon_{\mu \rightarrow h}(l_2)\delta^{\tau_\mu\tau_{h1}}(l_1, l_2) + \epsilon_{\mu \rightarrow h}(l_1)\delta^{\tau_\mu\tau_{h1}}(l_2, l_1)$$

where  $\epsilon_{\mu \rightarrow h}^{\tau_\mu\tau_{h1}}(l_1, l_2)$  is the misidentification probability, when one of the muons is identified as a charged hadron, passing the selection for the  $\tau_\mu\tau_{h1}$  channel. This rate is thus composed from two contributions whether the first or second muon is misidentified. The misidentification rate for single muon is denoted as  $\epsilon_{\mu \rightarrow h}(l)$ . The term  $\delta^{\tau_\mu\tau_{h1}}(l_1, l_2)$  has a value of one when the di-muons satisfies the requirement of the  $\tau_\mu\tau_{h1}$  selection, with the first muon  $l_1$  satisfies  $\tau_\mu$  requirement, and the second muon  $l_2$  satisfies  $\tau_{h1}$  requirement. The double-counting correction term is negligible.

The misidentification rate for the single muon is determined from simulation and from a tag-and-probe analysis applied to real data and to the  $Z \rightarrow \mu\mu$  simulated sample as well. For the tag-and-probe analysis, the  $Z \rightarrow \mu\mu$  enriched sample is selected with one muon and a charged track. The probe is subsequently checked against the hadron identification. The results from three calculations are compared and found to be in agreement within their uncertainties, as shown in Fig. 6.2. More details on the misidentification rate validation are given in appendix B.

For the calculation of the background from  $\mu \rightarrow h$  misidentification, the data is analysed with identical selections as for  $\tau_\mu\tau_{h1}$ , with exception of the hadron identification criteria, which is replaced by a muon. The summation  $\sum^{\mu^- \mu^+}$  is performed over the selected opposite-sign (OS) di-muon sample where the misidentification rate is evaluated for each di-muon as a function of  $p_T$ . A similar procedure is performed but from the same-sign (SS) di-muon sample,  $\sum^{\mu^\pm \mu^\pm}$ , and result is subtracted from the opposite-sign one, to approximately account for the impurity in the di-muon selection.

The results from the computation are summarized in Table 6.2. The misidentification probability for each di-muon is also used to re-weight the distributions in a later stage, notably for the invariant mass distributions of Fig. 6.5 (more details in appendix C).

The associated uncertainty is calculated from the uncertainty on the misidentification rate (statistical uncertainty of used samples), and from the statistical uncertainty of selected di-muon samples, from both opposite-sign and same-sign selections.

Similarly,  $Z \rightarrow ee$  event can arise as a fake  $\tau_e\tau_{h1}$  candidate when one of electrons is misidentified as a charged hadron (denoted as  $e \rightarrow h$ ). The same technique as the one outlined above is used, where the  $e \rightarrow h$  rate is obtained from the simulated sample,

## Chapter 6. Background Estimation

and it is applied to (opposite-sign) di-electron sample selected from data. The same-sign counterpart is again used to subtract contamination from other processes.

For the channel  $\tau_\mu\tau_e$ , the same technique is also applied to obtain the fake candidate from  $Z \rightarrow \mu\mu$  (where one muon is misidentified as an electron, denoted as  $\mu \rightarrow e$ ) and  $Z \rightarrow ee$  (where one electron is misidentified as a muon, denoted as  $e \rightarrow \mu$ ). Both  $\mu \rightarrow e$  and  $e \rightarrow \mu$  rates are obtained from the simulated samples. The sum of both contributions is used as a total background in this channel. The misidentification probabilities as a function of the lepton  $p_T$  obtained from the simulation are shown in Fig. 6.3.

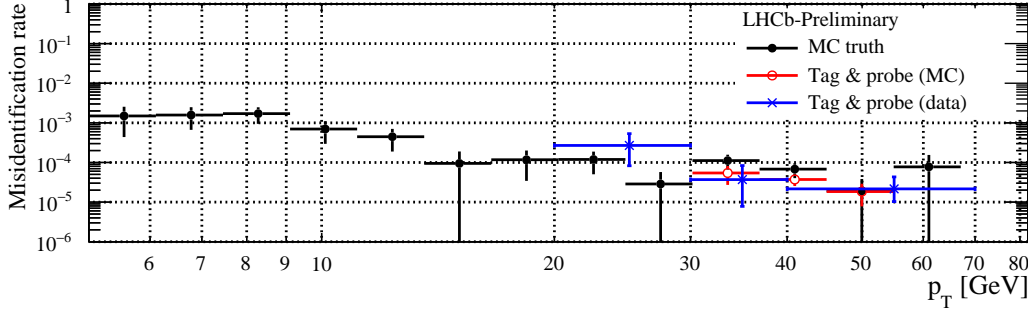


**Figure 6.2** – The  $\mu \rightarrow h$  misidentification probability as a function of the muon  $p_T$ . The results are from the simulated sample (black), and from the tag-and-probe in simulated sample (red), and in data (blue).

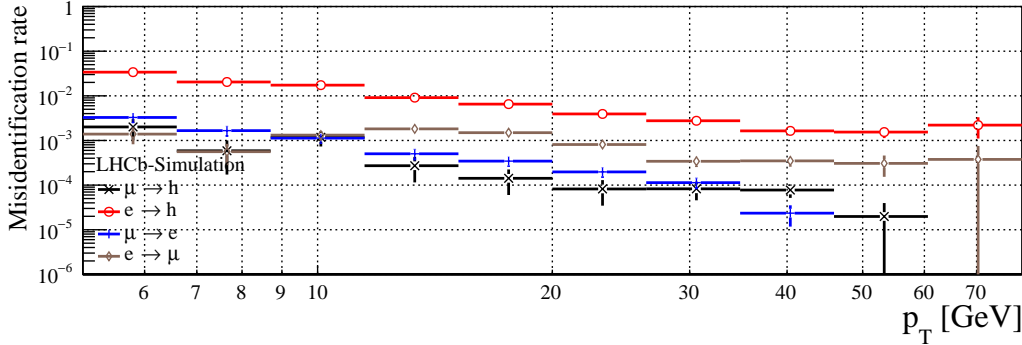


**Figure 6.3** – Summary of the lepton misidentification probabilities as a function of the lepton  $p_T$  which are used in the computation of the background from  $Z \rightarrow ll$  decays. The values are inferred from simulation: (black) muon misidentified as charged hadron, (red) electron misidentified as charged hadron, (blue) muon misidentified as electron, (brown) electron misidentified as muon.

**Table 6.2** – Estimation of the  $Z \rightarrow ll$  background for the  $\tau_\mu\tau_{h1}$ ,  $\tau_e\tau_{h1}$ , and  $\tau_\mu\tau_e$  channels. For illustration, the “Mean mis-id” column gives the lepton misidentification averaged over the  $p_T$  range of the selected di-lepton.

Channel	Background	Selected fake	SS/OS [%]	Expected $Z \rightarrow ll$	Mean mis-id [%]
$\tau_\mu\tau_{h1}$	$Z \rightarrow \mu\mu$	18756	$0.18 \pm 0.12$	$1.23 \pm 0.53$	$0.007 \pm 0.003$
$\tau_\mu\tau_e$	$Z \rightarrow \mu\mu$	112425	$0.20 \pm 0.11$	$5.41 \pm 2.41$	$0.005 \pm 0.002$
$\tau_e\tau_{h1}$	$Z \rightarrow ee$	7005	$1.93 \pm 0.39$	$16.09 \pm 2.18$	$0.234 \pm 0.031$
$\tau_\mu\tau_e$	$Z \rightarrow ee$	44717	$1.61 \pm 0.52$	$19.94 \pm 4.79$	$0.045 \pm 0.011$

## 6.2 QCD and $Vj$ Processes

The background from QCD events,  $N_{\text{QCD}}$ , and the one originated from the decay of a single electroweak boson in association with a jet ( $W+\text{jet}$ ,  $Z+\text{jet}$ ),  $N_{Vj}$ , are estimated by a data-driven method. As a first step, the same-sign di-tau candidates are used as a control sample and are selected from the data using the same criteria as signal, but requiring two tau candidates to have identical electric charge. The total number of same-sign candidates in the data is assumed to be mainly from QCD and  $Vj$  process, as well as a trace amount from the cross-feed  $Z \rightarrow \tau\tau$ :

$$N^{\text{SS}} = N_{\text{QCD}}^{\text{SS}} + N_{Vj}^{\text{SS}} + N_{Z \rightarrow \tau\tau}^{\text{SS}}$$

These processes are expected to be dominant. This is checked using simulated events, as listed in Table 6.8. The amount of  $N_{Z \rightarrow \tau\tau}^{\text{SS}}$  is only used to obtain the correct amount of other two species. The number of expected opposite-sign candidates for the background process, indexed by  $i$ , is subsequently expressed as:

$$N_i^{\text{OS}} = r_i \cdot N_i^{\text{SS}}$$

where  $r_i$  is determined separately for each process  $i$ . The procedures to determine  $N_i^{\text{SS}}$  and  $r_i$  will be discussed below.

In order to separate the contribution from each processes, the distribution of  $p_{\text{T}}(\tau_1) - p_{\text{T}}(\tau_2)$  is used for all di-tau channels, where  $\tau_{1(2)}$  denotes the first (second) tau of the di-tau candidate. This variable has been used in a previous analysis [107], and provides a good discriminant between those processes.

The distribution template for the QCD process is obtained from the data using an *anti-isolation* selection on both tau candidates, requiring  $(\vec{p}_{\text{cone}})_{\text{T}} > 10 \text{ GeV}/c$  and  $\hat{I}_{p_{\text{T}}} < 0.6$ , whilst keeping the other cuts unchanged. The same selection is also applied on the simulated samples to verify that there are only QCD processes selected by this cut (results can be found in Table C.5).

For the  $Vj$  process, the distribution template is obtained from the simulation. The selection criteria are identical to the main analysis. The distribution of  $p_{\text{T}}(\tau_1) - p_{\text{T}}(\tau_2)$  in  $W+\text{jet}$  and  $Z+\text{jet}$  from simulation are similar enough, so only the distribution from  $W+\text{jet}$  is used (by virtue of the larger simulated sample from central production). The  $W(\rightarrow \mu\nu\mu) + \text{jet}$  sample is used in the fitting procedure relative to the  $\tau_{\mu}\tau_{\mu}$ ,  $\tau_{\mu}\tau_{h1}$ , and  $\tau_{\mu}\tau_{h3}$  channels, and the  $W(\rightarrow e\nu_e) + \text{jet}$  sample in the case of  $\tau_e\tau_e$ ,  $\tau_e\tau_{h1}$ , and  $\tau_e\tau_{h3}$ . Both samples are needed for the  $\tau_{\mu}\tau_e$  channel.

For the same-sign  $Z \rightarrow \tau\tau$  template, the distribution from a simulated sample is used. Various histogram bin sizes for  $p_{\text{T}}(\tau_1) - p_{\text{T}}(\tau_2)$  are tested as this strongly affects the convergence of the fit<sup>1</sup>. Among those leading to convergence, the compatibility with the expected same-sign candidates given in Table 6.8 is checked. The fitting is compatible if the number of same-sign  $Vj$  background matches the expected number from simulation within 2 standard deviations. After the incompatible ones are removed, the one with lowest  $\chi^2$  is

<sup>1</sup>The fit is performed by the ROOT algorithm `TFractionFitter` [126].

## Chapter 6. Background Estimation

chosen. In order to ensure better fitting convergence, the fraction of same-sign  $Z \rightarrow \tau\tau$  is constrained to lie within 2 standard deviations from the expected number from simulation. The results for all the channels are shown in Table 6.3 and Fig. 6.4 (more details, including correlation matrices of fit results, are available in appendix C, Table C.3).

The factor  $r$  is obtained by dividing number of the selected opposite-sign candidates by the number of the selected same-sign candidates for each distribution template used. For  $r_{\text{QCD}}$ , the number  $N_{\text{QCD}}^{\text{OS}}$ ,  $N_{\text{QCD}}^{\text{SS}}$  are taken from data using the anti-isolation selection previously defined. In the case of  $r_{Vj}$ , it is calculated from simulation as a weighted-average of the  $r$  values for  $W$ +jet and  $Z$ +jet;

$$r_{Vj} = \frac{r_{Wj}N_{Wj}^{\text{SS}} + r_{Zj}N_{Zj}^{\text{SS}}}{N_{Wj}^{\text{SS}} + N_{Zj}^{\text{SS}}}; \quad r_{Wj} = \frac{N_{Wj}^{\text{OS}}}{N_{Wj}^{\text{SS}}}; \quad r_{Zj} = \begin{cases} 1, & \text{if channel } \tau_\mu\tau_\mu, \tau_e\tau_e \\ N_{Zj}^{\text{OS}}/N_{Zj}^{\text{SS}} & \text{otherwise} \end{cases}$$

where  $N_{Wj,[Zj]}^{\text{OS(SS)}}$  is the expected number of opposite(same)-sign  $W$ +jet [ $Z$ +jet] candidates obtained from simulation normalized to the integrated luminosity used. This allows the effect of systematic uncertainty to be minimized. The value of  $r_{Zj}$  is estimated to be unity in channels  $\tau_\mu\tau_\mu, \tau_e\tau_e$  as the computation from the simulated sample is impractical. In case of insufficient statistics in the simulated sample, the  $r_{Vj}$  factor is calculated without the isolation requirement.

For the channel  $\tau_\mu\tau_e$ , two  $r_{Vj}$  factors are calculated. One from the  $W(\rightarrow \mu\nu_\mu) + \text{jet}$  template and one using  $W(\rightarrow e\nu_e) + \text{jet}$  template. The expected number of  $Vj$  candidate in this channel is calculated from the sum of both projections. A check on the simulated sample was performed to ensure that there is no double-counting of candidates (The list of the  $r_i$  values calculated for QCD and  $Vj$  processes for each channel is given in Tables C.2 and C.7).

The systematic uncertainty is taken from the fitting uncertainty on  $N^{\text{SS}}$ , combined with the uncertainty on  $r_i$  which is statistical. The correlation between fitting variables are taken into account during the uncertainty propagation.

**Table 6.3** – Results of the fit of the  $p_{\text{T}}(\tau_1) - p_{\text{T}}(\tau_2)$  variable for same-sign di-tau candidates. “hard  $e$ ” and “hard  $\mu$ ” indicates which of the two particles has the larger  $p_{\text{T}}$ .

Channel	$N^{\text{SS}}$	$\chi^2/\text{ndf}$	$N_{\text{QCD}}^{\text{SS}}$	$N_{Vj}^{\text{SS}}$	$N_{Z \rightarrow \tau\tau}^{\text{SS}}$	$r_{\text{QCD}}$	$r_{Vj}$
$\tau_\mu\tau_\mu$	50	0.827	$39.8 \pm 7.8$	$9.8 \pm 5.7$	$0.4 \pm 0.4$	$1.30 \pm 0.05$	$1.44 \pm 0.11$
$\tau_\mu\tau_{h1}$	293	0.978	$232.1 \pm 18.9$	$60.9 \pm 16.4$	$0.0 \pm 0.8$	$1.02 \pm 0.01$	$2.37 \pm 0.30$
$\tau_\mu\tau_{h3}$	25	0.582	$20.6 \pm 5.1$	$4.4 \pm 3.0$	$0.0 \pm 1.1$	$1.03 \pm 0.03$	$1.14 \pm 0.11$
$\tau_e\tau_e$	58	1.068	$40.6 \pm 8.7$	$16.4 \pm 7.4$	$1.0 \pm 0.7$	$1.04 \pm 0.06$	$1.05 \pm 0.08$
$\tau_e\tau_{h1}$	380	0.879	$331.4 \pm 22.4$	$46.7 \pm 13.2$	$1.9 \pm 1.3$	$1.00 \pm 0.01$	$1.46 \pm 0.07$
$\tau_e\tau_{h3}$	28	0.625	$19.8 \pm 5.2$	$8.2 \pm 4.1$	$0.0 \pm 0.8$	$0.94 \pm 0.05$	$1.37 \pm 0.23$
$\tau_\mu\tau_e$ (hard $e$ )	186	0.528	$151.1 \pm 15.6$	$15.1 \pm 8.3$	$0.0 \pm 3.5$	$1.06 \pm 0.02$	$2.32 \pm 0.49$
$\tau_\mu\tau_e$ (hard $\mu$ )				$19.9 \pm 7.9$			$1.53 \pm 0.26$

## 6.2. QCD and $V_j$ Processes

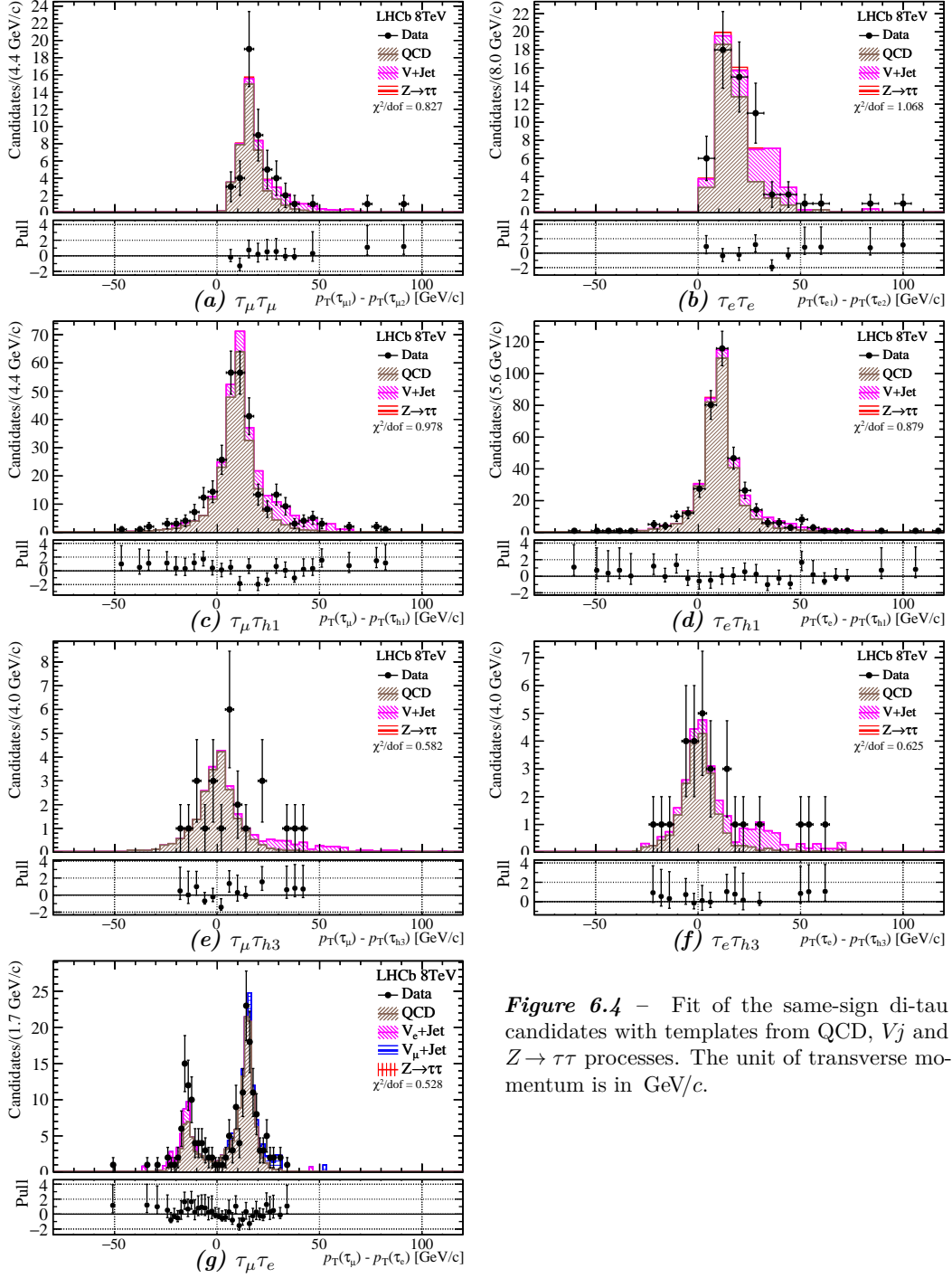


**Figure 6.4** – Fit of the same-sign di-tau candidates with templates from QCD,  $V_j$  and  $Z \rightarrow \tau\tau$  processes. The unit of transverse momentum is in  $\text{GeV}/c$ .

### 6.3 $t\bar{t}$ , $WW$ , $WZ$ , $Z \rightarrow b\bar{b}$

The contributions to the background from  $t\bar{t}$ ,  $WW$ ,  $WZ$ ,  $Z \rightarrow b\bar{b}$ , are expected to be very small with respect to the other sources of backgrounds previously discussed. As such, the estimations are taken from simulation.

### 6.4 $Z \rightarrow \tau\tau$ Cross-feed

Some of the selected di-tau candidates may not truly be originated from the selected channel. For instance, a  $\tau_{h1}$  candidate may be falsely selected from a partially reconstructed  $\tau_{h3}$  candidate. Simulated  $Z \rightarrow \tau\tau$  are used to obtain the fraction of events from a process that is reconstructed as a given channel. The list of fractions is shown in Table 6.4, with statistical uncertainties.

**Table 6.4** –  $Z \rightarrow \tau\tau$  cross-feed probabilities from a given channel to another, given in percentage. Each column represents the di-tau final-state under study, whilst each row represents the true channel of origin. The last row shows the total percentage of cross-feed. The contributions inferior to 0.1% are omitted.

Channel Origin	$\tau_\mu\tau_\mu$	$\tau_\mu\tau_{h1}$	$\tau_\mu\tau_{h3}$	$\tau_e\tau_e$	$\tau_e\tau_{h1}$	$\tau_e\tau_{h3}$	$\tau_\mu\tau_e$
$\tau_\mu\tau_\mu$	$98.8 \pm 0.3$	-	-	$0.2 \pm 0.2$	-	$0.2 \pm 0.2$	-
$\tau_\mu\tau_{h1}$	$1.1 \pm 0.3$	$97.8 \pm 0.2$	$7.0 \pm 0.8$	$0.2 \pm 0.2$	-	$0.2 \pm 0.2$	$4.0 \pm 0.3$
$\tau_\mu\tau_{h3}$	$0.1 \pm 0.1$	$1.0 \pm 0.2$	$92.2 \pm 0.9$	$0.2 \pm 0.2$	-	$0.2 \pm 0.2$	-
$\tau_e\tau_e$	-	-	-	$90.8 \pm 1.4$	$0.2 \pm 0.1$	$0.2 \pm 0.2$	-
$\tau_e\tau_{h1}$	-	-	-	$8.6 \pm 1.4$	$96.3 \pm 0.4$	$6.8 \pm 1.4$	$0.9 \pm 0.2$
$\tau_e\tau_{h3}$	-	-	-	$0.4 \pm 0.3$	$1.0 \pm 0.2$	$90.9 \pm 1.5$	-
$\tau_\mu\tau_e$	-	$0.4 \pm 0.1$	-	$0.4 \pm 0.3$	-	$0.2 \pm 0.2$	$95.0 \pm 0.3$
$\tau_{h1}\tau_{h1}$	-	$0.8 \pm 0.1$	$0.2 \pm 0.1$	$0.4 \pm 0.3$	$2.5 \pm 0.4$	$0.2 \pm 0.2$	-
$\tau_{h1}\tau_{h3}$	-	-	$0.8 \pm 0.3$	$0.2 \pm 0.2$	-	$2.4 \pm 0.9$	-
$\tau_{h3}\tau_{h3}$	-	-	-	$0.2 \pm 0.2$	-	$0.2 \pm 0.2$	-
Total	$1.18 \pm 0.28$	$2.25 \pm 0.22$	$7.81 \pm 0.87$	$9.24 \pm 1.44$	$3.71 \pm 0.44$	$9.07 \pm 1.55$	$4.97 \pm 0.34$

### 6.5 Summary

The estimated number of background events is given in Table 6.5, as well as the observed number of candidates in data. The last line gives the estimated  $Z \rightarrow \tau\tau$  signal. The uncertainty on the signal is given by the uncertainties on the backgrounds, and the statistical uncertainty on the observed events; the correlations are accounted for. The corresponding di-tau mass distributions are shown in Fig. 6.5. The complete set of figures is available in appendix D.

The mass distributions are also shown with equiprobable bins in Fig. 6.6. The optimal number of bins for each channel follows the computation in [127], and the  $\chi^2$  is computed



as

$$\chi^2 = \sum_i^{\text{bins}} \left( \frac{N_i^{\text{obs}} - N_i^{\text{exp}}}{\sigma_i^{\text{obs}} \oplus \sigma_i^{\text{exp}}} \right)^2$$

where the summation is over each bin  $i$ , containing the number of observed candidates  $N_i^{\text{obs}} \pm \sigma_i^{\text{obs}}$ , and the sum of expected candidates  $N_i^{\text{exp}} \pm \sigma_i^{\text{exp}}$  over all processes. The uncertainty  $\sigma^{\text{obs}}$  is statistical and  $\sigma^{\text{exp}}$  is obtained from the previous table, assuming in each process that their relative error is independent of the bins. The results are summarized in Table 6.6.

**Table 6.5** – Estimated number of backgrounds candidates, number of observed candidates, and, in the last row, the inferred number of signal candidates. The uncertainties on the signal are statistical and systematic combined.

	$\tau_\mu\tau_\mu$	$\tau_\mu\tau_{h1}$	$\tau_\mu\tau_{h3}$	$\tau_e\tau_e$	$\tau_e\tau_{h1}$	$\tau_e\tau_{h3}$	$\tau_\mu\tau_e$
$Z \rightarrow ll$	$249.7 \pm 8.8$	$1.2 \pm 0.5$	$0.0 \pm 0.0$	$420.8 \pm 25.3$	$16.1 \pm 2.2$	$0.0 \pm 0.0$	$25.3 \pm 5.4$
QCD	$50.9 \pm 10.2$	$235.8 \pm 19.3$	$21.2 \pm 5.3$	$42.7 \pm 8.8$	$330.8 \pm 22.8$	$19.4 \pm 5.1$	$160.0 \pm 16.9$
$Vj$	$12.7 \pm 7.4$	$144.2 \pm 43.0$	$5.1 \pm 3.4$	$5.8 \pm 2.7$	$68.3 \pm 19.7$	$10.1 \pm 5.8$	$65.3 \pm 25.7$
VV	$0.2 \pm 0.1$	$1.2 \pm 0.2$	$0.2 \pm 0.1$	$0.2 \pm 0.1$	$0.8 \pm 0.1$	$0.2 \pm 0.1$	$10.0 \pm 0.5$
$t\bar{t}$	$1.0 \pm 0.2$	$2.2 \pm 0.2$	$0.6 \pm 0.1$	$0.2 \pm 0.0$	$0.7 \pm 0.1$	$0.1 \pm 0.0$	$5.5 \pm 0.2$
$Z \rightarrow b\bar{b}$	$0.8 \pm 0.4$	$0.3 \pm 0.2$	$0.1 \pm 0.1$	$0.1 \pm 0.1$	$0.3 \pm 0.2$	$0.1 \pm 0.1$	$0.3 \pm 0.2$
Cross-feed	$4.5 \pm 1.1$	$22.2 \pm 2.5$	$13.9 \pm 2.0$	$13.0 \pm 3.9$	$16.5 \pm 2.4$	$7.3 \pm 1.7$	$52.5 \pm 4.2$
Backgrounds	$319.9 \pm 12.7$	$407.1 \pm 37.5$	$41.1 \pm 5.3$	$482.7 \pm 24.2$	$433.5 \pm 22.0$	$37.2 \pm 5.8$	$318.9 \pm 23.6$
Observed	696	1373	205	610	861	110	1322
$Z \rightarrow \tau\tau$	$376.1 \pm 29.0$	$965.9 \pm 52.1$	$163.9 \pm 14.2$	$127.3 \pm 32.9$	$427.5 \pm 35.8$	$72.8 \pm 11.1$	$1003.1 \pm 41.8$

**Table 6.6** – Result of the  $\chi^2$  test between the observed and expected di-tau candidates using equiprobable binning. The two last rows give the purity of the signal in the analysis.

	$\tau_\mu\tau_\mu$	$\tau_\mu\tau_{h1}$	$\tau_\mu\tau_{h3}$	$\tau_e\tau_e$	$\tau_e\tau_{h1}$	$\tau_e\tau_{h3}$	$\tau_\mu\tau_e$
ndf	32	28	13	12	23	10	28
$\chi^2/\text{ndf}$	0.75	1.22	0.81	3.48	1.54	2.12	1.99
$S/B$	1.18	2.37	3.99	0.26	0.99	1.96	3.14
$S/\sqrt{(S+B)}$	14.26	26.07	11.45	5.16	14.57	6.94	27.59

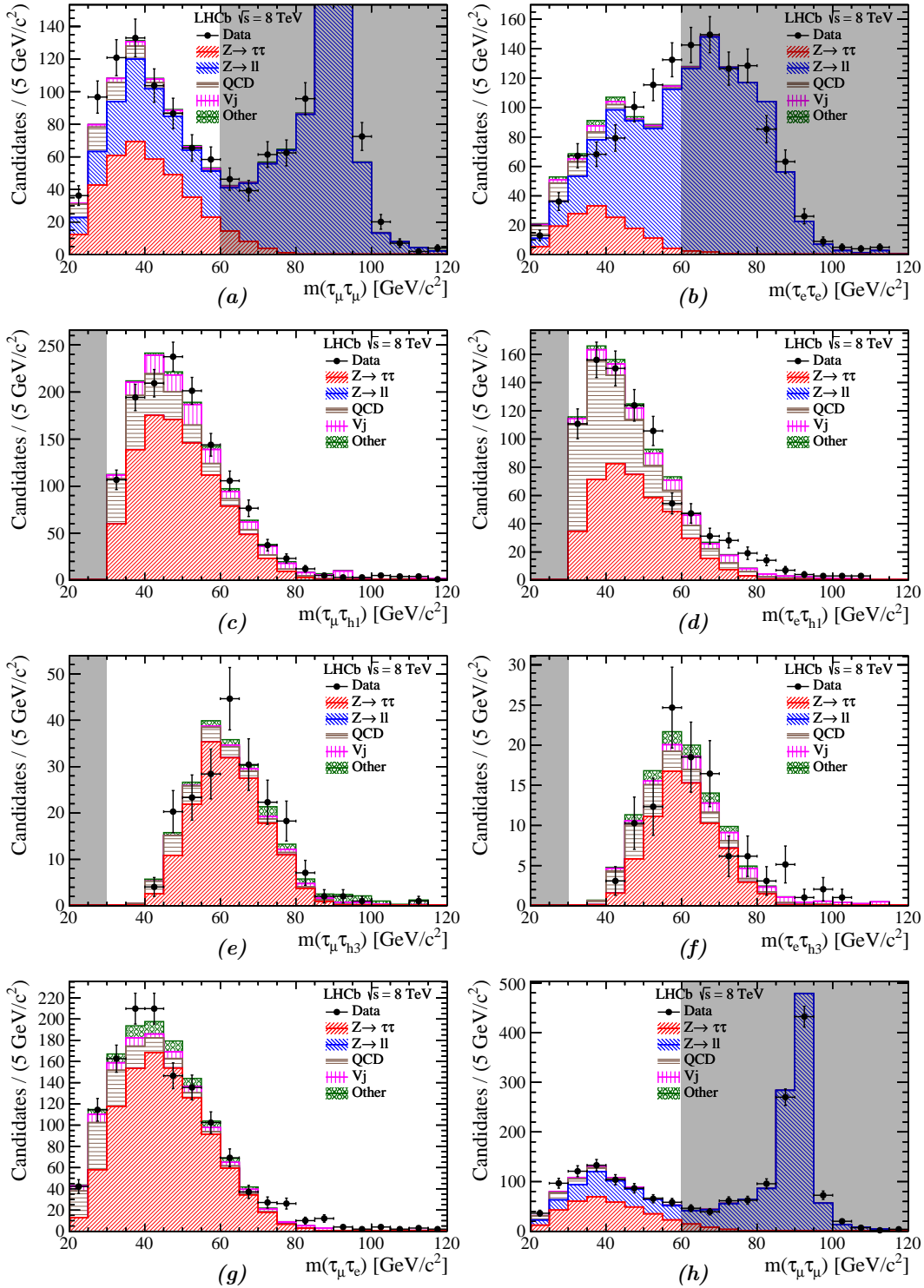


**Figure 6.5** – Invariant mass of the di-tau candidates. The contributions from each process is superposed. In grey, the areas which are excluded from the final computation of the signal. In (h),  $\tau_\mu\tau_\mu$  channel with full  $Z$ -peak normalization region shown.

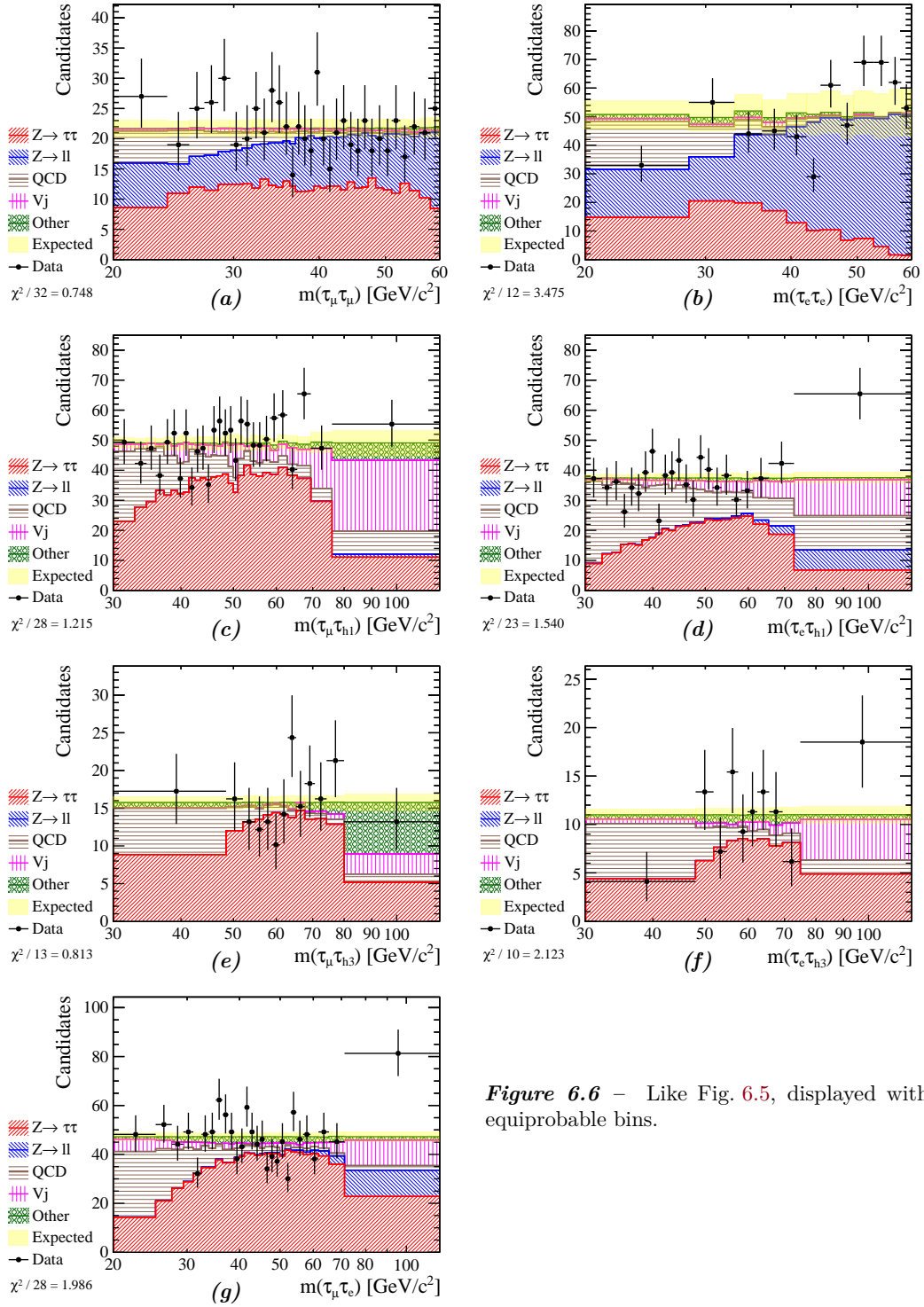


Figure 6.6 – Like Fig. 6.5, displayed with equiprobable bins.

**Table 6.7** – The numbers of expected opposite-sign di-tau candidates passing the analysis selection from simulation, normalized to the integrated luminosity (the raw number of selected candidates in bracket). The uncertainty is only statistical. In the last row, the number of observed candidates from data is given for comparison.

Process	ID	$\tau_\mu\tau_\mu$	$\tau_\mu\tau_{H1}$	$\tau_\mu\tau_{H3}$	$\tau_e\tau_e$	$\tau_e\tau_{H1}$	$\tau_e\tau_{H3}$	$\tau_e\tau_{H3}$	$\tau_\mu\tau_e$
$Z \rightarrow \tau\tau$	42100000	$278.6^{+8.5}_{-8.4}$ (1800)	$750.8^{+17.7}_{-17.6}$ (4850)	$151.2^{+5.7}_{-5.6}$ (977)	$66.1^{+3.6}_{-3.4}$ (427)	$303.7^{+9.0}_{-8.9}$ (1962)	$56.8^{+3.3}_{-3.1}$ (367)	$631.3^{+15.4}_{-15.3}$ (4078)	
$Z \rightarrow \mu\mu$	42112011	$239.0^{+9.9}_{-9.8}$ (1425)	$25.3^{+2.4}_{-2.2}$ (151)	$1.5^{+0.7}_{-0.5}$ (9)	$0.0^{+0.3}_{-0.3}$ (0)	$0.0^{+0.3}_{-0.3}$ (0)	$0.0^{+0.3}_{-0.3}$ (0)	$21.5^{+2.2}_{-2.0}$ (128)	
$Z \rightarrow ee$	42122011	$0.0^{+2.6}_{-0.0}$ (0)	$0.0^{+2.6}_{-0.0}$ (0)	$0.0^{+2.6}_{-0.0}$ (0)	$420.2^{+28.9}_{-27.6}$ (300)	$33.6^{+8.4}_{-6.9}$ (24)	$1.4^{+3.2}_{-1.2}$ (1)	$18.2^{+6.6}_{-5.0}$ (13)	
$Z \rightarrow b\bar{b}$	42150000	$0.7^{+0.4}_{-0.3}$ (6)	$0.2^{+0.3}_{-0.2}$ (2)	$0.0^{+0.2}_{-0.0}$ (0)	$0.0^{+0.2}_{-0.0}$ (0)	$0.2^{+0.2}_{-0.2}$ (2)	$0.0^{+0.2}_{-0.0}$ (0)	$0.2^{+0.3}_{-0.2}$ (2)	
$Z(\rightarrow\mu\mu) + \text{jet}$	42112022	$83.7^{+4.7}_{-4.5}$ (516)	$14.3^{+1.7}_{-1.6}$ (88)	$0.8^{+0.5}_{-0.4}$ (5)	$0.0^{+0.3}_{-0.0}$ (0)	$0.0^{+0.3}_{-0.0}$ (0)	$0.0^{+0.3}_{-0.0}$ (0)	$21.2^{+2.1}_{-2.0}$ (131)	
$W(\rightarrow\tau\nu_\tau) + \text{jet}$	42300010	$0.0^{+5.2}_{-0.0}$ (0)	$22.6^{+11.2}_{-7.9}$ (8)	$0.0^{+5.2}_{-0.0}$ (0)	$0.0^{+5.2}_{-0.0}$ (0)	$0.0^{+5.2}_{-0.0}$ (0)	$2.8^{+6.5}_{-2.3}$ (1)	$2.8^{+6.5}_{-2.3}$ (1)	
$W(\rightarrow\mu\nu_\mu) + \text{jet}$	42311011	$5.5^{+2.5}_{-1.8}$ (9)	$115.2^{+9.8}_{-9.2}$ (188)	$8.6^{+3.0}_{-2.3}$ (14)	$0.0^{+1.1}_{-0.0}$ (0)	$0.0^{+1.1}_{-0.0}$ (0)	$0.0^{+1.1}_{-0.0}$ (0)	$19.0^{+4.1}_{-3.4}$ (31)	
$W \rightarrow e\nu_e$	42321000	$0.0^{+1.7}_{-0.0}$ (0)	$0.0^{+1.7}_{-0.0}$ (0)	$0.0^{+1.7}_{-0.0}$ (0)	$4.7^{+3.2}_{-2.0}$ (5)	$73.9^{+9.4}_{-8.5}$ (78)	$8.5^{+3.9}_{-2.8}$ (9)	$4.7^{+3.2}_{-2.0}$ (5)	
$W(\rightarrow e\nu_e) + \text{jet}$	42321010	$0.0^{+6.4}_{-0.0}$ (0)	$0.0^{+6.4}_{-0.0}$ (0)	$0.0^{+6.4}_{-0.0}$ (0)	$6.9^{+9.1}_{-4.5}$ (2)	$62.3^{+18.5}_{-14.7}$ (18)	$3.5^{+8.0}_{-2.9}$ (1)	$3.5^{+8.0}_{-2.9}$ (1)	
$W(\rightarrow\mu\nu_\mu) + \text{jet}(\rightarrow\mu\dots)$	42311012	$5.4^{+0.4}_{-0.4}$ (195)	$0.0^{+0.1}_{-0.0}$ (0)	$0.0^{+0.1}_{-0.0}$ (0)	$0.0^{+0.1}_{-0.0}$ (0)	$0.0^{+0.1}_{-0.0}$ (0)	$0.0^{+0.1}_{-0.0}$ (0)	$0.0^{+0.1}_{-0.0}$ (0)	
$c\bar{c} \rightarrow e\dots$	49021004	$0.0^{+0.9}_{-0.0}$ (0)	$0.0^{+0.9}_{-0.0}$ (0)	$0.0^{+0.9}_{-0.0}$ (0)	$0.0^{+0.9}_{-0.0}$ (0)	$0.0^{+0.9}_{-0.0}$ (0)	$0.0^{+0.9}_{-0.0}$ (0)	$0.0^{+0.9}_{-0.0}$ (0)	
$c\bar{c} \rightarrow \mu\dots$	49011004	$9.4^{+2.9}_{-2.3}$ (19)	$31.2^{+4.3}_{-5.0}$ (63)	$21.3^{+4.3}_{-3.9}$ (43)	$0.0^{+0.9}_{-0.0}$ (0)	$0.0^{+0.9}_{-0.0}$ (0)	$0.0^{+0.9}_{-0.0}$ (0)	$11.9^{+3.2}_{-2.7}$ (24)	
$b\bar{b} \rightarrow e\dots$	49021005	$0.0^{+4.8}_{-0.0}$ (0)	$0.0^{+4.8}_{-0.0}$ (0)	$0.0^{+4.8}_{-0.0}$ (0)	$15.7^{+9.4}_{-6.3}$ (6)	$7.9^{+7.7}_{-4.3}$ (3)	$2.6^{+6.0}_{-2.2}$ (1)	$55.0^{+15.0}_{-12.1}$ (21)	
$b\bar{b} \rightarrow \mu\dots$	49011005	$141.6^{+22.4}_{-19.7}$ (55)	$67.0^{+16.1}_{-13.3}$ (26)	$10.3^{+8.2}_{-4.9}$ (4)	$0.0^{+4.7}_{-0.0}$ (0)	$0.0^{+4.7}_{-0.0}$ (0)	$0.0^{+4.7}_{-0.0}$ (0)	$61.8^{+15.5}_{-12.7}$ (24)	
$t\bar{t}$	41900010	$1.0^{+0.2}_{-0.2}$ (259)	$2.2^{+0.2}_{-0.2}$ (379)	$0.6^{+0.1}_{-0.1}$ (109)	$0.2^{+0.0}_{-0.0}$ (0)	$0.7^{+0.1}_{-0.1}$ (0)	$0.1^{+0.0}_{-0.0}$ (0)	$5.5^{+0.2}_{-0.2}$ (105)	
$WW \rightarrow \ell\ell\dots$	41922002	$0.0^{+0.0}_{-0.0}$ (2)	$0.0^{+0.0}_{-0.0}$ (0)	$0.0^{+0.0}_{-0.0}$ (0)	$0.0^{+0.0}_{-0.0}$ (0)	$0.0^{+0.0}_{-0.0}$ (0)	$0.0^{+0.0}_{-0.0}$ (0)	$8.5^{+0.3}_{-0.3}$ (1913)	
$WW \rightarrow \ell\dots$	42021000	$0.2^{+0.1}_{-0.1}$ (9)	$1.1^{+0.2}_{-0.2}$ (47)	$0.2^{+0.1}_{-0.1}$ (9)	$0.2^{+0.1}_{-0.1}$ (7)	$0.7^{+0.2}_{-0.1}$ (30)	$0.2^{+0.1}_{-0.1}$ (8)	$9.4^{+0.5}_{-0.5}$ (400)	
$WZ \rightarrow \ell\dots$	42021001	$0.0^{+0.0}_{-0.0}$ (5)	$0.1^{+0.0}_{-0.0}$ (19)	$0.0^{+0.0}_{-0.0}$ (1)	$0.0^{+0.0}_{-0.0}$ (6)	$0.1^{+0.0}_{-0.0}$ (12)	$0.0^{+0.0}_{-0.0}$ (2)	$0.5^{+0.1}_{-0.1}$ (92)	
Data		696	1373	205	610	861	110	1322	

Table 6.8 – Like Table 6.7, for same-sign candidates.

Process	ID	$\tau_\mu \tau_\mu$	$\tau_\mu \tau_{h1}$	$\tau_\mu \tau_{h3}$	$\tau_e \tau_e$	$\tau_e \tau_{h1}$	$\tau_e \tau_{h3}$	$\tau_\mu \tau_e$
$Z \rightarrow \tau\tau$	42100000	$0.0_{-0.3}^{+0.0}$ (0)	$0.6_{-0.3}^{+0.5}$ (4)	$0.5_{-0.3}^{+0.5}$ (3)	$0.3_{-0.2}^{+0.4}$ (2)	$0.9_{-0.4}^{+0.6}$ (6)	$0.2_{-0.1}^{+0.4}$ (1)	$2.2_{-0.6}^{+0.7}$ (14)
$Z \rightarrow \mu\mu$	42112011	$2.7_{-0.7}^{+0.9}$ (16)	$26.0_{-2.2}^{+2.4}$ (155)	$1.5_{-0.7}^{+0.7}$ (9)	$0.0_{-0.0}^{+0.3}$ (0)	$0.2_{-0.1}^{+0.4}$ (1)	$0.0_{-0.0}^{+0.3}$ (0)	$14.1_{-1.6}^{+1.8}$ (84)
$Z \rightarrow ee$	42122011	$0.0_{-0.0}^{+2.6}$ (0)	$0.0_{-0.0}^{+2.6}$ (0)	$0.0_{-0.0}^{+2.6}$ (0)	$4.2_{-2.3}^{+4.1}$ (3)	$12.6_{-4.1}^{+5.8}$ (9)	$1.4_{-1.2}^{+3.2}$ (1)	$1.4_{-1.2}^{+3.2}$ (1)
$Z \rightarrow b\bar{b}$	42150000	$0.0_{-0.0}^{+0.2}$ (0)	$0.1_{-0.1}^{+0.3}$ (1)	$0.0_{-0.0}^{+0.2}$ (0)	$0.0_{-0.0}^{+0.2}$ (0)	$0.0_{-0.0}^{+0.2}$ (0)	$0.1_{-0.1}^{+0.3}$ (1)	$0.5_{-0.2}^{+0.4}$ (4)
$Z(\rightarrow \mu\mu) + \text{jet}$	42112022	$2.1_{-0.6}^{+0.8}$ (13)	$12.8_{-1.5}^{+1.7}$ (79)	$1.1_{-0.4}^{+0.6}$ (7)	$0.0_{-0.0}^{+0.3}$ (0)	$0.0_{-0.0}^{+0.3}$ (0)	$0.0_{-0.0}^{+0.3}$ (0)	$16.7_{-1.7}^{+1.9}$ (103)
$W(\rightarrow \tau\nu_\tau) + \text{jet}$	42300010	$0.0_{-0.0}^{+5.2}$ (0)	$8.5_{-4.6}^{+8.3}$ (3)	$0.0_{-0.0}^{+5.2}$ (0)	$0.0_{-0.0}^{+5.2}$ (0)	$0.0_{-0.0}^{+5.2}$ (0)	$0.0_{-0.0}^{+5.2}$ (0)	$2.8_{-2.3}^{+6.5}$ (1)
$W(\rightarrow \mu\nu_\mu) + \text{jet}$	42311011	$0.6_{-0.5}^{+1.4}$ (1)	$41.7_{-5.2}^{+5.9}$ (68)	$4.3_{-1.6}^{+2.3}$ (7)	$0.0_{-0.0}^{+1.1}$ (0)	$0.6_{-0.5}^{+1.4}$ (1)	$0.0_{-0.0}^{+1.1}$ (0)	$12.3_{-2.7}^{+3.4}$ (20)
$W \rightarrow e\nu_e$	42321000	$0.0_{-0.0}^{+1.7}$ (0)	$0.0_{-0.0}^{+1.7}$ (0)	$0.0_{-0.0}^{+1.7}$ (0)	$1.9_{-1.2}^{+2.5}$ (2)	$20.8_{-3.0}^{+5.5}$ (22)	$4.7_{-2.0}^{+3.2}$ (5)	$3.8_{-1.8}^{+3.0}$ (4)
$W(\rightarrow e\nu_e) + \text{jet}$	42321010	$0.0_{-0.0}^{+6.4}$ (0)	$0.0_{-0.0}^{+6.4}$ (0)	$0.0_{-0.0}^{+6.4}$ (0)	$3.5_{-2.9}^{+8.0}$ (1)	$41.5_{-11.9}^{+15.8}$ (12)	$3.5_{-2.9}^{+8.0}$ (1)	$10.4_{-5.7}^{+10.1}$ (3)
$W(\rightarrow \mu\nu_\mu) + \text{jet}(\rightarrow \mu\dots)$	42311012	$2.6_{-0.3}^{+0.3}$ (93)	$0.0_{-0.0}^{+0.1}$ (0)	$0.0_{-0.0}^{+0.1}$ (0)	$0.0_{-0.0}^{+0.1}$ (0)	$0.0_{-0.0}^{+0.1}$ (0)	$0.0_{-0.0}^{+0.1}$ (0)	$0.0_{-0.0}^{+0.1}$ (0)
$c\bar{c} \rightarrow e\dots$	49021004	$0.0_{-0.0}^{+0.9}$ (0)	$0.0_{-0.0}^{+0.9}$ (0)	$0.0_{-0.0}^{+0.9}$ (0)	$0.0_{-0.0}^{+0.9}$ (0)	$1.4_{-0.8}^{+1.4}$ (3)	$0.5_{-0.4}^{+1.1}$ (1)	$0.9_{-0.6}^{+1.2}$ (2)
$c\bar{c} \rightarrow \mu\dots$	49011004	$0.0_{-0.0}^{+0.9}$ (0)	$12.9_{-2.8}^{+3.3}$ (26)	$7.9_{-2.1}^{+2.6}$ (16)	$0.0_{-0.0}^{+0.9}$ (0)	$0.0_{-0.0}^{+0.9}$ (0)	$0.0_{-0.0}^{+0.9}$ (0)	$2.0_{-1.0}^{+1.6}$ (4)
$b\bar{b} \rightarrow e\dots$	49021005	$0.0_{-0.0}^{+4.8}$ (0)	$0.0_{-0.0}^{+4.8}$ (0)	$0.0_{-0.0}^{+4.8}$ (0)	$0.0_{-0.0}^{+4.8}$ (0)	$7.9_{-4.3}^{+7.7}$ (3)	$0.0_{-0.0}^{+4.8}$ (0)	$5.2_{-3.4}^{+6.9}$ (2)
$b\bar{b} \rightarrow \mu\dots$	49011005	$23.2_{-7.6}^{+10.6}$ (9)	$36.1_{-9.6}^{+12.5}$ (14)	$10.3_{-4.9}^{+8.2}$ (4)	$0.0_{-0.0}^{+4.7}$ (0)	$0.0_{-0.0}^{+4.7}$ (0)	$0.0_{-0.0}^{+4.7}$ (0)	$18.0_{-6.7}^{+9.7}$ (7)
$t\bar{t}$	41900010	$0.5_{-0.1}^{+0.1}$ (160)	$1.0_{-0.2}^{+0.2}$ (331)	$0.3_{-0.1}^{+0.1}$ (96)	$0.0_{-0.0}^{+0.0}$ (0)	$0.0_{-0.0}^{+0.0}$ (0)	$0.0_{-0.0}^{+0.0}$ (0)	$0.3_{-0.1}^{+0.1}$ (82)
$WW \rightarrow \ell\ell\dots$	41922002	$0.0_{-0.0}^{+0.0}$ (0)	$0.0_{-0.0}^{+0.0}$ (0)	$0.0_{-0.0}^{+0.0}$ (0)	$0.0_{-0.0}^{+0.0}$ (0)	$0.0_{-0.0}^{+0.0}$ (0)	$0.0_{-0.0}^{+0.0}$ (0)	$0.0_{-0.0}^{+0.0}$ (5)
$WW \rightarrow \ell\dots$	42021000	$0.0_{-0.0}^{+0.0}$ (0)	$0.0_{-0.0}^{+0.1}$ (1)	$0.0_{-0.0}^{+0.0}$ (0)	$0.0_{-0.0}^{+0.0}$ (0)	$0.0_{-0.0}^{+0.0}$ (0)	$0.0_{-0.0}^{+0.0}$ (0)	$0.0_{-0.0}^{+0.1}$ (2)
$WZ \rightarrow \ell\dots$	42021001	$0.0_{-0.0}^{+0.0}$ (1)	$0.1_{-0.0}^{+0.0}$ (14)	$0.0_{-0.0}^{+0.0}$ (4)	$0.0_{-0.0}^{+0.0}$ (4)	$0.0_{-0.0}^{+0.0}$ (8)	$0.0_{-0.0}^{+0.0}$ (1)	$0.4_{-0.1}^{+0.1}$ (77)
Data		48	293	25	44	380	28	186



# 7 Reconstruction Efficiencies

The reconstruction efficiency of the di-tau candidate,  $\varepsilon_{\text{rec}}$ , depends on the kinematic of di-tau candidate. As such, it is computed as the average over the selected candidates. The components of  $\varepsilon_{\text{rec}}$  can be expressed as:

$$\varepsilon_{\text{rec}} := \langle \varepsilon_{\text{track}}(\eta_i, p_i, \text{nTracks}) \cdot \varepsilon_{\text{kine}} \cdot \varepsilon_{\text{PID}}(\eta_i, p_{T_i}) \cdot \varepsilon_{\text{GEC}} \cdot \varepsilon_{\text{trig}}(\eta_i, p_{T_i}) \rangle \quad (7.1)$$

where  $\varepsilon_{\text{track}}$  is the tracking efficiency,  $\varepsilon_{\text{kine}}$  the kinematic preselection efficiency,  $\varepsilon_{\text{PID}}$  the identification efficiency,  $\varepsilon_{\text{GEC}}$  the global event cut efficiency, and  $\varepsilon_{\text{trig}}$  the trigger efficiency. A round bracket indicates dependency on a di-tau candidate, and a subscript  $i$  includes all particles used to reconstruct a candidate. The efficiencies are determined cumulatively starting from the left-most term, *e.g.*, the identification efficiency is defined for di-tau candidates which passed the kinematic selection. Each of the efficiencies in eq. 7.1 along with their uncertainties are described in detail in following sections. By default, the efficiencies are determined from the simulated sample of  $Z \rightarrow \tau\tau$ . When possible, a data-driven method is applied. The usages are summarized in Table 7.1. Most uncertainties from fractional quantities (*e.g.*, in the form of  $N_{\text{pass}}/N_{\text{total}}$ ) are determined using the Clopper-Pearson method [125] at 68.3% confidence level<sup>1</sup>. The complete tables of efficiencies are also available in appendix E.1.

**Table 7.1** – Summary of calculation methods for different reconstruction efficiency components

	$\varepsilon_{\text{track}}$	$\varepsilon_{\text{kine}}$	$\varepsilon_{\text{PID}}$	$\varepsilon_{\text{GEC}}$	$\varepsilon_{\text{trig}}$
$\tau_{\mu}$	Data	MC	Data	Data	Data
$\tau_e$	MC+correction	MC	Data	Data	Data
$\tau_h$	MC+correction	MC	Data	-	-

<sup>1</sup>via the ROOT.TEfficiency class

## 7.1 Tracking Efficiencies

The tracking efficiency is defined as the probability that a charged particle inside the LHCb acceptance is reconstructed and satisfy the quality criteria described in Section 5.4.1. This is determined separately for muons (for  $\tau_\mu$ ), electrons (for  $\tau_e$ ), and charged hadrons (for  $\tau_{h1}$ ,  $\tau_{h3}$ ). As explained in the following sections, the efficiency for muons is obtained from data, while the simulation is used for electrons and hadrons. Corrections factors, functions of  $p_T$  and  $\eta$ , are used to match data and simulation. Averages of the corrections applied to the selected candidates are provided for illustration in Table 7.2 for each process considered. For  $\tau_{h3}$  a special treatment is needed, as explained in Section 7.1.3.

Finally, the tracking efficiency for the detection of a di-tau candidate is calculated as the product  $\varepsilon_{\text{track}} = \varepsilon_{\text{track},\tau_1}\varepsilon_{\text{track},\tau_2}$  assuming that the  $\varepsilon_{\text{track}}$  for the two  $\tau$  decay products are uncorrelated. Using simulated  $Z \rightarrow \tau\tau$  events this is verified to be a valid assumption.

### 7.1.1 Muon Tracking

For  $\tau_\mu$ , the muon tracking efficiency is determined using tag-and-probe method applied to data. The results from LHCb high- $p_T$  muon reconstruction study [128] are used for the present analysis. As the previous study noted that the efficiency is independent of the muon  $p_T$ , only the dependency in  $\eta$  is considered. The results are shown in Fig. 7.1a, compared to the efficiency obtained from simulation, which is seen to over-estimate the efficiency close to the detector edges.

### 7.1.2 Electron Tracking

For  $\tau_e$ , the electron tracking efficiency dependency on  $\eta$  and event tracks multiplicity (**nTracks**) is determined from the simulated sample of  $Z \rightarrow \tau\tau$  events, giving the results of Fig. 7.1b.

Subsequently two kind of simulation-to-data correction factors are applied. Their average values are given in Table 7.2, for each decay process:

1. As outlined in [129], the event is initially weighted to match the **nTracks** distribution in data (examples of **nTracks** distributions are shown in Fig. 7.4). The correction factors binned in track momentum and pseudorapidity are shown in Fig. 7.2. They are applied to each track of the signal candidate.
2. The second correction is taken from the study on  $\varepsilon_{\text{track},\mu}$  of the previous Section. As seen before the simulation is found to over-estimate the efficiency close to the edges of the detector. The correction factors are binned in  $\eta$  values of the particle track.

The uncertainties are a combination of the statistical uncertainty from simulated sample, of the per-track correction uncertainty, and of the overall correction uncertainty of 0.4%, for data versus MC 2012 as determined by the LHCb tracking group<sup>2</sup>.

<sup>2</sup> <https://twiki.cern.ch/twiki/bin/view/LHCb/TrackingEffStatus2012S20>



## 7.1. Tracking Efficiencies

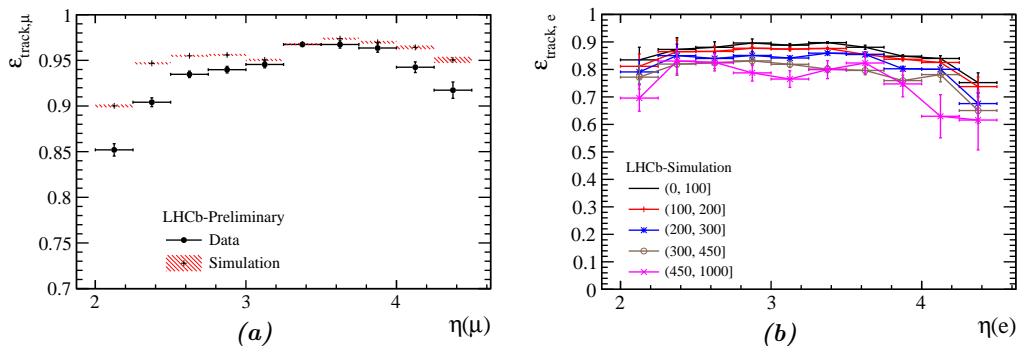


**Figure 7.1** – (a)  $\varepsilon_{\text{track},\mu}$  as a function of the  $\eta$  of the muon. The results from data and simulation are compared. (b)  $\varepsilon_{\text{track},e}$  from simulation as a function of the electron  $\eta$  and of the track multiplicity in the event.

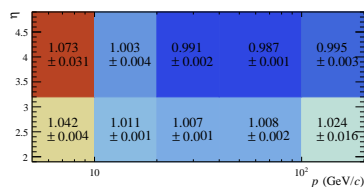


**Figure 7.2** – The single-track simulation-to-data correction factor for the calculation of  $\varepsilon_{\text{track}}$ , binned in track momentum and pseudorapidity.

**Table 7.2** – Correction factors applied to the tracking efficiency calculation, for each analysis channel. The values are averages over the candidates. The tracks of same kind are ordered in descending  $p_T$ .

Channel	Track	Correction1	Correction2
$\tau_\mu\tau_\mu$	$\tau_\mu$	—	—
$\tau_\mu\tau_{h1}$	$\tau_{h1}$	$1.012 \pm 0.009$	$0.978 \pm 0.005$
	$\tau_\mu$	—	—
$\tau_\mu\tau_{h3}$	$\tau_{h3}$ (1st-prong)	$1.012 \pm 0.009$	$0.980 \pm 0.004$
	$\tau_{h3}$ (2nd-prong)	$1.006 \pm 0.005$	$0.980 \pm 0.004$
	$\tau_{h3}$ (3rd-prong)	$1.004 \pm 0.004$	$0.980 \pm 0.004$
	$\tau_\mu$	—	—
$\tau_e\tau_e$	$\tau_e$ (1st-electron)	$1.015 \pm 0.012$	$0.978 \pm 0.005$
	$\tau_e$ (2nd-electron)	$1.008 \pm 0.006$	$0.978 \pm 0.005$
$\tau_e\tau_{h1}$	$\tau_e$	$1.014 \pm 0.011$	$0.979 \pm 0.005$
	$\tau_{h1}$	$1.011 \pm 0.009$	$0.978 \pm 0.005$
$\tau_e\tau_{h3}$	$\tau_e$	$1.015 \pm 0.012$	$0.978 \pm 0.005$
	$\tau_{h3}$ (1st-prong)	$1.011 \pm 0.008$	$0.980 \pm 0.004$
	$\tau_{h3}$ (2nd-prong)	$1.006 \pm 0.005$	$0.980 \pm 0.004$
	$\tau_{h3}$ (3rd-prong)	$1.004 \pm 0.004$	$0.980 \pm 0.004$
$\tau_\mu\tau_e$	$\tau_e$	$1.012 \pm 0.009$	$0.978 \pm 0.005$
	$\tau_\mu$	—	—

7.1.3 Charged Hadron Tracking

For  $\tau_{h1}$  and  $\tau_{h3}$ , the calculation of the charged hadron tracking efficiency also begins from values estimated from simulation. The hadron traverses approximately 20% of a hadronic interaction length of material before the last tracking plane, which can result in early showering, with subsequent reduction of the tracking efficiency. This efficiency is found to depend on the di-tau channel under consideration. For  $\tau_{h1}$ , the tracking efficiency is determined as a function of  $\eta$  and of the event track multiplicity. For  $\tau_{h3}$ , all 3 prongs are required to pass the track requirements simultaneously. The tracking efficiency is determined only as a function of the event track multiplicity. The simulation-to-data tracking efficiency correction is applied in the same manner as for the electron. The efficiencies are shown in Fig. 7.3, and the averages of the correction factors in Table 7.2.

The uncertainties are taken from the statistical uncertainty of the sample used, from the per-track correction uncertainty, from the overall correction uncertainty (again 0.4%). In addition, a 1.4% relative uncertainty contribution is added, due to the hadronic interaction simulation precision, as proposed in [129].

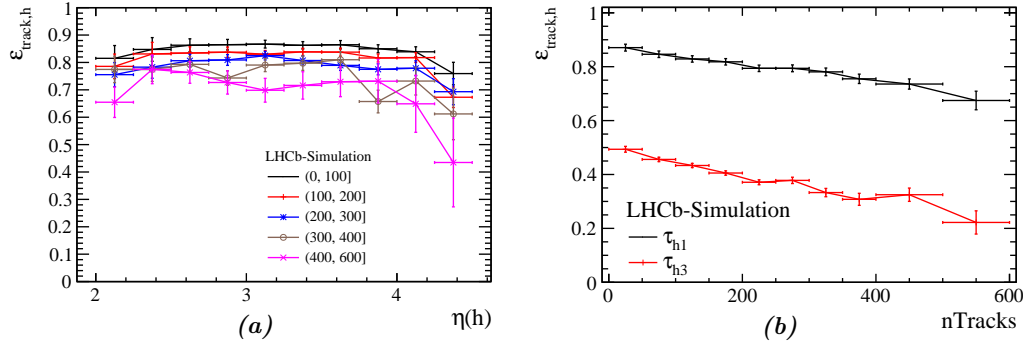


Figure 7.3 – (a)  $\epsilon_{\text{track},h}$  of  $\tau_{h1}$  as a function of  $\eta$  and of the event track multiplicity. (b)  $\epsilon_{\text{track}}$  of  $\tau_{h1}$  (black) and  $\tau_{h3}$  (red) as a function of the event track multiplicity.

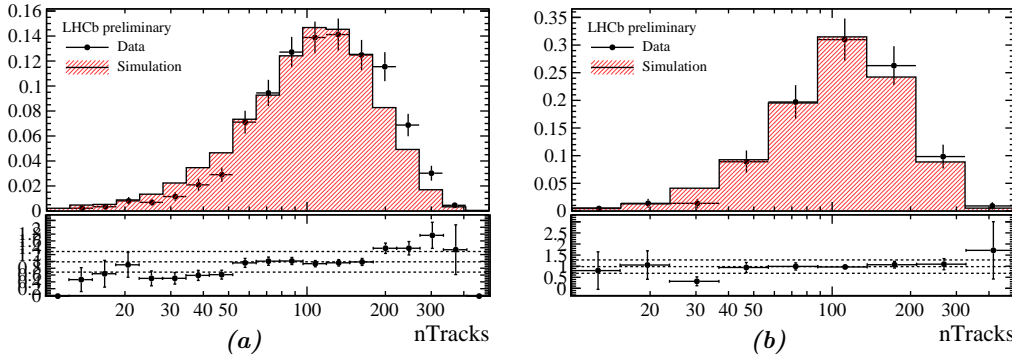


Figure 7.4 – Comparison of  $n\text{Tracks}$  distributions from data (black) and simulated  $Z \rightarrow \tau\tau$  (red), from the channel (a)  $\tau_{\mu}\tau_{h1}$ , and (b)  $\tau_{\mu}\tau_{h3}$ . The ratio is used to reweight the events prior to the computation of  $\epsilon_{\text{track}}$ .

## 7.2 Efficiencies of the Kinematic Preselection

These efficiencies are defined as the fraction of di-tau candidates satisfying acceptance and the track quality criteria, which also satisfies the kinematic selections on  $p_T$ ,  $\eta$ , and  $m$ , listed in Section 5.5. This is especially important for the channels with electrons, because of the imperfect correction for bremsstrahlung losses. The efficiencies are determined for each di-tau channel from simulated  $Z \rightarrow \tau\tau$  events.

The uncertainty has a statistical component from the number of the events of the samples used. A second component is taken from the study in [109], especially focused on the  $\tau_e$  candidate. The result of the study shows that the simulation reproduces very well the data, the electron  $p_T$  calibration factor is compatible with one:  $1.000 \pm 0.005$ . This small uncertainty is taken as a contribution to the uncertainty on  $\varepsilon_{\text{kin}}$  for each channel.

## 7.3 PID Efficiencies

The particle identification efficiency is defined as the probability that the reconstructed track passing the kinematic preselection satisfies the PID criteria described in Section 5.4.2. The calculation is performed independently for muons, electrons, and charged hadrons. The  $\varepsilon_{\text{PID}}$  of the di-tau candidate is calculated as a product of efficiencies from each particle, in a similar way as for  $\varepsilon_{\text{track}}$ . The tag-and-probe method is used to determine  $\varepsilon_{\text{PID}}$  from data, where the procedures are largely derived from the `PIDCalib` package [130], including decay modes, calibration datasets, fit models, and background removal via *sWeight* technique [131]. The `PIDCalib` package cannot be used directly as the PID selections of this analysis are not part of the ones considered in the original code.

### 7.3.1 Muon Identification

The muon identification efficiency,  $\varepsilon_{\text{PID},\mu}$ , is determined from data as a function of muon  $\eta$  and  $p_T$ . Since the muon  $p_T$  can range from 5 GeV/ $c$  to 70 GeV/ $c$ , it is determined using the combination of the analysis of two data sub-sets: the high- $p_T$  region ( $p_T > 20$  GeV/ $c$ ) uses  $Z \rightarrow \mu^+\mu^-$  events as studied in [128], while the low- $p_T$  region ( $5 < p_T < 20$  GeV/ $c$ ) uses  $J/\psi \rightarrow \mu^+\mu^-$  events.

In the low- $p_T$  region, the stripping `StrippingMuIDCalib_JpsiFromBNoPIDNoMip` allows to obtain the  $J/\psi \rightarrow \mu^+\mu^-$  sample, where the probe muon has no identification applied. The  $J/\psi$  candidates from this selection contain some background, so a maximum likelihood fit is used to identify the true number of muon probes. The  $J/\psi$  signal is modeled with a Voigtian distribution, whereas the background is modeled with a decaying exponential function. The result of the fit, and associated *sWeight* are shown in Fig. 7.5. The probe muons are binned in  $\eta$ ,  $p_T$ . The  $\varepsilon_{\text{PID},\mu}$  is calculated for each bin as the sum of *sWeight* of probes passing the identification requirement, over the sum of *sWeight* in that bin. The choice of bins is governed by the statistical precision.

The muon probes bi-parametric distribution can be seen in Fig. 7.6. where the two sub-sets are merged. The efficiencies in the overlapped region at  $p_T$  [20,25] GeV/ $c$  is computed via BLUE (best linear unbiased estimator) technique [132], assuming conservatively that the

## Chapter 7. Reconstruction Efficiencies

uncertainties are fully correlated. The efficiencies from simulation and data-driven methods are found to agree, as shown in Fig. 7.7.

The uncertainty in the high- $p_T$  region is estimated from the background contamination of the tag-and-probe sample. The uncertainty of the low- $p_T$  region follows the guideline of PIDCalib: For each track 0.1% systematic uncertainty is assigned, as well as from the choice of binning. The uncertainty of the latter is made by recomputing  $\varepsilon_{\text{PID},\mu}$  at doubled/halved number of bins from the nominal choice, and the variations are used as systematics. This is combined in quadrature with the statistical uncertainty of the calibration sample. The results are summarized in Table 7.3.

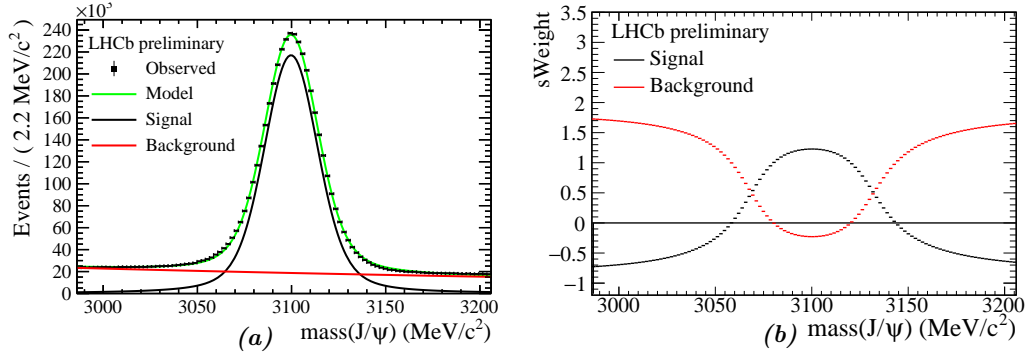


**Figure 7.5** – Results from the background-removal fit of  $J/\psi \rightarrow \mu^+\mu^-$  muon calibration sample. (a) contribution of processes projected on distribution of  $J/\psi$  mass, (b) distribution of  $sWeight$  from different fitted processes as a function of  $J/\psi$  mass.

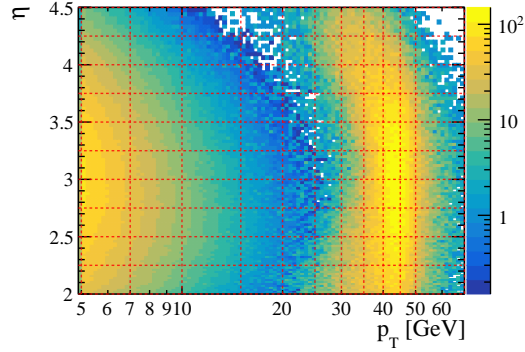


**Figure 7.6** – Bi-parametric distribution in  $\eta$  and  $p_T$  of the probe muon from  $J/\psi \rightarrow \mu^+\mu^-$  and  $Z \rightarrow \mu^+\mu^-$  calibration samples combined. The red dashed lines show the binning choice.

**Table 7.3** – Comparison of the average signal  $\varepsilon_{\text{PID}}$  from the data-driven method for three different  $\varepsilon_{\text{PID},\mu}(p_T,\eta)$  binning, and the corresponding systematic uncertainty.

$\varepsilon_{\text{PID}}$ [%]	Nominal	Doubled	Halved	Systematics [%]
$\tau_\mu$ from $\tau_\mu\tau_e$	$98.5 \pm 0.2$	$98.6 \pm 0.2$	$98.6 \pm 0.1$	0.02
$\tau_\mu$ (low- $p_T$ ) from $\tau_\mu\tau_\mu$	$98.6 \pm 0.1$	$98.6 \pm 0.2$	$98.6 \pm 0.1$	0.02

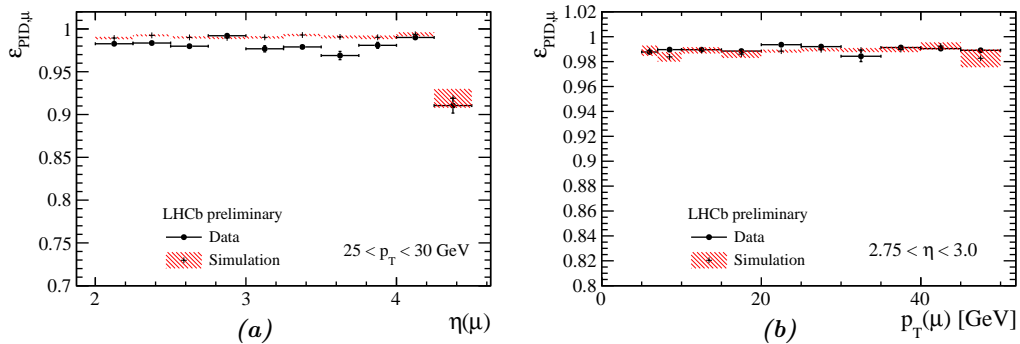


**Figure 7.7** – Examples of  $\epsilon_{\text{PID},\mu}$  from data (black) as a function of muon  $\eta$  (a), and  $p_T$  (b). The efficiency from simulation (red) is also shown. The values are taken from Table E.5.

### 7.3.2 Electron Identification

The electron identification efficiency,  $\epsilon_{\text{PID},e}$ , is determined from data as a function of electron's  $\eta$  and  $p_T$ . The tag-and-probe data-driven method treats electrons into two separate regions as a function of their  $p_T$ , similar to the procedure for  $\epsilon_{\text{PID},\mu}$ : the high- $p_T$  region ( $p_T > 20 \text{ GeV}/c$ ) using  $Z \rightarrow ee$  as studied in [109]; and the low- $p_T$  region ( $5 < p_T < 20 \text{ GeV}/c$ ) using  $B^+ \rightarrow J/\psi(\rightarrow e^+e^-)K^+$ .

For the high- $p_T$  region **StrippingWeLine** is used (requiring one electron of  $p_T > 20 \text{ GeV}/c$ ). The  $Z$  boson is required to have a reconstructed invariant mass greater than  $60 \text{ GeV}/c^2$ , with the two electrons  $\Delta\phi > 2.8$ . Both electrons are also required to pass the isolation  $\hat{I}_{p_T} > 0.9$ . The tag electron satisfies all the track, identification, and trigger requirements, while the probe only needs to pass the track requirement. The efficiency is evaluated as the number of probes passing electron identification over the number of total probes. The potential background is estimated from same-sign di-electrons and found to be negligible for this selection.

In the low- $p_T$  region, the  $B^+ \rightarrow J/\psi(\rightarrow e^+e^-)K^+$  process is selected, where the probe electron has no identification required. The  $J/\psi$  selection contains considerable amount of background, so a maximum likelihood fit of the reconstructed invariant mass is performed, where the signal PDF is modeled by a CrystalBall function, and the background by a linear function. The result of the fit and its associated *sWeight* are shown in Fig. 7.8.

The two regions are combined together with the overlapping  $p_T$  bins  $[8,20] \text{ GeV}/c$  computed via the BLUE technique, in the same manner as  $\epsilon_{\text{PID},\mu}$ . The probe coverage is shown in Fig. 7.9. The comparison of the efficiencies from simulation and from the data-driven method are shown in Fig. 7.10. They are mostly in agreement within their statistical uncertainty except toward the detector edge ( $\eta < 2.25$ ,  $\eta > 3.75$ ). The uncertainties for both high- $p_T$  and low- $p_T$  regions are obtained in the same way as  $\epsilon_{\text{PID},\mu}$ . The results are summarized in Table 7.4.

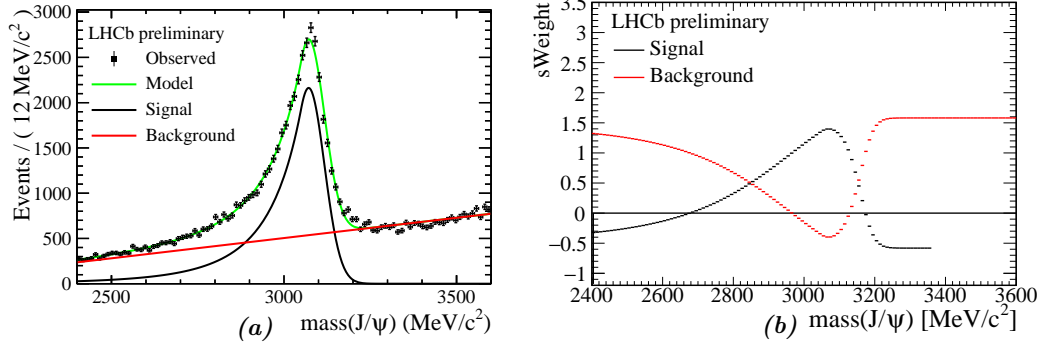


**Figure 7.8** – Results from the background-removal fit of  $B^+ \rightarrow J/\psi(\rightarrow e^+e^-)K^+$  electron calibration sample. (a) contribution of processes projected on distribution of  $J/\psi$  mass, (b) distribution of  $sWeight$  from different fitted processes as a function of  $J/\psi$  mass.

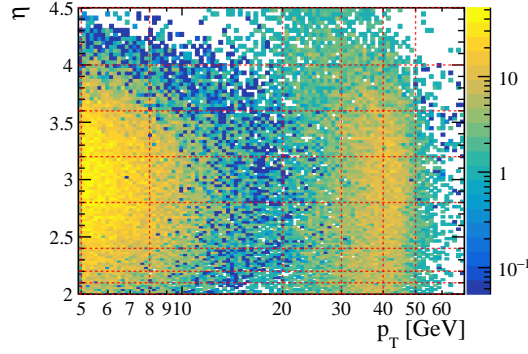


**Figure 7.9** – Bi-parametric distribution in  $\eta$  and  $p_T$  of the probe electron from  $J/\psi \rightarrow ee$  and  $Z \rightarrow ee$  calibration samples combined. The red dashed lines show the choice of bins.

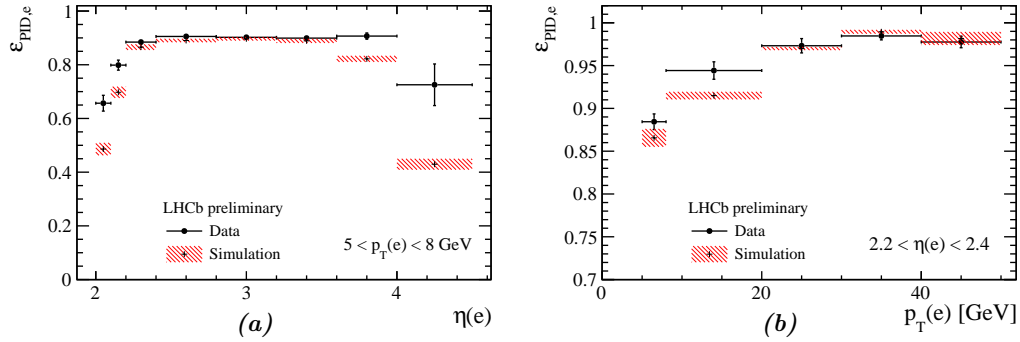


**Figure 7.10** – Examples of  $\epsilon_{PID,e}$  from data (black) as a function of electron  $\eta$  (a), and  $p_T$  (b). The efficiency from simulation (red) is also shown.

**Table 7.4** – Comparison of the average signal  $\epsilon_{PID}$  from the data-driven method for three different  $\epsilon_{PID,e}(p_T, \eta)$  binnings, and the corresponding systematic uncertainty.

$\epsilon_{PID}$ [%]	Doubled	Halved	Nominal	Systematics [%]
$\tau_e$ (higher- $p_T$ ) from $\tau_e\tau_e$	$95.4 \pm 1.2$	$94.9 \pm 0.7$	$95.1 \pm 0.9$	0.32
$\tau_e$ (lower- $p_T$ ) from $\tau_e\tau_e$	$92.2 \pm 0.5$	$92.0 \pm 0.4$	$91.9 \pm 0.4$	0.24
$\tau_e$ from $\tau_e\tau_{h1}$	$95.3 \pm 1.2$	$94.9 \pm 0.7$	$95.0 \pm 0.9$	0.39
$\tau_e$ from $\tau_e\tau_{h3}$	$95.3 \pm 1.2$	$94.9 \pm 0.7$	$95.1 \pm 0.9$	0.29
$\tau_e$ from $\tau_\mu\tau_e$	$93.8 \pm 0.7$	$93.4 \pm 0.4$	$93.4 \pm 0.5$	0.39

### 7.3.3 Charged Hadron Identification

The charged hadron identification efficiency,  $\varepsilon_{\text{PID},h}$ , is determined from data using the  $D^{*+} \rightarrow D^0(\rightarrow K^-\pi^+)\pi^+$  calibration sample, as a function of the charged hadron  $p_T$  and  $\eta$ . The pion without identification from  $D^0$  is used as a probe, covering adequately the kinematic region needed by the  $\tau_{h1}$  and  $\tau_{h3}$ . The candidates are taken from `StrippingNoPIDstarWithD02RSKPiLine`. The background is determined from two-dimensional fit of the distribution of reconstructed  $D^0$  mass, versus the difference in mass between the  $D^*$  and  $D^0$  (denoted here as  $\Delta m_D$ ). Four processes are considered for the maximum likelihood fit:

1. Signal process, modeled as a bi-Gaussian distribution in both dimensions.
2. Combinatorial backgrounds, modeled as a linear background in  $D^0$  mass and a decaying exponential in  $\Delta m_D$ .
3. Background of poor  $\Delta m_D$ , (*e.g.* random slow pion), modeled as signal in  $D^0$  mass and decaying exponential in  $\Delta m_D$ .
4. Background of fake  $D^0$ , modeled as an exponential in  $D^0$  mass and as signal in  $\Delta m_D$ .

The fit results, shown in Fig. 7.11, are used to calculate the *sWeight* for each process, for a given calibration dataset, see Fig. 7.12. The probes coverage is shown in Fig. 7.13, which are divided into bins in  $\eta$  and  $p_T$ . The  $\varepsilon_{\text{PID},h}$  is finally calculated for each subset as the sum of *sWeight* of the probes passing the identification requirement over the sum of *sWeight* in that bin. The efficiency distributions are shown in Fig. 7.14. Unlike  $\varepsilon_{\text{PID},e}$ , efficiencies from simulation and data-driven method are not in full agreement; only the values from the data-driven method are used. The systematic uncertainty follows the same manner as  $\varepsilon_{\text{PID},\mu}$  in the previous section. The results are summarized in Table 7.5.

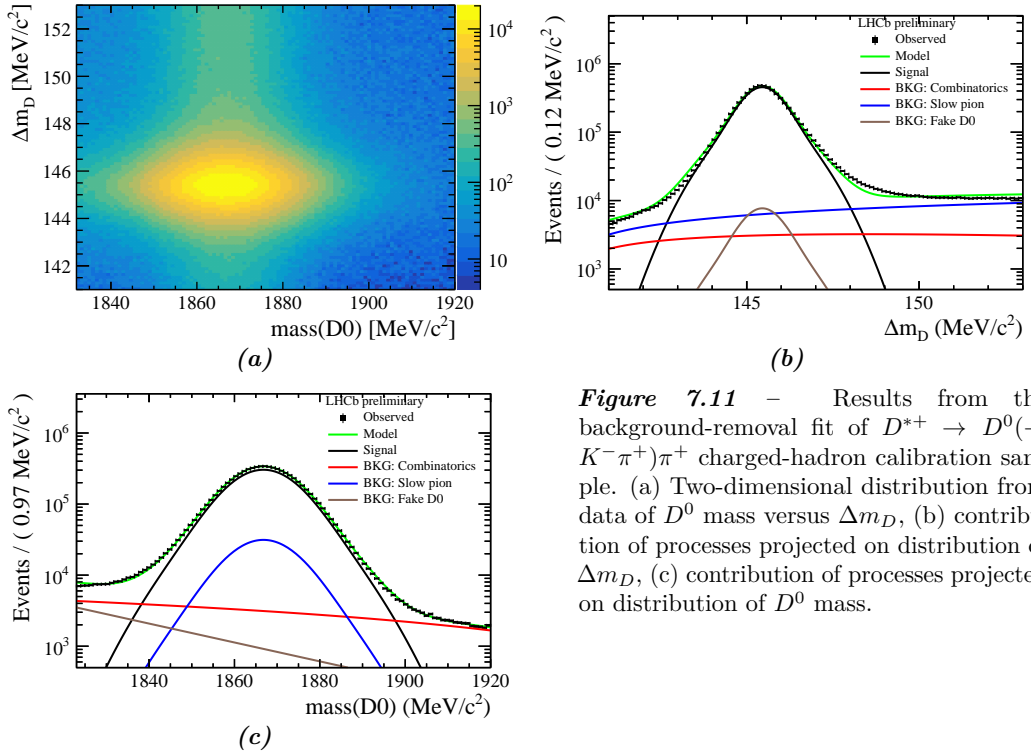


**Figure 7.11** – Results from the background-removal fit of  $D^{*+} \rightarrow D^0(\rightarrow K^-\pi^+)\pi^+$  charged-hadron calibration sample. (a) Two-dimensional distribution from data of  $D^0$  mass versus  $\Delta m_D$ , (b) contribution of processes projected on distribution of  $\Delta m_D$ , (c) contribution of processes projected on distribution of  $D^0$  mass.

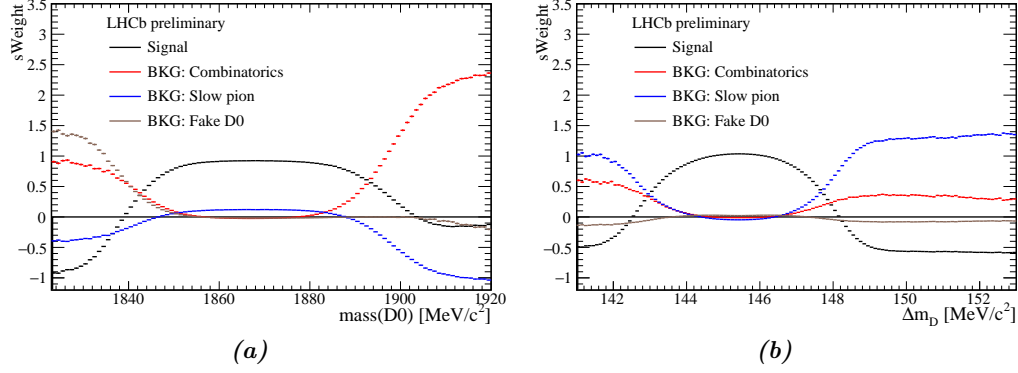


**Figure 7.12** – Distribution of  $sWeight$  from different fitted processes as a function of two parameters of interest; (a) mass of  $D^0$ , (b)  $\Delta m_D$ .

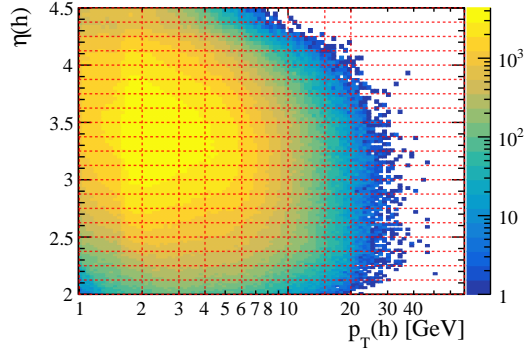


**Figure 7.13** – Bi-parametric distribution for the probe hadron in  $\eta$  and  $p_T$ . The red dashed lines show the choice of bins.

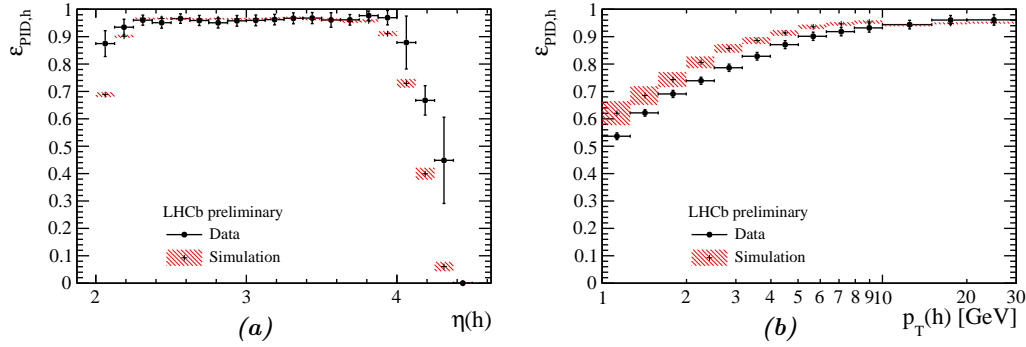


**Figure 7.14** – Examples of  $\epsilon_{PID,h}$  from data (black) as a function of charged hadron  $\eta$  (a), and  $p_T$  (b) (channel  $\tau_\mu\tau_{h1}$ ). The efficiency from simulation is also shown (in red).

**Table 7.5** – Comparison of the average signal  $\epsilon_{PID}$  from the data-driven method for three different  $\epsilon_{PID,h}$  ( $p_T, \eta$ ) binnings, and the corresponding systematic uncertainty.

$\epsilon_{PID}$ [%]	Doubled	Halved	Nominal	Systematics [%]
$\tau_{h1}$ from $\tau_\mu\tau_{h1}$	$95.1 \pm 1.0$	$95.0 \pm 0.5$	$95.2 \pm 0.9$	0.16
$\tau_{h1}$ from $\tau_e\tau_{h1}$	$95.1 \pm 1.0$	$95.0 \pm 0.5$	$95.1 \pm 0.9$	0.14
$\tau_{h3}$ from $\tau_\mu\tau_{h3}$	$74.2 \pm 1.0$	$73.1 \pm 0.5$	$74.1 \pm 0.8$	1.46
$\tau_{h3}$ from $\tau_e\tau_{h3}$	$74.6 \pm 1.0$	$73.5 \pm 0.5$	$74.8 \pm 0.8$	1.64



## 7.4 Global Event Cut Efficiency

The Global event cut (GEC) is the requirement of SPD hits  $< 600$  in the L0Muon and L0Electron triggers, so the cut is identical for all di-tau channel. The corresponding efficiency,  $\varepsilon_{\text{GEC}}$ , is estimated from data for each channel as the following:

**Channels  $\tau_\mu\tau_\mu$ ,  $\tau_e\tau_e$**  The event topology of  $Z \rightarrow \mu\mu$  is similar to  $\tau_\mu\tau_\mu$ , and  $Z \rightarrow ee$  to the  $\tau_e\tau_e$  channel, thus the results from those analyses are used. The efficiency can be determined from data via a method outlined in [108] for  $Z \rightarrow \mu\mu$ , yielding  $(93.00 \pm 0.32)\%$  and [109] for  $Z \rightarrow ee$ , yielding  $(91.60 \pm 0.60)\%$ .

**Channel  $\tau_\mu\tau_e$**  The  $\varepsilon_{\text{GEC}}$  in this channel is taken as the average of the  $\varepsilon_{\text{GEC}}$  values for the  $\tau_\mu\tau_\mu$  and  $\tau_e\tau_e$  channels, with the half of their difference used as a systematic uncertainty.

**Channels  $\tau_\mu\tau_{h1}$ ,  $\tau_\mu\tau_{h3}$**  From the simulated sample of  $Z \rightarrow \tau\tau$  events, it is found that the differences in  $\varepsilon_{\text{GEC}}$  between the channel  $\tau_\mu\tau_\mu$ ,  $\tau_\mu\tau_{h1}$ ,  $\tau_\mu\tau_{h3}$  are very small (shown in Fig. 7.15). Thus the  $\varepsilon_{\text{GEC}}$  inferred from  $\tau_\mu\tau_\mu$  is used for those channels. A systematic uncertainty for a given channel is computed from the difference in  $\varepsilon_{\text{GEC}}$  for that channel with respect to the reference  $\tau_\mu\tau_\mu$ , computed at the point where  $\varepsilon_{\text{GEC}}$  of  $\tau_\mu\tau_\mu$  in the simulated sample matches with  $\varepsilon_{\text{GEC}}$  of  $Z \rightarrow \mu\mu$  from data.

**Channels  $\tau_e\tau_{h1}$ ,  $\tau_e\tau_{h3}$**  The same procedure as the previous point is used where  $\tau_\mu\tau_e$  is used as the reference channel to  $\tau_e\tau_{h1}$ ,  $\tau_e\tau_{h3}$  channel.

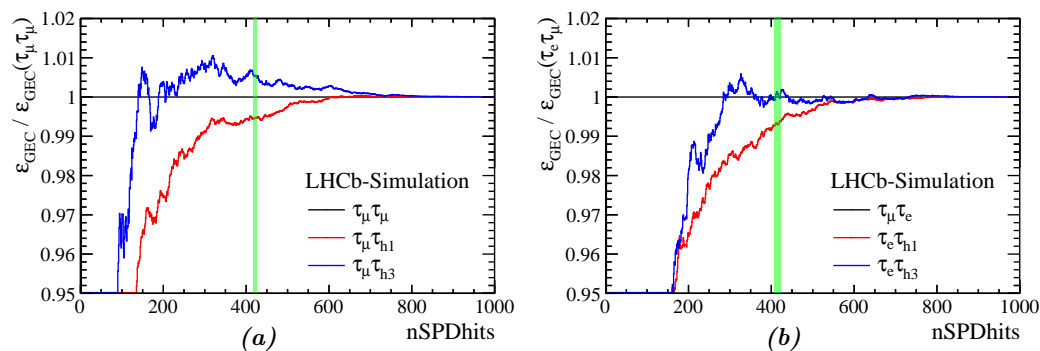


**Figure 7.15** – Relative  $\varepsilon_{\text{GEC}}$  as a function of maximum number of SPD hits obtained from the  $Z \rightarrow \tau\tau$  simulated sample normalized to the reference value. (a): channels  $\tau_\mu\tau_{h1}$  (red) and  $\tau_\mu\tau_{h3}$  (blue) relative to  $\tau_\mu\tau_\mu$ , (b): channels  $\tau_e\tau_{h1}$  (red) and  $\tau_e\tau_{h3}$  (blue) relative to  $\tau_\mu\tau_e$ . The green band denotes the region where the  $\varepsilon_{\text{GEC}}$  of the reference channel in simulation matches the efficiency obtained from data.

## 7.5 Trigger Efficiencies

The trigger efficiency,  $\varepsilon_{\text{trig}}$ , is evaluated separately for muon and electron triggers, listed in Table 5.1.  $\varepsilon_{\text{trig}}$  is evaluated as a function of the lepton  $p_T$ , and  $\eta$ . For the di-tau channel having only one leptonic tau candidate, the trigger efficiency is evaluated for that lepton type. In the case of two leptonic tau decays ( $\tau_\mu\tau_\mu$ ,  $\tau_\mu\tau_e$ ,  $\tau_e\tau_e$ ), either of the leptons can trigger the event, so the efficiency is calculated as  $\varepsilon_{\text{trig}} = \varepsilon_{\text{trig},1} + \varepsilon_{\text{trig},2} - \varepsilon_{\text{trig},1} \varepsilon_{\text{trig},2}$  where  $\varepsilon_{\text{trig},1(2)}$  is the trigger efficiency evaluated for the first (second) leptonic decaying tau candidate.

### 7.5.1 Muon Trigger

The muon trigger efficiency is determined from data using a tag-and-probe method described in [128]. The efficiency and uncertainty are taken from that analysis, as shown in Fig. 7.16.

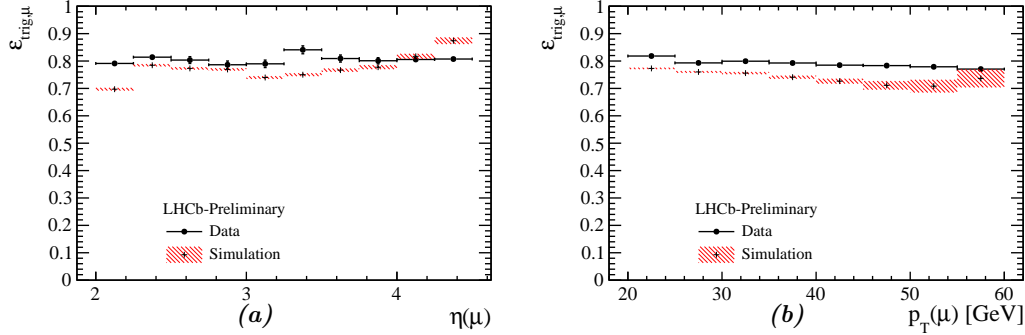


Figure 7.16 –  $\varepsilon_{\text{trig},\mu}$  from data (black) as a function of muon (a)  $\eta$ , (b)  $p_T$ . The efficiency from simulation is shown in red.

### 7.5.2 Electron Trigger

The electron trigger efficiency is determined from data using a tag-and-probe method. The  $Z \rightarrow ee$  events are selected from data via `StrippingZ02eeLine`, where the tag is an electron passing the track, PID, and trigger requirement, and the probe is another opposite-charge electron passing the track and PID requirement. Both tag and probe are required to have  $p_T > 20 \text{ GeV}/c$ ,  $2.0 < \eta < 4.5$ , and be isolated with  $\hat{I}_{p_T} > 0.9$ . The  $Z$  boson is required to have an invariant mass in the 70–120  $\text{GeV}/c^2$  range. The results are shown in Fig. 7.17, with the statistical uncertainties of the  $Z \rightarrow ee$  sample used.

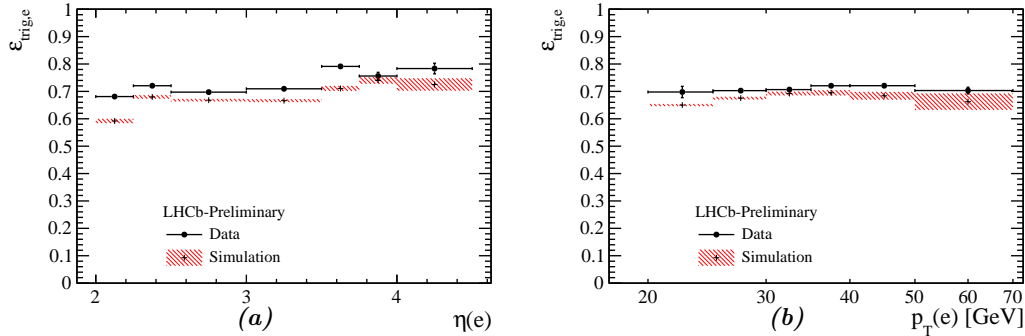


Figure 7.17 –  $\varepsilon_{\text{trig},e}$  from data (black) as a function of electron's (a)  $\eta$ , (b)  $p_T$ . The efficiency from simulation is shown in red.

## 7.6 Summary

The efficiency product of eq. 7.1 is calculated on a per-event basis. In order to quantify the efficiency for each di-tau channel, an *equivalent efficiency* is computed as

$$\varepsilon_x := \frac{N_{\text{signal}}}{N_{\text{obs}} \langle \varepsilon_x^{-1} \rangle_{\text{obs}} - \sum_i N_{\text{bkg},i} \langle \varepsilon_x^{-1} \rangle_{\text{bkg},i}} \quad (7.2)$$

$$N_{\text{signal}} = N_{\text{obs}} - \sum_i N_{\text{bkg},i}$$

where  $x$  is the efficiency kind under consideration (tracking, PID, trigger, rec). It can be regarded as the weighted harmonic average of the per-event efficiency, with  $N_{\text{signal}}$  is the number of expected signal candidates,  $N_{\text{obs}}$  is the number of observed candidates in data,  $N_{\text{bkg},i}$  is the number of expected background from process  $i$ , and  $\sum_i$  is the sum over all background processes. The quantity  $\langle \varepsilon_x^{-1} \rangle_{\text{obs}}$  is the average of  $\varepsilon_x^{-1}$  over all selected events from data, and  $\langle \varepsilon_x^{-1} \rangle_{\text{bkg},i}$  is the average over all selected background events of process  $i$ . The results are summarized for each efficiency and for each di-tau channel in Table 7.6. More details are provided in appendix E.

In general, the efficiencies for channels involving electrons are a factor of 2 lower than the corresponding channel with muons. This is mainly due to the momentum loss for the electron, from bremsstrahlung.

**Table 7.6** – Summary of the *equivalent* reconstruction efficiencies for each di-tau channel at each stage of the selection, given in percentage.

	$\tau_\mu\tau_\mu$	$\tau_\mu\tau_{h1}$	$\tau_\mu\tau_{h3}$	$\tau_e\tau_e$	$\tau_e\tau_{h1}$	$\tau_e\tau_{h3}$	$\tau_\mu\tau_e$
$\varepsilon_{\text{track}}$	$85.6 \pm 0.9$	$75.5 \pm 1.5$	$36.9 \pm 1.8$	$71.8 \pm 2.2$	$67.8 \pm 1.9$	$32.6 \pm 1.7$	$78.2 \pm 1.2$
$\varepsilon_{\text{kine}}$	$100.0 \pm 0.0$	$100.0 \pm 0.0$	$100.1 \pm 0.0$	$62.3 \pm 0.8$	$61.3 \pm 0.8$	$62.3 \pm 0.8$	$81.7 \pm 0.9$
$\varepsilon_{\text{PID}}$	$96.0 \pm 0.5$	$93.1 \pm 0.8$	$74.7 \pm 1.3$	$87.9 \pm 1.4$	$87.5 \pm 1.3$	$67.6 \pm 1.5$	$90.9 \pm 0.7$
$\varepsilon_{\text{GEC}}$	$93.0 \pm 0.3$	$93.0 \pm 0.6$	$93.0 \pm 0.6$	$91.6 \pm 0.6$	$92.3 \pm 1.0$	$92.3 \pm 0.7$	$92.3 \pm 0.7$
$\varepsilon_{\text{trig}}$	$84.7 \pm 1.5$	$80.4 \pm 1.7$	$80.4 \pm 1.8$	$79.5 \pm 2.0$	$69.2 \pm 3.0$	$70.1 \pm 2.7$	$84.8 \pm 1.3$
$\varepsilon_{\text{rec}}$	$64.8 \pm 1.4$	$52.6 \pm 1.6$	$20.8 \pm 1.2$	$28.8 \pm 1.3$	$23.3 \pm 1.3$	$8.9 \pm 0.6$	$45.7 \pm 1.2$



# 8 “Offline” Selection Efficiencies

The selection efficiency,  $\varepsilon_{\text{sel}}$ , is defined as the fraction of reconstructed signal candidates satisfying the “offline” selections presented in Section 5.6.  $\varepsilon_{\text{sel}}$  is calculated from the simulated sample of  $Z \rightarrow \tau\tau$  for each di-tau channel. The results are in Table 8.1.

Corrections to the simulation are needed before the calculation of  $\varepsilon_{\text{sel}}$ , as discussed in the following section. The resultant  $\varepsilon_{\text{sel}}$  after all corrections applied are summarized in Table 8.2. When the corrections are inferred from the comparison of  $Z \rightarrow \mu\mu$  candidates in data and simulation, the selection of such events requires muons with  $p_{\text{T}} > 20 \text{ GeV}/c$ ,  $2.0 < \eta < 4.5$ , at least one muon is required to fire the entire series of muon trigger lines, and the invariant mass of the di-muon must be in the 80–100  $\text{GeV}/c^2$  window.

**Table 8.1** – Selection efficiencies (in percentage) obtained from  $Z \rightarrow \tau\tau$  simulated events, for each of selection variables applied individually. The last line is the efficiency with all the criteria applied.

$\varepsilon_{\text{sel}}$ [%]	$\tau_{\mu}\tau_{\mu}$	$\tau_{\mu}\tau_{h1}$	$\tau_{\mu}\tau_{h3}$	$\tau_e\tau_e$	$\tau_e\tau_{h1}$	$\tau_e\tau_{h3}$	$\tau_{\mu}\tau_e$
$A_{p_{\text{T}}}$	83.6	—	—	85.4	—	—	89.3
di-tau mass	87.6	—	—	94.2	—	—	—
$\hat{I}_{p_{\text{T}}1}$	92.6	91.7	92.4	89.8	88.5	88.8	86.4
$\hat{I}_{p_{\text{T}}2}$	77.5	77.3	79.3	71.5	77.5	78.9	78.6
IP	51.7	61.3	—	47.1	61.3	—	—
$\Delta\phi$	81.8	82.3	81.8	80.9	82.2	80.8	81.6
Vertex $\chi^2/\text{ndf}$	—	—	94.7	—	—	93.8	—
$\Delta R_{\text{max}}/p_{\text{T}}$	—	—	77.0	—	—	77.2	—
Decay time	—	—	77.5	—	—	76.8	—
$m_{\text{corr}}$	—	—	80.7	—	—	79.4	—
(All)	23.5	35.6	33.7	20.4	34.6	31.5	51.7

## 8.1 Transverse Momentum Asymmetry ( $A_{p_T}$ )

A good agreement between data and simulation can be observed for the  $A_{p_T}$  variable applied to  $Z \rightarrow \mu\mu$  events, as shown in Fig. 8.1. Hence no correction is needed for the simulation. The uncertainty to  $\varepsilon_{\text{sel}}$  is calculated from the relative difference between the efficiencies of the  $A_{p_T}$  selection for data and simulation.

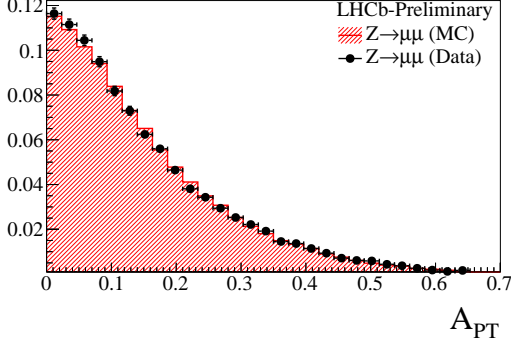


*Figure 8.1* – Comparison between  $Z \rightarrow \mu\mu$  from data (black) and simulation (red) for the  $A_{p_T}$  of di-muons.

## 8.2 Upper Cut on the Di-lepton Invariant Mass

This selection only applies to the same flavour di-leptons candidates. From the comparison of the invariant mass distributions in data and simulation for  $Z$  decay into di-muons and di-electron, there is a good agreement in this variable [133], hence no correction is applied to the simulation. The difference in position is estimated from the mean of the masses measured from 20 to 60  $\text{GeV}/c^2$ . The data and simulation differences are of 0.6  $\text{GeV}/c^2$  for di-muons and 1.6  $\text{GeV}/c^2$  for di-electrons. Moving the cuts by these amounts, the corresponding  $\varepsilon_{\text{sel}}$  variations are of 0.8% and 1.4%, which are taken as contributions to the systematic uncertainty.

## 8.3 Isolation ( $\hat{I}_{p_T}$ )

The comparison between data and the simulated sample of the muon isolation variable  $\hat{I}_{p_T}(\mu)$  is shown in Fig. 8.2a. The small disagreement especially at low  $p_T$  values is expected, because the track multiplicity of the underlying event is known to be underestimated in the simulation. The correction function for  $\varepsilon_{\text{sel}}$  as a function of  $p_T$  is determined from the ratio of isolation selection efficiencies from  $Z \rightarrow \mu\mu$  in data and simulation, requiring one muon to have  $\hat{I}_{p_T} > 0.9$ . This function is used to obtain the correction factors for the two tau candidates which are multiplied to obtain the event correction. This procedure is done independently for each di-tau channel, assuming that the correction function obtained for the muons is also valid for the other particles.

The uncertainty is calculated from the difference between the isolation selection efficiencies of  $Z \rightarrow \mu\mu$  and  $Z \rightarrow \tau_\mu\tau_\mu$  inferred from simulation. As both processes should have almost identical underlying event topologies, their efficiencies should match within uncertainty, see Fig. 8.2b. The effects on the efficiency are detailed in Table 8.2. The contribution to the systematic uncertainty is computed from the differences, function of  $p_T$ , averaged over all the candidates.

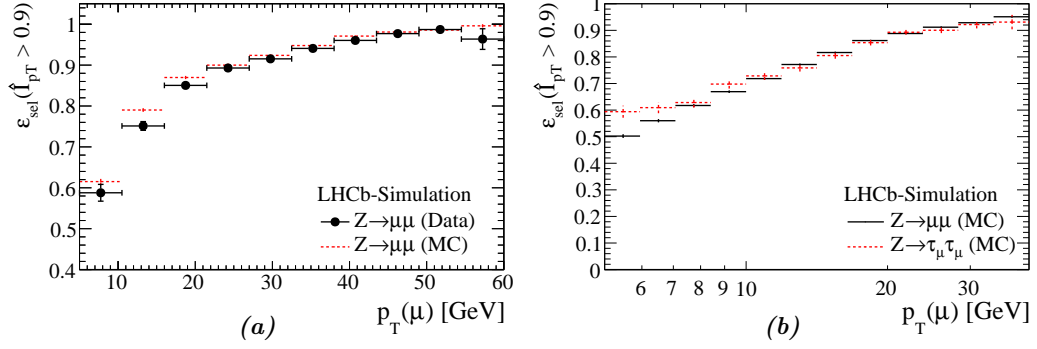


**Figure 8.2** – Comparison of the single muon selection efficiency as a function of  $p_T$  of the muon, (a) between  $Z \rightarrow \mu\mu$  from data and from the corresponding simulated sample; (b) between the simulated samples of  $Z \rightarrow \mu\mu$  and  $Z \rightarrow \tau_\mu\tau_\mu$ . The muon is required to be isolated with  $\hat{I}_{p_T} > 0.9$ .

## 8.4 Impact Parameter (IP)

The comparison between data and simulation of the muon IP distribution in  $Z \rightarrow \mu\mu$  is shown in Fig. 8.3. The IP resolution is slightly underestimated in the simulation[83], so an additional  $p_T$ -dependent resolution component is added prior to the  $\epsilon_{\text{sel}}$  computation. The VELO data and simulation 1-dimensional resolutions for 2012 data are

$$\sigma_{\text{data}} = 11.6 + 23.4/p_T \quad , \quad \sigma_{\text{MC}} = 11.6 + 22.6/p_T$$

where  $p_T$  is the track transverse momentum in GeV/c. Assuming the IP 2-dimensional resolution is  $\sqrt{2}$  times the above values, the additional contribution to the resolution is  $\delta(p_T) = \sqrt{2(\sigma_{\text{data}}^2 - \sigma_{\text{MC}}^2)}$ . This component is accounted for by smearing the simulated IP values. After this correction, the comparison using  $Z \rightarrow \mu\mu$  sample is shown in Fig. 8.3. A Kolmogorov test found that the smeared distribution has a better compatibility with the data (increasing from 0.04 to 0.18). The effects on the efficiency are detailed in Table 8.2. The uncertainty on  $\epsilon_{\text{sel}}$  is taken as the difference before and after correction.

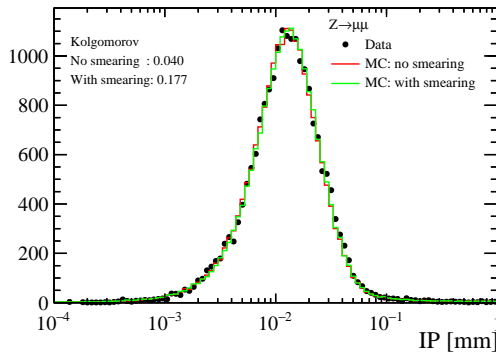


**Figure 8.3** – Comparison of  $Z \rightarrow \mu\mu$  from data (black) and simulation before smearing (red), and after smearing (green) of the distribution of muon IP.

## 8.5 Azimuthal Separation ( $\Delta\phi$ )

A calibration inferred from  $Z \rightarrow \mu\mu$  events is applied to correct for differences in simulation and data. The calibration is based on the function  $\Delta\phi \rightarrow (\pi - f_{\text{scale}}(\pi - \Delta\phi))$ , where  $f_{\text{scale}}$  is a multiplicative calibration constant such that the  $\chi^2$  between the distributions from data and from the simulated samples is minimized. The function ensures that the domain  $\Delta\phi \in [0, \pi]$  is respected. The  $\chi^2$  profile is shown in Fig. 8.4a where the points are fitted with a parabolic function, giving a minimum for  $f_{\text{scale}} = 0.9177$ . The calibrated distribution in  $Z \rightarrow \mu\mu$  is shown in Fig. 8.4b. The effects on the efficiency are detailed in Table 8.2. The difference of  $Z \rightarrow \tau\tau$  selection efficiency before and after the calibration is taken as a contribution to the systematic uncertainty.

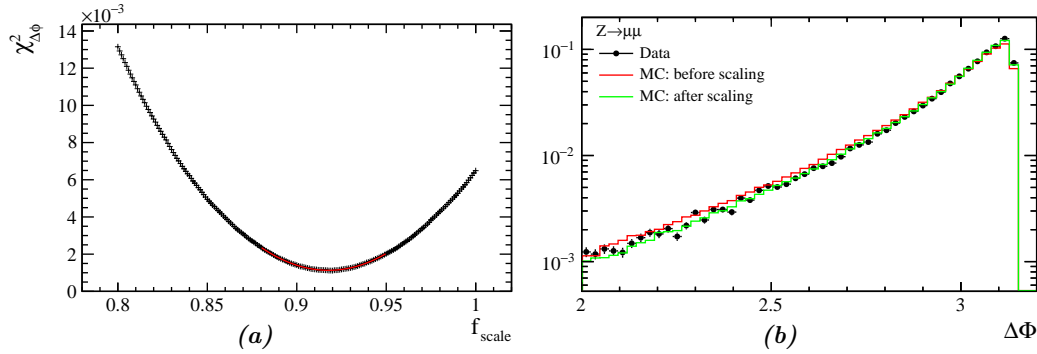


**Figure 8.4** – (a) Distribution of  $\chi^2_{\Delta\phi}(f_{\text{scale}})$  used to calibrate  $\Delta\phi$ , (b) Comparison of  $Z \rightarrow \mu\mu$  from data (black) and simulation before calibration (red), and after calibration (green) of the distribution of  $\pi - \Delta\phi$  of di-muon.

## 8.6 Variables for the Di-tau Channels with $\tau_{h3}$

There is no reliable high- $p_T$  three prongs decay to probe this channel. In an analogous context, the efficiency to detect displaced vertices from long-living particle (LLP)[134] was studied by exploiting re-weighted  $B^0 \rightarrow J/\psi K^{*0}$  followed by the four-particle final state  $J/\psi \rightarrow \mu^+\mu^-$  and  $K^{*0} \rightarrow K^+\pi^-$ . A discrepancy of at most 2% between the LLP efficiencies in data and simulation was inferred.

A more direct approach is the comparison of the  $\tau_{h3}$  distributions in data to the simulation. To enhance the statistical precision, the selection conditions are relaxed; in particular the minimal value of the decay time variable is lowered from 60 fs to 40 fs, requiring a re-fit of the background and signal components. The results are shown in Fig. 8.5.

The differences in the average of the  $m_{\text{corr}}$  distribution is of the order of less than 0.1 GeV (computed in the range 0.5-2.4 GeV). By moving the cuts by these amounts, the data/simulation discrepancy is of 0.7% which is taken as systematic uncertainty to the efficiency. A similar procedure for vertex  $\chi^2/\text{ndf}$  gives a difference between data and simulated distributions which is smaller than 0.1. Taking a value of one, the change in efficiency is less than 0.5%.

In the case of  $\Delta R_{\text{max}}/p_T$  and of the decay time variables, the same method indicates very small discrepancies, from the averages taken in the ranges 0.–0.006, and 60–1000 fs,



## 8.6. Variables for the Di-tau Channels with $\tau_{h3}$

respectively. As an alternative, an exponential fit is done in the region of the nominal cut, as shown in Fig. 8.6. From the data/simulation differences in the fitted parameters, the systematic uncertainties on the efficiency are estimated to be 1.5% and 2.7% respectively.

In conclusion, the contribution of these four observables to the systematic uncertainty on  $\varepsilon_{\text{sel}}$  is 3.2%.

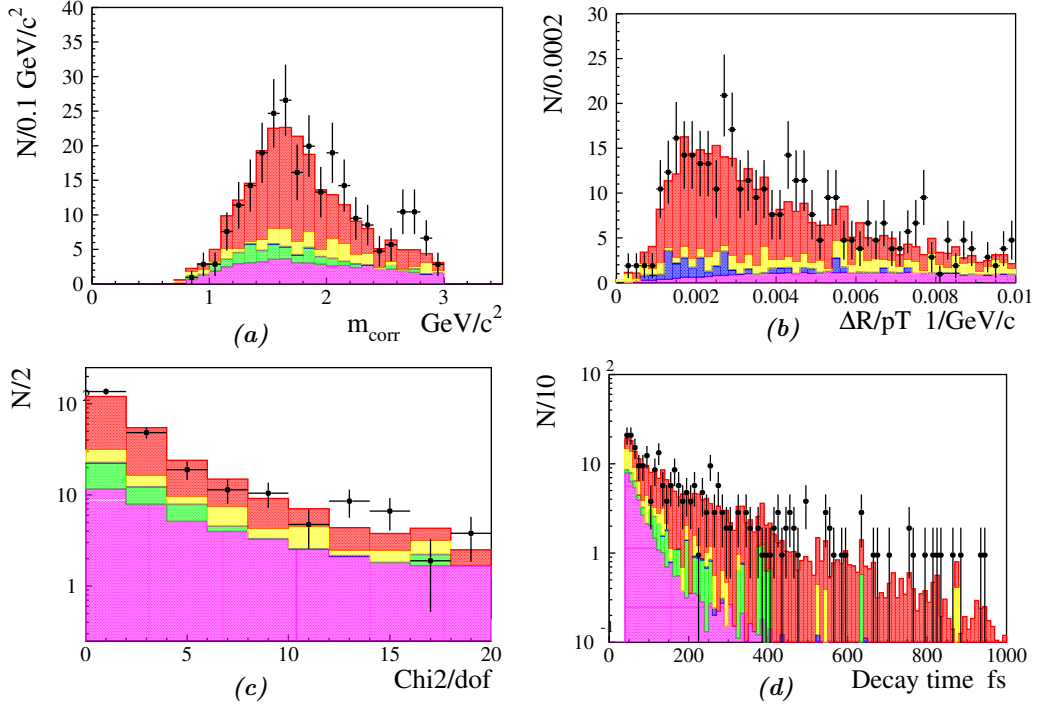


**Figure 8.5** – Comparison data/simulation for the variables relevant to the  $\tau_{h3}$  selection: (a)  $m_{\text{corr}}$  (b)  $\Delta R_{\eta\phi}/p_T$  (c) Vertex  $\chi^2/\text{ndf}$  (d) Decay time. The signal component is in red, the background QCD component in purple, cross-feed in green, di-boson in blue, and boson plus jets in yellow.

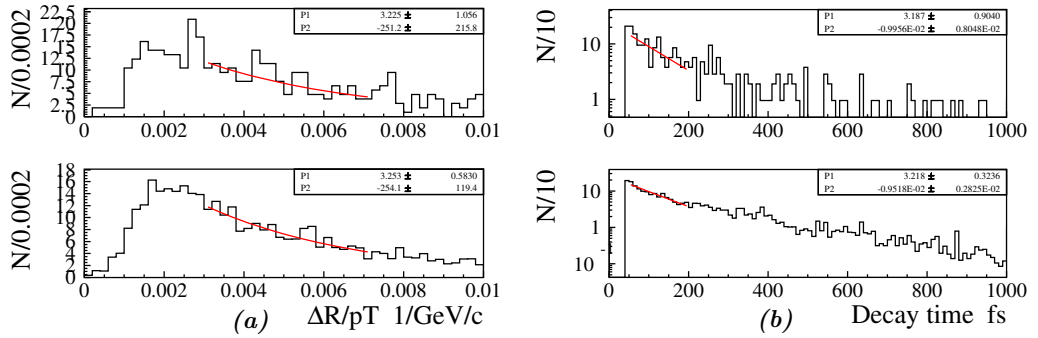


**Figure 8.6** – Comparison data (top plots) and simulation (bottom) for (a)  $\Delta R_{\eta\phi}/p_T$  and (b) decay time, with the result of the exponential fit (in red) in the region of the cut.

## Chapter 8. “Offline” Selection Efficiencies

---

**Table 8.2** – The values of  $\epsilon_{\text{sel}}$  for each di-tau channel, and the absolute changes induced by the corrections. The values are given in percentage.

$\epsilon_{\text{sel}} [\%]$	$\tau_{\mu}\tau_{\mu}$	$\tau_{\mu}\tau_{h1}$	$\tau_{\mu}\tau_{h3}$	$\tau_e\tau_e$	$\tau_e\tau_{h1}$	$\tau_e\tau_{h3}$	$\tau_{\mu}\tau_e$
Before correction	$23.5 \pm 0.3$	$35.6 \pm 0.2$	$33.7 \pm 0.5$	$20.4 \pm 0.4$	$34.6 \pm 0.3$	$31.5 \pm 0.7$	$51.7 \pm 0.3$
IP <sub>2</sub>	+0.04	+0.01	—	+0.05	+0.02	—	—
$\hat{I}_{p_{\Gamma 1}}$	-0.21	-0.35	-0.33	-0.21	-0.37	-0.33	-0.94
$\hat{I}_{p_{\Gamma 2}}$	-1.07	-0.92	-0.25	-1.03	-0.90	-0.22	-1.36
$\Delta\phi$	+0.55	+0.83	+0.76	+0.53	+0.80	+0.74	+1.28
After correction	$22.8 \pm 1.1$	$35.2 \pm 1.2$	$33.9 \pm 1.6$	$19.7 \pm 1.1$	$34.2 \pm 1.2$	$31.6 \pm 1.6$	$50.6 \pm 2.0$

# 9 Uncertainties

Sources of uncertainties for the determination of  $Z$  cross-section in eq. 4.1 are identified in this section, where the relative uncertainty is denoted as  $\delta\sigma_{pp \rightarrow Z \rightarrow \tau\tau}$ . Table 9.1 summarizes uncertainties associated to determination of the background, hence of the signal yield,  $N_{\text{sig}}$ . The contributions to the systematic uncertainties on  $\varepsilon_{\text{rec}}$  and  $\varepsilon_{\text{sel}}$  are in Tables 9.2 and 9.3 respectively. The uncertainty on the branching fractions are taken from the PDG (details in Section 2.4.1), where correlations between di-tau channels are dictated by the tau decay channel involved. The contributions to the total uncertainty are summarized in Table 9.4.

In addition to the already discussed contributions, the following sources of uncertainties are also considered:

- The partonic luminosity uncertainty affects the estimate of the acceptance. The corresponding uncertainty is computed by generating  $Z \rightarrow \tau\tau$  events with different eigenmembers of MSTW08NL090c1 PDF set [116], and determining the variation of  $\mathcal{A}$ . An uncertainty of 1.3% is found for channel  $\tau_l\tau_l$ , 1.9% for channel  $\tau_l\tau_{h1}$ , and 1.5% for channel  $\tau_l\tau_{h3}$ .
- The uncertainty of the LHC beam energy is studied in [135], where the relative uncertainty is determined to be less than 0.1%. This is propagated to the cross-section uncertainty via the variation of  $pp \rightarrow Z \rightarrow ll$  production cross-section inside LHCb fiducial region using DYNNLO 1.5 event generator [136] with MSTW20081o68c1 PDF. The cross-section as a function of  $\sqrt{s}$  is shown in Fig. 9.1, with the linear fit providing a relative systematic uncertainty of 0.18% for a 0.1% change of  $\sqrt{s}$ . This is applied identically to all channels.

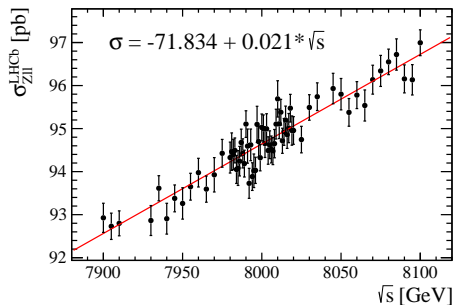


**Figure 9.1** – Production cross-section of  $pp \rightarrow Z \rightarrow ll$  inside LHCb fiducial region generated from DYNNLO as a function of  $\sqrt{s}$ .

## Chapter 9. Uncertainties

**Table 9.1** – Relative uncertainties due to the background estimate. The uncertainties associated to the QCD and  $Vj$  backgrounds are correlated, because obtained from the same fit.

$\delta\sigma_{pp\rightarrow Z\rightarrow\tau\tau}$ [%]	$\tau_\mu\tau_\mu$	$\tau_\mu\tau_{h1}$	$\tau_\mu\tau_{h3}$	$\tau_e\tau_e$	$\tau_e\tau_{h1}$	$\tau_e\tau_{h3}$	$\tau_\mu\tau_e$
$Z\rightarrow ll$	2.34	0.05	—	19.85	0.51	—	0.53
QCD	2.72	2.00	3.21	6.89	5.33	6.96	1.68
$Vj$	1.97	4.45	2.10	2.09	4.60	7.94	2.56
VV	0.02	0.02	0.05	0.04	0.03	0.11	0.05
$t\bar{t}$	0.04	0.02	0.05	0.02	0.02	0.04	0.02
$Z\rightarrow b\bar{b}$	0.09	0.02	0.07	0.09	0.05	0.15	0.02
Cross-feed	0.30	0.26	1.19	3.07	0.56	2.28	0.42
Backgrounds	3.37	3.88	3.23	19.04	5.15	7.98	2.36

**Table 9.2** – Relative uncertainties of reconstruction efficiencies, shown in percentage. The subscript 1(2) refers to tau candidate labeled at position 1(2) of di-tau channel. In case of  $\tau_{h3}$ , the uncertainty from product of 3-prongs is shown.

$\delta\sigma_{pp\rightarrow Z\rightarrow\tau\tau}$ [%]	$\tau_\mu\tau_\mu$	$\tau_\mu\tau_{h1}$	$\tau_\mu\tau_{h3}$	$\tau_e\tau_e$	$\tau_e\tau_{h1}$	$\tau_e\tau_{h3}$	$\tau_\mu\tau_e$
$\varepsilon_{\text{track}}$	1.02	1.92	4.76	3.07	2.85	5.34	1.55
$\hookrightarrow\varepsilon_{\text{track},1}$	0.49	0.48	0.45	1.70	1.58	1.65	0.48
$\hookrightarrow\varepsilon_{\text{track},2}$	0.53	1.86	4.74	1.39	1.88	4.70	1.48
$\varepsilon_{\text{kine}}$	0.00	0.01	0.01	1.25	1.23	1.27	1.10
$\varepsilon_{\text{PID}}$	0.50	0.81	1.72	1.60	1.46	2.25	0.77
$\hookrightarrow\varepsilon_{\text{PID},1}$	0.37	0.39	0.36	1.00	1.19	1.27	0.31
$\hookrightarrow\varepsilon_{\text{PID},2}$	0.13	0.72	1.68	0.80	0.86	1.89	0.70
$\varepsilon_{\text{GEC}}$	0.34	0.66	0.66	0.66	1.06	0.77	0.76
$\varepsilon_{\text{trig}}$	1.77	2.16	2.22	2.55	4.27	3.89	1.55
$\varepsilon_{\text{rec}}$	2.13	3.08	5.56	4.53	5.42	7.06	2.68

**Table 9.3** – Relative uncertainties of selection efficiencies, shown in percentage.

$\delta\sigma_{pp\rightarrow Z\rightarrow\tau\tau}$ [%]	$\tau_\mu\tau_\mu$	$\tau_\mu\tau_{h1}$	$\tau_\mu\tau_{h3}$	$\tau_e\tau_e$	$\tau_e\tau_{h1}$	$\tau_e\tau_{h3}$	$\tau_\mu\tau_e$
$A_{p_T}$	1.11	—	—	1.11	—	—	0.01
di-tau mass	0.90	—	—	1.44	—	—	—
$\hat{I}_{p_T1}$	1.56	1.49	1.51	1.45	1.42	1.42	1.89
$\hat{I}_{p_T2}$	3.74	2.06	1.71	3.99	2.06	1.74	2.22
IP <sub>2</sub>	0.17	0.04	—	0.22	0.05	—	—
$\Delta\phi$	2.36	2.32	2.24	2.60	2.31	2.36	2.47
Vertex $\chi^2/\text{ndf}$	—	—	0.50	—	—	0.50	—
$\Delta R_{\text{max}}/p_T$	—	—	1.50	—	—	1.50	—
Decay time	—	—	2.70	—	—	2.70	—
$m_{\text{corr}}$	—	—	0.70	—	—	0.70	—
Statistical	1.10	0.61	1.41	2.04	0.92	2.15	0.53
Total	5.03	3.50	4.74	5.69	3.53	5.05	3.86

**Table 9.4** – Summary of the relative uncertainties of the various contributions affecting the cross-section measurement, given in percentage.

$\delta\sigma_{pp\rightarrow Z\rightarrow\tau\tau}$ [%]	$\tau_\mu\bar{\tau}_\mu$	$\tau_\mu\bar{\tau}_{h1}$	$\tau_\mu\bar{\tau}_{h3}$	$\tau_e\bar{\tau}_e$	$\tau_e\bar{\tau}_{h1}$	$\tau_e\bar{\tau}_{h3}$	$\tau_\mu\bar{\tau}_e$
$\mathcal{B}$	0.46	0.29	0.53	0.45	0.29	0.53	0.32
$\mathcal{A}$ (PDF)	1.31	1.90	1.50	1.30	1.90	1.50	1.30
$\varepsilon_{\text{rec}}$	2.13	3.08	5.56	4.53	5.41	7.04	2.68
$\varepsilon_{\text{sel}}$	5.03	3.50	4.74	5.69	3.53	5.05	3.86
$N_{\text{sig}}$	3.37	3.88	3.23	19.04	5.15	7.98	2.36
Beam energy	0.18	0.18	0.18	0.18	0.18	0.18	0.18
Luminosity	1.16	1.16	1.16	1.16	1.16	1.16	1.16
Statistical	6.93	3.75	8.05	17.61	6.61	13.10	3.44
Total	9.62	7.48	11.52	26.99	10.81	17.73	6.53



# 10 Results

## 10.1 Fiducial Cross-sections

The production cross-sections of  $Z \rightarrow \tau\tau$  in LHCb fiducial region for each di-tau channels calculated with eq. 4.1 are the following:

$$\begin{aligned}
 \sigma(\tau_\mu\tau_\mu) &= 109.28 \pm 7.57 \pm 7.18 \pm 0.20 \pm 1.27 \text{ pb} \\
 \sigma(\tau_\mu\tau_{h1}) &= 98.87 \pm 3.71 \pm 6.29 \pm 0.18 \pm 1.15 \text{ pb} \\
 \sigma(\tau_\mu\tau_{h3}) &= 94.72 \pm 7.63 \pm 7.72 \pm 0.17 \pm 1.10 \text{ pb} \\
 \sigma(\tau_e\tau_e) &= 94.20 \pm 16.58 \pm 19.25 \pm 0.17 \pm 1.09 \text{ pb} \\
 \sigma(\tau_e\tau_{h1}) &= 100.98 \pm 6.67 \pm 8.56 \pm 0.18 \pm 1.17 \text{ pb} \\
 \sigma(\tau_e\tau_{h3}) &= 104.30 \pm 13.67 \pm 12.40 \pm 0.19 \pm 1.21 \text{ pb} \\
 \sigma(\tau_\mu\tau_e) &= 91.50 \pm 3.15 \pm 4.96 \pm 0.16 \pm 1.06 \text{ pb}
 \end{aligned}$$

where uncertainty values are statistical, systematic, associated with the LHC beam energy uncertainty, and with the integrated luminosity uncertainty, respectively. The values of each term in eq. 4.1 are reproduced in Table 10.1, with more detail in appendix F.

The BLUE (best linear unbiased estimator) technique [132] is used to combine the measurements from all channels, taking into account their correlations. The combined result is

$$\sigma_{Z \rightarrow \tau^+\tau^-} = 95.20 \pm 2.13 \pm 4.79 \pm 0.17 \pm 1.10 \text{ pb}$$

with a  $\chi^2/\text{ndf}$  value of 0.70. More details of the combination procedure can be found in appendix G. The results can be compared with the previous  $Z \rightarrow \mu\mu$  and  $Z \rightarrow ee$  measurements inside the same fiducial region at 8 TeV, which are presented in Fig. 10.1, along with the predictions from various theoretical models [108].

**Table 10.1** – Summary of the quantities used in the calculation of cross-section, shown in percentage.

	$\tau_\mu\tau_\mu$	$\tau_\mu\tau_{h1}$	$\tau_\mu\tau_{h3}$	$\tau_e\tau_e$	$\tau_e\tau_{h1}$	$\tau_e\tau_{h3}$	$\tau_\mu\tau_e$
$\mathcal{B}$	$3.03 \pm 0.01$	$17.45 \pm 0.05$	$5.07 \pm 0.03$	$3.18 \pm 0.01$	$17.87 \pm 0.05$	$5.20 \pm 0.03$	$6.21 \pm 0.02$
$\varepsilon_{\text{tot}}$	$5.75 \pm 0.32$	$2.83 \pm 0.14$	$1.73 \pm 0.13$	$2.15 \pm 0.16$	$1.20 \pm 0.08$	$0.68 \pm 0.06$	$8.93 \pm 0.44$
$\mathcal{A}$	$38.95 \pm 0.51$	$15.31 \pm 0.29$	$24.53 \pm 0.37$	$37.89 \pm 0.49$	$15.07 \pm 0.29$	$24.16 \pm 0.36$	$38.55 \pm 0.50$
$\varepsilon_{\text{rec}}$	$64.76 \pm 1.38$	$52.63 \pm 1.62$	$20.75 \pm 1.15$	$28.77 \pm 1.30$	$23.28 \pm 1.26$	$8.89 \pm 0.63$	$45.81 \pm 1.23$
$\varepsilon_{\text{sel}}$	$22.78 \pm 1.14$	$35.17 \pm 1.23$	$33.92 \pm 1.61$	$19.73 \pm 1.12$	$34.18 \pm 1.21$	$31.65 \pm 1.60$	$50.59 \pm 1.95$

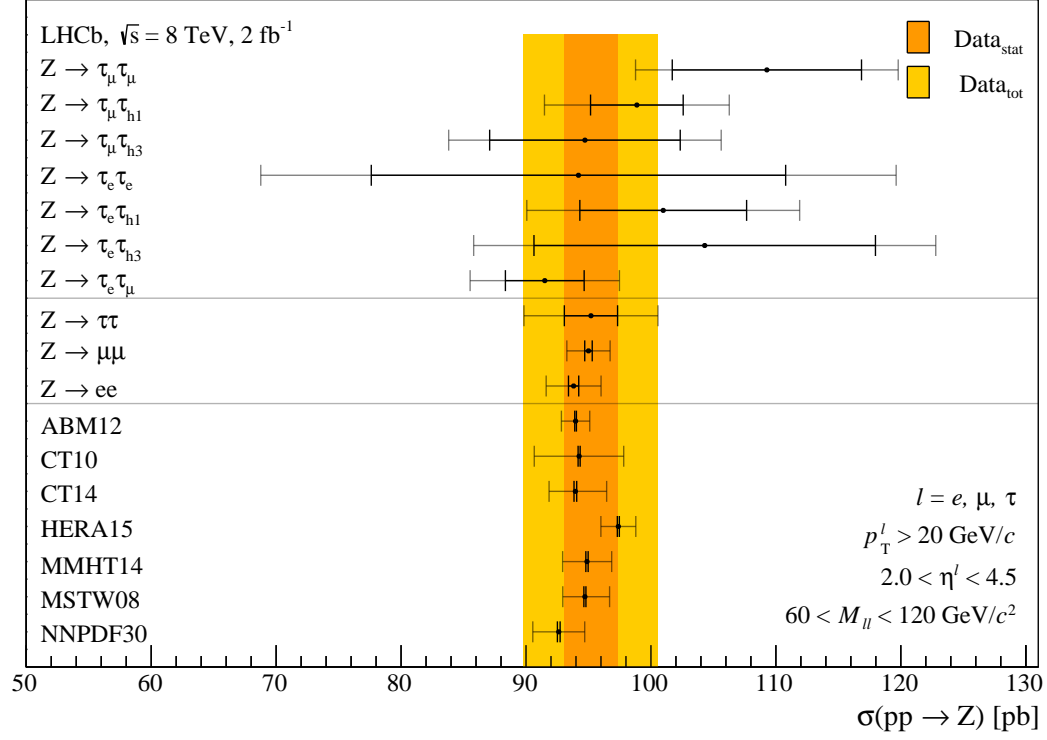


**Figure 10.1** – Summary of the measurements of  $Z \rightarrow ll$  production cross-section inside the LHCb fiducial region at 8 TeV. The dark inner error bar corresponds to the statistical uncertainty, whilst the light outer error bar is the total uncertainty. The colored band corresponds to the combined measurement of from  $Z \rightarrow \tau\tau$  of this analysis. The last 7 rows represent the NNLO predictions with different parameterizations of the PDFs [108].

## 10.2 Cross-section Ratios at Different Centre-of-mass Energies

The ratio of the  $Z \rightarrow \tau\tau$  cross-sections at  $\sqrt{s} = 8 \text{ TeV}$  and  $7 \text{ TeV}$  using LHCb results is

$$\frac{\sigma_{Z \rightarrow \tau\tau}^{8 \text{ TeV}}}{\sigma_{Z \rightarrow \tau\tau}^{7 \text{ TeV}}} = 1.333 \pm 0.088$$

where the systematic uncertainty is conservatively assumed to be fully correlated as the procedure between the two analyses are closely related, whereas the statistical and luminosity uncertainties are assumed to be uncorrelated as the analyses use different datasets. The results can be compared with the ratios from  $Z \rightarrow ee$ ,  $Z \rightarrow \mu\mu$  analyses:

$$\frac{\sigma_{Z \rightarrow ee}^{8 \text{ TeV}}}{\sigma_{Z \rightarrow ee}^{7 \text{ TeV}}} = 1.234 \pm 0.049 \quad , \quad \frac{\sigma_{Z \rightarrow \mu\mu}^{8 \text{ TeV}}}{\sigma_{Z \rightarrow \mu\mu}^{7 \text{ TeV}}} = 1.250 \pm 0.034$$

The ratio is found to be in a good agreement with the theoretical prediction from DYNLO [137] using MSTW08 [116] as a PDF, yielding the ratio of  $1.272 \pm 0.009$ .



### 10.3 Lepton Universality

The lepton universality hypothesis in  $Z$  decays can be tested from the ratio of the leptonic cross-sections:

$$\frac{\sigma_{Z \rightarrow \tau\tau}^{8 \text{ TeV}}}{\sigma_{Z \rightarrow \mu\mu}^{8 \text{ TeV}}} = 1.002 \pm 0.057 \quad , \quad \frac{\sigma_{Z \rightarrow \tau\tau}^{8 \text{ TeV}}}{\sigma_{Z \rightarrow ee}^{8 \text{ TeV}}} = 1.015 \pm 0.059 \quad , \quad \frac{\sigma_{Z \rightarrow \mu\mu}^{8 \text{ TeV}}}{\sigma_{Z \rightarrow ee}^{8 \text{ TeV}}} = 1.013 \pm 0.018$$

where the uncertainties in beam energy and luminosity are assumed to be fully correlated as the three analyses were performed at the same 2012 condition, whilst the statistical and systematic uncertainties are assumed to be uncorrelated. This can be compared with the lepton universality tests performed on 7 TeV data [138, 139, 107]:

$$\frac{\sigma_{Z \rightarrow \tau\tau}^{7 \text{ TeV}}}{\sigma_{Z \rightarrow \mu\mu}^{7 \text{ TeV}}} = 0.939 \pm 0.062 \quad , \quad \frac{\sigma_{Z \rightarrow \tau\tau}^{7 \text{ TeV}}}{\sigma_{Z \rightarrow ee}^{7 \text{ TeV}}} = 0.939 \pm 0.065 \quad , \quad \frac{\sigma_{Z \rightarrow \mu\mu}^{7 \text{ TeV}}}{\sigma_{Z \rightarrow ee}^{7 \text{ TeV}}} = 1.000 \pm 0.034$$

### 10.4 Tau Lepton Decay Branching Fraction

The four branching fractions of  $\tau$  lepton decay to electron, muon, one and three hadrons, can be obtained by treating them as unknown parameters and fitted to the cross-section measurements listed in Section 10.1. The  $Z \rightarrow \mu\mu$  cross section is used as reference, as it has the smallest uncertainty. The minimized  $\chi^2$  is,

$$\chi^2 = \sum_i^{7 \text{ channels}} \left( \frac{\sigma_{Z \rightarrow \tau\tau}^i - \sigma_{Z \rightarrow \mu\mu}}{\delta(\sigma_{Z \rightarrow \tau\tau}^i)} \right)^2$$

with  $\sigma_{Z \rightarrow \tau\tau}^i \pm \delta(\sigma_{Z \rightarrow \tau\tau}^i)$  the  $Z \rightarrow \tau\tau$  cross-section measurement with associated uncertainty. The uncertainty contains only the relevant elements (statistical and systematic, excluding the luminosity and beam energy uncertainties). The 4 unknown  $\tau$  lepton branching fractions are fitted using MIGRAD, and the fit results with errors are given in Table 10.2. They are found to be compatible with the values found in the PDG, also displayed.

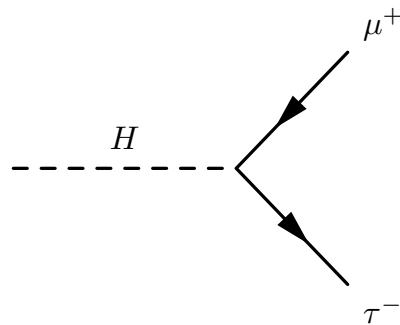
**Table 10.2** – The  $\tau$  lepton branching fractions obtained from the fit of the  $Z \rightarrow \tau\tau$  cross-section measurements. The values from the PDG are given in the bottom row.

$\mathcal{B}$ [%]	$\tau_e$	$\tau_{h1}$	$\tau_{h3}$	$\tau_\mu$
Fit	$17.31 \pm 0.91$	$51.93 \pm 3.19$	$14.67 \pm 1.22$	$17.90 \pm 0.72$
PDG	$17.83 \pm 0.04$	$50.11 \pm 0.09$	$14.57 \pm 0.07$	$17.41 \pm 0.04$



## Part III

### Search for CLFV of a Higgs-like scalar decay $H \rightarrow \mu\tau$





# 11 $H \rightarrow \mu\tau$ at LHCb

The search for model-independent CLFV decay,  $H \rightarrow \mu\tau$ , of a CP-even Higgs-like scalar with a mass ranging from 45 to 195 GeV/ $c^2$  is presented in this Section. The production cross-section to this decay mode is denoted as  $\sigma_{gg \rightarrow H \rightarrow \mu\tau}$ . The theoretical motivation for CLFV as a gateway for new physics, as well as recent searches and constraints are discussed in Section 2.3. The performance of tau identification and reconstruction at LHCb has been studied extensively with  $Z \rightarrow \tau\tau$  decay in Part II. A good performance on tau identification and background rejection is expected, based on a precise tracking and vertex resolution of the LHCb detector.

The analysis is separated into 4 channels depending on the final state of the  $\tau$  lepton decay: (i) single muon ( $\mu\tau_\mu$ ), (ii) single electron ( $\mu\tau_e$ ), (iii) single charged hadron ( $\mu\tau_{h1}$ ), and (iv) three-prongs charged hadrons ( $\mu\tau_{h3}$ ). The selection of the  $H \rightarrow \mu\tau$  candidates will be discussed in Chapter 12.

The main sources of background are  $Z \rightarrow \tau\tau$  decays, QCD processes with heavy flavour production, electroweak boson production accompanied with jets. The estimation of these backgrounds will be discussed in Chapter 13, and the determination of signal efficiencies in Chapter 14 and associated uncertainties in Chapter 15. Finally, the statistical treatment of signal likelihood and its upper limit will be discussed in Chapter 16, with results presented in Chapter 17.

## 11.1 Data Samples

The dataset collected by LHCb at  $\sqrt{s} = 8$  TeV is used, which is the same dataset used in the  $Z \rightarrow \tau\tau$  analysis (Section 4.3), corresponding to a total integrated luminosity of  $1976.2 \pm 22.9$  pb $^{-1}$ . The  $H \rightarrow \mu\tau$  signal samples are generated by PYTHIA 8.175, using SM Higgs produced via  $gg$ -fusion only<sup>1</sup>. The Higgs decay modes are modified to only produce  $H \rightarrow \mu\tau$ , with masses  $m_H$  from 45 to 195 GeV/ $c^2$ , by step of 10 GeV/ $c^2$ . The number of events is  $10^5$  per sample. The simulated samples discussed in Section 4.3.2 are also used in this analysis as background processes.

---

<sup>1</sup> Corresponding to PYTHIA flag `HiggsSM:gg2H`.



# 12 Signal Selection

The analysis described in this section is largely inspired by the  $Z \rightarrow \tau\tau$  analysis described in Chapter 5. The summary of the selection requirements in the tabulated form is provided in Section 12.4.

## 12.1 Acceptance

The “acceptance” is defined by the kinematic requirements (after final state radiation) on the observables  $p_T$ ,  $\eta$  of the prompt muon and of the  $\tau$  lepton decay products, and on  $m$ , the invariant mass of the pair.  $m$  is an approximation of the Higgs-like particle mass. All the particles must be in the geometrical acceptance defined by the pseudorapidity range  $2.0 < \eta < 4.5$ . Other acceptance criteria depend on the channel:

**Channel  $\mu\tau_e$**  Requiring one muon and one electron with  $p_T > 5 \text{ GeV}/c$ , one of them with  $p_T > 20 \text{ GeV}/c$ . The invariant mass of the pair must be greater than  $20 \text{ GeV}/c^2$ .

**Channel  $\mu\tau_{h1}$**  Requiring one muon of  $p_T > 20 \text{ GeV}/c$ , and a single charged hadron of  $p_T > 10 \text{ GeV}/c$ . The invariant mass of the pair must be greater than  $30 \text{ GeV}/c^2$ .

**Channel  $\mu\tau_{h3}$**  Requiring one muon of  $p_T > 20 \text{ GeV}/c$ , and three charged hadrons all having  $p_T > 1 \text{ GeV}/c$  with at least one of them having  $p_T > 6 \text{ GeV}/c$ . The total transverse momentum from three charged hadrons must be above  $12 \text{ GeV}/c$ , and the invariant mass within  $0.7\text{--}1.5 \text{ GeV}/c^2$ . The invariant mass calculated from the four-momenta sum of muon and the three charged hadrons must be greater than  $30 \text{ GeV}/c^2$ .

**Channel  $\mu\tau_\mu$**  Requiring one muon with  $p_T > 20 \text{ GeV}/c$ , and a second muon of  $p_T > 5 \text{ GeV}/c$ . The invariant mass of the pair must be greater than  $20 \text{ GeV}/c^2$ .

These acceptance definitions are identical to their counterpart in  $Z \rightarrow \tau\tau$  analysis defined in Section 5.2, mapping  $\mu\tau_e$  to  $\tau_\mu\tau_e$  channel,  $\mu\tau_{h1}$  to  $\tau_\mu\tau_{h1}$ ,  $\mu\tau_{h3}$  to  $\tau_\mu\tau_{h3}$ , and  $\mu\tau_\mu$  to  $\tau_\mu\tau_\mu$ . Distributions of the relevant kinematic variables obtained at the generator level are available in appendix H.

## 12.2 Trigger and Reconstruction Requirements

The trigger and reconstruction requirements for  $H \rightarrow \mu\tau$  candidates are identical to the ones used in  $Z \rightarrow \tau\tau$  analysis, described in Sections 5.3 to 5.5.

## 12.3 Offline Selection

The offline selection is applied to reconstructed  $\mu\tau$  candidates, with the selection optimization based on the figure-of-merit (FOM)  $\varepsilon_{\text{sel}}/(1 + \sqrt{N_{\text{obs}}})$  [140], where  $\varepsilon_{\text{sel}}$  is the efficiency of signal selection (to be outlined below) from simulation, and  $N_{\text{obs}}$  is the number of selected candidates in data.

Because of the wide range of  $m_H$ , three different selection *regimes* are considered such that each regime is optimized for particular range of  $m_H$ . The *central* selection regime is similar to the one chosen for the  $Z \rightarrow \tau\tau$  analysis; as such, it is optimized for  $m_H \sim m_Z$ . The *low-mass* regime is optimized for  $45 < m_H \ll m_Z$ , and *high-mass* regime is optimized for  $m_Z \ll m_H < 195$ . Details about the criteria for the 3 regimes are given in the following sections, and summarized in Section 12.4. In practice the analysis is carried out running the selection corresponding to the three regimes in parallel (in the following, we will indicate with the word “regime” the Higgs mass range and the corresponding selection criteria). Only at the end the choice is placed on the result with the best FOM. For instance, we can anticipate that for the  $\mu\tau_e$  channel the high-mass regime will be preferred for  $m_H$  above  $100 \text{ GeV}/c^2$ , the central regime for the region  $65\text{--}100 \text{ GeV}/c^2$ , and the low-mass regime below  $65 \text{ GeV}/c^2$ . For illustration, the FOM values for the three regimes and the four channels are given in Fig. 12.2 as a function of  $m_H$ , obtained at the end of the analysis process with all the selection criteria applied. Distributions of some kinematic variables from simulation are given in appendix I.

### 12.3.1 Transverse Momentum

The selection requires a prompt muon  $p_T > 20 \text{ GeV}/c$  for the low-mass regime,  $p_T > 30 \text{ GeV}/c$  for the central regime, and  $p_T > 40 \text{ GeV}/c$  for the high-mass regime. Additionally,  $p_T > 20 \text{ GeV}/c$  is also required for  $\tau_e, \tau_{h1}, \tau_{h3}$  in the high-mass regime. This is not required for  $\tau_\mu$  as  $Z \rightarrow \mu\mu$  is the dominating background and this criterion does not improve the FOM.

### 12.3.2 Combination Quality of $\tau_{h3}$

Using the definition in Section 5.6.1.1, a reconstructed 3-prongs vertex with  $\chi^2/\text{ndf} < 9$  is required. The distance in  $\eta\text{--}\phi$  space,  $\Delta R_{\eta\phi}$ , between any pair of charged hadrons is expected to be small for true 3-prongs candidates and becomes smaller as the  $p_T$  sum of the prongs increases. To ensure collimation, the selection requires  $\Delta R_{\text{max}}/p_T < 0.01 (\text{GeV}/c)^{-1}$  (see Fig. 12.1). This is not used for the low-mass regime because of the relatively low boost of the  $\tau_{h3}$  system.

### 12.3.3 Isolation

Using the definition of isolation variables in Section 5.6.1.2, the selection requires  $\hat{I}_{p_T} > 0.9$  for muon and tau candidates for all channels and regimes. In addition, at low-mass regime, the additional requirement  $\vec{p}_{\text{cone}})_T < 2 \text{ GeV}/c$ , is applied to muon and tau candidates, as their  $p_T$  can be low, making the  $\hat{I}_{p_T}$  requirement less effective to reject background.



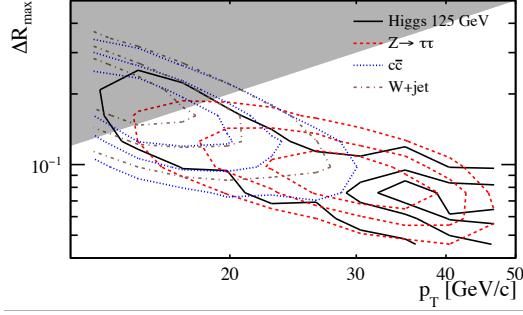


**Figure 12.1** –  $\Delta R_{\max}$  vs.  $p_T$  for different processes. The grey area is discarded by the selection.

### 12.3.4 Decay Time and Corrected Mass of $\tau_{h3}$

Using the definition of *decay time* and corrected mass in Section 5.6.1.3, a minimum decay time of 30 fs and a corrected mass  $m_{\text{corr}} < 3 \text{ GeV}/c^2$  are required in all regimes.

### 12.3.5 Impact Parameter

The decay  $H \rightarrow \mu\tau$  is supposed to be prompt, hence the IP is expected to be small for the muon, and relatively large for the  $\tau$  lepton decay products. The selection in all regimes requires  $\text{IP} < 0.05 \text{ mm}$  for the muon,  $\text{IP} > 0.01 \text{ mm}$  for  $\tau_e, \tau_{h1}$ , and  $\text{IP} > 0.05 \text{ mm}$  for  $\tau_\mu$  to suppress  $Z \rightarrow \mu\mu$  background.

### 12.3.6 Azimuthal Separation

The *azimuthal separation*,  $\Delta\phi \in [0, \pi]$ , is defined as the angle between the  $\mu$  and the  $\tau$  candidate in the transverse plane. The selection requires  $\Delta\phi > 2.7$  for all channels across all regimes.

### 12.3.7 Transverse Momentum Asymmetry

Using the definition of transverse momentum asymmetry defined in Section 5.6.2.3, the selection requires  $A_{p_T} > 0.3$  in the  $\mu\tau_\mu$  channel where the background is expected to be largely dominated by  $Z \rightarrow \mu\mu$ , and becomes  $A_{p_T} > 0.4$  in the high-mass regime. In  $\mu\tau_{h1}$  channel, the background from electroweak processes can be suppressed requiring  $A_{p_T} < 0.5(0.4)$  in the central (low-mass) regime. The requirement  $A_{p_T} < 0.6$  is also adopted for the low-mass  $\mu\tau_e$  channel. The cut is looser because the  $p_T$  of  $\tau_e$  is softer than  $\tau_{h1}$ . Lastly, channel  $\mu\tau_e$  also requires the muon  $p_T$  to be larger than the  $p_T$  of  $\tau_e$ , to suppress the  $W/Z \rightarrow (e) + \text{jet}$  background. This also allows a simplification of the background estimation procedure described in the Chapter 13.

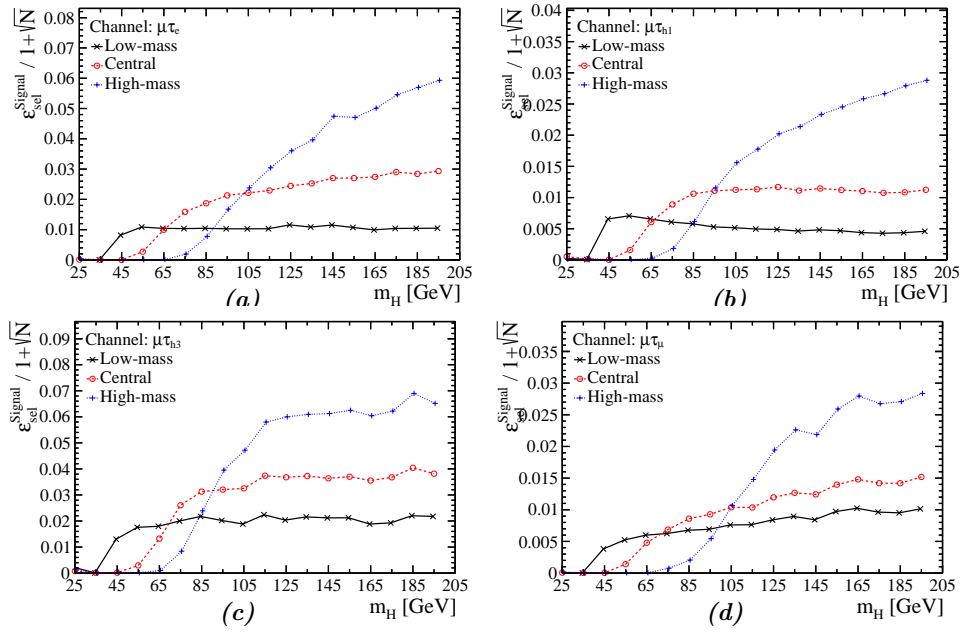


Figure 12.2 – Figure-of-merit as a function of  $m_H$  for different channels and regimes.

## 12.4 Summary of Selections

**Table 12.1** – Summary of the acceptance requirements, where  $\tau_x$  denotes the  $\tau$  decay channel.

Variables	Unit	$\mu\tau_e$	$\mu\tau_{h1}$	$\mu\tau_{h3}$	$\mu\tau_\mu$
$p_T(\mu)$	GeV/c	$> 20$	$> 20$	$> 20$	$> 20$
$p_T(\tau_x)$	GeV/c	$> 5$	$> 10$	$> 12$	$> 5$
$\eta(\mu)$	-	[2.0, 4.5]	[2.0, 4.5]	[2.0, 4.5]	[2.0, 4.5]
$\eta(\tau_x)$	-	[2.0, 4.5]	[2.0, 4.5]	—	[2.0, 4.5]
$m(\mu\tau_x)$	GeV/c <sup>2</sup>	$> 20$	$> 30$	$> 30$	$> 20$

**Table 12.2** – Additional acceptance requirements for  $\tau_{h3}$  in  $\mu\tau_{h3}$  channel, where  $h$  denotes one of the charged hadrons used in the reconstruction of the 3-prongs.

Variables	Unit	Cut
$\min(p_T(h))$	GeV/c	$> 1$
$\max(p_T(h))$	GeV/c	$> 6$
$\eta(h)$	-	[2.0, 4.5]
$m(\tau_{h3})$	MeV/c <sup>2</sup>	[700, 1500]

**Table 12.3** – Tracking selections, applied identically to muons, charged hadrons, and electrons.

Variables	Cut
Track type	LONG
Track prob. $\chi^2$	$> 0.01$

**Table 12.4** – Summary of the particle identification criteria.

Variables	Unit	Muons	Charged hadrons	Electrons
ISMUON	-	True	-	-
ISMUONLOOSE	-	-	False	False
InAccPrs	-	-	-	True
InAccEcal	-	-	-	True
InAccHcal	-	-	True	True
$E_{PRS}$	MeV	-	-	$> 50$
$E_{ECAL}/p$	-	-	-	$> 0.1$
$E_{HCAL}/p$	-	-	$> 0.05$	$< 0.05$

**Table 12.5** – Offline selections for  $\tau_{h3}$  in the  $\mu\tau_{h3}$  channel, for the three analysis regimes.

Variables	Unit	Central, High-mass	Low-mass
Vertex $\chi^2/\text{ndf}$	-	$< 9$	$< 9$
$\Delta R_{\text{max}}/p_{\text{T}}$	$(\text{GeV}/c)^{-1}$	$< 0.01$	-
$m_{\text{corr}}$	$\text{GeV}/c^2$	$< 3.0$	$< 3.0$
Decay time	fs	$> 30$	$> 30$

**Table 12.6** – Selections in common to all analysis regimes

Variables	Unit	$\mu\tau_e$	$\mu\tau_{h1}$	$\mu\tau_{h3}$	$\mu\tau_{\mu}$
$\hat{I}_{p_{\text{T}}}(\mu)$	-	$> 0.9$	$> 0.9$	$> 0.9$	$> 0.9$
$\hat{I}_{p_{\text{T}}}(\tau_x)$	-	$> 0.9$	$> 0.9$	$> 0.9$	$> 0.9$
IP( $\mu$ )	mm	[0, 0.05]	[0, 0.05]	[0, 0.05]	[0, 0.05]
IP( $\tau_x$ )	mm	$> 0.01$	$> 0.01$	-	$> 0.05$
$\Delta\phi$	rad	$> 2.7$	$> 2.7$	$> 2.7$	$> 2.7$
$p_{\text{T}}(\mu) - p_{\text{T}}(\tau_x)$	GeV/c	$> 0$	-	-	-

**Table 12.7** – Selections specific for each analysis regime.

Regime	Variables	Unit	$\mu\tau_e$	$\mu\tau_{h1}$	$\mu\tau_{h3}$	$\mu\tau_{\mu}$
Low-mass	$I_{p_{\text{T}}}(\mu)$	GeV/c	$< 2$	$< 2$	$< 2$	$< 2$
	$I_{p_{\text{T}}}(\tau_x)$	GeV/c	$< 2$	$< 2$	$< 2$	$< 2$
	$p_{\text{T}}(\mu)$	GeV/c	$> 20$	$> 20$	$> 20$	$> 20$
	$A_{p_{\text{T}}}$	-	$< 0.6$	$< 0.4$	-	$> 0.3$
Central	$p_{\text{T}}(\mu)$	GeV/c	$> 30$	$> 30$	$> 30$	$> 30$
	$A_{p_{\text{T}}}$	-	-	$< 0.5$	-	$> 0.3$
High-mass	$p_{\text{T}}(\mu)$	GeV/c	$> 40$	$> 40$	$> 40$	$> 50$
	$p_{\text{T}}(\tau_x)$	GeV/c	$> 20$	$> 20$	$> 20$	-
	$A_{p_{\text{T}}}$	-	-	-	-	$> 0.4$

# 13 Background Estimation

The estimation of the number of backgrounds for  $H \rightarrow \mu\tau$  candidates is discussed in this section. The results are summarized in Table 13.5. The methods are similar to the procedures described in Chapter 6.

## 13.1 $Z \rightarrow \tau\tau$

The  $Z \rightarrow \tau\tau$  process becomes a background when one of the  $\tau$  leptons decays to a muon. The number of expected background from this source is calculated from the expression:

$$N_{Z \rightarrow \tau\tau} = \mathcal{L} \cdot \sigma_{pp \rightarrow Z} \cdot \mathcal{B}_{Z \rightarrow \tau\tau} \cdot \mathcal{A}_{Z \rightarrow \tau\tau} \cdot \varepsilon_{\text{rec}, Z \rightarrow \tau\tau} \cdot \varepsilon_{\text{sel}, Z \rightarrow \tau\tau} \cdot \rho_{Z \rightarrow \tau\tau}^{-1} \quad (13.1)$$

The  $Z$  boson production cross-section in the LHCb  $Z \rightarrow ll$  fiducial region,  $\sigma_{pp \rightarrow Z}$ , is taken from the results of  $Z \rightarrow \mu\mu$  [108] and  $Z \rightarrow ee$  [109] combined, in which the fiducial region is defined as  $p_T(\ell) > 20 \text{ GeV}/c$ ,  $2.0 < \eta(\ell) < 4.5$ , and  $60 < m_{\ell\ell} < 120 \text{ GeV}/c^2$ .  $\mathcal{B}_{Z \rightarrow \tau\tau}$  is the branching fraction for  $Z$  decays to two tau leptons [123].

The acceptance factor,  $\mathcal{A}_{Z \rightarrow \tau\tau}$ , is the number of final states di-tau candidates satisfying the acceptance requirement of Section 12.1, divided by the number of di-tau candidates inside the fiducial acceptance. It is calculated from simulation, using POWHEG-BOX at the next-to-leading order with MSTW08NL090c1 PDF, showered by PYTHIA 8.175.

The reconstruction efficiency,  $\varepsilon_{\text{rec}, Z \rightarrow \tau\tau}$ , is the product of the tracking, kinematic, particle identification, global event cut, and trigger efficiencies. They are computed with the procedures described in Chapter 7 from the simulated samples and corrected by comparison with data where applicable.

The selection efficiency,  $\varepsilon_{\text{sel}, Z \rightarrow \tau\tau}$ , is determined from simulated samples of  $Z \rightarrow \tau\tau$  as the fraction of reconstructed di-tau candidates that passes the  $\mu\tau$  offline selections. The purity factor,  $\rho_{Z \rightarrow \tau\tau}$ , defines the fraction of selected di-tau candidates for a given channel which originates from  $Z \rightarrow \tau\tau$  of the identical channel.  $\rho_{Z \rightarrow \tau\tau}$  is determined from simulation.

The summary of the numerical values of the terms of eq. 13.1 is given in Table 13.1.

**Table 13.1** – Di-tau branching fraction, acceptance, reconstruction efficiency, offline selection efficiencies, and purity factor used in the computation of eq. 13.1, shown in percentage.

Regime	Channel	$\mathcal{B}_{Z \rightarrow \tau\tau}$	$\mathcal{A}_{Z \rightarrow \tau\tau}$	$\epsilon_{\text{rec}, Z \rightarrow \tau\tau}$	$\epsilon_{\text{sel}, Z \rightarrow \tau\tau}$	$\rho_{Z \rightarrow \tau\tau}$
Low-mass	$\mu\tau_e$	$6.21 \pm 0.02$	$38.60 \pm 0.03$	$45.54 \pm 1.59$	$17.53 \pm 0.20$	$94.45 \pm 0.60$
	$\mu\tau_{h1}$	$17.45 \pm 0.05$	$15.44 \pm 0.01$	$52.84 \pm 1.85$	$25.56 \pm 0.20$	$97.79 \pm 0.25$
	$\mu\tau_{h3}$	$5.07 \pm 0.03$	$24.53 \pm 0.03$	$19.15 \pm 1.15$	$28.89 \pm 0.47$	$93.39 \pm 0.90$
	$\mu\tau_\mu$	$3.03 \pm 0.01$	$39.14 \pm 0.04$	$63.68 \pm 1.91$	$9.82 \pm 0.18$	$98.97 \pm 0.40$
Central	$\mu\tau_e$	$6.21 \pm 0.02$	$38.60 \pm 0.03$	$46.36 \pm 1.62$	$9.10 \pm 0.15$	$92.59 \pm 0.98$
	$\mu\tau_{h1}$	$17.45 \pm 0.05$	$15.44 \pm 0.01$	$52.70 \pm 1.84$	$10.84 \pm 0.14$	$97.82 \pm 0.39$
	$\mu\tau_{h3}$	$5.07 \pm 0.03$	$24.53 \pm 0.03$	$19.30 \pm 1.16$	$12.93 \pm 0.35$	$92.74 \pm 1.43$
	$\mu\tau_\mu$	$3.03 \pm 0.01$	$39.14 \pm 0.04$	$65.40 \pm 1.96$	$4.99 \pm 0.13$	$98.83 \pm 0.64$
High-mass	$\mu\tau_e$	$6.21 \pm 0.02$	$38.60 \pm 0.03$	$53.16 \pm 1.86$	$0.52 \pm 0.04$	$87.92 \pm 7.31$
	$\mu\tau_{h1}$	$17.45 \pm 0.05$	$15.44 \pm 0.01$	$52.75 \pm 1.85$	$0.69 \pm 0.04$	$97.82 \pm 1.35$
	$\mu\tau_{h3}$	$5.07 \pm 0.03$	$24.53 \pm 0.03$	$19.43 \pm 1.17$	$1.84 \pm 0.14$	$91.61 \pm 4.49$
	$\mu\tau_\mu$	$3.03 \pm 0.01$	$39.14 \pm 0.04$	$63.99 \pm 1.92$	$0.14 \pm 0.02$	$92.89 \pm 7.11$

## 13.2 Drell-Yan Process

The Drell-Yan process,  $Z \rightarrow ll$ , contributes to the background in a way which depends on the analysis channel. This Section considers only the fake candidates originated directly from the  $Z \rightarrow ll$  decay. The contribution from  $Z$ +jet is treated in Section 13.3.

### 13.2.1 Channel $\mu\tau_\mu$

The  $Z \rightarrow \mu\mu$  background contribution is determined from data via *double-prompt* selection, where the impact parameter threshold of a displaced muon is changed to match a prompt muon, keeping other cuts unchanged. It is calculated from:

$$N_{\text{default}} = N_{\text{default}}^{\text{MC}} \frac{\hat{N}_{\text{double-prompt}}^{\text{data}}}{\hat{N}_{\text{double-prompt}}^{\text{MC}}}$$

where  $N^{\text{MC}}$  denotes number of candidates from  $Z \rightarrow \mu\mu$  simulated sample,  $N^{\text{data}}$  the number of candidates in data, subscripts “default”/“double-prompt” denote the selection used, and a hat above a variable indicates that the number of candidates is counted inside the  $Z$  mass peak window 80-100 GeV/ $c^2$ . The number of signal in  $\hat{N}_{\text{double-prompt}}^{\text{data}}$  is consequently negligible. The results are shown in Table 13.2, compared to the alternative method where a simulated sample of  $Z \rightarrow \mu\mu$  is used and scaled to data inside the  $Z$  mass peak window using default selection. The latter method assumes other processes including signal in the normalization window negligible. The results from both methods are compatible with each other. The quoted uncertainty is statistical.

**Table 13.2** – Numbers of estimated  $Z \rightarrow \mu\mu$  backgrounds.

Methods	Low-mass	Central	High-mass
Via double-prompt control region	$155.3 \pm 5.0$	$126.7 \pm 4.5$	$33.7 \pm 2.3$
Direct in signal selection	$155.0 \pm 22.1$	$133.1 \pm 16.9$	$30.2 \pm 6.6$

13.2.2 Channel  $\mu\tau_{h1}, \mu\tau_e$ 

The  $Z \rightarrow ll$  background can arise as a fake candidate when one of the lepton is misidentified as a charged hadron. The estimation of this background follows the procedures of Section 6.1.2. The results are summarized in Table 13.3.

**Table 13.3** – Statistics of  $Z \rightarrow ll$  background estimation in  $\mu\tau_{h1}, \mu\tau_e$  channel. The “Mean mis-id” gives the lepton misidentification averaged over the  $p_T$  range of the selected di-lepton. The uncertainties from the same background source are correlated.

Regime	Channel	Background	Mean mis-id $\times 10^4$	Selected fake	Expected $Z \rightarrow ll$
Low-mass	$\mu\tau_{h1}$	$Z \rightarrow \mu\mu$	$0.63 \pm 0.28$	63367	$4.02 \pm 1.75$
	$\mu\tau_e$	$Z \rightarrow \mu\mu$	$0.47 \pm 0.22$	42982	$2.04 \pm 0.94$
	$\mu\tau_e$	$Z \rightarrow ee$	$4.89 \pm 1.06$	12687	$6.17 \pm 1.35$
Central	$\mu\tau_{h1}$	$Z \rightarrow \mu\mu$	$0.60 \pm 0.25$	70980	$4.25 \pm 1.79$
	$\mu\tau_e$	$Z \rightarrow \mu\mu$	$0.30 \pm 0.18$	48317	$1.43 \pm 0.89$
	$\mu\tau_e$	$Z \rightarrow ee$	$4.55 \pm 1.03$	14612	$6.61 \pm 1.50$
High-mass	$\mu\tau_{h1}$	$Z \rightarrow \mu\mu$	$0.51 \pm 0.23$	49142	$2.51 \pm 1.13$
	$\mu\tau_e$	$Z \rightarrow \mu\mu$	$0.24 \pm 0.18$	37815	$0.89 \pm 0.70$
	$\mu\tau_e$	$Z \rightarrow ee$	$4.28 \pm 1.01$	8853	$3.76 \pm 0.89$

 13.3 QCD and  $V_j$  Processes

The backgrounds from QCD events,  $N_{\text{QCD}}$ , and from the decay of a single electroweak boson in association with a jet ( $W+\text{jet}$ ,  $Z+\text{jet}$ ),  $N_{V_j}$ , are obtained from a data-driven method. The procedure follows Section 6.2, using  $\mu$  and  $\tau$  candidates with the same electric charge. The same-sign candidates in the data are assumed to be mainly from QCD and  $V_j$  processes, ignoring contribution from  $Z \rightarrow \tau\tau$ . The distribution of  $\Delta p_T = p_T(\mu) - p_T(\tau_x)$  is used in the fit to separate contributions from both processes. When  $N^{\text{SS}}$  is too small ( $\lesssim 10$ ), which is found in the high-mass regime, the entire contribution is given to  $V_j$  as this process is more likely to pass the high- $p_T$  muon selection than the QCD process. The results for all channels and regimes are shown in Fig. 13.1 and Table 13.4.

**Table 13.4** – Results of the fit of the  $\Delta p_T$  variable for same-sign  $\mu\tau$  candidates.

Regime	Channel	$N^{\text{SS}}$	Fit $\chi^2/\text{ndf}$	$N_{\text{QCD}}^{\text{SS}}$	$N_{V_j}^{\text{SS}}$	$r_{\text{QCD}}$	$r_{V_j}$
Low-mass	$\mu\tau_e$	78	0.435	$67.1 \pm 10.3$	$10.9 \pm 7.4$	$1.01 \pm 0.03$	$1.33 \pm 0.27$
	$\mu\tau_{h1}$	509	1.025	$462.3 \pm 3.8$	$46.7 \pm 18.2$	$1.00 \pm 0.01$	$3.07 \pm 0.37$
	$\mu\tau_{h3}$	115	0.320	$93.8 \pm 10.9$	$21.2 \pm 7.3$	$0.99 \pm 0.02$	$1.89 \pm 0.36$
	$\mu\tau_\mu$	25	0.672	$17.7 \pm 4.9$	$7.3 \pm 3.9$	$1.10 \pm 0.06$	$1.46 \pm 0.13$
Central	$\mu\tau_e$	64	0.243	$11.4 \pm 16.0$	$52.6 \pm 17.4$	$0.87 \pm 0.06$	$0.92 \pm 0.12$
	$\mu\tau_{h1}$	219	0.932	$141.3 \pm 14.1$	$77.7 \pm 3.2$	$0.98 \pm 0.02$	$3.13 \pm 0.30$
	$\mu\tau_{h3}$	47	0.335	$30.5 \pm 9.1$	$16.5 \pm 8.7$	$0.98 \pm 0.04$	$1.87 \pm 0.41$
	$\mu\tau_\mu$	11	1.251	$5.6 \pm 3.2$	$5.4 \pm 3.2$	$1.09 \pm 0.13$	$1.45 \pm 0.13$
High-mass	$\mu\tau_e$	3	—	—	$3.0 \pm 1.7$	$0.81 \pm 0.26$	$1.17 \pm 0.56$
	$\mu\tau_{h1}$	54	1.117	$15.7 \pm 6.2$	$38.3 \pm 4.8$	$1.00 \pm 0.06$	$3.73 \pm 0.49$
	$\mu\tau_{h3}$	19	1.170	$12.0 \pm 6.1$	$7.0 \pm 5.8$	$0.81 \pm 0.09$	$2.66 \pm 0.88$
	$\mu\tau_\mu$	4	—	—	$4.0 \pm 2.0$	$0.67 \pm 0.25$	$1.95 \pm 0.25$

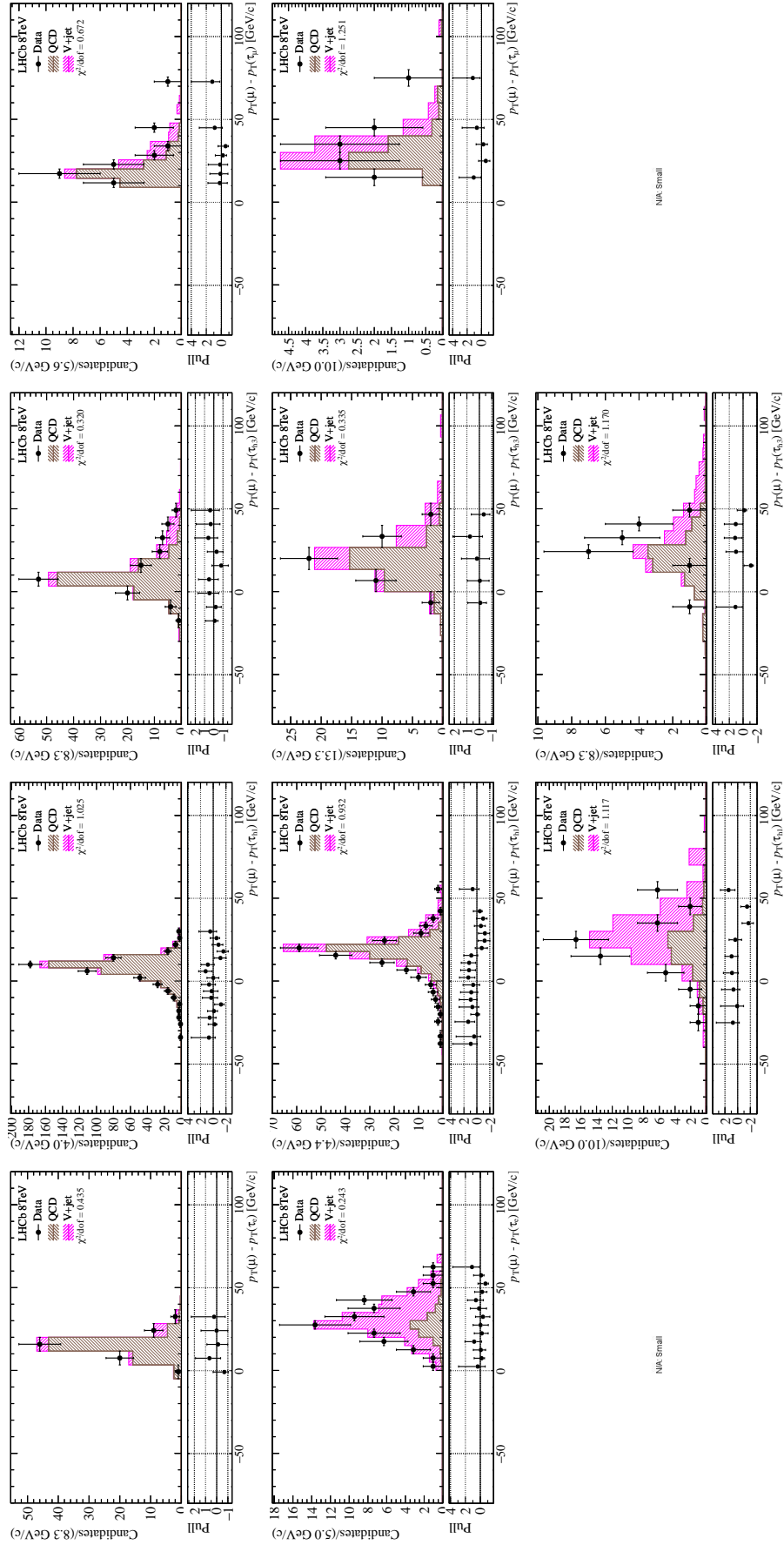


**Figure 13.1** –  $\Delta p_T$  distributions of same-sign  $\mu\tau$  candidates fitted with contributions from QCD and  $V_j$  processes. The top/middle/bottom rows correspond to the low-mass/central/high-mass regimes. From left to right:  $\mu\tau_e$ ,  $\mu\tau_{h1}$ ,  $\mu\tau_{h3}$ , and  $\mu\tau_\mu$ . Processes  $\mu\tau_e$  and  $\mu\tau_\mu$  have a too low statistics in the high-mass regime, the totality of the contribution is assigned to  $V_j$ .



### 13.4 $t\bar{t}$ , $WW$ , $WZ$ , $Z \rightarrow b\bar{b}$

The contributions to the background from  $t\bar{t}$ ,  $WW$ ,  $WZ$ ,  $Z \rightarrow b\bar{b}$  are expected to be very small with respect to the other sources of backgrounds. As such, the estimations are inferred from simulated samples. More details are available in appendix J.1.

### 13.5 Summary

The expected  $H \rightarrow \mu\tau$  background contributions are given in Table 13.5. The corresponding  $\mu\tau$  mass distributions are shown in Fig. 13.2, superposed to the distributions from data. The complete set of distributions is available in appendix J.2. The distributions in the equiprobable binning following the procedure indicated in [127] are shown in Fig. 13.3 and the results of the  $\chi^2$  test in Table 13.6.

For illustration, a comparisons with the Higgs-like boson signal distributions are also shown in Fig. 13.4, with the number of signal events chosen to be equal to the statistical uncertainty of the number of observed candidates.

**Table 13.6** – Result of the  $\chi^2$  test between the observed and expected  $\mu\tau$  candidates using the equiprobable binning technique.

Regime	Variable	$\mu\tau_e$	$\mu\tau_{h1}$	$\mu\tau_{h3}$	$\mu\tau_\mu$
Low-mass	ndf	18	27	14	16
	$\chi^2/\text{ndf}$	1.01	0.87	1.49	1.24
Central	ndf	15	21	10	14
	$\chi^2/\text{ndf}$	0.73	1.31	0.53	0.94
High-mass	ndf	5	12	6	6
	$\chi^2/\text{ndf}$	0.78	0.91	1.62	0.48

## Chapter 13. Background Estimation

**Table 13.5** – Expected number of background candidates, and the number of observed candidates.

Regime	Process	$\mu\tau_e$	$\mu\tau_{h1}$	$\mu\tau_{h3}$	$\mu\tau_\mu$
Low-mass	$Z \rightarrow \tau\tau$	$371.1 \pm 26.0$	$681.7 \pm 47.1$	$135.1 \pm 11.7$	$137.4 \pm 9.5$
	$Z \rightarrow ll$	$8.2 \pm 1.6$	$4.0 \pm 1.8$	—	$155.3 \pm 5.0$
	QCD	$67.5 \pm 10.6$	$463.6 \pm 5.4$	$93.1 \pm 10.9$	$19.4 \pm 5.5$
	$Vj$	$14.5 \pm 10.3$	$143.2 \pm 58.6$	$40.1 \pm 15.8$	$10.7 \pm 5.8$
	VV	$3.4 \pm 0.3$	$0.9 \pm 0.2$	$0.3 \pm 0.1$	$0.3 \pm 0.1$
	$t\bar{t}$	$1.7 \pm 0.1$	$1.3 \pm 0.1$	$0.7 \pm 0.1$	$1.3 \pm 0.2$
	$Z \rightarrow b\bar{b}$	$0.2 \pm 0.2$	$0.2 \pm 0.2$	$0.1 \pm 0.1$	$0.2 \pm 0.2$
	Total background	$466.6 \pm 28.0$	$1294.9 \pm 75.5$	$269.4 \pm 20.3$	$324.5 \pm 12.5$
Observed	$472.0 \pm 21.7$	$1284.0 \pm 35.8$	$240.0 \pm 15.5$	$344.0 \pm 18.5$	
Central	$Z \rightarrow \tau\tau$	$200.0 \pm 14.3$	$288.1 \pm 20.2$	$61.3 \pm 5.5$	$71.7 \pm 5.2$
	$Z \rightarrow ll$	$8.0 \pm 1.7$	$4.3 \pm 1.8$	—	$126.7 \pm 4.5$
	QCD	$10.0 \pm 14.0$	$137.9 \pm 14.0$	$29.9 \pm 9.0$	$6.1 \pm 3.6$
	$Vj$	$48.3 \pm 17.2$	$242.9 \pm 25.3$	$30.8 \pm 17.6$	$7.9 \pm 4.7$
	VV	$3.4 \pm 0.3$	$1.5 \pm 0.2$	$0.3 \pm 0.1$	$0.3 \pm 0.1$
	$t\bar{t}$	$2.5 \pm 0.1$	$1.6 \pm 0.1$	$0.7 \pm 0.1$	$1.5 \pm 0.2$
	$Z \rightarrow b\bar{b}$	$0.1 \pm 0.1$	$0.1 \pm 0.1$	$0.1 \pm 0.1$	$0.1 \pm 0.1$
	Total background	$272.3 \pm 17.8$	$676.4 \pm 35.2$	$123.1 \pm 15.0$	$214.3 \pm 8.1$
Observed	$296.0 \pm 17.2$	$679.0 \pm 26.1$	$123.0 \pm 11.1$	$235.0 \pm 15.3$	
High-mass	$Z \rightarrow \tau\tau$	$13.7 \pm 1.8$	$18.4 \pm 1.6$	$8.9 \pm 1.1$	$2.2 \pm 0.4$
	$Z \rightarrow ll$	$4.7 \pm 1.1$	$2.5 \pm 1.1$	—	$33.7 \pm 2.3$
	QCD	—	$15.8 \pm 6.3$	$9.7 \pm 5.1$	—
	$Vj$	$3.5 \pm 2.6$	$142.6 \pm 26.0$	$18.6 \pm 16.5$	$7.8 \pm 4.0$
	VV	$1.7 \pm 0.2$	$1.0 \pm 0.2$	$0.1 \pm 0.1$	$0.2 \pm 0.1$
	$t\bar{t}$	$1.2 \pm 0.1$	$0.9 \pm 0.1$	$0.4 \pm 0.1$	$0.8 \pm 0.1$
	$Z \rightarrow b\bar{b}$	$0.1 \pm 0.1$	$0.1 \pm 0.1$	$0.1 \pm 0.1$	$0.1 \pm 0.1$
	Total background	$24.9 \pm 3.4$	$181.2 \pm 26.7$	$37.8 \pm 13.6$	$44.7 \pm 4.6$
Observed	$27.0 \pm 5.2$	$184.0 \pm 13.6$	$37.0 \pm 6.1$	$39.0 \pm 6.2$	

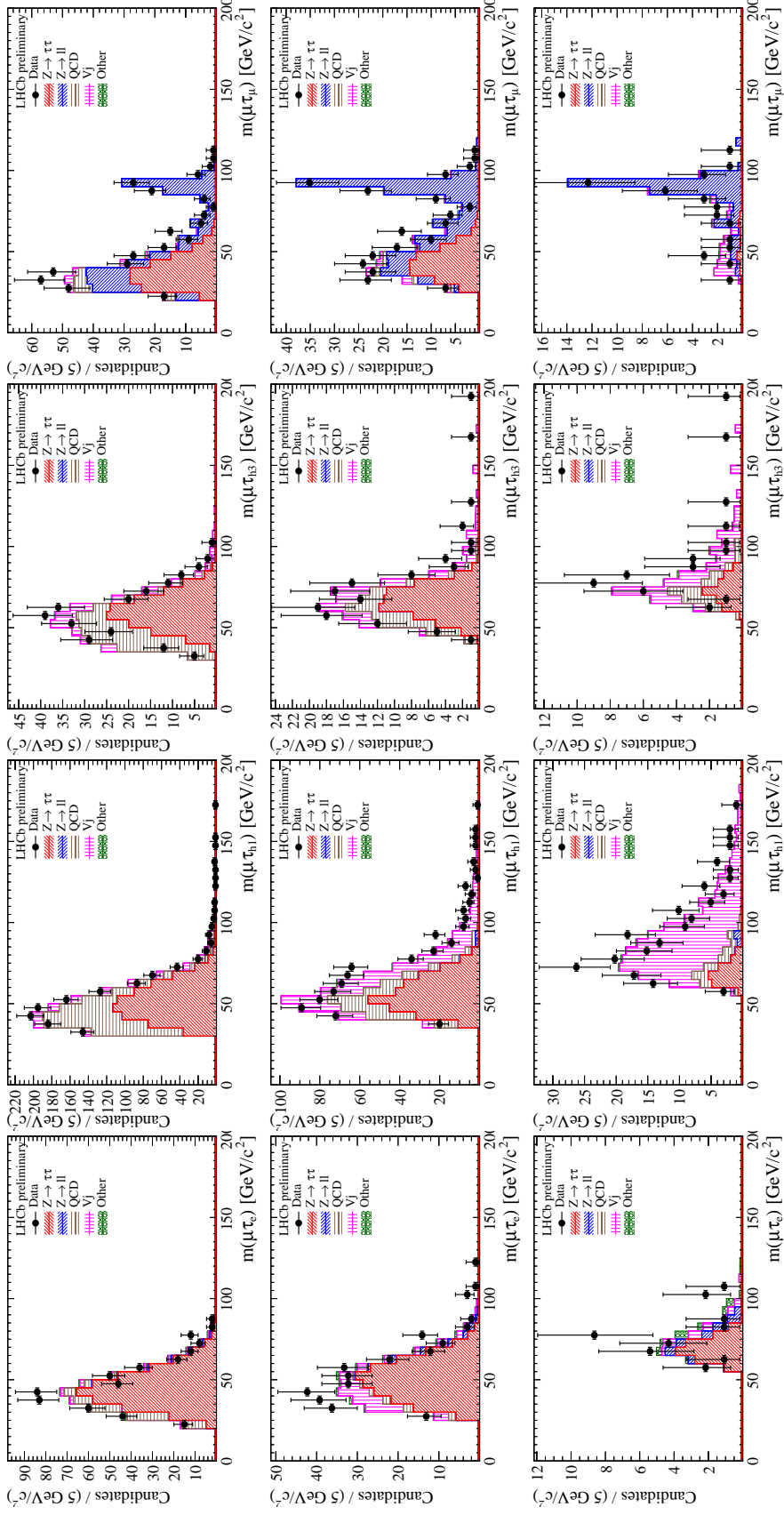


**Figure 13.2** – Invariant mass of the  $\mu\tau$  candidates from 4 analysis channels (column-wise;  $\mu\tau_e$ ,  $\mu\tau_{\mu 3}$ ,  $\mu\tau_{\mu 1}$ ), and at 3 selection regimes (row-wise; low-mass, central, high-mass). The contributions from each process is superposed.

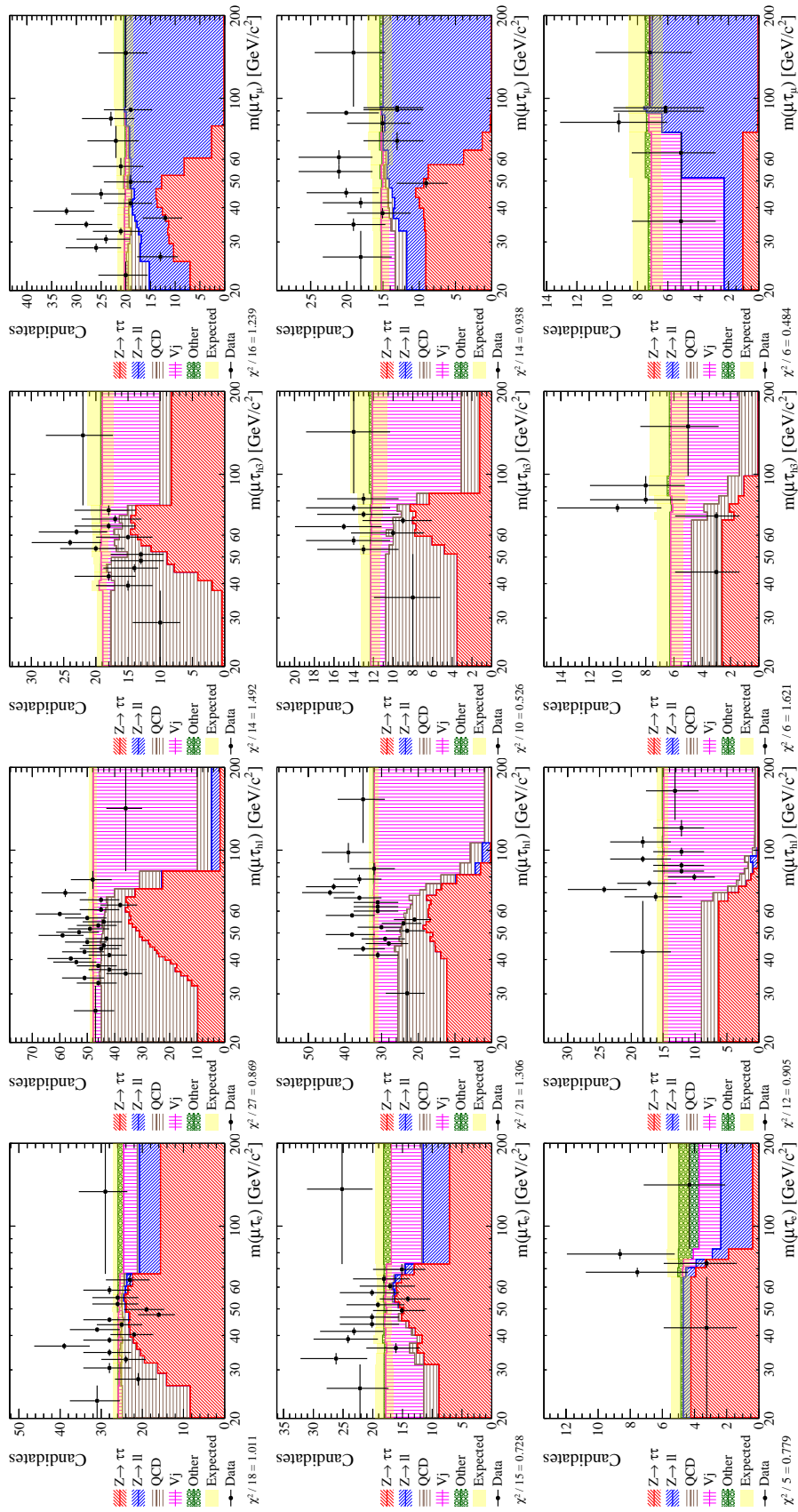
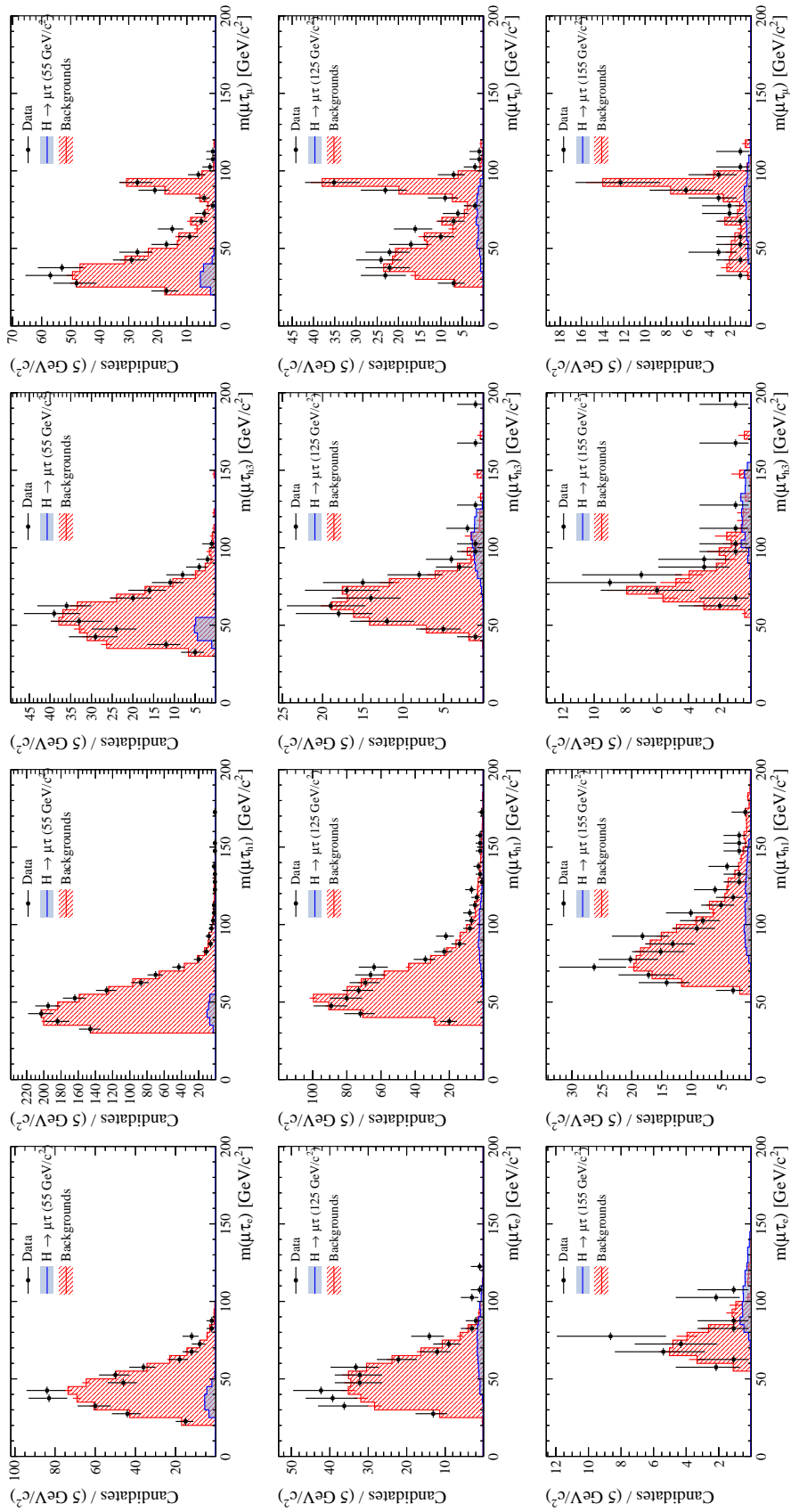


Figure 13.3 – Similar to Fig. 13.2, displayed with equiprobable bins.



**Figure 13.4** – Distribution of the observed  $\mu\tau$  candidates (black dots with error bars) and expected backgrounds (red histogram). The distributions expected for a signal (blue) are superposed, normalized to the statistical uncertainty.



# 14 Signal Efficiencies

The expected number of signal  $H \rightarrow \mu\tau$  candidates is calculated from the following expression:

$$N_{\text{sig}} = \mathcal{L} \cdot \sigma_{gg \rightarrow H \rightarrow \mu\tau}(m_H) \cdot \mathcal{B}_{\tau \rightarrow X} \cdot \varepsilon_{\text{tot}}(m_H) \quad (14.1)$$

where  $\mathcal{L}$  is the total integrated luminosity,  $\sigma_{gg \rightarrow H \rightarrow \mu\tau}$  is the model-independent inclusive Higgs-like boson production cross-section decaying to  $\mu\tau$ , which is a function of the boson mass  $m_H$ ,  $\mathcal{B}_{\tau \rightarrow X}$  is the  $\tau$  lepton final state branching fraction, and  $\varepsilon_{\text{tot}}(m_H)$  is the detection efficiency, which can be decomposed into

$$\varepsilon_{\text{tot}}(m_H) = \mathcal{A}(m_H) \cdot \varepsilon_{\text{rec}}(m_H) \cdot \varepsilon_{\text{sel}}(m_H) \quad (14.2)$$

with  $\mathcal{A}$  the acceptance factor (defined in Section 12.1),  $\varepsilon_{\text{rec}}$  the reconstruction efficiency (defined in Section 12.2), and  $\varepsilon_{\text{sel}}$  the offline selection efficiency (defined in Section 12.3). The computation of each term is discussed in this section. Additional details and plots can be found in appendix K.

## 14.1 Acceptance, $\mathcal{A}$

The acceptance factor is calculated from the generator-level simulated sample of  $H \rightarrow \mu\tau$  produced with POWHEG-BOX r2092 [112, 113, 114]. Only the  $gg$ -fusion production mode [141] is enabled. The generator uses MMHT2014n1o68c1 [142] as the proton PDF set via LHAPDF 6.1.6 [117]. Of the order of  $10^6$  events are generated for each  $H$  mass value. The parton shower is performed with PYTHIA 8.186 [118, 119]. Two acceptance factors are computed, corresponding to a full solid angle normalization of the cross-section, and inside the LHCb geometrical acceptance, defined as  $2.0 < \eta_{\mu,\tau} < 4.5$ .

The  $\mathcal{A}$  values are computed for each analysis channel.  $\mathcal{A}$  is the number of events passing the acceptance requirement listed in Section 12.1, divided by the number of events in the geometrical acceptance ( $4\pi$  or LHCb). The results are shown in Fig. 14.1. The uncertainty associated to the parton luminosity is computed from the sum in quadrature of differences in  $\mathcal{A}$  between each eigenmembers in the PDF set against the central member. The uncertainty from scale variations (factorization scale ( $\mu_F$ ), and normalization scale ( $\mu_R$ )) are computed by varying scales in the range  $[0.5\mu < \mu < 2\mu]$  with  $0.5 < \mu_F/\mu_R < 2$ .

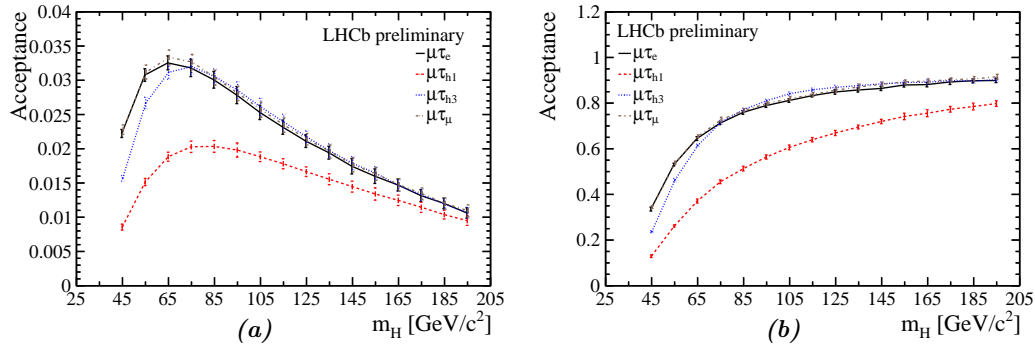


**Figure 14.1** – Acceptances for a Higgs-like boson signal as a function of  $m_H$  and the four analysis channels; (a)  $4\pi$  production, (b) production inside LHCb geometrical acceptance.

## 14.2 Reconstruction Efficiency, $\varepsilon_{\text{rec}}$

The reconstruction efficiency is calculated using simulated signal samples following the procedures outlined in Chapter 7, where efficiencies from simulation are corrected by comparison to data when possible. The reconstruction efficiency depends on the kinematics of the  $H \rightarrow \mu\tau$  candidate as well as event properties such as the event track multiplicities. The efficiency is averaged over the selected signal candidates directly (without using the definition of equivalent efficiency, eq. 7.2), and is computed for each analysis channel and selection regime. For illustration, the results for the central regime are shown in Fig. 14.2. The difference with the other regimes is small.

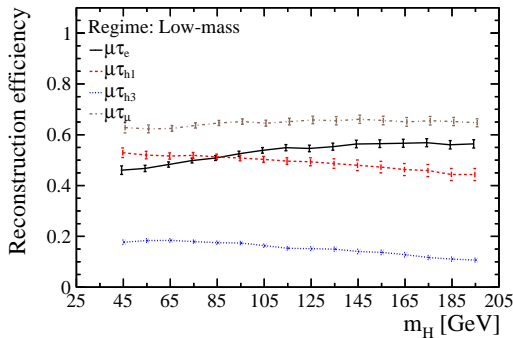


**Figure 14.2** – Reconstruction efficiency of  $\mu\tau$  candidates from low-mass selection regime as a function of  $m_H$ .



### 14.3 Selection Efficiency, $\varepsilon_{\text{sel}}$

The selection efficiency is calculated from simulation, as the fraction of reconstructed events which also pass the offline selections, Section 12.3. The results are shown in Fig. 14.3, with statistical uncertainties.

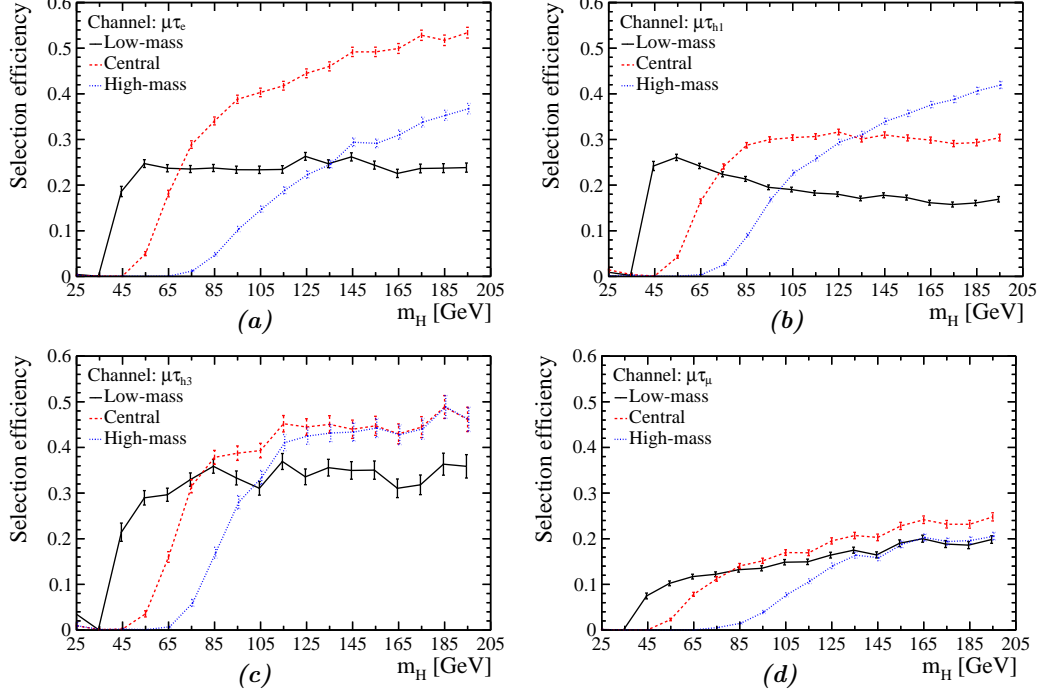


Figure 14.3 –  $\varepsilon_{\text{sel}}$  of  $\mu\tau$  candidates as a function of  $m_H$ : (a)  $\mu\tau_e$ , (b)  $\mu\tau_{h1}$ , (c)  $\mu\tau_{h3}$ , (d)  $\mu\tau_{\mu}$ .



# 15 Uncertainties

The list of uncertainties which affects the cross-section calculation (eq. 14.1) are summarized in Table 15.1. The level of correlation of the uncertainties across channels is summarized in Table 15.2.

The uncertainty on the integrated luminosity is taken from [89]. The uncertainty on the branching fractions are from the PDG [123]. The uncertainty on  $\mathcal{A}$  is mainly from the PDF uncertainty in the gluon-gluon production of the Higgs-like boson, with a minor contribution from scales variation, as shown in Fig. 15.1. The uncertainties on  $\varepsilon_{\text{rec}}$  are inferred from the simulation statistics and from the uncertainty associated with data-driven method. The uncertainties of  $\varepsilon_{\text{sel}}$  are taken from statistical uncertainties of simulated signal samples. The relative uncertainties on the number of expected background events, computed from values of Table 13.5, are summarized in Table 15.3.

**Table 15.1** – Systematic uncertainties on the parameters for the cross-section calculation, given in percentages. When the uncertainty depends on more parameters (*e.g.*,  $m_H$ , selection regime), only the range is indicated.

[%]	$\mu\tau_e$	$\mu\tau_{h1}$	$\mu\tau_{h3}$	$\mu\tau_\mu$
Luminosity	1.16	1.16	1.16	1.16
$\mathcal{B}_{\tau \rightarrow X}$	0.22	0.18	0.48	0.23
$\mathcal{A}$	2.9–7.4	3.6–7.4	2.8–7.5	3.3–8.1
$\hookrightarrow$ PDF	2.6–7.1	3.5–7.2	2.6–7.3	3.0–7.9
$\hookrightarrow$ Scales	0.9–1.9	0.8–1.7	0.9–1.7	0.9–1.9
$\varepsilon_{\text{rec}}$	1.8–3.6	1.5–5.4	3.3–7.1	1.5–3.3
$\varepsilon_{\text{sel}}$	2.5–6.0	1.9–4.1	4.0–9.3	3.8–8.5

**Table 15.2** – Correlation across channels for each term in the cross-section computation.

Uncertainty	Correlation level across channels
luminosity	fully correlated
$\mathcal{B}_{\tau \rightarrow X}$	uncorrelated
$\mathcal{A}$	fully correlated
$\varepsilon_{\text{rec}}$	corr( $\varepsilon_{\text{rec}}$ )
$\varepsilon_{\text{sel}}$	uncorrelated
$N_{\text{bkg}}$	uncorrelated

## Chapter 15. Uncertainties

A partial correlation is inferred for  $\varepsilon_{\text{rec}}$ . The correlation matrix (on average) is

$$\text{corr}(\varepsilon_{\text{rec}}) = \begin{pmatrix} 1 & 0.75 & 0.62 & 0.66 \\ 0.75 & 1 & 0.73 & 0.74 \\ 0.62 & 0.73 & 1 & 0.54 \\ 0.66 & 0.74 & 0.54 & 1 \end{pmatrix}$$

**Table 15.3** – Relative uncertainties on the number of expected backgrounds, shown in percentages.

Regime	Process	$\mu\tau_e$	$\mu\tau_{h1}$	$\mu\tau_{h3}$	$\mu\tau_\mu$
Low-mass	$Z \rightarrow \tau\tau$	5.56	3.64	4.33	2.92
	$Z \rightarrow ll$	0.35	0.14	0.00	6.83
	QCD	2.28	0.42	4.06	1.70
	$Vj$	2.21	4.52	5.87	1.78
	Other	0.08	0.02	0.06	0.09
	Total	6.00	5.83	7.52	7.68
Central	$Z \rightarrow \tau\tau$	5.25	2.98	4.48	2.33
	$Z \rightarrow ll$	0.64	0.26	0.00	7.68
	QCD	5.13	2.06	7.33	1.61
	$Vj$	6.32	3.75	14.27	2.13
	Other	0.13	0.04	0.13	0.12
	Total	6.54	5.21	12.19	8.26
High-mass	$Z \rightarrow \tau\tau$	7.30	0.91	2.95	1.04
	$Z \rightarrow ll$	4.55	0.63	0.00	16.07
	QCD	0.00	3.46	13.35	0.00
	$Vj$	10.61	14.32	43.59	9.74
	Other	1.01	0.12	0.37	0.44
	Total	13.69	14.75	35.85	18.83

**Table 15.4** – Correlation factors between QCD and  $Vj$  background uncertainties.

Regime	$\mu\tau_e$	$\mu\tau_{h1}$	$\mu\tau_{h3}$	$\mu\tau_\mu$
Low-mass	-0.51	0.02	-0.28	-0.37
Central	-0.79	-0.01	-0.62	-0.49
High-mass	-	-0.01	-0.69	-

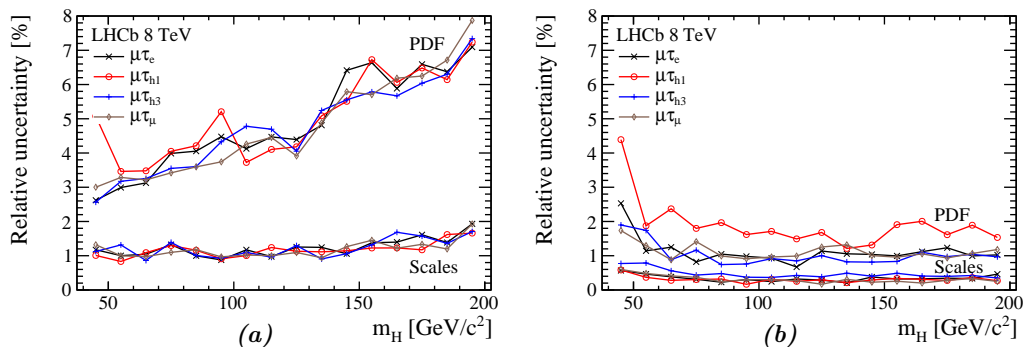


**Figure 15.1** – Relative uncertainties of  $\mathcal{A}$  from PDF uncertainty and scales variation (normalization, factorization) for (a)  $4\pi$ , and (b) LHCb acceptance.

# 16 Signal Likelihood

The best fit for signal production cross-section  $\sigma_{gg \rightarrow H \rightarrow \mu\tau}$  and exclusion limit via CL<sub>s</sub> method at 95% confidence level are obtained using `Roostats` framework, taken a large inspiration from the statistical treatment in  $H \rightarrow \tau^+\tau^-$  analysis [64]. A brief discussion on hypothesis testing and test statistics is provided in Section 16.1. The extended likelihood approach is used, defined with one parameter of interest,  $\sigma_{gg \rightarrow H \rightarrow \mu\tau}$ . The observables are the invariant mass distributions of  $H \rightarrow \mu\tau$  candidates from signal and background processes. The result for each  $m_H$  is shown for the selection regime with the best figure-of-merit  $\varepsilon_{\text{sel}}/(1 + \sqrt{N_{\text{obs}}})$  as discussed in Section 12.3.

The numbers of background candidates are normalized to the results of Table 13.5, with efficiencies and luminosity taken from Chapter 14. The background processes for which we expect zero candidates are excluded from the likelihood. The likelihood is simultaneously fit across the 4 analysis channels. More details on the fit procedure are given in Section 16.2

Systematic uncertainties listed in Chapter 15 are included in the likelihood, where each of them is treated as nuisance parameter with Gaussian distribution. The correlation between uncertainties are expressed as a product of conditional probability distributions. The treatment of uncertainties and their correlation are discussed in Sections 16.3 to 16.4.

Finally, the procedure for the determination of a cross-section upper limit via CL<sub>s</sub> method and inverted hypothesis testing is described in Section 16.5. The validation of likelihood model is presented in Section 16.6. Full detail of model validations can be found in appendix L.

## 16.1 Test Statistics

The exclusion limit of  $\sigma_{gg \rightarrow H \rightarrow \mu\tau}$  is performed using hypothesis testing between the background-only hypothesis,  $H_0$ , and the signal-plus-background hypothesis,  $H_1$ . The test statistic, which is a function of chosen observables in the analysis, is used to build the probability density function (PDF) for a given hypothesis  $H_\mu$ , denoted as  $f(q|\mu)$ . The fractional signal strength,  $\mu$ , varies between 0–1, and corresponds to background-only hypothesis for  $\mu = 0$ , and signal-plus-background hypothesis for  $\mu = 1$

The test statistic  $q_\mu = -2 \ln \lambda(\mu)$  is commonly chosen for the hypothesis test, where the

profile likelihood ratio,  $\lambda(\mu)$ , is defined as:

$$\lambda(\mu) = \frac{L(\mu, \hat{\boldsymbol{\theta}}(\mu) | \mathbf{x})}{L(\hat{\mu}, \hat{\boldsymbol{\theta}} | \mathbf{x})}$$

at the selected choice of likelihood model  $L$  (its explicit form discussed in the following section). The likelihood  $L(\mu, \boldsymbol{\theta} | \mathbf{x})$  is defined as a function of signal strength  $\mu$ , considered as the *parameter of interest* (POI), and  $\boldsymbol{\theta}$  the collection of *nuisance parameters*, whose values are not known *a priori* and need to be obtained from the data, evaluated in correspondence of the measured observables  $\mathbf{x}$ . Here,  $\hat{\mu}$ ,  $\hat{\boldsymbol{\theta}}$  are their maximum-likelihood estimator (thus the denominator of  $\lambda(\mu)$  can be considered as the global maximum likelihood), and  $\hat{\boldsymbol{\theta}}(\mu)$  is the conditional maximum-likelihood estimator of  $\boldsymbol{\theta}$  at the specified  $\mu$ . The presence of  $\boldsymbol{\theta}$  reflects the systematic uncertainties in the analysis and thus the loss of information in  $\mu$ .

For the purpose of establishing the upper limit on  $\mu$ , the test statistic is proposed [143] to be redefined as,

$$q_\mu = \begin{cases} -2 \ln \lambda(\mu) & \hat{\mu} \geq \mu \\ 0 & \text{otherwise} \end{cases}$$

The distribution of  $q_\mu$  can be obtained from various approaches. One is the use of Monte Carlo simulation to generate the pseudo-experiment data,  $\vec{x}_{\text{sim}}$  in order to build the distribution of  $f(q|\mu)$ . Whilst this approach robustly treats the uncertainties in a frequentist way, it can be computationally demanding as large generated samples are required. Alternatively, in the case where there is only one POI, the asymptotic formulae [143] can be employed, where it shows that the distribution of  $q_\mu$  follows the noncentral  $\chi^2$  for one degree of freedom, when the Wald approximation [144] is assumed. The use of an Asimov dataset allows the noncentrality parameter to be estimated. The formulae are valid and reasonably accurate for a small sample, and its implementation in `Roostats.AsymptoticCalculator` is used in this analysis.

## 16.2 Likelihood Model

The likelihood model,  $L(\mu, \boldsymbol{\theta} | \mathbf{x})$ , by construction should yield the value discriminating between the two hypotheses. Consider the counting experiment where  $N_{\text{obs}}$  candidates are observed given the expected candidates of  $N_{\text{exp}} = N_{\text{bkg}} + \mu N_{\text{sig}}$ , composed of the expected background candidates (from a single source) and the potential signal candidates at given signal strength. The likelihood can be written as the Poisson PDF,

$$L(\mu | N_{\text{obs}}) = \text{Pois}(N_{\text{obs}} | N_{\text{exp}}(\mu)) = \frac{N_{\text{exp}}(\mu)^{N_{\text{obs}}} e^{-N_{\text{exp}}}}{N_{\text{obs}}!} \quad (16.1)$$

Instead of the single number of observed events,  $N_{\text{obs}}$ , additional per-event information can be used to further discriminate between the signal and background candidates. In particular for this analysis, the distribution of the invariant mass of the  $H \rightarrow \mu\tau$  candidates is used, denoted as  $f_k(m)$  for the process  $k$ . Given the measurement of the observed

candidate invariant mass,  $\mathbf{m}$ , the extended likelihood can be written as,

$$L(\mu|\mathbf{m}) = \text{Pois}(N_{\text{obs}}|N_{\text{exp}}(\mu)) \prod_{i=0}^{m_i \in \mathbf{m}} (N_{\text{bkg}} f_{\text{bkg}} + \mu N_{\text{sig}} f_{\text{sig}})(m_i) \quad (16.2)$$

where  $f_{\text{bkg}}, f_{\text{sig}}$  are the invariant mass distribution for the background and signal process respectively. The product is applied over all observed candidates. The distribution of  $f_k(m)$  is taken empirically from its respective simulated sample and made into a PDF by kernel density estimation (`Roofit.RooKeysPdf`).

The model can be generalized from single background source to multiple sources:

$$L(\mu|\mathbf{m}) = \text{Pois}(N_{\text{obs}}|N_{\text{exp}}(\mu)) \prod_{i=0}^{m_i \in \mathbf{m}} \left( \sum_k^{\text{processes}} N_{\text{bkg},k} f_{\text{bkg},k} + \mu N_{\text{sig}} f_{\text{sig}} \right) (m_i)$$

where the summation loops over each background,  $k$ , with expected candidates  $N_{\text{bkg},k} > 0$  and invariant mass distribution  $f_{\text{bkg},k}$ . The number of expected candidates becomes

$$N_{\text{exp}}(\mu) = \sum_k^{\text{processes}} N_{\text{bkg},k} + \mu N_{\text{sig}}$$

As the POI of this analysis is  $\sigma_{gg \rightarrow H \rightarrow \mu\tau}$ , the instances of  $N_{\text{sig}}$  can be substituted with an expression similar to eq. 14.1:

$$N_{\text{sig}} \rightarrow N_{\text{sig}}^X = \mathcal{L} \sigma_{gg \rightarrow H \rightarrow \mu\tau} \mathcal{B}_{\tau \rightarrow X} \varepsilon^X$$

where  $\mathcal{L}$  is the integrated luminosity,  $\mathcal{B}_{\tau \rightarrow X}$  is the branching fraction of  $\tau$  lepton to one of the 4 channels of  $\tau$  lepton decay performed in this analysis ( $\tau_e, \tau_\mu, \tau_{h1}, \tau_{h3}$ ), and  $\varepsilon^X$  is the total efficiency (acceptance, reconstruction, selection) to yield signal candidates of this channel. The superscript  $X$  denotes the channel. The channel-dependent likelihood can now be expressed as:

$$L^X(\mu|\mathbf{m}) = \text{Pois}(N_{\text{obs}}^X|N_{\text{exp}}^X(\mu)) \prod_{i=0}^{m_i \in \mathbf{m}^X} F^X(m_i) \quad (16.3)$$

$$F^X(m) = \left( \sum_k^{\text{processes}} N_{\text{bkg},k}^X f_{\text{bkg},k}^X + \mu (\mathcal{L} \sigma_{gg \rightarrow H \rightarrow \mu\tau} \mathcal{B}_{\tau \rightarrow X} \varepsilon^X) f_{\text{sig}}^X \right) (m)$$

which allows the simultaneous fit of all analysis channels. The likelihood model operates on each selection regime separately.

### 16.3 Uncertainties

The uncertainties are introduced into the statistic test by the mean of nuisance parameters  $\theta$ . Consider a term in eq. 16.3 having associated systematic uncertainty,  $v \pm \delta_v$ : its corresponding nuisance parameter,  $v'$ , is substituted into the likelihood expression in place of  $v$ , and the likelihood is multiplied by a normally-distributed constraint term, *i.e.*,

$$L(\mu|\mathbf{m}) \rightarrow L(\mu, \theta|\mathbf{m}) N(v; v', \delta_v^2) \quad , \quad v' \in \theta$$

where the parameter  $v'$ , acts as an unknown true mean of  $N$ , is left floating for the fitting procedure<sup>1</sup>. It can be seen that in the case where all other parameters are fixed, the likelihood expression is maximized for  $v' = v$  (having the normal distribution constraint term equals unity), and as  $v'$  deviates from  $v$ , the likelihood decreases. The usage can be generalized for multiple uncorrelated uncertainties by repeating the procedure above, adding the constraint term to the likelihood product.

In the concrete implementation inside `Roostats` framework, the class `ModelConfig` is used for binding likelihood models and its parameters. The collection of  $v'$  are floating nuisance parameters,  $v$  are the *global observables* fixed constant, and  $\delta_v$  are the *constraint parameters* also fixed constant.

### 16.4 Correlated Uncertainties

For correlated uncertainties, they can be considered as nuisance parameters in a multivariate normal distribution. The above procedure can be applied by redefining the constraint term to be a product of an appropriate conditional distribution.

In general, given an  $N$ -dimensional array of random variable  $\mathbf{x}$ , with its mean  $\boldsymbol{\mu}$  and covariance matrix  $\boldsymbol{\sigma}$ , such that it is partitioned as:

$$\mathbf{x} = \begin{pmatrix} \mathbf{x}_1 \\ \mathbf{x}_2 \end{pmatrix}, \boldsymbol{\mu} = \begin{pmatrix} \boldsymbol{\mu}_1 \\ \boldsymbol{\mu}_2 \end{pmatrix} \quad \text{with sizes} \quad \begin{pmatrix} q \times 1 \\ (N - q) \times 1 \end{pmatrix}$$

$$\boldsymbol{\sigma} = \begin{pmatrix} \boldsymbol{\sigma}_{11} & \boldsymbol{\sigma}_{12} \\ \boldsymbol{\sigma}_{21} & \boldsymbol{\sigma}_{22} \end{pmatrix} \quad \text{with sizes} \quad \begin{pmatrix} q \times q & q \times (N - q) \\ (N - q) \times q & (N - q) \times (N - q) \end{pmatrix}$$

The distribution of  $\mathbf{x}_2$  conditional on  $\mathbf{x}_1 = \hat{\mathbf{x}}_1$  can be expressed as a multivariate normal distribution of transformed mean and variance,  $\mathcal{N}(\bar{\boldsymbol{\mu}}_2, \bar{\boldsymbol{\sigma}}_2)$ , where

$$\bar{\boldsymbol{\mu}}_2 = \boldsymbol{\mu}_2 + \mathbf{C}(\hat{\mathbf{x}}_1 - \boldsymbol{\mu}_1) \quad , \quad \bar{\boldsymbol{\sigma}}_2 = \boldsymbol{\sigma}_{22} - \mathbf{C}\boldsymbol{\sigma}_{12} \quad , \quad \mathbf{C} = \boldsymbol{\sigma}_{21}\boldsymbol{\sigma}_{11}^{-1}$$

where  $\mathbf{C}_i$  is known as the *matrix of regression coefficients*. It's worth noting that while the new mean  $\bar{\boldsymbol{\mu}}_2$  is shifted as a function of conditioned variables, the new variance  $\bar{\boldsymbol{\sigma}}_2$  is not affected, but only depends on the choice of conditioning order.

<sup>1</sup>This choice of “inverted” arguments (floating mean, and fixed observed value and variance) is conventionally used by physicists, not necessary statisticians. The shorthand notation  $N(v; v', \delta_v^2) = \mathcal{N}(v, \delta_v^2)$  will be used throughout this section.



In this analysis, the following systems of correlated uncertainties are treated:

- $\varepsilon_{\text{rec}}$  between channels: 4 correlated variables.
- Numbers of QCD and  $Vj$  backgrounds: 2 correlated variables.
- Acceptance, luminosity, and Higgs cross-section: 4 fully correlated variables

The treatment for specific system will be discussed in this section, where the explicit form is derived such that it can be easily parsed into the `Roostats` framework.

### 16.4.1 System of 4 Correlated Variables

In a system of 4 correlated nuisance parameters ( $v'_1, v'_2, v'_3, v'_4$ ), *e.g.*, in correlated  $\varepsilon_{\text{rec}}$ , their means and a covariance matrix are given as:

$$\boldsymbol{\mu} = \begin{pmatrix} v_1 \\ v_2 \\ v_3 \\ v_4 \end{pmatrix}, \quad \boldsymbol{\sigma} = \begin{pmatrix} \sigma_{11} & \sigma_{12} & \sigma_{13} & \sigma_{14} \\ \sigma_{21} & \sigma_{22} & \sigma_{23} & \sigma_{24} \\ \sigma_{31} & \sigma_{32} & \sigma_{33} & \sigma_{34} \\ \sigma_{41} & \sigma_{42} & \sigma_{43} & \sigma_{44} \end{pmatrix}$$

The multivariate normal distribution can be written as:

$$F(v'_1, v'_2, v'_3, v'_4) = F_1(v'_1) F_2(v'_2|v'_1) F_3(v'_3|v'_1, v'_2) F_4(v'_4|v'_1, v'_2, v'_3)$$

where each  $F_i$  retains the normal distribution shape but with the mean and variance modified,  $F_i \sim \mathcal{N}(\bar{v}_i, \bar{\delta}_i^2)$  as a function of conditional variables as well as  $\boldsymbol{\mu}$  and  $\boldsymbol{\sigma}$ . The explicit form of  $\bar{v}_i, \bar{\delta}_i^2$  can be written for each  $F_i$ :

$$\begin{aligned} \bar{v}_1 &= v_1 & \bar{\delta}_1^2 &= \sigma_{11} \\ \bar{v}_2 &= v_2 + \mathbf{C}_2 \begin{pmatrix} v'_1 - v_1 \end{pmatrix} & \bar{\delta}_2^2 &= \sigma_{22} - \mathbf{C}_2 \sigma_{12} & \mathbf{C}_2 &= \sigma_{21} \sigma_{11}^{-1} \\ \bar{v}_3 &= v_3 + \mathbf{C}_3 \begin{pmatrix} v'_1 - v_1 \\ v'_2 - v_2 \end{pmatrix} & \bar{\delta}_3^2 &= \sigma_{33} - \mathbf{C}_3 \begin{pmatrix} \sigma_{13} \\ \sigma_{23} \end{pmatrix} & \mathbf{C}_3 &= \begin{pmatrix} \sigma_{31} & \sigma_{32} \end{pmatrix} \begin{pmatrix} \sigma_{11} & \sigma_{12} \\ \sigma_{21} & \sigma_{22} \end{pmatrix}^{-1} \\ \bar{v}_4 &= v_4 + \mathbf{C}_4 \begin{pmatrix} v'_1 - v_1 \\ v'_2 - v_2 \\ v'_3 - v_3 \end{pmatrix} & \bar{\delta}_4^2 &= \sigma_{44} - \mathbf{C}_4 \begin{pmatrix} \sigma_{14} \\ \sigma_{24} \\ \sigma_{34} \end{pmatrix} & \mathbf{C}_4 &= \begin{pmatrix} \sigma_{41} & \sigma_{42} & \sigma_{43} \end{pmatrix} \begin{pmatrix} \sigma_{11} & \sigma_{12} & \sigma_{13} \\ \sigma_{21} & \sigma_{22} & \sigma_{23} \\ \sigma_{31} & \sigma_{32} & \sigma_{33} \end{pmatrix}^{-1} \end{aligned}$$

### 16.4.2 System of 2 Correlated Variables

In case of 2 correlated variables, *e.g.* the correlation between numbers of QCD and  $Vj$  backgrounds, the expression for conditional PDF is greatly simplified. The bivariate normal distribution of two nuisance parameters ( $v'_1, v'_2$ ) can be written as:

$$F(v'_1, v'_2) = F_1(v'_1) F_2(v'_2|v'_1)$$

with means and a covariance matrix:

$$\boldsymbol{\mu} = \begin{pmatrix} v_1 \\ v_2 \end{pmatrix}, \quad \boldsymbol{\sigma} = \begin{pmatrix} \delta_1^2 & \rho \delta_1 \delta_2 \\ \rho \delta_1 \delta_2 & \delta_2^2 \end{pmatrix}$$

Their explicit forms are:

$$F_1 \sim \mathcal{N}(v_1, \delta_1^2) \quad , \quad F_2 \sim \mathcal{N}\left(v_2 + \rho \frac{\delta_2}{\delta_1}(v_1' - v_1), (1 - \rho^2)\delta_2^2\right)$$

An example of constraint term based on this system is shown in Fig. 16.1.

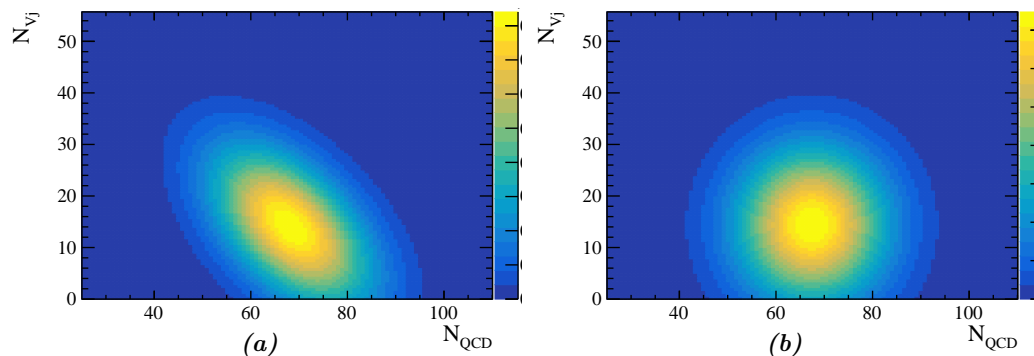


**Figure 16.1** – Bivariate normal distribution as constraint term of  $N_{\text{QCD}}, N_{Vj}$  backgrounds in the extended likelihood model. The result is taken from  $\mu\tau_e$  channel at nominal regime, with the correlation coefficient between their uncertainties of (a)  $-0.5$  as found in the analysis, (b)  $0$ , *i.e.*, uncorrelated, for comparison.

### 16.4.3 System of Fully Correlated Variables

In a system of fully correlated uncertainties, the easiest approach is to factorize the nuisance parameter and its constraint term to be based on the same instance across models (*e.g.*, luminosity uncertainty). However, when factorization is not applicable (*e.g.*, acceptance), it is computationally stable to express the variables as a linear transformation of a standard normal distribution, thus having only one nuisance parameter in a model. For example, given  $\mathcal{A}$  across 4 channels of

$$\mathcal{A}_{\mu\tau_e} = v_1 \pm \delta_1 \quad , \quad \mathcal{A}_{\mu\tau_{h1}} = v_2 \pm \delta_2 \quad , \quad \mathcal{A}_{\mu\tau_{h3}} = v_3 \pm \delta_3 \quad , \quad \mathcal{A}_{\mu\tau_\mu} = v_4 \pm \delta_4$$

Defining a nuisance parameter obeying a standard normal distribution,  $v' \sim \mathcal{N}(0, 1)$ , the acceptance factor in each model is expressed as a function of the nuisance parameter  $\mathcal{A}'_i = v_i + \delta_i v'$ .

## 16.5 Upper Limit

With the likelihood model well defined, the upper limit can be computed given the experimentally observed value of test statistic,  $q_{\text{obs}}$ . The confidence limit of the background only hypothesis,  $\text{CL}_b$ , is defined as  $\text{CL}_b = 1 - \int_{q_{\text{obs}}}^{\infty} f(q|0) dq$ , whereas for the signal plus background hypothesis it's defined as  $\text{CL}_{s+b} = \int_{-\infty}^{q_{\text{obs}}} f(q|1) dq$ . The exclusion of signal plus background hypothesis can be defined as when  $1 - \text{CL}_{s+b} > 95\%$ . However, in order to account for the possible downward fluctuation of the background which leads to erroneous exclusion limit, the  $\text{CL}_s$  method [145] is preferred in this analysis where  $\text{CL}_s = 1 - \text{CL}_{s+b}/\text{CL}_b$ , and the exclusion is defined as when  $1 - \text{CL}_s > 95\%$ . This

computation uses the `Roostats.HypoTestInverter` class to “scan” for the upper limit of given POI until the exclusion requirement is satisfied. The example of the  $CL_s$  scan is shown in Fig. 16.2. Prior to the scan, the best fit result of given POI is also computed.

A simple upper limit is also computed outside the statistical framework, in order to provide a baseline for validation. Consider the number of “best-fit” numbers of signal candidates and its systematic and statistical uncertainties, computed from the excess in the observed candidates:

$$N_{\text{sig}}^{\text{best}} = N_{\text{sig}} \pm \delta_{N_{\text{sig}}}^{\text{sys}} \pm \delta_{N_{\text{sig}}}^{\text{stat}} = (N_{\text{obs}} - N_{\text{bkg}}) \pm \delta_{N_{\text{bkg}}}^{\text{sys}} \pm \sqrt{N_{\text{obs}}}$$

where the systematic uncertainties is taken entirely from  $N_{\text{bkg}}$ . The value of  $\sigma\mathcal{B}$  can be computed with its uncertainties propagated and grouped in a similar fashion:

$$\sigma\mathcal{B}^{\text{best}} = \sigma\mathcal{B} \pm \delta_{\sigma\mathcal{B}}^{\text{sys}} \pm \delta_{\sigma\mathcal{B}}^{\text{stat}}$$

The baseline 95% confidence-level upper limit is then approximated by:

$$\sigma\mathcal{B}^{\text{ulim}} \simeq \sigma\mathcal{B} + 2(\delta_{\sigma\mathcal{B}}^{\text{sys}} \oplus \delta_{\sigma\mathcal{B}}^{\text{stat}}) \quad (16.4)$$

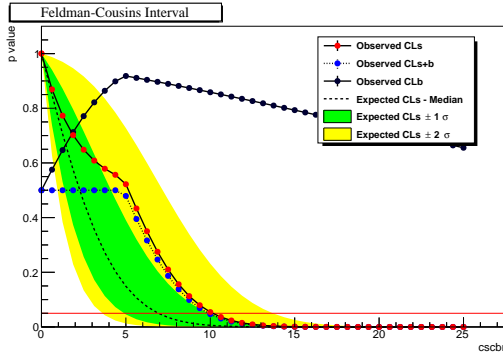


*Figure 16.2* – Example of hypothesis test with CLs method for 95% confidence level upper limit determination (shown here  $m_H = 125 \text{ GeV}/c^2$  at central regime, using simultaneous fit based on eq. 16.3).

## 16.6 Validation

Because of the complexity of the likelihood, several validations are made in order to check the validity of the procedure. Additional information is given in appendix L.

To assess the impact of simultaneous fit over all channels in contrast to independent fits, the expected upper limit of  $\sigma_{gg \rightarrow H \rightarrow \mu\tau}$  is computed for each analysis channel independently, and compared with the simultaneous fit. The results are shown in Fig. 16.3a. With each channel being statistically independent, the simultaneous fit yields the largest exclusion power, as expected.

The impact of uncertainties on the upper limit is shown in Fig. 16.3b. As expected, the upper limits degrade when the uncertainties are included in the calculation as nuisance parameters.

The uncertainty associated to the mass shape PDF used in the extended likelihood is

assessed by using different methods to represent such PDF: (i) continuous distribution (`RooKeysPdf`), (ii) histogram (`RooHistPdf`) with fixed bin-width, (iii) histogram with statistical-dependent bin-width. The expected upper limits are shown in Fig. 16.3c, and found to be consistent with each other. Thus, the shape uncertainty is handled by choosing the method with weakest limits overall, which is method (i).

The pull values for the nuisance parameters after the fit are shown in Fig. 16.4, where the pull is defined as  $(v' - v)/\delta_v$ , with  $v \pm \delta_v$  the nominal value and its uncertainty determined prior to the fit, and  $v'$  is the corresponding nuisance parameter.

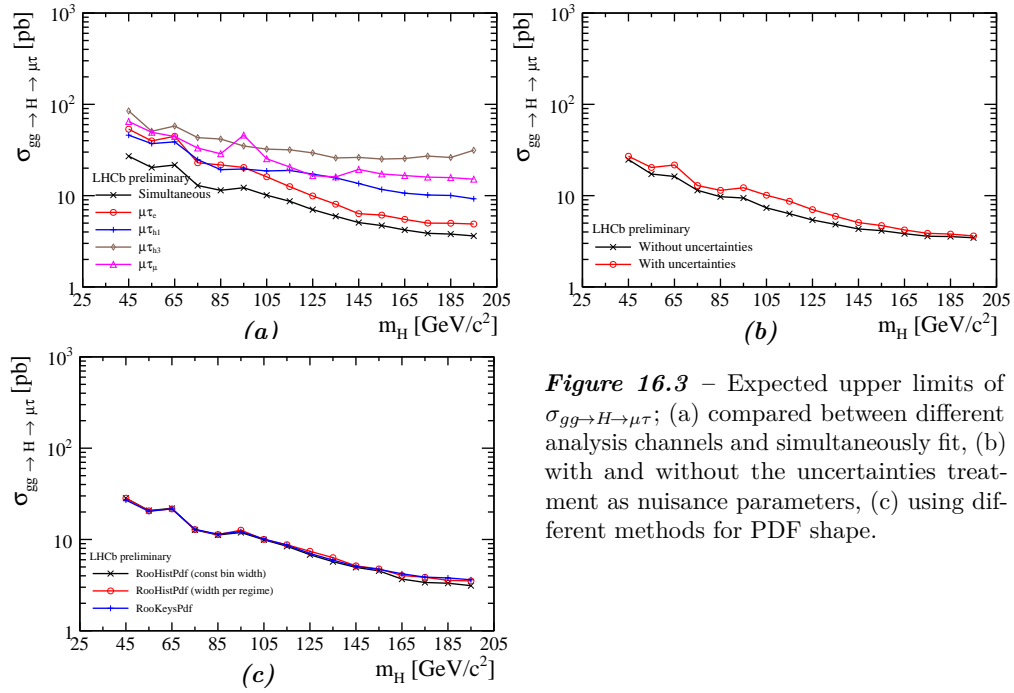


**Figure 16.3** – Expected upper limits of  $\sigma_{gg \rightarrow H \rightarrow \mu\tau}$ ; (a) compared between different analysis channels and simultaneously fit, (b) with and without the uncertainties treatment as nuisance parameters, (c) using different methods for PDF shape.

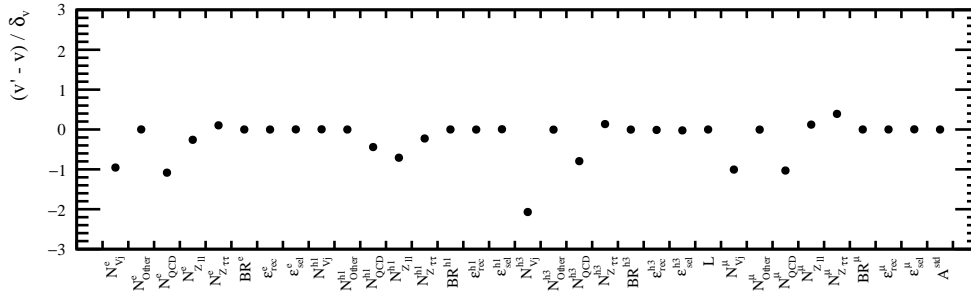


**Figure 16.4** – Pulls of the nuisance parameters from the likelihood simultaneously fit over all channels, for  $m_H = 125 \text{ GeV}/c^2$ .

# 17 Results

## 17.1 Signal upper limit

The extended maximum likelihood is performed simultaneously across all analysis channels to obtain the best fit of  $N_{\text{sig}}$  (eq. 16.3). The results are summarized in Fig. 17.2 for each tau decay channel and for each  $m_H$  value. The corresponding invariant mass distributions for the  $H \rightarrow \mu\tau$  candidates after the fit are shown in Fig. 17.1.

The same procedure is applied to the calculation of  $\sigma_{gg \rightarrow H \rightarrow \mu\tau}$ . The results are shown in Fig. 17.3, and Fig. 17.4, corresponding to 95% CL upper limits. The results are quoted for the  $4\pi$  acceptance as well as for the LHCb geometrical acceptance. No statistically significant excess is observed.

The best fit for the branching fraction,  $\mathcal{B}_{H \rightarrow \mu\tau}$ , as well as the upper limit can be computed for a given theoretical model of Higgs production. The results shown in Fig. 17.5 are obtained in the MSSM context, following cross-sections provided by the ‘‘LHC Higgs Cross Section Working Group’’<sup>1</sup>, with uncertainties (PDF, scale,  $\alpha_s$ ) fully correlated across channels.

Alternatively, for the SM Higgs of  $m_H = 125 \text{ GeV}/c^2$ , the same computation gives the best fit  $\mathcal{B}(H \rightarrow \mu\tau) = -1.68_{-12.26}^{+13.85}\%$ , and an observed upper limit  $\mathcal{B}(H \rightarrow \mu\tau) < 25.7\%$ . The result from SM Higgs can be interpreted in terms of the LFV Yukawa couplings [30] on  $\mu\tau$  using the following expression:

$$\mathcal{B}(H \rightarrow \mu\tau) = \frac{\Gamma(H \rightarrow \mu\tau)}{\Gamma(H \rightarrow \mu\tau) + \Gamma_{\text{SM}}} \quad , \quad \Gamma(H \rightarrow \mu\tau) = \frac{m_H}{8\pi} (|Y_{\mu\tau}|^2 + |Y_{\tau\mu}|^2)$$

Assuming  $\Gamma_{\text{SM}} = 4.1 \text{ MeV}/c^2$ , this gives an upper limit<sup>2</sup> of  $\sqrt{|Y_{\mu\tau}|^2 + |Y_{\tau\mu}|^2} < 1.69 \times 10^{-2}$ . Supplementary results are available in appendix M.

<sup>1</sup> <https://twiki.cern.ch/twiki/bin/view/LHCPhysics/CERNYellowReportPageBSMA8TeV>

<sup>2</sup> In contrast, the world best limit as of 2017 October is  $\sqrt{|Y_{\mu\tau}|^2 + |Y_{\tau\mu}|^2} < 1.43 \times 10^{-3}$  [52].

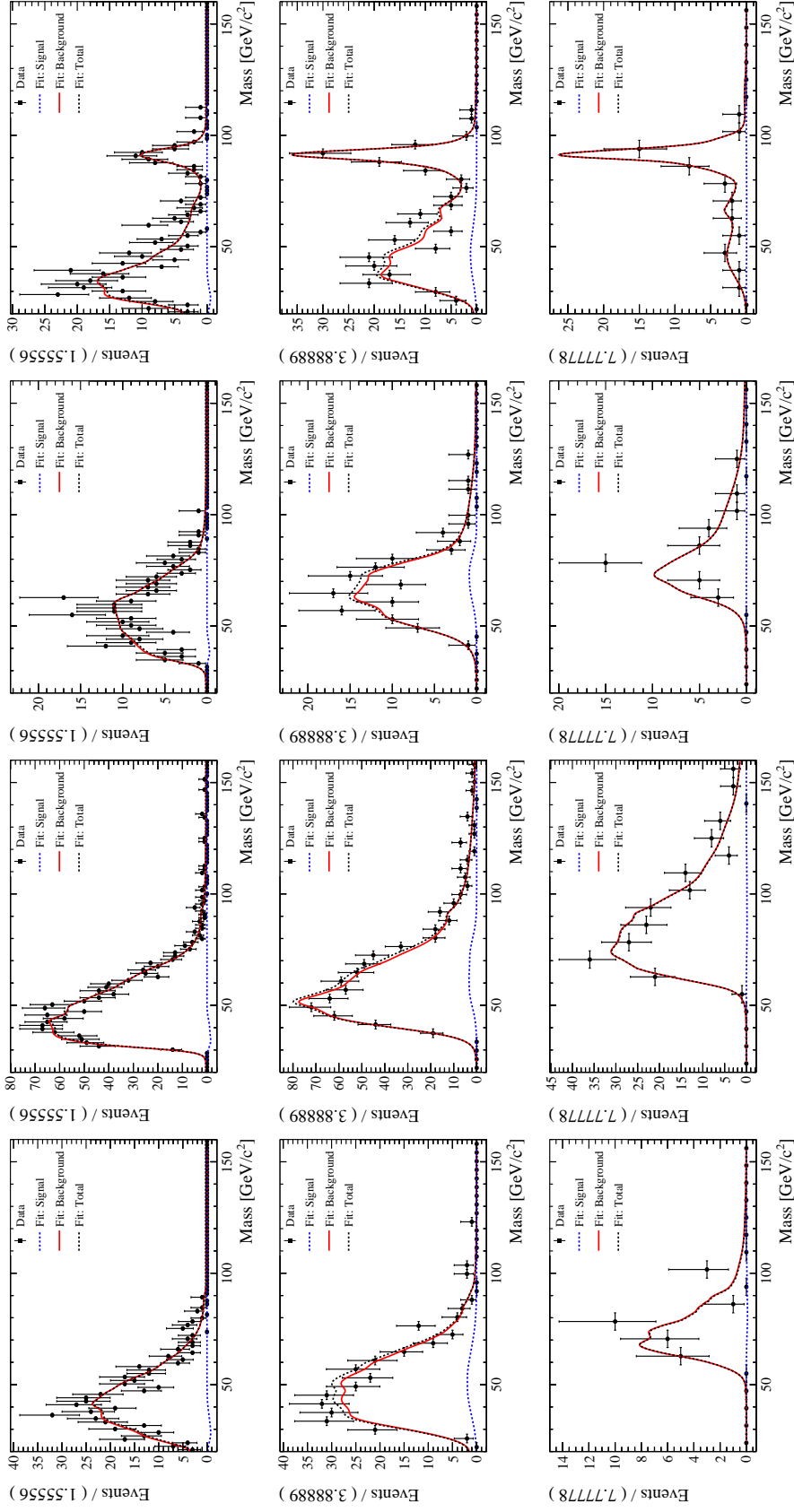


**Figure 17.1** – Simultaneous fit of the distribution of  $H \rightarrow \mu\pi$  candidates invariant mass for the 4 analysis channels (columns-wise;  $\mu\tau_e$ ,  $\mu\tau_{h1}$ ,  $\mu\tau_{h3}$ ,  $\mu\tau_\mu$ ) at 3 different selection regimes (row-wise; low-mass  $m_H = 45 \text{ GeV}/c^2$ , central  $m_H = 85 \text{ GeV}/c^2$ , high-mass  $m_H = 125 \text{ GeV}/c^2$ ).

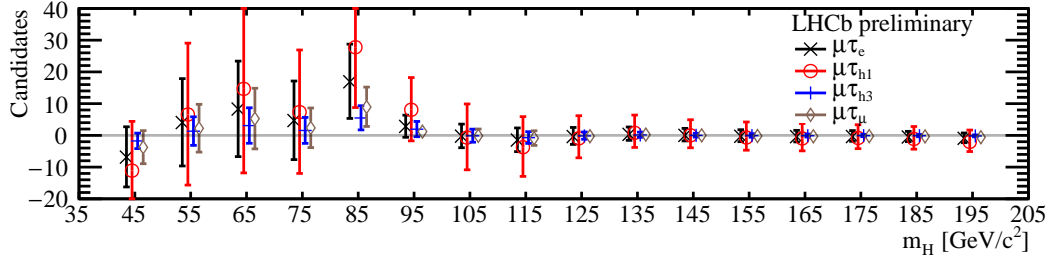


Figure 17.2 – Best fit number of signal candidates at different  $m_H$ .

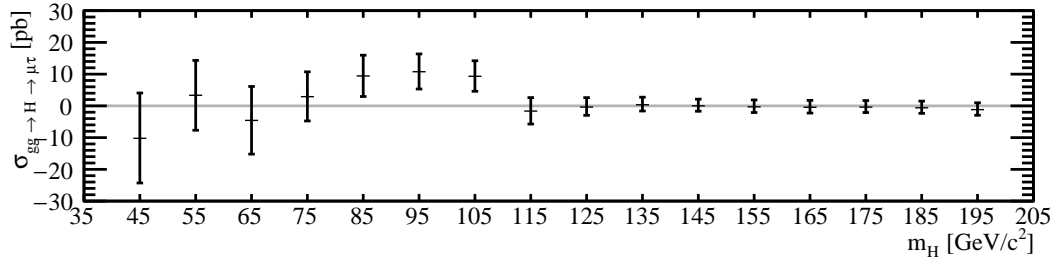


Figure 17.3 – Best fit of  $\sigma_{gg \rightarrow H \rightarrow \mu\tau}$  with all analysis channels simultaneously fit, and with selection regimes of best FOM, from inclusive production.

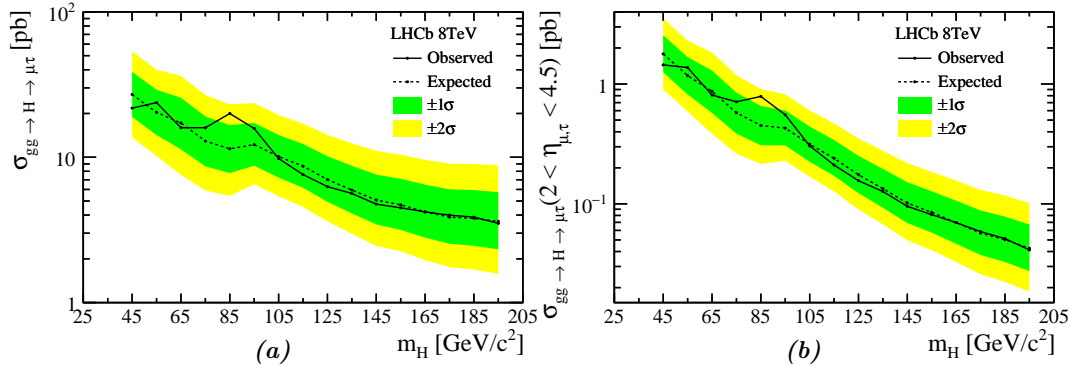


Figure 17.4 – 95% CLs upper limits of  $\sigma_{gg \rightarrow H \rightarrow \mu\tau}$  with all analysis channels simultaneously fit: (a) inclusive  $H \rightarrow \mu\tau$  production, (b)  $H \rightarrow \mu\tau$  production with lepton daughters inside LHCb geometrical acceptance.

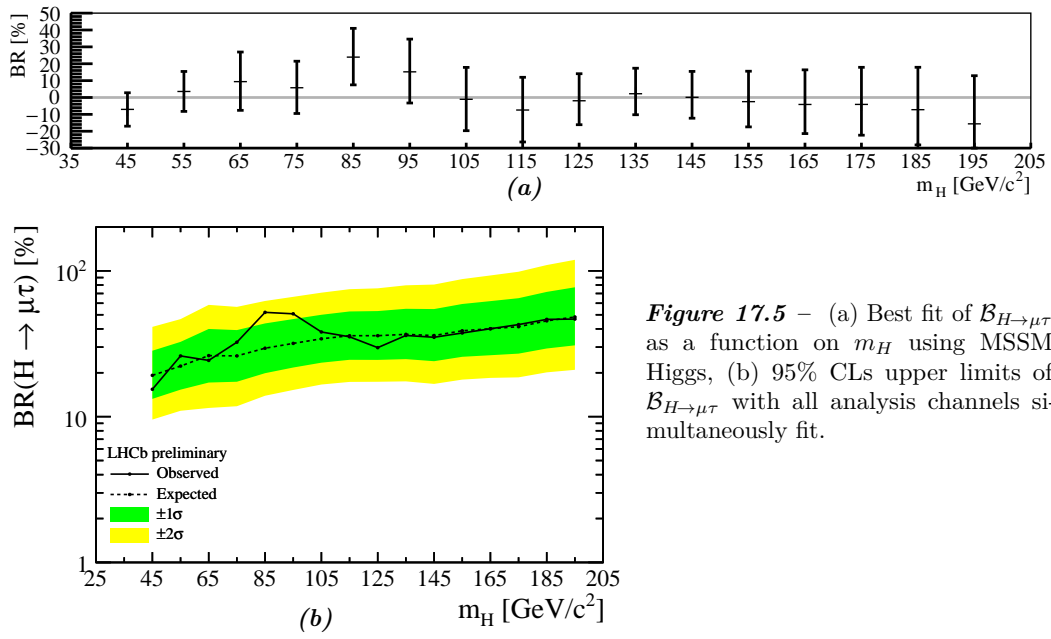


Figure 17.5 – (a) Best fit of  $\mathcal{B}_{H \rightarrow \mu\tau}$  as a function on  $m_H$  using MSSM Higgs, (b) 95% CLs upper limits of  $\mathcal{B}_{H \rightarrow \mu\tau}$  with all analysis channels simultaneously fit.



## 17.2 Future prospect

The estimation for  $H \rightarrow \mu\tau$  signal yield at  $\sqrt{s} = 13$  TeV during Run-II (2015-2018) is presented in this Section, which is calculated using the following expression:

$$N_{\text{sig}} = \mathcal{L} \sigma_{gg \rightarrow H} \mathcal{B}_{H \rightarrow \mu\tau} \mathcal{B}_{\tau \rightarrow X} \varepsilon_{\text{geo}} \varepsilon_{p_T} \varepsilon_{\text{rec}} \varepsilon_{\text{sel}}$$

The expected signal yields,  $N_{\text{sig}}$ , are summarized in Table 17.2. The meaning and estimation for each terms are the following:

$\mathcal{L}$ , **integrated luminosity**, assuming the expected integrated luminosity of  $5 \text{ fb}^{-1}$  collected throughout Run-II.

$\sigma_{gg \rightarrow H}$ , **BSM Higgs production cross-section** at 13 TeV via gluon-gluon fusion, taken from the LHCHXWG [146]. The cross-sections are computed at N3LO QCD [147], using PDF4LHC15\_nnlo\_100 PDF set [148]. The uncertainty includes QCD scales, PDF, and theory.

$\mathcal{B}_{H \rightarrow \mu\tau}$ , **branching fraction of  $H \rightarrow \mu\tau$** , assuming 0.25% from the world upper limit [52].

$\mathcal{B}_{\tau \rightarrow X}$ , **branching fraction of tau lepton**, taken from the PDG [123].

$\varepsilon_{\text{geo}}$ , **geometrical acceptance**, requiring prompt muon and tau lepton decay product to be inside the LHCb geometrical acceptance,  $2.0 < \eta < 4.5$ . The values are computed from the simulated samples using PYTHIA 8, and shown in Fig. 17.6.

$\varepsilon_{p_T}$ , **kinematic cut efficiency**, requiring prompt muon and tau lepton decay product to satisfy the minimum transverse momentum thresholds identical to the definition in Section 12.1. The values are computed from the simulated samples using PYTHIA 8, and shown in Fig. 17.7a.

$\varepsilon_{\text{rec}}$ , **reconstruction efficiency**. The reconstruction requirements are expected to differ between Run-I and Run-II. It is assumed that the performance remains similar to Section 14.2. For simplicity, the values are assumed independent from  $m_H$ , as shown in Table 17.1.

$\varepsilon_{\text{sel}}$ , **signal selection efficiency**. It is assumed that the performance remains similar to Section 14.3, with values assumed to be independent from  $m_H$ , as shown in Table 17.1.

Additionally, the efficiency  $\varepsilon_{p_T}$  can be improved in the future analysis by lowering the thresholds to better suit the Run-II triggers. Considering the high- $p_T$  muon trigger (H1t2EWSingleMuonVHighPt), the  $p_T$  threshold on prompt muon is placed at  $12.5 \text{ GeV}/c$ . With  $p_T$  threshold on other charged particles placed at  $1 \text{ GeV}/c$ , the improved expected signal yields are shown in Table 17.3. The future analysis is expected to improve the background rejection by employing a more sophisticated selection, such as using a multivariate technique. The results from Table 17.3 shows that there is a prospect to further constrain the limit especially in the region where  $m_H < m_Z$ , despite the reduced geometrical acceptance at LHCb.

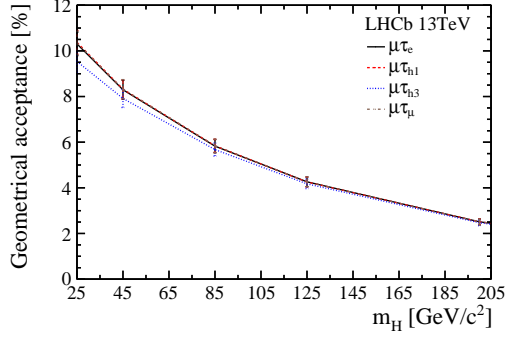

 Figure 17.6 –  $\varepsilon_{\text{geo}}$  as a function of  $m_H$ .

 Table 17.1 – Approximate efficiencies of  $\varepsilon_{\text{rec}}$  and  $\varepsilon_{\text{sel}}$  used in the estimation of future prospect.

[%]	$\varepsilon_{\text{rec}}$	$\varepsilon_{\text{sel}}$
$\mu\tau_e$	60	25
$\mu\tau_{h1}$	65	20
$\mu\tau_{h3}$	20	30
$\mu\tau_\mu$	75	10

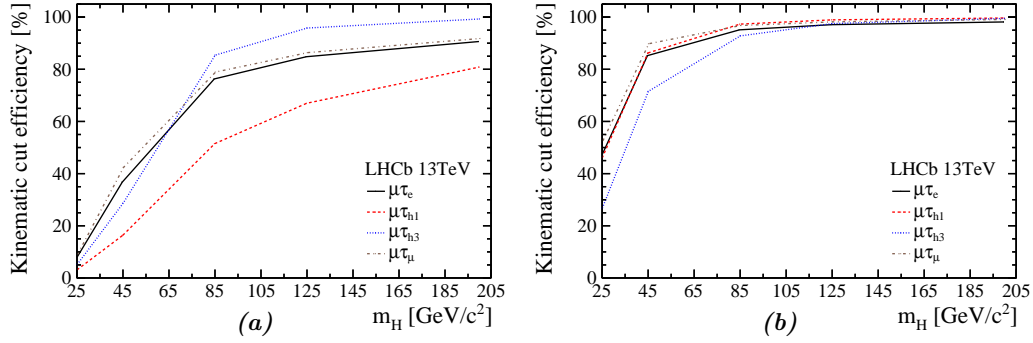

 Figure 17.7 –  $\varepsilon_{p_T}$  using (a) current selection, (b) improved selection.

Table 17.2 – Estimated Run-II signal yield using current selection.

$m_H$ [GeV/ $c^2$ ]	$\mu\tau_e$	$\mu\tau_{h1}$	$\mu\tau_{h3}$	$\mu\tau_\mu$	Total
25	1.62	1.62	0.34	0.97	4.56
45	2.76	3.00	0.67	1.56	7.98
85	1.39	2.29	0.49	0.70	4.87
125	0.55	1.05	0.20	0.27	2.06
200	0.13	0.28	0.05	0.06	0.52

Table 17.3 – Estimated Run-II signal yield using improved kinematic selection.

$m_H$ [GeV/ $c^2$ ]	$\mu\tau_e$	$\mu\tau_{h1}$	$\mu\tau_{h3}$	$\mu\tau_\mu$	Total
25	10.17	24.43	1.76	5.61	41.97
45	6.40	15.81	1.67	3.30	27.18
85	1.73	4.32	0.54	0.86	7.45
125	0.63	1.55	0.20	0.31	2.69
200	0.14	0.35	0.05	0.07	0.60

# Conclusion



# Conclusion and Outlook

The search for  $H \rightarrow \mu\tau$  decay has been presented in this thesis, where  $H$  is Higgs-like boson, with mass in the range 45 to 195 GeV/ $c^2$ . The theoretical introduction and the experimental setup have been discussed in Part I. The capability of LHCb to detect the tau lepton has been demonstrated with the reconstruction of the  $Z \rightarrow \tau\tau$  process, in Part II.

~

The measurement of the  $Z \rightarrow \tau^+\tau^-$  production cross-section in LHCb at  $\sqrt{s} = 8$  TeV is performed, in the kinematical fiducial region defined by a di-tau of invariant mass between 60 and 120 GeV/ $c^2$ , with the tau lepton having a transverse momentum greater than 20 GeV/ $c$ , and a pseudorapidity between 2 and 4.5. The forward phasespace explored by this analysis is complementary to the ones covered by the central detectors, ATLAS and CMS.

The reconstruction of di-tau candidates is performed in the leptonic and hadronic decay modes of the tau lepton, but requiring at least one tau decaying leptonically. The reconstruction of high- $p_T$  tau leptons in the 3-prongs decay mode is performed for the first time in LHCb, which is added to the set of tau lepton identification modes. This additional decay mode, as well as the combined treatment of  $\tau_\mu\tau_e$  and  $\tau_e\tau_\mu$  final states in a single channel, complements the analysis performed at 7 TeV.

The main sources of background are QCD processes and  $W$  and  $Z$  bosons produced in association with jets. They are estimated by a data-driven method. The measured production cross-section, combined from all the measured decay channels, is of  $95.20 \pm 5.36$  pb, resulting in a precision of 5.6%, an improvement from 7.2% in the previous analysis. However, the statistical uncertainty (2.2%) is no longer dominating; presently the most important component is from selection efficiency (3.7%). An improvement of this measurement would require the identification of control processes to calibrate the selection variables, as well as the use of multivariate technique for background discrimination.

The result presented in this thesis is compatible with the previous measurement performed by LHCb, with the World average (PDG), and with the NNLO SM prediction. The lepton universality hypothesis is verified.

~

In Part III, a direct search for model-independent Higgs-like bosons decaying via a lepton flavour violating process  $H \rightarrow \mu\tau$  has been performed using the same experimental condition, tau identification, and dataset as  $Z \rightarrow \tau\tau$  analysis. The tau lepton is reconstructed in both leptonic and hadronic modes as a 1-prong or 3-prongs, covering 99% of its decay modes. No statistically significant excess is observed over the range of the boson mass  $m_H$  45–195 GeV/ $c^2$ . An upper limit for the Higgs-like production cross-section times branching-ratio to  $\mu\tau$  is computed for each  $m_H$  value, ranging from about 23 pb for  $m_H = 45$  GeV/ $c^2$  to 4 pb at 195 GeV/ $c^2$ . Assuming SM Higgs, the limit on branching fraction is at  $\mathcal{B}(H \rightarrow \mu\tau) < 25.7\%$ , corresponding to a Yukawa coupling of  $\sqrt{|Y_{\mu\tau}|^2 + |Y_{\tau\mu}|^2} < 1.69 \times 10^{-2}$ . Whilst the upper limit is weaker than results obtained from ATLAS and CMS, the result excludes the  $H \rightarrow \mu\tau$  production in the forward region, as well as covering low-mass region inaccessible by aforementioned collaborations. Being a model-independent search, the result allows a flexible reinterpretation by theoreticians to constrain future HCLFV models.

Like previously mentioned about the  $Z \rightarrow \tau\tau$  analysis, a possible improvement is the usage of multivariate technique for discriminating signal and background candidates. Instead of using 3 selection regimes, a multivariate technique can be trained and evaluated for each  $m_H$  individually, allowing a seamless transition. A dedicated search for  $H \rightarrow \mu\tau$  at low-mass ( $m_H < 40$  GeV/ $c^2$ ) at LHCb would be another promising prospect, as it is a region inaccessible by ATLAS and CMS. The search would be more difficult because it could not rely on high- $p_T$   $\mu$  and  $\tau$ , and would require to change the trigger, in order to maximize the kinematical acceptance. Another possible development is to include the decay to  $\mu e$  and  $\tau e$  final states as well, enabling an inclusive coverage of CLFV couplings in one analysis.

~

The  $Z \rightarrow \tau\tau$  and  $H \rightarrow \mu\tau$  analyses can be considered “foreign” at LHCb, where the main programme focuses on the  $b$ -physics. Being less mainstream in the collaboration may seem like a hindrance, but the potential is truly unique. Having less personpower invested in this field deemed challenging, but that makes the QEE group compact, agile, and passionate in what we do. Whilst the collected results are statistically limited, the foundation and techniques for future analyses become increasingly firm and enticing, gradually decreasing the competition gap between collaborations. The New Physics may have already lay dormant amidst the pile of collected data, awaiting, for the awakening...

# Appendix





# A Selection of $Z \rightarrow \tau\tau$

## A.1 Acceptance

The acceptance region of the di-tau candidate (shown as visible area outside grey mask) is compared against the entire fiducial region of  $Z \rightarrow \tau\tau$ , which is studied at the generator-level. The sample is generated at next-to-leading order with POWHEG-BOX r2092 and showered with PYTHIA 8.175.

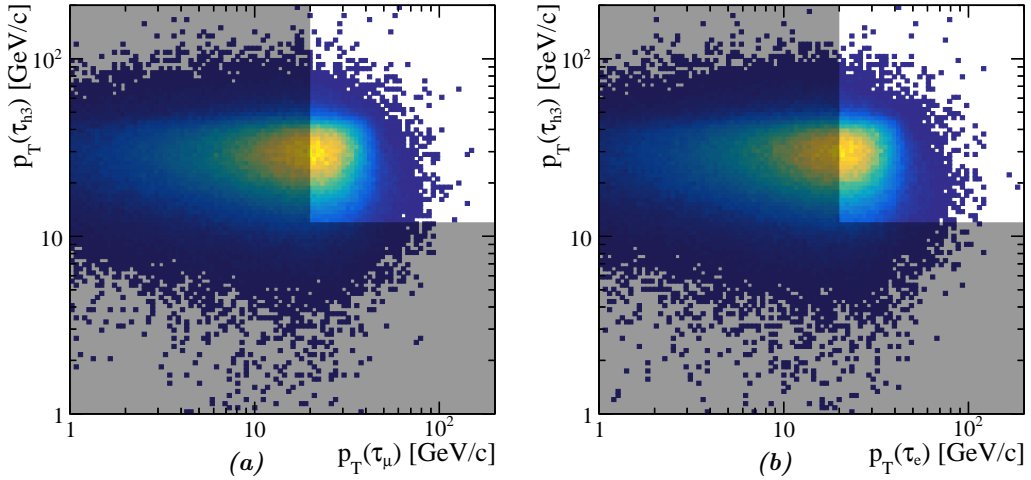


**Figure A.1** – The acceptance region as a function of transverse momentum of  $\tau_l$  and  $\tau_{h3}$  (sum of momenta of 3 charged hadrons) (a)  $\tau_\mu\tau_{h3}$  (b)  $\tau_e\tau_{h3}$ .

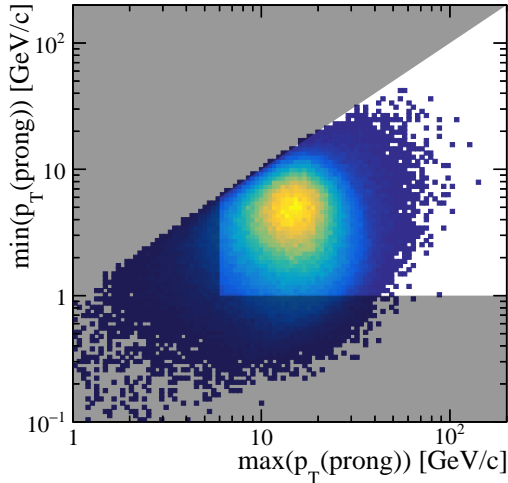


**Figure A.2** – For the  $\tau_{h3}$  from  $\tau_\mu\tau_{h3}$  channel, the acceptance region as a function of maximum  $p_T$  of the 3 tracks, and minimum  $p_T$  of prongs. No difference is observed for the same plot using  $\tau_{h3}$  from  $\tau_e\tau_{h3}$  channel.

## Appendix A. Selection of $Z \rightarrow \tau\tau$

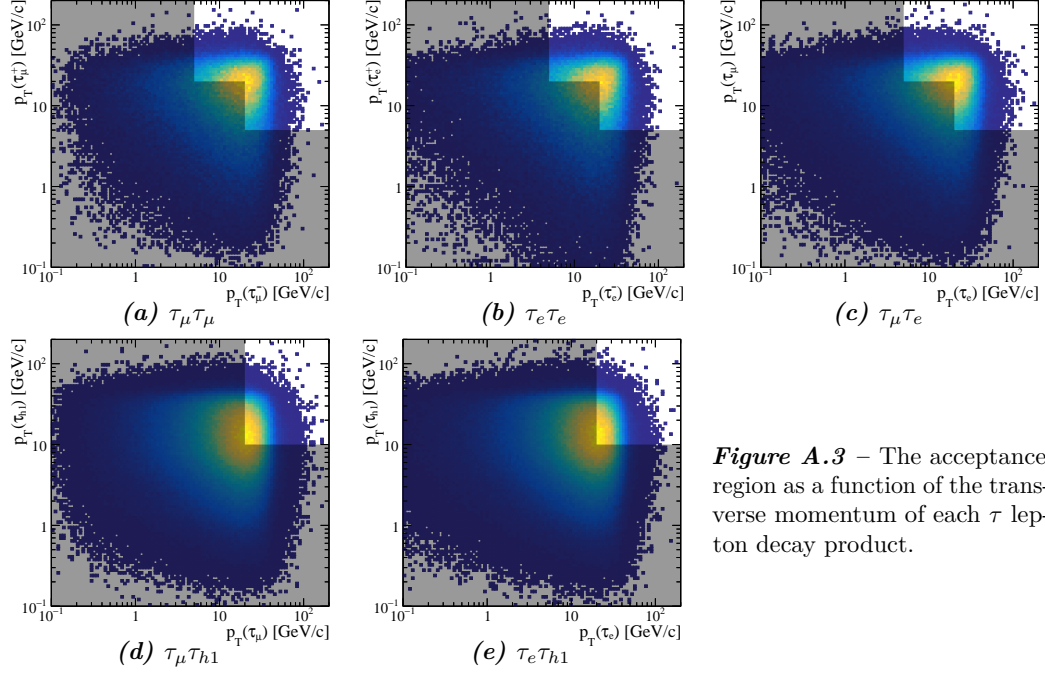


**Figure A.3** – The acceptance region as a function of each  $\tau$  lepton decay product.

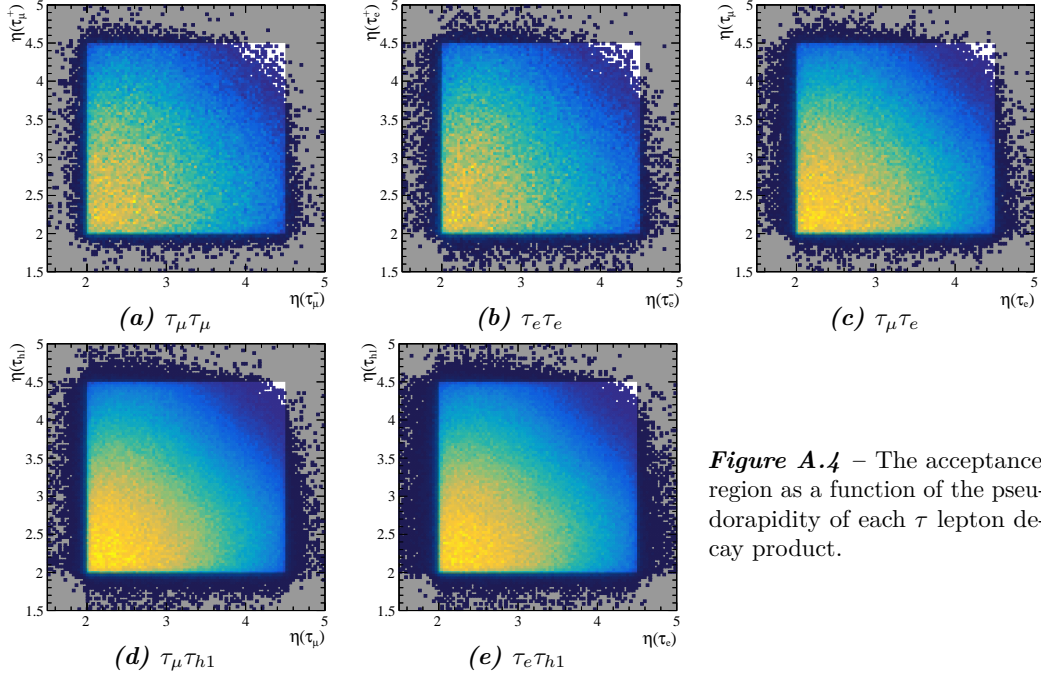


**Figure A.4** – The acceptance region as a function of the pseudorapidity of each  $\tau$  lepton decay product.

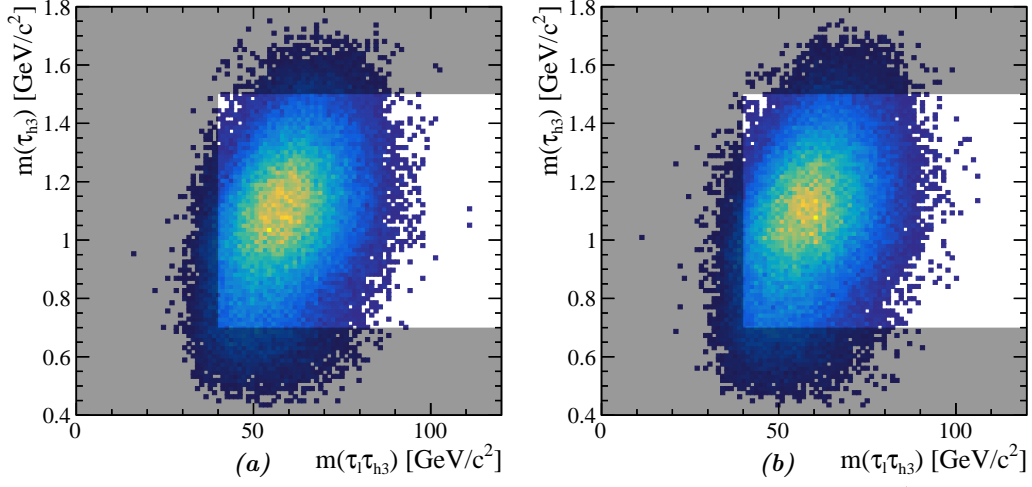


**Figure A.5** – The acceptance region as a function of the invariant masses of  $\tau_{h3}$  (vertical axis) and di-tau (horizontal axis), with all  $p_T$  and  $\eta$  acceptance cuts applied for channel (a)  $\tau_\mu\tau_{h3}$  (b)  $\tau_e\tau_{h3}$ .

**Table A.1** – Signal retention from the mass window cut at the acceptance level (with all other cuts on  $p_T$  and  $\eta$  applied).

Channel	Sample size	with lower bound [%]	with upper bound [%]	with both bound [%]
$\tau_\mu\tau_\mu$	94090	99.8895	99.6185	99.5079
$\tau_\mu\tau_{h1}$	164323	99.0847	100.0000	99.0847
$\tau_\mu\tau_{h3}$	75474	99.9762	100.0000	99.9762
$\tau_e\tau_e$	96048	99.8813	99.6346	99.5159
$\tau_e\tau_{h1}$	164655	99.1139	100.0000	99.1139
$\tau_e\tau_{h3}$	76635	99.9622	100.0000	99.9622
$\tau_\mu\tau_e$	190707	99.8757	100.0000	99.8757

## A.2 Trigger-Stripping Specification

*Table A.2* – Muon-alley specification for trigger–stripping.

Trigger/Stripping	Prescale	min $p_T(\mu)$ [GeV/c]	Other cuts
L0Muon	1.0	1.76	SPD mult < 600
Hlt1SingleMuonHighPT	1.0	4.8	L0Muon    L0MuonNoSPD VELO hits > 0 VELO missing hits < 999 Track upgrade <b>Tight</b> Track hits > 0 Track $\chi^2/\text{ndf}$ < 4 $p > 3$ GeV
Hlt2SingleMuonHighPT	1.0	10	—
Stripping20: Z02TauTau_MuX [ $Z \rightarrow \mu^- X^+$ ]cc	1.0	15	TRPCHI2 > 0.001 $p_T(X) > 5$ GeV $m_{\mu X} > 20$ GeV

*Table A.3* – Electron-alley specification for trigger–stripping.

Trigger/Stripping	Prescale	min $p_T(e)$ [GeV/c]	Other cuts
L0Electron	1.0	—	SPD mult < 600 $E_T > 2720$ MeV
Hlt1SingleElectronNoIP	1.0	10	L0Electron VELO hits > 0 VELO missing hits < 999 Track upgrade <b>Tight</b> Track hits > 0 Track $\chi^2/\text{ndf}$ < 3 $p > 20$ GeV
Hlt2SingleTFVHighPtElectron	1.0	15	Track $\chi^2/\text{ndf}$ < 20 $E_{PS} > 50$ MeV $E_{ECAL}/p > 0.1$ $E_{HCAL}/p < 0.05$
Stripping20: Z02TauTau_EX [ $Z \rightarrow e^- X^+$ ]cc	1.0	15	TRPCHI2 > 0.001 $E_{PS}(e) > 50$ MeV $E_{ECAL}/p(e) > 0.1$ $E_{HCAL}/p(e) < 0.05$ $p_T(X) > 5$ GeV $m_{eX} > 20$ GeV

## A.2. Trigger-Stripping Specification

**Table A.4** – StrippingZ02MuMuLine from StrippingZ02MuMu.py, used as control sample for  $\epsilon_{\text{sel}}$  systematics.

Particle	Selection
$\mu^\pm$	From StdAllLooseMuons PT > 3*GeV
Z	Decay descriptor: Z0 -> mu+ mu- MM > 40*GeV

**Table A.5** – StrippingMuIDCalib\_JpsiFromBNoPIDNoMip from StrippingMuIDCalib.py, used for low- $p_T$  muon tag-and-probe  $\epsilon_{\text{PID},\mu}$ .

Particle	Selection
$\mu^\pm$	From StdNoPIDsMuon P > 3*GeV PT > 800*MeV TRCHI2DOF < 3 ISLONG MIPCHI2DV(PRIMARY)>10
$J/\psi$	Decay descriptor: J/psi(1S) -> mu+ mu- ADAMASS('J/psi(1S)') < 200*MeV VCHI2PDOF < 8 BPVVDCHI2 > 225
tag $\mu^\pm$	ISMUON P > 6*GeV PT > 1.5*GeV MIPCHI2DV(PRIMARY)>25

**Table A.6** – StrippingWMuLine from StrippingWMu.py, used for high- $p_T$  muon tag-and-probe  $\epsilon_{\text{PID},\mu}$ , and for muon misidentification study.

Particle	Selection
$\mu^\pm$	From StdAllLooseMuons PT > 20*GeV

## Appendix A. Selection of $Z \rightarrow \tau\tau$

**Table A.7** – StrippingJpsi2eeForElectronIDBu2JpsiKLine from StrippingElectronID.py, used for low- $p_T$  electron tag-and-probe  $\varepsilon_{\text{PID},e}$ .

Particle	Selection
$e^\pm$	From StdNoPIDsElectrons PPINFO(LHCb.ProtoParticle.InAccEcal,-1) > 0.5 PT > 500*MeV TRCHI2DOF < 5 MINTREE('e+'==ABSID,BPVIPCHI2()) > 9
$J/\psi$	Decay descriptor: J/psi(1S) -> e+ e- VFASPF(VCHI2) < 9 in_range(2200*MeV, MM, 4200*MeV) BPVDLS > 5
tag $e^\pm$	PT > 1500*MeV PIDE > 5.0 P > 6000*MeV BPVIPCHI2() > 9.0
probe $e^\pm$	PT > 500*MeV P > 3000*MeV BPVIPCHI2() > 9.0
$K^\pm$	From StdTightKaons TRCHI2DOF < 4 PT > 1.0*GeV PIDK > 0 BPVIPCHI2()>9
$B^\pm$	Decay descriptor: [B+ -> J/psi(1S) K+]cc in_range(4.2*GeV, M, 6.0*GeV) VCHI2PDOF < 9

**Table A.8** – StrippingWeLine from StrippingWe.py, used for high- $p_T$  electron tag-and-probe  $\varepsilon_{\text{PID},e}$ , and  $\varepsilon_{\text{trig},e}$ .

Particle	Selection
$e^\pm$	From StdAllNoPIDsElectrons PPINFO(LHCb.ProtoParticle.CaloPrsE,0) > 50 PPINFO(LHCb.ProtoParticle.CaloEcalE,0) > P*0.1) PPINFO(LHCb.ProtoParticle.CaloHcalE,99999) < P*0.05 PT > 20*GeV HASTRACK TRCUT(0<TrIDC('isTT'))

## A.2. Trigger-Stripping Specification

**Table A.9** – StrippingNoPIDStarWithD02RSKPiLine from StrippingNoPIDStarWithD02RSKPi.py, used for charged hadron tag-and-probe  $\varepsilon_{\text{PID},h}$ .

Particle	Selection
$K^\pm$	From StdAllNoPIDsKaons PT > 250.0 P > 2000.0 TRCHI2DOF < 5 MIPCHI2DV(PRIMARY) > 16
$\pi^\pm$	From StdAllNoPIDsPions PT > 250.0 P > 2000.0 TRCHI2DOF < 5 MIPCHI2DV(PRIMARY) > 16
$D^0$	Decay descriptor: [D0 -> K- pi+]cc PT > 1500.0 VCHI2PDOF < 13 BPVVDCHI2 > 49 BPVDIRA > 0.9999 BPVIPCHI2() < 30 ADMASS('D0') < 75.0 ADWM('D0', WM('pi-', 'K+')) > 25.0 ADWM('D0', WM('K-', 'K+')) > 25.0 ADWM('D0', WM('pi-', 'pi+')) > 25.0
$D^{*\pm}$	Decay descriptor: [D*(2010)+ -> D0 pi+]cc APT > 2200.0 ADAMASS('D*(2010)+') < 75) AM - AM1 < 165*MeV VCHI2PDOF < 13 M-MAXTREE('D0'==ABSID,M)<155.0 M-MAXTREE('D0'==ABSID,M)>130.0

## A.3 Kinematic Preselection

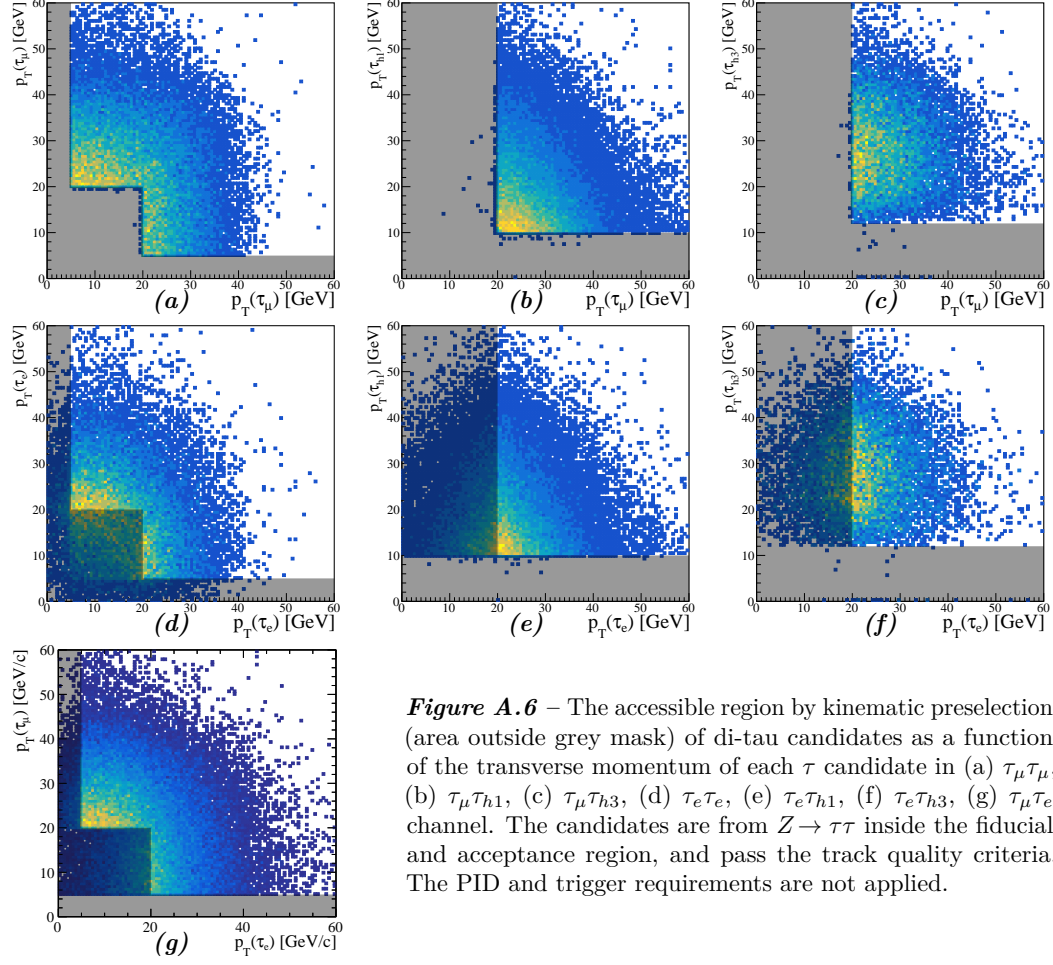


**Figure A.6** – The accessible region by kinematic preselection (area outside grey mask) of di-tau candidates as a function of the transverse momentum of each  $\tau$  candidate in (a)  $\tau_\mu\tau_\mu$ , (b)  $\tau_\mu\tau_{h1}$ , (c)  $\tau_\mu\tau_{h3}$ , (d)  $\tau_e\tau_e$ , (e)  $\tau_e\tau_{h1}$ , (f)  $\tau_e\tau_{h3}$ , (g)  $\tau_\mu\tau_e$  channel. The candidates are from  $Z \rightarrow \tau\tau$  inside the fiducial and acceptance region, and pass the track quality criteria. The PID and trigger requirements are not applied.



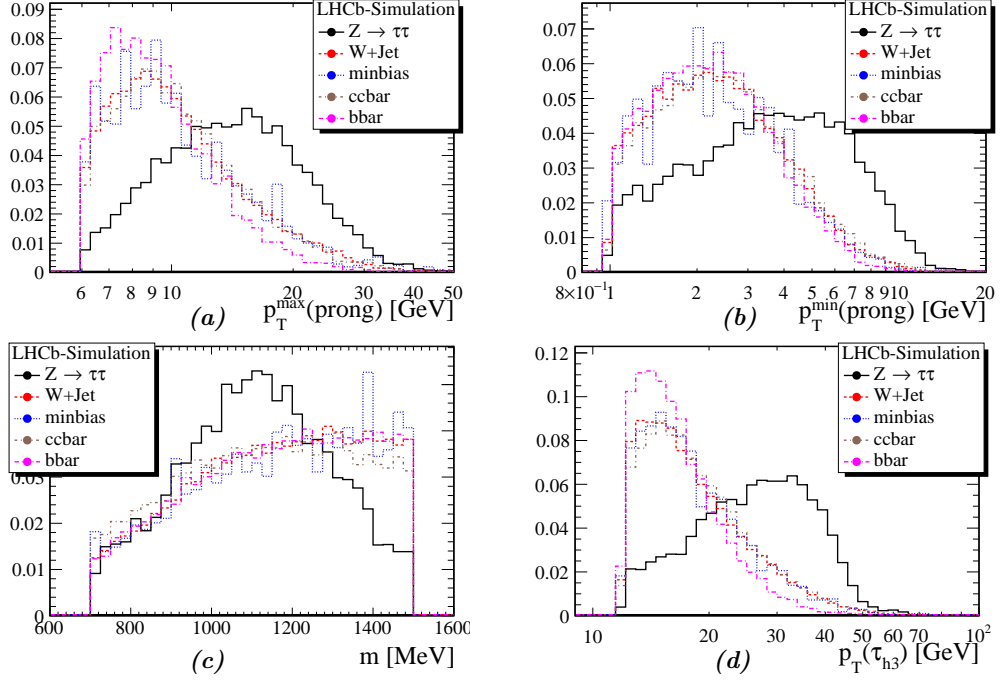


Figure A.7 – Variables of  $\tau_{h3}$  used in preselection of  $\tau_{\mu}\tau_{h3}$  candidates. Comparison between signal (black) and various background, all from simulation. The preselection cut is applied and shown as black vertical line. (a) largest  $p_T$  of  $\tau_{h3}$  prongs, (b) smallest  $p_T$  of  $\tau_{h3}$  prongs, (c) invariant mass of  $\tau_{h3}$ , (d)  $p_T$  of  $\tau_{h3}$ . The case for  $\tau_e\tau_{h3}$  produces similar results.

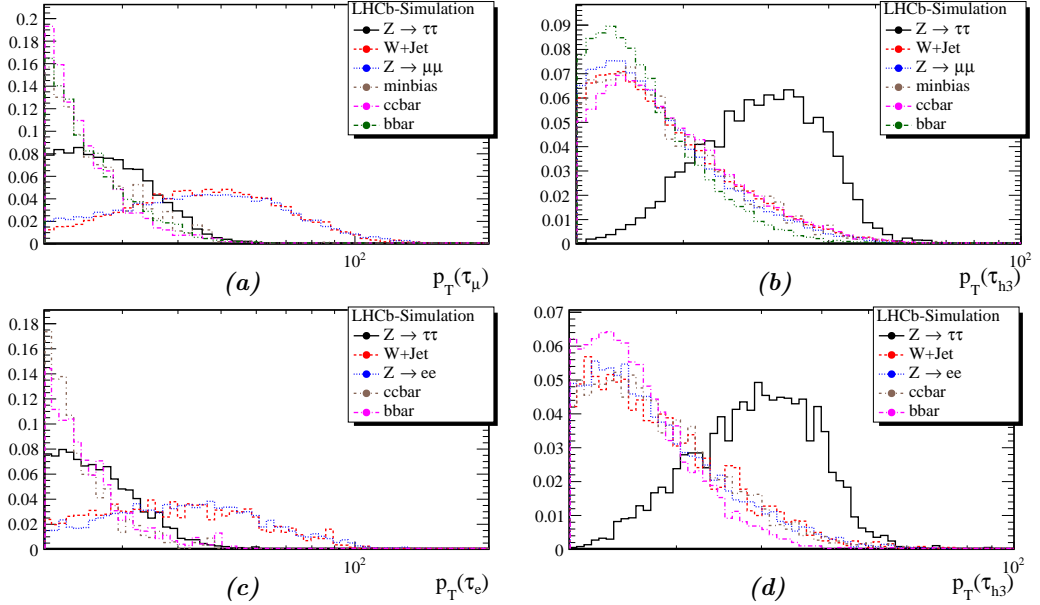
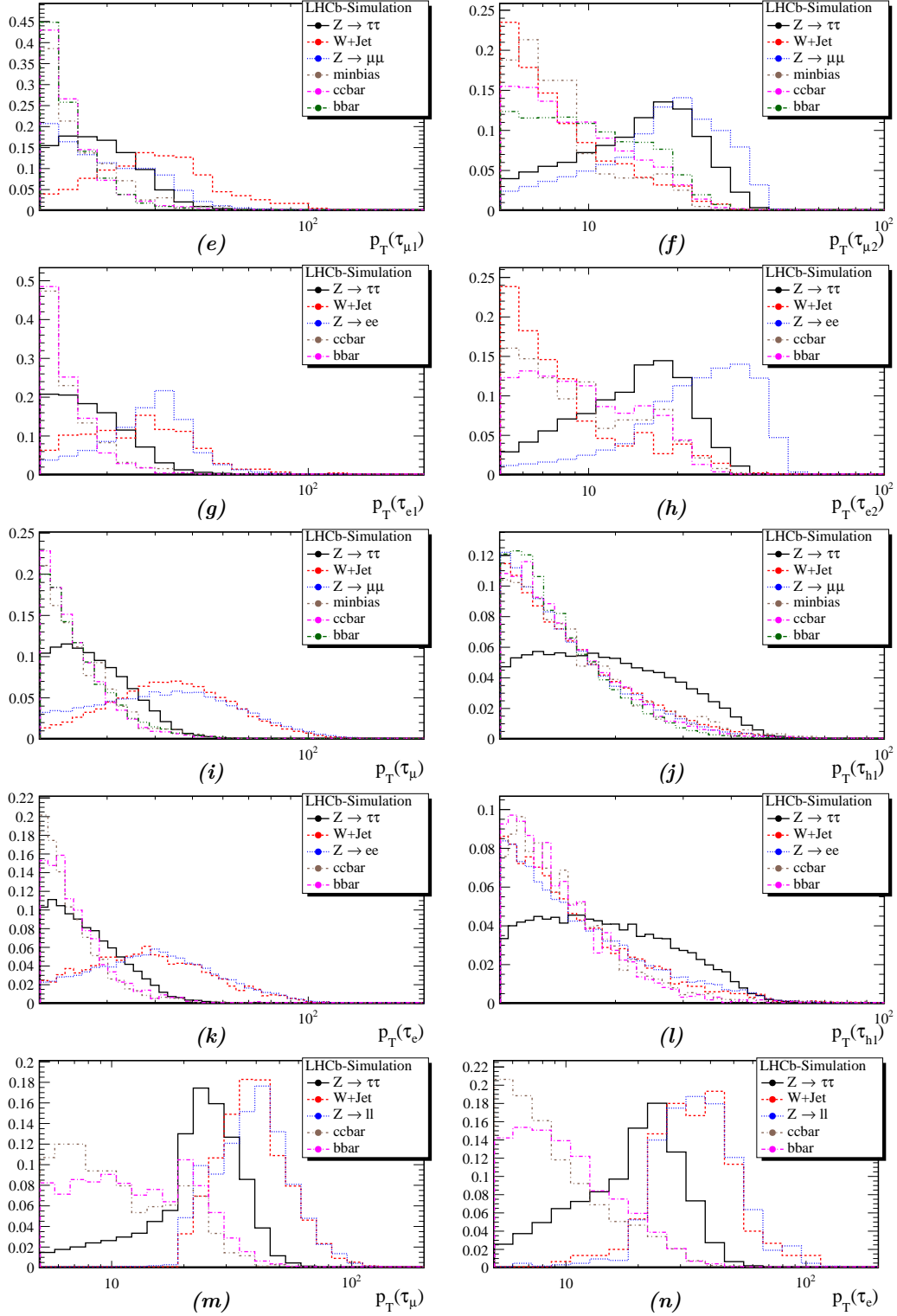


Figure A.8 – Transverse momentum of the tau in each di-tau candidates after preselection. Comparison of signal and backgrounds from simulation. (a,b)  $\tau_{\mu}\tau_{h3}$ , (c,d)  $\tau_e\tau_{h3}$ ,

## Appendix A. Selection of $Z \rightarrow \tau\tau$



**Figure A.8** – Transverse momentum of tau in each di-tau candidates after preselection. Comparison of signal and backgrounds from simulation. (a,b)  $\tau_\mu\tau_\mu$ , (c,d)  $\tau_e\tau_e$ , (e,f)  $\tau_\mu\tau_{h1}$ , (g,h)  $\tau_e\tau_{h1}$ , (i,j)  $\tau_\mu\tau_e$ .

## A.4 Assisted Candidate Selection

### A.4.1 Variables Correlation Matrix

The correlation matrix of the variables are calculated for each di-tau channel, using the TMVA package and simulated  $Z \rightarrow \tau\tau$  sample.

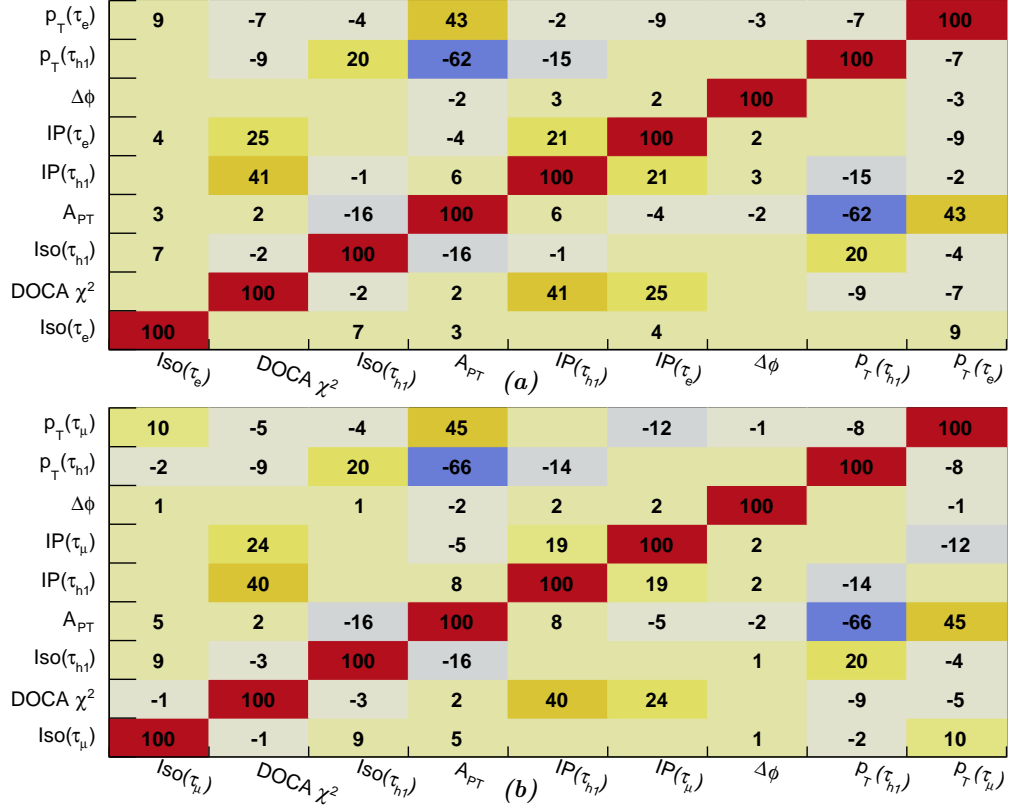


Figure A.9 – Variable correlation matrix in offline selection of (a)  $\tau_e \tau_{h1}$ , (b)  $\tau_\mu \tau_{h1}$  candidates.

## Appendix A. Selection of $Z \rightarrow \tau\tau$

$p_T(\tau_{e1})$	6	-7	1	28	-5	-10	-2	15	100
$p_T(\tau_{e2})$	2	-8	25	-90	-18		1	100	15
$\Delta\phi$	2	-1	1	-2		2	100	1	-2
$IP(\tau_{e1})$	6	24	2	-4	18	100	2		-10
$IP(\tau_{e2})$		43	4	15	100	18		-18	-5
$A_{PT}$		5	-24	100	15	-4	-2	-90	28
$ISO(\tau_{e2})$	6	2	100	-24	4	2	1	25	1
$DOCA \chi^2$		100	2	5	43	24	-1	-8	-7
$ISO(\tau_{e1})$	100		6			6	2	2	6
	$ISO(\tau_{e1})$	$DOCA \chi^2$	$ISO(\tau_{e2})$	$A_{PT}$	$IP(\tau_{e2})$	$IP(\tau_{e1})$	$\Delta\phi$	$p_T(\tau_{e2})$	$p_T(\tau_{e1})$
(c)									
$p_T(\tau_{\mu})$	29	-9	-14	-17	7	-25		-40	100
$p_T(\tau_e)$	-14	-5	30	-52	-23	9	1	100	-40
$\Delta\phi$	1		1	-3	1	3	100	1	
$IP(\tau_{\mu})$	-5	32	2	3	17	100	3	9	-25
$IP(\tau_e)$	3	33	1	13	100	17	1	-23	7
$A_{PT}$	-8	7	-18	100	13	3	-3	-52	-17
$ISO(\tau_e)$	5		100	-18	1	2	1	30	-14
$DOCA \chi^2$	-3	100		7	33	32		-5	-9
$ISO(\tau_{\mu})$	100	-3	5	-8	3	-5	1	-14	29
	$ISO(\tau_{\mu})$	$DOCA \chi^2$	$ISO(\tau_e)$	$A_{PT}$	$IP(\tau_e)$	$IP(\tau_{\mu})$	$\Delta\phi$	$p_T(\tau_e)$	$p_T(\tau_{\mu})$
(d)									
$p_T(\tau_{\mu1})$	10	-8	2	23	-6	-12	-4	20	100
$p_T(\tau_{\mu2})$	3	-14	28	-89	-24	-3	2	100	20
$\Delta\phi$			3	-4	2	2	100	2	-4
$IP(\tau_{\mu1})$		19		-2	24	100	2	-3	-12
$IP(\tau_{\mu2})$		45	-4	21	100	24	2	-24	-6
$A_{PT}$	1	11	-26	100	21	-2	-4	-89	23
$ISO(\tau_{\mu2})$	15	-3	100	-26	-4		3	28	2
$DOCA \chi^2$	-2	100	-3	11	45	19		-14	-8
$ISO(\tau_{\mu1})$	100	-2	15	1				3	10
	$ISO(\tau_{\mu1})$	$DOCA \chi^2$	$ISO(\tau_{\mu2})$	$A_{PT}$	$IP(\tau_{\mu2})$	$IP(\tau_{\mu1})$	$\Delta\phi$	$p_T(\tau_{\mu2})$	$p_T(\tau_{\mu1})$
(e)									

**Figure A.9** – Variable correlation matrix in offline selection of (c)  $\tau_e\tau_e$ , (d)  $\tau_{\mu}\tau_e$ , (e)  $\tau_{\mu}\tau_{\mu}$  candidates.

### A.4. Assisted Candidate Selection

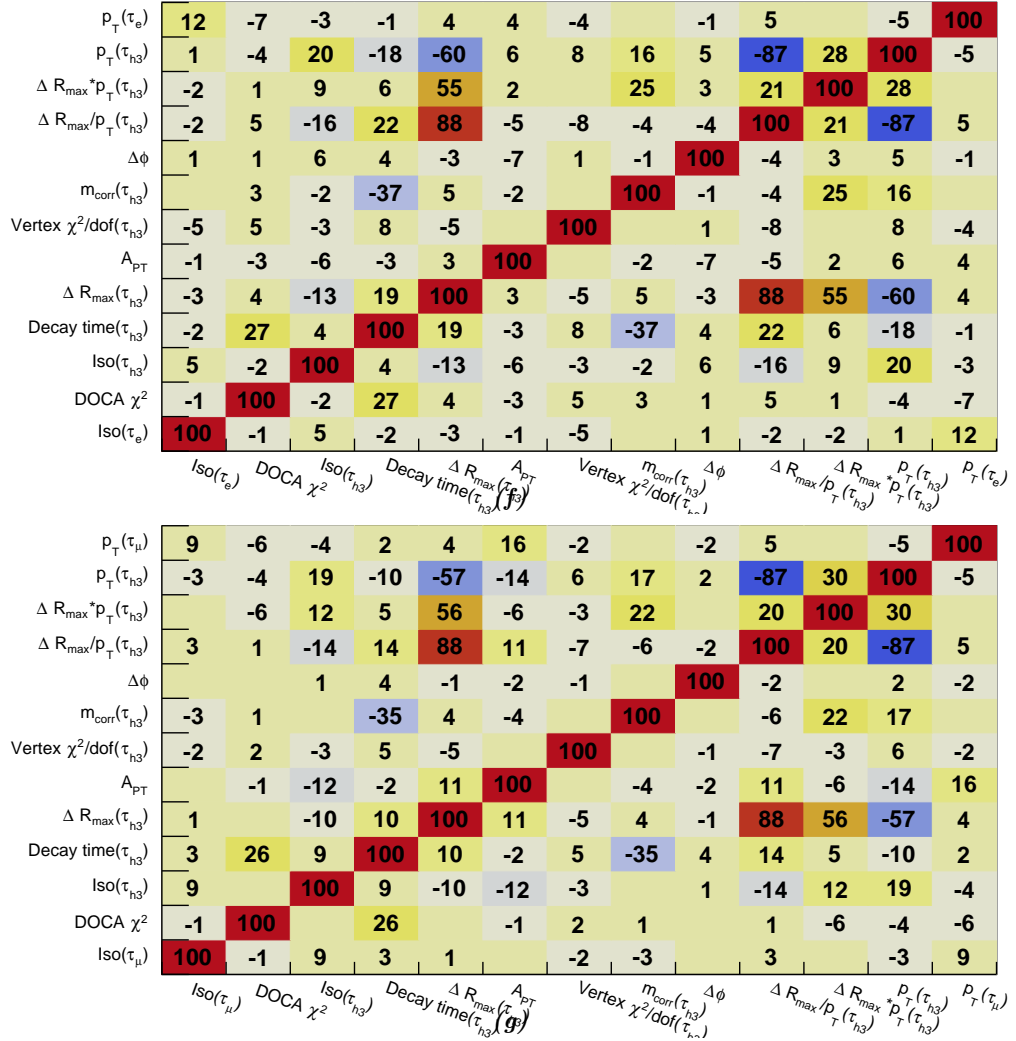


Figure A.9 – Variable correlation matrix in offline selection of (f)  $\tau_e \tau_{h3}$ , (g)  $\tau_\mu \tau_{h3}$  candidates.

## Appendix A. Selection of $Z \rightarrow \tau\tau$

### A.4.2 Variables Ranking

The list of available variables for di-tau candidate selection is processed with TMVA for the separation ranking (method unspecific) with respect to the background process in each channel. The signal is simulated  $Z \rightarrow \tau\tau$  sample, whereas the background process can be same-sign di-tau candidates from data, or  $Z \rightarrow \mu\mu$ ,  $Z \rightarrow ee$ ,  $W$ +jet simulated samples.

SIG: [MC] Z -> tau tau -> mu mu  
BKG: [Data] Same-sign

Variable	: Separation
Iso(#tau_{#mu2})	: 6.619e-01
Iso(#tau_{#mu1})	: 5.624e-01
p_{T}(#tau_{#mu2})	: 2.260e-01
A_{PT}	: 2.081e-01
DOCA #chi^2	: 9.416e-02
#Delta#phi	: 9.284e-02
IP(#tau_{#mu2})	: 8.975e-02
IP(#tau_{#mu1})	: 8.601e-02
p_{T}(#tau_{#mu1})	: 7.971e-02

SIG: [MC] Z -> tau tau -> e e  
BKG: [MC] Z -> e e

Variable	: Separation
DOCA #chi^2	: 3.563e-01
IP(#tau_{e2})	: 3.234e-01
p_{T}(#tau_{e1})	: 2.679e-01
IP(#tau_{e1})	: 2.094e-01
p_{T}(#tau_{e2})	: 1.939e-01
A_{PT}	: 3.239e-02
Iso(#tau_{e2})	: 2.930e-02
Iso(#tau_{e1})	: 9.234e-03
#Delta#phi	: 1.506e-03

SIG: [MC] Z -> tau tau -> mu mu  
BKG: [MC] Z -> mu mu

Variable	: Separation
DOCA #chi^2	: 3.763e-01
IP(#tau_{#mu2})	: 3.529e-01
IP(#tau_{#mu1})	: 2.164e-01
#Delta#phi	: 8.255e-02
p_{T}(#tau_{#mu2})	: 5.581e-02
A_{PT}	: 4.014e-02
p_{T}(#tau_{#mu1})	: 3.160e-02
Iso(#tau_{#mu2})	: 7.846e-03
Iso(#tau_{#mu1})	: 4.237e-03

SIG: [MC] Z -> tau tau -> e mu  
BKG: [Data] Same-sign

Variable	: Separation
Iso(#tau_{e})	: 5.726e-01
Iso(#tau_{#mu})	: 5.236e-01
A_{PT}	: 2.177e-01
p_{T}(#tau_{e})	: 2.135e-01
DOCA #chi^2	: 9.116e-02
#Delta#phi	: 8.642e-02
p_{T}(#tau_{#mu})	: 8.173e-02
IP(#tau_{e})	: 7.129e-02
IP(#tau_{#mu})	: 5.271e-02

SIG: [MC] Z -> tau tau -> e e  
BKG: [Data] Same-sign

Variable	: Separation
Iso(#tau_{e2})	: 5.824e-01
Iso(#tau_{e1})	: 4.043e-01
p_{T}(#tau_{e2})	: 2.601e-01
A_{PT}	: 2.217e-01
DOCA #chi^2	: 1.159e-01
IP(#tau_{e2})	: 1.134e-01
IP(#tau_{e1})	: 7.787e-02
#Delta#phi	: 7.311e-02
p_{T}(#tau_{e1})	: 4.913e-02

SIG: [MC] Z -> tau tau -> mu h1  
BKG: [Data] Same-sign

Variable	: Separation
Iso(#tau_{h1})	: 6.819e-01
Iso(#tau_{#mu})	: 6.175e-01
IP(#tau_{h1})	: 1.368e-01
p_{T}(#tau_{h1})	: 8.509e-02
DOCA #chi^2	: 6.417e-02
IP(#tau_{#mu})	: 4.921e-02
p_{T}(#tau_{#mu})	: 4.646e-02
A_{PT}	: 4.136e-02
#Delta#phi	: 1.735e-02

## A.4. Assisted Candidate Selection

SIG: [MC] Z -> tau tau -> mu h1  
 BKG: [MC] W(->mu) + jet

```
-----
Variable           : Separation
-----
Iso(#tau_{h1})    : 5.037e-01
p_{T}(#tau_{#mu}) : 3.752e-01
A_{PT}            : 3.209e-01
#Delta#phi        : 2.585e-01
IP(#tau_{#mu})    : 2.516e-01
DOCA #chi^{2}     : 2.474e-01
IP(#tau_{h1})     : 2.222e-01
p_{T}(#tau_{h1})  : 7.208e-02
Iso(#tau_{#mu})   : 2.763e-02
-----
```

SIG: [MC] Z -> tau tau -> e h1  
 BKG: [Data] Same-sign

```
-----
Variable           : Separation
-----
Iso(#tau_{h1})    : 6.385e-01
Iso(#tau_{e})     : 5.179e-01
IP(#tau_{h1})     : 1.707e-01
p_{T}(#tau_{h1})  : 1.114e-01
DOCA #chi^{2}     : 1.032e-01
A_{PT}            : 7.336e-02
IP(#tau_{e})      : 6.570e-02
p_{T}(#tau_{e})   : 4.033e-02
#Delta#phi        : 2.300e-02
-----
```

SIG: [MC] Z -> tau tau -> e h1  
 BKG: [MC] W(->e) + jet

```
-----
Variable           : Separation
-----
Iso(#tau_{h1})    : 5.410e-01
p_{T}(#tau_{e})   : 2.861e-01
A_{PT}            : 2.508e-01
DOCA #chi^{2}     : 2.497e-01
#Delta#phi        : 2.490e-01
IP(#tau_{e})      : 2.329e-01
IP(#tau_{h1})     : 2.282e-01
p_{T}(#tau_{h1})  : 6.979e-02
Iso(#tau_{e})     : 1.605e-02
-----
```

SIG: [MC] Z -> tau tau -> mu h3  
 BKG: [Data] Same-sign

```
-----
Variable           : Separation
-----
Iso(#tau_{#mu})   : 6.739e-01
Iso(#tau_{h3})    : 6.696e-01
#Delta R_{max}/p_{T}(#tau_{h3}) : 3.461e-01
p_{T}(#tau_{h3})  : 3.337e-01
#Delta R_{max}(\#tau_{h3}) : 2.730e-01
Decay time(\#tau_{h3}) : 2.656e-01
m_{corr}(\#tau_{h3}) : 2.311e-01
Vertex #chi^{2}/dof(\#tau_{h3}) : 1.253e-01
DOCA #chi^{2}     : 8.202e-02
A_{PT}            : 8.054e-02
p_{T}(\#tau_{#mu}) : 4.463e-02
#Delta R_{max}*p_{T}(\#tau_{h3}) : 1.925e-02
#Delta#phi        : 1.059e-02
-----
```

SIG: [MC] Z -> tau tau -> e h3  
 BKG: [Data] Same-sign

```
-----
Variable           : Separation
-----
Iso(#tau_{h3})    : 6.157e-01
Iso(#tau_{e})     : 5.763e-01
p_{T}(\#tau_{h3}) : 3.611e-01
#Delta R_{max}/p_{T}(\#tau_{h3}) : 3.601e-01
#Delta R_{max}(\#tau_{h3}) : 2.898e-01
Decay time(\#tau_{h3}) : 2.496e-01
m_{corr}(\#tau_{h3}) : 1.979e-01
Vertex #chi^{2}/dof(\#tau_{h3}) : 7.862e-02
A_{PT}            : 6.475e-02
DOCA #chi^{2}     : 4.858e-02
p_{T}(\#tau_{e})   : 3.250e-02
#Delta R_{max}*p_{T}(\#tau_{h3}) : 2.478e-02
#Delta#phi        : 2.296e-02
-----
```

### A.4.3 Suggested Cut-based Selection

The tables below provide the cut-based selection suggested by TMVA for the selection of di-tau candidates against different backgrounds. The considered backgrounds are

- Same-sign candidates
- $Z \rightarrow \mu\mu, Z \rightarrow ee$
- $W(\rightarrow \mu\nu_\mu) + \text{jet}, W(\rightarrow e\nu_e) + \text{jet}$

The signal and background candidates in each channel are required to pass the preselection, as well as  $\hat{I}_{p_T} > 0.9, \Delta\phi > 2.7$  prior to the optimization, and a vertex  $\chi^2 > 20$  for  $\tau_{h3}$ . This provides a good starting point where the number of backgrounds are reduced by these high-rank variables, and a reduction of the number of variables for the optimization.

The values of thresholds yielding the largest significance,  $S/\sqrt{S+B}$  is obtained. The number of expected signal,  $S$ , and background,  $B$ , is obtained from the simulated sample for each process respectively, using the relation  $N = \mathcal{L} \sigma \varepsilon_{\text{gen}} \varepsilon_{\text{presele}}$ . In case of the same-sign background, the number is already normalized.

#### A.4.3.1 Against $Z \rightarrow ll$ candidates (MC)

```
## simult_isodphi_zll_ee
=====
( #signal, #backgr.)  Optimal-cut  S/sqrt(S+B)      NSig      NBkg  EffSig  EffBkg
-----
(      372,      28994)      0.4250      4.2655  152.8629  1131.428  0.4109  0.03902
-----
APT > 6.8360211267647589e-02
IP1 > 10 ** -4.6399129385732394e+00
IP2 > 10 ** -1.2780244925880315e+00

## simult_isodphi_zll_mumu
=====
( #signal, #backgr.)  Optimal-cut  S/sqrt(S+B)      NSig      NBkg  EffSig  EffBkg
-----
(      872,      17174)      0.4250      13.3191  367.2817  393.1333  0.4212  0.02289
-----
APT > 1.0936455298611278e-01
IP1 > 10 ** -4.3144337307749199e+00
IP2 > 10 ** -1.3001493876349879e+00
```



## A.4. Assisted Candidate Selection

### A.4.3.2 Against $W(\rightarrow \mu\nu_\mu) + \text{jet}$ candidates (MC)

```

## simult_isodphi_EWKmu_mumu
=====
( #signal, #backgr.)  Optimal-cut  S/sqrt(S+B)      NSig      NBkg  EffSig  EffBkg
-----
(      873,      23)      0.9950      29.0557  861.7569  17.88889  0.9871  0.7778
-----

APT < 7.2502802341830264e-01
IP1 > 10 ** -3.5443412942648349e+00
IP2 > 10 ** -3.1454161540373429e+00

## simult_isodphi_EWKmu_emu
=====
( #signal, #backgr.)  Optimal-cut  S/sqrt(S+B)      NSig      NBkg  EffSig  EffBkg
-----
(     1156,      88)      0.9950      32.8389  1144.063  69.66667  0.9897  0.7917
-----

APT < 7.2217117046508394e-01
IP1 > 10 ** -3.9617222624510440e+00
IP2 > 10 ** -4.5753108020043554e+00

## simult_isodphi_EWKmu_h1mu
=====
( #signal, #backgr.)  Optimal-cut  S/sqrt(S+B)      NSig      NBkg  EffSig  EffBkg
-----
(     1550,     823)      0.9350      33.5301  1444.926  412.1133  0.9322  0.5007
-----

APT < 4.6614505450218630e-01
IP1 > 10 ** -3.9666054592171780e+00
IP2 > 10 ** -3.4534922502484604e+00

## simult_isodphi_EWKmu_h3mu
=====
( #signal, #backgr.)  Optimal-cut  S/sqrt(S+B)      NSig      NBkg  EffSig  EffBkg
-----
(      298,     607)      0.8050      14.7348  239.6289  24.84795  0.8041  0.04094
-----

BPVLTIME > 10 ** -4.2305614771463809e+00 ns
APT < 3.8423459830820855e-01
BPV CORR M < 6.8551420716383100 GeV
DR/PT < 10 ** -2.0289323727727218e+00 GeV^-1

```

## Appendix A. Selection of $Z \rightarrow \tau\tau$

---

### A.4.3.3 Against $W(\rightarrow e\nu_e) + \text{jet}$ candidates (MC)

```
## simult_isodphi_EWKe_ee
=====
( #signal, #backgr.)  Optimal-cut  S/sqrt(S+B)      NSig      NBkg  EffSig  EffBkg
-----
(    372,    54)      0.9250      18.5641  344.6259        0  0.9264    0
-----

APT < 6.0243040342372633e-01
IP1 > 10 ** -3.2661964516577076e+00
IP2 < 10 ** 1.5078199960067988e+00

## simult_isodphi_EWKe_emu
=====
( #signal, #backgr.)  Optimal-cut  S/sqrt(S+B)      NSig      NBkg  EffSig  EffBkg
-----
(    116,    14)      0.9950      10.171  115.9419        14  0.9995    1
-----

APT < 8.3813491542383622e-01
IP1 > 10 ** -3.8224147990620461e+00
IP2 > 10 ** -3.5859037105913734e+00

## simult_isodphi_EWKe_eh1
=====
( #signal, #backgr.)  Optimal-cut  S/sqrt(S+B)      NSig      NBkg  EffSig  EffBkg
-----
(    674,   318)      0.9750      22.1831  654.8594  216.6087  0.9716  0.6812
-----

APT < 5.1324978734905013e-01
IP1 > 10 ** -3.0377129174140722e+00
IP2 > 10 ** -3.6007375896638223e+00

## simult_isodphi_EWKe_eh3
=====
( #signal, #backgr.)  Optimal-cut  S/sqrt(S+B)      NSig      NBkg  EffSig  EffBkg
-----
(    121,   288)      0.9050      8.25604  108.4041        64  0.8959  0.2222
-----

BPVLTIME > 10 ** -4.7320814543784575e+00 ns
APT < 3.5063748202448525e-01
BPVCORRM < 4.9143853775397938 GeV
DR/PT < 10 ** -1.9312037762137901e+00 GeV^-1
```

## A.4. Assisted Candidate Selection

### A.4.3.4 Against same-sign candidates (data)

```
## simult_isodphi_ss_ee
=====
( #signal, #backgr.)  Optimal-cut  S/sqrt(S+B)      NSig      NBkg  EffSig  EffBkg
-----
(    372,    763)      0.7650      14.1405  285.4656    122.08  0.7674   0.16
-----

APT < 5.7914370671523152e-01
IP1 > 10 ** -2.7405750462305196e+00
IP2 > 10 ** -1.8899656928354722e+00

## simult_isodphi_ss_eh1
=====
( #signal, #backgr.)  Optimal-cut  S/sqrt(S+B)      NSig      NBkg  EffSig  EffBkg
-----
(    674,   2450)      0.6750      17.7147  450.3793     196  0.6682   0.08
-----

APT < 5.5036137648043537e-01
IP1 > 10 ** -2.0363326793101724e+00
IP2 > 10 ** -1.7901504963988963e+00

## simult_isodphi_ss_emu
=====
( #signal, #backgr.)  Optimal-cut  S/sqrt(S+B)      NSig      NBkg  EffSig  EffBkg
-----
(   1156,    416)      0.9050      29.5404  1046.137     208  0.905   0.5
-----

APT < 8.4704262057793822e-01
IP1 > 10 ** -2.1752836485063605e+00
IP2 < 10 ** 6.2696457836681674e-01

## simult_isodphi_ss_h1mu
=====
( #signal, #backgr.)  Optimal-cut  S/sqrt(S+B)      NSig      NBkg  EffSig  EffBkg
-----
(   1550,   1811)      0.5450      29.0847  845.9193         0  0.5458   0
-----

APT < 3.8792737577067893e-01
IP1 > 10 ** -4.3240011986543641e+00
IP2 > 10 ** -1.6232090556894088e+00

## simult_isodphi_ss_mumu
=====
( #signal, #backgr.)  Optimal-cut  S/sqrt(S+B)      NSig      NBkg  EffSig  EffBkg
-----
(    872,    117)      0.9950      27.541  861.5185     117  0.988   1
-----

APT > 2.0868180732041587e-04
IP1 > 10 ** -2.7980521481468532e+00
IP2 > 10 ** -3.8634912225844613e+00
```

## Appendix A. Selection of $Z \rightarrow \tau\tau$

---

## simult\_isodphi\_ss\_h3mu

```
=====
( #signal, #backgr.) Optimal-cut S/sqrt(S+B) NSig NBkg EffSig EffBkg
-----
( 298, 471) 0.8150 15.5789 242.701 0 0.8144 0
-----
```

```
BPVLTIME > 10 ** -4.3113518959556467e+00 ns
APT > -3.5266384280254934e-03
BPVCORRM < 8.8521342853887054 GeV
DR/PT < 10 ** -2.1244006050998601e+00 GeV^-1
```

## simult\_isodphi\_ss\_eh3

```
=====
( #signal, #backgr.) Optimal-cut S/sqrt(S+B) NSig NBkg EffSig EffBkg
-----
( 122, 581) 0.7250 9.41807 88.7 0 0.727 0
-----
```

```
BPVLTIME > 10 ** -5.2657394692961761e+00 ns
APT < 3.4313728239372127e-01
BPVCORRM < 3.0111604147612998 GeV
DR/PT < 10 ** -2.2110161773546668e+00 GeV^-1
```

## A.5 Tau Candidate Selection

### A.5.1 Isolation

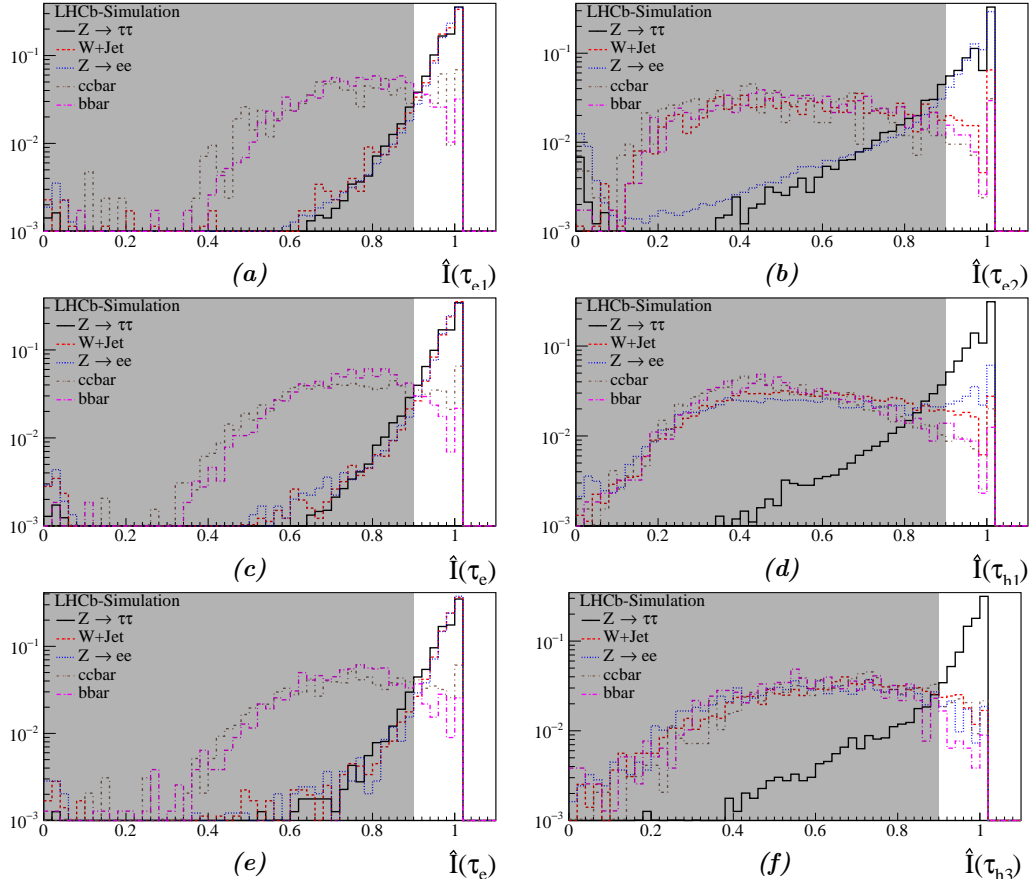


**Figure A.10** – Isolation of the tau in each di-tau candidates after preselection. Comparison of signal and backgrounds from simulation. (a,b)  $\tau_e\tau_e$ , (c,d)  $\tau_e\tau_{h1}$ , (e,f)  $\tau_e\tau_{h3}$ .

## Appendix A. Selection of $Z \rightarrow \tau\tau$

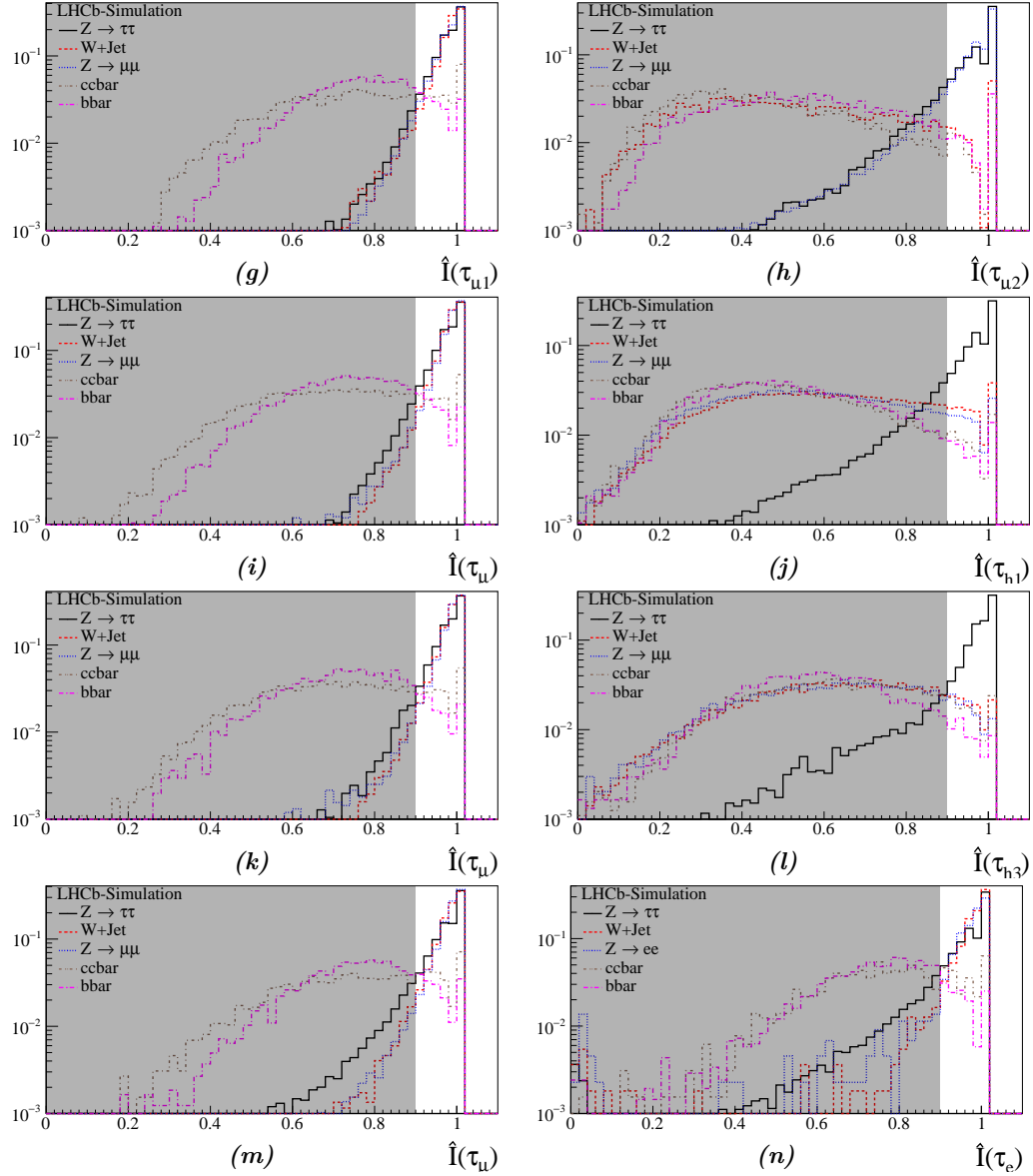


Figure A.10 – Isolation of tau in each di-tau candidates after preselection. Comparison of signal and backgrounds from simulation. (a,b)  $\tau_{\mu}\tau_{\mu}$ , (c,d)  $\tau_{\mu}\tau_{h1}$ , (e,f)  $\tau_{\mu}\tau_{h3}$ , (g,h)  $\tau_{\mu}\tau_e$ .

A.5.2 Decay Time and Corrected Mass of  $\tau_{h3}$

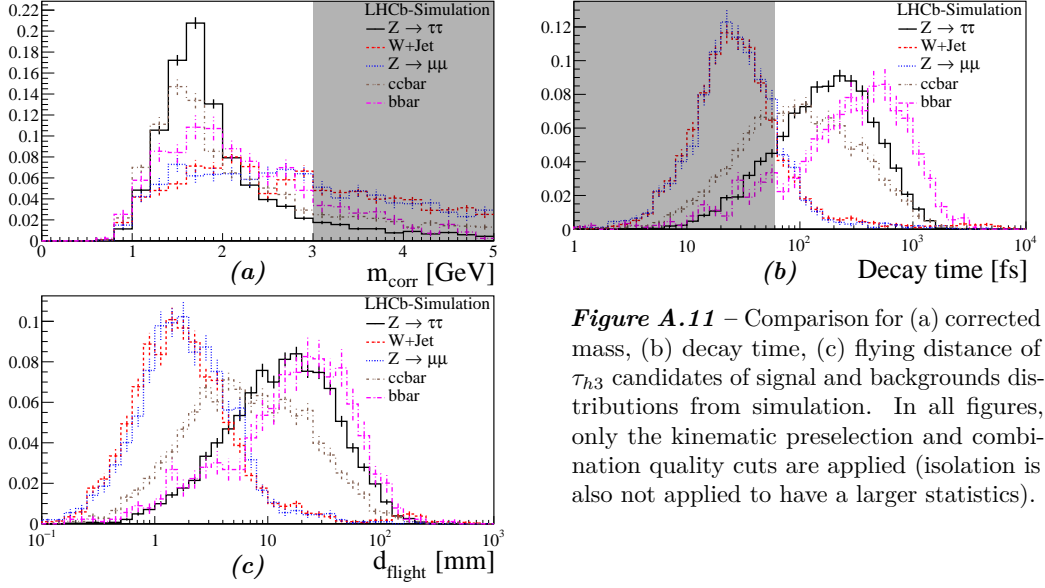


Figure A.11 – Comparison for (a) corrected mass, (b) decay time, (c) flying distance of  $\tau_{h3}$  candidates of signal and backgrounds distributions from simulation. In all figures, only the kinematic preselection and combination quality cuts are applied (isolation is also not applied to have a larger statistics).

A.5.3 Impact Parameter

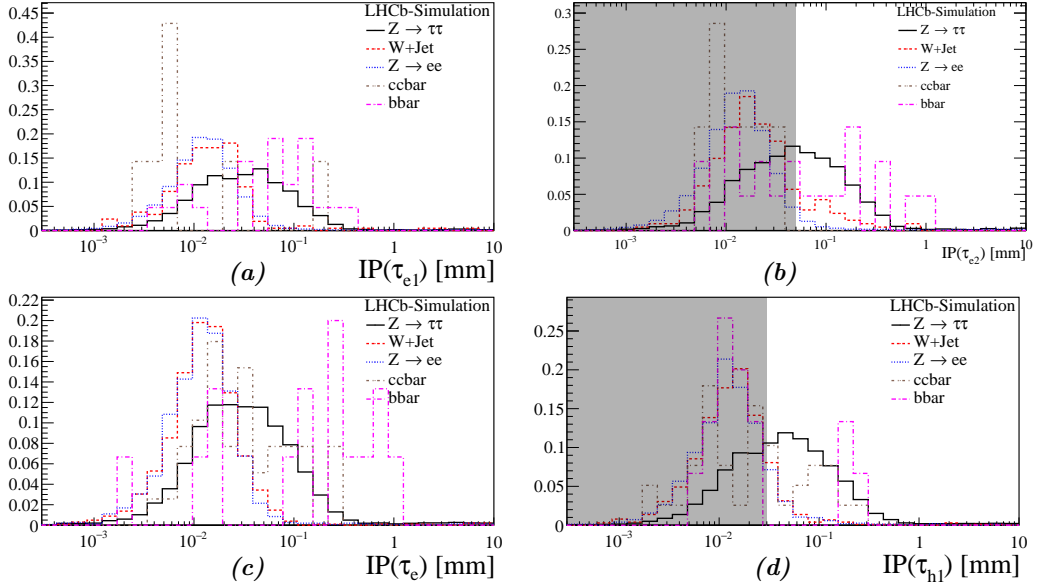
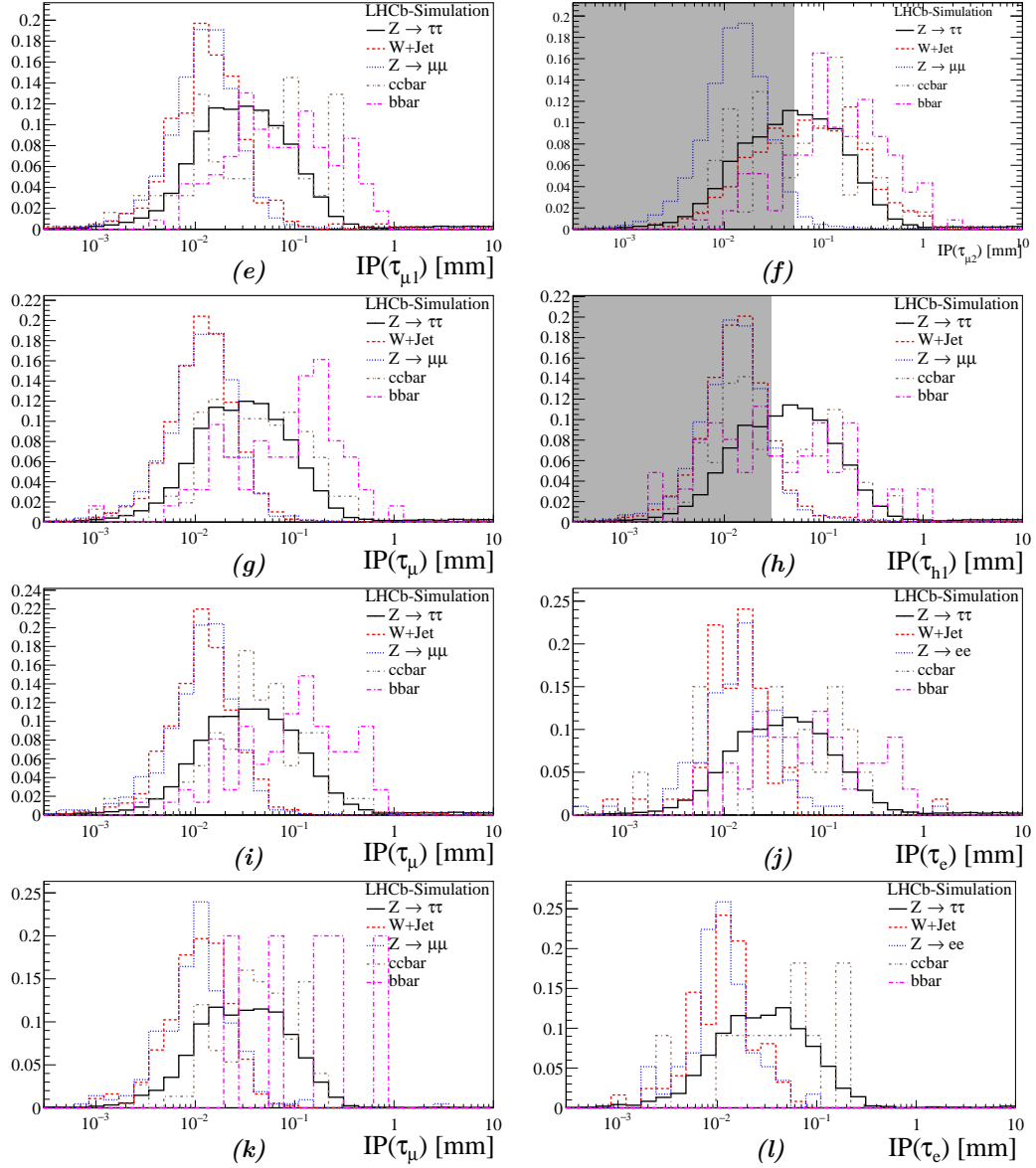


Figure A.12 – Impact parameter of tau in each di-tau candidates after isolation cut. Comparison of signal and backgrounds from simulation. (a,b)  $\tau_e \tau_e$ , (c,d)  $\tau_e \tau_{h1}$ .

## Appendix A. Selection of $Z \rightarrow \tau\tau$



**Figure A.12** – Impact parameter of tau in each di-tau candidates after isolation cut. Comparison of signal and backgrounds from simulation. (e,f)  $\tau_{\mu}\tau_{\mu}$ , (g,h)  $\tau_{\mu}\tau_{h1}$ , (i,j)  $\tau_{\mu}\tau_e$ , (k)  $\tau_{\mu}\tau_{h3}$ , (l)  $\tau_e\tau_{h3}$ .



## A.6 Di-tau Candidate Selection

### A.6.1 Azimuthal Separation

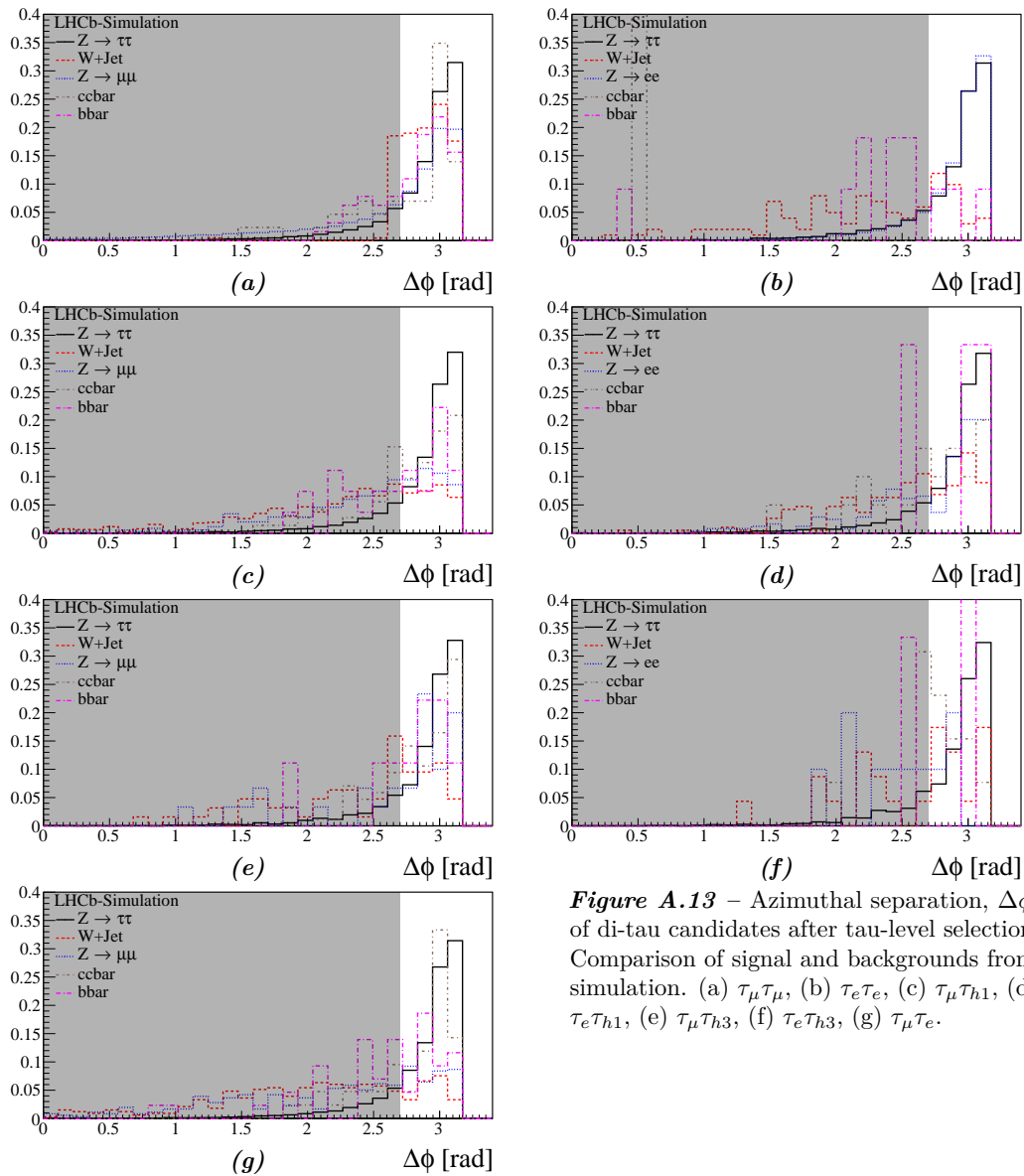


**Figure A.13** – Azimuthal separation,  $\Delta\phi$ , of di-tau candidates after tau-level selection. Comparison of signal and backgrounds from simulation. (a)  $\tau_\mu\tau_\mu$ , (b)  $\tau_e\tau_e$ , (c)  $\tau_\mu\tau_{h1}$ , (d)  $\tau_e\tau_{h1}$ , (e)  $\tau_\mu\tau_{h3}$ , (f)  $\tau_e\tau_{h3}$ , (g)  $\tau_\mu\tau_e$ .

## A.6.2 Transverse Momentum Asymmetry

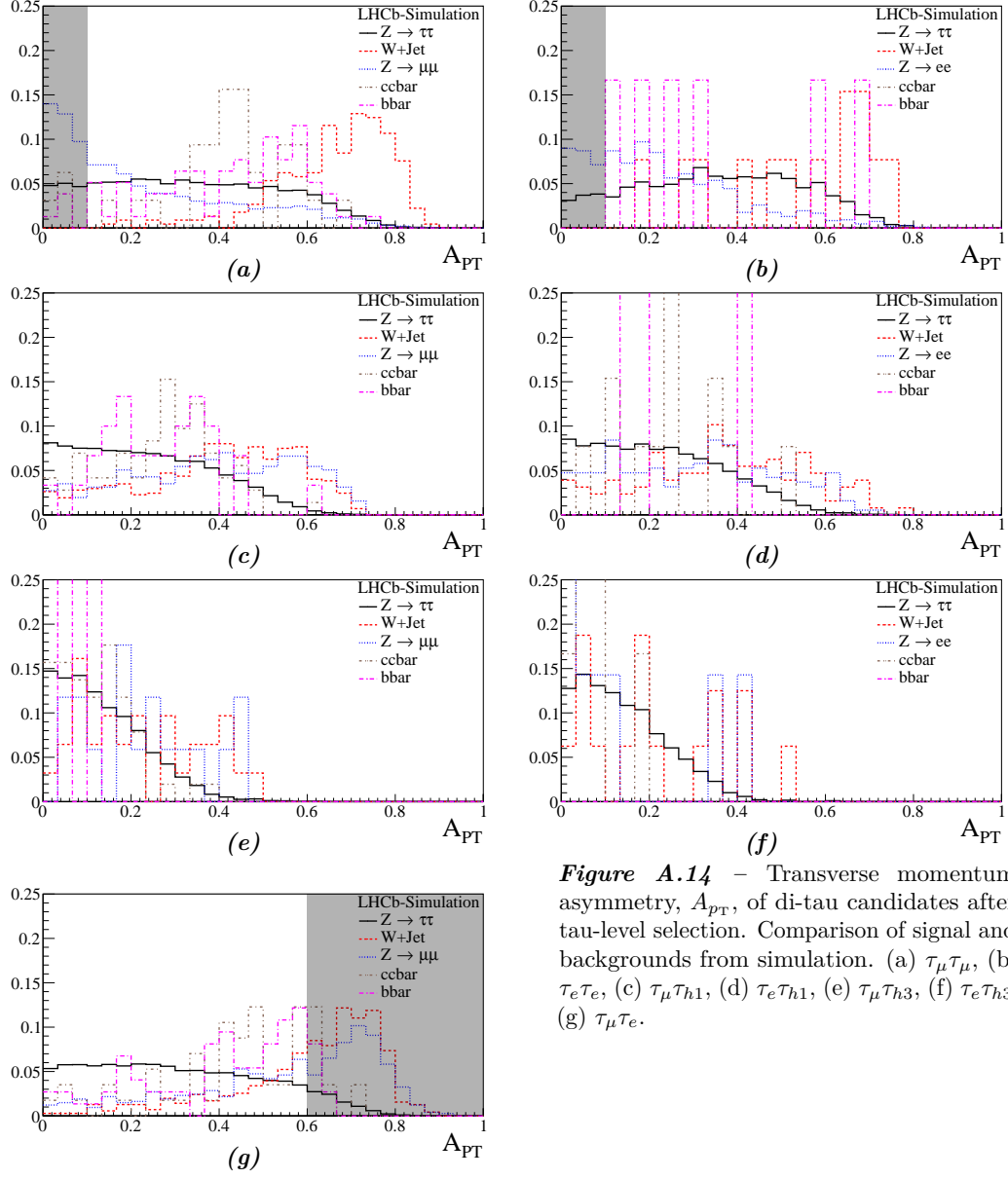


**Figure A.14** – Transverse momentum asymmetry,  $A_{pT}$ , of di-tau candidates after tau-level selection. Comparison of signal and backgrounds from simulation. (a)  $\tau_\mu\tau_\mu$ , (b)  $\tau_e\tau_e$ , (c)  $\tau_\mu\tau_{h1}$ , (d)  $\tau_e\tau_{h1}$ , (e)  $\tau_\mu\tau_{h3}$ , (f)  $\tau_e\tau_{h3}$ , (g)  $\tau_\mu\tau_e$ .

# B Muon Misidentification

The probability of muon misidentification as a charged hadron is determined using a data-driven method, cross-checked with the result found from the simulation. The tag-and-probe method using  $Z \rightarrow \mu\mu$  decays is employed, where the tag is a muon passing the track quality selection, identified as muon, and fires the muon trigger, and having  $p_T > 20 \text{ GeV}/c$ . The probe is a charged track passing the track quality selection, but with no particle identification and trigger requirement imposed. The invariant mass of tag and probe combined is between 70–110  $\text{GeV}/c^2$ , with the vertex  $\chi^2 < 5$ . The muon-misidentified-as-hadron rate ( $\mu \rightarrow h$ ) is in principle defined as the number of probes passing charged hadron identification over the total number of probes. However, because of the possible background contribution to the tag-and-probe sample, an additional step of background fitting is performed. The tag-and-probe sample is separated into 2 sets of selection, one requiring the probe to pass the charged hadron identification criteria, and another without. The samples are binned in 3 bins of probe's  $p_T$  at the interval between 20, 30, 40, 70  $\text{GeV}/c$ . The fitting using ROOFIT is performed over the distribution of mass of the candidates, with the following definition:

$$f(x) = n_{\text{probe}} f_{\text{probe}}(x) + n_{\text{bkg}} f_{\text{bkg}}(x)$$

$$f_{\text{probe}}(x) = \begin{cases} \text{Gaussian}(x; \bar{x}, \sigma) & (1) \\ \text{CrystalBall}(x; \bar{x}, \sigma, \alpha, n) & (2) \\ \text{Voigtian}(x; \bar{x}, \sigma, \sigma_{\text{gauss}}) & (3) \end{cases}$$

$$f_{\text{bkg}} = \text{Exponential}(x; c)$$

where the distribution of the probe,  $f_{\text{probe}}$ , is (1) Gaussian, in sample of the hadron-identified probe, which exhibits a very low statistic of genuine  $Z \rightarrow \mu\mu$  candidates, (2) CrystalBall, in the sample of unidentified probe, where the long tail on the lower-mass side of the distribution agrees with data, and (3) Voigtian (convoluted Breit-Wigner and Gaussian) in the last  $p_T$  bin of the sample of unidentified probe, where a high purity of  $Z \rightarrow \mu\mu$  is expected.

The fitted distributions are shown in Fig. B.1, with the results in Table B.1. The misidentification probability is thus computed per bin of probe's  $p_T$  as the number of background-excluded hadron-identified probes over the total number of background-excluded probes. The systematic uncertainty is combined in quadrature from the errors of  $n_{\text{probe}}$  yielded the fitting, with the uncertainty from the division using Clopper-Pearson 68% confidence interval.

## Appendix B. Muon Misidentification

**Table B.1** – Muon misidentification tag-and-probe fitting results.

Interval	Unprobed		Probed		Misid rate $\times 10^4$
	$n_{\text{probe}}$	$n_{\text{bkg}}$	$n_{\text{probe}}$	$n_{\text{bkg}}$	
[20, 30]	$12856 \pm 216$	$6695 \pm 201$	$3.46 \pm 1.75$	$3456.7 \pm 16.0$	$2.69^{+2.65}_{-1.86}$
[30, 40]	$63220 \pm 344$	$6734 \pm 249$	$2.34 \pm 1.32$	$2473.6 \pm 239.2$	$0.37^{+0.47}_{-0.29}$
[40, 70]	$124213 \pm 452$	$3174 \pm 294$	$2.68 \pm 0.54$	$2677.3 \pm 15.9$	$0.22^{+0.22}_{-0.11}$

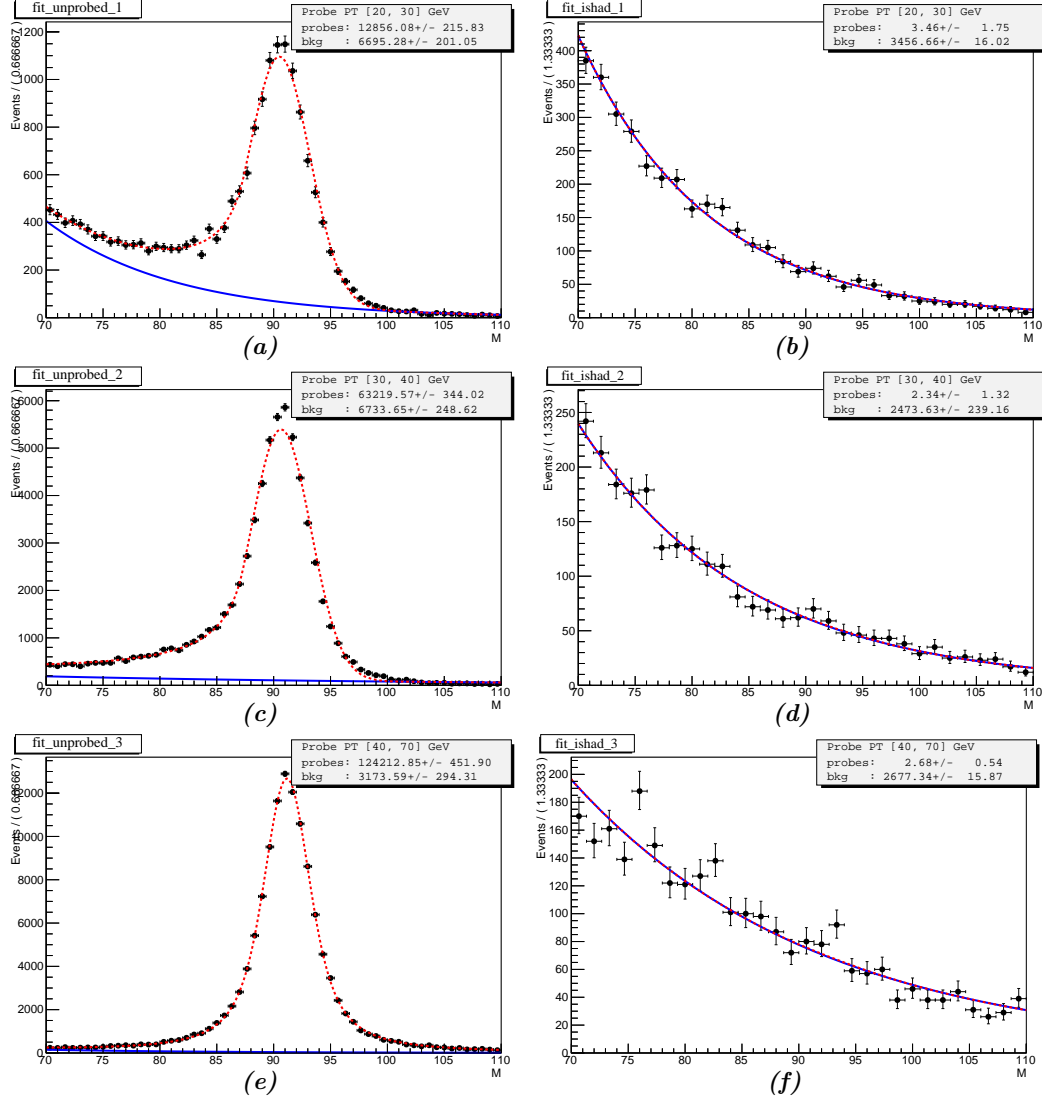


**Figure B.1** – Background-removal fit in muon misidentification tag-and-probe study, where each row is different  $p_T$  range. The probe muon at unprobed state is on the left column, and probed state on the right column.

# C Backgrounds of $Z \rightarrow \tau\tau$

**Table C.1** – Numbers of expected opposite-sign di-lepton candidates in  $\tau_\mu\tau_e$  channel, allowing the estimation of dominating processes in faking  $Z \rightarrow ll$  background in  $\tau_\mu\tau_{h1}$ ,  $\tau_e\tau_{h1}$ ,  $\tau_\mu\tau_e$  channels.

Process	ID	di-muon	di-electron
$Z \rightarrow \tau\tau$	42100000	$420.3^{+11.3}_{-11.2}$ (2715)	$94.4^{+4.3}_{-4.2}$ (610)
$Z \rightarrow \mu\mu$	42112011	$5324^{+169.5}_{-169.4}$ (31740)	$0.0^{+0.3}_{-0.0}$ (0)
$Z \rightarrow ee$	42122011	$0.0^{+2.6}_{-0.0}$ (0)	$2127^{+87.2}_{-86.3}$ (1519)
$Z \rightarrow b\bar{b}$	42150000	$0.9^{+0.5}_{-0.3}$ (8)	$0.0^{+0.2}_{-0.0}$ (0)
$Z(\rightarrow\mu\mu) + \text{jet}$	42112022	$9422^{+303.3}_{-303.3}$ (58105)	$0.0^{+0.3}_{-0.0}$ (0)
$W(\rightarrow\tau\nu_\tau) + \text{jet}$	42300010	$0.0^{+5.2}_{-0.0}$ (0)	$0.0^{+5.2}_{-0.0}$ (0)
$W(\rightarrow\mu\nu_\mu) + \text{jet}$	42311011	$25.7^{+4.7}_{-4.0}$ (42)	$0.0^{+1.1}_{-0.0}$ (0)
$W \rightarrow e\nu_e$	42321000	$0.0^{+1.7}_{-0.0}$ (0)	$15.2^{+4.8}_{-3.8}$ (16)
$W(\rightarrow e\nu_e) + \text{jet}$	42321010	$0.0^{+6.4}_{-0.0}$ (0)	$13.8^{+11.0}_{-6.6}$ (4)
$W(\rightarrow\mu\nu_\mu) + \text{jet}(\rightarrow\mu\dots)$	42311012	$6.9^{+0.5}_{-0.5}$ (249)	$0.0^{+0.1}_{-0.0}$ (0)
$c\bar{c} \rightarrow e\dots$	49021004	$0.0^{+0.9}_{-0.0}$ (0)	$0.0^{+0.9}_{-0.0}$ (0)
$c\bar{c} \rightarrow \mu\dots$	49011004	$16.8^{+3.8}_{-3.3}$ (34)	$0.0^{+0.9}_{-0.0}$ (0)
$b\bar{b} \rightarrow e\dots$	49021005	$0.0^{+4.8}_{-0.0}$ (0)	$23.6^{+10.8}_{-7.8}$ (9)
$b\bar{b} \rightarrow \mu\dots$	49011005	$236.9^{+28.6}_{-26.1}$ (92)	$0.0^{+4.7}_{-0.0}$ (0)
$t\bar{t}$	41900010	$14.4^{+2.6}_{-2.6}$ (4636)	$0.0^{+0.0}_{-0.0}$ (0)
$WW \rightarrow ll\dots$	41922002	$1.0^{+0.1}_{-0.1}$ (214)	$0.4^{+0.0}_{-0.0}$ (100)
$WW \rightarrow \ell\dots$	42021000	$2.6^{+0.3}_{-0.3}$ (109)	$1.1^{+0.2}_{-0.2}$ (46)
$WZ \rightarrow \ell\dots$	42021001	$1.1^{+0.1}_{-0.1}$ (193)	$0.5^{+0.1}_{-0.1}$ (91)
Data		5242	2020

## Appendix C. Backgrounds of $Z \rightarrow \tau\tau$

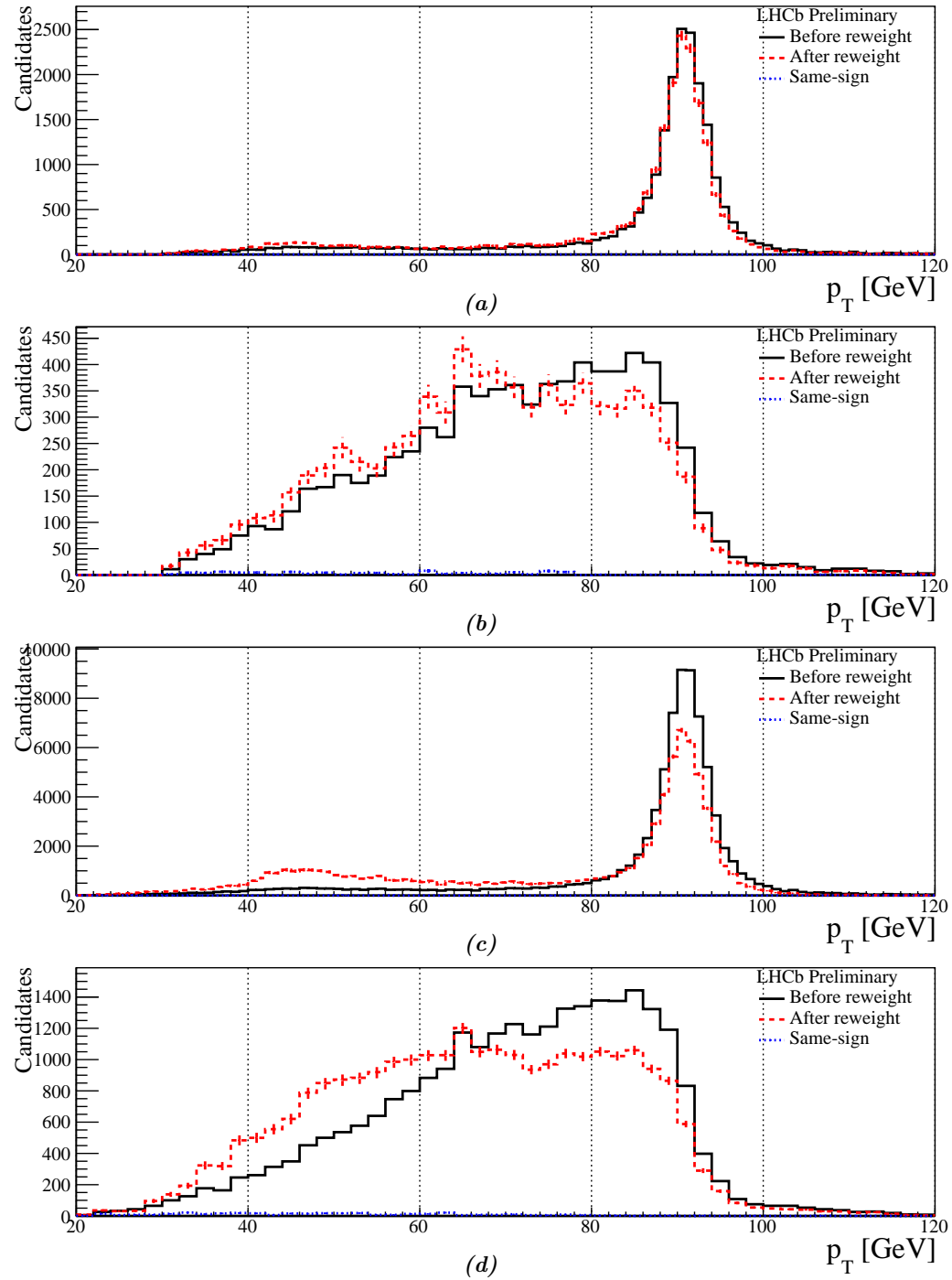


**Figure C.1** – Comparison of the di-lepton invariant mass distribution before and after the reweighting to the misidentification probability. (a)  $\mu \rightarrow h$  (b)  $e \rightarrow h$  (c)  $\mu \rightarrow e$  (d)  $e \rightarrow \mu$ .

**Table C.2** – Number of observed candidates in data and projection factor  $r$  for the calculation of QCD background.

Channel	OS	SS	$r_{\text{QCD}}$
$\tau_\mu\tau_\mu$	1522	1167	$1.304 \pm 0.051$
$\tau_\mu\tau_{h1}$	25162	24768	$1.016 \pm 0.009$
$\tau_\mu\tau_{h3}$	2205	2139	$1.031 \pm 0.031$
$\tau_e\tau_e$	684	658	$1.040 \pm 0.057$
$\tau_e\tau_{h1}$	11375	11394	$0.998 \pm 0.013$
$\tau_e\tau_{h3}$	791	841	$0.941 \pm 0.047$
$\tau_\mu\tau_e$	4505	4253	$1.059 \pm 0.023$

**Table C.3** – Detailed result from the fitting of same-sign candidates to different compositions via ROOT.TFractionFitter class.

Channel	src	Amount	Correlation matrix					
mumu	QCD	39.2251+/-	8.1054	1.0000	-0.5426	0.0607		
	EWK	10.3473+/-	6.1484	-0.5426	1.0000	0.0045		
	Ztau	0.4277+/-	0.4178	0.0607	0.0045	1.0000		
h1mu	QCD	232.0730+/-	18.8591	1.0000	-0.5078	-0.0138		
	EWK	60.9270+/-	16.3939	-0.5078	1.0000	0.0153		
	Ztau	0.0000+/-	0.8278	-0.0138	0.0153	1.0000		
h3mu	QCD	21.1058+/-	7.0829	1.0000	-0.3823	0.5735		
	EWK	3.8941+/-	2.8508	-0.3823	1.0000	-0.2248		
	Ztau	0.0000+/-	1.2259	0.5735	-0.2248	1.0000		
ee	QCD	36.7870+/-	7.9141	1.0000	-0.4191	0.0178		
	EWK	20.1890+/-	7.2010	-0.4191	1.0000	0.0051		
	Ztau	1.0240+/-	0.8407	0.0178	0.0051	1.0000		
eh1	QCD	318.4637+/-	21.9221	1.0000	-0.4479	-0.0518		
	EWK	59.5910+/-	13.9446	-0.4479	1.0000	0.0118		
	Ztau	1.9454+/-	1.3145	-0.0518	0.0118	1.0000		
eh3	QCD	19.2638+/-	5.2128	1.0000	-0.3860	-0.0185		
	EWK	8.7362+/-	4.2796	-0.3860	1.0000	-0.0010		
	Ztau	0.0000+/-	0.6603	-0.0185	-0.0010	1.0000		
mue	QCD	151.0642+/-	15.6013	1.0000	-0.3957	-0.2994	-0.0306	
	EWKe	15.0847+/-	8.3304	-0.3957	1.0000	0.1231	0.0072	
	EWKmu	19.8511+/-	7.9494	-0.2994	0.1231	1.0000	-0.0055	
	Ztau	0.0000+/-	3.5091	-0.0306	0.0072	-0.0055	1.0000	

**Table C.4** – The number of expected opposite-sign di-tau candidates using QCD data-driven cuts. The values are normalized by the integrated luminosity, with cross-section and  $\varepsilon_{\text{gen}}$  from Table 4.2. The number of selected candidates before normalization is in the bracket.

Process	ID	$\tau_\mu\tau_\mu$	$\tau_\mu\tau_{h1}$	$\tau_\mu\tau_{h3}$	$\tau_e\tau_e$	$\tau_e\tau_{h1}$	$\tau_e\tau_{h3}$	$\tau_\mu\tau_e$
$Z \rightarrow \tau\tau$	42100000	$0.0^{+0.3}_{-0.0}$ (0)	$0.6^{+0.5}_{-0.3}$ (4)	$0.0^{+0.3}_{-0.0}$ (0)	$0.0^{+0.3}_{-0.0}$ (0)	$0.6^{+0.5}_{-0.3}$ (4)	$0.0^{+0.3}_{-0.0}$ (0)	$0.6^{+0.5}_{-0.3}$ (4)
$Z \rightarrow \mu\mu$	42112011	$1.7^{+0.7}_{-0.5}$ (10)	$6.4^{+1.2}_{-1.0}$ (38)	$0.5^{+0.5}_{-0.3}$ (3)	$0.0^{+0.3}_{-0.0}$ (0)	$0.0^{+0.3}_{-0.0}$ (0)	$0.0^{+0.3}_{-0.0}$ (0)	$0.7^{+0.5}_{-0.3}$ (4)
$Z \rightarrow ee$	42122011	$0.0^{+2.6}_{-0.0}$ (0)	$0.0^{+2.6}_{-0.0}$ (0)	$0.0^{+2.6}_{-0.0}$ (0)	$5.6^{+4.4}_{-2.7}$ (4)	$12.6^{+5.8}_{-4.1}$ (9)	$0.0^{+2.6}_{-0.0}$ (0)	$1.4^{+3.2}_{-1.2}$ (1)
$Z \rightarrow b\bar{b}$	42150000	$8.6^{+1.2}_{-1.0}$ (73)	$23.0^{+1.9}_{-1.8}$ (195)	$1.8^{+0.6}_{-0.5}$ (15)	$1.1^{+0.5}_{-0.3}$ (9)	$6.8^{+1.0}_{-0.9}$ (58)	$0.4^{+0.3}_{-0.2}$ (3)	$7.2^{+1.1}_{-0.9}$ (61)
$Z(\rightarrow\mu\mu) + \text{jet}$	42112022	$0.8^{+0.5}_{-0.4}$ (5)	$0.8^{+0.5}_{-0.4}$ (5)	$0.0^{+0.3}_{-0.0}$ (0)	$0.0^{+0.3}_{-0.0}$ (0)	$0.0^{+0.3}_{-0.0}$ (0)	$0.0^{+0.3}_{-0.0}$ (0)	$0.8^{+0.5}_{-0.4}$ (5)
$W(\rightarrow\tau\nu_\tau) + \text{jet}$	42300010	$0.0^{+5.2}_{-0.0}$ (0)	$0.0^{+5.2}_{-0.0}$ (0)	$0.0^{+5.2}_{-0.0}$ (0)	$0.0^{+5.2}_{-0.0}$ (0)	$5.7^{+7.5}_{-3.7}$ (2)	$0.0^{+5.2}_{-0.0}$ (0)	$0.0^{+5.2}_{-0.0}$ (0)
$W(\rightarrow\nu\mu) + \text{jet}$	42311011	$0.0^{+1.1}_{-0.0}$ (0)	$5.5^{+1.8}_{-1.8}$ (9)	$0.0^{+1.1}_{-0.0}$ (0)	$0.0^{+1.1}_{-0.0}$ (0)	$0.0^{+1.1}_{-0.0}$ (0)	$0.0^{+1.1}_{-0.0}$ (0)	$0.0^{+1.1}_{-0.0}$ (0)
$W \rightarrow e\nu_e$	42321000	$0.0^{+1.7}_{-0.0}$ (0)	$0.0^{+1.7}_{-0.0}$ (0)	$0.0^{+1.7}_{-0.0}$ (0)	$0.9^{+2.2}_{-0.8}$ (1)	$23.7^{+5.8}_{-4.7}$ (25)	$0.0^{+1.7}_{-0.0}$ (0)	$0.9^{+2.2}_{-0.8}$ (1)
$W(\rightarrow e\nu_e) + \text{jet}$	42321010	$0.0^{+6.4}_{-0.0}$ (0)	$0.0^{+6.4}_{-0.0}$ (0)	$0.0^{+6.4}_{-0.0}$ (0)	$3.5^{+8.0}_{-2.9}$ (1)	$17.3^{+11.7}_{-7.5}$ (5)	$0.0^{+6.4}_{-0.0}$ (0)	$3.5^{+8.0}_{-2.9}$ (1)
$W(\rightarrow \nu\mu) + \text{jet}(\rightarrow \mu\dots)$	42311012	$0.2^{+0.1}_{-0.1}$ (6)	$0.0^{+0.1}_{-0.0}$ (0)	$0.0^{+0.1}_{-0.0}$ (0)	$0.0^{+0.1}_{-0.0}$ (0)	$0.0^{+0.1}_{-0.0}$ (0)	$0.0^{+0.1}_{-0.0}$ (0)	$0.0^{+0.1}_{-0.0}$ (0)
$c\bar{c} \rightarrow e\dots$	49021004	$0.0^{+0.9}_{-0.0}$ (0)	$14.9^{+3.5}_{-3.1}$ (32)	$0.5^{+1.1}_{-0.4}$ (1)	$4.2^{+2.0}_{-1.4}$ (9)	$64.8^{+9.3}_{-9.0}$ (139)	$7.9^{+2.6}_{-2.1}$ (17)	$22.4^{+4.4}_{-4.0}$ (48)
$c\bar{c} \rightarrow \mu\dots$	49011004	$102.1^{+12.9}_{-12.6}$ (206)	$731.7^{+77.1}_{-76.9}$ (1477)	$111.5^{+13.9}_{-13.6}$ (225)	$0.0^{+0.9}_{-0.0}$ (0)	$1.0^{+1.3}_{-0.6}$ (2)	$0.5^{+1.1}_{-0.4}$ (1)	$67.4^{+9.3}_{-9.0}$ (136)
$b\bar{b} \rightarrow e\dots$	49021005	$7.9^{+7.7}_{-4.3}$ (3)	$94.4^{+18.8}_{-16.0}$ (36)	$7.9^{+7.7}_{-4.3}$ (3)	$91.7^{+18.6}_{-15.8}$ (35)	$532.0^{+44.3}_{-41.8}$ (203)	$57.7^{+15.2}_{-12.4}$ (22)	$254.2^{+29.9}_{-27.3}$ (97)
$b\bar{b} \rightarrow \mu\dots$	49011005	$674.7^{+50.4}_{-48.1}$ (262)	$2515^{+122.0}_{-120.3}$ (977)	$270.4^{+30.6}_{-28.0}$ (105)	$0.0^{+4.7}_{-0.0}$ (0)	$10.3^{+8.2}_{-4.9}$ (4)	$2.6^{+5.9}_{-2.1}$ (1)	$383.7^{+36.7}_{-34.2}$ (149)
$t\bar{t}$	41900010	$1.4^{+0.3}_{-0.3}$ (452)	$7.2^{+1.3}_{-1.3}$ (2317)	$1.0^{+0.2}_{-0.2}$ (327)	$0.0^{+0.0}_{-0.0}$ (5)	$0.2^{+0.0}_{-0.0}$ (67)	$0.0^{+0.0}_{-0.0}$ (4)	$0.5^{+0.1}_{-0.1}$ (173)
$WW \rightarrow \ell\ell\dots$	41922002	$0.0^{+0.0}_{-0.0}$ (0)	$0.0^{+0.0}_{-0.0}$ (0)	$0.0^{+0.0}_{-0.0}$ (0)	$0.0^{+0.0}_{-0.0}$ (0)	$0.0^{+0.0}_{-0.0}$ (0)	$0.0^{+0.0}_{-0.0}$ (0)	$0.0^{+0.0}_{-0.0}$ (1)
$WW \rightarrow \ell\dots$	42021000	$0.0^{+0.0}_{-0.0}$ (0)	$0.0^{+0.0}_{-0.0}$ (2)	$0.0^{+0.1}_{-0.0}$ (4)	$0.0^{+0.0}_{-0.0}$ (0)	$0.1^{+0.1}_{-0.1}$ (5)	$0.0^{+0.1}_{-0.0}$ (2)	$0.0^{+0.1}_{-0.0}$ (1)
$WZ \rightarrow \ell\dots$	42021001	$0.0^{+0.0}_{-0.0}$ (0)	$0.0^{+0.0}_{-0.0}$ (1)	$0.0^{+0.0}_{-0.0}$ (0)	$0.0^{+0.0}_{-0.0}$ (0)	$0.0^{+0.0}_{-0.0}$ (7)	$0.0^{+0.0}_{-0.0}$ (2)	$0.0^{+0.0}_{-0.0}$ (2)
Data		1545	25162	2205	701	11375	791	4505



**Table C.5** – The number of expected same-sign di-tau candidates using QCD data-driven cuts. The values are normalized by the integrated luminosity, with cross-section and  $\varepsilon_{\text{gen}}$  from Table 4.2. The number of selected candidates before normalization is in the bracket.

Process	ID	$\tau_\mu\tau_\mu$	$\tau_\mu\tau_h$	$\tau_\mu\tau_{h3}$	$\tau_e\tau_e$	$\tau_e\tau_h$	$\tau_e\tau_{h3}$	$\tau_\mu\tau_e$
$Z \rightarrow \tau\tau$	42100000	$0.0^{+0.3}_{-0.0}$ (0)	$0.0^{+0.3}_{-0.0}$ (0)	$0.0^{+0.3}_{-0.0}$ (0)	$0.0^{+0.3}_{-0.0}$ (0)	$0.2^{+0.4}_{-0.1}$ (1)	$0.0^{+0.3}_{-0.0}$ (0)	$0.0^{+0.3}_{-0.0}$ (0)
$Z \rightarrow \mu\mu$	42112011	$0.5^{+0.5}_{-0.3}$ (3)	$4.9^{+1.1}_{-0.9}$ (29)	$0.5^{+0.5}_{-0.3}$ (3)	$0.0^{+0.3}_{-0.0}$ (0)	$0.0^{+0.3}_{-0.0}$ (0)	$0.0^{+0.3}_{-0.0}$ (0)	$0.3^{+0.4}_{-0.2}$ (2)
$Z \rightarrow ee$	42122011	$0.0^{+2.6}_{-0.0}$ (0)	$0.0^{+2.6}_{-0.0}$ (0)	$0.0^{+2.6}_{-0.0}$ (0)	$5.6^{+4.4}_{-2.7}$ (4)	$7.0^{+4.7}_{-3.0}$ (5)	$0.0^{+2.6}_{-0.0}$ (0)	$0.0^{+2.6}_{-0.0}$ (0)
$Z \rightarrow b\bar{b}$	42150000	$4.6^{+0.9}_{-0.7}$ (39)	$19.7^{+1.8}_{-1.7}$ (167)	$1.5^{+0.6}_{-0.4}$ (13)	$0.7^{+0.4}_{-0.3}$ (6)	$5.2^{+0.9}_{-0.8}$ (44)	$0.7^{+0.4}_{-0.3}$ (6)	$5.9^{+1.0}_{-0.9}$ (50)
$Z(\rightarrow\mu\mu) + \text{jet}$	42112022	$0.3^{+0.4}_{-0.2}$ (2)	$0.8^{+0.5}_{-0.4}$ (5)	$0.0^{+0.3}_{-0.0}$ (0)	$0.0^{+0.3}_{-0.0}$ (0)	$0.0^{+0.3}_{-0.0}$ (0)	$0.0^{+0.3}_{-0.0}$ (0)	$0.0^{+0.3}_{-0.0}$ (0)
$W(\rightarrow\tau\nu_\tau) + \text{jet}$	42300010	$0.0^{+5.2}_{-0.0}$ (0)	$0.0^{+5.2}_{-0.0}$ (0)	$0.0^{+5.2}_{-0.0}$ (0)	$0.0^{+5.2}_{-0.0}$ (0)	$2.8^{+6.5}_{-2.3}$ (1)	$0.0^{+5.2}_{-0.0}$ (0)	$0.0^{+5.2}_{-0.0}$ (0)
$W(\rightarrow\mu\nu_\mu) + \text{jet}$	42311011	$1.2^{+1.6}_{-0.8}$ (2)	$3.1^{+2.1}_{-1.3}$ (5)	$0.0^{+1.1}_{-0.0}$ (0)	$0.0^{+1.1}_{-0.0}$ (0)	$0.0^{+1.1}_{-0.0}$ (0)	$0.0^{+1.1}_{-0.0}$ (0)	$0.0^{+1.1}_{-0.0}$ (0)
$W \rightarrow e\nu_e$	42321000	$0.0^{+1.7}_{-0.0}$ (0)	$0.0^{+1.7}_{-0.0}$ (0)	$0.0^{+1.7}_{-0.0}$ (0)	$0.9^{+2.2}_{-0.8}$ (1)	$11.4^{+4.3}_{-3.2}$ (12)	$0.9^{+2.2}_{-0.8}$ (1)	$0.0^{+1.7}_{-0.0}$ (0)
$W(\rightarrow e\nu_e) + \text{jet}$	42321010	$0.0^{+6.4}_{-0.0}$ (0)	$0.0^{+6.4}_{-0.0}$ (0)	$0.0^{+6.4}_{-0.0}$ (0)	$3.5^{+8.0}_{-2.9}$ (1)	$58.8^{+18.1}_{-14.3}$ (17)	$0.0^{+6.4}_{-0.0}$ (0)	$0.0^{+6.4}_{-0.0}$ (0)
$W(\rightarrow\mu\nu_\mu) + \text{jet}(\rightarrow\mu\dots)$	42311012	$0.0^{+0.1}_{-0.0}$ (1)	$0.0^{+0.1}_{-0.0}$ (0)	$0.0^{+0.1}_{-0.0}$ (0)	$0.0^{+0.1}_{-0.0}$ (0)	$0.0^{+0.1}_{-0.0}$ (0)	$0.0^{+0.1}_{-0.0}$ (0)	$0.0^{+0.1}_{-0.0}$ (0)
$c\bar{c} \rightarrow e\dots$	49021004	$0.0^{+0.9}_{-0.0}$ (0)	$11.2^{+3.0}_{-2.6}$ (24)	$0.0^{+0.9}_{-0.0}$ (0)	$0.9^{+1.2}_{-0.6}$ (2)	$69.0^{+9.7}_{-9.4}$ (148)	$6.1^{+2.3}_{-1.8}$ (13)	$4.7^{+2.1}_{-1.5}$ (10)
$c\bar{c} \rightarrow \mu\dots$	49011004	$13.9^{+3.5}_{-3.0}$ (28)	$732.2^{+77.1}_{-77.0}$ (1478)	$76.3^{+10.2}_{-9.9}$ (154)	$0.0^{+0.9}_{-0.0}$ (0)	$2.0^{+1.6}_{-1.0}$ (4)	$0.5^{+1.1}_{-0.1}$ (1)	$35.2^{+5.9}_{-5.5}$ (71)
$b\bar{b} \rightarrow e\dots$	49021005	$15.7^{+9.4}_{-6.3}$ (6)	$73.4^{+16.9}_{-14.0}$ (28)	$7.9^{+7.7}_{-4.3}$ (3)	$55.0^{+15.0}_{-12.1}$ (21)	$325.0^{+33.9}_{-31.4}$ (124)	$41.9^{+13.4}_{-10.5}$ (16)	$89.1^{+18.3}_{-13.3}$ (34)
$b\bar{b} \rightarrow \mu\dots$	49011005	$381.1^{+36.6}_{-34.1}$ (148)	$1784^{+94.7}_{-92.8}$ (693)	$224.0^{+27.8}_{-25.3}$ (87)	$0.0^{+4.7}_{-0.0}$ (0)	$5.2^{+6.8}_{-3.3}$ (2)	$0.0^{+4.7}_{-0.0}$ (0)	$175.1^{+24.7}_{-22.1}$ (68)
$t\bar{t}$	41900010	$1.3^{+0.3}_{-0.3}$ (432)	$6.9^{+1.3}_{-1.3}$ (2238)	$0.9^{+0.2}_{-0.2}$ (303)	$0.0^{+0.0}_{-0.0}$ (0)	$0.2^{+0.0}_{-0.0}$ (68)	$0.0^{+0.0}_{-0.0}$ (9)	$0.5^{+0.1}_{-0.1}$ (172)
$WW \rightarrow \ell\ell\dots$	41922002	$0.0^{+0.0}_{-0.0}$ (0)	$0.0^{+0.0}_{-0.0}$ (0)	$0.0^{+0.0}_{-0.0}$ (0)	$0.0^{+0.0}_{-0.0}$ (0)	$0.0^{+0.0}_{-0.0}$ (1)	$0.0^{+0.0}_{-0.0}$ (1)	$0.0^{+0.0}_{-0.0}$ (0)
$WW \rightarrow \ell\dots$	42021000	$0.0^{+0.0}_{-0.0}$ (0)	$0.0^{+0.0}_{-0.0}$ (0)	$0.0^{+0.0}_{-0.0}$ (0)	$0.0^{+0.0}_{-0.0}$ (0)	$0.1^{+0.1}_{-0.0}$ (4)	$0.0^{+0.1}_{-0.0}$ (1)	$0.0^{+0.1}_{-0.0}$ (1)
$WZ \rightarrow \ell\dots$	42021001	$0.0^{+0.0}_{-0.0}$ (1)	$0.0^{+0.0}_{-0.0}$ (0)	$0.0^{+0.0}_{-0.0}$ (0)	$0.0^{+0.0}_{-0.0}$ (0)	$0.0^{+0.0}_{-0.0}$ (6)	$0.0^{+0.0}_{-0.0}$ (2)	$0.0^{+0.0}_{-0.0}$ (0)
Data		1187	24768	2139	674	11394	841	4253

**Table C.6** – The number of expected di-tau candidates from simulation, using offline selection in the region of the  $Z$ -peak (an invariant mass between  $[80,100]\text{GeV}/c^2$  for the  $\tau_\mu\tau_\mu$  channel, and  $[70,100]\text{GeV}/c^2$  for the  $\tau_e\tau_e$  channel).

Process	ID	$\tau_\mu\tau_\mu$	$\tau_e\tau_e$
$Z \rightarrow \tau\tau$	42100000	$0.8^{+0.5}_{-0.3}$ (5)	$1.9^{+0.7}_{-0.5}$ (12)
$Z \rightarrow \mu\mu$	42112011	$100542^{+3151}_{-3151}$ (599370)	$0.0^{+0.3}_{-0.0}$ (0)
$Z \rightarrow ee$	42122011	$0.0^{+2.6}_{-0.0}$ (0)	$30260^{+972.7}_{-972.4}$ (21602)
$Z \rightarrow b\bar{b}$	42150000	$0.0^{+0.2}_{-0.0}$ (0)	$0.0^{+0.2}_{-0.0}$ (0)
$Z(\rightarrow\mu\mu) + \text{jet}$	42112022	$178746^{+5707}_{-5707}$ (1102263)	$0.0^{+0.3}_{-0.0}$ (0)
$W(\rightarrow\tau\nu_\tau) + \text{jet}$	42300010	$0.0^{+5.2}_{-0.0}$ (0)	$0.0^{+5.2}_{-0.0}$ (0)
$W(\rightarrow\mu\nu_\mu) + \text{jet}$	42311011	$11.0^{+3.3}_{-2.6}$ (18)	$0.0^{+1.1}_{-0.0}$ (0)
$W \rightarrow e\nu_e$	42321000	$0.0^{+1.7}_{-0.0}$ (0)	$20.8^{+5.5}_{-4.4}$ (22)
$W(\rightarrow e\nu_e) + \text{jet}$	42321010	$0.0^{+6.4}_{-0.0}$ (0)	$34.6^{+14.8}_{-10.8}$ (10)
$W(\rightarrow\mu\nu_\mu) + \text{jet}(\rightarrow\mu\dots)$	42311012	$4.4^{+0.4}_{-0.4}$ (160)	$0.0^{+0.1}_{-0.0}$ (0)
$c\bar{c} \rightarrow e\dots$	49021004	$0.0^{+0.9}_{-0.0}$ (0)	$0.9^{+1.2}_{-0.6}$ (2)
$c\bar{c} \rightarrow \mu\dots$	49011004	$6.4^{+2.4}_{-1.9}$ (13)	$0.0^{+0.9}_{-0.0}$ (0)
$b\bar{b} \rightarrow e\dots$	49021005	$0.0^{+4.8}_{-0.0}$ (0)	$0.0^{+4.8}_{-0.0}$ (0)
$b\bar{b} \rightarrow \mu\dots$	49011005	$23.2^{+10.6}_{-7.6}$ (9)	$0.0^{+4.7}_{-0.0}$ (0)
$t\bar{t}$	41900010	$94.0^{+17.0}_{-17.0}$ (30307)	$0.0^{+0.0}_{-0.0}$ (0)
$WW \rightarrow \ell\ell\dots$	41922002	$3.6^{+0.1}_{-0.1}$ (807)	$2.5^{+0.1}_{-0.1}$ (564)
$WW \rightarrow \ell\dots$	42021000	$4.2^{+0.3}_{-0.3}$ (176)	$2.7^{+0.3}_{-0.3}$ (115)
$WZ \rightarrow \ell\dots$	42021001	$32.6^{+0.8}_{-0.8}$ (5763)	$10.3^{+0.3}_{-0.3}$ (1825)
Data		103103	29346

**Table C.7** – Number of selected candidates from simulation and projection factor  $r$  for the calculation of  $V_j$  background.

Channels	$N_W^{SS}$	$N_Z^{SS}$	$N_W^{OS}$	$r_W$	$r_Z$	$r_{V_j}$
$\tau_e\tau_e$	$48.8 \pm 7.3$	$209.4 \pm 19.0$	$61.1 \pm 8.1$	$1.25 \pm 0.25$	$1.00 \pm 0.09$	$1.05 \pm 0.08$
$\tau_e\tau_{h1}$	$695.6 \pm 29.2$	$237.4 \pm 20.3$	$1037.5 \pm 37.3$	$1.49 \pm 0.08$	$1.38 \pm 0.16$	$1.46 \pm 0.07$
$\tau_e\tau_{h3}$	$62.1 \pm 8.2$	$14.8 \pm 5.2$	$84.8 \pm 9.5$	$1.37 \pm 0.24$	$1.38 \pm 0.63$	$1.37 \pm 0.23$
$\tau_\mu\tau_{h1}$	$42.0 \pm 5.5$	$12.9 \pm 1.6$	$115.5 \pm 9.5$	$2.75 \pm 0.43$	$1.11 \pm 0.19$	$2.37 \pm 0.30$
$\tau_\mu\tau_{h3}$	$108.1 \pm 9.2$	$28.9 \pm 2.5$	$125.3 \pm 10.0$	$1.16 \pm 0.13$	$1.06 \pm 0.13$	$1.14 \pm 0.11$
$\tau_\mu\tau_\mu$	$2.7 \pm 0.3$	$5.0 \pm 1.0$	$6.1 \pm 0.4$	$2.26 \pm 0.29$	$1.00 \pm 0.20$	$1.44 \pm 0.11$
emu_raw	$21.4 \pm 4.9$	$24.6 \pm 6.5$	$55.4 \pm 7.8$	$2.60 \pm 0.70$	$2.08 \pm 0.67$	$2.32 \pm 0.49$
mue_raw	$12.6 \pm 3.1$	$14.2 \pm 1.7$	$19.3 \pm 3.8$	$1.53 \pm 0.48$	$1.52 \pm 0.23$	$1.53 \pm 0.26$

**Table C.8** – Same-sign candidates fit results at different  $Z \rightarrow \tau\tau$  fit constraints, where constraints are the multipliers applied to the  $2\text{-}\sigma$  upper limit on same-sign  $Z \rightarrow \tau\tau$  from simulation.

Channel	Constraint	$N^{SS}$	$N_{QCD}^{SS}$	$N_{V_j}^{SS}$	$N_{Z \rightarrow \tau\tau}^{SS}$	$N_{QCD+V_j}^{OS}$
$\tau_\mu\tau_\mu$	x0	50	$39.6 \pm 8.1$	$10.4 \pm 6.1$	-	$66.7 \pm 9.7$
	x1	50	$39.2 \pm 8.1$	$10.3 \pm 6.1$	$0.4 \pm 0.4$	$66.1 \pm 9.7$
	x1.5	50	$39.4 \pm 7.4$	$9.9 \pm 5.4$	$0.6 \pm 0.6$	$65.7 \pm 9.9$
	x2	50	$39.6 \pm 7.4$	$9.5 \pm 5.1$	$0.9 \pm 0.7$	$65.4 \pm 9.8$
$\tau_\mu\tau_{h1}$	x0	293	$229.9 \pm 19.3$	$63.1 \pm 17.1$	-	$382.9 \pm 39.2$
	x1	293	$232.1 \pm 18.9$	$60.9 \pm 16.4$	$0.0 \pm 0.8$	$379.9 \pm 38.3$
	x1.5	293	$232.1 \pm 18.6$	$60.9 \pm 16.8$	$0.0 \pm 1.2$	$379.9 \pm 38.0$
	x2	293	$229.9 \pm 18.8$	$63.1 \pm 17.0$	$0.0 \pm 1.6$	$382.9 \pm 39.0$
$\tau_\mu\tau_{h3}$	x0	25	$21.1 \pm 4.7$	$3.9 \pm 2.7$	-	$26.2 \pm 5.1$
	x1	25	$21.1 \pm 7.1$	$3.9 \pm 2.9$	$0.0 \pm 1.2$	$26.2 \pm 6.8$
	x1.5	25	$21.1 \pm 5.0$	$3.9 \pm 2.7$	$0.0 \pm 1.5$	$26.2 \pm 5.4$
	x2	25	$21.1 \pm 5.1$	$3.9 \pm 2.7$	$0.0 \pm 1.4$	$26.2 \pm 5.5$
$\tau_e\tau_e$	x0	58	$37.6 \pm 7.9$	$20.4 \pm 7.2$	-	$60.5 \pm 8.9$
	x1	58	$36.8 \pm 7.9$	$20.2 \pm 7.2$	$1.0 \pm 0.8$	$59.4 \pm 8.9$
	x1.5	58	$36.4 \pm 7.9$	$20.1 \pm 7.2$	$1.5 \pm 1.5$	$58.9 \pm 8.9$
	x2	58	$36.0 \pm 7.9$	$20.0 \pm 7.2$	$2.1 \pm 2.1$	$58.3 \pm 8.9$
$\tau_e\tau_{h1}$	x0	380	$331.7 \pm 21.0$	$48.3 \pm 14.5$	-	$401.9 \pm 22.8$
	x1	380	$318.5 \pm 21.9$	$59.6 \pm 13.9$	$1.9 \pm 1.3$	$405.2 \pm 23.1$
	x1.5	380	$325.6 \pm 21.5$	$51.4 \pm 13.4$	$2.9 \pm 0.6$	$400.4 \pm 22.8$
	x2	380	$326.8 \pm 21.4$	$49.3 \pm 13.1$	$3.9 \pm 0.6$	$398.4 \pm 22.7$
$\tau_e\tau_{h3}$	x0	28	$19.3 \pm 5.2$	$8.7 \pm 4.3$	-	$30.1 \pm 6.4$
	x1	28	$19.3 \pm 5.2$	$8.7 \pm 4.3$	$0.0 \pm 0.7$	$30.1 \pm 6.4$
	x1.5	28	$19.3 \pm 5.2$	$8.7 \pm 4.3$	$0.0 \pm 1.1$	$30.1 \pm 6.4$
	x2	28	$19.3 \pm 5.2$	$8.7 \pm 4.3$	$0.0 \pm 1.5$	$30.1 \pm 6.4$
$\tau_\mu\tau_e$ (hard $e$ )	x0	186	$151.1 \pm 15.6$	$15.1 \pm 8.3$	-	$195.0 \pm 21.5$
	x1	186	$151.1 \pm 15.6$	$15.1 \pm 8.3$	$0.0 \pm 3.5$	$195.0 \pm 21.5$
	x1.5	186	$151.1 \pm 15.9$	$15.1 \pm 8.3$	$0.0 \pm 4.9$	$195.0 \pm 21.6$
	x2	186	$150.6 \pm 15.1$	$21.3 \pm 8.7$	$0.0 \pm 6.7$	$209.0 \pm 24.3$
$\tau_\mu\tau_e$ (hard $\mu$ )	x0	186	$151.1 \pm 15.6$	$19.9 \pm 8.0$	-	$190.3 \pm 18.3$
	x1	186	$151.1 \pm 15.6$	$19.9 \pm 7.9$	$0.0 \pm 3.5$	$190.3 \pm 18.4$
	x1.5	186	$151.1 \pm 15.9$	$19.9 \pm 7.9$	$0.0 \pm 4.9$	$190.3 \pm 18.6$
	x2	186	$150.6 \pm 15.1$	$14.1 \pm 7.4$	$0.0 \pm 6.7$	$181.0 \pm 17.1$



# D Combined Plots of $Z \rightarrow \tau\tau$

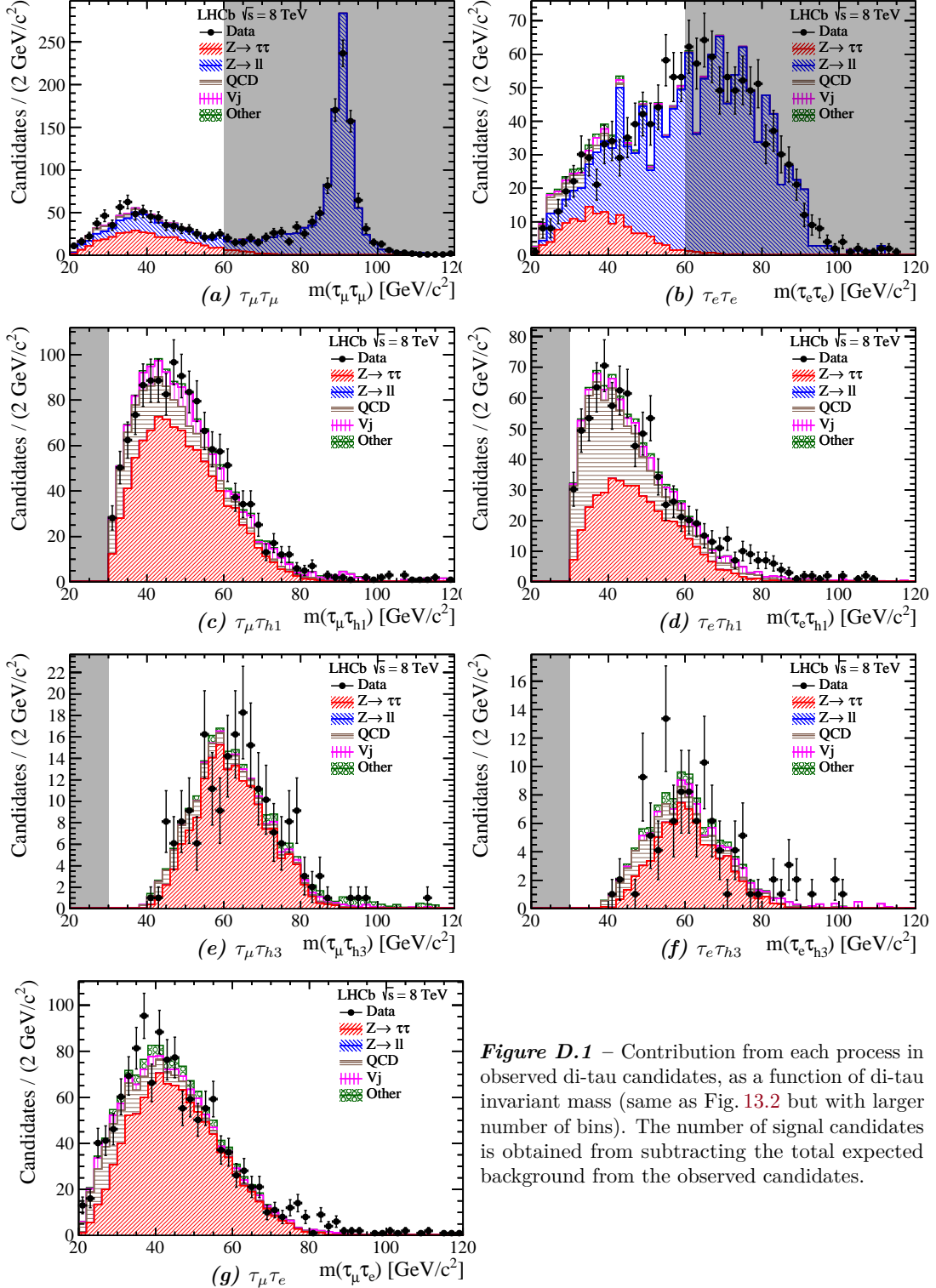


*Figure D.1* – Contribution from each process in observed di-tau candidates, as a function of di-tau invariant mass (same as Fig. 13.2 but with larger number of bins). The number of signal candidates is obtained from subtracting the total expected background from the observed candidates.

## Appendix D. Combined Plots of $Z \rightarrow \tau\tau$

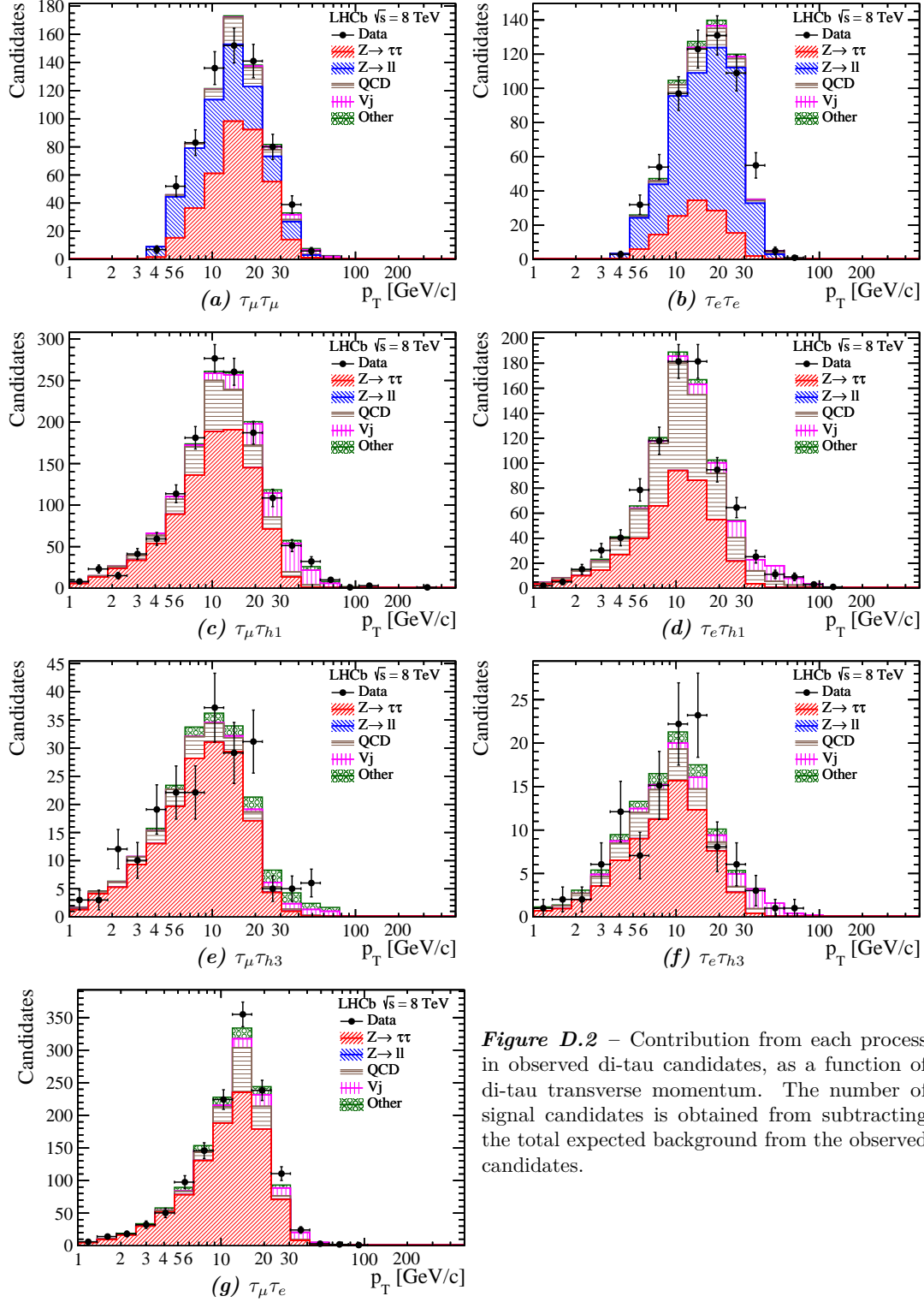


**Figure D.2** – Contribution from each process in observed di-tau candidates, as a function of di-tau transverse momentum. The number of signal candidates is obtained from subtracting the total expected background from the observed candidates.

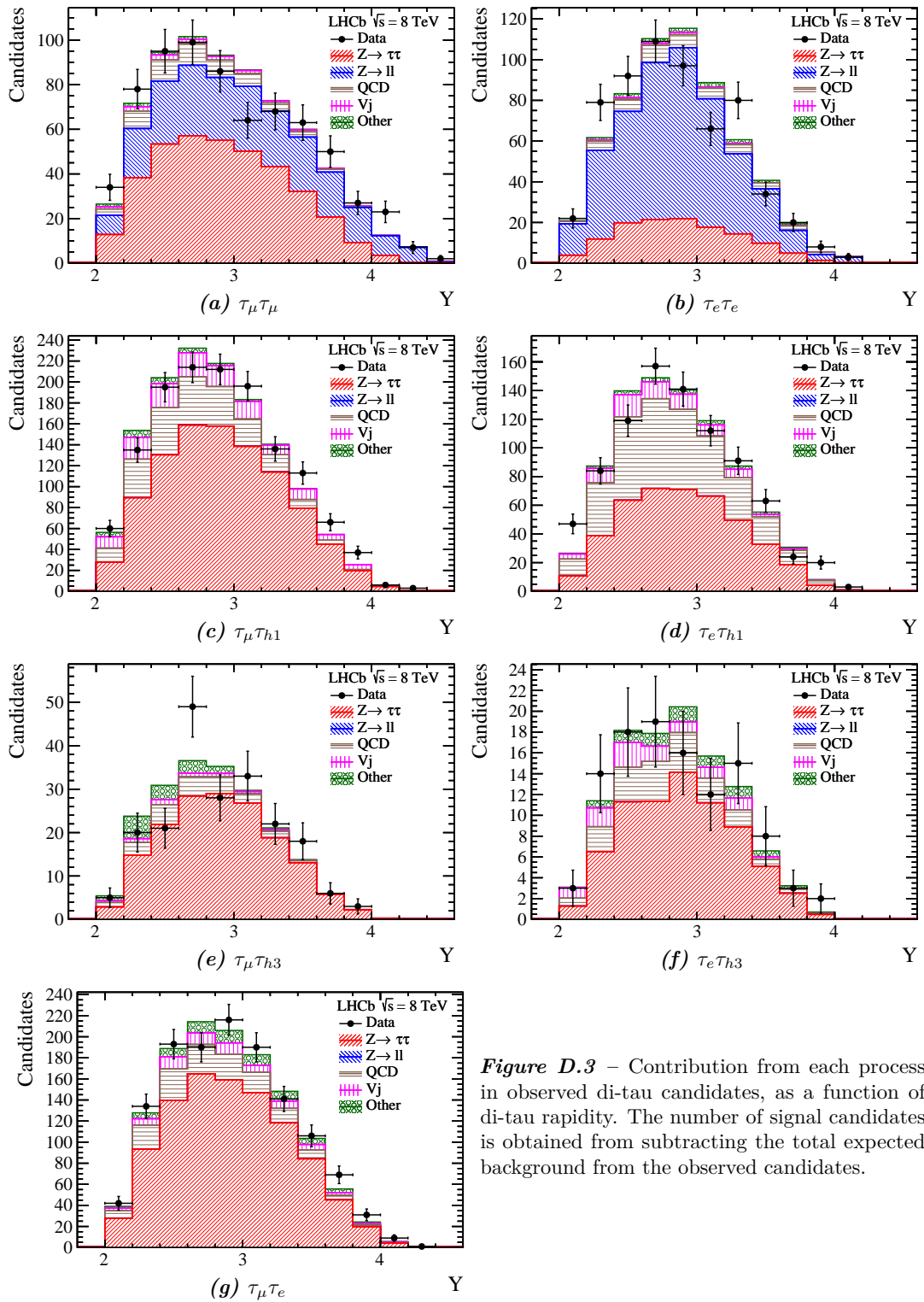


**Figure D.3** – Contribution from each process in observed di-tau candidates, as a function of di-tau rapidity. The number of signal candidates is obtained from subtracting the total expected background from the observed candidates.

## Appendix D. Combined Plots of $Z \rightarrow \tau\tau$

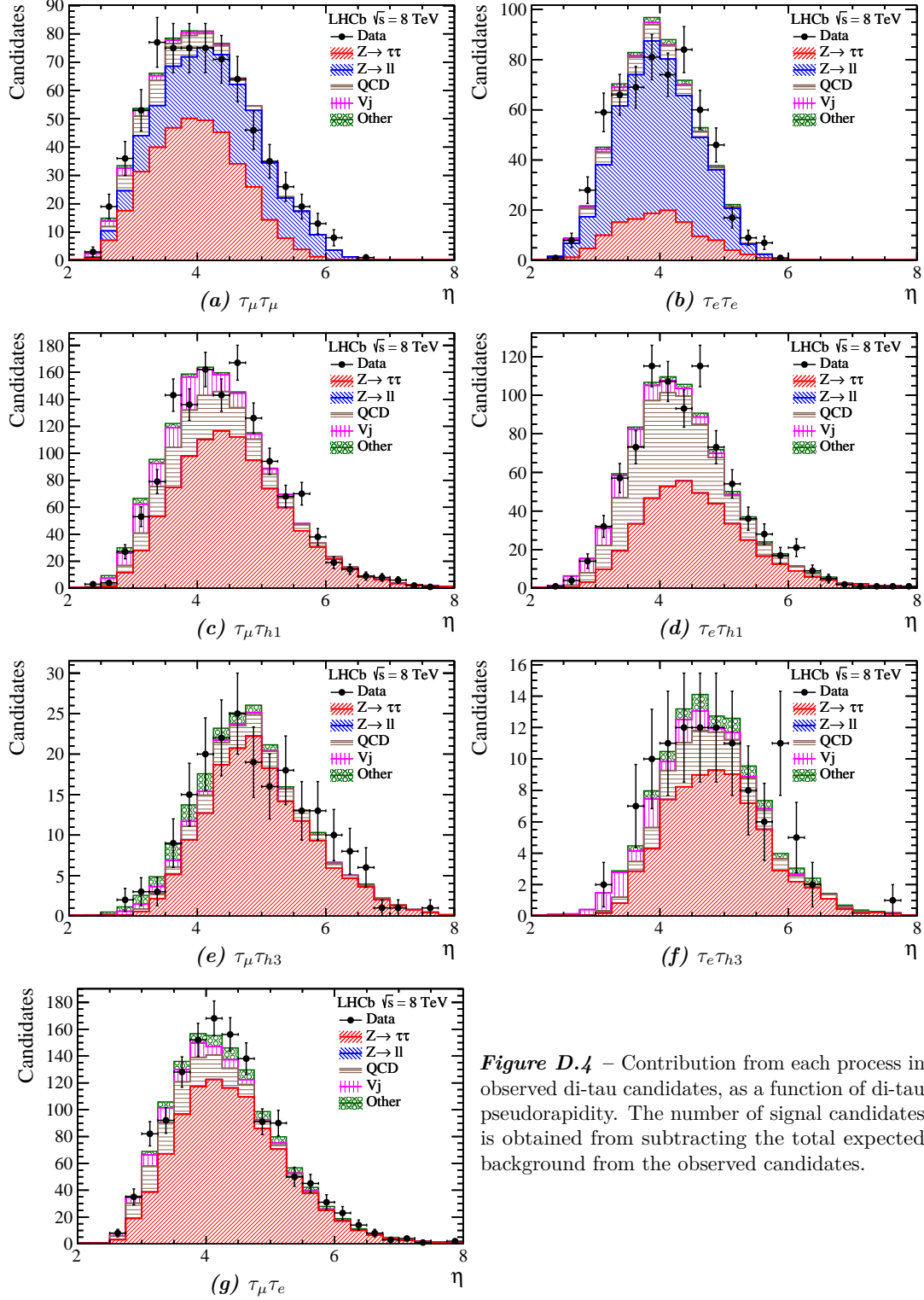


**Figure D.4** – Contribution from each process in observed di-tau candidates, as a function of di-tau pseudorapidity. The number of signal candidates is obtained from subtracting the total expected background from the observed candidates.



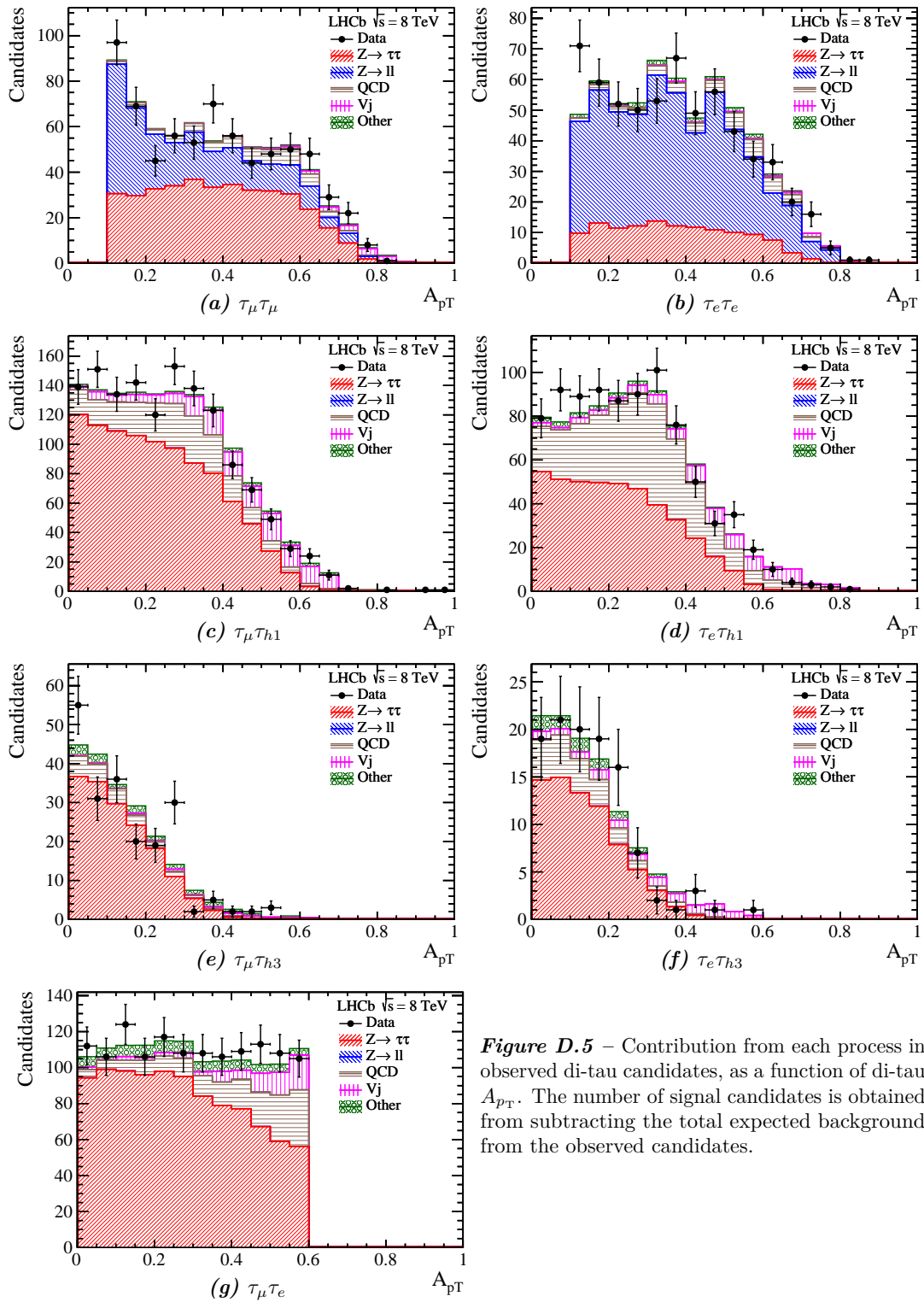


**Figure D.5** – Contribution from each process in observed di-tau candidates, as a function of di-tau  $A_{pT}$ . The number of signal candidates is obtained from subtracting the total expected background from the observed candidates.

## Appendix D. Combined Plots of $Z \rightarrow \tau\tau$

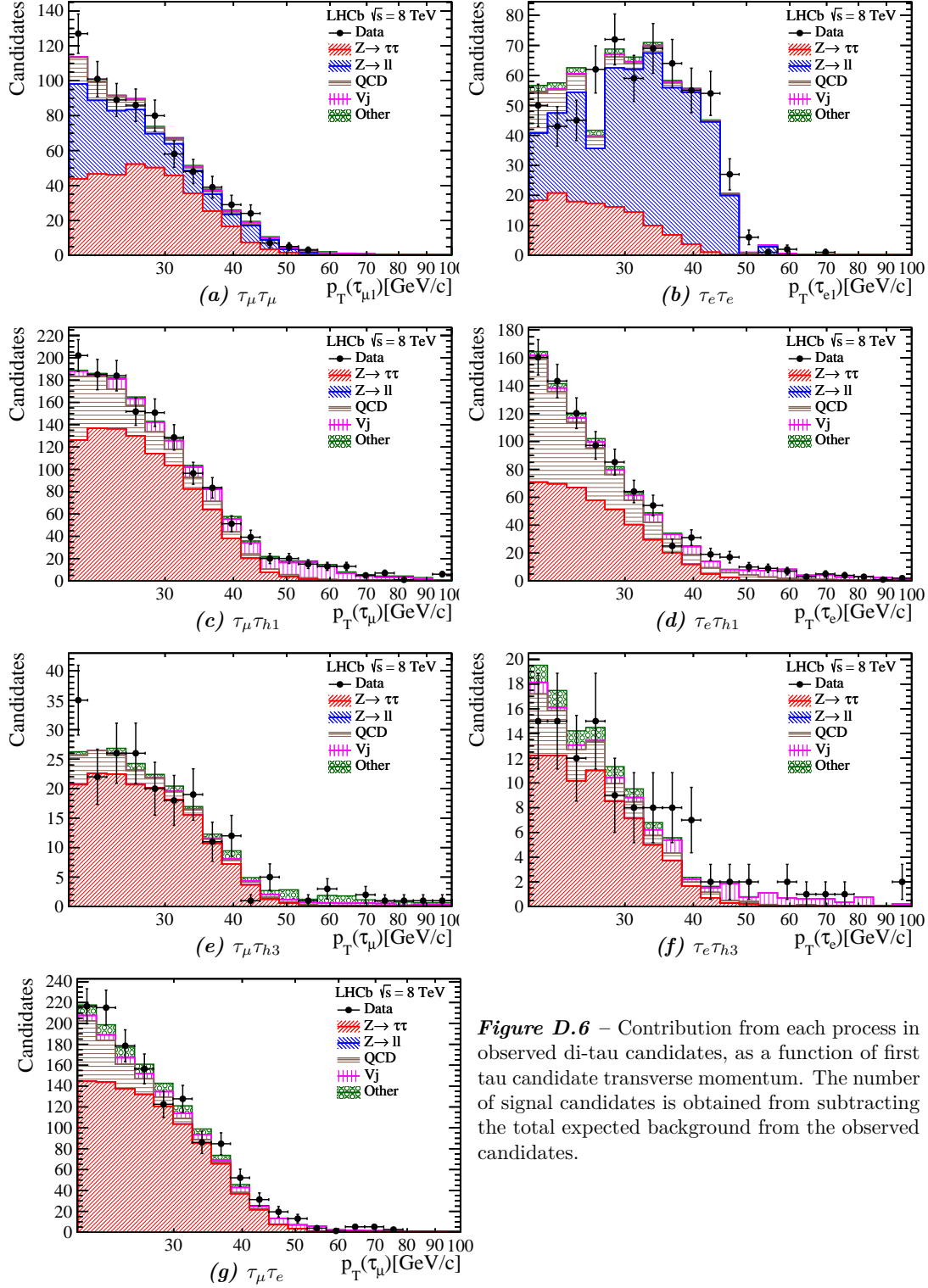


**Figure D.6** – Contribution from each process in observed di-tau candidates, as a function of first tau candidate transverse momentum. The number of signal candidates is obtained from subtracting the total expected background from the observed candidates.

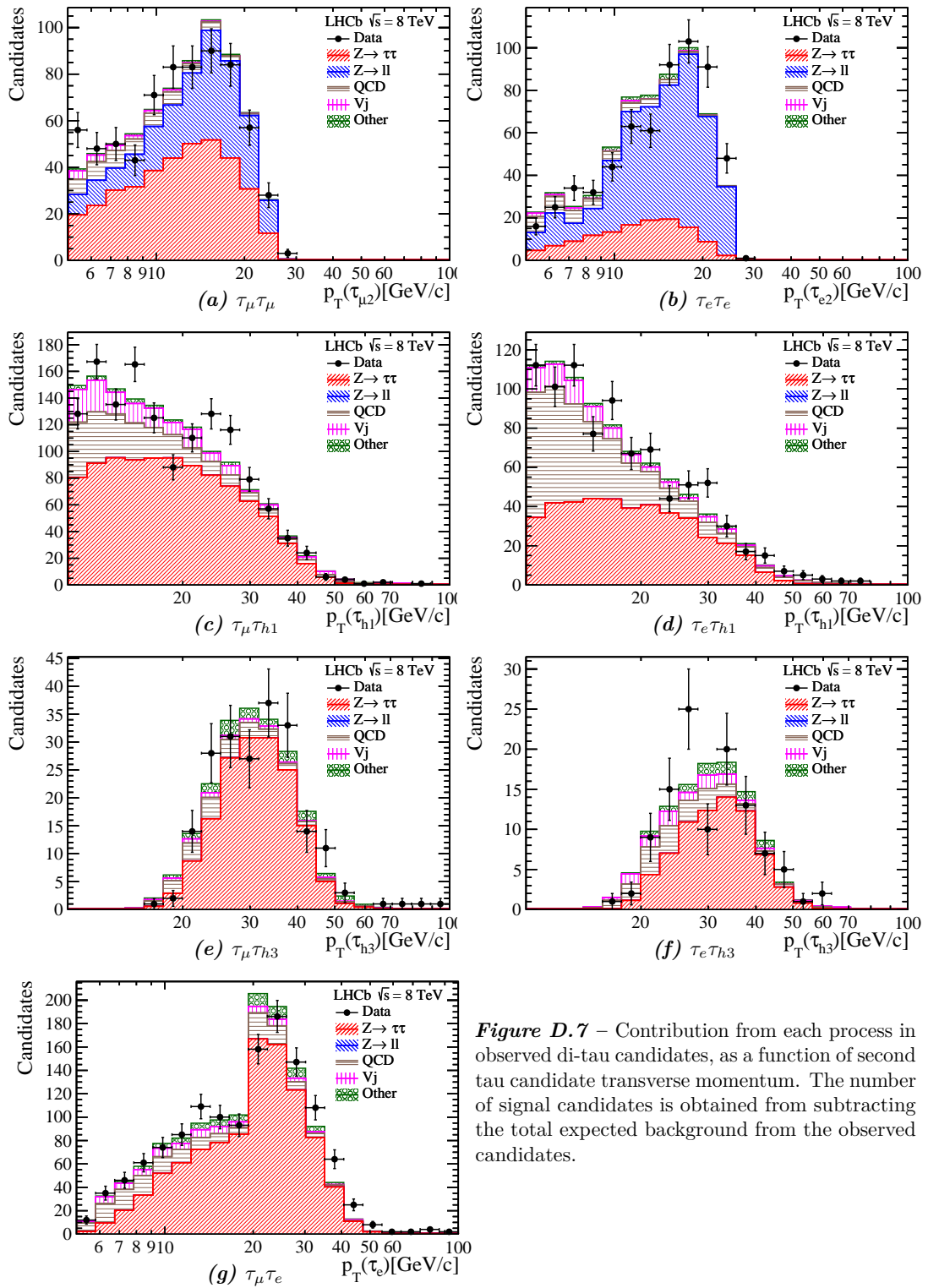


*Figure D.7* – Contribution from each process in observed di-tau candidates, as a function of second tau candidate transverse momentum. The number of signal candidates is obtained from subtracting the total expected background from the observed candidates.

## Appendix D. Combined Plots of $Z \rightarrow \tau\tau$

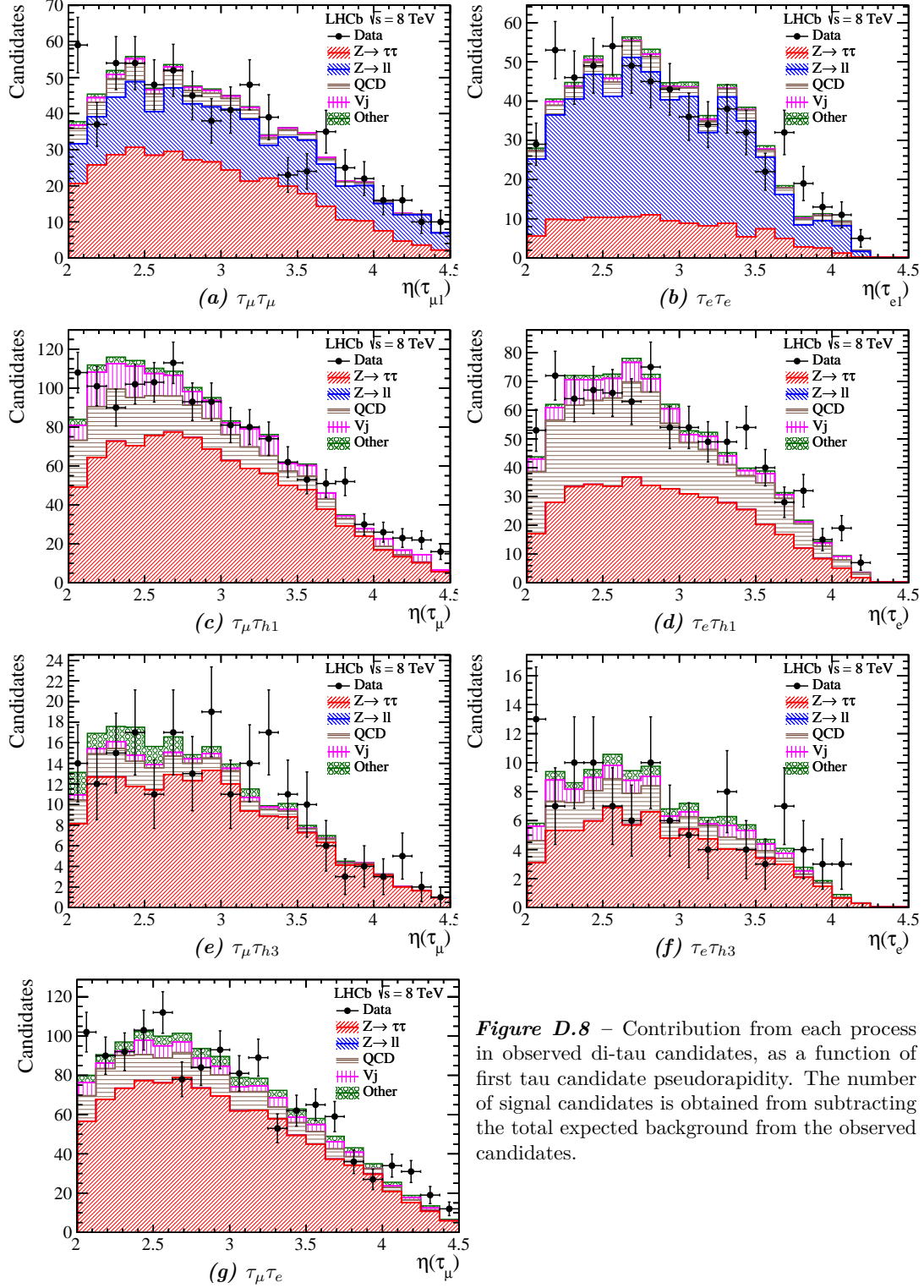


**Figure D.8** – Contribution from each process in observed di-tau candidates, as a function of first tau candidate pseudorapidity. The number of signal candidates is obtained from subtracting the total expected background from the observed candidates.

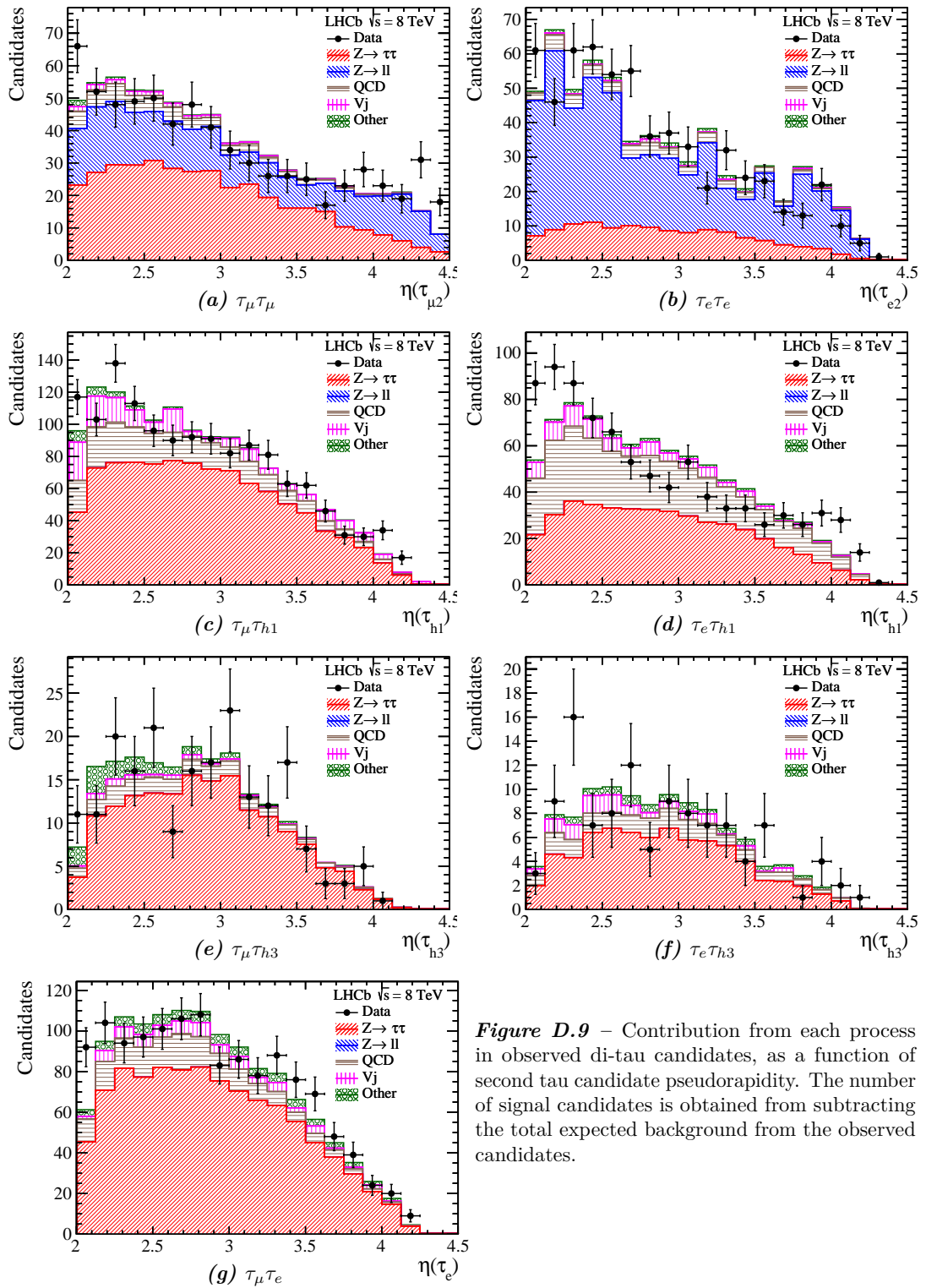


**Figure D.9** – Contribution from each process in observed di-tau candidates, as a function of second tau candidate pseudorapidity. The number of signal candidates is obtained from subtracting the total expected background from the observed candidates.



# E Reconstruction Efficiencies

## E.1 Binned Efficiencies

The efficiencies used in Chapter 7 are tabulated here, all shown in percentages.

**Table E.1** –  $\varepsilon_{\text{track},\mu}$  as a function of muon  $\eta$

$\eta$	$\varepsilon_{\text{track},\mu}$
2.00 – 2.25	$85.20 \pm 0.68$
2.25 – 2.50	$90.41 \pm 0.48$
2.50 – 2.75	$93.47 \pm 0.35$
2.75 – 3.00	$93.98 \pm 0.36$
3.00 – 3.25	$94.55 \pm 0.37$
3.25 – 3.50	$96.74 \pm 0.30$
3.50 – 3.75	$96.74 \pm 0.39$
3.75 – 4.00	$96.35 \pm 0.46$
4.00 – 4.25	$94.25 \pm 0.58$
4.25 – 4.50	$91.73 \pm 0.89$

**Table E.2** –  $\varepsilon_{\text{track},e}$  as a function of electron  $\eta$  and event track multiplicity.

$\eta \setminus \text{nTracks}$	0 – 100	100 – 300	300 – 600
2.00 – 2.25	$82.73 \pm 0.94$	$80.06 \pm 0.90$	$75.61 \pm 1.25$
2.25 – 2.50	$86.63 \pm 0.97$	$85.27 \pm 0.94$	$81.75 \pm 1.20$
2.50 – 2.75	$87.42 \pm 0.98$	$85.22 \pm 0.94$	$81.60 \pm 1.21$
2.75 – 3.00	$88.58 \pm 0.99$	$86.23 \pm 0.95$	$81.91 \pm 1.22$
3.00 – 3.25	$88.00 \pm 0.99$	$85.63 \pm 0.95$	$81.14 \pm 1.28$
3.25 – 3.50	$88.70 \pm 1.00$	$86.31 \pm 0.96$	$80.47 \pm 1.36$
3.50 – 3.75	$87.21 \pm 1.00$	$84.61 \pm 0.96$	$78.89 \pm 1.56$
3.75 – 4.00	$83.94 \pm 1.02$	$81.84 \pm 0.97$	$73.89 \pm 1.89$
4.00 – 4.25	$82.86 \pm 1.08$	$80.68 \pm 1.02$	$75.17 \pm 2.45$
4.25 – 4.50	$74.57 \pm 1.28$	$71.29 \pm 1.16$	$64.66 \pm 3.36$

**Table E.3** –  $\varepsilon_{\text{track},h}$  as a function of charged hadron  $\eta$  and event track multiplicity, for  $\tau_\mu\tau_{h1}$  channel.

$\eta \setminus \text{nTracks}$	0 – 100	100 – 300	300 – 600
2.00 – 2.25	$81.02 \pm 1.30$	$77.31 \pm 1.21$	$74.36 \pm 2.12$
2.25 – 2.50	$84.09 \pm 1.32$	$81.25 \pm 1.24$	$76.47 \pm 2.04$
2.50 – 2.75	$85.59 \pm 1.32$	$81.93 \pm 1.25$	$77.71 \pm 2.00$
2.75 – 3.00	$85.60 \pm 1.33$	$82.00 \pm 1.25$	$72.55 \pm 2.13$
3.00 – 3.25	$85.72 \pm 1.34$	$81.71 \pm 1.26$	$75.78 \pm 2.17$
3.25 – 3.50	$85.00 \pm 1.36$	$81.52 \pm 1.28$	$76.61 \pm 2.42$
3.50 – 3.75	$85.04 \pm 1.40$	$80.13 \pm 1.31$	$77.10 \pm 2.68$
3.75 – 4.00	$82.98 \pm 1.48$	$77.00 \pm 1.37$	$63.61 \pm 3.73$
4.00 – 4.25	$82.08 \pm 1.70$	$77.61 \pm 1.56$	$68.50 \pm 4.61$
4.25 – 4.50	$74.13 \pm 2.30$	$64.78 \pm 1.97$	$52.89 \pm 7.77$

**Table E.4** –  $\varepsilon_{\text{track},h}$  as a function of charged hadron  $\eta$  and event track multiplicity, for  $\tau_e\tau_{h1}$  channel.

$\eta \setminus \text{nTracks}$	0 – 100	100 – 300	300 – 600
2.00 – 2.25	$80.59 \pm 1.31$	$77.49 \pm 1.21$	$71.06 \pm 2.14$
2.25 – 2.50	$84.35 \pm 1.32$	$81.94 \pm 1.25$	$78.57 \pm 1.99$
2.50 – 2.75	$84.81 \pm 1.32$	$81.80 \pm 1.25$	$78.46 \pm 1.99$
2.75 – 3.00	$84.92 \pm 1.33$	$82.38 \pm 1.26$	$79.45 \pm 2.04$
3.00 – 3.25	$84.42 \pm 1.34$	$81.71 \pm 1.26$	$78.06 \pm 2.18$
3.25 – 3.50	$85.39 \pm 1.36$	$82.46 \pm 1.29$	$76.29 \pm 2.43$
3.50 – 3.75	$84.95 \pm 1.41$	$80.89 \pm 1.32$	$76.51 \pm 2.74$
3.75 – 4.00	$81.91 \pm 1.49$	$79.08 \pm 1.39$	$74.44 \pm 3.32$
4.00 – 4.25	$83.25 \pm 1.68$	$78.05 \pm 1.55$	$69.81 \pm 5.09$
4.25 – 4.50	$72.58 \pm 2.28$	$63.01 \pm 1.99$	$67.57 \pm 6.95$

Table E.5 –  $\varepsilon_{\text{PID},\mu}$  as a function of muon  $\eta$ ,  $p_{\text{T}}$ .

$p_{\text{T}}$ [GeV/c] \ $\eta$	2.00 – 2.25	2.25 – 2.50	2.50 – 2.75	2.75 – 3.00	3.00 – 3.25	3.25 – 3.50	3.50 – 3.75	3.75 – 4.00	4.00 – 4.25
5 – 7	99.17 ± 0.02	99.16 ± 0.03	99.27 ± 0.02	98.77 ± 0.05	98.81 ± 0.05	98.24 ± 0.07	98.23 ± 0.04	98.58 ± 0.06	98.61 ± 0.09
7 – 10	99.05 ± 0.05	99.26 ± 0.04	98.92 ± 0.03	98.96 ± 0.03	98.66 ± 0.04	98.45 ± 0.05	97.91 ± 0.08	98.57 ± 0.07	98.96 ± 0.08
10 – 15	99.09 ± 0.07	99.15 ± 0.05	99.13 ± 0.06	98.96 ± 0.05	98.65 ± 0.09	97.95 ± 0.10	97.72 ± 0.13	98.94 ± 0.13	96.90 ± 0.33
15 – 20	99.08 ± 0.05	99.25 ± 0.04	99.09 ± 0.04	98.85 ± 0.05	98.18 ± 0.06	98.18 ± 0.06	98.09 ± 0.09	98.09 ± 0.09	96.57 ± 0.30
20 – 25	98.12 ± 0.28	97.15 ± 0.32	97.52 ± 0.33	99.36 ± 0.22	97.53 ± 0.45	97.57 ± 0.45	96.13 ± 0.44	96.19 ± 0.43	97.24 ± 1.22
25 – 30	98.27 ± 0.20	98.35 ± 0.20	97.98 ± 0.24	99.20 ± 0.19	97.68 ± 0.36	97.90 ± 0.34	96.89 ± 0.48	98.08 ± 0.34	99.00 ± 0.30
30 – 35	98.12 ± 0.28	98.94 ± 0.25	98.38 ± 0.35	98.43 ± 0.43	97.71 ± 0.59	98.17 ± 0.50	97.30 ± 0.49	98.31 ± 0.35	99.02 ± 0.30
35 – 40	98.67 ± 0.21	99.12 ± 0.18	99.28 ± 0.18	99.13 ± 0.20	98.63 ± 0.25	98.58 ± 0.26	97.08 ± 0.35	98.68 ± 0.27	99.32 ± 0.27
40 – 45	98.56 ± 0.19	99.13 ± 0.14	99.36 ± 0.12	99.05 ± 0.14	98.81 ± 0.16	98.91 ± 0.17	97.17 ± 0.31	98.51 ± 0.31	98.99 ± 0.38
45 – 50	98.55 ± 0.24	99.32 ± 0.16	99.30 ± 0.15	98.91 ± 0.18	99.10 ± 0.18	99.05 ± 0.21	97.89 ± 0.36	98.75 ± 0.42	99.06 ± 0.74
50 – 70	98.12 ± 0.45	98.86 ± 0.35	98.95 ± 0.33	98.96 ± 0.33	98.68 ± 0.40	99.01 ± 0.44	97.07 ± 0.79	98.45 ± 1.07	97.65 ± 2.35
70 – 300	98.12 ± 0.45	98.86 ± 0.35	98.95 ± 0.33	98.96 ± 0.33	98.68 ± 0.40	99.01 ± 0.44	97.07 ± 0.79	98.45 ± 1.07	97.65 ± 2.35

 Table E.6 –  $\varepsilon_{\text{PID},e}$  as a function of electron  $\eta$ ,  $p_{\text{T}}$ .

$p_{\text{T}}$ [GeV/c] \ $\eta$	2.00 – 2.10	2.10 – 2.20	2.20 – 2.40	2.40 – 2.80	2.80 – 3.20	3.20 – 3.60	3.60 – 4.00	4.00 – 4.50
5 – 8	65.68 ± 2.94	79.86 ± 1.87	88.44 ± 0.91	90.54 ± 0.46	90.22 ± 0.45	89.92 ± 0.57	90.68 ± 1.16	72.55 ± 7.75
8 – 20	76.87 ± 3.30	83.61 ± 2.61	94.42 ± 1.02	96.04 ± 0.53	97.39 ± 0.47	94.36 ± 0.87	99.80 ± 0.35	20.34 ± 4.11
20 – 30	73.52 ± 2.98	86.41 ± 2.39	97.32 ± 0.84	96.05 ± 0.76	96.49 ± 0.84	97.51 ± 0.74	96.40 ± 0.94	32.69 ± 2.46
30 – 40	77.31 ± 2.22	88.41 ± 1.66	98.46 ± 0.46	98.40 ± 0.35	98.70 ± 0.32	98.67 ± 0.35	96.61 ± 0.77	45.31 ± 3.18
40 – 50	80.73 ± 2.85	88.89 ± 2.02	97.76 ± 0.67	98.96 ± 0.30	98.93 ± 0.31	97.96 ± 0.49	96.84 ± 1.04	48.61 ± 5.89



**Table E.7** –  $\epsilon_{\text{PID},h}$  as a function of charged hadron  $\eta$ ,  $p_{\text{T}}$ .

$\eta \setminus p_{\text{T}}$ [GeV/c]	1 – 2	2 – 3	3 – 4	4 – 6	6 – 10	10 – 15	15 – 20	20 – 70
2.000 – 2.125	44.95 ± 0.58	63.52 ± 0.47	70.07 ± 0.51	76.41 ± 0.45	84.77 ± 0.27	89.12 ± 0.44	92.31 ± 0.75	93.64 ± 1.14
2.125 – 2.250	50.19 ± 0.43	65.84 ± 0.34	76.71 ± 0.36	84.53 ± 0.28	84.77 ± 0.27	89.12 ± 0.44	92.31 ± 0.75	93.64 ± 1.14
2.250 – 2.375	53.68 ± 0.33	67.96 ± 0.27	77.87 ± 0.29	86.28 ± 0.23	91.62 ± 0.15	94.49 ± 0.21	96.55 ± 0.32	97.25 ± 0.47
2.375 – 2.500	58.57 ± 0.25	70.16 ± 0.22	78.34 ± 0.25	85.96 ± 0.20	91.62 ± 0.15	94.49 ± 0.21	96.55 ± 0.32	97.25 ± 0.47
2.500 – 2.625	61.98 ± 0.21	72.33 ± 0.19	79.32 ± 0.22	86.30 ± 0.18	91.16 ± 0.13	93.89 ± 0.19	96.01 ± 0.33	96.90 ± 0.52
2.625 – 2.750	63.26 ± 0.18	72.73 ± 0.17	79.47 ± 0.19	85.85 ± 0.16	91.16 ± 0.13	93.89 ± 0.19	96.01 ± 0.33	96.90 ± 0.52
2.750 – 2.875	64.64 ± 0.16	73.23 ± 0.15	79.83 ± 0.17	86.51 ± 0.15	92.00 ± 0.12	93.94 ± 0.19	96.15 ± 0.34	96.07 ± 0.64
2.875 – 3.000	65.84 ± 0.14	74.92 ± 0.14	81.66 ± 0.16	88.14 ± 0.14	92.00 ± 0.12	93.94 ± 0.19	96.15 ± 0.34	96.07 ± 0.64
3.000 – 3.125	67.28 ± 0.14	77.23 ± 0.13	83.86 ± 0.15	89.54 ± 0.13	93.59 ± 0.12	95.13 ± 0.18	96.27 ± 0.35	96.50 ± 0.67
3.125 – 3.250	69.05 ± 0.13	79.84 ± 0.13	85.84 ± 0.14	90.87 ± 0.13	93.59 ± 0.12	95.13 ± 0.18	96.27 ± 0.35	96.50 ± 0.67
3.250 – 3.375	70.24 ± 0.13	82.10 ± 0.12	87.36 ± 0.14	91.67 ± 0.12	94.44 ± 0.12	96.00 ± 0.18	96.84 ± 0.36	97.10 ± 0.77
3.375 – 3.500	70.91 ± 0.13	83.91 ± 0.12	88.97 ± 0.13	92.47 ± 0.12	94.44 ± 0.12	96.00 ± 0.18	96.84 ± 0.36	97.10 ± 0.77
3.500 – 3.625	68.76 ± 0.13	86.14 ± 0.12	90.47 ± 0.13	93.51 ± 0.12	95.41 ± 0.12	96.00 ± 0.21	96.36 ± 0.53	95.80 ± 1.52
3.625 – 3.750	65.82 ± 0.14	84.31 ± 0.13	91.56 ± 0.14	94.04 ± 0.13	95.41 ± 0.12	96.00 ± 0.21	96.36 ± 0.53	95.80 ± 1.52
3.750 – 3.875	64.08 ± 0.14	77.42 ± 0.15	88.09 ± 0.16	93.20 ± 0.14	94.71 ± 0.15	95.64 ± 0.32	96.05 ± 0.96	98.46 ± 1.69
3.875 – 4.000	63.84 ± 0.15	70.21 ± 0.17	80.62 ± 0.20	87.51 ± 0.19	94.71 ± 0.15	95.64 ± 0.32	96.05 ± 0.96	98.46 ± 1.69
4.000 – 4.125	59.97 ± 0.17	65.37 ± 0.20	71.99 ± 0.25	77.68 ± 0.27	76.10 ± 0.40	81.31 ± 1.32	90.26 ± 4.41	90.26 ± 4.41
4.125 – 4.250	52.65 ± 0.19	53.04 ± 0.24	55.26 ± 0.34	54.92 ± 0.41	76.10 ± 0.40	81.31 ± 1.32	90.26 ± 4.41	90.26 ± 4.41
4.250 – 4.375	36.92 ± 0.23	32.94 ± 0.30	26.26 ± 0.44	18.81 ± 0.53	18.81 ± 0.53	18.81 ± 0.53	18.81 ± 0.53	18.81 ± 0.53
4.375 – 4.500	34.29 ± 0.25	19.60 ± 0.31	7.89 ± 0.39	7.89 ± 0.39	7.89 ± 0.39	7.89 ± 0.39	7.89 ± 0.39	7.89 ± 0.39

Table E.8 –  $\varepsilon_{\text{trig},\mu}$  as a function of muon  $\eta$ ,  $p_T$ .

$p_T$ [GeV/c] \ $\eta$	2.00 – 2.25	2.25 – 2.50	2.50 – 2.75	2.75 – 3.00	3.00 – 3.25	3.25 – 3.50	3.50 – 3.75	3.75 – 4.00	4.00 – 4.25	4.25 – 4.50
20 – 25	80.67 ± 1.55	82.21 ± 1.99	79.27 ± 2.90	80.30 ± 3.18	82.18 ± 3.37	89.05 ± 3.34	81.14 ± 2.94	82.89 ± 2.43	79.78 ± 2.06	81.12 ± 1.74
25 – 30	78.47 ± 0.94	81.58 ± 1.10	82.00 ± 1.51	76.67 ± 1.95	75.05 ± 2.01	80.94 ± 1.89	80.71 ± 1.75	77.73 ± 1.51	81.48 ± 1.14	80.29 ± 1.19
30 – 35	78.68 ± 0.73	80.64 ± 0.76	80.53 ± 0.91	78.53 ± 1.10	79.44 ± 1.23	81.19 ± 1.12	81.58 ± 0.99	78.12 ± 0.93	80.78 ± 0.94	80.86 ± 1.16
35 – 40	76.90 ± 0.65	80.11 ± 0.63	80.03 ± 0.67	78.73 ± 0.71	78.42 ± 0.75	80.70 ± 0.73	79.88 ± 0.74	79.39 ± 0.81	80.73 ± 0.98	78.45 ± 1.43
40 – 45	75.60 ± 0.59	78.58 ± 0.54	79.62 ± 0.51	78.35 ± 0.52	79.04 ± 0.53	79.37 ± 0.57	78.58 ± 0.69	79.55 ± 0.87	80.83 ± 1.15	78.17 ± 2.09
45 – 50	75.03 ± 0.73	79.50 ± 0.63	79.08 ± 0.61	77.67 ± 0.63	78.33 ± 0.66	79.20 ± 0.72	79.56 ± 0.88	78.31 ± 1.22	81.32 ± 1.96	79.73 ± 3.83
50 – 55	74.66 ± 1.24	79.28 ± 1.11	79.49 ± 1.07	75.88 ± 1.14	76.02 ± 1.23	79.90 ± 1.32	77.66 ± 1.70	78.12 ± 2.41	78.72 ± 3.99	79.59 ± 7.38
55 – 60	72.16 ± 1.96	76.63 ± 1.77	77.83 ± 1.71	75.79 ± 1.77	79.49 ± 1.94	79.12 ± 2.20	76.95 ± 2.92	84.30 ± 4.01	78.85 ± 7.17	50.00 ± 25.60
60 – 65	71.38 ± 2.78	79.51 ± 2.30	78.81 ± 2.38	74.21 ± 2.67	78.89 ± 2.66	76.16 ± 3.68	84.87 ± 4.00	79.25 ± 7.06	76.47 ± 14.67	100.00 ± 45.71
65 – 70	74.52 ± 3.36	73.22 ± 3.66	79.79 ± 3.34	75.90 ± 3.76	83.45 ± 3.66	75.00 ± 4.39	70.49 ± 6.95	71.43 ± 13.08	87.50 ± 23.13	66.67 ± 41.33

 Table E.9 –  $\varepsilon_{\text{trig},e}$  as a function of electron  $\eta$ ,  $p_T$ .

$p_T$ [GeV/c] \ $\eta$	2.00 – 2.25	2.25 – 2.50	2.50 – 3.00	3.00 – 3.50	3.50 – 3.75	3.75 – 4.00	4.00 – 4.50
20 – 25	64.12 ± 3.49	62.67 ± 4.48	72.28 ± 3.89	67.59 ± 4.58	71.33 ± 5.13	71.34 ± 4.93	82.26 ± 4.80
25 – 30	63.45 ± 2.09	68.70 ± 2.14	64.42 ± 1.85	66.40 ± 2.08	78.81 ± 2.71	76.27 ± 2.86	82.60 ± 3.53
30 – 35	66.16 ± 1.58	68.30 ± 1.60	66.70 ± 1.26	70.04 ± 1.34	78.02 ± 1.91	76.12 ± 2.32	78.28 ± 3.32
35 – 40	66.96 ± 1.41	72.26 ± 1.32	69.79 ± 0.96	71.40 ± 0.99	78.27 ± 1.67	81.80 ± 2.17	81.50 ± 3.66
40 – 50	69.30 ± 1.29	74.17 ± 1.07	69.68 ± 0.74	71.84 ± 0.78	80.74 ± 1.43	75.20 ± 2.41	75.82 ± 4.36
50 – 70	70.43 ± 2.91	72.17 ± 2.59	68.64 ± 1.80	70.97 ± 2.03	77.88 ± 4.03	78.21 ± 6.57	73.48 ± 11.86

## E.2 Equivalent Efficiencies

The list of reconstruction efficiencies and their components are shown here, for each di-tau channel. The value in each entry is an harmonic averaged value over the list of candidates passing final selection. In cases where the value of 0 is possible (notably the probability of the second lepton to optionally trigger an event), an arithmetic average is shown instead. The values are in percentage.

The first column (“MC”) refers to the efficiency obtain from Monte-Carlo truth by simply dividing the number of candidate passing such selection over the number at previous stage (the “cut-and-count” method). The rest of the columns are efficiencies evaluated as a function of binning variable given selected candidates from respective source. The values in the column “Equivalent” are determined from eq. 7.2, and the last column ( $Z \rightarrow \tau\tau$ ) uses candidates from simulated sample of  $Z \rightarrow \tau\tau$ . Only  $\varepsilon_{\text{rec}}$  from “Equivalent” column is used in the cross-section computation.

The next-to-last row, “Size”, refers to the size of samples used to perform the average, reflecting the quality of the average. The last row, “Expected”, refers to the expected number of that process in data.

*Table E.10* – Channel  $\tau_\mu\tau_\mu$

	MC	Observed	$Z \rightarrow ll$	QCD	$Vj$	Others	Equivalent	$Z \rightarrow \tau\tau$
$\varepsilon_{\text{track}}$	90.2	$85.7 \pm 0.9$	$86.4 \pm 0.9$	$84.7 \pm 0.8$	$84.4 \pm 0.8$	$81.7 \pm 0.9$	$85.6 \pm 0.9$	$86.3 \pm 0.8$
$\varepsilon_{\text{track},\mu 1}$	95.0	$92.8 \pm 0.5$	$93.3 \pm 0.5$	$92.3 \pm 0.4$	$92.2 \pm 0.4$	$90.7 \pm 0.5$	$92.6 \pm 0.5$	$93.0 \pm 0.4$
$\varepsilon_{\text{track},\mu 2}$	94.8	$92.4 \pm 0.5$	$92.6 \pm 0.5$	$91.8 \pm 0.5$	$91.5 \pm 0.5$	$90.1 \pm 0.5$	$92.4 \pm 0.5$	$92.8 \pm 0.4$
$\varepsilon_{\text{kine}}$	100.0	$100.0 \pm 0.0$	$100.0 \pm 0.0$	$100.0 \pm 0.0$	$100.0 \pm 0.0$	$100.0 \pm 0.0$	$100.0 \pm 0.0$	$100.0 \pm 0.0$
$\varepsilon_{\text{PID}}$	97.8	$96.0 \pm 0.5$	$95.7 \pm 0.6$	$96.8 \pm 0.4$	$97.4 \pm 0.4$	$97.2 \pm 0.4$	$96.0 \pm 0.5$	$96.5 \pm 0.4$
$\varepsilon_{\text{PID},\mu 1}$	98.9	$97.8 \pm 0.4$	$97.5 \pm 0.4$	$97.9 \pm 0.3$	$98.5 \pm 0.3$	$98.5 \pm 0.3$	$97.9 \pm 0.4$	$98.0 \pm 0.3$
$\varepsilon_{\text{PID},\mu 2}$	98.8	$98.2 \pm 0.1$	$98.1 \pm 0.2$	$98.9 \pm 0.1$	$98.8 \pm 0.0$	$98.6 \pm 0.1$	$98.1 \pm 0.1$	$98.5 \pm 0.1$
$\varepsilon_{\text{GEC}}$	99.2	$93.0 \pm 0.3$	$93.0 \pm 0.3$	$93.0 \pm 0.3$	$93.0 \pm 0.3$	$93.0 \pm 0.3$	$93.0 \pm 0.3$	$93.0 \pm 0.3$
$\varepsilon_{\text{trig}}$	80.4	$85.6 \pm 1.6$	$88.2 \pm 1.5$	$82.6 \pm 2.0$	$78.3 \pm 1.6$	$81.7 \pm 1.4$	$84.7 \pm 1.5$	$85.5 \pm 1.5$
$\varepsilon_{\text{trig},\mu 1}$	75.7	$80.4 \pm 1.8$	$80.5 \pm 1.9$	$80.8 \pm 2.1$	$78.0 \pm 1.6$	$77.8 \pm 1.5$	$80.4 \pm 1.6$	$80.3 \pm 1.7$
$\varepsilon_{\text{trig},\mu 2}$	18.6	$26.4 \pm 1.2$	$39.2 \pm 1.7$	$8.7 \pm 0.4$	$1.3 \pm 0.1$	$18.6 \pm 0.8$	$100.1 \pm 3.1$	$26.0 \pm 1.2$
$\varepsilon_{\text{rec}}$	70.0	$65.6 \pm 1.4$	$67.8 \pm 1.4$	$63.0 \pm 1.7$	$59.9 \pm 1.4$	$60.3 \pm 1.3$	$64.8 \pm 1.4$	$66.2 \pm 1.4$
Size	—	696	1425	1518	2125	259	—	6456
Expected	—	696	249.7	50.9	12.7	5.8	376.1	376.1

## Appendix E. Reconstruction Efficiencies

**Table E.11** – Channel  $\tau_\mu\tau_{h1}$

	MC	Observed	$Z \rightarrow ll$	QCD	$Vj$	Others	Equivalent	$Z \rightarrow \tau\tau$
$\epsilon_{\text{track}}$	77.5	$74.9 \pm 1.4$	$74.9 \pm 1.6$	$73.8 \pm 1.4$	$73.2 \pm 1.4$	$71.4 \pm 1.4$	$75.5 \pm 1.5$	$75.6 \pm 1.5$
$\epsilon_{\text{track},\mu}$	95.0	$92.7 \pm 0.4$	$93.0 \pm 0.5$	$91.7 \pm 0.5$	$92.1 \pm 0.5$	$91.1 \pm 0.5$	$93.1 \pm 0.4$	$93.0 \pm 0.4$
$\epsilon_{\text{track},h}$	81.4	$80.8 \pm 1.5$	$80.6 \pm 1.6$	$80.5 \pm 1.5$	$79.4 \pm 1.4$	$78.3 \pm 1.5$	$81.1 \pm 1.5$	$81.2 \pm 1.5$
$\epsilon_{\text{kine}}$	100.0	$100.0 \pm 0.0$	$100.0 \pm 0.0$	$100.0 \pm 0.0$	$100.0 \pm 0.0$	$100.0 \pm 0.0$	$100.0 \pm 0.0$	$100.0 \pm 0.0$
$\epsilon_{\text{PID}}$	91.1	$92.9 \pm 0.7$	$94.0 \pm 1.1$	$92.5 \pm 0.5$	$91.8 \pm 0.6$	$92.2 \pm 0.7$	$93.1 \pm 0.8$	$93.3 \pm 0.7$
$\epsilon_{\text{PID},\mu}$	99.0	$97.9 \pm 0.4$	$98.2 \pm 0.3$	$98.0 \pm 0.3$	$98.3 \pm 0.4$	$98.5 \pm 0.3$	$97.8 \pm 0.4$	$97.9 \pm 0.3$
$\epsilon_{\text{PID},h}$	91.8	$94.9 \pm 0.6$	$95.7 \pm 1.0$	$94.4 \pm 0.5$	$93.4 \pm 0.5$	$93.6 \pm 0.6$	$95.3 \pm 0.7$	$95.3 \pm 0.6$
$\epsilon_{\text{GEC}}$	99.2	$93.0 \pm 0.6$	$93.0 \pm 0.6$	$93.0 \pm 0.6$	$93.0 \pm 0.6$	$93.0 \pm 0.6$	$93.0 \pm 0.6$	$93.0 \pm 0.6$
$\epsilon_{\text{trig}}$	76.0	$80.1 \pm 1.8$	$79.2 \pm 1.0$	$80.6 \pm 1.9$	$78.3 \pm 1.6$	$76.9 \pm 1.9$	$80.4 \pm 1.7$	$80.3 \pm 1.7$
$\epsilon_{\text{rec}}$	52.7	$51.9 \pm 1.6$	$52.0 \pm 1.4$	$51.2 \pm 1.6$	$49.0 \pm 1.4$	$47.2 \pm 1.5$	$52.6 \pm 1.6$	$52.7 \pm 1.6$
Size	—	1371	18750	25150	188	377	—	17278
Expected	—	1373	1.2	235.8	144.2	25.7	965.9	965.9

**Table E.12** – Channel  $\tau_\mu\tau_{h3}$

	MC	Observed	$Z \rightarrow ll$	QCD	$Vj$	Others	Equivalent	$Z \rightarrow \tau\tau$
$\epsilon_{\text{track}}$	38.9	$36.5 \pm 1.7$	—	$35.6 \pm 1.7$	$35.3 \pm 1.7$	$34.3 \pm 1.7$	$36.9 \pm 1.8$	$36.6 \pm 1.7$
$\epsilon_{\text{track},\mu}$	95.0	$93.0 \pm 0.4$	—	$91.5 \pm 0.5$	$91.8 \pm 0.5$	$90.8 \pm 0.5$	$93.4 \pm 0.4$	$93.0 \pm 0.4$
$\epsilon_{\text{track},\tau_{h3}}$	40.7	$39.3 \pm 1.9$	—	$39.0 \pm 1.8$	$38.4 \pm 1.8$	$37.8 \pm 1.8$	$39.5 \pm 1.9$	$39.4 \pm 1.9$
$\epsilon_{\text{kine}}$	100.1	$100.1 \pm 0.0$	—	$100.1 \pm 0.0$	$100.1 \pm 0.0$	$100.1 \pm 0.0$	$100.1 \pm 0.0$	$100.1 \pm 0.0$
$\epsilon_{\text{PID}}$	76.7	$72.8 \pm 1.3$	—	$66.9 \pm 1.1$	$66.6 \pm 1.2$	$65.4 \pm 1.2$	$74.7 \pm 1.3$	$73.1 \pm 1.3$
$\epsilon_{\text{PID},\mu}$	98.9	$98.0 \pm 0.3$	—	$98.0 \pm 0.3$	$98.6 \pm 0.4$	$98.6 \pm 0.3$	$97.9 \pm 0.4$	$97.9 \pm 0.3$
$\epsilon_{\text{PID},h1}$	93.2	$95.0 \pm 0.4$	—	$94.3 \pm 0.4$	$94.1 \pm 0.4$	$94.3 \pm 0.5$	$95.2 \pm 0.4$	$95.2 \pm 0.4$
$\epsilon_{\text{PID},h2}$	91.9	$92.3 \pm 0.2$	—	$89.9 \pm 0.2$	$90.0 \pm 0.2$	$89.0 \pm 0.3$	$93.0 \pm 0.2$	$92.4 \pm 0.2$
$\epsilon_{\text{PID},h3}$	84.0	$84.5 \pm 0.2$	—	$80.2 \pm 0.2$	$79.3 \pm 0.2$	$78.5 \pm 0.2$	$85.9 \pm 0.2$	$84.7 \pm 0.2$
$\epsilon_{\text{PID},\tau_{h3}}$	77.1	$74.3 \pm 1.3$	—	$68.2 \pm 1.1$	$67.5 \pm 1.2$	$66.3 \pm 1.2$	$76.3 \pm 1.3$	$74.6 \pm 1.3$
$\epsilon_{\text{GEC}}$	99.5	$93.0 \pm 0.6$	—	$93.0 \pm 0.6$	$93.0 \pm 0.6$	$93.0 \pm 0.6$	$93.0 \pm 0.6$	$93.0 \pm 0.6$
$\epsilon_{\text{trig}}$	75.8	$80.1 \pm 1.8$	—	$80.4 \pm 1.9$	$75.1 \pm 2.5$	$77.9 \pm 1.8$	$80.4 \pm 1.8$	$80.3 \pm 1.7$
$\epsilon_{\text{rec}}$	22.1	$19.9 \pm 1.1$	—	$17.9 \pm 1.0$	$16.5 \pm 1.0$	$16.3 \pm 0.9$	$20.8 \pm 1.2$	$20.1 \pm 1.1$
Size	—	205	—	2205	204	109	—	3425
Expected	—	205	—	21.2	5.1	14.7	163.9	163.9

**Table E.13** – Channel  $\tau_e\tau_e$

	MC	Observed	$Z \rightarrow ll$	QCD	$Vj$	Others	Equivalent	$Z \rightarrow \tau\tau$
$\epsilon_{\text{track}}$	72.2	$71.0 \pm 2.2$	$70.7 \pm 2.2$	$70.8 \pm 2.0$	$71.0 \pm 2.1$	$71.9 \pm 2.1$	$71.8 \pm 2.2$	$71.6 \pm 2.1$
$\epsilon_{\text{track},e1}$	85.4	$84.7 \pm 1.4$	$85.1 \pm 1.4$	$84.7 \pm 1.4$	$84.7 \pm 1.5$	$85.1 \pm 1.4$	$83.6 \pm 1.4$	$85.0 \pm 1.4$
$\epsilon_{\text{track},e2}$	84.3	$83.7 \pm 1.2$	$83.1 \pm 1.2$	$83.6 \pm 1.1$	$83.8 \pm 1.1$	$84.4 \pm 1.1$	$85.9 \pm 1.2$	$84.2 \pm 1.1$
$\epsilon_{\text{kine}}$	62.3	$62.3 \pm 0.8$	$62.3 \pm 0.8$	$62.3 \pm 0.8$	$62.3 \pm 0.8$	$62.3 \pm 0.8$	$62.3 \pm 0.8$	$62.3 \pm 0.8$
$\epsilon_{\text{PID}}$	81.0	$86.2 \pm 1.1$	$85.8 \pm 1.0$	$85.0 \pm 1.1$	$86.5 \pm 1.4$	$87.4 \pm 1.0$	$87.9 \pm 1.4$	$88.1 \pm 1.0$
$\epsilon_{\text{PID},e1}$	90.8	$94.4 \pm 0.9$	$95.0 \pm 0.8$	$93.7 \pm 1.1$	$95.7 \pm 1.2$	$94.7 \pm 0.9$	$92.6 \pm 0.9$	$95.1 \pm 0.9$
$\epsilon_{\text{PID},e2}$	89.0	$91.4 \pm 0.5$	$90.2 \pm 0.5$	$90.7 \pm 0.5$	$90.4 \pm 1.0$	$92.3 \pm 0.4$	$95.5 \pm 0.8$	$92.6 \pm 0.4$
$\epsilon_{\text{GEC}}$	99.2	$91.6 \pm 0.6$	$91.6 \pm 0.6$	$91.6 \pm 0.6$	$91.6 \pm 0.6$	$91.6 \pm 0.6$	$91.6 \pm 0.6$	$91.6 \pm 0.6$
$\epsilon_{\text{trig}}$	70.4	$74.2 \pm 2.2$	$73.5 \pm 2.0$	$69.0 \pm 3.4$	$69.8 \pm 2.3$	$70.1 \pm 2.9$	$79.5 \pm 2.0$	$70.2 \pm 2.8$
$\epsilon_{\text{trig},e1}$	66.8	$70.1 \pm 2.1$	$69.7 \pm 2.0$	$68.8 \pm 3.4$	$69.4 \pm 2.3$	$68.9 \pm 2.9$	$71.9 \pm 2.1$	$68.6 \pm 2.8$
$\epsilon_{\text{trig},e2}$	10.7	$13.3 \pm 0.8$	$12.4 \pm 0.8$	$0.7 \pm 0.0$	$1.4 \pm 0.1$	$3.5 \pm 0.2$	$-2.2 \pm 0.1$	$5.0 \pm 0.3$
$\epsilon_{\text{rec}}$	25.2	$26.1 \pm 1.2$	$25.6 \pm 1.2$	$23.7 \pm 1.4$	$24.6 \pm 1.2$	$25.2 \pm 1.3$	$28.8 \pm 1.3$	$25.4 \pm 1.3$
Size	—	610	300	683	58	458	—	1966
Expected	—	610	420.8	42.7	5.8	13.3	127.3	127.3

## E.2. Equivalent Efficiencies

*Table E.14* – Channel  $\tau_e\tau_{h1}$

	MC	Observed	$Z \rightarrow ll$	QCD	$Vj$	Others	Equivalent	$Z \rightarrow \tau\tau$
$\varepsilon_{\text{track}}$	70.6	$68.0 \pm 1.9$	$68.4 \pm 2.1$	$68.2 \pm 1.9$	$68.1 \pm 2.0$	$69.2 \pm 2.0$	$67.8 \pm 1.9$	$69.2 \pm 2.0$
$\varepsilon_{\text{track},e}$	86.4	$84.6 \pm 1.4$	$84.6 \pm 1.4$	$84.5 \pm 1.4$	$84.6 \pm 1.5$	$85.0 \pm 1.4$	$84.5 \pm 1.3$	$85.0 \pm 1.4$
$\varepsilon_{\text{track},h}$	81.6	$80.4 \pm 1.5$	$80.9 \pm 1.6$	$80.7 \pm 1.5$	$80.4 \pm 1.5$	$81.4 \pm 1.5$	$80.1 \pm 1.5$	$81.4 \pm 1.5$
$\varepsilon_{\text{kine}}$	61.3	$61.3 \pm 0.8$	$61.3 \pm 0.8$	$61.3 \pm 0.8$	$61.3 \pm 0.8$	$61.3 \pm 0.8$	$61.3 \pm 0.8$	$61.3 \pm 0.8$
$\varepsilon_{\text{PID}}$	85.9	$88.1 \pm 1.2$	$90.2 \pm 1.2$	$88.7 \pm 1.1$	$87.9 \pm 1.6$	$90.7 \pm 1.1$	$87.5 \pm 1.3$	$90.5 \pm 1.1$
$\varepsilon_{\text{PID},e}$	93.0	$93.3 \pm 1.1$	$94.3 \pm 1.0$	$94.0 \pm 1.1$	$93.2 \pm 1.6$	$95.1 \pm 0.9$	$92.7 \pm 1.1$	$95.0 \pm 0.9$
$\varepsilon_{\text{PID},h}$	91.9	$94.4 \pm 0.6$	$95.6 \pm 0.9$	$94.4 \pm 0.5$	$94.4 \pm 0.4$	$95.4 \pm 0.6$	$94.3 \pm 0.8$	$95.3 \pm 0.6$
$\varepsilon_{\text{GEC}}$	99.2	$92.3 \pm 1.0$	$92.3 \pm 1.0$	$92.3 \pm 1.0$	$92.3 \pm 1.0$	$92.3 \pm 1.0$	$92.3 \pm 1.0$	$92.3 \pm 1.0$
$\varepsilon_{\text{trig}}$	66.7	$68.9 \pm 3.2$	$70.1 \pm 2.2$	$68.3 \pm 3.4$	$70.1 \pm 3.8$	$68.8 \pm 2.9$	$69.2 \pm 3.0$	$68.7 \pm 2.9$
$\varepsilon_{\text{rec}}$	24.2	$23.4 \pm 1.3$	$24.5 \pm 1.2$	$23.5 \pm 1.4$	$23.8 \pm 1.6$	$24.5 \pm 1.3$	$23.3 \pm 1.3$	$24.4 \pm 1.3$
Size	—	861	7005	11370	312	1981	—	7840
Expected	—	861	16.1	330.8	68.3	17.9	427.5	427.5

*Table E.15* – Channel  $\tau_e\tau_{h3}$

	MC	Observed	$Z \rightarrow ll$	QCD	$Vj$	Others	Equivalent	$Z \rightarrow \tau\tau$
$\varepsilon_{\text{track}}$	35.3	$32.6 \pm 1.7$	—	$32.6 \pm 1.7$	$32.3 \pm 1.7$	$33.3 \pm 1.8$	$32.6 \pm 1.7$	$33.3 \pm 1.8$
$\varepsilon_{\text{track},e}$	86.6	$84.1 \pm 1.4$	—	$84.1 \pm 1.4$	$84.1 \pm 1.4$	$85.0 \pm 1.4$	$84.0 \pm 1.4$	$84.9 \pm 1.4$
$\varepsilon_{\text{track},\tau_{h3}}$	40.6	$38.7 \pm 1.8$	—	$38.8 \pm 1.8$	$38.4 \pm 1.8$	$39.2 \pm 1.9$	$38.7 \pm 1.8$	$39.2 \pm 1.9$
$\varepsilon_{\text{kine}}$	62.3	$62.3 \pm 0.8$	—	$62.3 \pm 0.8$	$62.3 \pm 0.8$	$62.3 \pm 0.8$	$62.3 \pm 0.8$	$62.3 \pm 0.8$
$\varepsilon_{\text{PID}}$	71.8	$66.9 \pm 1.5$	—	$64.8 \pm 1.4$	$63.7 \pm 1.6$	$70.3 \pm 1.5$	$67.6 \pm 1.5$	$71.2 \pm 1.5$
$\varepsilon_{\text{PID},e}$	93.0	$92.6 \pm 1.2$	—	$94.4 \pm 1.1$	$93.8 \pm 1.7$	$94.3 \pm 0.9$	$91.9 \pm 1.2$	$95.0 \pm 0.9$
$\varepsilon_{\text{PID},h1}$	93.4	$94.8 \pm 0.5$	—	$94.1 \pm 0.4$	$94.1 \pm 0.3$	$95.4 \pm 0.5$	$95.0 \pm 0.5$	$95.1 \pm 0.4$
$\varepsilon_{\text{PID},h2}$	91.7	$91.7 \pm 0.2$	—	$89.8 \pm 0.2$	$90.5 \pm 0.2$	$92.5 \pm 0.2$	$92.3 \pm 0.3$	$92.4 \pm 0.2$
$\varepsilon_{\text{PID},h3}$	83.9	$82.6 \pm 0.2$	—	$80.9 \pm 0.2$	$79.3 \pm 0.2$	$84.2 \pm 0.2$	$83.4 \pm 0.2$	$85.0 \pm 0.2$
$\varepsilon_{\text{PID},\tau_{h3}}$	77.2	$72.1 \pm 1.3$	—	$68.7 \pm 1.3$	$67.9 \pm 1.2$	$74.5 \pm 1.4$	$73.5 \pm 1.4$	$74.9 \pm 1.4$
$\varepsilon_{\text{GEC}}$	99.2	$92.3 \pm 0.7$	—	$92.3 \pm 0.7$	$92.3 \pm 0.7$	$92.3 \pm 0.7$	$92.3 \pm 0.7$	$92.3 \pm 0.7$
$\varepsilon_{\text{trig}}$	66.9	$69.5 \pm 3.0$	—	$67.6 \pm 3.4$	$69.5 \pm 4.4$	$69.1 \pm 3.0$	$70.1 \pm 2.7$	$68.7 \pm 2.9$
$\varepsilon_{\text{rec}}$	10.2	$8.7 \pm 0.6$	—	$8.3 \pm 0.6$	$8.3 \pm 0.7$	$9.3 \pm 0.7$	$8.9 \pm 0.6$	$9.4 \pm 0.7$
Size	—	110	—	791	89	410	—	1533
Expected	—	110	—	19.4	10.1	7.6	72.8	72.8

## Appendix E. Reconstruction Efficiencies

**Table E.16** – Channel  $\tau_\mu\tau_e$

	MC	Observed	$Z \rightarrow \mu\mu$	$Z \rightarrow ee$	QCD	$V_\mu + \text{jett}$	$V_e + \text{jett}$	Others	Equivalent	$Z \rightarrow \tau\tau$
$\epsilon_{\text{track}}$	81.3	$78.2 \pm 1.2$	$78.4 \pm 1.3$	$78.1 \pm 1.3$	$77.5 \pm 1.1$	$77.6 \pm 1.1$	$79.5 \pm 1.5$	$78.7 \pm 1.2$	$78.2 \pm 1.2$	$78.7 \pm 1.2$
$\epsilon_{\text{track},\mu}$	95.0	$92.8 \pm 0.4$	$93.0 \pm 0.5$	$92.6 \pm 0.4$	$92.3 \pm 0.4$	$91.8 \pm 0.5$	$91.4 \pm 0.5$	$93.1 \pm 0.4$	$92.9 \pm 0.4$	$93.0 \pm 0.4$
$\epsilon_{\text{track},e}$	85.4	$84.3 \pm 1.2$	$84.3 \pm 1.3$	$84.4 \pm 1.4$	$84.0 \pm 1.2$	$84.6 \pm 1.2$	$86.9 \pm 1.6$	$84.5 \pm 1.3$	$84.2 \pm 1.2$	$84.6 \pm 1.3$
$\epsilon_{\text{kine}}$	81.7	$81.7 \pm 0.9$	$81.7 \pm 0.9$	$81.7 \pm 0.9$	$81.7 \pm 0.9$	$81.7 \pm 0.9$	$81.7 \pm 0.9$	$81.7 \pm 0.9$	$81.7 \pm 0.9$	$81.7 \pm 0.9$
$\epsilon_{\text{PID}}$	88.6	$91.0 \pm 0.7$	$90.9 \pm 0.9$	$92.5 \pm 1.0$	$90.1 \pm 0.6$	$92.4 \pm 0.6$	$97.2 \pm 0.6$	$91.6 \pm 0.7$	$90.9 \pm 0.7$	$92.2 \pm 0.7$
$\epsilon_{\text{PID},\mu}$	98.9	$98.0 \pm 0.3$	$97.5 \pm 0.4$	$98.5 \pm 0.2$	$98.0 \pm 0.3$	$97.9 \pm 0.4$	$99.1 \pm 0.1$	$98.0 \pm 0.3$	$98.0 \pm 0.3$	$98.1 \pm 0.3$
$\epsilon_{\text{PID},e}$	89.4	$92.8 \pm 0.6$	$93.3 \pm 0.9$	$93.8 \pm 1.0$	$91.9 \pm 0.6$	$94.4 \pm 0.5$	$98.1 \pm 0.6$	$93.4 \pm 0.6$	$92.7 \pm 0.7$	$94.0 \pm 0.6$
$\epsilon_{\text{GEC}}$	99.3	$92.3 \pm 0.7$	$92.3 \pm 0.7$	$92.3 \pm 0.7$	$92.3 \pm 0.7$	$92.3 \pm 0.7$	$92.3 \pm 0.7$	$92.3 \pm 0.7$	$92.3 \pm 0.7$	$92.3 \pm 0.7$
$\epsilon_{\text{trig}}$	76.5	$83.8 \pm 1.4$	$91.7 \pm 0.8$	$91.4 \pm 0.8$	$80.1 \pm 1.8$	$84.6 \pm 1.3$	$69.8 \pm 1.7$	$83.8 \pm 1.3$	$84.8 \pm 1.3$	$84.3 \pm 1.3$
$\epsilon_{\text{trig},\mu}$	53.5	$68.1 \pm 1.7$	$79.8 \pm 1.4$	$71.5 \pm 1.3$	$64.5 \pm 1.8$	$77.0 \pm 1.6$	$0.0 \pm 0$	$68.2 \pm 1.7$	$70.5 \pm 1.8$	$68.3 \pm 1.7$
$\epsilon_{\text{trig},e}$	32.6	$36.3 \pm 1.5$	$57.7 \pm 1.7$	$69.9 \pm 2.5$	$21.9 \pm 1.1$	$26.1 \pm 1.1$	$69.8 \pm 1.7$	$36.5 \pm 1.6$	$39.9 \pm 1.6$	$39.1 \pm 1.7$
$\epsilon_{\text{rec}}$	44.5	$45.2 \pm 1.2$	$49.5 \pm 1.3$	$49.9 \pm 1.3$	$42.2 \pm 1.3$	$45.9 \pm 1.2$	$40.7 \pm 1.4$	$45.7 \pm 1.2$	$45.7 \pm 1.2$	$46.3 \pm 1.2$
Size	—	1322	5622	2236	4503	31	5	4252	—	17600
Expected	—	1322	19.9	5.4	160.0	30.3	35.0	68.0	1003.1	1003.1

# F $Z \rightarrow \tau\tau$ Cross-section Measurement

**Table F.1** – Statistics for the calculation of the acceptance factor  $\mathcal{A}$ . The migration into acceptance refers to the fraction of di-tau candidates found inside acceptance that are from outside the fiducial region.

	$\tau_\mu\tau_\mu$	$\tau_\mu\tau_{h1}$	$\tau_\mu\tau_{h3}$	$\tau_e\tau_e$	$\tau_e\tau_{h1}$	$\tau_e\tau_{h3}$	$\tau_\mu\tau_e$
In fiducial, in acceptance	461441	1054037	506099	472507	1061476	512560	936645
In fiducial, not in acceptance	741924	5906753	1569761	793962	6061430	1621009	1531234
Not in fiducial, in acceptance	7327	11526	3010	7389	11700	2998	14769
Migration into $\mathcal{A}$ [%]	$1.56 \pm 0.02$	$1.08 \pm 0.01$	$0.59 \pm 0.01$	$1.54 \pm 0.02$	$1.09 \pm 0.01$	$0.58 \pm 0.01$	$1.55 \pm 0.01$
Effective $\mathcal{A}$ [%]	$38.95 \pm 0.51$	$15.31 \pm 0.29$	$24.53 \pm 0.37$	$37.89 \pm 0.49$	$15.07 \pm 0.29$	$24.16 \pm 0.36$	$38.55 \pm 0.50$

**Table F.2** – Statistics for the calculation of the kinematic selection efficiency  $\varepsilon_{\text{kine}}$ . The first five rows refers to the number of di-tau candidates from the simulated  $Z \rightarrow \tau\tau$  sample after the given selection is applied: **acc** for the acceptance selection, **trk** for the track quality selection, and **kine** the kinematical selection. The migration into  $\varepsilon_{\text{kine}}$  refers to the fraction of di-tau candidates passing the track and kinematic selections but are from outside the acceptance region.

	$\tau_\mu\tau_\mu$	$\tau_\mu\tau_{h1}$	$\tau_\mu\tau_{h3}$	$\tau_e\tau_e$	$\tau_e\tau_{h1}$	$\tau_e\tau_{h3}$	$\tau_\mu\tau_e$
<b>acc, trk</b>	36089	69872	16763	29279	64155	15440	66122
<b>acc, trk, kine</b>	35885	69220	16489	18013	38690	9381	53711
<b>trk, kine</b>	36095	69862	16785	18237	39351	9615	54047
Migration into $\varepsilon_{\text{kine}}$ [%]	$0.58 \pm 0.04$	$0.92 \pm 0.04$	$1.77 \pm 0.10$	$1.23 \pm 0.08$	$1.68 \pm 0.07$	$2.44 \pm 0.16$	$0.62 \pm 0.03$
Effective $\varepsilon_{\text{kine}}$ [%]	$100.02 \pm 0.00$	$99.98 \pm 0.01$	$100.13 \pm 0.01$	$62.29 \pm 0.78$	$61.34 \pm 0.76$	$62.27 \pm 0.79$	$81.74 \pm 0.90$

## Appendix F. $Z \rightarrow \tau\tau$ Cross-section Measurement

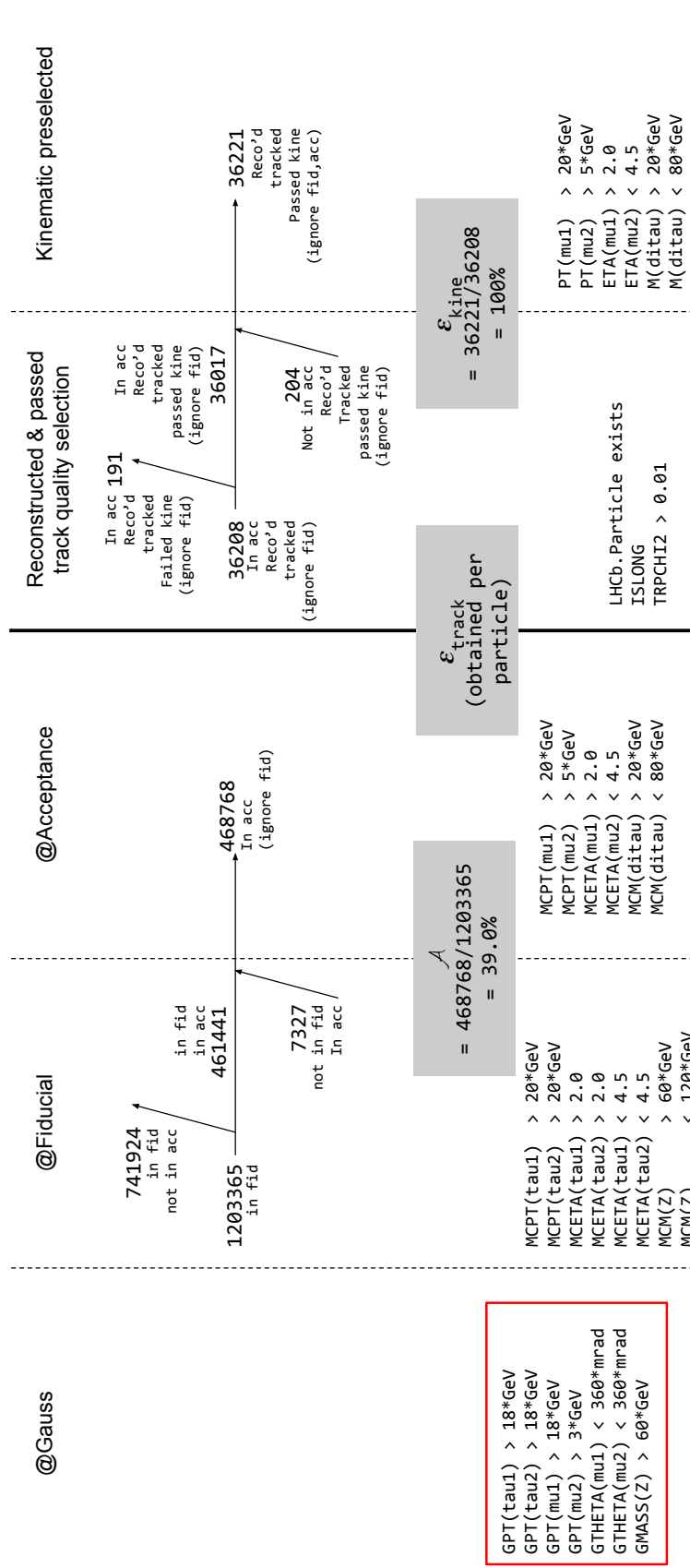


**Figure F.1** – Schematic representation of the migrations at relevant selection stages. The values from  $\tau_{\mu}\tau_{\mu}$  channel is shown here, where the values from other channels can be replaced by those found in Table F.1, and Table F.2.



# G Combining Cross-sections with Uncertainties

The uncertainties of the cross-section measurement is combined across all di-tau channels using the method of best linear unbiased estimator outlined in [132]. The computation is assisted by the python packages `pandas` [149] and `uncertainties` [150] which allows the manipulation of variables attached with uncertainty and correlation being tracked by their usages.

The summary of the correlation for each uncertainty terms is listed in Table G.1. The correlation matrices of the fully correlated and uncorrelated quantity can be represented as a  $7 \times 7$  identity matrix, and square matrix of ones respectively. The terms  $\mathcal{B}$ ,  $\varepsilon_{\text{rec}}$ ,  $\varepsilon_{\text{sel}}$  are partially correlated across channels, with their correlation matrices are also listed below. The order of rows and columns in the matrix is the following:  $\tau_\mu\tau_\mu$ ,  $\tau_\mu\tau_{h1}$ ,  $\tau_\mu\tau_{h3}$ ,  $\tau_e\tau_e$ ,  $\tau_e\tau_{h1}$ ,  $\tau_e\tau_{h3}$ ,  $\tau_\mu\tau_e$ . The correlation in  $\mathcal{B}$ ,  $\varepsilon_{\text{rec}}$  is dictated by the tau decay channel involved. The  $\varepsilon_{\text{rec}}$  is not factorized into a product of efficiencies as done in the previous analysis to ensure that the average of products is used consistently instead of the product of averages. For  $\varepsilon_{\text{sel}}$ , the correlation of systematic uncertainties is dictated by which selection cuts are common between each channel. The uncertainty from the size of the simulated samples is also included, but is completely uncorrelated between channels.

**Table G.1** – Summary of correlation across channels for each term in the cross-section computation, and their contributions to combined cross-section uncertainties.

Uncertainty	Correlation across channels	$\delta\sigma_{pp \rightarrow Z \rightarrow \tau\tau}$ [pb]	[%]
statistical	uncorrelated	2.13	2.24
luminosity	fully correlated	1.10	1.16
LHC beam	fully correlated	0.17	0.18
$\mathcal{B}$	corr( $\mathcal{B}$ )	0.26	0.27
$\mathcal{A}$	fully correlated	1.44	1.51
$\varepsilon_{\text{rec}}$	corr( $\varepsilon_{\text{rec}}$ )	2.41	2.53
$\varepsilon_{\text{sel}}$	corr( $\varepsilon_{\text{sel}}$ )	3.54	3.72
$N_{\text{sig}}$	uncorrelated	1.57	1.65

## Appendix G. Combining Cross-sections with Uncertainties

---

$$\text{corr}(\mathcal{B}) = \begin{pmatrix} 1 & 0.7878 & 0.4314 & 0 & 0 & 0 & 0.7155 \\ 0.7878 & 1 & 0.3399 & 0 & 0.3849 & 0 & 0.5637 \\ 0.4314 & 0.3399 & 1 & 0 & 0 & 0.8174 & 0.3087 \\ 0 & 0 & 0 & 1 & 0.7806 & 0.4231 & 0.6986 \\ 0 & 0.3849 & 0 & 0.7806 & 1 & 0.3303 & 0.5454 \\ 0 & 0 & 0.8174 & 0.4231 & 0.3303 & 1 & 0.2956 \\ 0.7155 & 0.5637 & 0.3087 & 0.6986 & 0.5454 & 0.2956 & 1 \end{pmatrix}$$

$$\text{corr}(\varepsilon_{\text{rec}}) = \begin{pmatrix} 1 & 0.7071 & 0.3955 & 0 & 0 & 0 & 0.5407 \\ 0.7071 & 1 & 0.7963 & 0.1556 & 0.2727 & 0.4257 & 0.5165 \\ 0.3955 & 0.7963 & 1 & 0.1685 & 0.3528 & 0.6285 & 0.3541 \\ 0 & 0.1556 & 0.1685 & 1 & 0.7548 & 0.6087 & 0.5912 \\ 0 & 0.2727 & 0.3528 & 0.7548 & 1 & 0.8093 & 0.4995 \\ 0 & 0.4257 & 0.6285 & 0.6087 & 0.8093 & 1 & 0.4152 \\ 0.5407 & 0.5165 & 0.3541 & 0.5912 & 0.4995 & 0.4152 & 1 \end{pmatrix}$$

$$\text{corr}(\varepsilon_{\text{sel}}) = \begin{pmatrix} 1 & 0.9164 & 0.6959 & 0.9238 & 0.9028 & 0.6358 & 0.7758 \\ 0.9164 & 1 & 0.7636 & 0.8847 & 0.9636 & 0.6982 & 0.8244 \\ 0.6959 & 0.7636 & 1 & 0.6694 & 0.7547 & 0.7755 & 0.9043 \\ 0.9238 & 0.8847 & 0.6694 & 1 & 0.8724 & 0.6130 & 0.7424 \\ 0.9028 & 0.9636 & 0.7547 & 0.8724 & 1 & 0.6908 & 0.8127 \\ 0.6358 & 0.6982 & 0.7755 & 0.6130 & 0.6908 & 1 & 0.8247 \\ 0.7758 & 0.8244 & 0.9043 & 0.7424 & 0.8127 & 0.8247 & 1 \end{pmatrix}$$

The covariance and correlation matrices from all uncertainties combined are

$$V = \text{cov}(\sigma) = \begin{pmatrix} 111.5182 & 30.2456 & 22.1989 & 33.8307 & 25.8508 & 19.3245 & 22.0803 \\ 30.2456 & 56.4879 & 26.6455 & 25.0313 & 24.6544 & 25.0151 & 18.5448 \\ 22.1989 & 26.6455 & 109.9349 & 19.4277 & 24.3388 & 38.9752 & 18.1980 \\ 33.8307 & 25.0313 & 19.4277 & 618.1798 & 40.4465 & 36.2090 & 23.2731 \\ 25.8508 & 24.6544 & 24.3388 & 40.4465 & 118.6728 & 47.8153 & 21.6196 \\ 19.3245 & 25.0151 & 38.9752 & 36.2090 & 47.8153 & 330.2145 & 22.6144 \\ 22.0803 & 18.5448 & 18.1980 & 23.2731 & 21.6196 & 22.6144 & 35.3756 \end{pmatrix}$$

$$\text{corr}(\sigma) = \begin{pmatrix} 1 & 0.3811 & 0.2005 & 0.1288 & 0.2247 & 0.1007 & 0.3515 \\ 0.3811 & 1 & 0.3381 & 0.1340 & 0.3011 & 0.1832 & 0.4149 \\ 0.2005 & 0.3381 & 1 & 0.0745 & 0.2131 & 0.2046 & 0.2918 \\ 0.1288 & 0.1340 & 0.0745 & 1 & 0.1493 & 0.0801 & 0.1574 \\ 0.2247 & 0.3011 & 0.2131 & 0.1493 & 1 & 0.2415 & 0.3337 \\ 0.1007 & 0.1832 & 0.2046 & 0.0801 & 0.2415 & 1 & 0.2092 \\ 0.3515 & 0.4149 & 0.2918 & 0.1574 & 0.3337 & 0.2092 & 1 \end{pmatrix}$$

The weights to each di-tau channel is  $\lambda = (U^T V^{-1} U)^{-1} (U^T V^{-1})$ , where  $U$  is the column vector of ones of length 7.

$$\lambda = (0.0497 \quad 0.2196 \quad 0.0850 \quad 0.0061 \quad 0.0568 \quad 0.0088 \quad 0.5739)$$

# H Generator-level $H \rightarrow \mu\tau$

The plots are from the generator-level  $H \rightarrow \mu\tau$ , using POWHEG-BOX inclusive production.

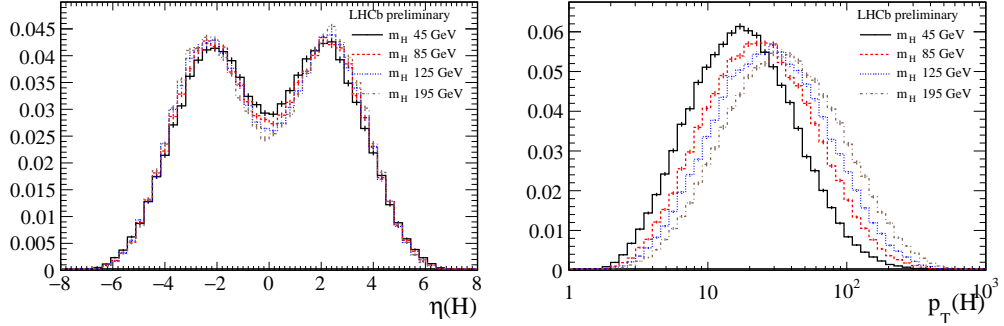


Figure H.1 –  $\eta$  and  $p_T$  distribution of Higgs-like boson.

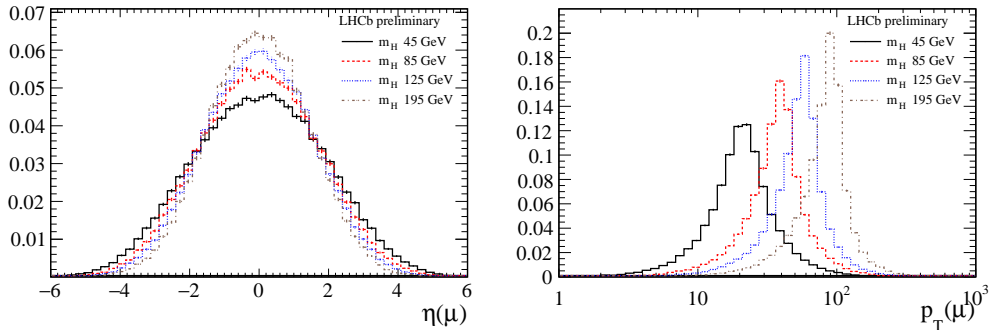


Figure H.2 –  $\eta$  and  $p_T$  distribution of prompt muon.

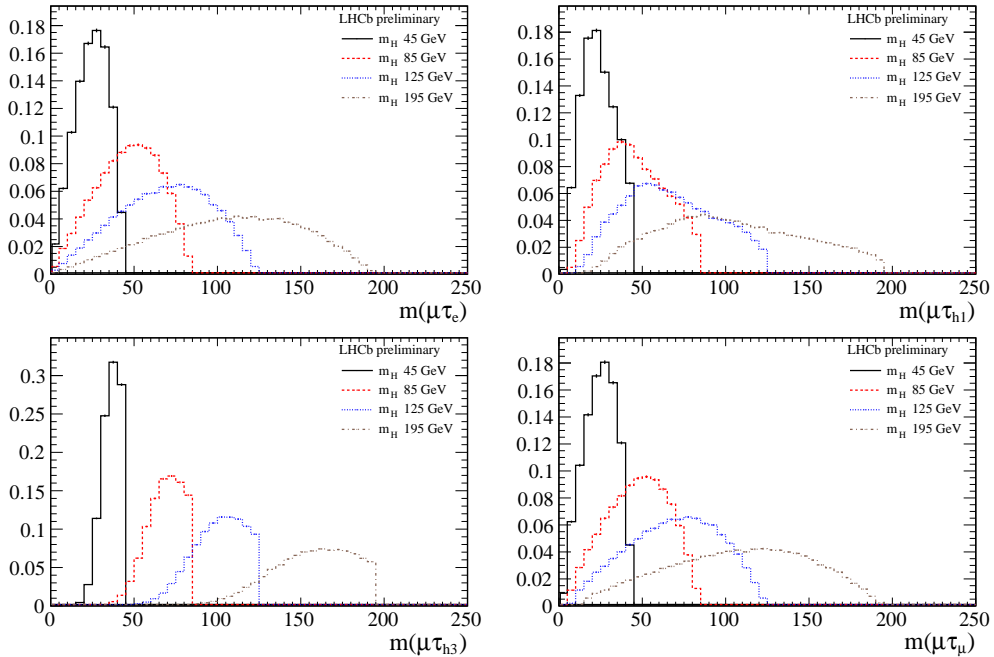


Figure H.3 – Invariant mass distributions of  $\mu\tau$  candidates from different channels

## Appendix H. Generator-level $H \rightarrow \mu\tau$

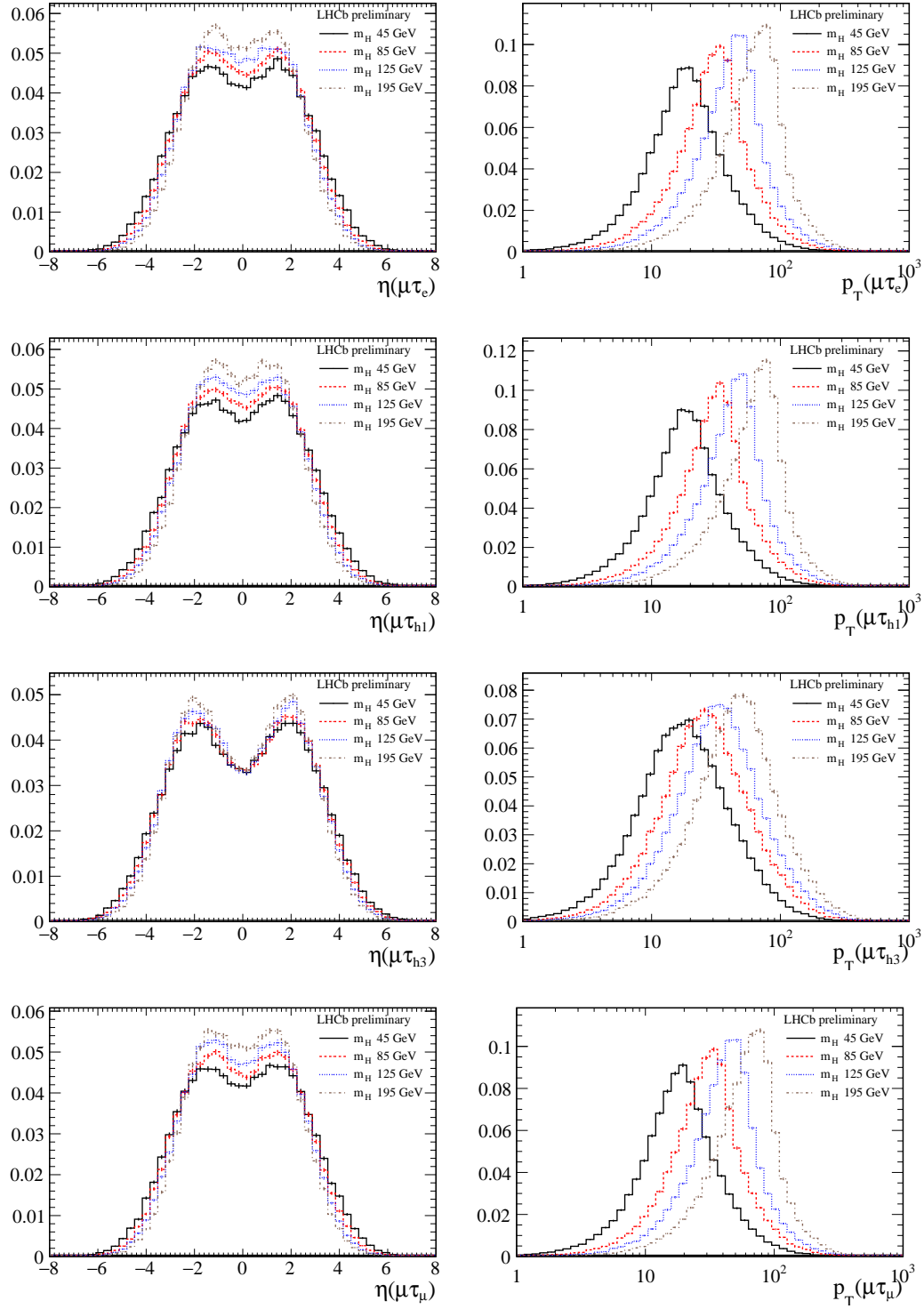


Figure H.4 –  $\eta$  and  $p_T$  distributions of  $\mu\tau$  candidates from different channels.

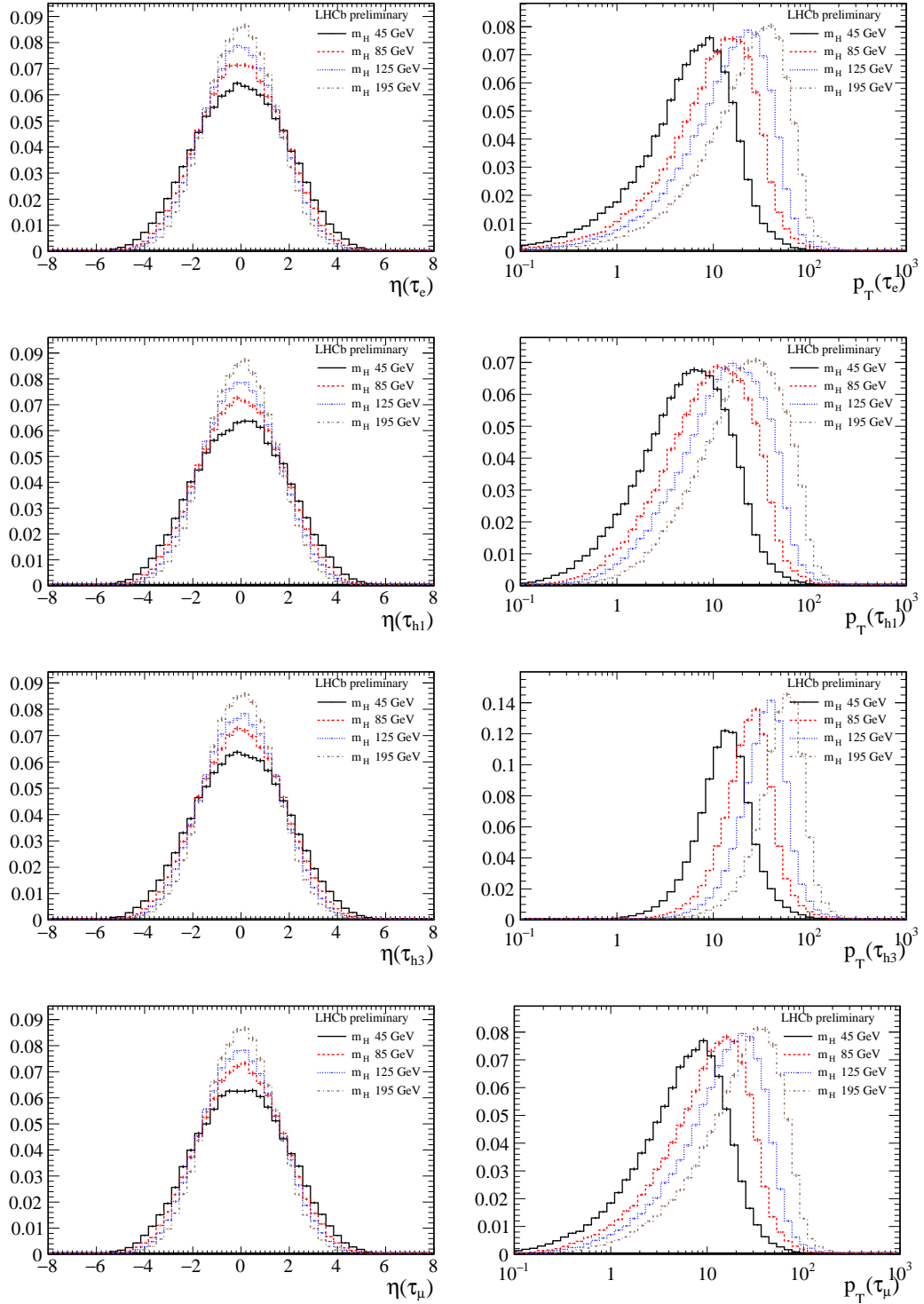


Figure H.5 –  $\eta$  and  $p_T$  distributions of  $\tau$  candidates from different channels.



# I Selection of $H \rightarrow \mu\tau$

These figures are obtained after the kinematic selections on  $p_T$ ,  $\eta$ ,  $m$ , as described in Section 12.3. The left column is Higgs signal at different  $m_H$ , the right column is different backgrounds.

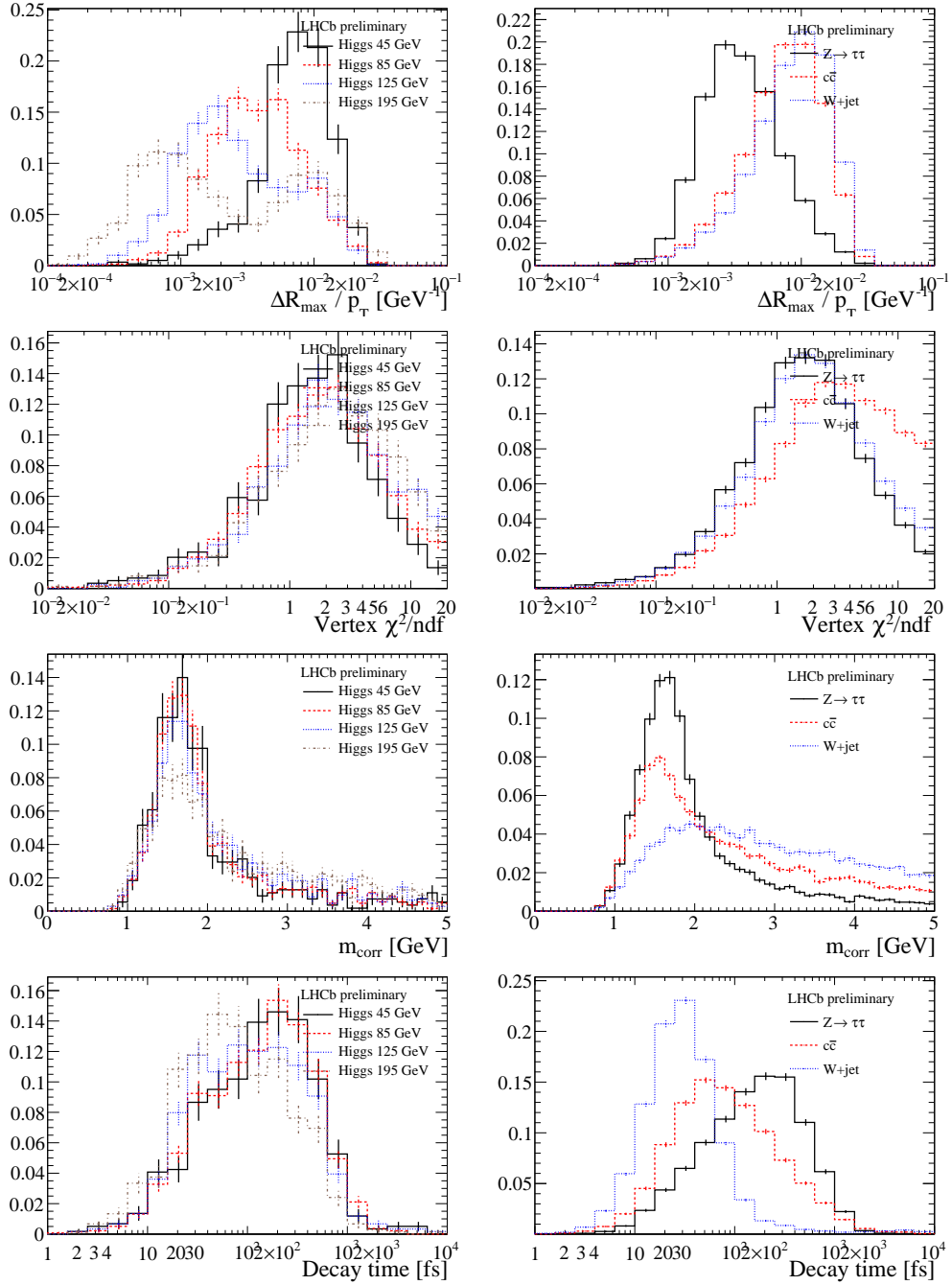


Figure I.1 –  $\tau_{h3}$  variables in  $\mu\tau_{h3}$

## Appendix I. Selection of $H \rightarrow \mu\tau$

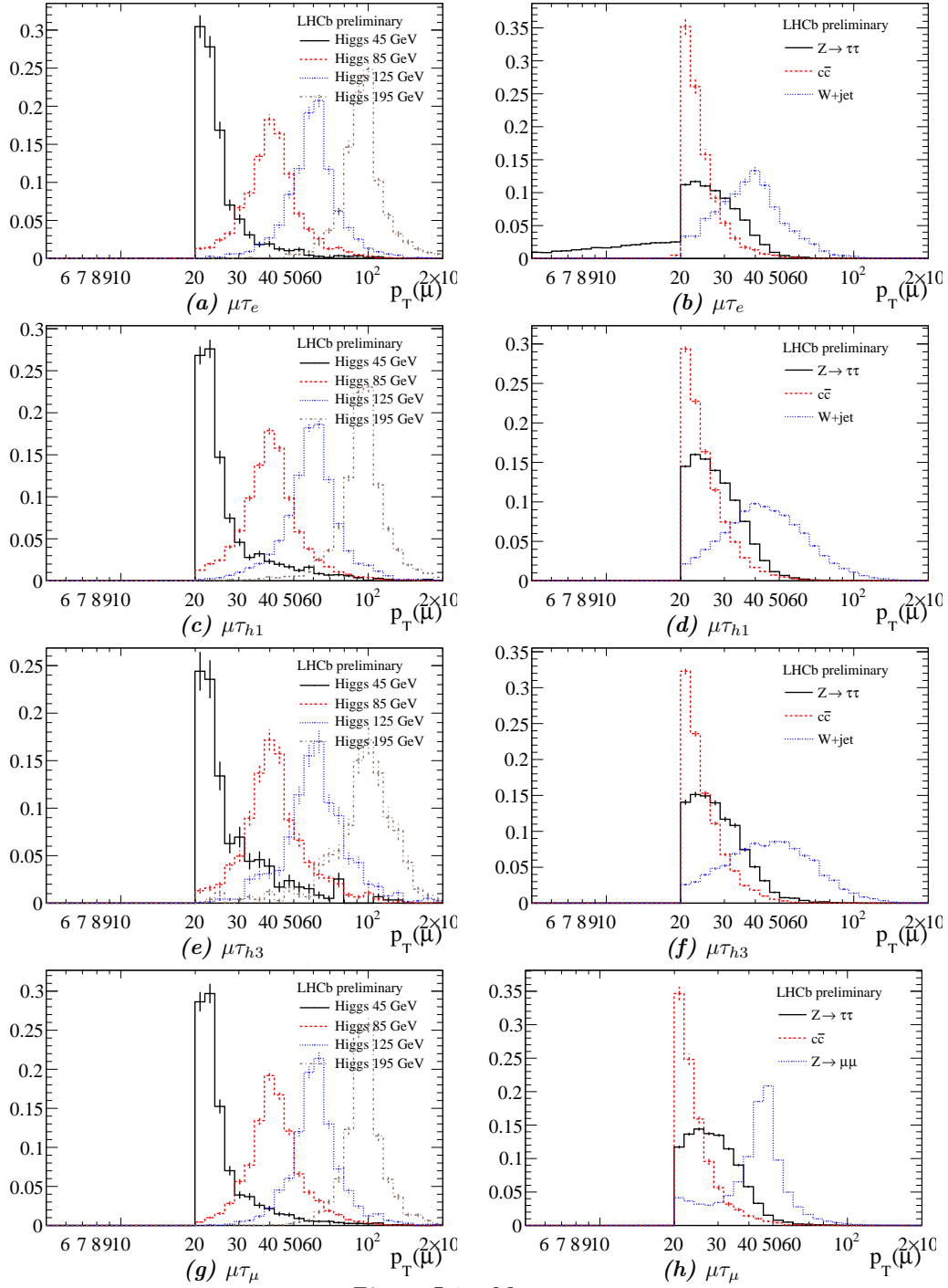


Figure I.2 – Muon  $p_T$



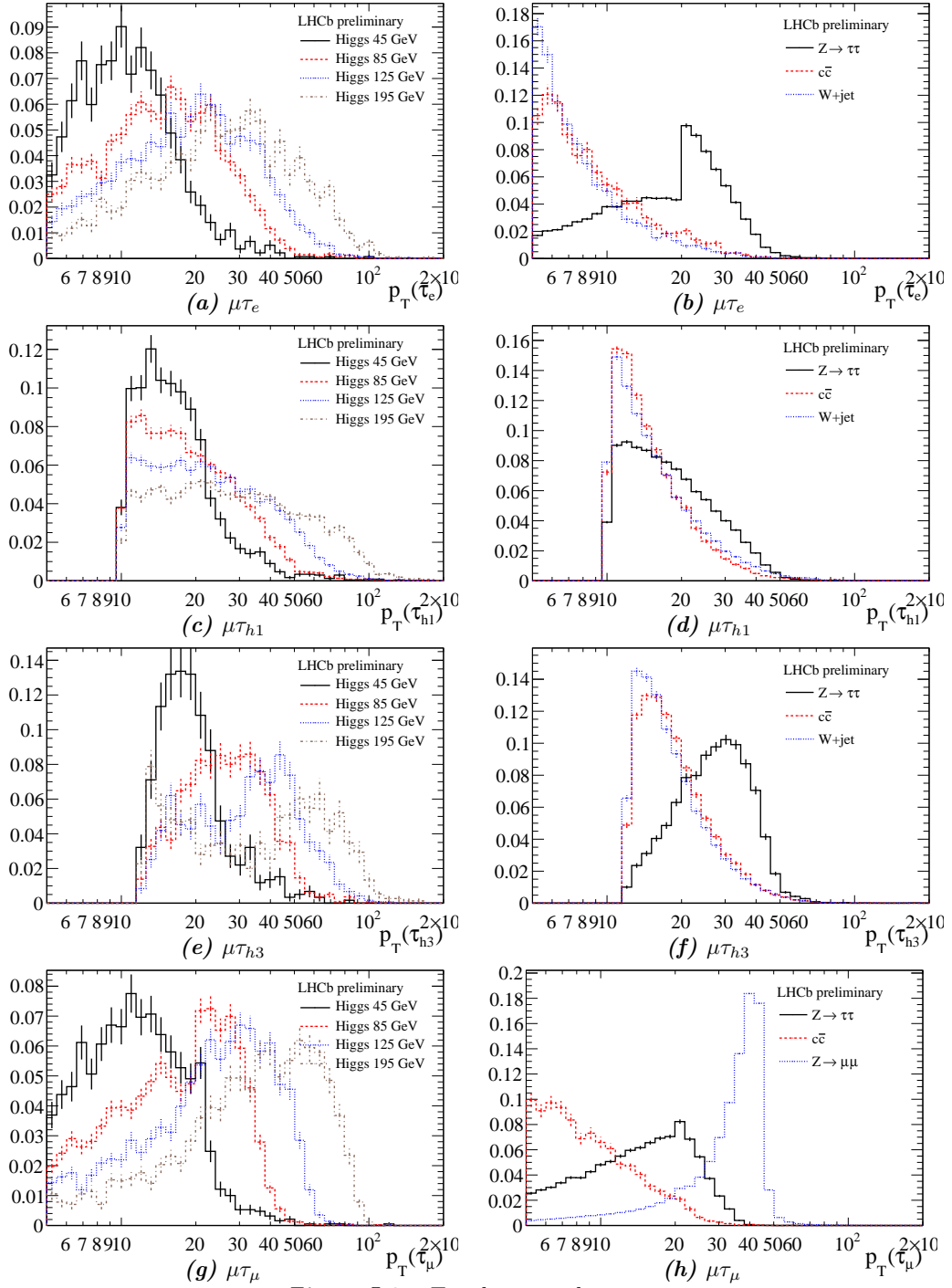
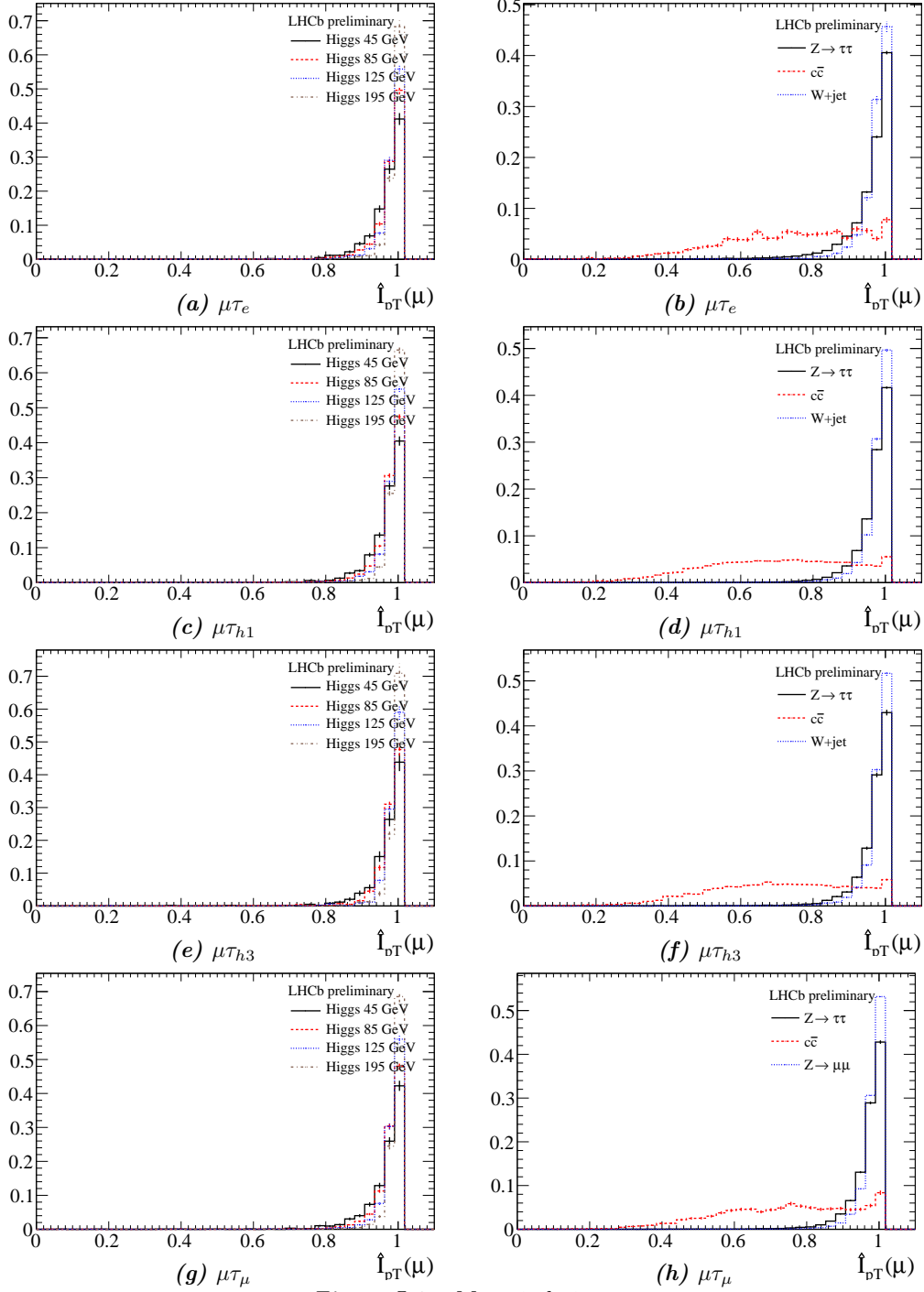


Figure I.3 – Tau decay product  $p_T$

## Appendix I. Selection of $H \rightarrow \mu\tau$



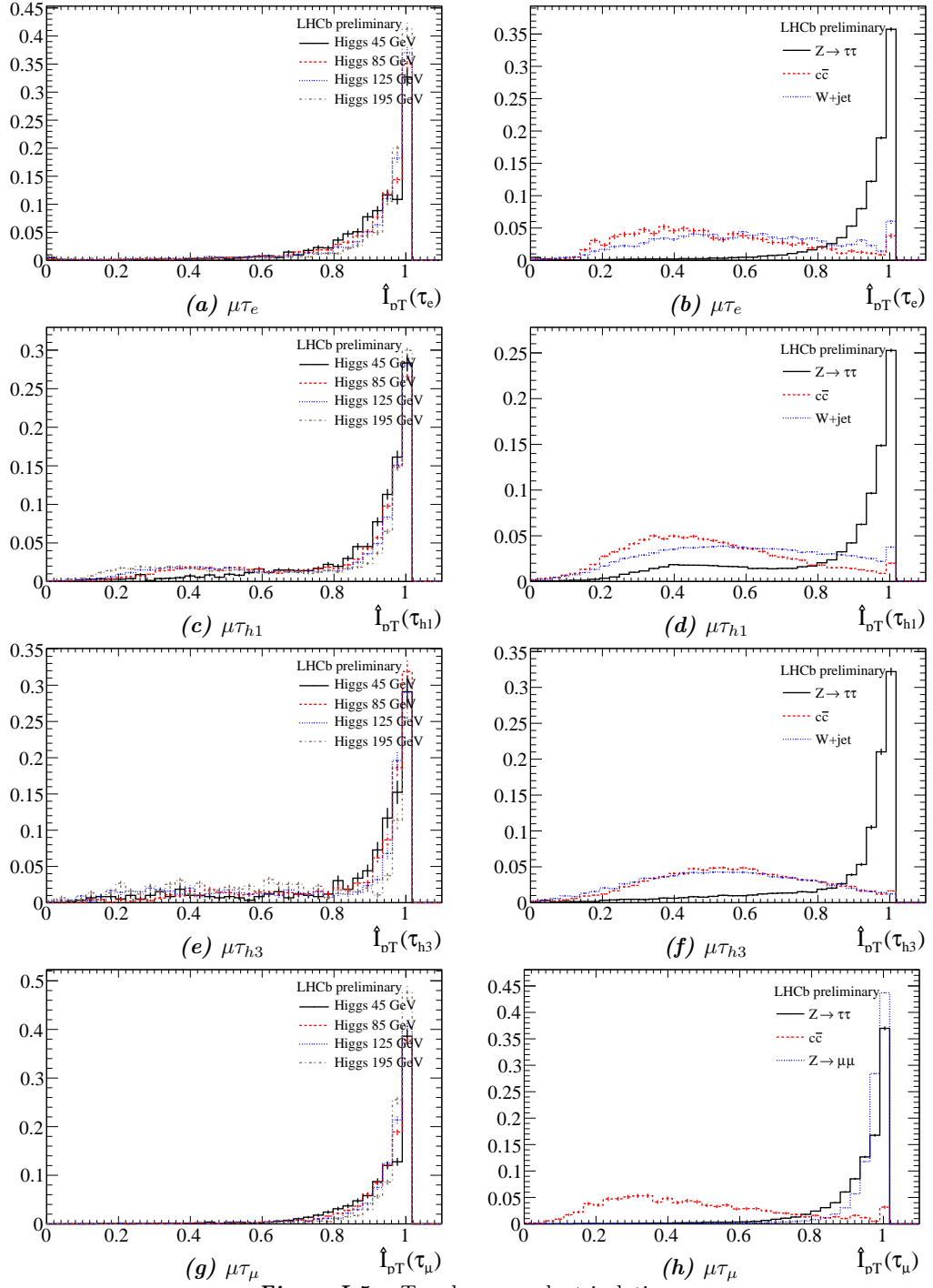
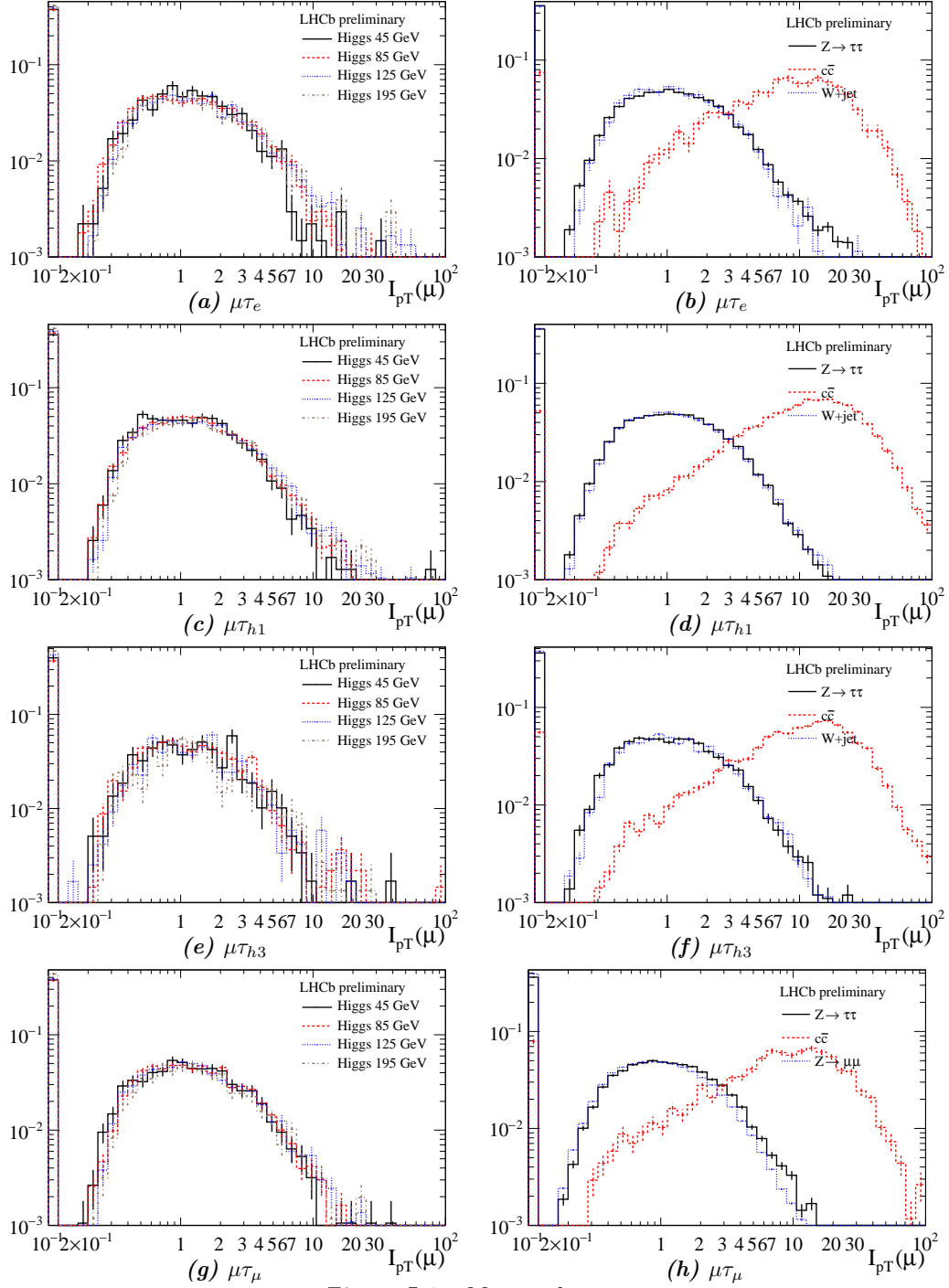


Figure 1.5 – Tau decay product isolation

## Appendix I. Selection of $H \rightarrow \mu\tau$



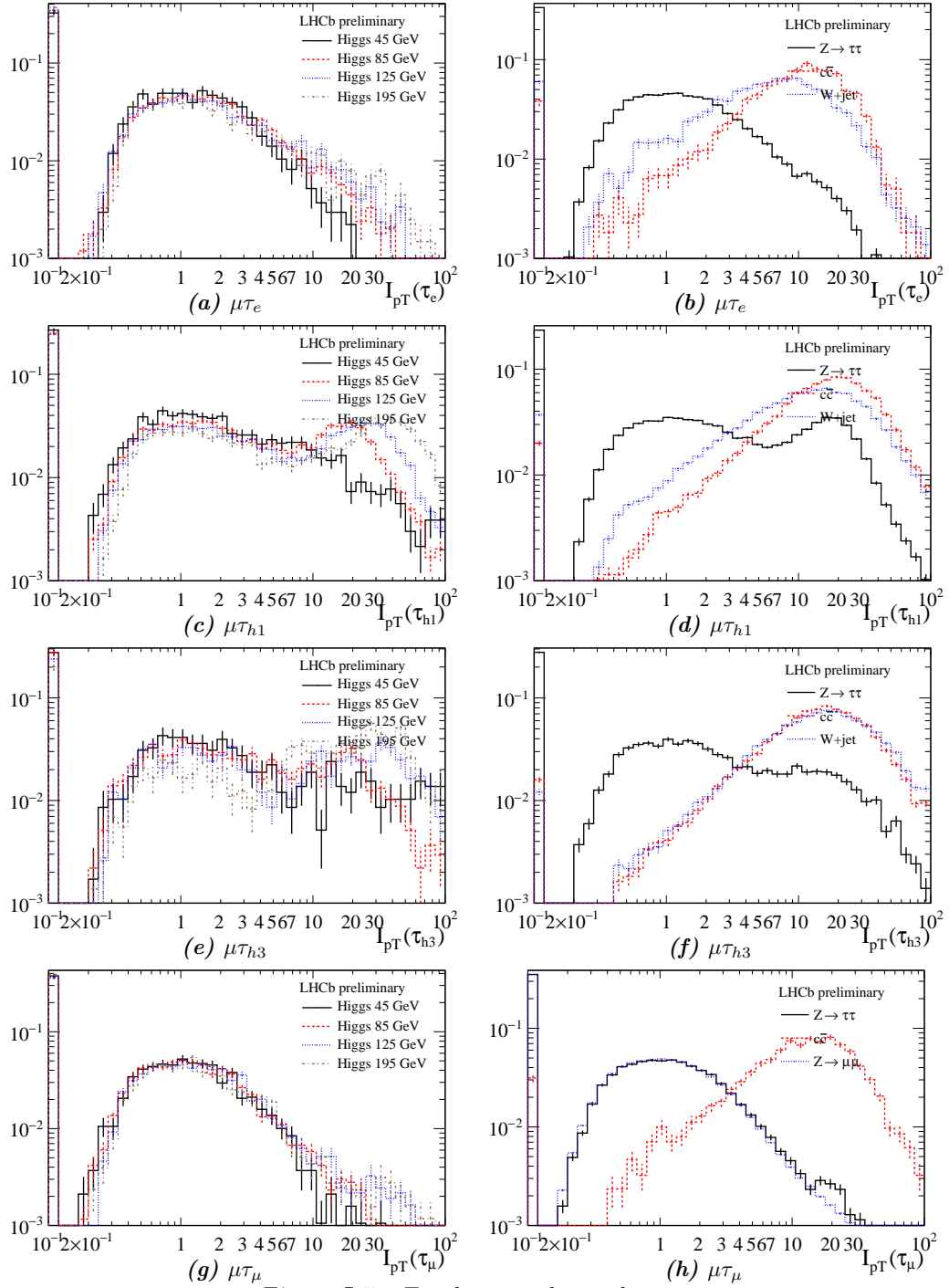


Figure I.7 – Tau decay product isolation

Appendix I. Selection of  $H \rightarrow \mu\tau$

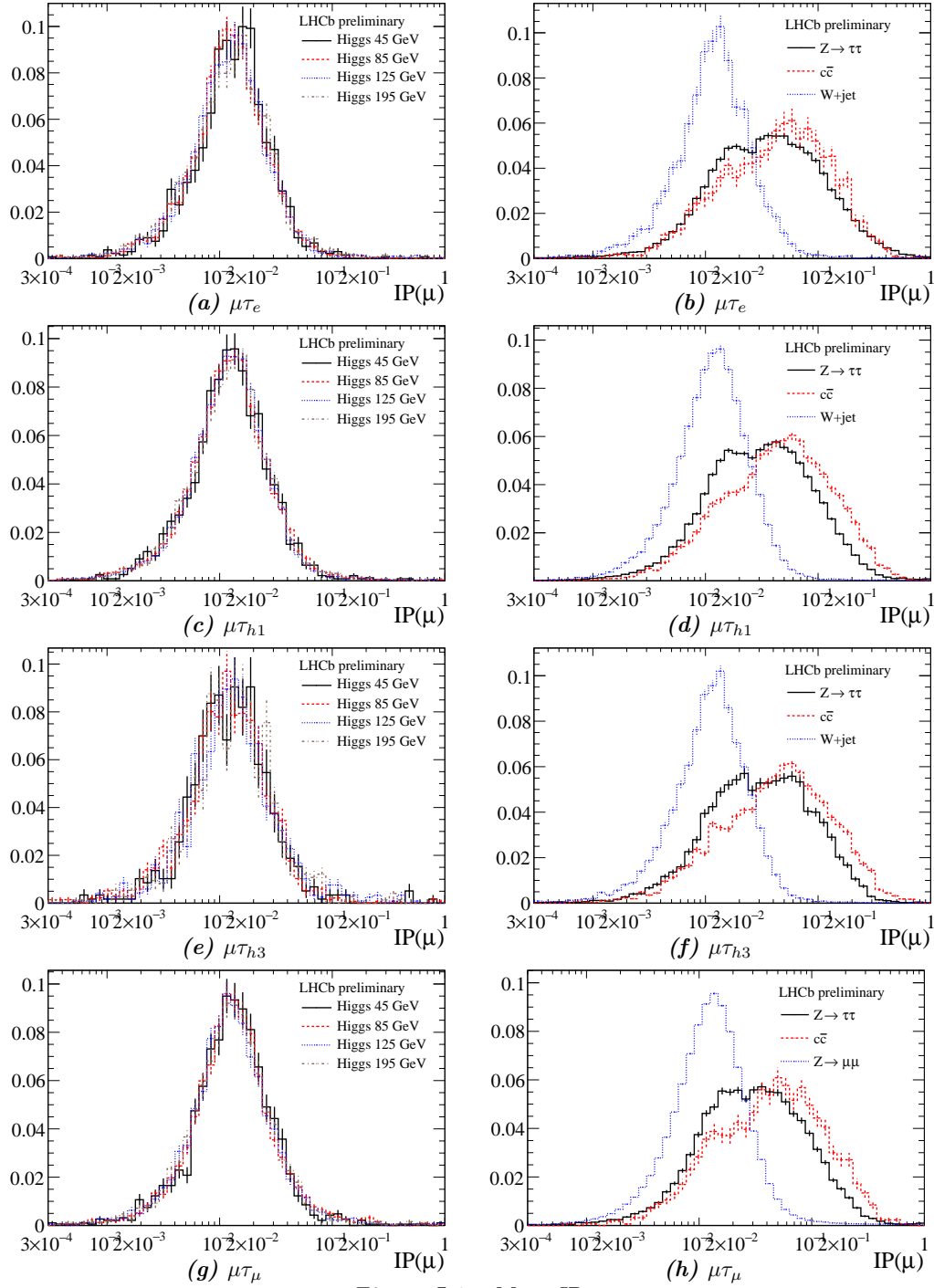


Figure I.8 – Muon IP

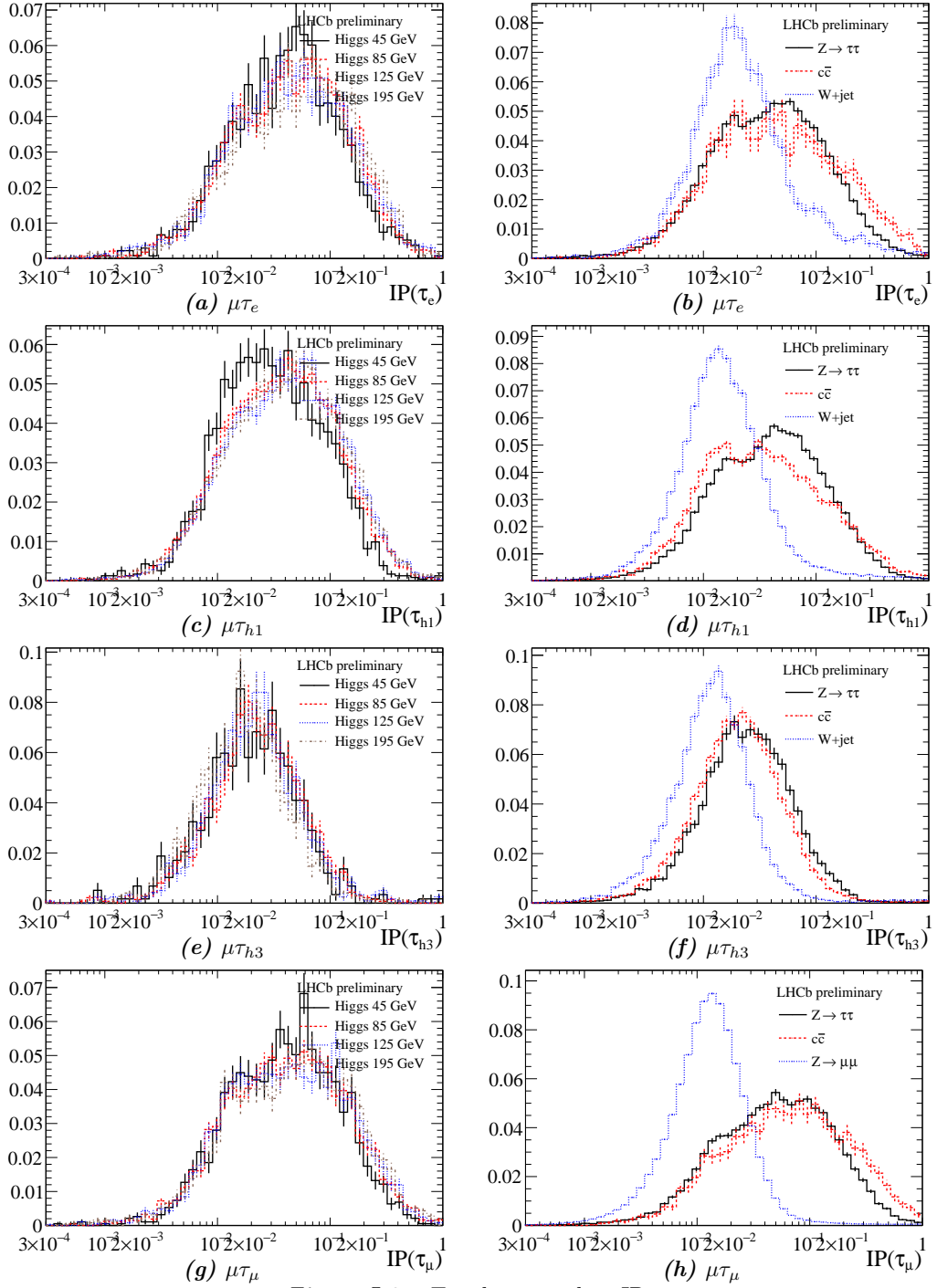


Figure I.9 – Tau decay product IP

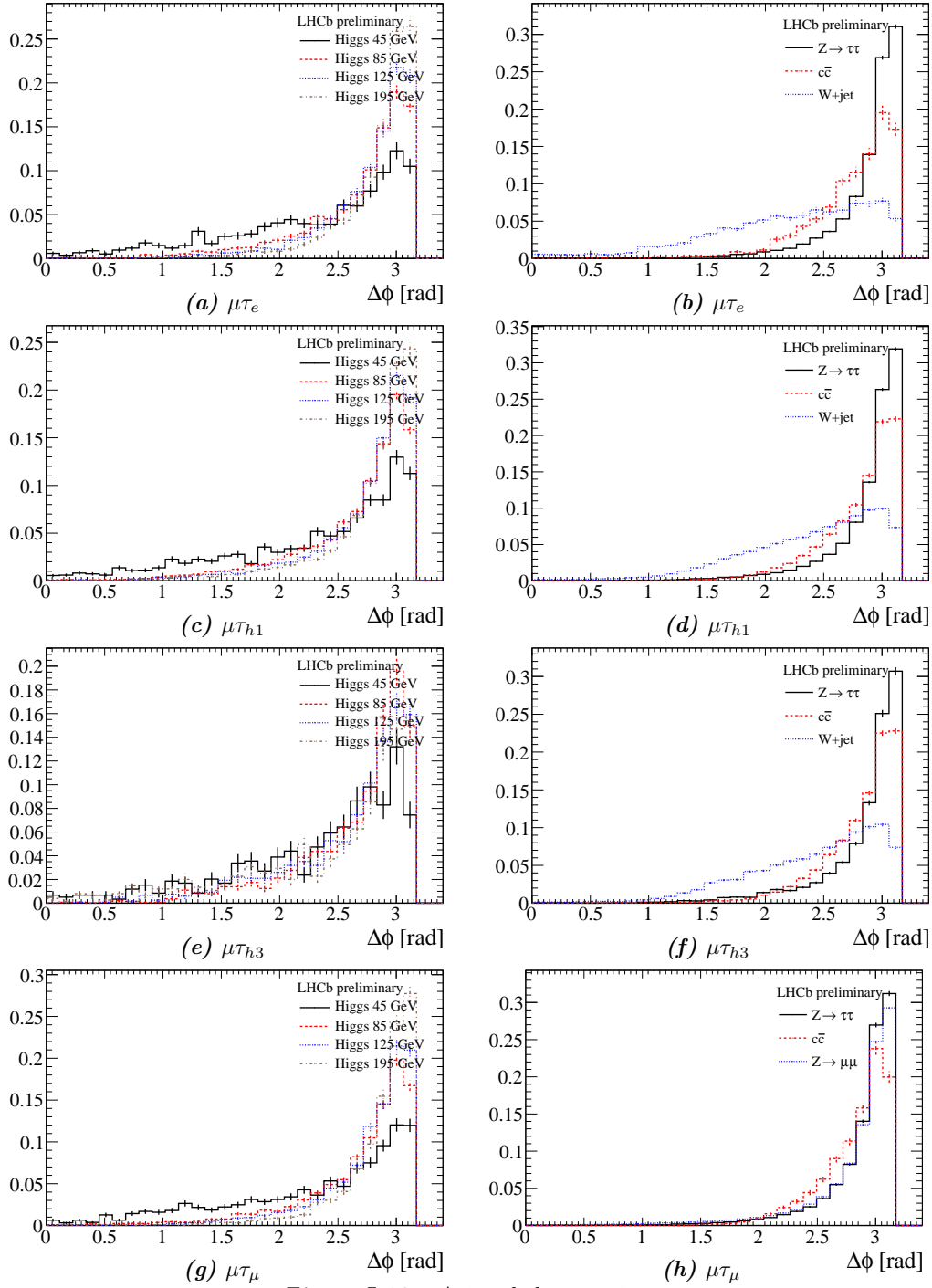


Figure I.10 – Azimuthal separation



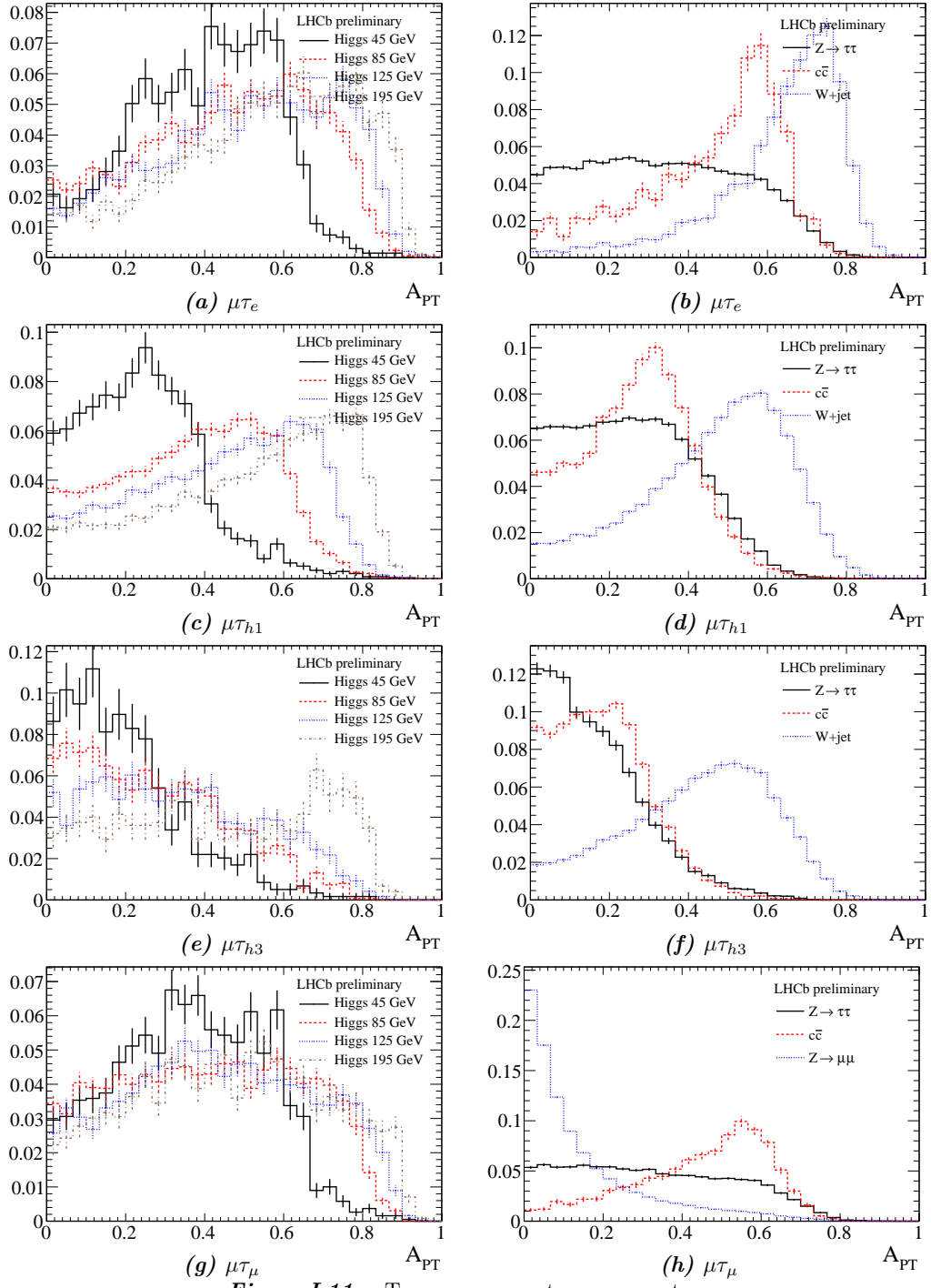


Figure I.11 – Transverse momentum asymmetry

## Appendix I. Selection of $H \rightarrow \mu\tau$

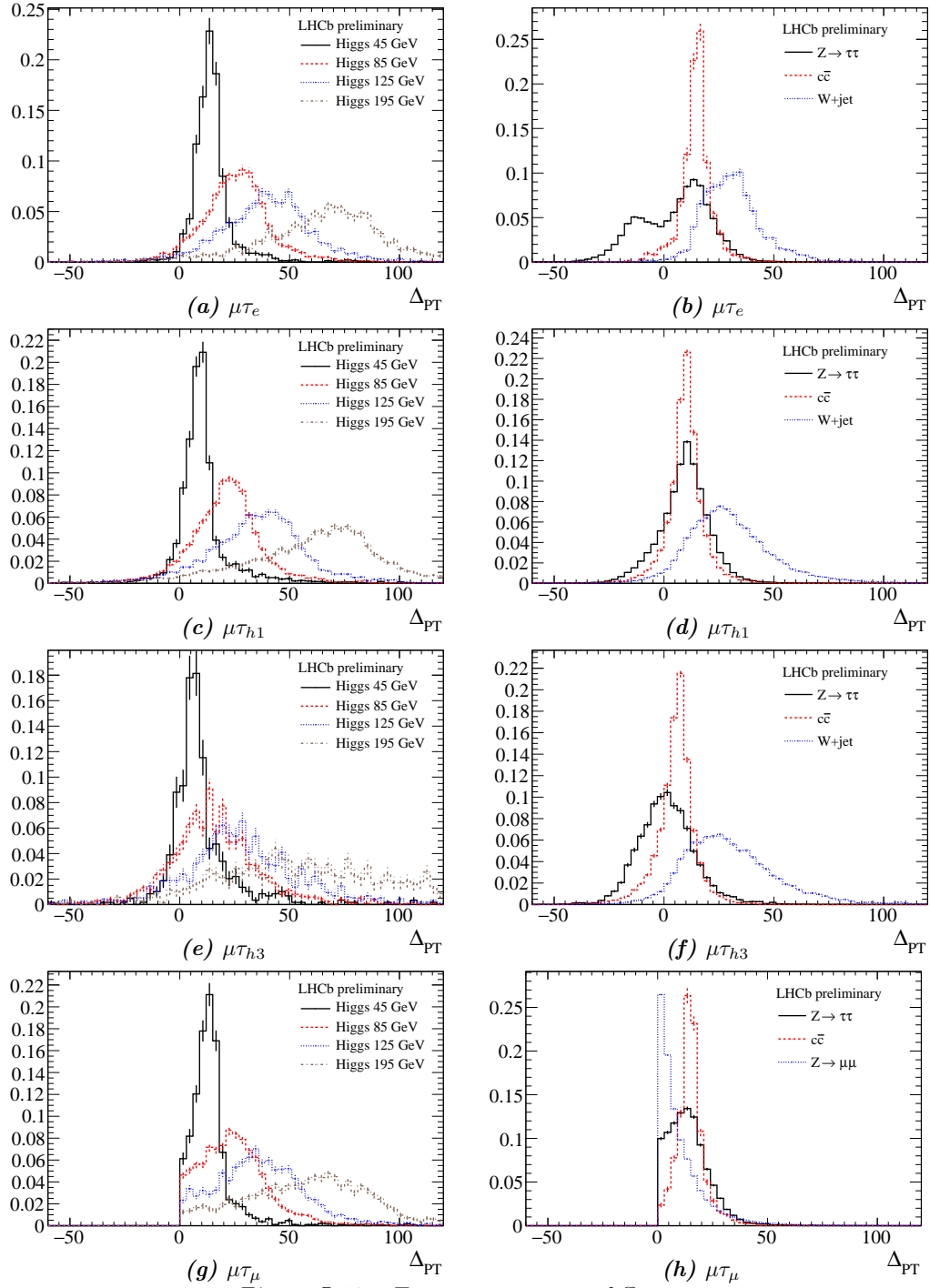


Figure I.12 – Transverse momentum difference

# J Background estimation of $H \rightarrow \mu\tau$

## J.1 Estimation from Simulation

Table J.1 – Opposite-sign low-mass selection

Process	ID	$\mu\tau_e$	$\mu\tau_{h1}$	$\mu\tau_{h3}$	$\mu\tau_\mu$
$t\bar{t}$	41900006	$0.7^{+0.1}_{-0.1}$ (97)	$0.5^{+0.1}_{-0.1}$ (63)	$0.2^{+0.0}_{-0.0}$ (24)	$0.1^{+0.0}_{-0.0}$ (9)
$t\bar{t}$	41900007	$0.8^{+0.1}_{-0.1}$ (250)	$0.4^{+0.0}_{-0.0}$ (118)	$0.1^{+0.0}_{-0.0}$ (39)	$0.2^{+0.0}_{-0.0}$ (56)
$t\bar{t}$	41900010	$0.2^{+0.0}_{-0.0}$ (62)	$0.4^{+0.1}_{-0.1}$ (140)	$0.4^{+0.1}_{-0.1}$ (129)	$1.0^{+0.2}_{-0.2}$ (325)
$WW \rightarrow \ell\ell\dots$	41922002	$2.8^{+0.1}_{-0.1}$ (629)	$0.0^{+0.0}_{-0.0}$ (1)	$0.0^{+0.0}_{-0.0}$ (0)	$0.0^{+0.0}_{-0.0}$ (2)
$WW \rightarrow \ell\dots$	42021000	$3.2^{+0.3}_{-0.3}$ (136)	$0.9^{+0.2}_{-0.2}$ (36)	$0.2^{+0.1}_{-0.1}$ (9)	$0.2^{+0.1}_{-0.1}$ (8)
$WZ \rightarrow \ell\dots$	42021001	$0.1^{+0.0}_{-0.0}$ (25)	$0.1^{+0.0}_{-0.0}$ (14)	$0.1^{+0.0}_{-0.0}$ (9)	$0.1^{+0.0}_{-0.0}$ (20)
$Z \rightarrow \tau\tau$	42100000	$226.8^{+6.9}_{-6.8}$ (1465)	$575.6^{+12.8}_{-12.7}$ (3718)	$120.6^{+4.8}_{-4.7}$ (779)	$124.2^{+4.9}_{-4.7}$ (802)
$Z \rightarrow \mu\mu$	42112011	$14.4^{+1.8}_{-1.6}$ (86)	$61.7^{+3.8}_{-3.7}$ (368)	$12.6^{+1.7}_{-1.5}$ (75)	$142.6^{+6.6}_{-6.4}$ (850)
$Z(\rightarrow\mu\mu) + \text{jet}$	42112022	$11.2^{+1.6}_{-1.4}$ (69)	$16.5^{+1.9}_{-1.7}$ (102)	$3.7^{+0.8}_{-0.8}$ (23)	$122.6^{+5.2}_{-5.8}$ (756)
$Z \rightarrow ee$	42122011	$2.8^{+3.7}_{-1.8}$ (2)	$0.0^{+2.6}_{-0.0}$ (0)	$0.0^{+2.6}_{-0.0}$ (0)	$0.0^{+2.6}_{-0.0}$ (0)
$Z \rightarrow b\bar{b}$	42150000	$0.1^{+0.3}_{-0.1}$ (1)	$0.1^{+0.3}_{-0.1}$ (1)	$0.0^{+0.2}_{-0.0}$ (0)	$0.1^{+0.3}_{-0.1}$ (1)
$W(\rightarrow\tau\nu_\tau) + \text{jet}$	42300010	$0.0^{+5.2}_{-0.0}$ (0)	$14.1^{+3.6}_{-6.1}$ (5)	$0.0^{+0.0}_{-0.0}$ (0)	$0.0^{+5.2}_{-0.0}$ (0)
$W(\rightarrow\mu\nu_\mu) + \text{jet}$	42311011	$13.5^{+3.6}_{-2.9}$ (22)	$155.0^{+11.4}_{-10.9}$ (253)	$46.6^{+6.1}_{-5.5}$ (76)	$4.9^{+2.4}_{-1.7}$ (8)
$W(\rightarrow\mu\nu_\mu) + \text{jet}(\rightarrow\mu\dots)$	42311012	$0.0^{+0.1}_{-0.0}$ (0)	$0.0^{+0.1}_{-0.0}$ (0)	$0.0^{+0.1}_{-0.0}$ (0)	$4.9^{+0.4}_{-0.4}$ (175)
$W \rightarrow e\nu_e$	42321000	$0.0^{+0.0}_{-0.0}$ (0)	$0.0^{+0.0}_{-0.0}$ (0)	$0.0^{+0.0}_{-0.0}$ (0)	$0.0^{+0.0}_{-0.0}$ (0)
$W(\rightarrow e\nu_e) + \text{jet}$	42321010	$0.0^{+6.4}_{-0.0}$ (0)	$0.0^{+6.4}_{-0.0}$ (0)	$0.0^{+6.4}_{-0.0}$ (0)	$0.0^{+6.4}_{-0.0}$ (0)
$c\bar{c} \rightarrow \mu\dots$	49011004	$7.4^{+2.6}_{-2.0}$ (15)	$19.3^{+4.1}_{-3.6}$ (39)	$18.8^{+4.1}_{-3.6}$ (38)	$2.0^{+1.6}_{-1.0}$ (4)
$b\bar{b} \rightarrow \mu\dots$	49011005	$7.7^{+7.5}_{-4.2}$ (3)	$20.6^{+10.2}_{-7.2}$ (8)	$15.5^{+9.2}_{-6.2}$ (6)	$28.3^{+11.4}_{-8.5}$ (11)
$c\bar{c} \rightarrow e\dots$	49021004	$0.5^{+1.1}_{-0.4}$ (1)	$0.0^{+0.9}_{-0.0}$ (0)	$0.0^{+0.9}_{-0.0}$ (0)	$0.0^{+0.9}_{-0.0}$ (0)
$b\bar{b} \rightarrow e\dots$	49021005	$2.6^{+6.0}_{-2.2}$ (1)	$0.0^{+4.8}_{-0.0}$ (0)	$0.0^{+4.8}_{-0.0}$ (0)	$0.0^{+4.8}_{-0.0}$ (0)
Data		472	1284	240	344

Table J.2 – Same-sign low-mass selection

Process	ID	$\mu\tau_e$	$\mu\tau_{h1}$	$\mu\tau_{h3}$	$\mu\tau_\mu$
$t\bar{t}$	41900006	$0.0^{+0.0}_{-0.0}$ (0)	$0.0^{+0.0}_{-0.0}$ (0)	$0.0^{+0.0}_{-0.0}$ (0)	$0.0^{+0.0}_{-0.0}$ (0)
$t\bar{t}$	41900007	$0.0^{+0.0}_{-0.0}$ (0)	$0.0^{+0.0}_{-0.0}$ (0)	$0.0^{+0.0}_{-0.0}$ (0)	$0.0^{+0.0}_{-0.0}$ (0)
$t\bar{t}$	41900010	$0.0^{+0.0}_{-0.0}$ (0)	$0.0^{+0.0}_{-0.0}$ (0)	$0.0^{+0.0}_{-0.0}$ (0)	$0.0^{+0.0}_{-0.0}$ (0)
$WW \rightarrow \ell\ell\dots$	41922002	$0.0^{+0.0}_{-0.0}$ (0)	$0.0^{+0.0}_{-0.0}$ (0)	$0.0^{+0.0}_{-0.0}$ (0)	$0.0^{+0.0}_{-0.0}$ (0)
$WW \rightarrow \ell\dots$	42021000	$0.0^{+0.0}_{-0.0}$ (0)	$0.0^{+0.0}_{-0.0}$ (0)	$0.0^{+0.0}_{-0.0}$ (0)	$0.0^{+0.0}_{-0.0}$ (0)
$WZ \rightarrow \ell\dots$	42021001	$0.0^{+0.0}_{-0.0}$ (0)	$0.0^{+0.0}_{-0.0}$ (0)	$0.0^{+0.0}_{-0.0}$ (0)	$0.0^{+0.0}_{-0.0}$ (0)
$Z \rightarrow \tau\tau$	42100000	$1.7^{+0.7}_{-0.5}$ (11)	$0.5^{+0.5}_{-0.3}$ (3)	$0.5^{+0.5}_{-0.3}$ (3)	$0.0^{+0.3}_{-0.0}$ (0)
$Z \rightarrow \mu\mu$	42112011	$9.4^{+1.5}_{-1.3}$ (56)	$57.5^{+3.7}_{-3.5}$ (343)	$11.6^{+1.6}_{-1.4}$ (69)	$2.7^{+0.9}_{-0.7}$ (16)
$Z(\rightarrow\mu\mu) + \text{jet}$	42112022	$11.7^{+1.6}_{-1.4}$ (72)	$14.6^{+1.8}_{-1.6}$ (90)	$6.2^{+1.2}_{-1.0}$ (38)	$3.1^{+0.9}_{-0.7}$ (19)
$Z \rightarrow ee$	42122011	$0.0^{+2.6}_{-0.0}$ (0)	$0.0^{+2.6}_{-0.0}$ (0)	$0.0^{+2.6}_{-0.0}$ (0)	$0.0^{+2.6}_{-0.0}$ (0)
$Z \rightarrow b\bar{b}$	42150000	$0.0^{+0.2}_{-0.0}$ (0)	$0.0^{+0.2}_{-0.0}$ (0)	$0.0^{+0.2}_{-0.0}$ (0)	$0.0^{+0.2}_{-0.0}$ (0)
$W(\rightarrow\tau\nu_\tau) + \text{jet}$	42300010	$0.0^{+5.2}_{-0.0}$ (0)	$2.8^{+6.5}_{-2.3}$ (1)	$0.0^{+5.2}_{-0.0}$ (0)	$0.0^{+5.2}_{-0.0}$ (0)
$W(\rightarrow\mu\nu_\mu) + \text{jet}$	42311011	$6.7^{+2.7}_{-2.0}$ (11)	$41.0^{+5.8}_{-5.2}$ (67)	$20.2^{+4.2}_{-3.6}$ (33)	$0.6^{+1.4}_{-0.5}$ (1)
$W(\rightarrow\mu\nu_\mu) + \text{jet}(\rightarrow\mu\dots)$	42311012	$0.0^{+0.1}_{-0.0}$ (0)	$0.0^{+0.1}_{-0.0}$ (0)	$0.0^{+0.1}_{-0.0}$ (0)	$2.3^{+0.3}_{-0.3}$ (83)
$W \rightarrow e\nu_e$	42321000	$0.0^{+1.7}_{-0.0}$ (0)	$0.0^{+1.7}_{-0.0}$ (0)	$0.0^{+1.7}_{-0.0}$ (0)	$0.0^{+1.7}_{-0.0}$ (0)
$W(\rightarrow e\nu_e) + \text{jet}$	42321010	$0.0^{+6.4}_{-0.0}$ (0)	$0.0^{+6.4}_{-0.0}$ (0)	$0.0^{+6.4}_{-0.0}$ (0)	$0.0^{+6.4}_{-0.0}$ (0)
$c\bar{c} \rightarrow \mu\dots$	49011004	$1.5^{+1.5}_{-0.8}$ (3)	$10.9^{+3.1}_{-2.6}$ (22)	$5.4^{+2.3}_{-1.7}$ (11)	$0.0^{+0.9}_{-0.0}$ (0)
$b\bar{b} \rightarrow \mu\dots$	49011005	$2.6^{+5.9}_{-2.1}$ (1)	$12.9^{+8.7}_{-5.6}$ (5)	$2.6^{+5.9}_{-2.1}$ (1)	$5.2^{+6.8}_{-3.3}$ (2)
$c\bar{c} \rightarrow e\dots$	49021004	$0.5^{+1.1}_{-0.4}$ (1)	$0.0^{+0.9}_{-0.0}$ (0)	$0.0^{+0.9}_{-0.0}$ (0)	$0.0^{+0.9}_{-0.0}$ (0)
$b\bar{b} \rightarrow e\dots$	49021005	$0.0^{+4.8}_{-0.0}$ (0)	$0.0^{+4.8}_{-0.0}$ (0)	$0.0^{+4.8}_{-0.0}$ (0)	$0.0^{+4.8}_{-0.0}$ (0)
Data		78	509	115	25

## Appendix J. Background estimation of $H \rightarrow \mu\tau$

**Table J.3** – Opposite-sign central selection

Process	ID	$\mu\tau_e$	$\mu\tau_{h1}$	$\mu\tau_{h3}$	$\mu\tau_\mu$
$t\bar{t}$	41900006	$0.9^{+0.1}_{-0.1}$ (119)	$0.4^{+0.1}_{-0.1}$ (57)	$0.2^{+0.0}_{-0.0}$ (23)	$0.1^{+0.0}_{-0.0}$ (9)
$t\bar{t}$	41900007	$1.1^{+0.1}_{-0.1}$ (347)	$0.5^{+0.0}_{-0.0}$ (155)	$0.1^{+0.0}_{-0.0}$ (40)	$0.2^{+0.0}_{-0.0}$ (56)
$t\bar{t}$	41900010	$0.4^{+0.1}_{-0.1}$ (144)	$0.6^{+0.1}_{-0.1}$ (202)	$0.4^{+0.1}_{-0.1}$ (127)	$1.2^{+0.2}_{-0.2}$ (385)
$WW \rightarrow \ell\ell\dots$	41922002	$3.2^{+0.1}_{-0.1}$ (715)	$0.0^{+0.0}_{-0.0}$ (2)	$0.0^{+0.0}_{-0.0}$ (0)	$0.0^{+0.0}_{-0.0}$ (3)
$WW \rightarrow \ell\dots$	42021000	$3.2^{+0.3}_{-0.3}$ (135)	$1.4^{+0.2}_{-0.2}$ (60)	$0.2^{+0.1}_{-0.1}$ (9)	$0.2^{+0.1}_{-0.1}$ (8)
$WZ \rightarrow \ell\dots$	42021001	$0.2^{+0.0}_{-0.0}$ (33)	$0.1^{+0.0}_{-0.0}$ (17)	$0.0^{+0.0}_{-0.0}$ (6)	$0.1^{+0.0}_{-0.0}$ (24)
$Z \rightarrow \tau\tau$	42100000	$114.1^{+4.7}_{-4.5}$ (737)	$242.0^{+7.2}_{-7.1}$ (1563)	$54.6^{+3.2}_{-3.0}$ (353)	$58.7^{+3.3}_{-3.1}$ (379)
$Z \rightarrow \mu\mu$	42112011	$19.1^{+2.0}_{-1.9}$ (114)	$49.5^{+3.4}_{-3.2}$ (295)	$6.9^{+1.3}_{-1.1}$ (41)	$112.2^{+5.6}_{-5.4}$ (669)
$Z(\rightarrow\mu\mu) + \text{jet}$	42112022	$20.3^{+2.1}_{-1.9}$ (125)	$29.5^{+2.5}_{-2.4}$ (182)	$4.5^{+1.0}_{-0.9}$ (28)	$138.0^{+6.4}_{-6.3}$ (851)
$Z \rightarrow ee$	42122011	$2.8^{+3.7}_{-1.8}$ (2)	$0.0^{+2.6}_{-0.0}$ (0)	$0.0^{+2.6}_{-0.0}$ (0)	$0.0^{+2.6}_{-0.0}$ (0)
$Z \rightarrow b\bar{b}$	42150000	$0.0^{+0.2}_{-0.0}$ (0)	$0.0^{+0.2}_{-0.0}$ (0)	$0.0^{+0.2}_{-0.0}$ (0)	$0.0^{+0.2}_{-0.0}$ (0)
$W(\rightarrow \tau\nu_\tau) + \text{jet}$	42300010	$0.0^{+5.2}_{-0.0}$ (0)	$28.3^{+12.1}_{-8.8}$ (10)	$0.0^{+5.2}_{-0.0}$ (0)	$0.0^{+5.2}_{-0.0}$ (0)
$W(\rightarrow \mu\nu_\mu) + \text{jet}$	42311011	$39.2^{+5.7}_{-5.0}$ (64)	$245.6^{+15.0}_{-14.4}$ (401)	$33.7^{+5.3}_{-4.6}$ (55)	$3.7^{+1.5}_{-1.5}$ (6)
$W(\rightarrow \mu\nu_\mu) + \text{jet}(\rightarrow \mu\dots)$	42311012	$0.0^{+0.1}_{-0.0}$ (0)	$0.0^{+0.1}_{-0.0}$ (0)	$0.0^{+0.1}_{-0.0}$ (0)	$4.4^{+0.4}_{-0.4}$ (158)
$W \rightarrow e\nu_e$	42321000	$0.0^{+1.7}_{-0.0}$ (0)	$0.0^{+1.7}_{-0.0}$ (0)	$0.0^{+1.7}_{-0.0}$ (0)	$0.0^{+1.7}_{-0.0}$ (0)
$W(\rightarrow e\nu_e) + \text{jet}$	42321010	$0.0^{+6.4}_{-0.0}$ (0)	$0.0^{+6.4}_{-0.0}$ (0)	$0.0^{+6.4}_{-0.0}$ (0)	$0.0^{+6.4}_{-0.0}$ (0)
$c\bar{c} \rightarrow \mu\dots$	49011004	$1.5^{+1.5}_{-0.8}$ (3)	$5.4^{+2.3}_{-1.7}$ (11)	$2.5^{+1.7}_{-1.1}$ (5)	$0.5^{+1.1}_{-0.4}$ (1)
$b\bar{b} \rightarrow \mu\dots$	49011005	$0.0^{+4.7}_{-0.0}$ (0)	$5.2^{+6.8}_{-3.3}$ (2)	$0.0^{+4.7}_{-0.0}$ (0)	$0.0^{+4.7}_{-0.0}$ (0)
$c\bar{c} \rightarrow e\dots$	49021004	$0.0^{+0.9}_{-0.0}$ (0)	$0.0^{+0.9}_{-0.0}$ (0)	$0.0^{+0.9}_{-0.0}$ (0)	$0.0^{+0.9}_{-0.0}$ (0)
$b\bar{b} \rightarrow e\dots$	49021005	$0.0^{+4.8}_{-0.0}$ (0)	$0.0^{+4.8}_{-0.0}$ (0)	$0.0^{+4.8}_{-0.0}$ (0)	$0.0^{+4.8}_{-0.0}$ (0)
Data		296	679	123	235

**Table J.4** – Same-sign central selection

Process	ID	$\mu\tau_e$	$\mu\tau_{h1}$	$\mu\tau_{h3}$	$\mu\tau_\mu$
$t\bar{t}$	41900006	$0.0^{+0.0}_{-0.0}$ (0)	$0.0^{+0.0}_{-0.0}$ (0)	$0.0^{+0.0}_{-0.0}$ (0)	$0.0^{+0.0}_{-0.0}$ (0)
$t\bar{t}$	41900007	$0.0^{+0.0}_{-0.0}$ (0)	$0.0^{+0.0}_{-0.0}$ (0)	$0.0^{+0.0}_{-0.0}$ (0)	$0.0^{+0.0}_{-0.0}$ (0)
$t\bar{t}$	41900010	$0.0^{+0.0}_{-0.0}$ (0)	$0.0^{+0.0}_{-0.0}$ (0)	$0.0^{+0.0}_{-0.0}$ (0)	$0.0^{+0.0}_{-0.0}$ (0)
$WW \rightarrow \ell\ell\dots$	41922002	$0.0^{+0.0}_{-0.0}$ (0)	$0.0^{+0.0}_{-0.0}$ (0)	$0.0^{+0.0}_{-0.0}$ (0)	$0.0^{+0.0}_{-0.0}$ (0)
$WW \rightarrow \ell\dots$	42021000	$0.0^{+0.0}_{-0.0}$ (0)	$0.0^{+0.0}_{-0.0}$ (0)	$0.0^{+0.0}_{-0.0}$ (0)	$0.0^{+0.0}_{-0.0}$ (0)
$WZ \rightarrow \ell\dots$	42021001	$0.0^{+0.0}_{-0.0}$ (0)	$0.0^{+0.0}_{-0.0}$ (0)	$0.0^{+0.0}_{-0.0}$ (0)	$0.0^{+0.0}_{-0.0}$ (0)
$Z \rightarrow \tau\tau$	42100000	$0.6^{+0.5}_{-0.3}$ (4)	$0.3^{+0.4}_{-0.2}$ (2)	$0.2^{+0.4}_{-0.1}$ (1)	$0.0^{+0.3}_{-0.0}$ (0)
$Z \rightarrow \mu\mu$	42112011	$14.6^{+1.8}_{-1.6}$ (87)	$43.8^{+3.2}_{-3.0}$ (261)	$7.2^{+1.3}_{-1.1}$ (43)	$2.0^{+0.8}_{-0.6}$ (12)
$Z(\rightarrow\mu\mu) + \text{jet}$	42112022	$19.5^{+2.0}_{-1.9}$ (120)	$29.5^{+2.5}_{-2.4}$ (182)	$3.7^{+1.0}_{-0.8}$ (23)	$3.2^{+0.9}_{-0.7}$ (20)
$Z \rightarrow ee$	42122011	$0.0^{+2.6}_{-0.0}$ (0)	$0.0^{+2.6}_{-0.0}$ (0)	$0.0^{+2.6}_{-0.0}$ (0)	$0.0^{+2.6}_{-0.0}$ (0)
$Z \rightarrow b\bar{b}$	42150000	$0.0^{+0.2}_{-0.0}$ (0)	$0.0^{+0.2}_{-0.0}$ (0)	$0.0^{+0.2}_{-0.0}$ (0)	$0.0^{+0.2}_{-0.0}$ (0)
$W(\rightarrow \tau\nu_\tau) + \text{jet}$	42300010	$0.0^{+5.2}_{-0.0}$ (0)	$0.0^{+5.2}_{-0.0}$ (0)	$0.0^{+5.2}_{-0.0}$ (0)	$0.0^{+5.2}_{-0.0}$ (0)
$W(\rightarrow \mu\nu_\mu) + \text{jet}$	42311011	$45.3^{+6.1}_{-5.4}$ (74)	$58.2^{+6.8}_{-6.2}$ (95)	$16.5^{+3.9}_{-3.2}$ (27)	$0.0^{+1.1}_{-0.0}$ (0)
$W(\rightarrow \mu\nu_\mu) + \text{jet}(\rightarrow \mu\dots)$	42311012	$0.0^{+0.1}_{-0.0}$ (0)	$0.0^{+0.1}_{-0.0}$ (0)	$0.0^{+0.1}_{-0.0}$ (0)	$2.0^{+0.3}_{-0.2}$ (71)
$W \rightarrow e\nu_e$	42321000	$0.9^{+2.2}_{-0.8}$ (1)	$0.0^{+1.7}_{-0.0}$ (0)	$0.0^{+1.7}_{-0.0}$ (0)	$0.0^{+1.7}_{-0.0}$ (0)
$W(\rightarrow e\nu_e) + \text{jet}$	42321010	$0.0^{+6.4}_{-0.0}$ (0)	$0.0^{+6.4}_{-0.0}$ (0)	$0.0^{+6.4}_{-0.0}$ (0)	$0.0^{+6.4}_{-0.0}$ (0)
$c\bar{c} \rightarrow \mu\dots$	49011004	$0.5^{+1.1}_{-0.4}$ (1)	$1.5^{+1.5}_{-0.8}$ (3)	$0.0^{+0.9}_{-0.0}$ (0)	$0.0^{+0.9}_{-0.0}$ (0)
$b\bar{b} \rightarrow \mu\dots$	49011005	$2.6^{+5.9}_{-2.1}$ (1)	$2.6^{+5.9}_{-2.1}$ (1)	$0.0^{+4.7}_{-0.0}$ (0)	$0.0^{+4.7}_{-0.0}$ (0)
$c\bar{c} \rightarrow e\dots$	49021004	$0.0^{+0.9}_{-0.0}$ (0)	$0.0^{+0.9}_{-0.0}$ (0)	$0.0^{+0.9}_{-0.0}$ (0)	$0.0^{+0.9}_{-0.0}$ (0)
$b\bar{b} \rightarrow e\dots$	49021005	$0.0^{+4.8}_{-0.0}$ (0)	$0.0^{+4.8}_{-0.0}$ (0)	$0.0^{+4.8}_{-0.0}$ (0)	$0.0^{+4.8}_{-0.0}$ (0)
Data		64	219	47	11

Table J.5 – Opposite-sign high-mass selection

Process	ID	$\mu\mathcal{T}_e$	$\mu\mathcal{T}_{h1}$	$\mu\mathcal{T}_{h3}$	$\mu\mathcal{T}_\mu$
$t\bar{t}$	41900006	$0.4^{+0.1}_{-0.1}$ (59)	$0.2^{+0.0}_{-0.0}$ (29)	$0.1^{+0.0}_{-0.0}$ (14)	$0.1^{+0.0}_{-0.0}$ (7)
$t\bar{t}$	41900007	$0.7^{+0.1}_{-0.1}$ (200)	$0.3^{+0.0}_{-0.0}$ (102)	$0.1^{+0.0}_{-0.0}$ (25)	$0.1^{+0.0}_{-0.0}$ (31)
$t\bar{t}$	41900010	$0.1^{+0.0}_{-0.0}$ (19)	$0.3^{+0.1}_{-0.1}$ (105)	$0.2^{+0.0}_{-0.0}$ (71)	$0.7^{+0.1}_{-0.1}$ (212)
$WW \rightarrow \ell\ell\dots$	41922002	$2.0^{+0.0}_{-0.1}$ (455)	$0.0^{+0.0}_{-0.0}$ (2)	$0.0^{+0.0}_{-0.0}$ (0)	$0.0^{+0.0}_{-0.0}$ (0)
$WW \rightarrow \ell\dots$	42021000	$1.6^{+0.2}_{-0.2}$ (68)	$0.9^{+0.2}_{-0.1}$ (39)	$0.1^{+0.1}_{-0.0}$ (4)	$0.1^{+0.1}_{-0.0}$ (4)
$WZ \rightarrow \ell\dots$	42021001	$0.1^{+0.0}_{-0.0}$ (16)	$0.1^{+0.0}_{-0.0}$ (11)	$0.0^{+0.0}_{-0.0}$ (2)	$0.1^{+0.0}_{-0.0}$ (13)
$Z \rightarrow \tau\tau$	42100000	$3.4^{+0.9}_{-0.7}$ (22)	$22.9^{+2.1}_{-1.9}$ (148)	$7.1^{+1.2}_{-1.1}$ (46)	$1.2^{+0.6}_{-0.4}$ (8)
$Z \rightarrow \mu\mu$	42112011	$2.2^{+0.8}_{-0.6}$ (13)	$21.0^{+2.1}_{-2.0}$ (125)	$3.2^{+0.9}_{-0.7}$ (19)	$32.0^{+2.7}_{-2.5}$ (191)
$Z(\rightarrow\mu\mu) + \text{jet}$	42112022	$2.3^{+0.8}_{-0.5}$ (14)	$18.6^{+2.0}_{-1.8}$ (115)	$3.4^{+0.9}_{-0.7}$ (21)	$31.5^{+2.6}_{-2.4}$ (194)
$Z \rightarrow ee$	42122011	$1.4^{+3.5}_{-1.2}$ (1)	$0.0^{+2.5}_{-0.0}$ (0)	$0.0^{+2.5}_{-0.0}$ (0)	$0.0^{+2.5}_{-0.0}$ (0)
$Z \rightarrow b\bar{b}$	42150000	$0.0^{+0.2}_{-0.0}$ (0)	$0.0^{+0.2}_{-0.0}$ (0)	$0.0^{+0.2}_{-0.0}$ (0)	$0.0^{+0.2}_{-0.0}$ (0)
$W(\rightarrow\tau\nu_\tau) + \text{jet}$	42300010	$0.0^{+5.2}_{-0.0}$ (0)	$14.1^{+9.6}_{-6.1}$ (5)	$0.0^{+5.2}_{-0.0}$ (0)	$0.0^{+5.2}_{-0.0}$ (0)
$W(\rightarrow\mu\nu_\mu) + \text{jet}$	42311011	$2.5^{+1.9}_{-1.2}$ (4)	$124.4^{+10.1}_{-9.5}$ (203)	$18.4^{+4.0}_{-3.4}$ (30)	$0.6^{+1.4}_{-0.5}$ (1)
$W(\rightarrow\mu\nu_\mu) + \text{jet}(\rightarrow\mu\dots)$	42311012	$0.0^{+0.1}_{-0.0}$ (0)	$0.0^{+0.1}_{-0.0}$ (0)	$0.0^{+0.1}_{-0.0}$ (0)	$1.5^{+0.2}_{-0.0}$ (55)
$W \rightarrow e\nu_e$	42321000	$0.0^{+1.7}_{-0.0}$ (0)	$0.0^{+1.7}_{-0.0}$ (0)	$0.0^{+1.7}_{-0.0}$ (0)	$0.0^{+1.7}_{-0.0}$ (0)
$W(\rightarrow e\nu_e) + \text{jet}$	42321010	$0.0^{+6.4}_{-0.0}$ (0)	$0.0^{+6.4}_{-0.0}$ (0)	$0.0^{+6.4}_{-0.0}$ (0)	$0.0^{+6.4}_{-0.0}$ (0)
$c\bar{c} \rightarrow \mu\dots$	49011004	$0.5^{+1.1}_{-0.4}$ (1)	$0.0^{+0.9}_{-0.0}$ (0)	$0.5^{+1.1}_{-0.4}$ (1)	$0.0^{+0.9}_{-0.0}$ (0)
$b\bar{b} \rightarrow \mu\dots$	49011005	$0.0^{+4.7}_{-0.0}$ (0)	$0.0^{+4.7}_{-0.0}$ (0)	$0.0^{+4.7}_{-0.0}$ (0)	$0.0^{+4.7}_{-0.0}$ (0)
$c\bar{c} \rightarrow e\dots$	49021004	$0.0^{+0.9}_{-0.0}$ (0)	$0.0^{+0.9}_{-0.0}$ (0)	$0.0^{+0.9}_{-0.0}$ (0)	$0.0^{+0.9}_{-0.0}$ (0)
$b\bar{b} \rightarrow e\dots$	49021005	$0.0^{+4.8}_{-0.0}$ (0)	$0.0^{+4.8}_{-0.0}$ (0)	$0.0^{+4.8}_{-0.0}$ (0)	$0.0^{+4.8}_{-0.0}$ (0)
Data		27	184	37	39

Table J.6 – Same-sign high-mass selection

Process	ID	$\mu\mathcal{T}_e$	$\mu\mathcal{T}_{h1}$	$\mu\mathcal{T}_{h3}$	$\mu\mathcal{T}_\mu$
$t\bar{t}$	41900006	$0.0^{+0.0}_{-0.0}$ (0)	$0.0^{+0.0}_{-0.0}$ (0)	$0.0^{+0.0}_{-0.0}$ (0)	$0.0^{+0.0}_{-0.0}$ (0)
$t\bar{t}$	41900007	$0.0^{+0.0}_{-0.0}$ (0)	$0.0^{+0.0}_{-0.0}$ (0)	$0.0^{+0.0}_{-0.0}$ (0)	$0.0^{+0.0}_{-0.0}$ (0)
$t\bar{t}$	41900010	$0.0^{+0.0}_{-0.0}$ (0)	$0.0^{+0.0}_{-0.0}$ (0)	$0.0^{+0.0}_{-0.0}$ (0)	$0.0^{+0.0}_{-0.0}$ (0)
$WW \rightarrow \ell\ell\dots$	41922002	$0.0^{+0.0}_{-0.0}$ (0)	$0.0^{+0.0}_{-0.0}$ (0)	$0.0^{+0.0}_{-0.0}$ (0)	$0.0^{+0.0}_{-0.0}$ (0)
$WW \rightarrow \ell\dots$	42021000	$0.0^{+0.0}_{-0.0}$ (0)	$0.0^{+0.0}_{-0.0}$ (0)	$0.0^{+0.0}_{-0.0}$ (0)	$0.0^{+0.0}_{-0.0}$ (0)
$WZ \rightarrow \ell\dots$	42021001	$0.0^{+0.0}_{-0.0}$ (0)	$0.0^{+0.0}_{-0.0}$ (0)	$0.0^{+0.0}_{-0.0}$ (0)	$0.0^{+0.0}_{-0.0}$ (0)
$Z \rightarrow \tau\tau$	42100000	$0.0^{+0.3}_{-0.0}$ (0)	$0.0^{+0.3}_{-0.0}$ (0)	$0.0^{+0.3}_{-0.0}$ (0)	$0.0^{+0.3}_{-0.0}$ (0)
$Z \rightarrow \mu\mu$	42112011	$1.3^{+0.7}_{-0.5}$ (8)	$17.8^{+2.0}_{-1.8}$ (106)	$3.9^{+1.0}_{-0.8}$ (23)	$0.8^{+0.6}_{-0.4}$ (5)
$Z(\rightarrow\mu\mu) + \text{jet}$	42112022	$2.1^{+0.8}_{-0.6}$ (13)	$17.8^{+1.9}_{-1.8}$ (110)	$1.8^{+0.7}_{-0.5}$ (11)	$0.8^{+0.5}_{-0.4}$ (5)
$Z \rightarrow ee$	42122011	$0.0^{+2.6}_{-0.0}$ (0)	$0.0^{+2.6}_{-0.0}$ (0)	$0.0^{+2.6}_{-0.0}$ (0)	$0.0^{+2.6}_{-0.0}$ (0)
$Z \rightarrow b\bar{b}$	42150000	$0.0^{+0.2}_{-0.0}$ (0)	$0.0^{+0.2}_{-0.0}$ (0)	$0.0^{+0.2}_{-0.0}$ (0)	$0.0^{+0.2}_{-0.0}$ (0)
$W(\rightarrow\tau\nu_\tau) + \text{jet}$	42300010	$0.0^{+5.2}_{-0.0}$ (0)	$0.0^{+5.2}_{-0.0}$ (0)	$0.0^{+5.2}_{-0.0}$ (0)	$0.0^{+5.2}_{-0.0}$ (0)
$W(\rightarrow\mu\nu_\mu) + \text{jet}$	42311011	$1.8^{+1.8}_{-1.0}$ (3)	$20.2^{+4.2}_{-3.6}$ (33)	$6.1^{+2.6}_{-1.9}$ (10)	$0.0^{+1.1}_{-0.0}$ (0)
$W(\rightarrow\mu\nu_\mu) + \text{jet}(\rightarrow\mu\dots)$	42311012	$0.0^{+0.1}_{-0.0}$ (0)	$0.0^{+0.1}_{-0.0}$ (0)	$0.0^{+0.1}_{-0.0}$ (0)	$0.3^{+0.1}_{-0.1}$ (12)
$W \rightarrow e\nu_e$	42321000	$0.9^{+2.2}_{-0.8}$ (1)	$0.0^{+1.7}_{-0.0}$ (0)	$0.0^{+1.7}_{-0.0}$ (0)	$0.0^{+1.7}_{-0.0}$ (0)
$W(\rightarrow e\nu_e) + \text{jet}$	42321010	$0.0^{+6.4}_{-0.0}$ (0)	$0.0^{+6.4}_{-0.0}$ (0)	$0.0^{+6.4}_{-0.0}$ (0)	$0.0^{+6.4}_{-0.0}$ (0)
$c\bar{c} \rightarrow \mu\dots$	49011004	$0.0^{+0.9}_{-0.0}$ (0)	$0.5^{+1.1}_{-0.4}$ (1)	$0.0^{+0.9}_{-0.0}$ (0)	$0.0^{+0.9}_{-0.0}$ (0)
$b\bar{b} \rightarrow \mu\dots$	49011005	$0.0^{+4.7}_{-0.0}$ (0)	$0.0^{+4.7}_{-0.0}$ (0)	$0.0^{+4.7}_{-0.0}$ (0)	$0.0^{+4.7}_{-0.0}$ (0)
$c\bar{c} \rightarrow e\dots$	49021004	$0.0^{+0.9}_{-0.0}$ (0)	$0.0^{+0.9}_{-0.0}$ (0)	$0.0^{+0.9}_{-0.0}$ (0)	$0.0^{+0.9}_{-0.0}$ (0)
$b\bar{b} \rightarrow e\dots$	49021005	$0.0^{+4.8}_{-0.0}$ (0)	$0.0^{+4.8}_{-0.0}$ (0)	$0.0^{+4.8}_{-0.0}$ (0)	$0.0^{+4.8}_{-0.0}$ (0)
Data		3	54	19	4

## J.2 Combined Plots of $H \rightarrow \mu\tau$

On each page: column-wise;  $\mu\tau_e$ ,  $\mu\tau_{h,1}$ ,  $\mu\tau_{h,3}$ ,  $\mu\tau_{\mu}$ , row-wise; low-mass, central, high-mass.

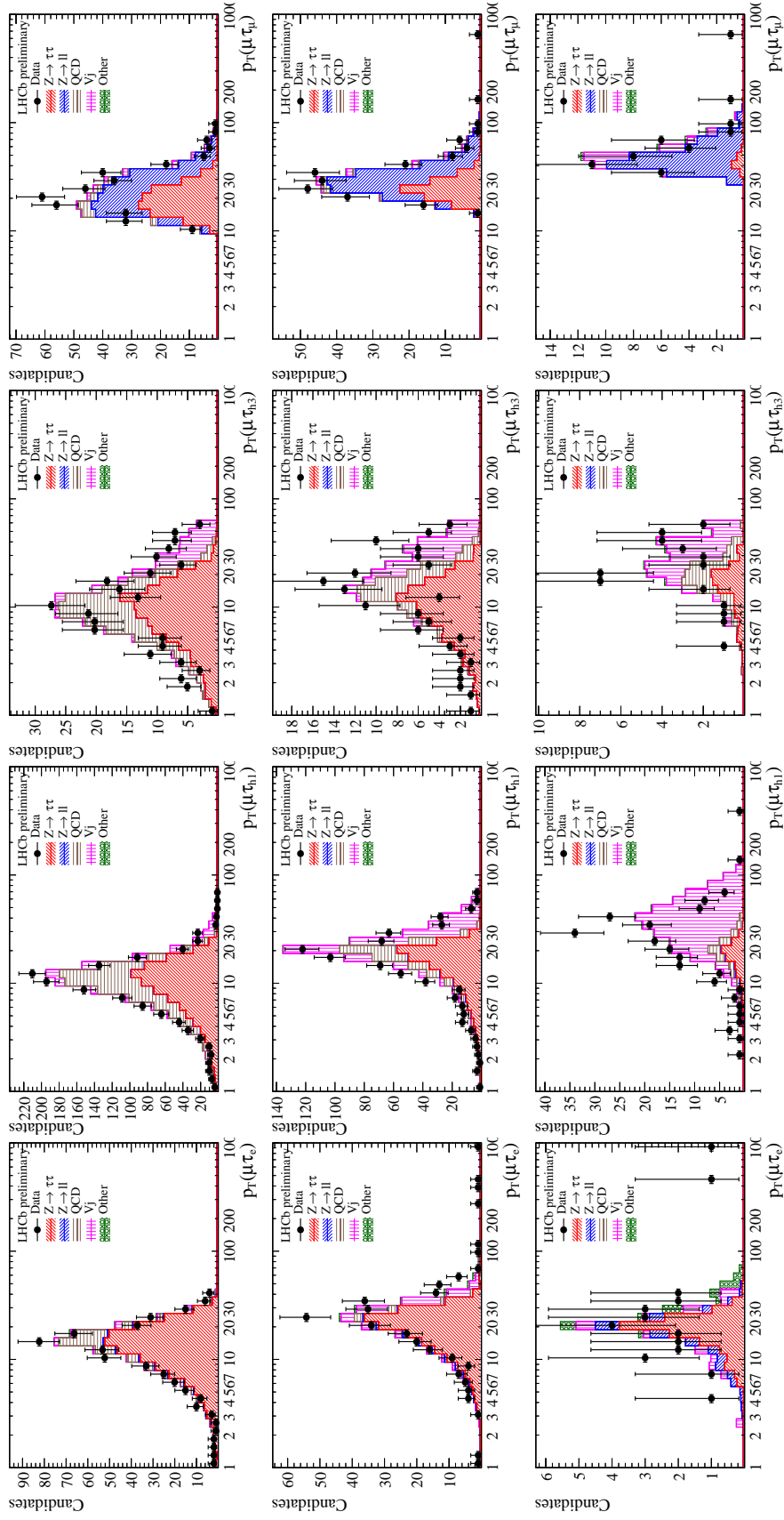


Figure J.1 – Backgrounds contribution of  $\mu\tau$  candidates as a function of its  $p_T$ .

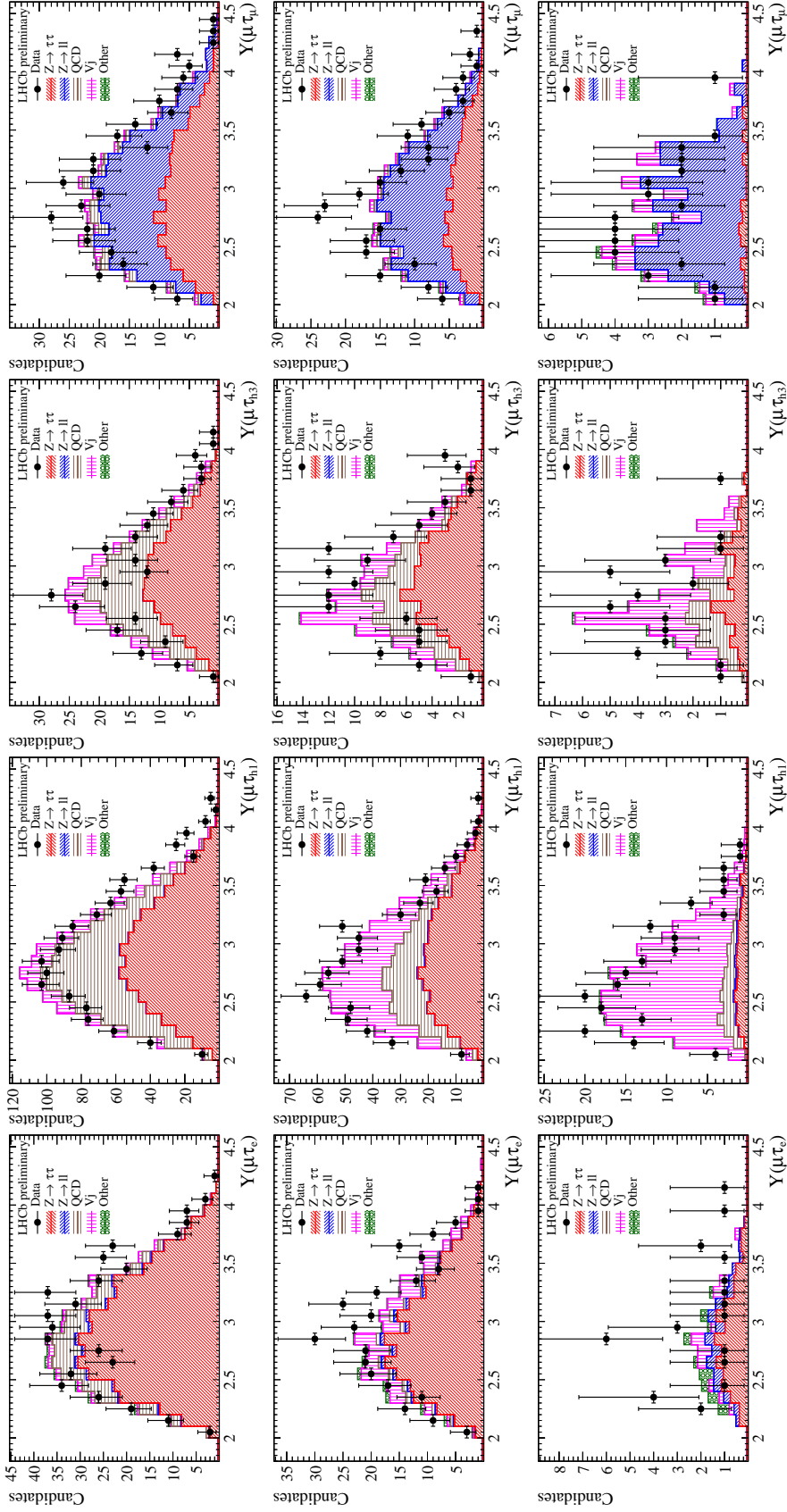
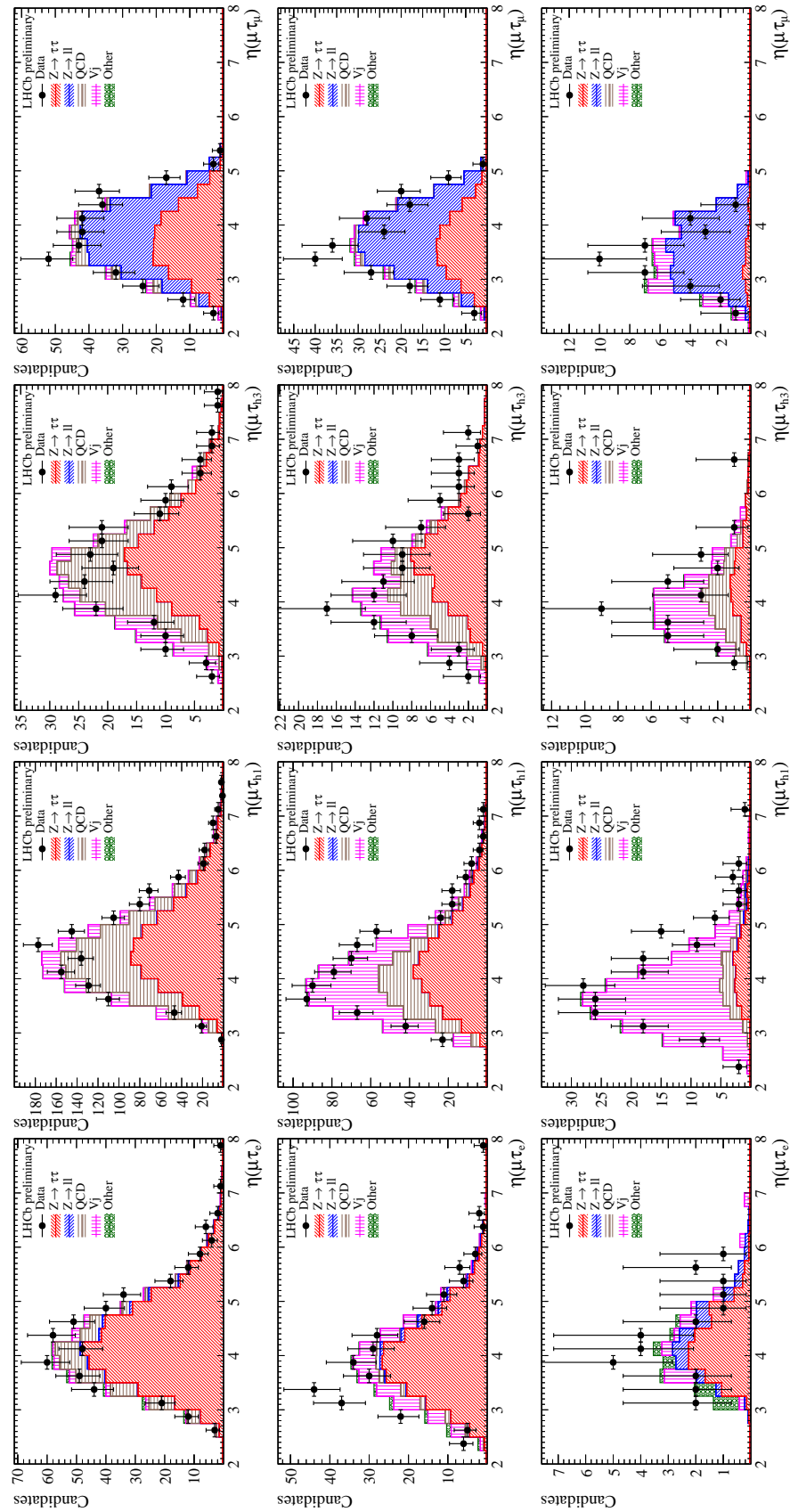


Figure J.2 – Background contribution of  $\mu\tau$  candidates as a function of its rapidity.


 Figure J.3 – Backgrounds contribution of  $\mu\tau$  candidates as a function of its pseudorapidity.



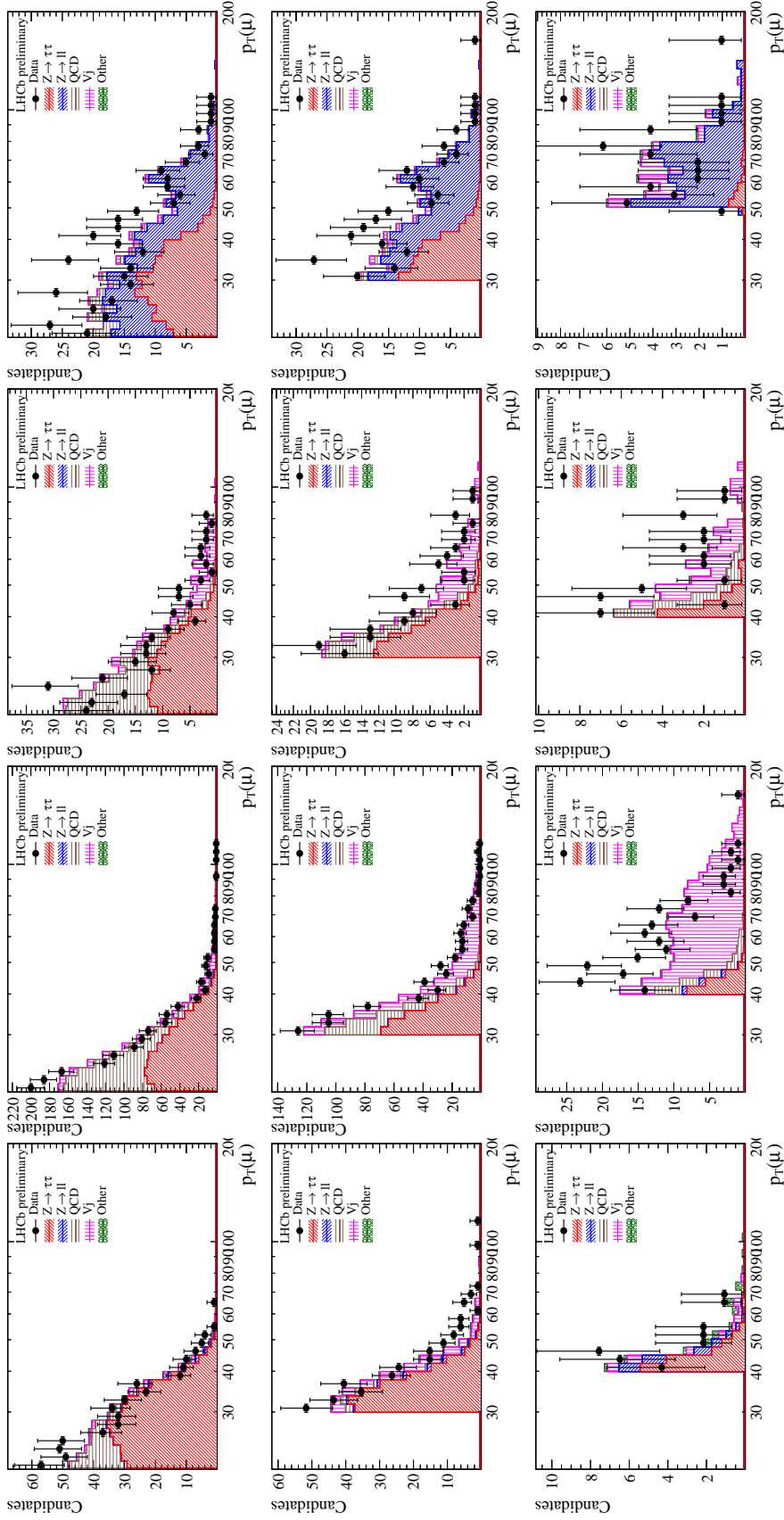


Figure J.4 – Backgrounds contribution of  $\mu\tau$  candidates as a function of hard muon  $p_T$ .

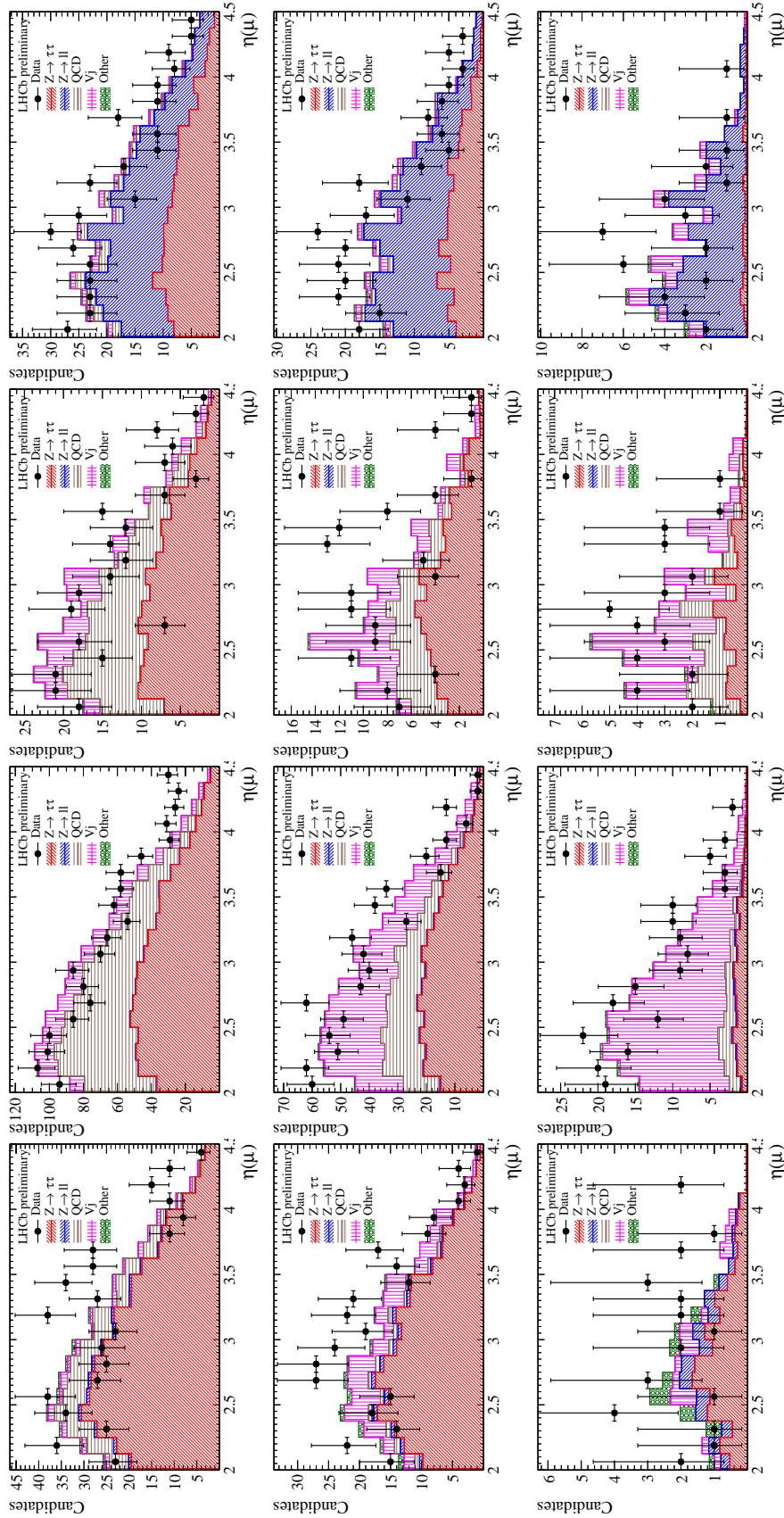


Figure J.5 – Backgrounds contribution of  $\mu\tau$  candidates as a function of hard muon  $\eta$ .

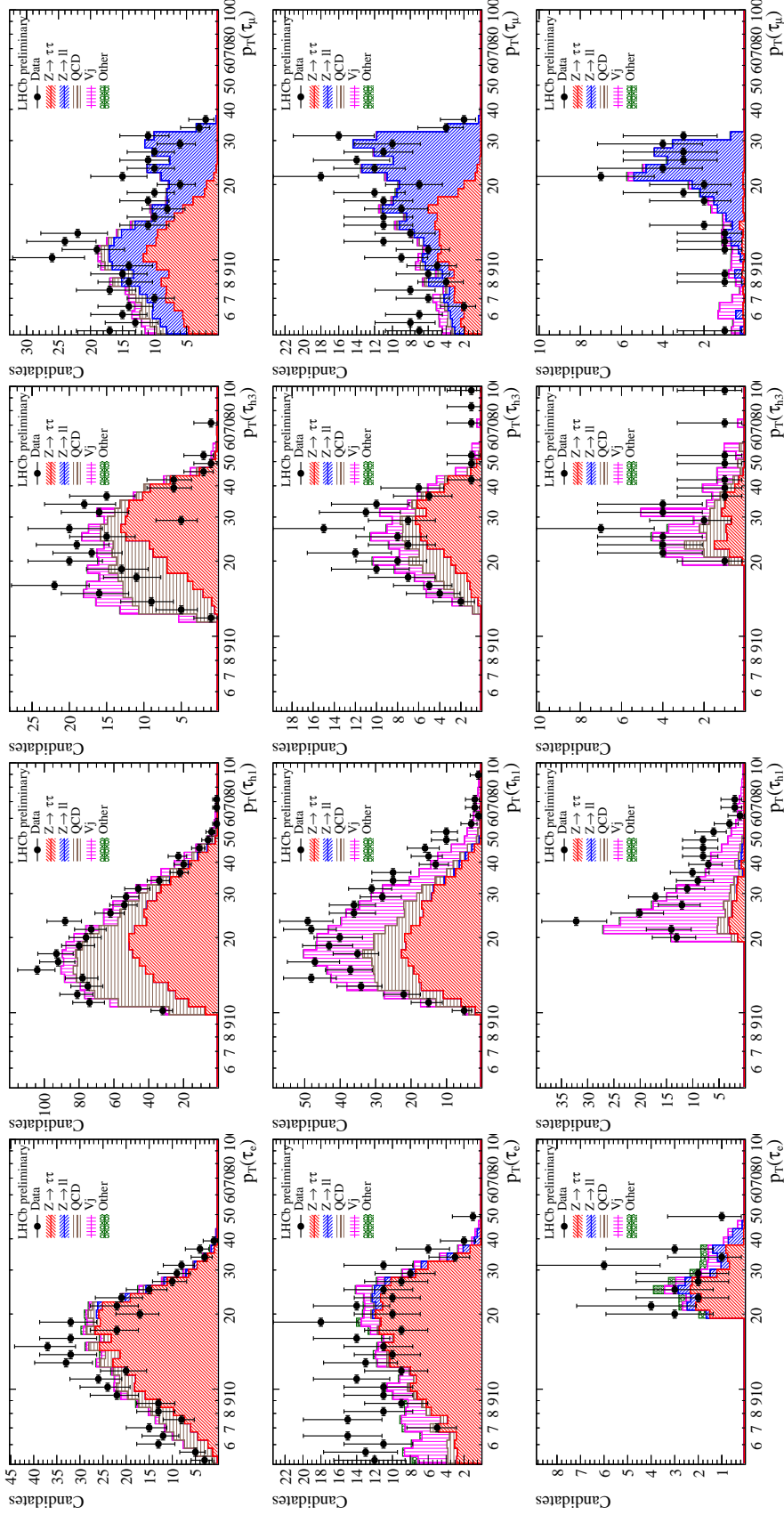
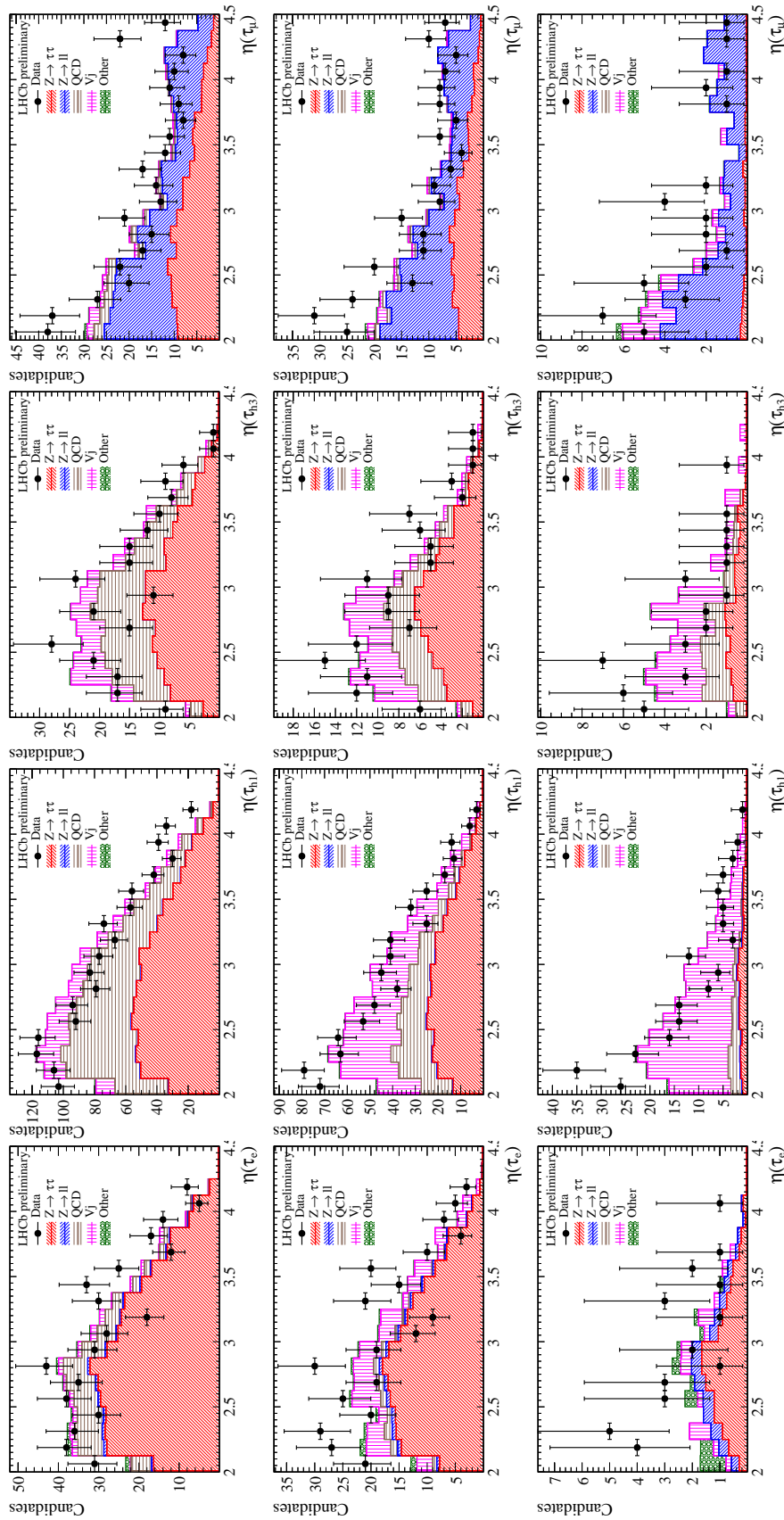


Figure J.6 – Backgrounds contribution of  $\tau$  lepton candidates as a function of  $\mu$  lepton candidate  $p_T$ .


 Figure J.7 – Backgrounds contribution of  $\mu\tau$  candidates as a function of  $\tau$  lepton candidate  $\eta$ .

# K $H \rightarrow \mu\tau$ Efficiencies

**Table K.1** – Signal acceptance from inclusive ( $4\pi$ ) production for different channel at different selection regimes, shown in percentage.

$m_H$ [GeV/ $c^2$ ]	$\mu\tau_e$	$\mu\tau_{h1}$	$\mu\tau_{h3}$	$\mu\tau_\mu$
45	$2.22 \pm 0.06$	$0.86 \pm 0.04$	$1.57 \pm 0.04$	$2.28 \pm 0.07$
55	$3.08 \pm 0.10$	$1.51 \pm 0.05$	$2.67 \pm 0.09$	$3.12 \pm 0.11$
65	$3.25 \pm 0.11$	$1.88 \pm 0.07$	$3.12 \pm 0.10$	$3.34 \pm 0.11$
75	$3.18 \pm 0.13$	$2.03 \pm 0.09$	$3.20 \pm 0.12$	$3.27 \pm 0.12$
85	$3.01 \pm 0.13$	$2.03 \pm 0.09$	$3.06 \pm 0.11$	$3.04 \pm 0.11$
95	$2.78 \pm 0.13$	$1.98 \pm 0.10$	$2.85 \pm 0.13$	$2.81 \pm 0.11$
105	$2.53 \pm 0.11$	$1.88 \pm 0.07$	$2.61 \pm 0.13$	$2.57 \pm 0.11$
115	$2.32 \pm 0.11$	$1.78 \pm 0.08$	$2.39 \pm 0.11$	$2.35 \pm 0.11$
125	$2.11 \pm 0.10$	$1.67 \pm 0.07$	$2.17 \pm 0.09$	$2.14 \pm 0.09$
135	$1.94 \pm 0.10$	$1.56 \pm 0.08$	$1.97 \pm 0.10$	$1.96 \pm 0.10$
145	$1.74 \pm 0.11$	$1.45 \pm 0.08$	$1.79 \pm 0.10$	$1.76 \pm 0.10$
155	$1.60 \pm 0.11$	$1.34 \pm 0.09$	$1.64 \pm 0.10$	$1.63 \pm 0.10$
165	$1.47 \pm 0.09$	$1.25 \pm 0.08$	$1.46 \pm 0.09$	$1.47 \pm 0.09$
175	$1.32 \pm 0.09$	$1.15 \pm 0.08$	$1.33 \pm 0.08$	$1.34 \pm 0.09$
185	$1.20 \pm 0.08$	$1.04 \pm 0.07$	$1.19 \pm 0.08$	$1.20 \pm 0.08$
195	$1.06 \pm 0.08$	$0.95 \pm 0.07$	$1.07 \pm 0.08$	$1.09 \pm 0.09$

**Table K.2** – Signal acceptance from production inside LHCb fiducial volume for different channel at different selection regimes, shown in percentage.

$m_H$ [GeV/ $c^2$ ]	$\mu\tau_e$	$\mu\tau_{h1}$	$\mu\tau_{h3}$	$\mu\tau_\mu$
45	$33.58 \pm 0.87$	$12.93 \pm 0.57$	$23.66 \pm 0.48$	$34.45 \pm 0.63$
55	$53.05 \pm 0.65$	$26.15 \pm 0.50$	$46.20 \pm 0.88$	$53.88 \pm 0.75$
65	$64.44 \pm 0.84$	$37.10 \pm 0.89$	$61.43 \pm 0.64$	$65.48 \pm 0.64$
75	$71.16 \pm 0.62$	$45.55 \pm 0.83$	$71.58 \pm 0.89$	$72.77 \pm 1.06$
85	$75.91 \pm 0.81$	$51.30 \pm 1.02$	$77.21 \pm 0.68$	$76.84 \pm 0.78$
95	$78.90 \pm 0.81$	$56.40 \pm 0.92$	$81.08 \pm 0.68$	$79.87 \pm 0.77$
105	$81.13 \pm 0.78$	$60.60 \pm 1.05$	$84.14 \pm 0.83$	$82.01 \pm 0.83$
115	$83.25 \pm 0.62$	$63.96 \pm 0.97$	$85.84 \pm 0.82$	$83.82 \pm 0.86$
125	$84.88 \pm 1.00$	$66.91 \pm 1.14$	$86.93 \pm 0.93$	$85.74 \pm 1.08$
135	$85.75 \pm 0.92$	$69.52 \pm 0.86$	$87.68 \pm 0.84$	$87.11 \pm 1.18$
145	$86.42 \pm 0.95$	$71.95 \pm 0.97$	$88.49 \pm 0.80$	$88.30 \pm 0.91$
155	$87.93 \pm 0.92$	$74.16 \pm 1.44$	$89.01 \pm 0.86$	$89.30 \pm 0.89$
165	$88.12 \pm 1.03$	$75.57 \pm 1.53$	$89.17 \pm 1.05$	$89.68 \pm 0.96$
175	$89.26 \pm 1.14$	$77.30 \pm 1.27$	$89.86 \pm 0.95$	$90.21 \pm 0.88$
185	$89.80 \pm 0.94$	$78.50 \pm 1.51$	$89.65 \pm 1.01$	$90.65 \pm 1.01$
195	$89.91 \pm 1.01$	$79.80 \pm 1.24$	$90.22 \pm 0.93$	$91.52 \pm 1.10$

Appendix K.  $H \rightarrow \mu\tau$  Efficiencies

 Table K.3 – Detail of  $\epsilon_{\text{rec}}$  in  $\mu\tau_e$  channel.

Regime	$m_H$	$m_H$ [GeV/ $c^2$ ]	$\epsilon_{\text{track}}$	$\epsilon_{\text{track},\mu}$	$\epsilon_{\text{track},\tau_e}$	$\epsilon_{\text{kin}}$	$\epsilon_{\text{PID}}$	$\epsilon_{\text{PID},\mu}$	$\epsilon_{\text{PID},\tau_e}$	$\epsilon_{\text{GEC}}$	$\epsilon_{\text{trig}}$	$\epsilon_{\text{trig},\mu}$	$\epsilon_{\text{trig},\tau_e}$	$\epsilon_{\text{rec}}$
Low-mass	45	75.7 ± 0.8	92.8 ± 0.4	81.5 ± 0.8	87.9 ± 0.5	91.1 ± 0.6	97.8 ± 0.3	93.2 ± 0.5	92.3 ± 0.7	82.1 ± 2.7	82.0 ± 2.7	0.9 ± 0.1	46.1 ± 1.7	
	55	75.5 ± 0.8	92.0 ± 0.5	82.1 ± 0.8	90.1 ± 0.4	91.1 ± 0.6	98.0 ± 0.3	93.0 ± 0.5	92.3 ± 0.7	81.5 ± 1.8	80.5 ± 1.9	5.2 ± 0.3	46.7 ± 1.2	
	65	75.5 ± 0.8	92.2 ± 0.4	81.9 ± 0.8	92.7 ± 0.4	91.1 ± 0.6	98.1 ± 0.3	92.8 ± 0.5	92.3 ± 0.7	81.9 ± 1.2	79.7 ± 1.3	11.0 ± 0.6	48.3 ± 1.0	
	75	76.0 ± 0.9	92.1 ± 0.5	82.6 ± 0.9	92.9 ± 0.4	91.5 ± 0.6	98.4 ± 0.3	93.0 ± 0.6	92.3 ± 0.7	83.4 ± 0.8	79.4 ± 0.9	19.2 ± 1.0	49.8 ± 0.9	
	85	75.9 ± 0.9	92.0 ± 0.5	82.5 ± 0.9	93.9 ± 0.3	92.0 ± 0.6	98.5 ± 0.3	93.4 ± 0.6	92.3 ± 0.7	83.8 ± 0.7	78.8 ± 0.8	23.4 ± 1.1	50.8 ± 0.9	
	95	76.6 ± 1.0	91.7 ± 0.5	83.5 ± 1.0	94.2 ± 0.3	92.4 ± 0.7	98.7 ± 0.3	93.9 ± 0.6	92.3 ± 0.7	85.2 ± 0.7	78.3 ± 0.9	31.6 ± 1.4	52.5 ± 1.0	
	105	75.9 ± 1.1	91.7 ± 0.5	82.8 ± 1.1	95.3 ± 0.3	92.7 ± 0.7	98.7 ± 0.3	93.9 ± 0.6	92.3 ± 0.7	86.8 ± 0.7	77.8 ± 1.1	40.2 ± 1.6	53.9 ± 1.1	
	115	76.4 ± 1.1	91.7 ± 0.5	83.3 ± 1.2	95.3 ± 0.3	92.8 ± 0.8	98.7 ± 0.3	94.0 ± 0.8	92.3 ± 0.7	87.9 ± 0.9	77.3 ± 1.1	46.3 ± 1.7	54.9 ± 1.2	
	125	75.6 ± 1.1	91.3 ± 0.5	82.8 ± 1.2	96.0 ± 0.3	92.3 ± 0.9	98.6 ± 0.4	93.6 ± 0.8	92.3 ± 0.7	88.1 ± 1.1	76.6 ± 2.1	48.4 ± 1.8	54.6 ± 1.3	
	135	75.3 ± 1.2	91.0 ± 0.5	82.8 ± 1.3	95.8 ± 0.3	92.6 ± 1.0	98.6 ± 0.4	93.8 ± 0.9	92.3 ± 0.7	89.4 ± 1.2	76.1 ± 2.7	55.2 ± 1.9	55.3 ± 1.4	
	145	75.4 ± 1.3	90.8 ± 0.5	83.0 ± 1.3	96.6 ± 0.3	92.7 ± 1.1	98.6 ± 0.4	94.0 ± 1.0	92.3 ± 0.7	90.2 ± 1.3	75.3 ± 3.1	60.2 ± 2.0	56.4 ± 1.5	
	155	75.3 ± 1.3	90.7 ± 0.5	83.0 ± 1.3	96.9 ± 0.3	92.5 ± 1.1	98.6 ± 0.4	93.8 ± 1.1	92.3 ± 0.7	90.5 ± 1.3	74.7 ± 3.3	62.0 ± 1.9	56.5 ± 1.5	
	165	75.1 ± 1.3	90.8 ± 0.5	82.7 ± 1.4	96.8 ± 0.3	92.7 ± 1.3	98.6 ± 0.4	94.0 ± 1.2	92.3 ± 0.7	90.9 ± 1.3	73.6 ± 3.5	65.2 ± 2.0	56.7 ± 1.6	
	175	75.3 ± 1.3	90.7 ± 0.5	83.1 ± 1.4	96.6 ± 0.3	92.8 ± 1.3	98.7 ± 0.4	94.1 ± 1.3	92.3 ± 0.7	91.1 ± 1.3	72.9 ± 3.5	66.8 ± 2.1	56.9 ± 1.6	
	185	74.7 ± 1.3	90.3 ± 0.5	82.8 ± 1.4	97.3 ± 0.3	91.7 ± 1.5	98.6 ± 0.4	93.0 ± 1.4	92.3 ± 0.7	90.9 ± 1.3	71.7 ± 3.6	67.5 ± 2.1	56.1 ± 1.6	
	195	75.3 ± 1.4	90.5 ± 0.5	83.3 ± 1.4	96.7 ± 0.4	92.4 ± 1.4	98.6 ± 0.4	93.7 ± 1.4	92.3 ± 0.7	90.6 ± 1.3	70.5 ± 3.5	68.0 ± 2.2	56.4 ± 1.6	
	Central	75	76.1 ± 0.9	92.1 ± 0.4	82.5 ± 0.8	92.9 ± 0.4	91.6 ± 0.6	98.6 ± 0.3	92.9 ± 0.5	92.3 ± 0.7	82.6 ± 0.7	79.2 ± 0.8	16.3 ± 0.8	49.5 ± 0.9
		85	75.9 ± 0.9	92.0 ± 0.4	82.5 ± 0.9	93.9 ± 0.3	91.7 ± 0.6	98.7 ± 0.2	92.8 ± 0.5	92.3 ± 0.7	82.7 ± 0.7	78.6 ± 0.8	19.2 ± 0.9	50.0 ± 0.9
		95	76.6 ± 0.9	91.8 ± 0.5	83.4 ± 0.9	94.2 ± 0.3	92.2 ± 0.6	98.8 ± 0.3	93.4 ± 0.6	92.3 ± 0.7	83.2 ± 0.8	78.1 ± 0.9	23.2 ± 1.0	51.2 ± 1.0
105		75.9 ± 0.9	91.9 ± 0.4	82.6 ± 0.9	95.3 ± 0.3	92.1 ± 0.6	98.7 ± 0.3	93.2 ± 0.6	92.3 ± 0.7	84.0 ± 1.0	77.7 ± 1.3	28.4 ± 1.1	51.8 ± 1.1	
115		76.1 ± 1.0	91.6 ± 0.5	83.1 ± 1.0	95.3 ± 0.3	92.1 ± 0.7	98.7 ± 0.3	93.3 ± 0.6	92.3 ± 0.7	84.5 ± 1.2	77.0 ± 1.7	32.4 ± 1.2	52.3 ± 1.2	
125		75.6 ± 1.0	91.4 ± 0.5	82.7 ± 1.0	96.0 ± 0.3	91.9 ± 0.7	98.7 ± 0.4	93.1 ± 0.7	92.3 ± 0.7	84.7 ± 1.5	76.5 ± 2.2	34.6 ± 1.2	52.3 ± 1.3	
135		75.2 ± 1.0	91.1 ± 0.5	82.6 ± 1.1	95.8 ± 0.3	92.1 ± 0.8	98.6 ± 0.4	93.4 ± 0.7	92.3 ± 0.7	84.9 ± 1.8	75.9 ± 2.8	36.9 ± 1.2	52.2 ± 1.5	
145		75.4 ± 1.1	91.0 ± 0.5	82.8 ± 1.1	96.6 ± 0.3	92.2 ± 0.8	98.6 ± 0.4	93.4 ± 0.8	92.3 ± 0.7	85.3 ± 1.9	75.1 ± 3.2	41.1 ± 1.3	53.0 ± 1.6	
155		75.3 ± 1.1	91.0 ± 0.5	82.8 ± 1.1	96.9 ± 0.3	91.9 ± 0.9	98.6 ± 0.4	93.2 ± 0.8	92.3 ± 0.7	84.8 ± 2.1	73.4 ± 3.6	43.0 ± 1.4	52.5 ± 1.7	
165		75.0 ± 1.1	90.9 ± 0.5	82.5 ± 1.1	96.8 ± 0.3	92.2 ± 0.9	98.6 ± 0.4	93.4 ± 0.9	92.3 ± 0.7	84.8 ± 2.1	73.4 ± 3.6	43.0 ± 1.4	52.5 ± 1.7	
175		75.1 ± 1.1	90.8 ± 0.5	82.7 ± 1.2	96.6 ± 0.3	92.1 ± 0.9	98.6 ± 0.4	93.4 ± 0.9	92.3 ± 0.7	84.3 ± 2.1	72.3 ± 3.6	43.3 ± 1.4	52.2 ± 1.7	
185		74.8 ± 1.2	90.6 ± 0.5	82.6 ± 1.2	97.3 ± 0.3	91.8 ± 1.0	98.6 ± 0.4	93.1 ± 1.0	92.3 ± 0.7	84.8 ± 2.0	71.4 ± 3.6	47.0 ± 1.6	52.5 ± 1.7	
195		75.1 ± 1.2	90.5 ± 0.5	83.0 ± 1.2	96.7 ± 0.4	92.1 ± 1.1	98.6 ± 0.4	93.4 ± 1.0	92.3 ± 0.7	84.2 ± 1.9	69.9 ± 3.5	47.4 ± 1.7	52.2 ± 1.6	
High-mass		95	76.5 ± 1.2	91.3 ± 0.5	83.8 ± 1.3	94.2 ± 0.3	93.4 ± 1.1	98.9 ± 0.2	94.4 ± 1.0	92.3 ± 0.7	92.7 ± 0.7	77.7 ± 0.8	67.3 ± 2.9	57.7 ± 1.3
		105	76.0 ± 1.2	91.6 ± 0.5	83.0 ± 1.3	95.3 ± 0.3	93.5 ± 1.0	98.8 ± 0.3	94.7 ± 1.0	92.3 ± 0.7	92.7 ± 0.7	77.5 ± 1.2	67.7 ± 2.7	58.1 ± 1.3
		115	76.4 ± 1.3	91.5 ± 0.5	83.5 ± 1.3	95.3 ± 0.3	93.4 ± 1.1	98.7 ± 0.3	94.7 ± 1.0	92.3 ± 0.7	92.6 ± 0.8	77.0 ± 1.6	67.9 ± 2.5	58.2 ± 1.4
		125	75.6 ± 1.3	91.0 ± 0.5	83.0 ± 1.3	96.0 ± 0.3	93.2 ± 1.1	98.6 ± 0.4	94.5 ± 1.0	92.3 ± 0.7	92.4 ± 0.9	76.2 ± 2.2	68.0 ± 2.4	57.8 ± 1.4
		135	75.4 ± 1.3	90.8 ± 0.5	83.0 ± 1.3	95.8 ± 0.3	93.4 ± 1.1	98.6 ± 0.4	94.7 ± 1.1	92.3 ± 0.7	92.3 ± 1.0	75.7 ± 2.8	68.4 ± 2.3	57.6 ± 1.4
		145	75.6 ± 1.3	90.9 ± 0.5	83.1 ± 1.4	96.6 ± 0.3	93.0 ± 1.2	98.6 ± 0.4	94.3 ± 1.1	92.3 ± 0.7	92.1 ± 1.2	75.1 ± 3.2	68.2 ± 2.2	57.8 ± 1.5
	155	75.4 ± 1.3	90.7 ± 0.5	83.2 ± 1.4	96.9 ± 0.3	93.1 ± 1.2	98.6 ± 0.4	94.4 ± 1.2	92.3 ± 0.7	91.9 ± 1.2	74.4 ± 3.4	68.5 ± 2.1	57.9 ± 1.5	
	165	75.2 ± 1.3	90.9 ± 0.5	82.8 ± 1.4	96.8 ± 0.3	92.7 ± 1.3	98.6 ± 0.4	94.0 ± 1.3	92.3 ± 0.7	91.6 ± 1.3	73.4 ± 3.5	68.4 ± 2.2	57.2 ± 1.6	
	175	75.4 ± 1.3	90.7 ± 0.5	83.1 ± 1.4	96.6 ± 0.3	93.1 ± 1.3	98.7 ± 0.4	94.3 ± 1.3	92.3 ± 0.7	91.4 ± 1.3	72.5 ± 3.6	68.7 ± 2.2	57.2 ± 1.6	
	185	74.9 ± 1.3	90.5 ± 0.5	82.8 ± 1.4	97.3 ± 0.3	92.3 ± 1.4	98.6 ± 0.4	93.6 ± 1.4	92.3 ± 0.7	91.0 ± 1.3	71.4 ± 3.6	68.7 ± 2.3	56.7 ± 1.6	
	195	75.4 ± 1.4	90.5 ± 0.5	83.3 ± 1.4	96.7 ± 0.4	92.8 ± 1.4	98.6 ± 0.4	94.1 ± 1.4	92.3 ± 0.7	90.6 ± 1.3	70.0 ± 3.5	68.8 ± 2.4	56.7 ± 1.6	

Table K.4 – Detail of  $\epsilon_{\text{rec}}$  in  $\mu\tau_{h1}$  channel.

Regime	$m_H$ [GeV/ $c^2$ ]	$\epsilon_{\text{track}}$	$\epsilon_{\text{track},\mu}$	$\epsilon_{\text{track},\tau_{h1}}$	$\epsilon_{\text{kine}}$	$\epsilon_{\text{PID}}$	$\epsilon_{\text{PID},\mu}$	$\epsilon_{\text{PID},\tau_{h1}}$	$\epsilon_{\text{GEC}}$	$\epsilon_{\text{trig}}$	$\epsilon_{\text{rec}}$	
Low-mass	45	75.1 ± 0.9	92.6 ± 0.4	81.1 ± 0.8	100.3 ± 0.0	92.5 ± 0.5	97.6 ± 0.4	94.8 ± 0.4	93.0 ± 0.6	81.6 ± 2.6	52.9 ± 1.9	
	55	74.6 ± 0.9	92.4 ± 0.4	80.7 ± 0.9	99.8 ± 0.1	93.2 ± 0.6	97.9 ± 0.3	95.2 ± 0.5	93.0 ± 0.6	80.5 ± 1.9	52.0 ± 1.5	
	65	74.1 ± 0.9	92.0 ± 0.5	80.5 ± 0.9	100.0 ± 0.0	93.7 ± 0.7	98.0 ± 0.3	95.6 ± 0.6	93.0 ± 0.6	79.9 ± 1.4	51.6 ± 1.2	
	75	74.6 ± 1.0	92.2 ± 0.4	80.9 ± 1.0	99.9 ± 0.0	94.1 ± 0.7	98.4 ± 0.3	95.7 ± 0.7	93.0 ± 0.6	79.6 ± 1.1	51.9 ± 1.1	
	85	73.9 ± 1.1	92.0 ± 0.5	80.3 ± 1.1	99.9 ± 0.0	94.4 ± 0.8	98.6 ± 0.3	95.8 ± 0.7	93.0 ± 0.6	79.1 ± 0.9	51.3 ± 1.1	
	95	73.4 ± 1.1	91.9 ± 0.4	79.8 ± 1.2	100.0 ± 0.0	94.8 ± 0.8	98.7 ± 0.2	96.0 ± 0.7	93.0 ± 0.6	78.6 ± 0.8	50.8 ± 1.1	
	105	73.1 ± 1.2	91.7 ± 0.5	79.7 ± 1.2	100.0 ± 0.0	94.7 ± 0.8	98.7 ± 0.3	96.0 ± 0.8	93.0 ± 0.6	78.1 ± 1.0	50.3 ± 1.2	
	115	72.7 ± 1.2	91.7 ± 0.5	79.3 ± 1.2	99.9 ± 0.0	94.6 ± 0.8	98.6 ± 0.3	96.0 ± 0.8	93.0 ± 0.6	77.6 ± 1.4	49.6 ± 1.3	
	125	72.7 ± 1.2	91.7 ± 0.5	79.4 ± 1.3	100.1 ± 0.0	94.7 ± 0.8	98.6 ± 0.4	96.0 ± 0.8	93.0 ± 0.6	76.9 ± 1.9	49.4 ± 1.6	
	135	72.1 ± 1.2	91.5 ± 0.5	78.8 ± 1.3	99.9 ± 0.0	94.7 ± 0.8	98.6 ± 0.4	96.0 ± 0.7	93.0 ± 0.6	76.6 ± 2.5	48.7 ± 1.9	
	145	71.8 ± 1.2	91.3 ± 0.5	78.5 ± 1.3	99.8 ± 0.0	94.6 ± 0.8	98.6 ± 0.4	96.0 ± 0.8	93.0 ± 0.6	76.0 ± 2.9	48.0 ± 2.1	
	155	71.2 ± 1.2	91.2 ± 0.5	78.1 ± 1.3	100.0 ± 0.0	94.6 ± 0.9	98.6 ± 0.4	95.9 ± 0.8	93.0 ± 0.6	75.4 ± 3.2	47.3 ± 2.3	
	165	70.9 ± 1.3	90.8 ± 0.5	78.1 ± 1.3	100.0 ± 0.0	94.5 ± 0.9	98.6 ± 0.4	95.8 ± 0.8	93.0 ± 0.6	74.2 ± 3.5	46.3 ± 2.4	
	175	71.0 ± 1.2	91.0 ± 0.5	78.0 ± 1.3	100.0 ± 0.0	94.6 ± 0.8	98.6 ± 0.4	95.9 ± 0.8	93.0 ± 0.6	73.4 ± 3.5	45.9 ± 2.4	
	185	69.8 ± 1.2	90.7 ± 0.5	76.9 ± 1.3	100.0 ± 0.0	94.5 ± 0.9	98.6 ± 0.4	95.9 ± 0.8	93.0 ± 0.6	72.1 ± 3.5	44.4 ± 2.4	
	195	70.6 ± 1.3	90.8 ± 0.5	77.7 ± 1.3	99.9 ± 0.0	94.6 ± 0.8	98.6 ± 0.4	96.0 ± 0.7	93.0 ± 0.6	71.2 ± 3.5	44.3 ± 2.3	
	Central	75	74.6 ± 1.0	92.2 ± 0.4	80.9 ± 1.0	99.9 ± 0.0	94.2 ± 0.7	98.6 ± 0.3	95.5 ± 0.6	93.0 ± 0.6	79.3 ± 0.8	51.8 ± 1.0
		85	74.0 ± 1.0	92.1 ± 0.4	80.4 ± 1.0	99.9 ± 0.0	94.6 ± 0.7	98.7 ± 0.2	95.8 ± 0.7	93.0 ± 0.6	78.8 ± 0.8	51.3 ± 1.0
		95	73.3 ± 1.1	91.9 ± 0.4	79.8 ± 1.1	100.0 ± 0.0	94.8 ± 0.7	98.8 ± 0.2	95.9 ± 0.7	93.0 ± 0.6	78.4 ± 0.8	50.6 ± 1.0
105		73.0 ± 1.1	91.7 ± 0.5	79.7 ± 1.1	100.0 ± 0.0	94.8 ± 0.8	98.8 ± 0.3	96.0 ± 0.7	93.0 ± 0.6	77.9 ± 1.1	50.2 ± 1.2	
115		72.8 ± 1.1	91.8 ± 0.5	79.3 ± 1.2	99.9 ± 0.0	94.7 ± 0.8	98.7 ± 0.3	95.9 ± 0.7	93.0 ± 0.6	77.5 ± 1.5	49.7 ± 1.3	
125		72.6 ± 1.2	91.5 ± 0.5	79.4 ± 1.2	100.1 ± 0.0	94.7 ± 0.8	98.7 ± 0.4	96.0 ± 0.7	93.0 ± 0.6	76.7 ± 2.0	49.2 ± 1.6	
135		72.1 ± 1.2	91.5 ± 0.5	78.8 ± 1.2	99.9 ± 0.0	94.7 ± 0.8	98.6 ± 0.4	96.0 ± 0.7	93.0 ± 0.6	76.5 ± 2.5	48.6 ± 1.9	
145		71.8 ± 1.2	91.4 ± 0.5	78.5 ± 1.3	99.8 ± 0.0	94.6 ± 0.8	98.6 ± 0.4	96.0 ± 0.8	93.0 ± 0.6	75.9 ± 3.0	48.0 ± 2.1	
155		71.4 ± 1.2	91.3 ± 0.5	78.1 ± 1.3	100.0 ± 0.0	94.7 ± 0.8	98.7 ± 0.4	96.0 ± 0.8	93.0 ± 0.6	75.3 ± 3.3	47.4 ± 2.3	
165		71.2 ± 1.2	91.1 ± 0.5	78.2 ± 1.3	100.0 ± 0.0	94.6 ± 0.8	98.6 ± 0.4	95.9 ± 0.8	93.0 ± 0.6	74.2 ± 3.5	46.6 ± 2.4	
175		71.1 ± 1.2	91.0 ± 0.5	78.1 ± 1.3	100.0 ± 0.0	94.7 ± 0.8	98.6 ± 0.4	96.0 ± 0.8	93.0 ± 0.6	73.2 ± 3.5	45.9 ± 2.4	
185		69.8 ± 1.2	90.8 ± 0.5	76.9 ± 1.3	100.0 ± 0.0	94.6 ± 0.8	98.6 ± 0.4	95.9 ± 0.8	93.0 ± 0.6	72.1 ± 3.5	44.4 ± 2.4	
195		70.7 ± 1.2	90.9 ± 0.5	77.8 ± 1.3	99.9 ± 0.0	94.7 ± 0.8	98.7 ± 0.4	96.0 ± 0.7	93.0 ± 0.6	71.4 ± 3.5	44.5 ± 2.4	
High-mass		95	73.3 ± 1.2	91.7 ± 0.4	79.9 ± 1.2	100.0 ± 0.0	95.1 ± 0.8	98.9 ± 0.2	96.2 ± 0.8	93.0 ± 0.6	78.0 ± 0.9	50.6 ± 1.1
		105	73.1 ± 1.2	91.7 ± 0.4	79.8 ± 1.2	100.0 ± 0.0	95.0 ± 0.8	98.8 ± 0.3	96.2 ± 0.8	93.0 ± 0.6	77.5 ± 1.2	50.1 ± 1.3
		115	72.8 ± 1.2	91.7 ± 0.5	79.4 ± 1.2	99.9 ± 0.0	94.9 ± 0.8	98.8 ± 0.3	96.1 ± 0.8	93.0 ± 0.6	77.1 ± 1.7	49.5 ± 1.4
		125	72.6 ± 1.2	91.4 ± 0.5	79.4 ± 1.2	100.1 ± 0.0	94.8 ± 0.8	98.7 ± 0.4	96.1 ± 0.8	93.0 ± 0.6	76.4 ± 2.2	49.0 ± 1.7
		135	72.1 ± 1.2	91.4 ± 0.5	78.8 ± 1.2	99.9 ± 0.0	94.8 ± 0.8	98.7 ± 0.4	96.1 ± 0.8	93.0 ± 0.6	76.1 ± 2.7	48.4 ± 2.0
		145	71.7 ± 1.2	91.3 ± 0.5	78.6 ± 1.3	99.8 ± 0.0	94.7 ± 0.8	98.7 ± 0.4	96.0 ± 0.8	93.0 ± 0.6	75.5 ± 3.1	47.7 ± 2.2
	155	71.3 ± 1.2	91.3 ± 0.5	78.1 ± 1.3	100.0 ± 0.0	94.7 ± 0.8	98.7 ± 0.4	96.0 ± 0.8	93.0 ± 0.6	74.8 ± 3.4	47.1 ± 2.3	
	165	71.2 ± 1.2	91.0 ± 0.5	78.2 ± 1.3	100.0 ± 0.0	94.7 ± 0.8	98.7 ± 0.4	95.9 ± 0.8	93.0 ± 0.6	73.7 ± 3.5	46.3 ± 2.4	
	175	71.1 ± 1.2	91.0 ± 0.5	78.1 ± 1.3	100.0 ± 0.0	94.7 ± 0.8	98.7 ± 0.4	96.0 ± 0.8	93.0 ± 0.6	72.7 ± 3.5	45.6 ± 2.4	
185	69.7 ± 1.2	90.7 ± 0.5	76.9 ± 1.3	100.0 ± 0.0	94.6 ± 0.8	98.6 ± 0.4	95.9 ± 0.8	93.0 ± 0.6	71.7 ± 3.5	44.1 ± 2.4		
195	70.6 ± 1.2	90.8 ± 0.5	77.8 ± 1.3	99.9 ± 0.0	94.6 ± 0.8	98.6 ± 0.4	95.9 ± 0.8	93.0 ± 0.6	70.6 ± 3.5	44.0 ± 2.4		

Appendix K.  $H \rightarrow \mu\tau$  Efficiencies

 Table K.5 – Detail of  $\epsilon_{\text{rec}}$  in  $\mu\tau_{h3}$  channel.

Regime	$m_H$ [GeV/ $c^2$ ]	$\epsilon_{\text{track}}$	$\epsilon_{\text{track},\mu}$	$\epsilon_{\text{track},\tau_{h3}}$	$\epsilon_{\text{kin}}$	$\epsilon_{\text{PID}}$	$\epsilon_{\text{PID},\mu}$	$\epsilon_{\text{PID},\tau_{h3}}$	$\epsilon_{\text{GEC}}$	$\epsilon_{\text{trig}}$	$\epsilon_{\text{rec}}$
Low-mass											
	45	40.2 ± 1.1	92.7 ± 0.4	43.3 ± 1.2	100.5 ± 0.1	57.2 ± 0.9	97.6 ± 0.4	58.7 ± 0.9	93.0 ± 0.6	81.8 ± 2.7	17.7 ± 0.8
	55	38.7 ± 1.0	92.5 ± 0.4	41.9 ± 1.1	100.8 ± 0.0	62.6 ± 1.0	97.9 ± 0.3	64.0 ± 1.0	93.0 ± 0.6	80.3 ± 1.9	18.4 ± 0.7
	65	37.8 ± 1.0	92.6 ± 0.4	40.8 ± 1.0	100.6 ± 0.0	64.9 ± 1.1	98.1 ± 0.3	66.2 ± 1.1	93.0 ± 0.6	79.9 ± 1.3	18.4 ± 0.6
	75	35.9 ± 0.9	92.2 ± 0.4	38.9 ± 1.0	100.6 ± 0.0	67.1 ± 1.1	98.6 ± 0.3	68.1 ± 1.1	93.0 ± 0.6	79.3 ± 0.9	17.9 ± 0.6
	85	34.6 ± 0.9	92.3 ± 0.4	37.5 ± 1.0	100.6 ± 0.0	68.5 ± 1.2	98.6 ± 0.2	69.4 ± 1.2	93.0 ± 0.6	78.8 ± 0.9	17.5 ± 0.6
	95	33.6 ± 0.9	92.3 ± 0.4	36.4 ± 1.0	100.8 ± 0.0	70.3 ± 1.2	98.8 ± 0.3	71.2 ± 1.2	93.0 ± 0.6	78.2 ± 1.0	17.4 ± 0.6
	105	32.0 ± 0.9	91.6 ± 0.5	35.0 ± 1.0	100.5 ± 0.1	70.3 ± 1.3	98.7 ± 0.3	71.3 ± 1.2	93.0 ± 0.6	77.4 ± 1.5	16.3 ± 0.6
	115	30.0 ± 0.9	91.4 ± 0.5	32.8 ± 1.0	100.4 ± 0.1	70.9 ± 1.3	98.7 ± 0.4	71.9 ± 1.3	93.0 ± 0.6	76.7 ± 1.8	15.3 ± 0.7
	125	29.1 ± 0.9	91.7 ± 0.5	31.7 ± 1.0	100.9 ± 0.1	72.2 ± 1.3	98.6 ± 0.4	73.2 ± 1.3	93.0 ± 0.6	76.6 ± 2.3	15.2 ± 0.7
	135	28.3 ± 1.0	91.6 ± 0.5	30.9 ± 1.0	100.6 ± 0.1	74.4 ± 1.4	98.7 ± 0.4	75.5 ± 1.4	93.0 ± 0.6	75.7 ± 2.9	15.0 ± 0.8
	145	26.8 ± 1.0	91.2 ± 0.5	29.3 ± 1.0	100.6 ± 0.1	74.6 ± 1.4	98.6 ± 0.4	75.7 ± 1.4	93.0 ± 0.6	74.6 ± 3.4	14.0 ± 0.9
	155	26.4 ± 1.0	91.1 ± 0.5	29.0 ± 1.0	100.7 ± 0.1	74.7 ± 1.4	98.6 ± 0.4	75.7 ± 1.4	93.0 ± 0.6	73.8 ± 3.5	13.7 ± 0.9
	165	24.4 ± 0.9	91.2 ± 0.5	26.7 ± 1.0	100.7 ± 0.1	76.2 ± 1.5	98.7 ± 0.4	77.3 ± 1.5	93.0 ± 0.6	73.1 ± 3.6	12.8 ± 0.8
	175	22.8 ± 0.9	90.4 ± 0.5	25.3 ± 1.0	99.9 ± 0.1	76.2 ± 1.5	98.6 ± 0.4	77.3 ± 1.5	93.0 ± 0.6	71.6 ± 3.6	11.7 ± 0.8
	185	22.1 ± 0.9	90.7 ± 0.5	24.4 ± 1.0	100.6 ± 0.1	75.1 ± 1.6	98.5 ± 0.4	76.2 ± 1.6	93.0 ± 0.6	70.8 ± 3.8	11.0 ± 0.8
	195	21.0 ± 0.9	91.1 ± 0.5	23.0 ± 1.0	99.6 ± 0.3	77.4 ± 1.6	98.6 ± 0.4	78.5 ± 1.6	93.0 ± 0.6	70.4 ± 3.5	10.7 ± 0.7
Central											
	75	36.1 ± 1.0	92.5 ± 0.4	39.0 ± 1.0	100.6 ± 0.0	68.0 ± 1.1	98.7 ± 0.3	68.9 ± 1.1	93.0 ± 0.6	79.2 ± 0.8	18.2 ± 0.6
	85	34.6 ± 0.9	92.1 ± 0.4	37.5 ± 1.0	100.6 ± 0.0	68.9 ± 1.2	98.7 ± 0.2	69.7 ± 1.2	93.0 ± 0.6	78.7 ± 0.8	17.6 ± 0.6
	95	33.6 ± 0.9	92.3 ± 0.4	36.4 ± 1.0	100.8 ± 0.0	70.6 ± 1.2	98.8 ± 0.3	71.5 ± 1.2	93.0 ± 0.6	78.2 ± 0.9	17.5 ± 0.6
	105	32.2 ± 0.9	91.8 ± 0.5	35.1 ± 1.0	100.5 ± 0.1	70.8 ± 1.3	98.7 ± 0.3	71.8 ± 1.3	93.0 ± 0.6	77.4 ± 1.4	16.6 ± 0.7
	115	30.0 ± 0.9	91.5 ± 0.5	32.8 ± 1.0	100.4 ± 0.1	71.6 ± 1.3	98.7 ± 0.4	72.6 ± 1.3	93.0 ± 0.6	76.9 ± 1.8	15.5 ± 0.7
	125	29.2 ± 0.9	91.8 ± 0.5	31.8 ± 1.0	100.9 ± 0.1	73.1 ± 1.3	98.6 ± 0.4	74.2 ± 1.3	93.0 ± 0.6	76.7 ± 2.3	15.4 ± 0.8
	135	28.4 ± 1.0	91.8 ± 0.4	30.9 ± 1.0	100.6 ± 0.1	74.7 ± 1.4	98.7 ± 0.4	75.7 ± 1.4	93.0 ± 0.6	75.7 ± 2.9	15.1 ± 0.8
	145	26.8 ± 1.0	91.3 ± 0.5	29.3 ± 1.0	100.6 ± 0.1	75.1 ± 1.4	98.6 ± 0.4	76.1 ± 1.4	93.0 ± 0.6	74.6 ± 3.4	14.1 ± 0.9
	155	26.4 ± 1.0	91.1 ± 0.5	29.0 ± 1.0	100.7 ± 0.1	75.4 ± 1.4	98.6 ± 0.4	76.5 ± 1.4	93.0 ± 0.6	74.0 ± 3.4	13.9 ± 0.9
	165	24.4 ± 0.9	91.2 ± 0.5	26.7 ± 1.0	100.7 ± 0.1	76.3 ± 1.5	98.7 ± 0.4	77.3 ± 1.5	93.0 ± 0.6	73.3 ± 3.6	12.8 ± 0.8
	175	22.9 ± 0.9	90.5 ± 0.5	25.3 ± 1.0	99.9 ± 0.1	77.1 ± 1.5	98.6 ± 0.4	78.1 ± 1.5	93.0 ± 0.6	71.7 ± 3.5	11.8 ± 0.8
	185	22.3 ± 0.9	90.9 ± 0.5	24.5 ± 1.0	100.6 ± 0.1	75.5 ± 1.6	98.6 ± 0.4	76.6 ± 1.6	93.0 ± 0.6	71.2 ± 3.7	11.2 ± 0.8
	195	20.9 ± 0.9	90.9 ± 0.5	23.0 ± 1.0	99.6 ± 0.3	78.0 ± 1.6	98.6 ± 0.4	79.1 ± 1.6	93.0 ± 0.6	70.1 ± 3.5	10.7 ± 0.8
High-mass											
	95	33.6 ± 1.0	92.2 ± 0.4	36.5 ± 1.0	100.8 ± 0.0	70.9 ± 1.2	98.9 ± 0.2	71.8 ± 1.2	93.0 ± 0.6	77.9 ± 0.9	17.5 ± 0.6
	105	32.2 ± 1.0	91.7 ± 0.5	35.1 ± 1.0	100.5 ± 0.1	71.7 ± 1.3	98.8 ± 0.3	72.6 ± 1.3	93.0 ± 0.6	77.3 ± 1.4	16.7 ± 0.7
	115	30.0 ± 0.9	91.4 ± 0.5	32.8 ± 1.0	100.4 ± 0.1	72.3 ± 1.3	98.7 ± 0.4	73.3 ± 1.3	93.0 ± 0.6	76.8 ± 1.8	15.6 ± 0.7
	125	29.2 ± 0.9	91.7 ± 0.5	31.9 ± 1.0	100.9 ± 0.1	73.5 ± 1.3	98.6 ± 0.4	74.5 ± 1.3	93.0 ± 0.6	76.6 ± 2.4	15.5 ± 0.8
	135	28.4 ± 1.0	91.7 ± 0.4	30.9 ± 1.0	100.6 ± 0.1	75.2 ± 1.4	98.7 ± 0.4	76.2 ± 1.4	93.0 ± 0.6	75.7 ± 2.9	15.2 ± 0.8
	145	26.8 ± 1.0	91.4 ± 0.5	29.3 ± 1.0	100.6 ± 0.1	75.2 ± 1.4	98.6 ± 0.4	76.3 ± 1.4	93.0 ± 0.6	74.6 ± 3.4	14.2 ± 0.9
	155	26.4 ± 1.0	91.1 ± 0.5	29.0 ± 1.0	100.7 ± 0.1	75.6 ± 1.4	98.6 ± 0.4	76.6 ± 1.4	93.0 ± 0.6	74.0 ± 3.5	13.9 ± 0.9
	165	24.4 ± 0.9	91.2 ± 0.5	26.7 ± 1.0	100.7 ± 0.1	76.3 ± 1.5	98.7 ± 0.4	77.3 ± 1.5	93.0 ± 0.6	73.3 ± 3.6	12.8 ± 0.8
	175	23.0 ± 0.9	90.5 ± 0.5	25.4 ± 1.0	99.9 ± 0.1	77.2 ± 1.5	98.6 ± 0.4	78.3 ± 1.5	93.0 ± 0.6	71.7 ± 3.5	11.9 ± 0.8
	185	22.3 ± 0.9	90.9 ± 0.5	24.5 ± 1.0	100.6 ± 0.1	75.5 ± 1.6	98.6 ± 0.4	76.6 ± 1.6	93.0 ± 0.6	71.2 ± 3.7	11.2 ± 0.8
	195	20.9 ± 0.9	90.9 ± 0.5	23.0 ± 1.0	99.6 ± 0.3	78.0 ± 1.6	98.6 ± 0.4	79.1 ± 1.6	93.0 ± 0.6	70.1 ± 3.5	10.7 ± 0.8



Table K.6 – Detail of  $\varepsilon_{\text{rec}}$  in  $\mu\tau_\mu$  channel.

Regime	$m_H$	$[\text{GeV}/c^2]$	$\varepsilon_{\text{track}}$	$\varepsilon_{\text{track},\mu}$	$\varepsilon_{\text{track},\tau_\mu}$	$\varepsilon_{\text{kine}}$	$\varepsilon_{\text{PID}}$	$\varepsilon_{\text{PID},\mu}$	$\varepsilon_{\text{PID},\tau_\mu}$	$\varepsilon_{\text{GBC}}$	$\varepsilon_{\text{trig}}$	$\varepsilon_{\text{trig},\mu}$	$\varepsilon_{\text{trig},\tau_\mu}$	$\varepsilon_{\text{rec}}$	
Low-mass	45	$85.5 \pm 0.8$	$92.4 \pm 0.4$	$92.4 \pm 0.4$	$92.4 \pm 0.4$	$100.0 \pm 0.0$	$96.4 \pm 0.4$	$97.5 \pm 0.4$	$98.9 \pm 0.0$	$93.0 \pm 0.3$	$81.9 \pm 2.5$	$81.9 \pm 2.5$	$0.0 \pm 0.0$	$62.8 \pm 2.1$	
	55	$85.6 \pm 0.8$	$92.6 \pm 0.4$	$92.4 \pm 0.4$	$100.2 \pm 0.0$	$96.8 \pm 0.4$	$98.0 \pm 0.3$	$98.8 \pm 0.1$	$98.8 \pm 0.1$	$93.0 \pm 0.3$	$80.8 \pm 1.8$	$80.2 \pm 1.8$	$2.5 \pm 0.1$	$62.3 \pm 1.5$	
	65	$84.7 \pm 0.8$	$92.0 \pm 0.5$	$92.0 \pm 0.5$	$100.2 \pm 0.0$	$97.1 \pm 0.4$	$98.3 \pm 0.3$	$98.8 \pm 0.1$	$98.8 \pm 0.1$	$93.0 \pm 0.3$	$81.5 \pm 1.2$	$79.7 \pm 1.2$	$9.1 \pm 0.5$	$62.5 \pm 1.1$	
	75	$85.1 \pm 0.8$	$92.5 \pm 0.4$	$92.0 \pm 0.5$	$100.0 \pm 0.0$	$97.3 \pm 0.3$	$98.5 \pm 0.3$	$98.7 \pm 0.1$	$98.7 \pm 0.1$	$93.0 \pm 0.3$	$82.6 \pm 1.0$	$79.3 \pm 1.0$	$15.4 \pm 0.7$	$63.7 \pm 1.0$	
	85	$84.8 \pm 0.8$	$91.9 \pm 0.4$	$92.2 \pm 0.4$	$100.1 \pm 0.0$	$97.4 \pm 0.4$	$98.7 \pm 0.2$	$98.7 \pm 0.2$	$98.7 \pm 0.1$	$93.0 \pm 0.3$	$84.1 \pm 0.9$	$78.5 \pm 0.9$	$25.5 \pm 1.1$	$64.6 \pm 1.0$	
	95	$84.2 \pm 0.8$	$92.1 \pm 0.4$	$91.4 \pm 0.5$	$99.9 \pm 0.0$	$97.4 \pm 0.4$	$98.8 \pm 0.3$	$98.6 \pm 0.1$	$98.6 \pm 0.1$	$93.0 \pm 0.3$	$85.5 \pm 1.0$	$78.0 \pm 1.0$	$33.6 \pm 1.4$	$65.2 \pm 1.1$	
	105	$83.6 \pm 0.8$	$91.3 \pm 0.5$	$91.5 \pm 0.5$	$100.1 \pm 0.0$	$97.4 \pm 0.4$	$98.7 \pm 0.3$	$98.6 \pm 0.1$	$98.6 \pm 0.1$	$93.0 \pm 0.3$	$85.2 \pm 1.2$	$77.2 \pm 1.4$	$34.7 \pm 1.3$	$64.5 \pm 1.2$	
	115	$83.5 \pm 0.8$	$91.6 \pm 0.5$	$91.1 \pm 0.5$	$100.0 \pm 0.0$	$97.3 \pm 0.5$	$98.7 \pm 0.4$	$98.6 \pm 0.1$	$98.6 \pm 0.1$	$93.0 \pm 0.3$	$86.3 \pm 1.4$	$76.9 \pm 1.9$	$39.9 \pm 1.3$	$65.2 \pm 1.3$	
	125	$83.4 \pm 0.8$	$91.6 \pm 0.5$	$91.1 \pm 0.5$	$100.0 \pm 0.0$	$97.3 \pm 0.5$	$98.7 \pm 0.4$	$98.6 \pm 0.1$	$98.6 \pm 0.1$	$93.0 \pm 0.3$	$87.2 \pm 1.7$	$76.3 \pm 2.5$	$46.1 \pm 1.5$	$65.8 \pm 1.5$	
	135	$83.0 \pm 0.9$	$91.3 \pm 0.5$	$90.9 \pm 0.5$	$100.1 \pm 0.0$	$97.2 \pm 0.5$	$98.6 \pm 0.4$	$98.5 \pm 0.2$	$98.5 \pm 0.2$	$93.0 \pm 0.3$	$87.2 \pm 1.9$	$75.6 \pm 2.9$	$48.0 \pm 1.5$	$65.5 \pm 1.6$	
	145	$82.9 \pm 0.9$	$91.2 \pm 0.5$	$90.9 \pm 0.5$	$100.0 \pm 0.0$	$97.2 \pm 0.6$	$98.6 \pm 0.4$	$98.5 \pm 0.2$	$98.5 \pm 0.2$	$93.0 \pm 0.3$	$88.3 \pm 1.8$	$75.0 \pm 3.3$	$52.8 \pm 1.3$	$66.1 \pm 1.6$	
	155	$82.3 \pm 0.9$	$90.9 \pm 0.5$	$90.6 \pm 0.5$	$99.9 \pm 0.1$	$97.2 \pm 0.6$	$98.6 \pm 0.4$	$98.5 \pm 0.2$	$98.5 \pm 0.2$	$93.0 \pm 0.3$	$88.3 \pm 1.9$	$74.2 \pm 3.5$	$54.4 \pm 1.4$	$65.6 \pm 1.7$	
	165	$82.3 \pm 0.9$	$90.9 \pm 0.5$	$90.5 \pm 0.5$	$100.0 \pm 0.0$	$97.2 \pm 0.6$	$98.6 \pm 0.4$	$98.6 \pm 0.2$	$98.6 \pm 0.2$	$93.0 \pm 0.3$	$87.4 \pm 2.0$	$73.1 \pm 3.6$	$52.9 \pm 1.3$	$65.1 \pm 1.7$	
	175	$81.8 \pm 0.9$	$90.6 \pm 0.5$	$90.3 \pm 0.5$	$100.0 \pm 0.0$	$97.2 \pm 0.6$	$98.6 \pm 0.4$	$98.6 \pm 0.2$	$98.6 \pm 0.2$	$93.0 \pm 0.3$	$88.5 \pm 1.9$	$72.2 \pm 3.7$	$58.7 \pm 1.4$	$65.5 \pm 1.7$	
	185	$81.6 \pm 0.9$	$90.5 \pm 0.5$	$90.2 \pm 0.5$	$99.9 \pm 0.1$	$97.3 \pm 0.6$	$98.6 \pm 0.4$	$98.7 \pm 0.2$	$98.7 \pm 0.2$	$93.0 \pm 0.3$	$88.4 \pm 1.8$	$70.8 \pm 3.6$	$59.6 \pm 1.3$	$65.2 \pm 1.6$	
	195	$81.5 \pm 0.9$	$90.3 \pm 0.5$	$90.3 \pm 0.5$	$99.9 \pm 0.1$	$97.3 \pm 0.6$	$98.6 \pm 0.4$	$98.6 \pm 0.2$	$98.6 \pm 0.2$	$93.0 \pm 0.3$	$87.8 \pm 1.8$	$69.5 \pm 3.5$	$60.0 \pm 1.3$	$64.7 \pm 1.6$	
	Central	75	$85.3 \pm 0.8$	$92.7 \pm 0.4$	$92.0 \pm 0.5$	$100.0 \pm 0.0$	$97.5 \pm 0.3$	$98.7 \pm 0.3$	$98.8 \pm 0.1$	$98.8 \pm 0.1$	$93.0 \pm 0.3$	$83.2 \pm 0.9$	$79.2 \pm 0.8$	$19.1 \pm 0.9$	$64.4 \pm 1.0$
		85	$84.8 \pm 0.8$	$91.9 \pm 0.4$	$92.3 \pm 0.4$	$100.1 \pm 0.0$	$97.5 \pm 0.3$	$98.8 \pm 0.2$	$98.7 \pm 0.1$	$98.7 \pm 0.1$	$93.0 \pm 0.3$	$84.3 \pm 0.9$	$78.5 \pm 0.8$	$26.8 \pm 1.2$	$64.9 \pm 1.0$
		95	$84.3 \pm 0.8$	$92.1 \pm 0.4$	$91.5 \pm 0.5$	$99.3 \pm 0.0$	$97.5 \pm 0.4$	$98.8 \pm 0.3$	$98.7 \pm 0.1$	$98.7 \pm 0.1$	$93.0 \pm 0.3$	$85.6 \pm 1.0$	$78.0 \pm 1.0$	$34.5 \pm 1.4$	$65.4 \pm 1.0$
105		$83.6 \pm 0.8$	$91.4 \pm 0.5$	$91.4 \pm 0.5$	$100.1 \pm 0.0$	$97.4 \pm 0.4$	$98.7 \pm 0.3$	$98.6 \pm 0.1$	$98.6 \pm 0.1$	$93.0 \pm 0.3$	$85.6 \pm 1.2$	$77.3 \pm 1.4$	$36.4 \pm 1.4$	$64.9 \pm 1.2$	
115		$83.6 \pm 0.8$	$91.7 \pm 0.5$	$91.1 \pm 0.5$	$100.0 \pm 0.0$	$97.3 \pm 0.5$	$98.7 \pm 0.4$	$98.6 \pm 0.1$	$98.6 \pm 0.1$	$93.0 \pm 0.3$	$86.4 \pm 1.4$	$76.9 \pm 1.9$	$40.7 \pm 1.3$	$65.4 \pm 1.3$	
125		$83.5 \pm 0.8$	$91.7 \pm 0.5$	$91.1 \pm 0.5$	$100.0 \pm 0.0$	$97.3 \pm 0.5$	$98.7 \pm 0.4$	$98.6 \pm 0.2$	$98.6 \pm 0.2$	$93.0 \pm 0.3$	$87.7 \pm 1.6$	$76.3 \pm 2.4$	$48.1 \pm 1.5$	$66.3 \pm 1.4$	
135		$83.1 \pm 0.9$	$91.3 \pm 0.5$	$91.0 \pm 0.5$	$100.1 \pm 0.0$	$97.2 \pm 0.5$	$98.6 \pm 0.4$	$98.5 \pm 0.2$	$98.5 \pm 0.2$	$93.0 \pm 0.3$	$87.6 \pm 1.8$	$75.6 \pm 2.9$	$49.4 \pm 1.5$	$65.8 \pm 1.6$	
145		$82.8 \pm 0.9$	$91.2 \pm 0.5$	$90.9 \pm 0.5$	$100.0 \pm 0.0$	$97.2 \pm 0.6$	$98.6 \pm 0.4$	$98.5 \pm 0.2$	$98.5 \pm 0.2$	$93.0 \pm 0.3$	$88.8 \pm 1.8$	$75.0 \pm 3.3$	$54.8 \pm 1.4$	$66.5 \pm 1.6$	
155		$82.4 \pm 0.9$	$91.1 \pm 0.5$	$90.5 \pm 0.5$	$99.9 \pm 0.1$	$97.2 \pm 0.6$	$98.6 \pm 0.4$	$98.6 \pm 0.2$	$98.6 \pm 0.2$	$93.0 \pm 0.3$	$88.5 \pm 1.9$	$74.3 \pm 3.5$	$55.3 \pm 1.4$	$65.9 \pm 1.7$	
165		$82.4 \pm 0.9$	$91.1 \pm 0.5$	$90.4 \pm 0.5$	$100.0 \pm 0.0$	$97.2 \pm 0.6$	$98.6 \pm 0.4$	$98.6 \pm 0.4$	$98.6 \pm 0.2$	$93.0 \pm 0.3$	$88.0 \pm 1.9$	$73.3 \pm 3.6$	$54.6 \pm 1.3$	$65.6 \pm 1.7$	
175		$82.0 \pm 0.9$	$90.7 \pm 0.5$	$90.4 \pm 0.5$	$100.0 \pm 0.0$	$97.2 \pm 0.6$	$98.6 \pm 0.4$	$98.6 \pm 0.4$	$98.6 \pm 0.2$	$93.0 \pm 0.3$	$88.9 \pm 1.9$	$72.3 \pm 3.6$	$60.0 \pm 1.4$	$66.0 \pm 1.6$	
185		$81.7 \pm 0.9$	$90.5 \pm 0.5$	$90.2 \pm 0.5$	$99.9 \pm 0.1$	$97.3 \pm 0.6$	$98.6 \pm 0.4$	$98.6 \pm 0.2$	$98.6 \pm 0.2$	$93.0 \pm 0.3$	$88.6 \pm 1.8$	$70.8 \pm 3.5$	$60.4 \pm 1.3$	$65.4 \pm 1.6$	
195		$81.6 \pm 0.9$	$90.4 \pm 0.5$	$90.3 \pm 0.5$	$99.9 \pm 0.1$	$97.3 \pm 0.6$	$98.6 \pm 0.4$	$98.7 \pm 0.2$	$98.7 \pm 0.2$	$93.0 \pm 0.3$	$88.2 \pm 1.7$	$69.5 \pm 3.5$	$61.1 \pm 1.2$	$65.1 \pm 1.5$	
High-mass		95	$84.2 \pm 0.8$	$91.8 \pm 0.4$	$91.7 \pm 0.5$	$99.9 \pm 0.0$	$97.4 \pm 0.5$	$98.7 \pm 0.4$	$98.7 \pm 0.1$	$98.7 \pm 0.1$	$93.0 \pm 0.3$	$83.8 \pm 1.7$	$76.6 \pm 1.9$	$30.5 \pm 1.3$	$64.0 \pm 1.5$
		105	$83.3 \pm 0.8$	$91.2 \pm 0.5$	$91.3 \pm 0.5$	$100.1 \pm 0.0$	$97.4 \pm 0.5$	$98.6 \pm 0.4$	$98.8 \pm 0.1$	$98.8 \pm 0.1$	$93.0 \pm 0.3$	$83.6 \pm 1.7$	$76.4 \pm 2.0$	$30.6 \pm 1.3$	$63.2 \pm 1.5$
		115	$83.4 \pm 0.8$	$91.4 \pm 0.5$	$91.3 \pm 0.5$	$100.0 \pm 0.0$	$97.4 \pm 0.5$	$98.7 \pm 0.4$	$98.6 \pm 0.1$	$98.6 \pm 0.1$	$93.0 \pm 0.3$	$85.0 \pm 1.7$	$76.3 \pm 2.2$	$36.1 \pm 1.4$	$64.2 \pm 1.5$
		125	$83.5 \pm 0.8$	$91.6 \pm 0.4$	$91.1 \pm 0.5$	$100.0 \pm 0.0$	$97.3 \pm 0.5$	$98.7 \pm 0.4$	$98.6 \pm 0.1$	$98.6 \pm 0.1$	$93.0 \pm 0.3$	$86.0 \pm 1.9$	$76.0 \pm 2.7$	$42.7 \pm 1.6$	$65.1 \pm 1.6$
		135	$83.1 \pm 0.9$	$91.4 \pm 0.5$	$90.9 \pm 0.5$	$100.1 \pm 0.0$	$97.3 \pm 0.5$	$98.7 \pm 0.4$	$98.6 \pm 0.1$	$98.6 \pm 0.1$	$93.0 \pm 0.3$	$86.2 \pm 2.1$	$75.3 \pm 3.0$	$43.5 \pm 1.5$	$64.7 \pm 1.7$
		145	$82.9 \pm 0.9$	$91.1 \pm 0.5$	$91.0 \pm 0.5$	$100.0 \pm 0.0$	$97.2 \pm 0.6$	$98.6 \pm 0.4$	$98.6 \pm 0.2$	$98.6 \pm 0.2$	$93.0 \pm 0.3$	$87.4 \pm 2.0$	$74.8 \pm 3.4$	$49.7 \pm 1.5$	$65.5 \pm 1.7$
	155	$82.5 \pm 0.9$	$91.0 \pm 0.5$	$90.6 \pm 0.5$	$99.9 \pm 0.1$	$97.2 \pm 0.6$	$98.7 \pm 0.4$	$98.5 \pm 0.2$	$98.5 \pm 0.2$	$93.0 \pm 0.3$	$87.2 \pm 2.1$	$74.2 \pm 3.5$	$50.6 \pm 1.5$	$65.0 \pm 1.8$	
	165	$82.4 \pm 0.9$	$91.1 \pm 0.5$	$90.4 \pm 0.5$	$100.0 \pm 0.0$	$97.2 \pm 0.6$	$98.6 \pm 0.4$	$98.6 \pm 0.2$	$98.6 \pm 0.2$	$93.0 \pm 0.3$	$86.8 \pm 2.1$	$73.0 \pm 3.6$	$50.7 \pm 1.3$	$64.7 \pm 1.8$	
	175	$82.1 \pm 0.9$	$90.6 \pm 0.5$	$90.5 \pm 0.5$	$100.0 \pm 0.0$	$97.2 \pm 0.6$	$98.6 \pm 0.4$	$98.5 \pm 0.2$	$98.5 \pm 0.2$	$93.0 \pm 0.3$	$87.9 \pm 2.0$	$72.1 \pm 3.7$	$56.7 \pm 1.5$	$65.3 \pm 1.7$	
	185	$81.8 \pm 0.9$	$90.6 \pm 0.5$	$90.3 \pm 0.5$	$99.9 \pm 0.1$	$97.2 \pm 0.6$	$98.6 \pm 0.4$	$98.6 \pm 0.2$	$98.6 \pm 0.2$	$93.0 \pm 0.3$	$87.7 \pm 1.9$	$70.9 \pm 3.5$	$57.3 \pm 1.4$	$64.9 \pm 1.7$	
	195	$81.6 \pm 0.9$	$90.4 \pm 0.5$	$90.2 \pm 0.5$	$99.9 \pm 0.1$	$97.2 \pm 0.6$	$98.6 \pm 0.4$	$98.6 \pm 0.2$	$98.6 \pm 0.2$	$93.0 \pm 0.3$	$87.1 \pm 1.9$	$69.2 \pm 3.5$	$57.7 \pm 1.3$	$64.2 \pm 1.6$	

## Appendix K. $H \rightarrow \mu\tau$ Efficiencies

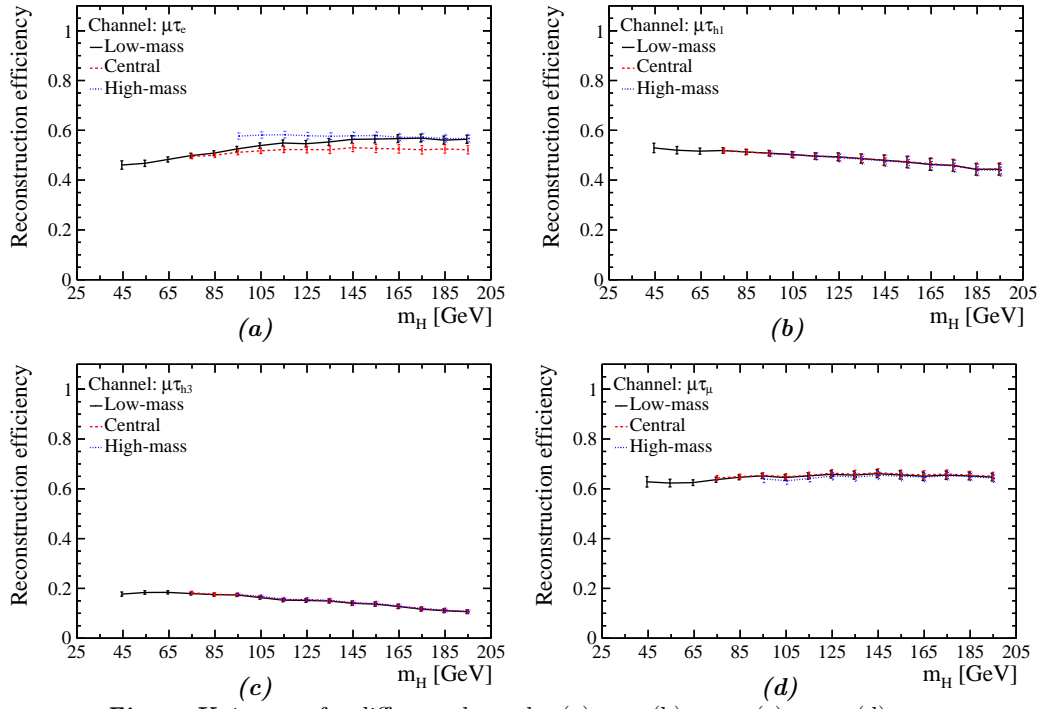


Figure K.1 –  $\varepsilon_{\text{rec}}$  for different channels: (a)  $\mu\tau_e$ , (b)  $\mu\tau_{h1}$ , (c)  $\mu\tau_{h3}$ , (d),  $\mu\tau_\mu$ .

**Table K.7** – Signal selection efficiencies for different channels at different selection regimes, shown in percentage.

Regime	$m_H$ [GeV/ $c^2$ ]	$\mu\tau_e$	$\mu\tau_{h1}$	$\mu\tau_{h3}$	$\mu\tau_\mu$
Low-mass	45	$18.6 \pm 1.1$	$24.2 \pm 1.0$	$21.4 \pm 2.0$	$7.5 \pm 0.6$
	55	$24.7 \pm 0.9$	$26.1 \pm 0.7$	$29.0 \pm 1.6$	$10.2 \pm 0.5$
	65	$23.7 \pm 0.8$	$24.2 \pm 0.6$	$29.6 \pm 1.4$	$11.7 \pm 0.5$
	75	$23.5 \pm 0.8$	$22.4 \pm 0.5$	$33.0 \pm 1.5$	$12.2 \pm 0.5$
	85	$23.8 \pm 0.8$	$21.4 \pm 0.5$	$35.9 \pm 1.5$	$13.2 \pm 0.5$
	95	$23.4 \pm 0.8$	$19.5 \pm 0.5$	$33.3 \pm 1.5$	$13.5 \pm 0.6$
	105	$23.4 \pm 0.8$	$19.0 \pm 0.5$	$31.1 \pm 1.5$	$14.9 \pm 0.6$
	115	$23.4 \pm 0.8$	$18.3 \pm 0.5$	$36.9 \pm 1.7$	$14.9 \pm 0.6$
	125	$26.3 \pm 0.9$	$18.0 \pm 0.5$	$33.6 \pm 1.7$	$16.4 \pm 0.6$
	135	$24.7 \pm 0.9$	$17.1 \pm 0.5$	$35.6 \pm 1.8$	$17.5 \pm 0.7$
	145	$26.2 \pm 0.9$	$17.8 \pm 0.5$	$35.0 \pm 1.9$	$16.5 \pm 0.7$
	155	$24.4 \pm 0.9$	$17.3 \pm 0.5$	$35.0 \pm 2.0$	$19.0 \pm 0.7$
	165	$22.6 \pm 0.9$	$16.2 \pm 0.5$	$31.1 \pm 2.0$	$20.0 \pm 0.8$
	175	$23.6 \pm 1.0$	$15.8 \pm 0.5$	$31.8 \pm 2.2$	$18.8 \pm 0.8$
	185	$23.7 \pm 1.0$	$16.1 \pm 0.6$	$36.3 \pm 2.4$	$18.6 \pm 0.8$
195	$23.8 \pm 1.0$	$16.9 \pm 0.6$	$35.9 \pm 2.6$	$19.8 \pm 0.8$	
Central	65	$18.2 \pm 0.7$	$16.5 \pm 0.5$	$16.0 \pm 1.2$	$7.8 \pm 0.4$
	75	$28.9 \pm 0.8$	$24.1 \pm 0.6$	$31.5 \pm 1.4$	$11.2 \pm 0.5$
	85	$34.1 \pm 0.9$	$28.7 \pm 0.6$	$37.8 \pm 1.5$	$14.0 \pm 0.5$
	95	$38.8 \pm 0.9$	$30.0 \pm 0.6$	$38.7 \pm 1.6$	$15.2 \pm 0.6$
	105	$40.3 \pm 0.9$	$30.4 \pm 0.6$	$39.3 \pm 1.6$	$17.0 \pm 0.6$
	115	$41.8 \pm 1.0$	$30.7 \pm 0.6$	$45.2 \pm 1.8$	$16.9 \pm 0.6$
	125	$44.5 \pm 1.0$	$31.6 \pm 0.6$	$44.5 \pm 1.8$	$19.5 \pm 0.7$
	135	$46.0 \pm 1.0$	$30.1 \pm 0.6$	$45.1 \pm 1.9$	$20.7 \pm 0.7$
	145	$49.2 \pm 1.0$	$31.0 \pm 0.7$	$44.0 \pm 2.0$	$20.3 \pm 0.7$
	155	$49.2 \pm 1.0$	$30.3 \pm 0.7$	$44.7 \pm 2.1$	$22.8 \pm 0.8$
	165	$49.9 \pm 1.1$	$29.9 \pm 0.7$	$43.0 \pm 2.2$	$24.2 \pm 0.8$
	175	$52.8 \pm 1.1$	$29.1 \pm 0.7$	$44.5 \pm 2.3$	$23.2 \pm 0.8$
	185	$51.7 \pm 1.1$	$29.3 \pm 0.7$	$48.9 \pm 2.5$	$23.2 \pm 0.8$
195	$53.4 \pm 1.2$	$30.4 \pm 0.7$	$46.1 \pm 2.7$	$24.8 \pm 0.9$	
High-mass	75	$1.2 \pm 0.2$	$2.7 \pm 0.2$	$5.9 \pm 0.8$	$0.6 \pm 0.1$
	85	$4.8 \pm 0.4$	$9.0 \pm 0.4$	$16.9 \pm 1.2$	$1.5 \pm 0.2$
	95	$10.4 \pm 0.6$	$16.8 \pm 0.5$	$28.0 \pm 1.5$	$4.0 \pm 0.3$
	105	$14.7 \pm 0.7$	$22.7 \pm 0.5$	$33.4 \pm 1.5$	$7.7 \pm 0.4$
	115	$18.9 \pm 0.8$	$25.9 \pm 0.6$	$41.1 \pm 1.8$	$10.7 \pm 0.5$
	125	$22.3 \pm 0.8$	$29.4 \pm 0.6$	$42.5 \pm 1.8$	$14.1 \pm 0.6$
	135	$24.6 \pm 0.9$	$31.1 \pm 0.6$	$43.2 \pm 1.9$	$16.4 \pm 0.6$
	145	$29.4 \pm 0.9$	$34.0 \pm 0.7$	$43.4 \pm 2.0$	$15.8 \pm 0.7$
	155	$29.1 \pm 0.9$	$35.7 \pm 0.7$	$44.3 \pm 2.1$	$18.8 \pm 0.7$
	165	$31.0 \pm 1.0$	$37.6 \pm 0.7$	$42.8 \pm 2.2$	$20.3 \pm 0.8$
	175	$33.8 \pm 1.1$	$38.8 \pm 0.7$	$44.1 \pm 2.3$	$19.4 \pm 0.8$
	185	$35.3 \pm 1.1$	$40.7 \pm 0.8$	$48.9 \pm 2.5$	$19.6 \pm 0.8$
	195	$36.7 \pm 1.1$	$41.9 \pm 0.8$	$46.1 \pm 2.7$	$20.6 \pm 0.8$



# L Validation of Fit Models

In order to outline the versatility of the likelihood model used in this analysis, the degree of freedom used to construct the model is summarized in Table L.1 for reference, which will be discussed in the following sections.

**Table L.1** – Summary of construction degree of freedom of models.

Spec	Choices
Upper limit strategy	“baseline”, “Poisson”, “extended LL”
Selection regime	Low-mass, Central, High-mass, Best FOM
Analysis channel	$\mu\tau_e$ , $\mu\tau_{h1}$ , $\mu\tau_{h3}$ , $\mu\tau_\mu$ , simultaneous
Systematics	With, without
PDF Shape	“keyspdf”, “histpdf”, “histstat”
Acceptance	$4\pi$ , LHCb
$m_H$	45–195
POI	$N_{\text{sig}}$ , $\sigma_{gg \rightarrow H \rightarrow \mu\tau}$ , $\mathcal{B}_{H \rightarrow \mu\tau}$

## L.1 Upper Limit Strategies

The validation compares expected upper limit from 3 exclusion strategies defined in the previous section, and shown in Fig. L.1: (1) The baseline upper limit, eq. 16.4, (2) Poisson counting model, eq. 16.1, (3) Extended likelihood model, eq. 16.3.

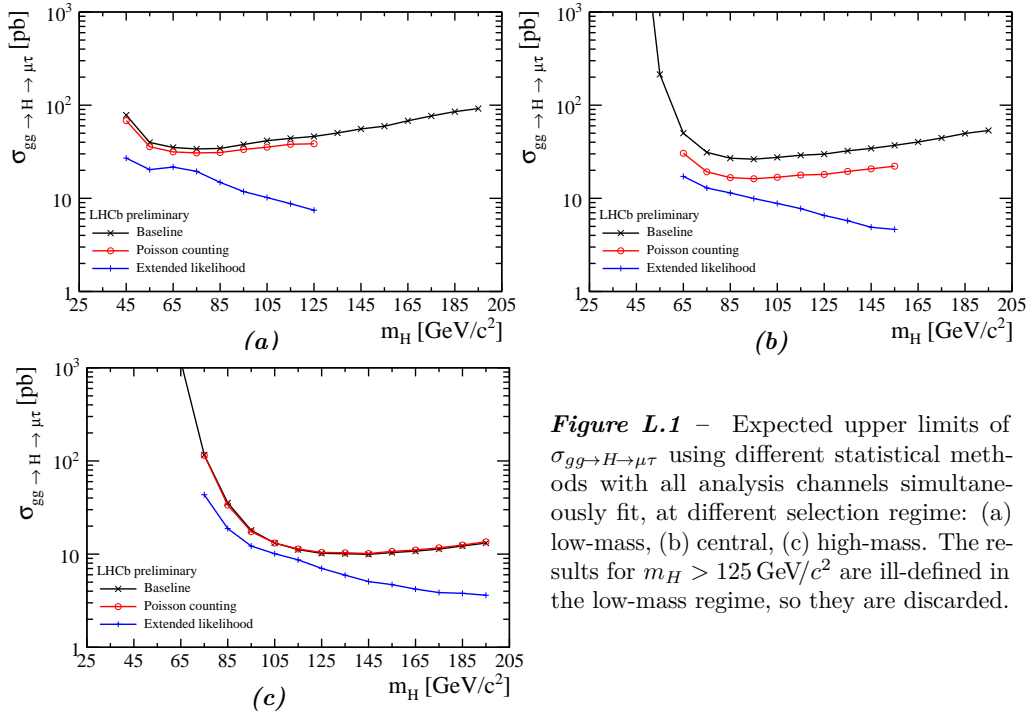


**Figure L.1** – Expected upper limits of  $\sigma_{gg \rightarrow H \rightarrow \mu\tau}$  using different statistical methods with all analysis channels simultaneously fit, at different selection regime: (a) low-mass, (b) central, (c) high-mass. The results for  $m_H > 125$  GeV/c<sup>2</sup> are ill-defined in the low-mass regime, so they are discarded.

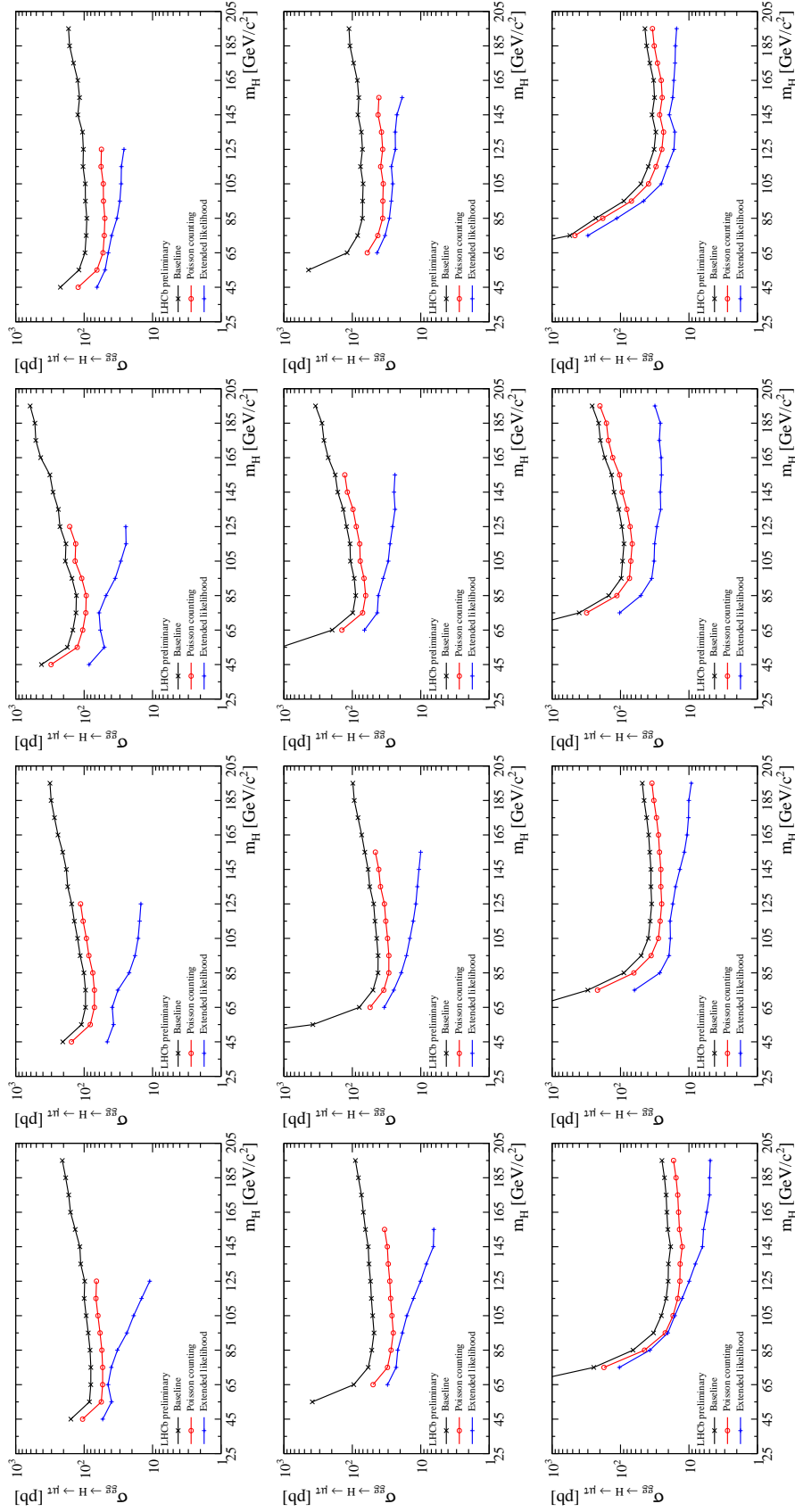
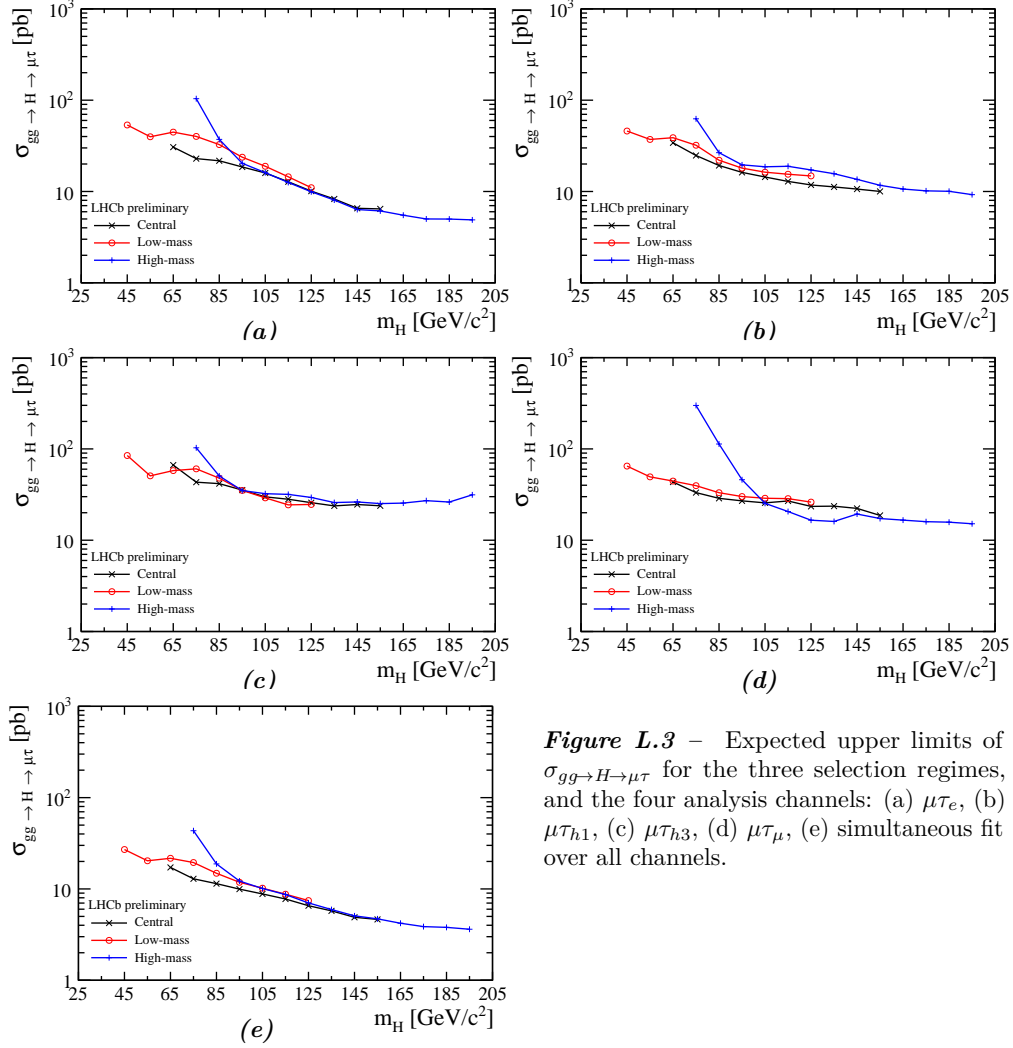


Figure 1.2 – Expected upper limits of  $\sigma_{gg \rightarrow H \rightarrow \mu\tau}$  using different statistical methods for 4 analysis channels (columns-wise) and 3 selection regimes (row-wise).

## L.2 Selection Regimes

The final result for each  $m_H$  is obtained by choosing the regime with the best figure-of-merit ( $\epsilon_{\text{sel}}/(1 + \sqrt{N_{\text{obs}}})$ ). Fig. L.3 compares the expected upper limits obtained with the three selection regimes. It can be seen that each selection regime has the strongest exclusion power at different and complementary subrange of  $m_H$ . The effect is consistent with Fig. 12.2.



**Figure L.3** – Expected upper limits of  $\sigma_{gg \rightarrow H \rightarrow \mu\tau}$  for the three selection regimes, and the four analysis channels: (a)  $\mu\tau_e$ , (b)  $\mu\tau_{h1}$ , (c)  $\mu\tau_{h3}$ , (d)  $\mu\tau_{\mu}$ , (e) simultaneous fit over all channels.

### L.3 Analysis Channels & Simultaneous Fit

The comparison of expected limits between different channel and the simultaneous fit is shown in Fig. L.4.

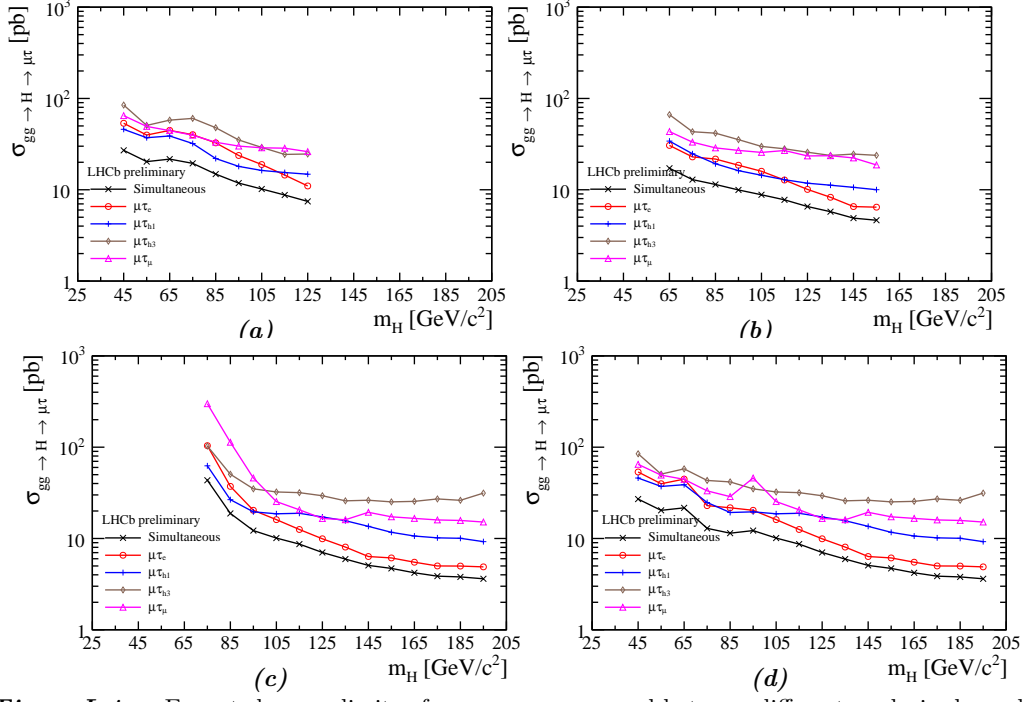


**Figure L.4** – Expected upper limits of  $\sigma_{gg \rightarrow H \rightarrow \mu\tau}$  compared between different analysis channels, at different selection regime: (a) low-mass, (b) central, (c) high-mass, (d) best FOM.



## L.4 Uncertainties as Nuisance Parameters

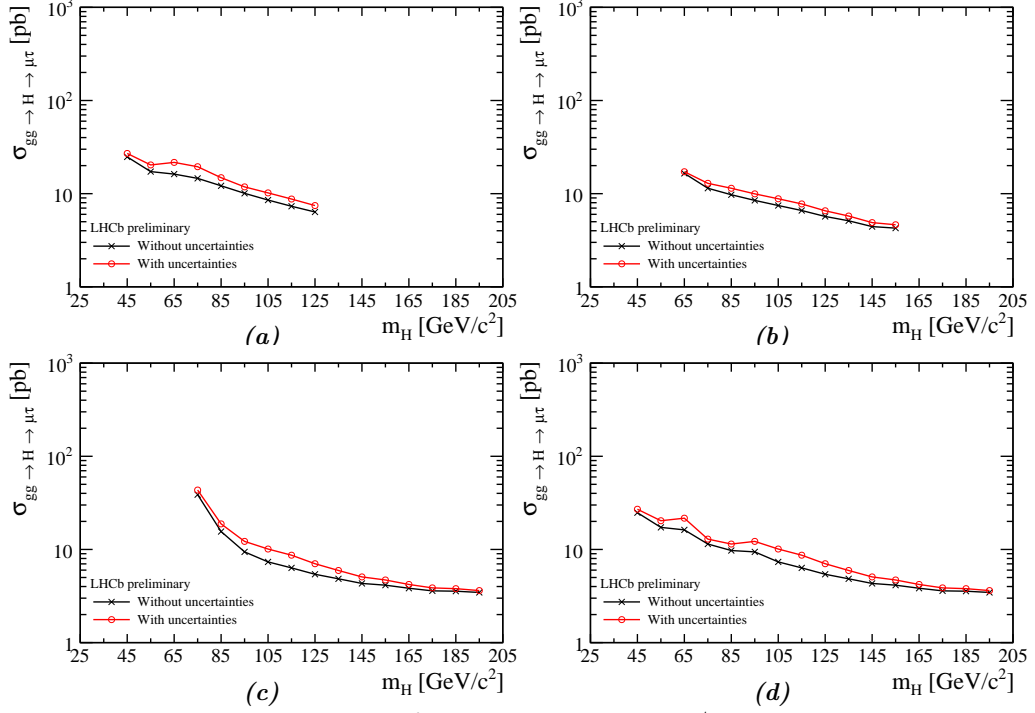


**Figure L.5** – Expected upper limits of  $\sigma_{gg \rightarrow H \rightarrow \mu\tau}$  compared with/without systematic uncertainties, with all analysis channels simultaneously fit, at different selection regime: (a) low-mass, (b) central, (c) high-mass, (d) best FOM.

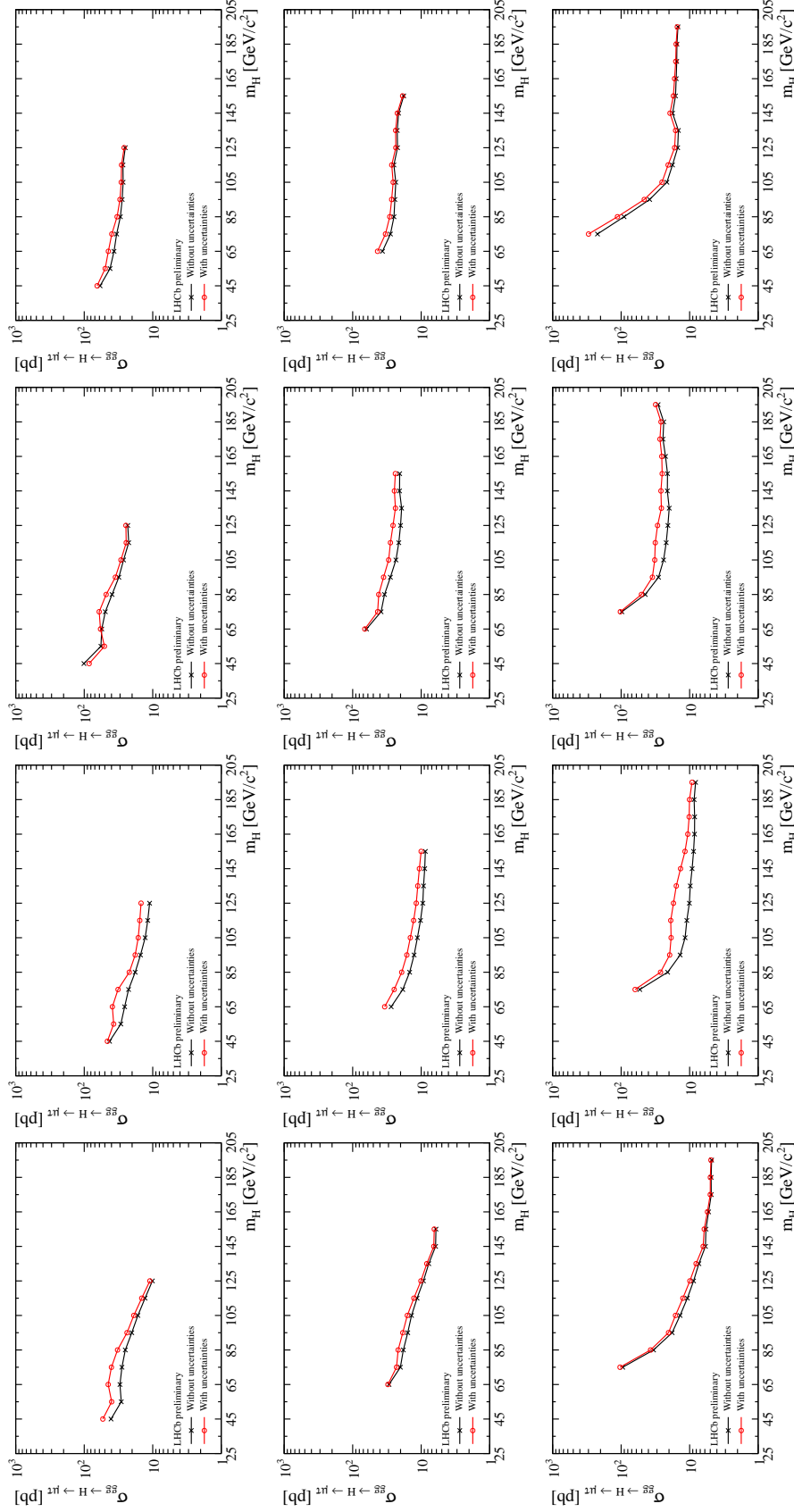


Figure L.6 – Expected upper limits of  $\sigma_{gg \rightarrow H \rightarrow \mu\tau}$  compared with/without systematic uncertainties, for 4 analysis channels (columns-wise) and 3 selection regimes (row-wise).

## L.5 Shape Uncertainty

In order to assess the uncertainty from PDF shape, three different methods to produce the candidate mass distribution are used:

1. Using `RooKeysPdf` class.
2. Using `RooHistPdf` class, with bin width fixed to  $10 \text{ GeV}/c^2$  (dubbed “histpdf”).
3. Using `RooHistPdf` class, with variable bins for each regime (dubbed “histstat”). The numbers of bins are 16 for low-mass, 12 for central, 8 for high-mass regime.

The comparison for each channel is shown in Fig. L.7, as well as samples of corresponding mass distributions best fit in Fig. L.8, Fig. L.9.

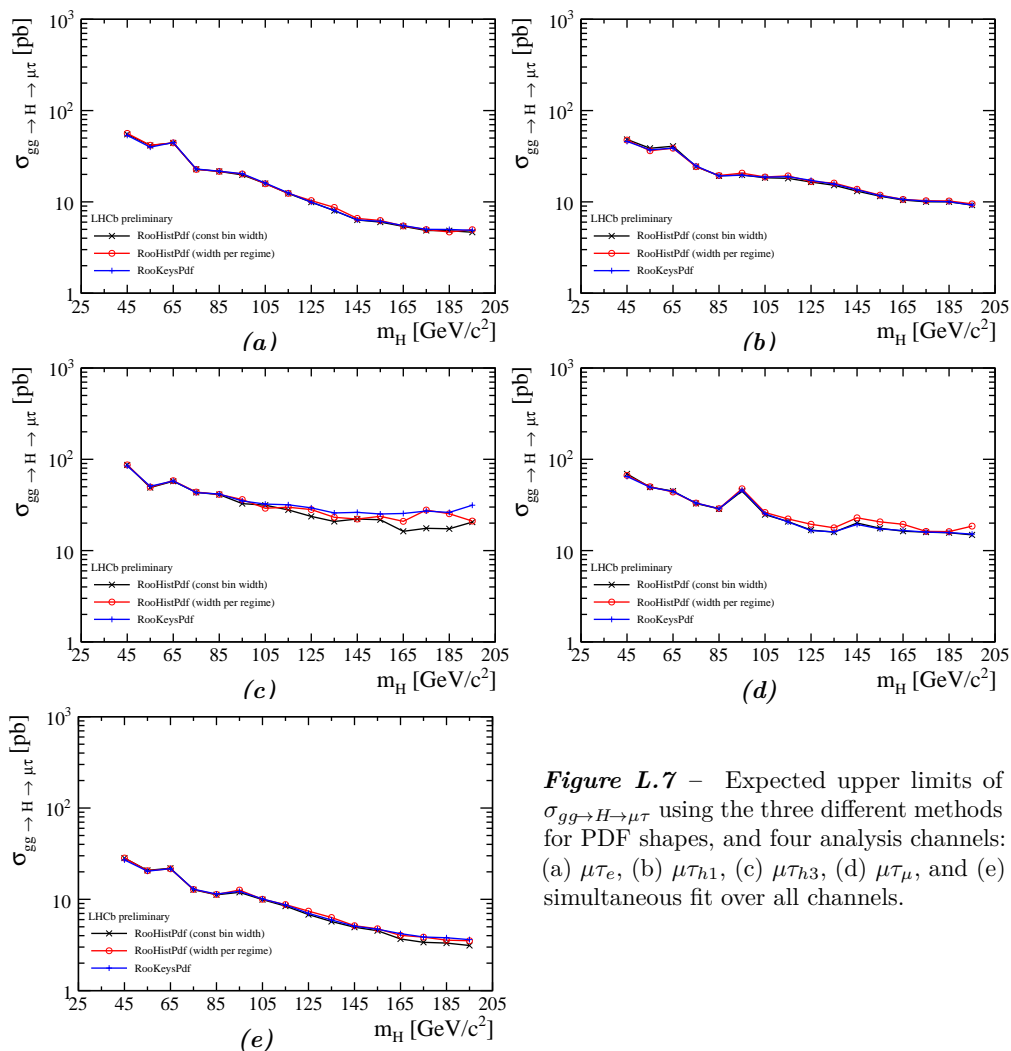


**Figure L.7** – Expected upper limits of  $\sigma_{gg \rightarrow H \rightarrow \mu\tau}$  using the three different methods for PDF shapes, and four analysis channels: (a)  $\mu\tau_e$ , (b)  $\mu\tau_{h1}$ , (c)  $\mu\tau_{h3}$ , (d)  $\mu\tau_\mu$ , and (e) simultaneous fit over all channels.

## Appendix L. Validation of Fit Models

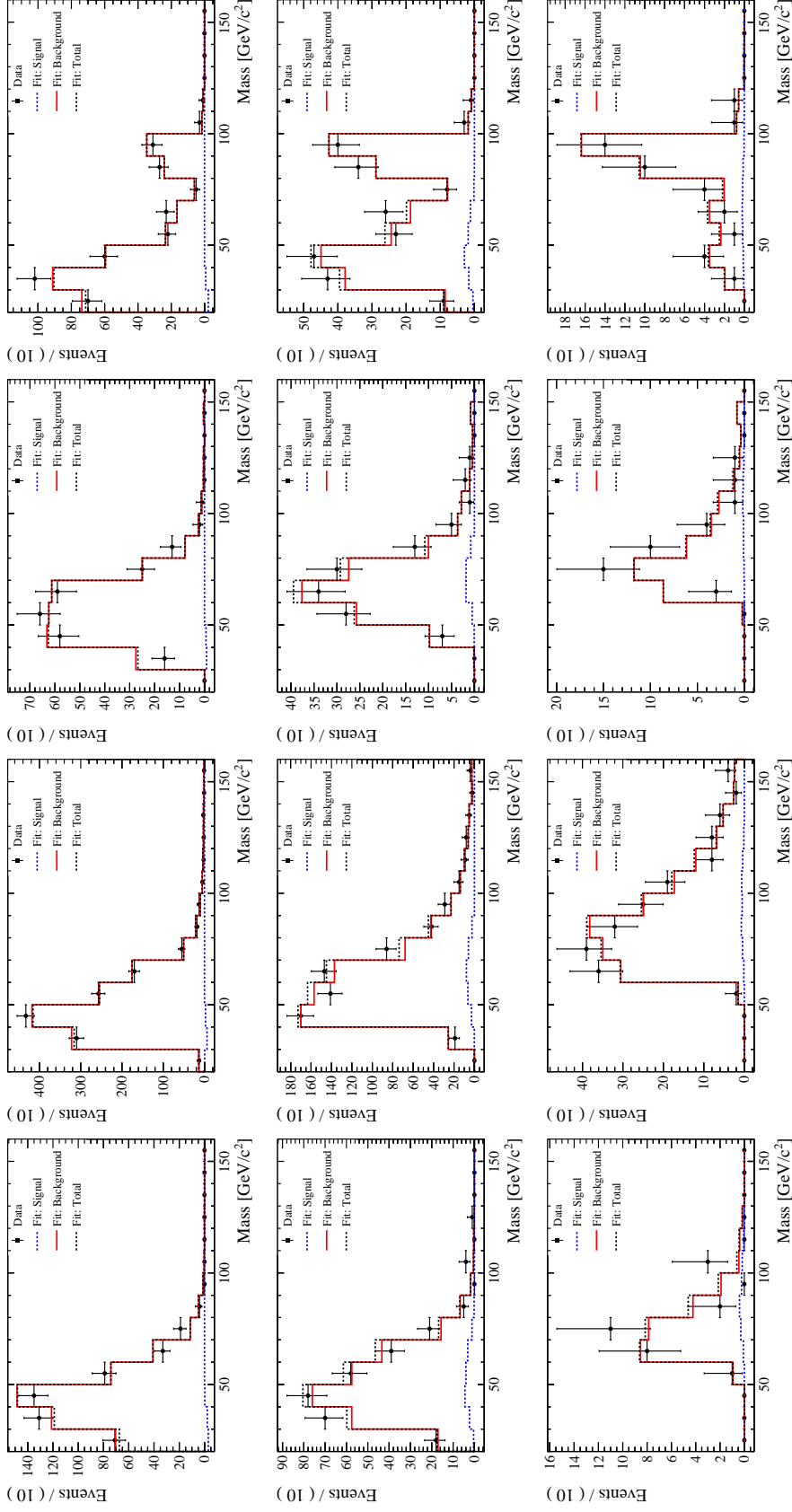


**Figure L.8** – Simultaneous fit of the distribution of  $H \rightarrow \mu\tau$  candidates invariant mass for the 4 analysis channels (columns-wise;  $\mu\tau_e$ ,  $\mu\tau_{h1}$ ,  $\mu\tau_{h3}$ ,  $\mu\tau_\mu$ ) at 3 different selection regimes (row-wise; low-mass  $m_H = 45 \text{ GeV}/c^2$ , central  $m_H = 85 \text{ GeV}/c^2$ , high-mass  $m_H = 125 \text{ GeV}/c^2$ ). The method of “histpdf” is used.

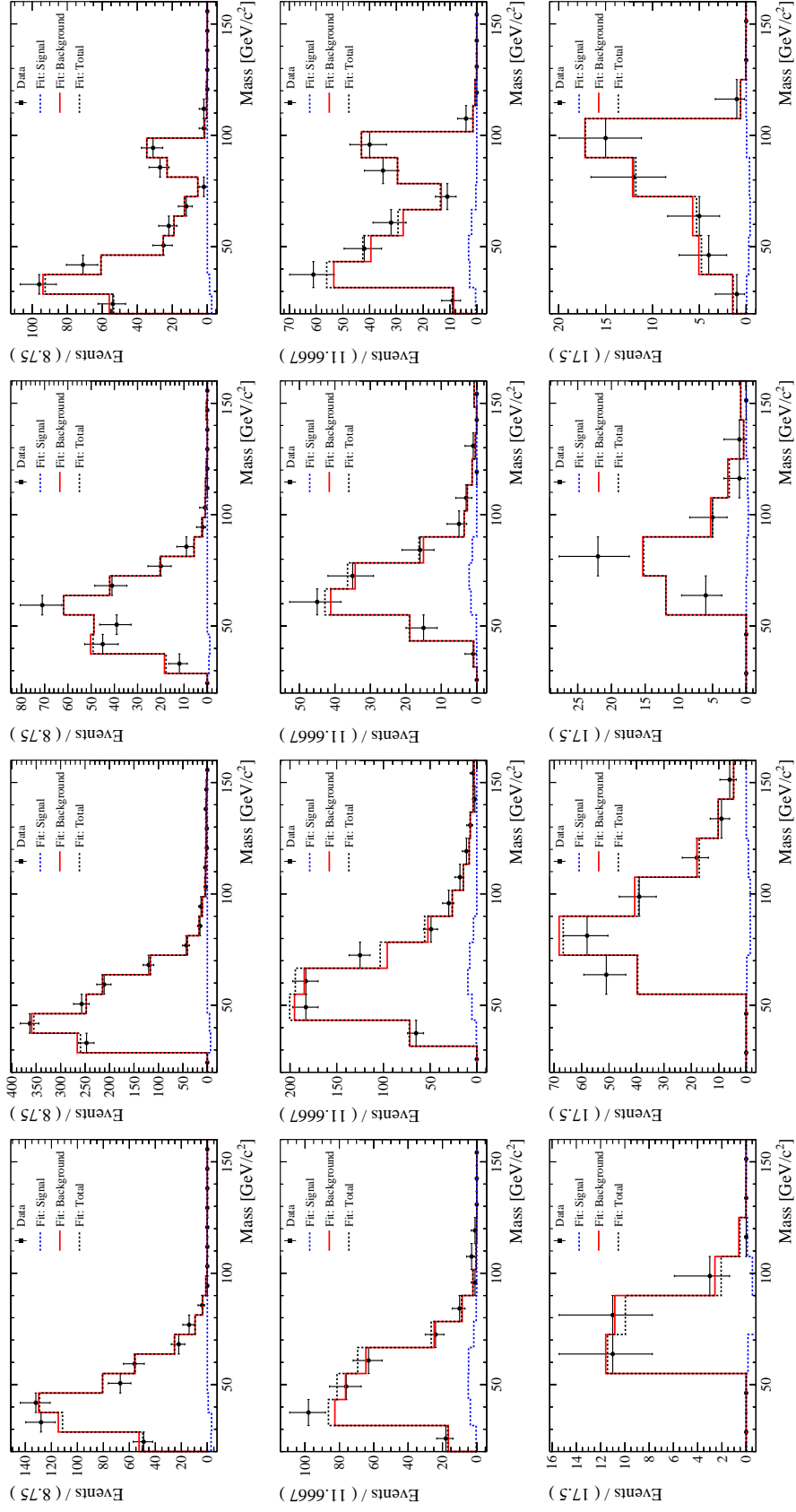


**Figure L.9** – Simultaneous fit of the distribution of  $H \rightarrow \mu\tau$  candidates invariant mass for the 4 analysis channels (columns-wise;  $\mu\tau_e$ ,  $\mu\tau_{h1}$ ,  $\mu\tau_{h3}$ ,  $\mu\tau_\mu$ ) at 3 different selection regimes (row-wise; low-mass  $m_H = 45 \text{ GeV}/c^2$ , central  $m_H = 85 \text{ GeV}/c^2$ , high-mass  $m_H = 125 \text{ GeV}/c^2$ ). The method of “h1stat” is used.

### L.6 RooKeysPdf as Distribution Shape

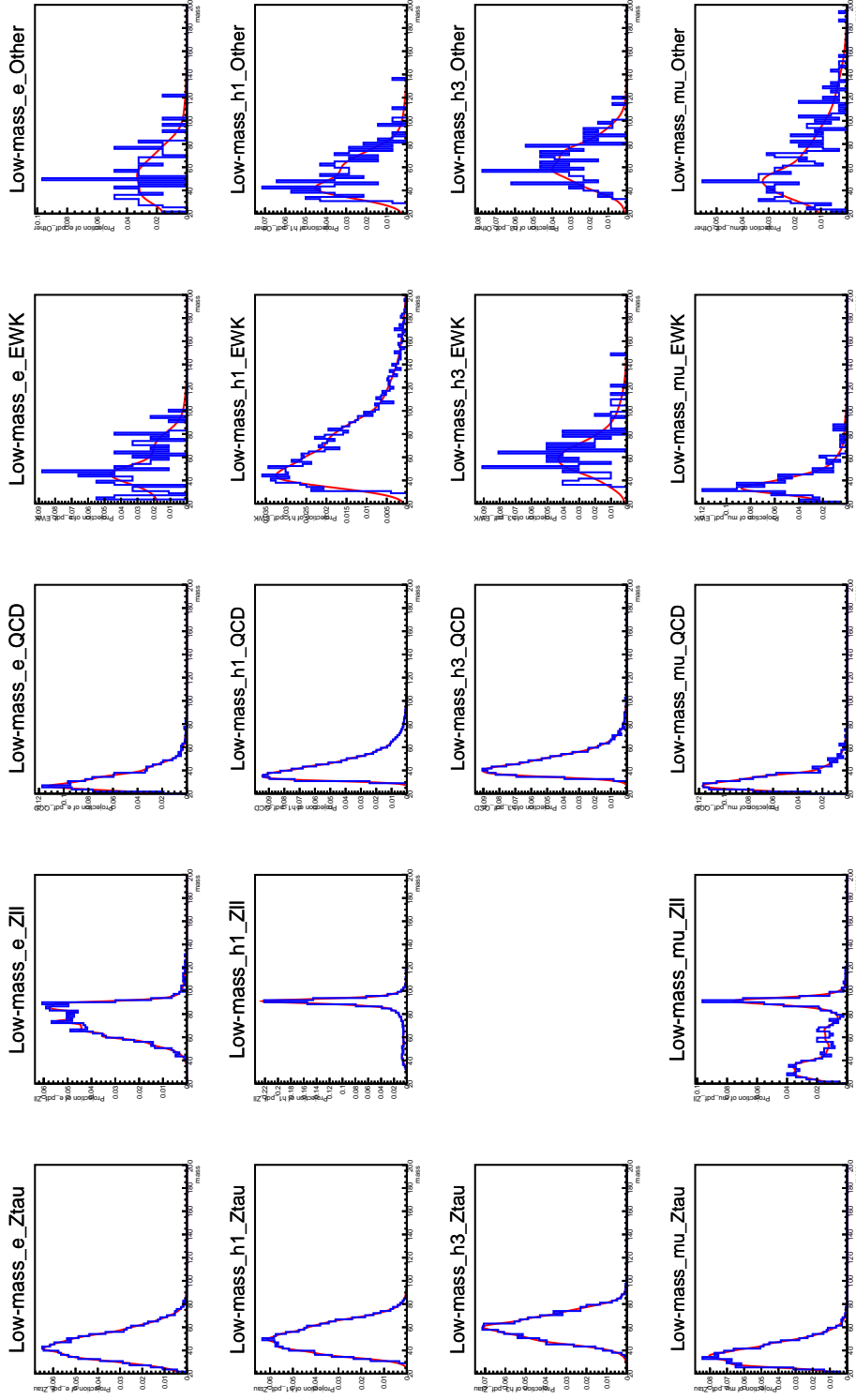


Figure L.10 – Transformation to RooKeysPdf for different backgrounds at low-mass regime.

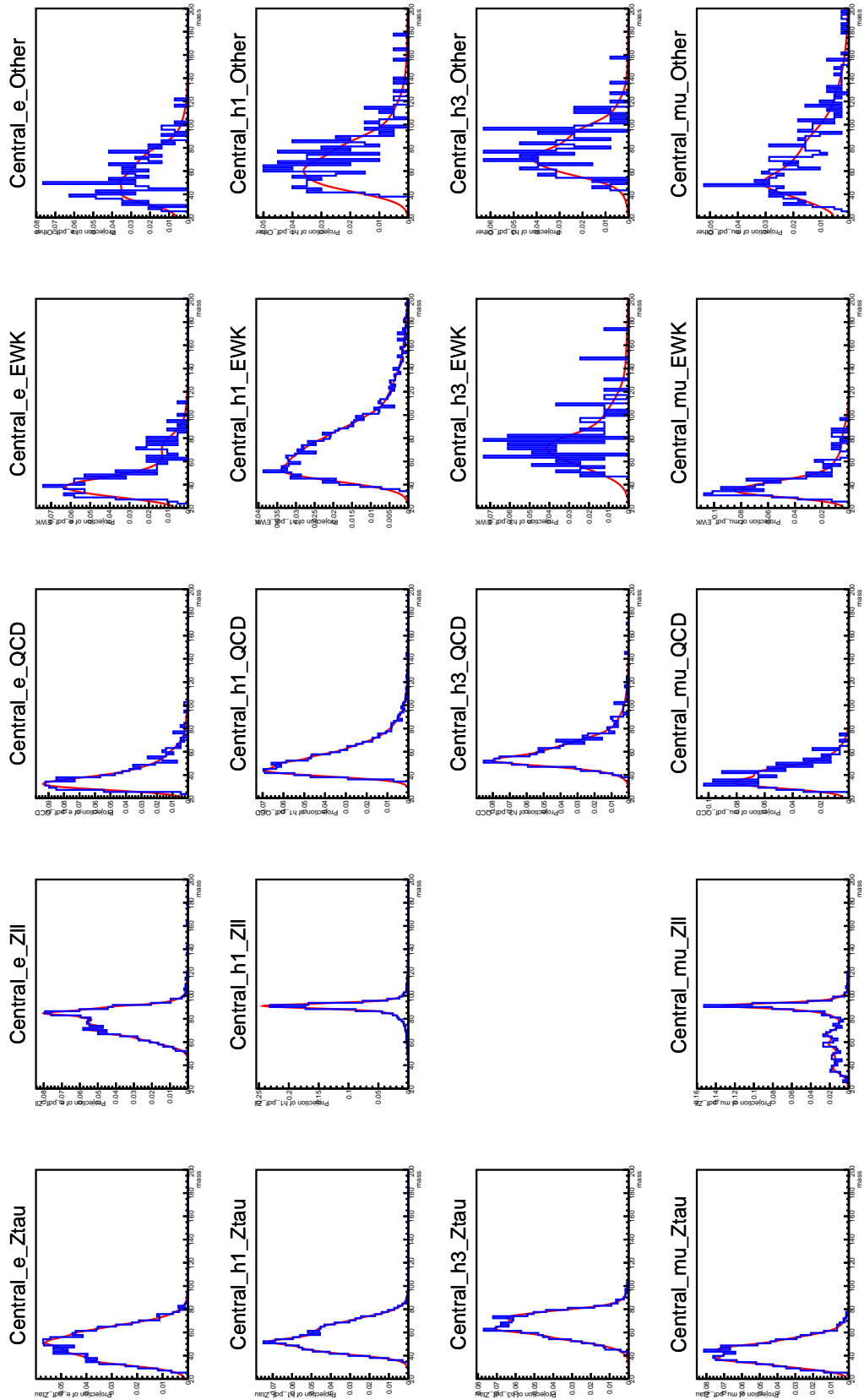


Figure L.11 – Transformation to RooKeysPdf for different backgrounds at central regime.

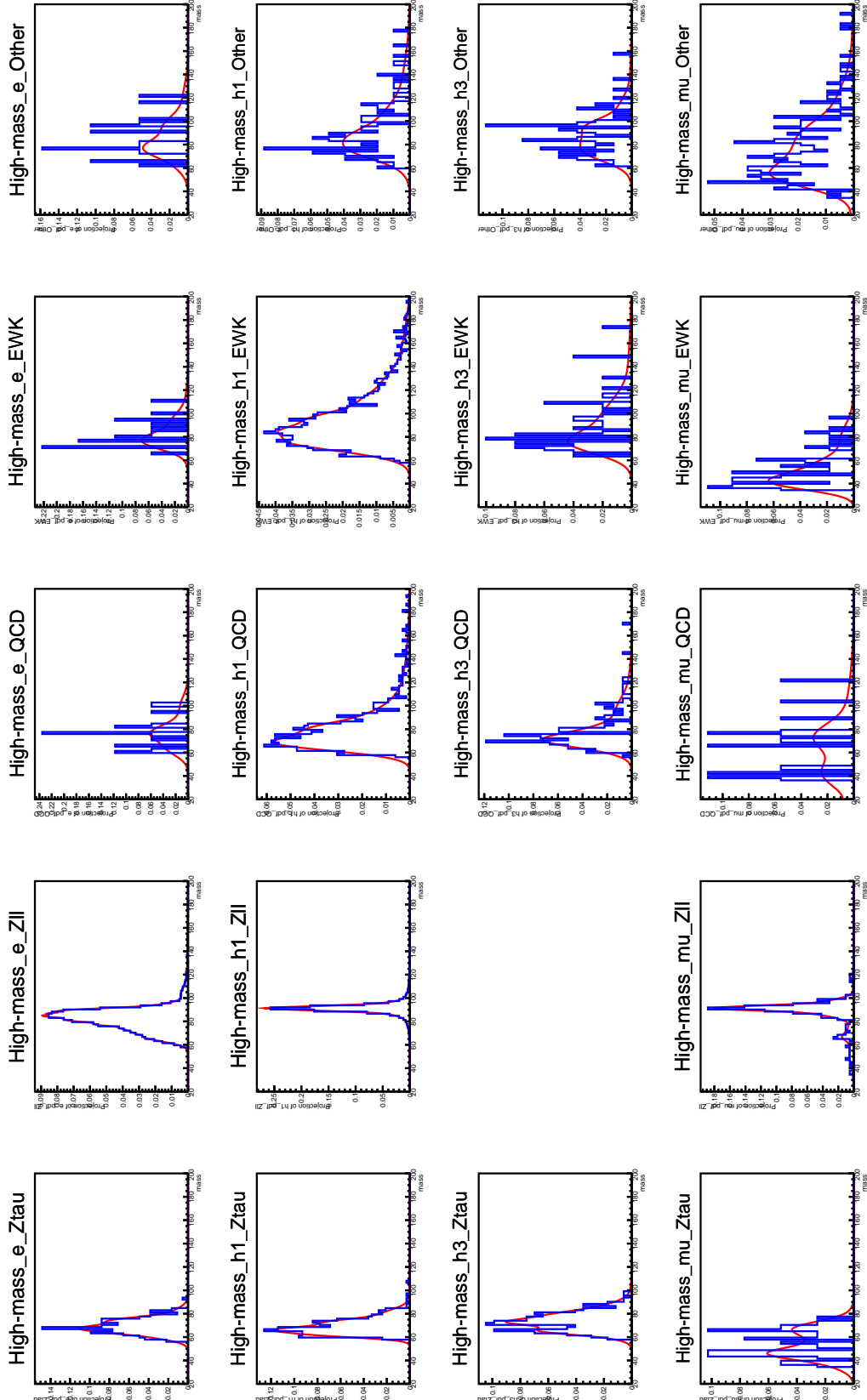
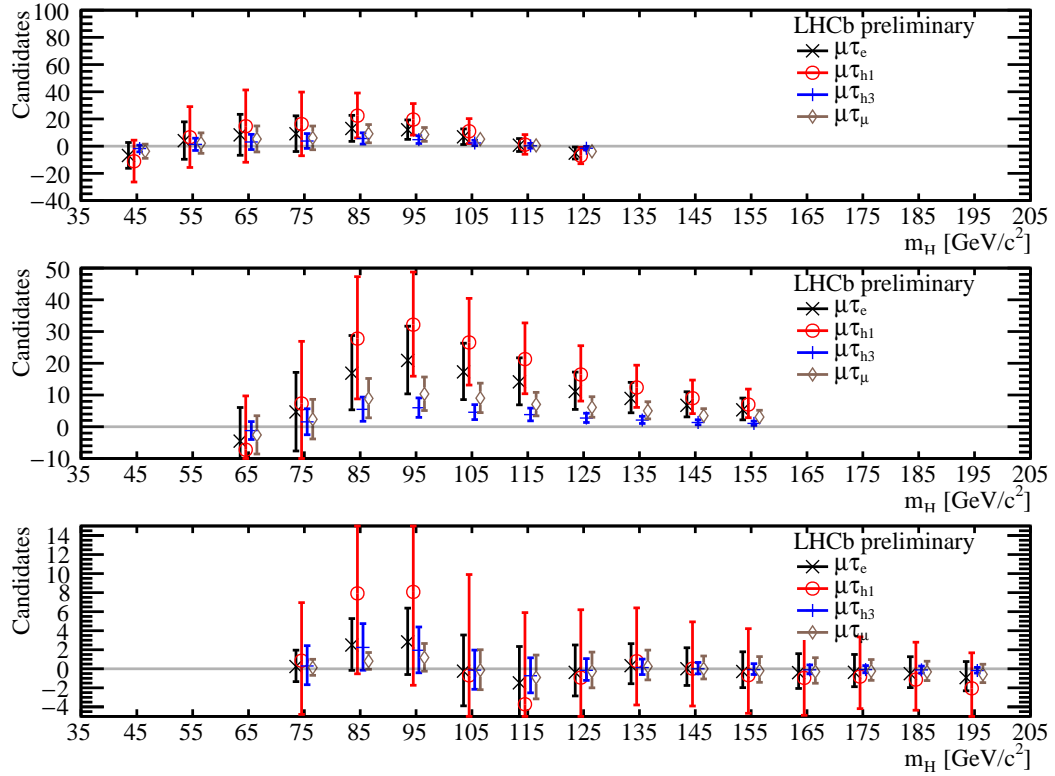


Figure L.12 – Transformation to RooKeysPdf for different backgrounds at high-mass regime.



# M Search for $H \rightarrow \mu\tau$ results

## M.1 Signal Yield



**Figure M.1** – Best fit number of signal candidates for different selection regimes: (top) low-mass, (middle) central, (bottom) high-mass.

## Appendix M. Search for $H \rightarrow \mu\tau$ results

**Table M.1** – Best fit signal yield using extended likelihood model for different channels at different selection regimes.

Regime	$m_H$ [GeV/ $c^2$ ]	$\mu\tau_e$	$\mu\tau_{h1}$	$\mu\tau_{h3}$	$\mu\tau_\mu$
Low-mass	45	$-6.86^{+9.56}_{-9.40}$	$-11.11^{+15.52}_{-15.25}$	$-1.76^{+2.47}_{-2.42}$	$-3.76^{+5.26}_{-5.17}$
	55	$4.04^{+13.84}_{-13.68}$	$6.57^{+22.50}_{-22.23}$	$1.32^{+4.53}_{-4.47}$	$2.21^{+7.57}_{-7.48}$
	65	$8.30^{+15.10}_{-15.00}$	$14.65^{+26.67}_{-26.48}$	$3.08^{+5.61}_{-5.57}$	$5.26^{+9.59}_{-9.52}$
	75	$9.12^{+13.20}_{-13.06}$	$16.25^{+23.52}_{-23.28}$	$3.78^{+5.47}_{-5.42}$	$6.04^{+8.76}_{-8.67}$
	85	$12.99^{+9.67}_{-9.47}$	$22.40^{+16.67}_{-16.33}$	$5.63^{+4.20}_{-4.11}$	$9.10^{+6.78}_{-6.64}$
	95	$12.05^{+7.24}_{-7.05}$	$19.57^{+11.75}_{-11.45}$	$4.78^{+2.88}_{-2.81}$	$8.56^{+5.15}_{-5.02}$
	105	$6.87^{+5.80}_{-5.66}$	$10.97^{+9.27}_{-9.04}$	$2.35^{+1.99}_{-1.94}$	$5.17^{+4.37}_{-4.26}$
	115	$0.72^{+4.87}_{-4.63}$	$1.10^{+7.41}_{-7.04}$	$0.27^{+1.80}_{-1.71}$	$0.54^{+3.62}_{-3.44}$
	125	$-5.14^{+4.51}_{-4.28}$	$-7.05^{+6.18}_{-5.87}$	$-1.53^{+1.34}_{-1.28}$	$-3.81^{+3.35}_{-3.18}$
Central	65	$-4.53^{+10.59}_{-10.48}$	$-7.24^{+16.95}_{-16.78}$	$-1.21^{+2.84}_{-2.81}$	$-2.59^{+6.06}_{-6.00}$
	75	$4.67^{+12.46}_{-12.30}$	$7.33^{+19.58}_{-19.32}$	$1.54^{+4.12}_{-4.06}$	$2.35^{+6.28}_{-6.20}$
	85	$16.88^{+11.86}_{-11.55}$	$27.77^{+19.52}_{-19.00}$	$5.48^{+3.86}_{-3.76}$	$8.93^{+6.28}_{-6.12}$
	95	$20.91^{+10.78}_{-10.55}$	$32.16^{+16.60}_{-16.23}$	$5.99^{+3.10}_{-3.03}$	$10.33^{+5.34}_{-5.23}$
	105	$17.29^{+9.04}_{-8.73}$	$26.56^{+13.89}_{-13.42}$	$4.57^{+2.40}_{-2.31}$	$9.01^{+4.72}_{-4.56}$
	115	$14.15^{+7.57}_{-7.24}$	$21.31^{+11.41}_{-10.92}$	$3.82^{+2.05}_{-1.96}$	$7.05^{+3.78}_{-3.62}$
	125	$11.10^{+6.12}_{-5.64}$	$16.46^{+9.08}_{-8.36}$	$2.74^{+1.51}_{-1.39}$	$6.10^{+3.37}_{-3.10}$
	135	$8.92^{+5.07}_{-4.52}$	$12.37^{+7.03}_{-6.27}$	$2.10^{+1.20}_{-1.07}$	$5.02^{+2.86}_{-2.55}$
	145	$6.75^{+4.28}_{-3.65}$	$9.00^{+5.71}_{-4.87}$	$1.34^{+0.85}_{-0.73}$	$3.48^{+2.21}_{-1.89}$
	155	$5.33^{+3.71}_{-3.15}$	$6.99^{+4.87}_{-4.14}$	$1.05^{+0.73}_{-0.62}$	$3.06^{+2.14}_{-1.82}$
High-mass	75	$0.24^{+1.72}_{-1.59}$	$0.85^{+6.10}_{-5.64}$	$0.30^{+2.13}_{-1.97}$	$0.12^{+0.88}_{-0.81}$
	85	$2.50^{+2.78}_{-2.66}$	$7.92^{+8.82}_{-8.45}$	$2.24^{+2.50}_{-2.40}$	$0.81^{+0.90}_{-0.86}$
	95	$2.82^{+3.55}_{-3.43}$	$8.07^{+10.15}_{-9.80}$	$1.94^{+2.45}_{-2.37}$	$1.18^{+1.48}_{-1.43}$
	105	$-0.25^{+3.80}_{-3.64}$	$-0.69^{+10.59}_{-10.16}$	$-0.14^{+2.10}_{-2.02}$	$-0.14^{+2.14}_{-2.05}$
	115	$-1.48^{+3.82}_{-3.65}$	$-3.73^{+9.63}_{-9.20}$	$-0.73^{+1.88}_{-1.80}$	$-0.91^{+2.35}_{-2.25}$
	125	$-0.37^{+2.88}_{-2.48}$	$-0.93^{+7.13}_{-6.14}$	$-0.16^{+1.23}_{-1.06}$	$-0.26^{+2.02}_{-1.74}$
	135	$0.33^{+2.31}_{-1.90}$	$0.80^{+5.60}_{-4.60}$	$0.13^{+0.89}_{-0.73}$	$0.24^{+1.72}_{-1.41}$
	145	$0.01^{+2.20}_{-1.76}$	$0.01^{+4.92}_{-3.92}$	$0.00^{+0.67}_{-0.53}$	$0.00^{+1.34}_{-1.07}$
	155	$-0.28^{+2.07}_{-1.70}$	$-0.67^{+4.89}_{-4.00}$	$-0.09^{+0.62}_{-0.51}$	$-0.20^{+1.48}_{-1.22}$
	165	$-0.41^{+1.99}_{-1.66}$	$-0.96^{+4.71}_{-3.93}$	$-0.10^{+0.51}_{-0.42}$	$-0.30^{+1.46}_{-1.22}$
	175	$-0.37^{+1.87}_{-1.51}$	$-0.82^{+4.17}_{-3.37}$	$-0.08^{+0.42}_{-0.34}$	$-0.24^{+1.21}_{-0.98}$
	185	$-0.51^{+1.78}_{-1.46}$	$-1.13^{+3.92}_{-3.22}$	$-0.11^{+0.40}_{-0.33}$	$-0.32^{+1.12}_{-0.92}$
195	$-0.93^{+1.69}_{-1.38}$	$-2.05^{+3.73}_{-3.05}$	$-0.18^{+0.33}_{-0.27}$	$-0.59^{+1.06}_{-0.87}$	

## M.2 Production Cross-section, $\sigma_{gg \rightarrow H \rightarrow \mu\tau}$

**Table M.2** – The best fit, expected, and observed upper limits of  $\sigma_{gg \rightarrow H \rightarrow \mu\tau}$  from full solid angle.

$m_H$ [GeV/ $c^2$ ]	Best fit [pb]	Expected limits [pb]	Observed limits [pb]
45	$-10.22^{+14.28}_{-14.07}$	$27.02^{+11.65}_{-8.08}$	21.77
55	$3.34^{+10.99}_{-11.02}$	$20.34^{+8.75}_{-6.14}$	23.75
65	$-4.58^{+10.69}_{-10.62}$	$17.20^{+8.47}_{-5.86}$	15.96
75	$2.91^{+7.82}_{-7.66}$	$12.91^{+6.15}_{-4.26}$	15.96
85	$9.43^{+6.54}_{-6.48}$	$11.43^{+5.22}_{-3.64}$	19.99
95	$10.76^{+5.61}_{-5.45}$	$12.21^{+5.01}_{-3.46}$	15.76
105	$9.32^{+4.90}_{-4.72}$	$10.11^{+4.13}_{-2.86}$	9.79
115	$-1.64^{+4.25}_{-4.09}$	$8.68^{+3.66}_{-2.51}$	7.60
125	$-0.37^{+2.97}_{-2.60}$	$7.03^{+3.13}_{-2.09}$	6.27
135	$0.35^{+2.39}_{-1.97}$	$5.95^{+2.79}_{-1.84}$	5.63
145	$0.01^{+2.11}_{-1.69}$	$5.07^{+2.52}_{-1.62}$	4.76
155	$-0.30^{+2.17}_{-1.79}$	$4.70^{+2.40}_{-1.54}$	4.49
165	$-0.44^{+2.18}_{-1.82}$	$4.21^{+2.26}_{-1.41}$	4.21
175	$-0.39^{+2.07}_{-1.71}$	$3.87^{+2.15}_{-1.33}$	3.99
185	$-0.61^{+2.11}_{-1.75}$	$3.79^{+2.15}_{-1.34}$	3.87
195	$-1.18^{+2.15}_{-1.78}$	$3.62^{+2.13}_{-1.29}$	3.50

**Table M.3** – The best fit, expected, and observed upper limits of  $\sigma_{gg \rightarrow H \rightarrow \mu\tau}$  with  $H \rightarrow \mu\tau$  inside LHCb geometrical acceptance.

$m_H$ [GeV/ $c^2$ ]	Best fit [fb]	Expected limits [fb]	Observed limits [fb]
45	$-67.74^{+94.63}_{-92.98}$	$178.47^{+76.74}_{-53.10}$	144.44
55	$18.70^{+64.08}_{-63.31}$	$117.47^{+50.36}_{-35.59}$	137.21
65	$-23.21^{+54.31}_{-53.75}$	$87.05^{+42.81}_{-29.67}$	80.84
75	$13.03^{+34.78}_{-34.33}$	$57.61^{+27.22}_{-19.05}$	71.05
85	$37.09^{+26.07}_{-25.38}$	$45.11^{+20.57}_{-14.31}$	78.80
95	$37.88^{+19.56}_{-19.13}$	$42.89^{+17.26}_{-12.13}$	55.31
105	$29.00^{+15.18}_{-14.66}$	$31.41^{+12.76}_{-8.96}$	30.49
115	$22.10^{+11.84}_{-11.33}$	$24.00^{+10.11}_{-6.88}$	21.08
125	$-0.97^{+7.45}_{-6.42}$	$17.49^{+7.66}_{-5.20}$	15.60
135	$0.77^{+5.40}_{-4.43}$	$13.38^{+6.19}_{-4.10}$	12.67
145	$0.01^{+4.26}_{-3.40}$	$10.16^{+4.98}_{-3.25}$	9.54
155	$-0.54^{+3.96}_{-3.24}$	$8.50^{+4.25}_{-2.75}$	8.12
165	$-0.74^{+3.62}_{-3.01}$	$6.98^{+3.65}_{-2.34}$	6.97
175	$-0.61^{+3.08}_{-2.49}$	$5.69^{+3.11}_{-1.95}$	5.87
185	$-0.81^{+2.81}_{-2.31}$	$5.03^{+2.80}_{-1.76}$	5.14
195	$-1.41^{+2.56}_{-2.09}$	$4.27^{+2.45}_{-1.52}$	4.12

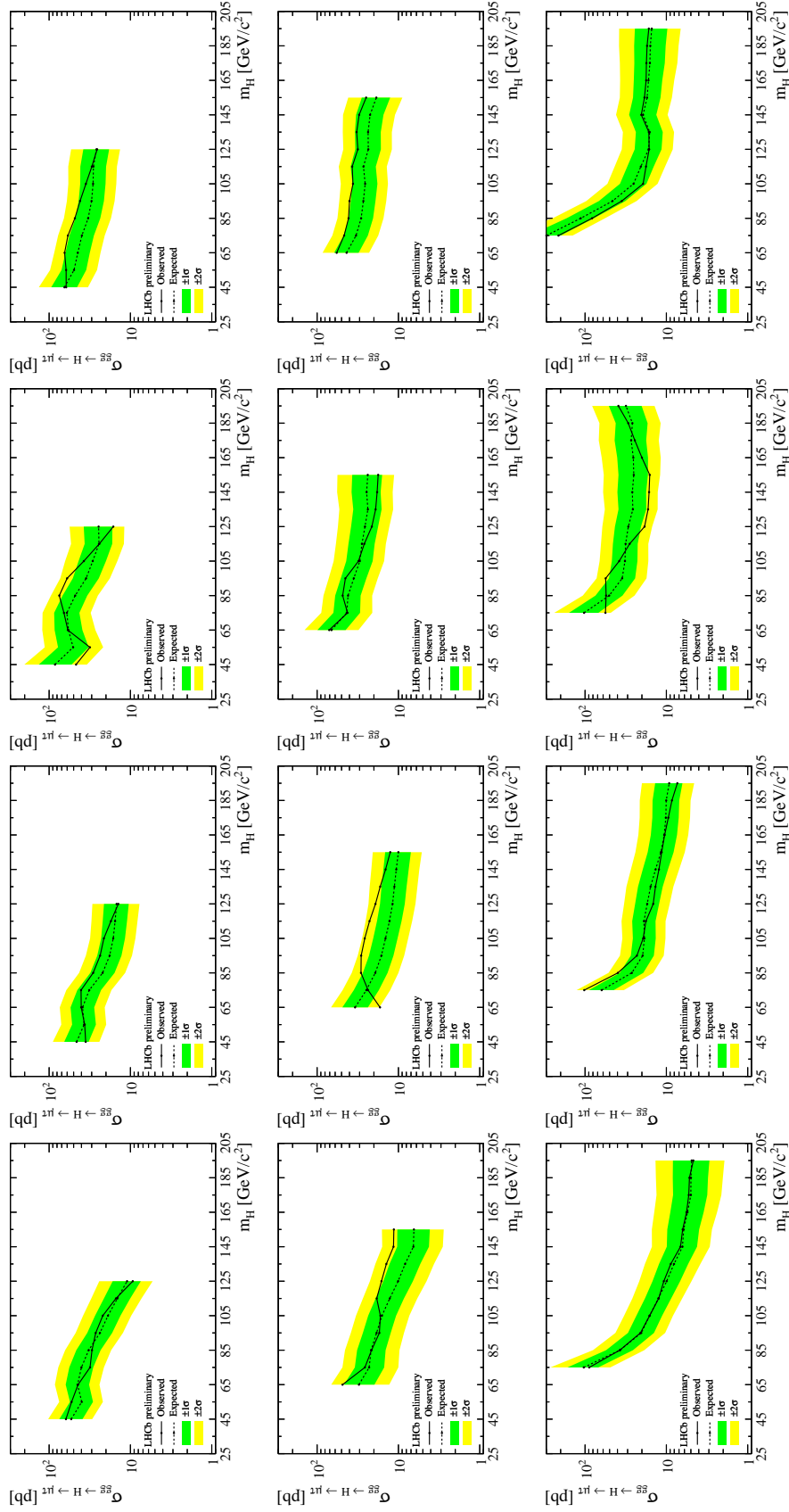
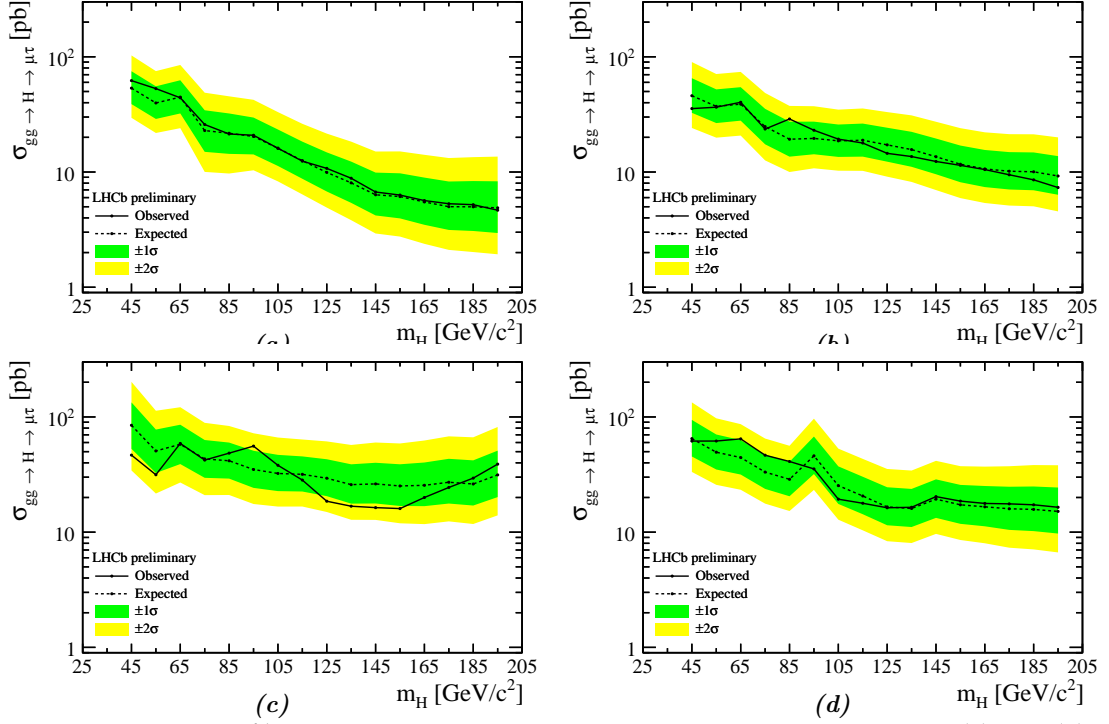
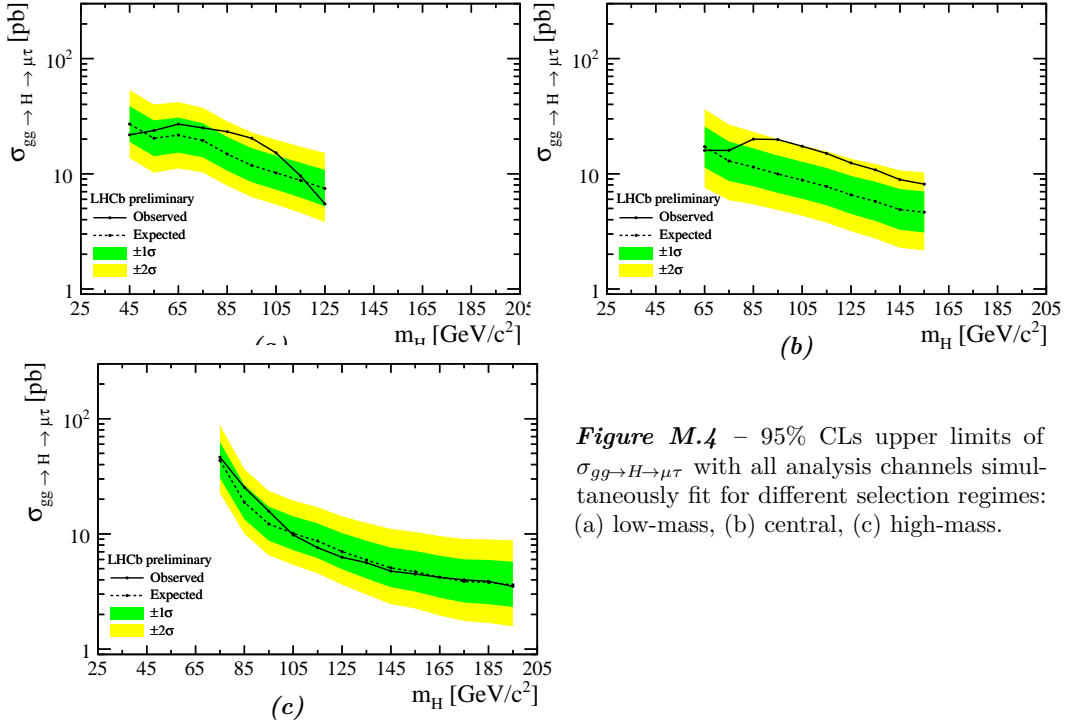


Figure M.2 – 95% CLs upper limits of  $\sigma_{qg \rightarrow H \rightarrow \mu\tau}$  for different analysis channels (column-wise;  $\mu\tau_e$ ,  $\mu\tau_{h1}$ ,  $\mu\tau_{h3}$ ,  $\mu\tau_\mu$ ) and for different selection regimes (row-wise; low-mass, central, high-mass).

## M.2. Production Cross-section, $\sigma_{gg \rightarrow H \rightarrow \mu\tau}$



**Figure M.3** – 95% CLs upper limits of  $\sigma_{gg \rightarrow H \rightarrow \mu\tau}$  for different analysis channels (a)  $\mu\tau_e$ , (b)  $\mu\tau_{h1}$ , (c)  $\mu\tau_{h3}$ , (d)  $\mu\tau_\mu$ .



**Figure M.4** – 95% CLs upper limits of  $\sigma_{gg \rightarrow H \rightarrow \mu\tau}$  with all analysis channels simultaneously fit for different selection regimes: (a) low-mass, (b) central, (c) high-mass.

## Appendix M. Search for $H \rightarrow \mu\tau$ results

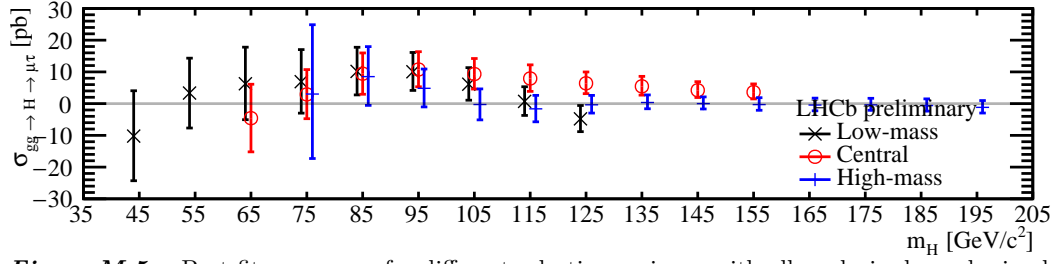


**Figure M.5** – Best fit  $\sigma_{gg \rightarrow H \rightarrow \mu\tau}$  for different selection regimes, with all analysis channels simultaneously fit.

### M.3 Branching Fraction, $\mathcal{B}_{H \rightarrow \mu\tau}$

**Table M.4** – The best fit, expected, and observed upper limits of  $\mathcal{B}_{H \rightarrow \mu\tau}$  using the BSM Higgs production cross-section from LHCHSWG.

$m_H$ [GeV/ $c^2$ ]	Best fit [%]	Expected limits [%]	Observed limits [%]
45	$-7.1^{+9.9}_{-10.0}$	$20.8 \pm 7.5$	15.4
55	$3.6^{+11.9}_{-11.8}$	$24.0 \pm 8.6$	26.1
65	$9.4^{+17.5}_{-17.0}$	$28.5 \pm 11.4$	24.3
75	$5.8^{+15.7}_{-15.3}$	$28.3 \pm 10.9$	32.4
85	$23.9^{+17.1}_{-16.4}$	$31.7 \pm 11.9$	51.9
95	$15.2^{+19.4}_{-18.5}$	$34.2 \pm 12.5$	50.8
105	$-1.1^{+18.9}_{-18.6}$	$36.7 \pm 13.3$	38.1
115	$-7.4^{+19.4}_{-18.9}$	$38.6 \pm 14.1$	35.3
125	$-1.9^{+16.0}_{-14.2}$	$38.8 \pm 14.2$	29.7
135	$2.2^{+15.1}_{-12.4}$	$39.9 \pm 15.1$	36.1
145	$0.1^{+15.4}_{-12.4}$	$39.4 \pm 15.4$	35.0
155	$-2.5^{+18.0}_{-15.0}$	$42.5 \pm 16.8$	37.5
165	$-4.1^{+20.5}_{-17.3}$	$44.2 \pm 17.8$	40.1
175	$-4.1^{+22.0}_{-18.2}$	$46.0 \pm 19.0$	42.8
185	$-7.2^{+25.1}_{-20.9}$	$50.6 \pm 21.2$	46.5
195	$-15.6^{+28.5}_{-23.8}$	$54.0 \pm 23.2$	46.7



# Bibliography

- [1] Michael E. Peskin and Daniel V. Schroeder. *An Introduction to quantum field theory*. Addison-Wesley, Reading, USA, 1995. URL: <http://www.slac.stanford.edu/~mpeskin/QFT.html>. [Page 5.]
- [2] Michele Maggiore. *A Modern introduction to quantum field theory*. 2005. [Page 5.]
- [3] C. Patrignani et al. Review of Particle Physics. *Chin. Phys.*, C40(10):100001, 2016. doi:10.1088/1674-1137/40/10/100001. [Pages 5 and 15.]
- [4] Wikimedia Commons. Elementary particle interactions in the standard model, 2014. URL: [https://commons.wikimedia.org/wiki/File:Elementary\\_particle\\_interactions\\_in\\_the\\_Standard\\_Model.png](https://commons.wikimedia.org/wiki/File:Elementary_particle_interactions_in_the_Standard_Model.png). [Page 6.]
- [5] Wikimedia Commons. Standard model of elementary particles, 2017. URL: [https://commons.wikimedia.org/wiki/File:Standard\\_Model\\_of\\_Elementary\\_Particles.svg](https://commons.wikimedia.org/wiki/File:Standard_Model_of_Elementary_Particles.svg). [Page 6.]
- [6] Serguei Chatrchyan et al. Observation of a new boson at a mass of 125 GeV with the CMS experiment at the LHC. *Phys. Lett.*, B716:30–61, 2012. arXiv:1207.7235, doi:10.1016/j.physletb.2012.08.021. [Page 5.]
- [7] Georges Aad et al. Observation of a new particle in the search for the Standard Model Higgs boson with the ATLAS detector at the LHC. *Phys. Lett.*, B716:1–29, 2012. arXiv:1207.7214, doi:10.1016/j.physletb.2012.08.020. [Page 5.]
- [8] Julia Woithe and Harriet Kim Jarlett. Sit down for coffee with the Standard Model. Apr 2017. URL: <https://cds.cern.ch/record/2261834>. [Page 6.]
- [9] Kaoru Hagiwara, A. D. Martin, Daisuke Nomura, and T. Teubner. Improved predictions for  $g-2$  of the muon and  $\alpha(\text{QED}) (M^{*2}(Z))$ . *Phys. Lett.*, B649:173–179, 2007. arXiv:hep-ph/0611102, doi:10.1016/j.physletb.2007.04.012. [Page 7.]
- [10] NASA. What is the universe made of?, 2014. URL: [https://map.gsfc.nasa.gov/universe/uni\\_matter.html](https://map.gsfc.nasa.gov/universe/uni_matter.html). [Pages 7 and 267.]
- [11] J. Charles, Andreas Hocker, H. Lacker, S. Laplace, F. R. Le Diberder, J. Malcles, J. Ocariz, M. Pivk, and L. Roos. CP violation and the CKM matrix: Assessing the impact of the asymmetric  $B$  factories. *Eur. Phys. J.*, C41(1):1–131, 2005. arXiv:hep-ph/0406184, doi:10.1140/epjc/s2005-02169-1. [Pages 7 and 267.]

## Bibliography

---

- [12] H. Georgi and S. L. Glashow. Unity of All Elementary Particle Forces. *Phys. Rev. Lett.*, 32:438–441, 1974. doi:10.1103/PhysRevLett.32.438. [Page 8.]
- [13] Stephen P. Martin. A Supersymmetry primer. 1997. [Adv. Ser. Direct. High Energy Phys.18,1(1998)]. arXiv:hep-ph/9709356, doi:10.1142/9789812839657\_0001, 10.1142/9789814307505\_0001. [Page 8.]
- [14] Nobel Media AB 2014. The 2004 nobel prize in physics - popular information. URL: [http://www.nobelprize.org/nobel\\_prizes/physics/laureates/2004/popular.html](http://www.nobelprize.org/nobel_prizes/physics/laureates/2004/popular.html). [Pages 8 and 267.]
- [15] R. D. Peccei and Helen R. Quinn. CP Conservation in the Presence of Instantons. *Phys. Rev. Lett.*, 38:1440–1443, 1977. doi:10.1103/PhysRevLett.38.1440. [Page 8.]
- [16] Javier Redondo. *Can the PVLAS particle be compatible with the astrophysical bounds?* PhD thesis, Barcelona, Autònoma U., 2007. URL: <https://inspirehep.net/record/791614/files/arXiv:0807.4329.pdf>, arXiv:0807.4329. [Pages 9 and 267.]
- [17] Gautam Bhattacharyya and Dipankar Das. Scalar sector of two-Higgs-doublet models: A minireview. *Pramana*, 87(3):40, 2016. arXiv:1507.06424, doi:10.1007/s12043-016-1252-4. [Page 9.]
- [18] K. Becker, M. Becker, and J. H. Schwarz. *String theory and M-theory: A modern introduction*. Cambridge University Press, 2006. [Page 9.]
- [19] James J Kolata. *Elementary Cosmology: From Aristotle’s Universe to the Big Bang and Beyond*. 2053-2571. Morgan & Claypool Publishers, 2015. URL: <http://dx.doi.org/10.1088/978-1-6817-4100-0>, doi:10.1088/978-1-6817-4100-0. [Pages 9 and 267.]
- [20] E. J. Konopinski and H. M. Mahmoud. The Universal Fermi interaction. *Phys. Rev.*, 92:1045–1049, 1953. doi:10.1103/PhysRev.92.1045. [Page 10.]
- [21] B. Pontecorvo. Inverse beta processes and nonconservation of lepton charge. *Sov. Phys. JETP*, 7:172–173, 1958. [Zh. Eksp. Teor. Fiz.34,247(1957)]. [Page 10.]
- [22] Ziro Maki, Masami Nakagawa, and Shoichi Sakata. Remarks on the unified model of elementary particles. *Prog. Theor. Phys.*, 28:870–880, 1962. doi:10.1143/PTP.28.870. [Page 10.]
- [23] Y. Fukuda et al. Evidence for oscillation of atmospheric neutrinos. *Phys. Rev. Lett.*, 81:1562–1567, 1998. arXiv:hep-ex/9807003, doi:10.1103/PhysRevLett.81.1562. [Pages 10 and 267.]
- [24] Robert H. Bernstein and Peter S. Cooper. Charged Lepton Flavor Violation: An Experimenter’s Guide. *Phys. Rept.*, 532:27–64, 2013. arXiv:1307.5787, doi:10.1016/j.physrep.2013.07.002. [Page 10.]
- [25] William J. Marciano, Toshinori Mori, and J. Michael Roney. Charged Lepton Flavor Violation Experiments. *Ann. Rev. Nucl. Part. Sci.*, 58:315–341, 2008. doi:10.1146/annurev.nucl.58.110707.171126. [Pages 10, 11, and 267.]



- [26] A. Vicente. FlavorKit: a brief overview. *Nucl. Part. Phys. Proc.*, 273-275:1423–1428, 2016. [arXiv:1410.2099](#), [doi:10.1016/j.nuclphysbps.2015.09.230](#). [Pages 11 and 267.]
- [27] Andre de Gouvea and Petr Vogel. Lepton Flavor and Number Conservation, and Physics Beyond the Standard Model. *Prog. Part. Nucl. Phys.*, 71:75–92, 2013. [arXiv:1303.4097](#), [doi:10.1016/j.pnpnp.2013.03.006](#). [Page 11.]
- [28] M. Raidal et al. Flavour physics of leptons and dipole moments. *Eur. Phys. J.*, C57:13–182, 2008. [arXiv:0801.1826](#), [doi:10.1140/epjc/s10052-008-0715-2](#). [Page 11.]
- [29] Bertrand Echenard. The mu2e experiment at fermilab, 2016. URL: <https://indico.cern.ch/event/432527/contributions/1071455>. [Pages 11 and 267.]
- [30] Roni Harnik, Joachim Kopp, and Jure Zupan. Flavor Violating Higgs Decays. *JHEP*, 03:026, 2013. [arXiv:1209.1397](#), [doi:10.1007/JHEP03\(2013\)026](#). [Pages 11, 12, 13, 133, and 277.]
- [31] J. D. Bjorken and Steven Weinberg. A Mechanism for Nonconservation of Muon Number. *Phys. Rev. Lett.*, 38:622, 1977. [doi:10.1103/PhysRevLett.38.622](#). [Page 12.]
- [32] J. Lorenzo Diaz-Cruz and J. J. Toscano. Lepton flavor violating decays of Higgs bosons beyond the standard model. *Phys. Rev.*, D62:116005, 2000. [arXiv:hep-ph/9910233](#), [doi:10.1103/PhysRevD.62.116005](#). [Page 12.]
- [33] Tao Han and Danny Marfatia.  $h \rightarrow \mu \tau$  at hadron colliders. *Phys. Rev. Lett.*, 86:1442–1445, 2001. [arXiv:hep-ph/0008141](#), [doi:10.1103/PhysRevLett.86.1442](#). [Page 12.]
- [34] Abdesslam Arhrib, Yifan Cheng, and Otto C. W. Kong. Comprehensive analysis on lepton flavor violating Higgs boson to  $\mu^\mp \tau^\pm$  decay in supersymmetry without  $R$  parity. *Phys. Rev.*, D87(1):015025, 2013. [arXiv:1210.8241](#), [doi:10.1103/PhysRevD.87.015025](#). [Page 12.]
- [35] M. Arana-Catania, E. Arganda, and M. J. Herrero. Non-decoupling SUSY in LFV Higgs decays: a window to new physics at the LHC. *JHEP*, 09:160, 2013. [Erratum: *JHEP*10,192(2015)]. [arXiv:1304.3371](#), [doi:10.1007/JHEP10\(2015\)192](#), [doi:10.1007/JHEP09\(2013\)160](#). [Page 12.]
- [36] Kaustubh Agashe and Roberto Contino. Composite Higgs-Mediated FCNC. *Phys. Rev.*, D80:075016, 2009. [arXiv:0906.1542](#), [doi:10.1103/PhysRevD.80.075016](#). [Page 12.]
- [37] Aleksandr Azatov, Manuel Toharia, and Lijun Zhu. Higgs Mediated FCNC’s in Warped Extra Dimensions. *Phys. Rev.*, D80:035016, 2009. [arXiv:0906.1990](#), [doi:10.1103/PhysRevD.80.035016](#). [Page 12.]
- [38] Joachim Kopp and Marco Nardecchia. Flavor and CP violation in Higgs decays. *JHEP*, 10:156, 2014. [arXiv:1406.5303](#), [doi:10.1007/JHEP10\(2014\)156](#). [Page 12.]
- [39] Georges Aad et al. Search for neutral MSSM Higgs bosons decaying to  $\tau^+ \tau^-$  pairs in proton-proton collisions at  $\sqrt{s} = 7$  TeV with the ATLAS detector. *Phys. Lett.*,

## Bibliography

---

- B705:174–192, 2011. [arXiv:1107.5003](#), [doi:10.1016/j.physletb.2011.10.001](#). [Page 12.]
- [40] Gilad Perez and Lisa Randall. Natural Neutrino Masses and Mixings from Warped Geometry. *JHEP*, 01:077, 2009. [arXiv:0805.4652](#), [doi:10.1088/1126-6708/2009/01/077](#). [Page 12.]
- [41] S. Casagrande, F. Goertz, U. Haisch, M. Neubert, and T. Pfoh. Flavor Physics in the Randall-Sundrum Model: I. Theoretical Setup and Electroweak Precision Tests. *JHEP*, 10:094, 2008. [arXiv:0807.4937](#), [doi:10.1088/1126-6708/2008/10/094](#). [Page 12.]
- [42] Hajime Ishimori, Tatsuo Kobayashi, Hiroshi Ohki, Yusuke Shimizu, Hiroshi Okada, and Morimitsu Tanimoto. Non-Abelian Discrete Symmetries in Particle Physics. *Prog. Theor. Phys. Suppl.*, 183:1–163, 2010. [arXiv:1003.3552](#), [doi:10.1143/PTPS.183.1](#). [Page 12.]
- [43] Monika Blanke, Andrzej J. Buras, Bjoern Duling, Stefania Gori, and Andreas Weiler.  $\Delta F=2$  Observables and Fine-Tuning in a Warped Extra Dimension with Custodial Protection. *JHEP*, 03:001, 2009. [arXiv:0809.1073](#), [doi:10.1088/1126-6708/2009/03/001](#). [Page 12.]
- [44] Gian F. Giudice and Oleg Lebedev. Higgs-dependent Yukawa couplings. *Phys. Lett.*, B665:79–85, 2008. [arXiv:0804.1753](#), [doi:10.1016/j.physletb.2008.05.062](#). [Page 12.]
- [45] J. A. Aguilar-Saavedra. A Minimal set of top-Higgs anomalous couplings. *Nucl. Phys.*, B821:215–227, 2009. [arXiv:0904.2387](#), [doi:10.1016/j.nuclphysb.2009.06.022](#). [Page 12.]
- [46] Michaela E. Albrecht, Monika Blanke, Andrzej J. Buras, Bjorn Duling, and Katrin Gemmler. Electroweak and Flavour Structure of a Warped Extra Dimension with Custodial Protection. *JHEP*, 09:064, 2009. [arXiv:0903.2415](#), [doi:10.1088/1126-6708/2009/09/064](#). [Page 12.]
- [47] Andreas Goudelis, Oleg Lebedev, and Jae-hyeon Park. Higgs-induced lepton flavor violation. *Phys. Lett.*, B707:369–374, 2012. [arXiv:1111.1715](#), [doi:10.1016/j.physletb.2011.12.059](#). [Page 12.]
- [48] David McKeen, Maxim Pospelov, and Adam Ritz. Modified Higgs branching ratios versus CP and lepton flavor violation. *Phys. Rev.*, D86:113004, 2012. [arXiv:1208.4597](#), [doi:10.1103/PhysRevD.86.113004](#). [Page 12.]
- [49] Ernesto Arganda, Ana M. Curiel, Maria J. Herrero, and David Temes. Lepton flavor violating Higgs boson decays from massive seesaw neutrinos. *Phys. Rev.*, D71:035011, 2005. [arXiv:hep-ph/0407302](#), [doi:10.1103/PhysRevD.71.035011](#). [Page 12.]
- [50] E. Arganda, M. J. Herrero, X. Marcano, and C. Weiland. Imprints of massive inverse seesaw model neutrinos in lepton flavor violating Higgs boson decays. *Phys. Rev.*, D91(1):015001, 2015. [arXiv:1405.4300](#), [doi:10.1103/PhysRevD.91.015001](#). [Page 12.]

- [51] Vardan Khachatryan et al. Search for lepton flavour violating decays of the Higgs boson to  $e\tau$  and  $e\mu$  in proton–proton collisions at  $\sqrt{s}=8$  TeV. *Phys. Lett.*, B763:472–500, 2016. [arXiv:1607.03561](#), [doi:10.1016/j.physletb.2016.09.062](#). [Page 13.]
- [52] CMS Collaboration. Search for lepton flavour violating decays of the Higgs boson to  $\mu\tau$  and  $e\tau$  in proton-proton collisions at  $\sqrt{s}=13$  TeV. 2017. [Pages 13, 133, and 137.]
- [53] Georges Aad et al. Search for lepton-flavour-violating decays of the Higgs and  $Z$  bosons with the ATLAS detector. *Eur. Phys. J.*, C77(2):70, 2017. [arXiv:1604.07730](#), [doi:10.1140/epjc/s10052-017-4624-0](#). [Page 13.]
- [54] Georges Aad et al. Search for lepton-flavour-violating  $H \rightarrow \mu\tau$  decays of the Higgs boson with the ATLAS detector. *JHEP*, 11:211, 2015. [arXiv:1508.03372](#), [doi:10.1007/JHEP11\(2015\)211](#). [Page 13.]
- [55] J. Beringer et al. Review of Particle Physics (RPP). *Phys. Rev.*, D86:010001, 2012. [doi:10.1103/PhysRevD.86.010001](#). [Page 13.]
- [56] U. Bellgardt et al. Search for the Decay  $\mu^+ \rightarrow e^+ e^+ e^-$ . *Nucl. Phys.*, B299:1–6, 1988. [doi:10.1016/0550-3213\(88\)90462-2](#). [Page 13.]
- [57] K. Hayasaka et al. Search for Lepton Flavor Violating Tau Decays into Three Leptons with 719 Million Produced Tau+Tau- Pairs. *Phys. Lett.*, B687:139–143, 2010. [arXiv:1001.3221](#), [doi:10.1016/j.physletb.2010.03.037](#). [Page 13.]
- [58] K. Nakamura et al. Review of particle physics. *J. Phys.*, G37:075021, 2010. [doi:10.1088/0954-3899/37/7A/075021](#). [Page 13.]
- [59] Wilhelm H. Bertl et al. A Search for muon to electron conversion in muonic gold. *Eur. Phys. J.*, C47:337–346, 2006. [doi:10.1140/epjc/s2006-02582-x](#). [Page 13.]
- [60] L. Willmann et al. New bounds from searching for muonium to anti-muonium conversion. *Phys. Rev. Lett.*, 82:49–52, 1999. [arXiv:hep-ex/9807011](#), [doi:10.1103/PhysRevLett.82.49](#). [Page 13.]
- [61] Nobel Media AB. The nobel prize in physics 1995, 2014. URL: [http://www.nobelprize.org/nobel\\_prizes/physics/laureates/1995](http://www.nobelprize.org/nobel_prizes/physics/laureates/1995). [Page 15.]
- [62] Antonio Pich. Lessons learnt from the heavy tau lepton. *CERN Cour.*, 40(1):20–2, 2000. URL: <https://cds.cern.ch/record/434853>. [Page 15.]
- [63] Alan J. Weinstein and Ryszard Stroynowski. The Tau lepton and its neutrino. *Ann. Rev. Nucl. Part. Sci.*, 43:457–528, 1993. [doi:10.1146/annurev.ns.43.120193.002325](#). [Page 15.]
- [64] Philip Ilten. *Electroweak and Higgs Measurements Using Tau Final States with the LHCb Detector*. PhD thesis, University Coll., Dublin, 2013-09-06. URL: <https://inspirehep.net/record/1278195/files/arXiv:1401.4902.pdf>, [arXiv:1401.4902](#). [Pages 15, 16, 22, 33, 125, and 267.]
- [65] Gregory Ciezarek, Manuel Franco Sevilla, Brian Hamilton, Robert Kowalewski, Thomas Kuhr, Vera Lüth, and Yutaro Sato. A Challenge to Lepton Universality in B Meson Decays. *Nature*, 546:227–233, 2017. [arXiv:1703.01766](#), [doi:10.1038/nature22346](#). [Page 17.]

## Bibliography

---

- [66] CERN.ch: Member states. Jan 2012. URL: <https://cds.cern.ch/record/1997223>. [Page 19.]
- [67] Cern.ch: Our mission. URL: <https://jobs.web.cern.ch/content/our-mission>. [Page 19.]
- [68] CERN.ch: The accelerator complex. Jan 2012. URL: <https://cds.cern.ch/record/1997193>. [Page 19.]
- [69] Cinzia De Melis. The CERN accelerator complex. Complexe des accélérateurs du CERN. Jul 2016. General Photo. URL: <https://cds.cern.ch/record/2197559>. [Pages 20 and 267.]
- [70] CERN.ch: Experiments. Jul 2012. URL: <https://cds.cern.ch/record/1997374>. [Pages 21 and 267.]
- [71] S. Chatrchyan et al. The CMS Experiment at the CERN LHC. *JINST*, 3:S08004, 2008. doi:10.1088/1748-0221/3/08/S08004. [Page 22.]
- [72] G. Aad et al. The ATLAS Experiment at the CERN Large Hadron Collider. *JINST*, 3:S08003, 2008. doi:10.1088/1748-0221/3/08/S08003. [Page 22.]
- [73] A. Augusto Alves, Jr. et al. The LHCb Detector at the LHC. *JINST*, 3:S08005, 2008. doi:10.1088/1748-0221/3/08/S08005. [Pages 22, 24, 26, 27, 28, 29, 31, 267, and 268.]
- [74] Mike Lamont. Status of the LHC. *J. Phys. Conf. Ser.*, 455:012001, 2013. doi:10.1088/1742-6596/455/1/012001. [Page 23.]
- [75] Summary of the analysis of the 19 September 2008 incident at the LHC. Résumé de l'analyse de l'incident survenu le 19 septembre 2008 au LHC. Technical report, CERN, Geneva, Oct 2008. URL: <https://cds.cern.ch/record/1135729>. [Page 23.]
- [76] G Apollinari, I Béjar Alonso, O Brüning, M Lamont, and L Rossi. High-Luminosity Large Hadron Collider (HL-LHC) : Preliminary Design Report. 2015. doi:10.5170/CERN-2015-005. [Page 23.]
- [77] by Rende Steerenberg for the Operations group and Stefania Pandolfi. LHC report: full house for the LHC. Jun 2017. URL: <https://cds.cern.ch/record/2272573>. [Pages 23 and 267.]
- [78] F. Follin and D. Jacquet. Implementation and experience with luminosity levelling with offset beam. In *Proceedings, ICFA Mini-Workshop on Beam-Beam Effects in Hadron Colliders (BB2013): CERN, Geneva, Switzerland, March 18-22 2013*, pages 183–187, 2014. [183(2014)]. URL: <https://inspirehep.net/record/1322139/files/arXiv:1410.3667.pdf>, arXiv:1410.3667, doi:10.5170/CERN-2014-004.183. [Page 24.]
- [79] Saranya Samik Ghosh. Performance of MET reconstruction and pileup mitigation techniques in CMS. *Nucl. Part. Phys. Proc.*, 273-275:2512–2514, 2016. arXiv:1502.05207, doi:10.1016/j.nuclphysbps.2015.09.442. [Page 24.]
- [80] Zachary Marshall. Simulation of Pile-up in the ATLAS Experiment. *J. Phys. Conf. Ser.*, 513:022024, 2014. doi:10.1088/1742-6596/513/2/022024. [Page 24.]
- [81] Rolf Lindner. LHCb layout. LHCb Collection., Feb 2008. URL: <https://cds.cern.ch/record/1087860>. [Pages 24 and 267.]

- [82] Roel Aaij et al. LHCb Detector Performance. *Int. J. Mod. Phys.*, A30(07):1530022, 2015. [arXiv:1412.6352](#), [doi:10.1142/S0217751X15300227](#). [Page 24.]
- [83] R. Aaij et al. Performance of the LHCb Vertex Locator. *JINST*, 9:09007, 2014. [arXiv:1405.7808](#), [doi:10.1088/1748-0221/9/09/P09007](#). [Pages 25, 26, 87, and 267.]
- [84] A Arefev, S Barsuk, I Belyaev, B Bobchenko, L Camilleri, V Egorychev, Yu Gilitsky, A Golutvin, O Gouchtchine, I Korolko, T Kvaratskheliia, I Machikhilian, M Martemyanov, E Melnikov, A Morozov, M Prokudin, D Roussinov, V Rusinov, A Schopper, S Schuvalov, A Soldatov, E Tarkovski, and K Voronchev. Beam Test Results of the LHCb Electromagnetic Calorimeter. Technical Report LHCb-2007-149. CERN-LHCb-2007-149, CERN, Geneva, May 2008. revised version submitted on 2008-05-15 09:09:53. URL: <https://cds.cern.ch/record/1103500>. [Page 28.]
- [85] In preparation. The HeRSChE detector: high rapidity shower counters for LHCb. Technical report, 2016. [Pages 29 and 268.]
- [86] M. Adinolfi et al. Performance of the LHCb RICH detector at the LHC. *Eur. Phys. J.*, C73:2431, 2013. [arXiv:1211.6759](#), [doi:10.1140/epjc/s10052-013-2431-9](#). [Page 32.]
- [87] Eduardo Picatoste Olloqui. LHCb preshower(PS) and scintillating pad detector (SPD): Commissioning, calibration, and monitoring. *J. Phys. Conf. Ser.*, 160:012046, 2009. [doi:10.1088/1742-6596/160/1/012046](#). [Page 32.]
- [88] Trigger schemes. URL: <https://lhcb.web.cern.ch/lhcb/speakersbureau/html/TriggerScheme.html>. [Pages 33 and 268.]
- [89] R. Aaij et al. Precision luminosity measurements at LHCb. *JINST*, 9:P12005, 2014. [arXiv:1410.0149](#), [doi:10.1088/1748-0221/9/12/P12005](#). [Pages 34 and 123.]
- [90] G. Barrand et al. GAUDI - A software architecture and framework for building HEP data processing applications. *Comput. Phys. Commun.*, 140:45–55, 2001. [doi:10.1016/S0010-4655\(01\)00254-5](#). [Page 34.]
- [91] The LHCb Collaboration. The BRUNEL Project. URL: <http://lhcb-release-area.web.cern.ch/LHCb-release-area/DOC/brunel>. [Page 34.]
- [92] The LHCb Collaboration. The DAVINCI Project. URL: <http://lhcb-release-area.web.cern.ch/LHCb-release-area/DOC/davinci>. [Page 34.]
- [93] The LHCb Collaboration. The GAUSS Project. URL: <http://lhcb-release-area.web.cern.ch/LHCb-release-area/DOC/gauss>. [Page 34.]
- [94] The LHCb Collaboration. The BOOLE Project. URL: <http://lhcb-release-area.web.cern.ch/LHCb-release-area/DOC/boole>. [Page 34.]
- [95] The LHCb Collaboration. The MOORE Project. URL: <http://lhcb-release-area.web.cern.ch/LHCb-release-area/DOC/moore>. [Page 34.]
- [96] P. Charpentier. LHCb Computing Resource usage in 2012(II). 2013. [Page 34.]
- [97] The LHCb Collaboration. The STRIPPING Project. URL: <http://lhcb-release-area.web.cern.ch/LHCb-release-area/DOC/stripping>. [Page 34.]

## Bibliography

---

- [98] Jamie Shiers. The Worldwide LHC Computing Grid (worldwide LCG). *Comput. Phys. Commun.*, 177:219–223, 2007. doi:10.1016/j.cpc.2007.02.021. [Page 34.]
- [99] A. Tsaregorodtsev. DIRAC Distributed Computing Services. *J. Phys. Conf. Ser.*, 513:032096, 2014. doi:10.1088/1742-6596/513/3/032096. [Page 34.]
- [100] J. T. Mościcki et al. Ganga : A tool for computational-task management and easy access to Grid resources. *Comput. Phys. Commun.*, 180:2303–2316, 2009. doi:10.1016/j.cpc.2009.06.016. [Page 34.]
- [101] Task Force on Core Software (TFCS). URL: <https://twiki.cern.ch/twiki/bin/view/LHCb/TaskForceCS>. [Page 34.]
- [102] LHCb Collaboration member list. URL: [https://lhcb.web.cern.ch/lhcb/lhcb\\_page/collaboration/organization/list\\_of\\_members/members\\_default.pdf](https://lhcb.web.cern.ch/lhcb/lhcb_page/collaboration/organization/list_of_members/members_default.pdf). [Page 34.]
- [103] The LHCb collaboration. URL: <http://lhcb-public.web.cern.ch/lhcb-public/en/Collaboration/Collaboration-en.html>. [Page 34.]
- [104] WLCG (Worldwide LHC Computing Grid). Tier centres. URL: <http://wlcg-public.web.cern.ch/tier-centres>. [Pages 36 and 268.]
- [105] Georges Aad et al. Measurement of the Z to tau tau Cross Section with the ATLAS Detector. *Phys. Rev.*, D84:112006, 2011. arXiv:1108.2016, doi:10.1103/PhysRevD.84.112006. [Page 39.]
- [106] Serguei Chatrchyan et al. Measurement of the Inclusive Z Cross Section via Decays to Tau Pairs in  $pp$  Collisions at  $\sqrt{s} = 7$  TeV. *JHEP*, 08:117, 2011. arXiv:1104.1617, doi:10.1007/JHEP08(2011)117. [Page 39.]
- [107] R. Aaij et al. A study of the Z production cross-section in  $pp$  collisions at  $\sqrt{s} = 7$  TeV using tau final states. *JHEP*, 01:111, 2013. arXiv:1210.6289, doi:10.1007/JHEP01(2013)111. [Pages 39, 43, 57, 61, and 97.]
- [108] R. Aaij et al. Measurement of forward W and Z boson production in  $pp$  collisions at  $\sqrt{s} = 8$  TeV. *JHEP*, 01:155, 2016. arXiv:1511.08039, doi:10.1007/JHEP01(2016)155. [Pages 39, 43, 81, 95, 96, 109, and 271.]
- [109] R. Aaij et al. Measurement of  $Z \rightarrow e^+e^-$  production at  $\sqrt{s} = 8$  TeV. *JHEP*, 05:109, 2015. arXiv:1503.00963, doi:10.1007/JHEP05(2015)109. [Pages 39, 43, 75, 77, 81, and 109.]
- [110] Roel Aaij et al. Precision luminosity measurements at LHCb. *JINST*, 9(12):P12005, 2014. arXiv:1410.0149, doi:10.1088/1748-0221/9/12/P12005. [Page 41.]
- [111] Simone Alioli, Paolo Nason, Carlo Oleari, and Emanuele Re. NLO vector-boson production matched with shower in POWHEG. *JHEP*, 07:060, 2008. arXiv:0805.4802, doi:10.1088/1126-6708/2008/07/060. [Pages 41 and 44.]
- [112] Paolo Nason. A New method for combining NLO QCD with shower Monte Carlo algorithms. *JHEP*, 11:040, 2004. arXiv:hep-ph/0409146, doi:10.1088/1126-6708/2004/11/040. [Pages 41, 44, and 119.]

- [113] Stefano Frixione, Paolo Nason, and Carlo Oleari. Matching NLO QCD computations with Parton Shower simulations: the POWHEG method. *JHEP*, 11:070, 2007. [arXiv:0709.2092](#), [doi:10.1088/1126-6708/2007/11/070](#). [Pages 41, 44, and 119.]
- [114] Simone Alioli, Paolo Nason, Carlo Oleari, and Emanuele Re. A general framework for implementing NLO calculations in shower Monte Carlo programs: the POWHEG BOX. *JHEP*, 06:043, 2010. [arXiv:1002.2581](#), [doi:10.1007/JHEP06\(2010\)043](#). [Pages 41, 44, and 119.]
- [115] Philip Ilten. Tau Decays in Pythia 8. *Nucl. Phys. Proc. Suppl.*, 253-255:77–80, 2014. [arXiv:1211.6730](#), [doi:10.1016/j.nuclphysbps.2014.09.019](#). [Page 42.]
- [116] A. D. Martin, W. J. Stirling, R. S. Thorne, and G. Watt. Parton distributions for the LHC. *Eur. Phys. J.*, C63:189–285, 2009. [arXiv:0901.0002](#), [doi:10.1140/epjc/s10052-009-1072-5](#). [Pages 44, 91, and 96.]
- [117] Andy Buckley, James Ferrando, Stephen Lloyd, Karl Nordström, Ben Page, Martin Rüfenacht, Marek Schönherr, and Graeme Watt. LHAPDF6: parton density access in the LHC precision era. *Eur. Phys. J.*, C75:132, 2015. [arXiv:1412.7420](#), [doi:10.1140/epjc/s10052-015-3318-8](#). [Pages 44 and 119.]
- [118] Torbjorn Sjostrand, Stephen Mrenna, and Peter Z. Skands. PYTHIA 6.4 Physics and Manual. *JHEP*, 05:026, 2006. [arXiv:hep-ph/0603175](#), [doi:10.1088/1126-6708/2006/05/026](#). [Pages 44 and 119.]
- [119] Torbjorn Sjostrand, Stephen Mrenna, and Peter Z. Skands. A Brief Introduction to PYTHIA 8.1. *Comput. Phys. Commun.*, 178:852–867, 2008. [arXiv:0710.3820](#), [doi:10.1016/j.cpc.2008.01.036](#). [Pages 44 and 119.]
- [120] Albert Puig. The LHCb trigger in 2011 and 2012. Technical Report LHCb-PUB-2014-046. CERN-LHCb-PUB-2014-046, CERN, Geneva, Nov 2014. URL: <https://cds.cern.ch/record/1970930>. [Page 45.]
- [121] Jan Therhaag. TMVA: Toolkit for multivariate data analysis. *AIP Conf. Proc.*, 1504:1013–1016, 2009. [doi:10.1063/1.4771869](#). [Page 47.]
- [122] Serguei Chatrchyan et al. Performance of tau-lepton reconstruction and identification in CMS. *JINST*, 7:P01001, 2012. [arXiv:1109.6034](#), [doi:10.1088/1748-0221/7/01/P01001](#). [Page 48.]
- [123] C. Patrignani et al. Review of particle physics. *Chin. Phys.*, C40:100001, 2016. [doi:10.1088/1674-1137/40/10/100001](#). [Pages 50, 109, 123, and 137.]
- [124] Wouter D. Hulsbergen. Decay chain fitting with a Kalman filter. *Nucl. Instrum. Meth.*, A552:566–575, 2005. [arXiv:physics/0503191](#), [doi:10.1016/j.nima.2005.06.078](#). [Page 50.]
- [125] C. J. Clopper and E. S. Pearson. The use of confidence or fiducial limits illustrated in the case of the binomial. *Biometrika*, 26(4):404–413, 1934. URL: <http://www.jstor.org/stable/2331986>. [Pages 57 and 71.]



## Bibliography

---

- [126] R. Brun and F. Rademakers. ROOT: An object oriented data analysis framework. *Nucl. Instrum. Meth.*, A389:81–86, 1997. doi:10.1016/S0168-9002(97)00048-X. [Page 61.]
- [127] Frederick James. *Statistical methods in experimental physics*. World Scientific, 2006. [Pages 64 and 113.]
- [128] The LHCb Collaboration. A measurement of high-pT muon reconstruction efficiencies in 2011 and 2012 data. 2014. [Pages 72, 75, and 82.]
- [129] R. Aaij et al. Measurement of the track reconstruction efficiency at LHCb. *JINST*, 10:P02007, 2015. arXiv:1408.1251, doi:10.1088/1748-0221/10/02/P02007. [Pages 72 and 74.]
- [130] Lucio Anderlini, Andrea Contu, Christopher Rob Jones, Sneha Sirirshkumar Malde, Dominik Muller, Stephen Ogilvy, Juan Martin Otalora Goicochea, Alex Pearce, Ivan Polyakov, Wenbin Qian, Barbara Sciascia, Ricardo Vazquez Gomez, and Yanxi Zhang. The PIDCalib package. Technical Report LHCb-PUB-2016-021. CERN-LHCb-PUB-2016-021, CERN, Geneva, Jul 2016. URL: <https://cds.cern.ch/record/2202412>. [Page 75.]
- [131] Muriel Pivk and Francois R. Le Diberder. SPlot: A Statistical tool to unfold data distributions. *Nucl. Instrum. Meth.*, A555:356–369, 2005. arXiv:physics/0402083, doi:10.1016/j.nima.2005.08.106. [Page 75.]
- [132] A. Valassi. Combining correlated measurements of several different physical quantities. *Nucl. Instrum. Meth.*, A500:391–405, 2003. doi:10.1016/S0168-9002(03)00329-2. [Pages 75, 95, and 201.]
- [133] R. Aaij et al. Measurement of the forward  $Z$  boson production cross-section in  $pp$  collisions at  $\sqrt{s} = 13$  TeV. *JHEP*, 09:136, 2016. submitted to JHEP. arXiv:1607.06495, doi:10.1007/JHEP09(2016)136. [Page 86.]
- [134] R. Aaij et al. Search for massive long-lived particles decaying semileptonically in the LHCb detector. 2016. submitted to EPJC. arXiv:1612.00945. [Page 88.]
- [135] Jorg Wenninger and Ezio Todesco. Large Hadron Collider momentum calibration and accuracy. Technical Report CERN-ACC-2017-0007, CERN, Geneva, Feb 2017. URL: <https://cds.cern.ch/record/2254678>. [Page 91.]
- [136] Stefano Catani, Leandro Cieri, Giancarlo Ferrera, Daniel de Florian, and Massimiliano Grazzini. Vector boson production at hadron colliders: a fully exclusive QCD calculation at NNLO. *Phys. Rev. Lett.*, 103:082001, 2009. arXiv:0903.2120, doi:10.1103/PhysRevLett.103.082001. [Page 91.]
- [137] Stefano Catani and Massimiliano Grazzini. An NNLO subtraction formalism in hadron collisions and its application to Higgs boson production at the LHC. *Phys. Rev. Lett.*, 98:222002, 2007. arXiv:hep-ph/0703012, doi:10.1103/PhysRevLett.98.222002. [Page 96.]
- [138] R. Aaij et al. Measurement of the cross-section for  $Z \rightarrow e^+e^-$  production in  $pp$  collisions at  $\sqrt{s} = 7$  TeV. *JHEP*, 02:106, 2013. arXiv:1212.4620, doi:10.1007/JHEP02(2013)106. [Page 97.]



- 
- [139] R Aaij et al. Inclusive  $W$  and  $Z$  production in the forward region at  $\sqrt{s} = 7 \text{ TeV}$ . *JHEP*, 06:058, 2012. [arXiv:1204.1620](#), [doi:10.1007/JHEP06\(2012\)058](#). [Page 97.]
- [140] Giovanni Punzi. Sensitivity of searches for new signals and its optimization. *eConf*, C030908:MODT002, 2003. [,79(2003)]. [arXiv:physics/0308063](#). [Page 104.]
- [141] Simone Alioli, Paolo Nason, Carlo Oleari, and Emanuele Re. NLO Higgs boson production via gluon fusion matched with shower in POWHEG. *JHEP*, 04:002, 2009. [arXiv:0812.0578](#), [doi:10.1088/1126-6708/2009/04/002](#). [Page 119.]
- [142] L. A. Harland-Lang, A. D. Martin, P. Motylinski, and R. S. Thorne. Parton distributions in the LHC era: MMHT 2014 PDFs. *Eur. Phys. J.*, C75(5):204, 2015. [arXiv:1412.3989](#), [doi:10.1140/epjc/s10052-015-3397-6](#). [Page 119.]
- [143] Glen Cowan, Kyle Cranmer, Eilam Gross, and Ofer Vitells. Asymptotic formulae for likelihood-based tests of new physics. *Eur. Phys. J.*, C71:1554, 2011. [Erratum: *Eur. Phys. J.*C73,2501(2013)]. [arXiv:1007.1727](#), [doi:10.1140/epjc/s10052-011-1554-0](#), [10.1140/epjc/s10052-013-2501-z](#). [Page 126.]
- [144] Abraham Wald. Tests of statistical hypotheses concerning several parameters when the number of observations is large. *Transactions of the American Mathematical Society*, 54(3):426–426, mar 1943. URL: <https://doi.org/10.1090/s0002-9947-1943-0012401-3>, [doi:10.1090/s0002-9947-1943-0012401-3](#). [Page 126.]
- [145] Alexander L. Read. Presentation of search results: The CL(s) technique. *J. Phys.*, G28:2693–2704, 2002. [,11(2002)]. [doi:10.1088/0954-3899/28/10/313](#). [Page 130.]
- [146] D. de Florian et al. Handbook of LHC Higgs Cross Sections: 4. Deciphering the Nature of the Higgs Sector. 2016. [arXiv:1610.07922](#), [doi:10.23731/CYRM-2017-002](#). [Page 137.]
- [147] Charalampos Anastasiou, Claude Duhr, Falko Dulat, Elisabetta Furlan, Thomas Gehrmann, Franz Herzog, Achilleas Lazopoulos, and Bernhard Mistlberger. CP-even scalar boson production via gluon fusion at the LHC. *JHEP*, 09:037, 2016. [arXiv:1605.05761](#), [doi:10.1007/JHEP09\(2016\)037](#). [Page 137.]
- [148] Jon Butterworth et al. PDF4LHC recommendations for LHC Run II. *J. Phys.*, G43:023001, 2016. [arXiv:1510.03865](#), [doi:10.1088/0954-3899/43/2/023001](#). [Page 137.]
- [149] Wes McKinney. Data Structures for Statistical Computing in Python. In Stéfan van der Walt and Jarrod Millman, editors, *Proceedings of the 9th Python in Science Conference*, pages 51–56, 2010. [Page 201.]
- [150] Eric O. Lebigot. Uncertainties: a Python package for calculations with uncertainties, 2016. URL: <https://pythonhosted.org/uncertainties/>. [Page 201.]



# List of Figures

2.1	Overview of the standard model of physics. . . . .	6
2.2	Current known distribution of matter in the observable universe [10]. . . . .	7
2.3	Current constraints on the CKM matrix [11]. . . . .	7
2.4	Changes on the running gauge couplings in the Minimal Supersymmetric SM, where the gauge coupling unification is observed at a higher energy scale, assuming $SU(5)$ symmetry group [14]. . . . .	8
2.5	Coupling of axion and photon can be exploit in the “light-shining-through-wall” experiment [16]. . . . .	9
2.6	Illustration of elements in M-theory [19]. . . . .	9
2.7	Observation of atmospheric neutrinos found to be compatible with the neutrino oscillation scenario [23]. . . . .	10
2.8	Highly-suppressed CLFV decay in the SM [26]. . . . .	11
2.9	Possible CLFV from the NP processes. The upper row can be classified as “loop” type, and the lower row as “contact” type. Diagrams adapted from [25, 29]. . . . .	11
2.10	Various low-energy measurements constraining HCLFV, shown with the relevant Yukawa couplings. . . . .	14
2.11	List of major decay channels of $\tau$ lepton, grouped into 4 channels in this analysis. Only the charged final state particle(s) marked in red are used for the reconstruction, denoted as (a) $\tau_\mu$ (b) $\tau_e$ (c) $\tau_{h1}$ (d) $\tau_{h3}$ . The conjugated mode is implied, as well as possible neutral hadrons (omitted from figure) from the hadronic decay of the $W$ . . . . .	15
2.12	Some of the possibilities of cross-feed $\tau_e$ candidate. (a) neutral pion decay in $\tau_{h1}$ , (b) pair-production from $\pi^0 \rightarrow \gamma\gamma$ decay, (c) bremsstrahlung to pair-production. . . . .	17
3.1	The accelerators complex at CERN [69]. . . . .	20
3.2	Experiments at CERN[70]. . . . .	21
3.3	Comparison of the detector components and their geometrical acceptance found in the major LHC experiments. Illustration from [64]. . . . .	22
3.4	Integrated luminosity delivered by year collected at the LHCb. One inverse femtobarn ( $\text{fb}^{-1}$ ) is roughly equivalent to 80 million million collisions [77]. . . . .	23
3.5	The LHCb detector [81]. . . . .	24
3.6	Schematic of the VELO module and sensors [73]. . . . .	26
3.7	VELO impact parameter resolution dependencies [83]. . . . .	26

## List of Figures

---

3.8	Schematic of 4-layer TT [73]. . . . .	27
3.9	Overview of the OT and IT [73]. . . . .	27
3.10	Lateral segmentation of the calorimeters, shown only single quadrant [73]. . . . .	28
3.11	Sideview of muon stations [73]. . . . .	29
3.12	Schematic of HERSCHEL stations around the interaction point at LHCb [85]. . . . .	29
3.13	Different track types classified in the LHCb event reconstruction with the subdetectors involved, shown with the corresponding $y$ -component magnetic field long the $z$ -axis of the LHCb detector. The momentum information can also be determined for the track types that pass through the magnetic field, where the curvature radius is inversely proportional to its momentum [73]. . . . .	31
3.14	Schematic illustration of bremsstrahlung correction [73]. . . . .	31
3.15	LHCb calorimetry responses. . . . .	32
3.16	LHCb trigger scheme in 2012 [88]. . . . .	33
3.17	Projects and their dependencies in the LHCb framework. . . . .	36
3.18	Layers of WLCG Tier-0, Tier-1, and Tier-2 sites as of June 2014 [104]. . . . .	36
4.1	List of major background processes in this study. (a) QCD from gluon-pair, (b) Drell-Yan, (c) $W$ +jet, (d) $Z$ +jet, (e) $t\bar{t}$ , (f) $WW$ . Note that the conjugated mode and topologically-equivalent diagrams are implied. . . . .	40
5.1	Schema of $Z \rightarrow \tau\tau$ candidates selection stages organized in this analysis. . . . .	43
5.2	The selected di-tau acceptance region is shown as the area not covered by the gray mask, for the $\tau_\mu\tau_e$ channel. The fiducial region requirement was applied. The distributions are shown as a function of (a) $p_T$ (b) $\eta$ of $\tau_e$ (horizontal axis) and $\tau_\mu$ (vertical axis). The plots are obtained at generator level. . . . .	45
5.3	The invariant mass of di-tau candidates at generator level for $Z \rightarrow \tau\tau$ in the fiducial region, with all $p_T$ and $\eta$ acceptance cuts applied. The $\tau_e$ and $\tau_\mu$ candidates are grouped together as $\tau_l$ . Note that the minimal invariant mass used in this analysis is $20 \text{ GeV}/c^2$ for $\tau_l\tau_l$ (black curve), and $30 \text{ GeV}/c^2$ for both $\tau_l\tau_{h1}$ (red) and $\tau_l\tau_{h3}$ (blue). . . . .	45
5.4	$p_T$ of the reconstructed muon vs $p_T$ of the reconstructed electron, in the $\tau_\mu\tau_e$ channel, from $Z \rightarrow \tau\tau$ simulated sample. The kinematic preselection excludes the shaded region. Notice that the reconstructed electrons can populate the region below this cut, because of the bremsstrahlung loss. . . . .	47
5.5	Illustration of $\tau_{h3}$ cone and distances $R_i$ between prongs. . . . .	48
5.6	Combination quality variables of $\tau_{h3}$ from $\tau_\mu\tau_{h3}$ channel: (a) vertex fitting $\chi^2/\text{ndf}$ , (b) $\Delta R_{\text{max}}$ , (c) $\Delta R_{\text{max}}$ and $p_T$ contours (d) $\Delta R_{\text{max}}$ between prongs divided by the $p_T$ of $\tau_{h3}$ . The $Z \rightarrow \tau\tau$ signal from simulation (black) is compared against other prominent backgrounds. . . . .	48
5.7	Illustration of neighbor tracks inside the cone around a tau candidate used to compute the isolation. . . . .	49
5.8	Isolation variable $\hat{I}_{p_T}$ for (a) $\tau_\mu$ , (b) $\tau_{h3}$ from $\tau_\mu\tau_{h3}$ channel, and (c) $\tau_e$ , (d) $\tau_{h1}$ from $\tau_e\tau_{h1}$ channel. . . . .	49
5.9	Variable used for $\tau_{h3}$ identification based on a secondary vertex, shown with $\tau_{h3}$ from $\tau_\mu\tau_{h3}$ candidates: (a) <i>decay time</i> , (b) <i>corrected mass</i> $m_{\text{corr}}$ . . . . .	50

5.10	Illustration of the impact parameter of a tau candidate. . . . .	51
5.11	Impact parameters of (a) second $\tau_e$ from $\tau_e\tau_e$ channel, (b) second $\tau_\mu$ from $\tau_\mu\tau_\mu$ channel, (c) $\tau_{h1}$ from $\tau_\mu\tau_{h1}$ channel. . . . .	51
5.12	Figure-of-merits as a function of maximum di-tau invariant mass selection, with all selections applied: (a) $S/\sqrt{S+B}$ , (b) $S/B$ . At the right-most bin, no mass cut is applied. . . . .	52
5.13	Illustration of $\Delta\phi$ between two $\tau$ candidate. . . . .	52
5.14	Azimuthal separation, $\Delta\phi$ , for (a) $\tau_\mu\tau_{h3}$ , (b) $\tau_e\tau_{h1}$ channel. . . . .	52
5.15	Transverse momentum asymmetry, $A_{p_T}$ , for (a) $\tau_\mu\tau_\mu$ , (b) $\tau_\mu\tau_e$ channel. . . . .	53
5.16	Distribution of $\chi^2_{\text{DOCA}}$ for $Z \rightarrow \mu\mu$ from data (black), $Z \rightarrow \mu\mu$ from simulated sample (red), $\tau_\mu\tau_\mu$ candidate of $Z \rightarrow \tau\tau$ from simulated sample (blue). The data-simulation disagreement can be observed in the vicinity of $\chi^2_{\text{DOCA}} \sim 10$ . . . . .	53
6.1	Mass distribution for (a) the $Z \rightarrow \mu\mu$ background after the $\tau_\mu\tau_\mu$ candidate selection, and (b) the $Z \rightarrow ee$ background in $\tau_e\tau_e$ candidates. The number of candidates in data (black dot) under the $Z$ peak is used to normalize the $Z \rightarrow ll$ background from simulated events (red). The distribution from $Z \rightarrow \tau\tau$ (blue) is shown for reference with an arbitrary normalization. . . . .	58
6.2	The $\mu \rightarrow h$ misidentification probability as a function of the muon $p_T$ . The results are from the simulated sample (black), and from the tag-and-probe in simulated sample (red), and in data (blue). . . . .	60
6.3	Summary of the lepton misidentification probabilities as a function of the lepton $p_T$ which are used in the computation of the background from $Z \rightarrow ll$ decays. The values are inferred from simulation: (black) muon misidentified as charged hadron, (red) electron misidentified as charged hadron, (blue) muon misidentified as electron, (brown) electron misidentified as muon. . . . .	60
6.4	Fit of the same-sign di-tau candidates with templates from QCD, $Vj$ and $Z \rightarrow \tau\tau$ processes. The unit of transverse momentum is in $\text{GeV}/c$ . . . . .	63
6.5	Invariant mass of the di-tau candidates. The contributions from each process is superposed. In grey, the areas which are excluded from the final computation of the signal. In (h), $\tau_\mu\tau_\mu$ channel with full $Z$ -peak normalization region shown. . . . .	66
6.6	Like Fig. 6.5, displayed with equiprobable bins. . . . .	67
7.1	(a) $\varepsilon_{\text{track},\mu}$ as a function of the $\eta$ of the muon. The results from data and simulation are compared. (b) $\varepsilon_{\text{track},e}$ from simulation as a function of the electron $\eta$ and of the track multiplicity in the event. . . . .	73
7.2	The single-track simulation-to-data correction factor for the calculation of $\varepsilon_{\text{track}}$ , binned in track momentum and pseudorapidity. . . . .	73
7.3	(a) $\varepsilon_{\text{track},h}$ of $\tau_{h1}$ as a function of $\eta$ and of the event track multiplicity. (b) $\varepsilon_{\text{track}}$ of $\tau_{h1}$ (black) and $\tau_{h3}$ (red) as a function of the event track multiplicity. . . . .	74
7.4	Comparison of <b>nTracks</b> distributions from data (black) and simulated $Z \rightarrow \tau\tau$ (red), from the channel (a) $\tau_\mu\tau_{h1}$ , and (b) $\tau_\mu\tau_{h3}$ . The ratio is used to reweight the events prior to the computation of $\varepsilon_{\text{track}}$ . . . . .	74

## List of Figures

---

7.5	Results from the background-removal fit of $J/\psi \rightarrow \mu^+\mu^-$ muon calibration sample. (a) contribution of processes projected on distribution of $J/\psi$ mass, (b) distribution of $sWeight$ from different fitted processes as a function of $J/\psi$ mass. . . . .	76
7.6	Bi-parametric distribution in $\eta$ and $p_T$ of the probe muon from $J/\psi \rightarrow \mu^+\mu^-$ and $Z \rightarrow \mu^+\mu^-$ calibration samples combined. The red dashed lines show the binning choice. . . . .	76
7.7	Examples of $\varepsilon_{PID,\mu}$ from data (black) as a function of muon $\eta$ (a), and $p_T$ (b). The efficiency from simulation (red) is also shown. The values are taken from Table E.5. . . . .	77
7.8	Results from the background-removal fit of $B^+ \rightarrow J/\psi(\rightarrow e^+e^-)K^+$ electron calibration sample. (a) contribution of processes projected on distribution of $J/\psi$ mass, (b) distribution of $sWeight$ from different fitted processes as a function of $J/\psi$ mass. . . . .	78
7.9	Bi-parametric distribution in $\eta$ and $p_T$ of the probe electron from $J/\psi \rightarrow ee$ and $Z \rightarrow ee$ calibration samples combined. The red dashed lines show the choice of bins. . . . .	78
7.10	Examples of $\varepsilon_{PID,e}$ from data (black) as a function of electron $\eta$ (a), and $p_T$ (b). The efficiency from simulation (red) is also shown. . . . .	78
7.11	Results from the background-removal fit of $D^{*+} \rightarrow D^0(\rightarrow K^-\pi^+)\pi^+$ charged-hadron calibration sample. (a) Two-dimensional distribution from data of $D^0$ mass versus $\Delta m_D$ , (b) contribution of processes projected on distribution of $\Delta m_D$ , (c) contribution of processes projected on distribution of $D^0$ mass. . . . .	79
7.12	Distribution of $sWeight$ from different fitted processes as a function of two parameters of interest; (a) mass of $D^0$ , (b) $\Delta m_D$ . . . . .	80
7.13	Bi-parametric distribution for the probe hadron in $\eta$ and $p_T$ . The red dashed lines show the choice of bins. . . . .	80
7.14	Examples of $\varepsilon_{PID,h}$ from data (black) as a function of charged hadron $\eta$ (a), and $p_T$ (b) (channel $\tau_\mu\tau_{h1}$ ). The efficiency from simulation is also shown (in red). . . . .	80
7.15	Relative $\varepsilon_{GEC}$ as a function of maximum number of SPD hits obtained from the $Z \rightarrow \tau\tau$ simulated sample normalized to the reference value. (a): channels $\tau_\mu\tau_{h1}$ (red) and $\tau_\mu\tau_{h3}$ (blue) relative to $\tau_\mu\tau_\mu$ , (b): channels $\tau_e\tau_{h1}$ (red) and $\tau_e\tau_{h3}$ (blue) relative to $\tau_\mu\tau_e$ . The green band denotes the region where the $\varepsilon_{GEC}$ of the reference channel in simulation matches the efficiency obtained from data. . . . .	81
7.16	$\varepsilon_{trig,\mu}$ from data (black) as a function of muon (a) $\eta$ , (b) $p_T$ . The efficiency from simulation is shown in red. . . . .	82
7.17	$\varepsilon_{trig,e}$ from data (black) as a function of electron's (a) $\eta$ , (b) $p_T$ . The efficiency from simulation is shown in red. . . . .	82
8.1	Comparison between $Z \rightarrow \mu\mu$ from data (black) and simulation (red) for the $A_{p_T}$ of di-muons. . . . .	86

8.2	Comparison of the single muon selection efficiency as a function of $p_T$ of the muon, (a) between $Z \rightarrow \mu\mu$ from data and from the corresponding simulated sample; (b) between the simulated samples of $Z \rightarrow \mu\mu$ and $Z \rightarrow \tau\mu\tau\mu$ . The muon is required to be isolated with $\hat{I}_{p_T} > 0.9$ . . . . .	87
8.3	Comparison of $Z \rightarrow \mu\mu$ from data (black) and simulation before smearing (red), and after smearing (green) of the distribution of muon IP. . . . .	87
8.4	(a) Distribution of $\chi^2_{\Delta\phi}(f_{\text{scale}})$ used to calibrate $\Delta\phi$ , (b) Comparison of $Z \rightarrow \mu\mu$ from data (black) and simulation before calibration (red), and after calibration (green) of the distribution of $\pi - \Delta\phi$ of di-muon. . . . .	88
8.5	Comparison data/simulation for the variables relevant to the $\tau_{h3}$ selection: (a) $m_{\text{corr}}$ (b) $\Delta R_{\eta\phi}/p_T$ (c) Vertex $\chi^2/\text{ndf}$ (d) Decay time. The signal component is in red, the background QCD component in purple, cross-feed in green, di-boson in blue, and boson plus jets in yellow. . . . .	89
8.6	Comparison data (top plots) and simulation (bottom) for (a) $\Delta R_{\eta\phi}/p_T$ and (b) decay time, with the result of the exponential fit (in red) in the region of the cut. . . . .	89
9.1	Production cross-section of $pp \rightarrow Z \rightarrow ll$ inside LHCb fiducial region generated from DYNLO as a function of $\sqrt{s}$ . . . . .	91
10.1	Summary of the measurements of $Z \rightarrow ll$ production cross-section inside the LHCb fiducial region at 8 TeV. The dark inner error bar corresponds to the statistical uncertainty, whilst the light outer error bar is the total uncertainty. The colored band corresponds to the combined measurement of from $Z \rightarrow \tau\tau$ of this analysis. The last 7 rows represent the NNLO predictions with different parameterizations of the PDFs [108]. . . . .	96
12.1	$\Delta R_{\text{max}}$ vs. $p_T$ for different processes. The grey area is discarded by the selection. . . . .	105
12.2	Figure-of-merit as a function of $m_H$ for different channels and regimes. . . . .	106
13.1	$\Delta p_T$ distributions of same-sign $\mu\tau$ candidates fitted with contributions from QCD and $Vj$ processes. The top/middle/bottom rows correspond to the low-mass/central/high-mass regimes. From left to right: $\mu\tau_e$ , $\mu\tau_{h1}$ , $\mu\tau_{h3}$ , and $\mu\tau_\mu$ . Processes $\mu\tau_e$ and $\mu\tau_\mu$ have a too low statistics in the high-mass regime, the totality of the contribution is assigned to $Vj$ . . . . .	112
13.2	Invariant mass of the $\mu\tau$ candidates from 4 analysis channels (column-wise; $\mu\tau_e$ , $\mu\tau_{h1}$ , $\mu\tau_{h3}$ , $\mu\tau_\mu$ ), and at 3 selection regimes (row-wise; low-mass, central, high-mass). The contributions from each process is superposed. . . . .	115
13.3	Similar to Fig. 13.2, displayed with equiprobable bins. . . . .	116
13.4	Distribution of the observed $\mu\tau$ candidates (black dots with error bars) and expected backgrounds (red histogram). The distributions expected for a signal (blue) are superposed, normalized to the statistical uncertainty. . . . .	117
14.1	Acceptances for a Higgs-like boson signal as a function of $m_H$ and the four analysis channels; (a) $4\pi$ production, (b) production inside LHCb geometrical acceptance. . . . .	120

## List of Figures

---

14.2	Reconstruction efficiency of $\mu\tau$ candidates from low-mass selection regime as a function of $m_H$ . . . . .	120
14.3	$\varepsilon_{\text{sel}}$ of $\mu\tau$ candidates as a function of $m_H$ : (a) $\mu\tau_e$ , (b) $\mu\tau_{h1}$ , (c) $\mu\tau_{h3}$ , (d) $\mu\tau_\mu$ . . . . .	121
15.1	Relative uncertainties of $\mathcal{A}$ from PDF uncertainty and scales variation (normalization, factorization) for (a) $4\pi$ , and (b) LHCb acceptance. . . . .	124
16.1	Bivariate normal distribution as constraint term of $N_{\text{QCD}}, N_{Vj}$ backgrounds in the extended likelihood model. The result is taken from $\mu\tau_e$ channel at nominal regime, with the correlation coefficient between their uncertainties of (a) $-0.5$ as found in the analysis, (b) $0$ , <i>i.e.</i> , uncorrelated, for comparison. . . . .	130
16.2	Example of hypothesis test with CLs method for 95% confidence level upper limit determination (shown here $m_H = 125 \text{ GeV}/c^2$ at central regime, using simultaneous fit based on eq. 16.3). . . . .	131
16.3	Expected upper limits of $\sigma_{gg \rightarrow H \rightarrow \mu\tau}$ ; (a) compared between different analysis channels and simultaneously fit, (b) with and without the uncertainties treatment as nuisance parameters, (c) using different methods for PDF shape. . . . .	132
16.4	Pulls of the nuisance parameters from the likelihood simultaneously fit over all channels, for $m_H = 125 \text{ GeV}/c^2$ . . . . .	132
17.1	Simultaneous fit of the distribution of $H \rightarrow \mu\tau$ candidates invariant mass for the 4 analysis channels (columns-wise; $\mu\tau_e, \mu\tau_{h1}, \mu\tau_{h3}, \mu\tau_\mu$ ) at 3 different selection regimes (row-wise; low-mass $m_H = 45 \text{ GeV}/c^2$ , central $m_H = 85 \text{ GeV}/c^2$ , high-mass $m_H = 125 \text{ GeV}/c^2$ ). . . . .	134
17.2	Best fit number of signal candidates at different $m_H$ . . . . .	135
17.3	Best fit of $\sigma_{gg \rightarrow H \rightarrow \mu\tau}$ with all analysis channels simultaneously fit, and with selection regimes of best FOM, from inclusive production. . . . .	135
17.4	95% CLs upper limits of $\sigma_{gg \rightarrow H \rightarrow \mu\tau}$ with all analysis channels simultaneously fit: (a) inclusive $H \rightarrow \mu\tau$ production, (b) $H \rightarrow \mu\tau$ production with lepton daughters inside LHCb geometrical acceptance. . . . .	135
17.5	(a) Best fit of $\mathcal{B}_{H \rightarrow \mu\tau}$ as a function on $m_H$ using MSSM Higgs, (b) 95% CLs upper limits of $\mathcal{B}_{H \rightarrow \mu\tau}$ with all analysis channels simultaneously fit. . . . .	136
17.6	$\varepsilon_{\text{geo}}$ as a function of $m_H$ . . . . .	138
17.7	$\varepsilon_{p_T}$ using (a) current selection, (b) improved selection. . . . .	138
A.1	The acceptance region as a function of transverse momentum of $\tau_l$ and $\tau_{h3}$ (sum of momenta of 3 charged hadrons) (a) $\tau_\mu\tau_{h3}$ (b) $\tau_e\tau_{h3}$ . . . . .	145
A.2	For the $\tau_{h3}$ from $\tau_\mu\tau_{h3}$ channel, the acceptance region as a function of maximum $p_T$ of the 3 tracks, and minimum $p_T$ of prongs. No difference is observed for the same plot using $\tau_{h3}$ from $\tau_e\tau_{h3}$ channel. . . . .	145
A.3	The acceptance region as a function of the transverse momentum of each $\tau$ lepton decay product. . . . .	146
A.4	The acceptance region as a function of the pseudorapidity of each $\tau$ lepton decay product. . . . .	146



A.5	The acceptance region as a function of the invariant masses of $\tau_{h3}$ (vertical axis) and di-tau (horizontal axis), with all $p_T$ and $\eta$ acceptance cuts applied for channel (a) $\tau_\mu\tau_{h3}$ (b) $\tau_e\tau_{h3}$ . . . . .	147
A.6	The accessible region by kinematic preselection (area outside grey mask) of di-tau candidates as a function of the transverse momentum of each $\tau$ candidate in (a) $\tau_\mu\tau_\mu$ , (b) $\tau_\mu\tau_{h1}$ , (c) $\tau_\mu\tau_{h3}$ , (d) $\tau_e\tau_e$ , (e) $\tau_e\tau_{h1}$ , (f) $\tau_e\tau_{h3}$ , (g) $\tau_\mu\tau_e$ channel. The candidates are from $Z \rightarrow \tau\tau$ inside the fiducial and acceptance region, and pass the track quality criteria. The PID and trigger requirements are not applied. . . . .	152
A.7	Variables of $\tau_{h3}$ used in preselection of $\tau_\mu\tau_{h3}$ candidates. Comparison between signal (black) and various background, all from simulation. The preselection cut is applied and shown as black vertical line. (a) largest $p_T$ of $\tau_{h3}$ prongs, (b) smallest $p_T$ of $\tau_{h3}$ prongs, (c) invariant mass of $\tau_{h3}$ , (d) $p_T$ of $\tau_{h3}$ . The case for $\tau_e\tau_{h3}$ produces similar results. . . . .	153
A.8	Transverse momentum of the tau in each di-tau candidates after preselection. Comparison of signal and backgrounds from simulation. (a,b) $\tau_\mu\tau_{h3}$ , (c,d) $\tau_e\tau_{h3}$ , . . . . .	153
A.8	Transverse momentum of tau in each di-tau candidates after preselection. Comparison of signal and backgrounds from simulation. (a,b) $\tau_\mu\tau_\mu$ , (c,d) $\tau_e\tau_e$ , (e,f) $\tau_\mu\tau_{h1}$ , (g,h) $\tau_e\tau_{h1}$ , (i,j) $\tau_\mu\tau_e$ . . . . .	154
A.9	Variable correlation matrix in offline selection of (a) $\tau_e\tau_{h1}$ , (b) $\tau_\mu\tau_{h1}$ candidates. . . . .	155
A.9	Variable correlation matrix in offline selection of (c) $\tau_e\tau_e$ , (d) $\tau_\mu\tau_e$ , (e) $\tau_\mu\tau_\mu$ candidates. . . . .	156
A.9	Variable correlation matrix in offline selection of (f) $\tau_e\tau_{h3}$ , (g) $\tau_\mu\tau_{h3}$ candidates. . . . .	157
A.10	Isolation of the tau in each di-tau candidates after preselection. Comparison of signal and backgrounds from simulation. (a,b) $\tau_e\tau_e$ , (c,d) $\tau_e\tau_{h1}$ , (e,f) $\tau_e\tau_{h3}$ . . . . .	165
A.10	Isolation of tau in each di-tau candidates after preselection. Comparison of signal and backgrounds from simulation. (a,b) $\tau_\mu\tau_\mu$ , (c,d) $\tau_\mu\tau_{h1}$ , (e,f) $\tau_\mu\tau_{h3}$ , (g,h) $\tau_\mu\tau_e$ . . . . .	166
A.11	Comparison for (a) corrected mass, (b) decay time, (c) flying distance of $\tau_{h3}$ candidates of signal and backgrounds distributions from simulation. In all figures, only the kinematic preselection and combination quality cuts are applied (isolation is also not applied to have a larger statistics). . . . .	167
A.12	Impact parameter of tau in each di-tau candidates after isolation cut. Comparison of signal and backgrounds from simulation. (a,b) $\tau_e\tau_e$ , (c,d) $\tau_e\tau_{h1}$ . . . . .	167
A.12	Impact parameter of tau in each di-tau candidates after isolation cut. Comparison of signal and backgrounds from simulation. (e,f) $\tau_\mu\tau_\mu$ , (g,h) $\tau_\mu\tau_{h1}$ , (i,j) $\tau_\mu\tau_e$ , (k) $\tau_\mu\tau_{h3}$ , (l) $\tau_e\tau_{h3}$ . . . . .	168
A.13	Azimuthal separation, $\Delta\phi$ , of di-tau candidates after tau-level selection. Comparison of signal and backgrounds from simulation. (a) $\tau_\mu\tau_\mu$ , (b) $\tau_e\tau_e$ , (c) $\tau_\mu\tau_{h1}$ , (d) $\tau_e\tau_{h1}$ , (e) $\tau_\mu\tau_{h3}$ , (f) $\tau_e\tau_{h3}$ , (g) $\tau_\mu\tau_e$ . . . . .	169
A.14	Transverse momentum asymmetry, $A_{p_T}$ , of di-tau candidates after tau-level selection. Comparison of signal and backgrounds from simulation. (a) $\tau_\mu\tau_\mu$ , (b) $\tau_e\tau_e$ , (c) $\tau_\mu\tau_{h1}$ , (d) $\tau_e\tau_{h1}$ , (e) $\tau_\mu\tau_{h3}$ , (f) $\tau_e\tau_{h3}$ , (g) $\tau_\mu\tau_e$ . . . . .	170

## List of Figures

---

B.1	Background-removal fit in muon misidentification tag-and-probe study, where each row is different $p_T$ range. The probe muon at unprobed state is on the left column, and probed state on the right column. . . . .	172
C.1	Comparison of the di-lepton invariant mass distribution before and after the reweighting to the misidentification probability. (a) $\mu \rightarrow h$ (b) $e \rightarrow h$ (c) $\mu \rightarrow e$ (d) $e \rightarrow \mu$ . . . . .	174
D.1	Contribution from each process in observed di-tau candidates, as a function of di-tau invariant mass (same as Fig. 13.2 but with larger number of bins). The number of signal candidates is obtained from subtracting the total expected background from the observed candidates. . . . .	181
D.2	Contribution from each process in observed di-tau candidates, as a function of di-tau transverse momentum. The number of signal candidates is obtained from subtracting the total expected background from the observed candidates. . . . .	182
D.3	Contribution from each process in observed di-tau candidates, as a function of di-tau rapidity. The number of signal candidates is obtained from subtracting the total expected background from the observed candidates. . . . .	183
D.4	Contribution from each process in observed di-tau candidates, as a function of di-tau pseudorapidity. The number of signal candidates is obtained from subtracting the total expected background from the observed candidates. . . . .	184
D.5	Contribution from each process in observed di-tau candidates, as a function of di-tau $A_{p_T}$ . The number of signal candidates is obtained from subtracting the total expected background from the observed candidates. . . . .	185
D.6	Contribution from each process in observed di-tau candidates, as a function of first tau candidate transverse momentum. The number of signal candidates is obtained from subtracting the total expected background from the observed candidates. . . . .	186
D.7	Contribution from each process in observed di-tau candidates, as a function of second tau candidate transverse momentum. The number of signal candidates is obtained from subtracting the total expected background from the observed candidates. . . . .	187
D.8	Contribution from each process in observed di-tau candidates, as a function of first tau candidate pseudorapidity. The number of signal candidates is obtained from subtracting the total expected background from the observed candidates. . . . .	188
D.9	Contribution from each process in observed di-tau candidates, as a function of second tau candidate pseudorapidity. The number of signal candidates is obtained from subtracting the total expected background from the observed candidates. . . . .	189
F.1	Schematic representation of the migrations at relevant selection stages. The values from $\tau_\mu\tau_\mu$ channel is shown here, where the values from other channels can be replaced by those found in Table F.1, and Table F.2. . . . .	200
H.1	$\eta$ and $p_T$ distribution of Higgs-like boson. . . . .	203
H.2	$\eta$ and $p_T$ distribution of prompt muon. . . . .	203

H.3	Invariant mass distributions of $\mu\tau$ candidates from different channels . . . . .	203
H.4	$\eta$ and $p_T$ distributions of $\mu\tau$ candidates from different channels. . . . .	204
H.5	$\eta$ and $p_T$ distributions of $\tau$ candidates from different channels. . . . .	205
I.1	$\tau_{h3}$ variables in $\mu\tau_{h3}$ . . . . .	207
I.2	Muon $p_T$ . . . . .	208
I.3	Tau decay product $p_T$ . . . . .	209
I.4	Muon isolation . . . . .	210
I.5	Tau decay product isolation . . . . .	211
I.6	Muon isolation . . . . .	212
I.7	Tau decay product isolation . . . . .	213
I.8	Muon IP . . . . .	214
I.9	Tau decay product IP . . . . .	215
I.10	Azimuthal separation . . . . .	216
I.11	Transver momentum asymmetry . . . . .	217
I.12	Transver momentum difference . . . . .	218
J.1	Backgrounds contribution of $\mu\tau$ candidates as a function of its $p_T$ . . . . .	222
J.2	Backgrounds contribution of $\mu\tau$ candidates as a function of its rapidity. . . . .	223
J.3	Backgrounds contribution of $\mu\tau$ candidates as a function of its pseudorapidity. . . . .	224
J.4	Backgrounds contribution of $\mu\tau$ candidates as a function of hard muon $p_T$ . . . . .	225
J.5	Backgrounds contribution of $\mu\tau$ candidates as a function of hard muon $\eta$ . . . . .	226
J.6	Backgrounds contribution of $\mu\tau$ candidates as a function of $\tau$ lepton candidate $p_T$ . . . . .	227
J.7	Backgrounds contribution of $\mu\tau$ candidates as a function of $\tau$ lepton candidate $\eta$ . . . . .	228
K.1	$\varepsilon_{\text{rec}}$ for different channels: (a) $\mu\tau_e$ , (b) $\mu\tau_{h1}$ , (c) $\mu\tau_{h3}$ , (d), $\mu\tau_\mu$ . . . . .	234
L.1	Expected upper limits of $\sigma_{gg \rightarrow H \rightarrow \mu\tau}$ using different statistical methods with all analysis channels simultaneously fit, at different selection regime: (a) low-mass, (b) central, (c) high-mass. The results for $m_H > 125 \text{ GeV}/c^2$ are ill-defined in the low-mass regime, so they are discarded. . . . .	237
L.2	Expected upper limits of $\sigma_{gg \rightarrow H \rightarrow \mu\tau}$ using different statistical methods for 4 analysis channels (columns-wise) and 3 selection regimes (row-wise). . . . .	238
L.3	Expected upper limits of $\sigma_{gg \rightarrow H \rightarrow \mu\tau}$ for the three selection regimes, and the four analysis channels: (a) $\mu\tau_e$ , (b) $\mu\tau_{h1}$ , (c) $\mu\tau_{h3}$ , (d) $\mu\tau_\mu$ , (e) simultaneous fit over all channels. . . . .	239
L.4	Expected upper limits of $\sigma_{gg \rightarrow H \rightarrow \mu\tau}$ compared between different analysis channels, at different selection regime: (a) low-mass, (b) central, (c) high-mass, (d) best FOM. . . . .	240
L.5	Expected upper limits of $\sigma_{gg \rightarrow H \rightarrow \mu\tau}$ compared with/without systematic uncertainties, with all analysis channels simultaneously fit, at different selection regime: (a) low-mass, (b) central, (c) high-mass, (d) best FOM. . . . .	241
L.6	Expected upper limits of $\sigma_{gg \rightarrow H \rightarrow \mu\tau}$ compared with/without systematic uncertainties, for 4 analysis channels (columns-wise) and 3 selection regimes (row-wise). . . . .	242

## List of Figures

---

L.7	Expected upper limits of $\sigma_{gg \rightarrow H \rightarrow \mu\tau}$ using the three different methods for PDF shapes, and four analysis channels: (a) $\mu\tau_e$ , (b) $\mu\tau_{h1}$ , (c) $\mu\tau_{h3}$ , (d) $\mu\tau_\mu$ , and (e) simultaneous fit over all channels. . . . .	243
L.8	Simultaneous fit of the distribution of $H \rightarrow \mu\tau$ candidates invariant mass for the 4 analysis channels (columns-wise; $\mu\tau_e$ , $\mu\tau_{h1}$ , $\mu\tau_{h3}$ , $\mu\tau_\mu$ ) at 3 different selection regimes (row-wise; low-mass $m_H = 45 \text{ GeV}/c^2$ , central $m_H = 85 \text{ GeV}/c^2$ , high-mass $m_H = 125 \text{ GeV}/c^2$ ). The method of “histpdf” is used. . . . .	244
L.9	Simultaneous fit of the distribution of $H \rightarrow \mu\tau$ candidates invariant mass for the 4 analysis channels (columns-wise; $\mu\tau_e$ , $\mu\tau_{h1}$ , $\mu\tau_{h3}$ , $\mu\tau_\mu$ ) at 3 different selection regimes (row-wise; low-mass $m_H = 45 \text{ GeV}/c^2$ , central $m_H = 85 \text{ GeV}/c^2$ , high-mass $m_H = 125 \text{ GeV}/c^2$ ). The method of “histstat” is used. . . . .	245
L.10	Transformation to RooKeysPdf for different backgrounds at low-mass regime. . . . .	246
L.11	Transformation to RooKeysPdf for different backgrounds at central regime. . . . .	247
L.12	Transformation to RooKeysPdf for different backgrounds at high-mass regime. . . . .	248
M.1	Best fit number of signal candidates for different selection regimes: (top) low-mass, (middle) central, (bottom) high-mass. . . . .	249
M.2	95% CLs upper limits of $\sigma_{gg \rightarrow H \rightarrow \mu\tau}$ for different analysis channels (column-wise; $\mu\tau_e$ , $\mu\tau_{h1}$ , $\mu\tau_{h3}$ , $\mu\tau_\mu$ ) and for different selection regimes (row-wise; low-mass, central, high-mass). . . . .	252
M.3	95% CLs upper limits of $\sigma_{gg \rightarrow H \rightarrow \mu\tau}$ for different analysis channels (a) $\mu\tau_e$ , (b) $\mu\tau_{h1}$ , (c) $\mu\tau_{h3}$ , (d) $\mu\tau_\mu$ . . . . .	253
M.4	95% CLs upper limits of $\sigma_{gg \rightarrow H \rightarrow \mu\tau}$ with all analysis channels simultaneously fit for different selection regimes: (a) low-mass, (b) central, (c) high-mass. . . . .	253
M.5	Best fit $\sigma_{gg \rightarrow H \rightarrow \mu\tau}$ for different selection regimes, with all analysis channels simultaneously fit. . . . .	254

# List of Tables

2.1	Constraints on HCLFV for a Higgs mass of $125 \text{ GeV}/c^2$ , adapted from [30]. . . . .	13
2.2	Branching fraction of each $\tau$ lepton decay channel, as grouped in this analysis. The conjugated mode is implied. Charged hadronic product represented by $h^\pm$ stands for $\pi^\pm$ or $K^\pm$ . “neutrals” stands for $\gamma$ 's and/or $\pi^0$ 's. . . . .	15
3.1	List of the working groups as organized at the LHCb collaboration. . . . .	35
4.1	Branching fraction of each di-tau decay channel, as considered in this analysis.	39
4.2	Details of simulated samples used in this analysis, sorted by <code>decfile-ID</code> as used in LHCb. The cross-section is at leading-order from PYTHIA 8, unless stated otherwise. Where relevant, the branching ratio is already applied to the cross-section. . . . .	41
5.1	List of triggers defined for each trigger alley. . . . .	45
5.2	Definition of the LHCb $Z$ -boson fiducial region. . . . .	54
5.3	Trigger and stripping requirements. . . . .	54
5.4	Acceptance cuts. The subscript 1(2) refers to the $\tau$ lepton decay product candidate labeled at position 1(2) of the respective di-tau channel. The $p_T$ cuts in channel $\tau_\mu\tau_\mu$ , $\tau_e\tau_e$ , and $\tau_\mu\tau_e$ are interchangeable between the two $\tau$ lepton decay product candidates. . . . .	54
5.5	Additional acceptance cuts for $\tau_{h3}$ in $\tau_\mu\tau_{h3}$ and $\tau_e\tau_{h3}$ channel, where $h$ denotes a single charged hadron used in the construction of 3-prongs $\tau_{h3}$ . . . . .	54
5.6	Particle identification cuts. . . . .	55
5.7	Tracking selection criteria. They are applied identically to all muons, charged hadrons, and electrons used in the reconstruction of the $\tau$ candidate. . . . .	55
5.8	Summary of the criteria for the offline selection. The subscript 1(2) refers to the $\tau$ lepton decay product candidate labeled at position 1(2) of the respective di-tau channel. . . . .	55
5.9	Additional offline selection criteria for $\tau_{h3}$ in $\tau_\mu\tau_{h3}$ and $\tau_e\tau_{h3}$ channels. . . . .	55
6.1	Determination of the $Z \rightarrow ll$ background in $\tau_\mu\tau_\mu$ and $\tau_e\tau_e$ channels. . . . .	58
6.2	Estimation of the $Z \rightarrow ll$ background for the $\tau_\mu\tau_{h1}$ , $\tau_e\tau_{h1}$ , and $\tau_\mu\tau_e$ channels. For illustration, the “Mean mis-id” column gives the lepton misidentification averaged over the $p_T$ range of the selected di-lepton. . . . .	60

## List of Tables

---

6.3	Results of the fit of the $p_T(\tau_1) - p_T(\tau_2)$ variable for same-sign di-tau candidates. “hard $e$ ” and “hard $\mu$ ” indicates which of the two particles has the larger $p_T$ . . . . .	62
6.4	$Z \rightarrow \tau\tau$ cross-feed probabilities from a given channel to another, given in percentage. Each column represents the di-tau final-state under study, whilst each row represents the true channel of origin. The last row shows the total percentage of cross-feed. The contributions inferior to 0.1% are omitted. . . . .	64
6.5	Estimated number of backgrounds candidates, number of observed candidates, and, in the last row, the inferred number of signal candidates. The uncertainties on the signal are statistical and systematic combined. . . . .	65
6.6	Result of the $\chi^2$ test between the observed and expected di-tau candidates using equiprobable binning. The two last rows give the purity of the signal in the analysis. . . . .	65
6.7	The numbers of expected opposite-sign di-tau candidates passing the analysis selection from simulation, normalized to the integrated luminosity (the raw number of selected candidates in bracket). The uncertainty is only statistical. In the last row, the number of observed candidates from data is given for comparison. . . . .	68
6.8	Like Table 6.7, for same-sign candidates. . . . .	69
7.1	Summary of calculation methods for different reconstruction efficiency components . . . . .	71
7.2	Correction factors applied to the tracking efficiency calculation, for each analysis channel. The values are averages over the candidates. The tracks of same kind are ordered in descending $p_T$ . . . . .	73
7.3	Comparison of the average signal $\varepsilon_{\text{PID}}$ from the data-driven method for three different $\varepsilon_{\text{PID},\mu}(p_T,\eta)$ binning, and the corresponding systematic uncertainty. . . . .	76
7.4	Comparison of the average signal $\varepsilon_{\text{PID}}$ from the data-driven method for three different $\varepsilon_{\text{PID},e}(p_T,\eta)$ binnings, and the corresponding systematic uncertainty. . . . .	78
7.5	Comparison of the average signal $\varepsilon_{\text{PID}}$ from the data-driven method for three different $\varepsilon_{\text{PID},h}(p_T,\eta)$ binnings, and the corresponding systematic uncertainty. . . . .	80
7.6	Summary of the <i>equivalent</i> reconstruction efficiencies for each di-tau channel at each stage of the selection, given in percentage. . . . .	83
8.1	Selection efficiencies (in percentage) obtained from $Z \rightarrow \tau\tau$ simulated events, for each of selection variables applied individually. The last line is the efficiency with all the criteria applied. . . . .	85
8.2	The values of $\varepsilon_{\text{sel}}$ for each di-tau channel, and the absolute changes induced by the corrections. The values are given in percentage. . . . .	90
9.1	Relative uncertainties due to the background estimate. The uncertainties associated to the QCD and $Vj$ backgrounds are correlated, because obtained from the same fit. . . . .	92

9.2	Relative uncertainties of reconstruction efficiencies, shown in percentage. The subscript 1(2) refers to tau candidate labeled at position 1(2) of di-tau channel. In case of $\tau_{h3}$ , the uncertainty from product of 3-prongs is shown. . . . .	92
9.3	Relative uncertainties of selection efficiencies, shown in percentage. . . . .	92
9.4	Summary of the relative uncertainties of the various contributions affecting the cross-section measurement, given in percentage. . . . .	93
10.1	Summary of the quantities used in the calculation of cross-section, shown in percentage. . . . .	95
10.2	The $\tau$ lepton branching fractions obtained from the fit of the $Z \rightarrow \tau\tau$ cross-section measurements. The values from the PDG are given in the bottom row. . . . .	97
12.1	Summary of the acceptance requirements, where $\tau_x$ denotes the $\tau$ decay channel. . . . .	107
12.2	Additional acceptance requirements for $\tau_{h3}$ in $\mu\tau_{h3}$ channel, where $h$ denotes one of the charged hadrons used in the reconstruction of the 3-prongs. . . . .	107
12.3	Tracking selections, applied identically to muons, charged hadrons, and electrons. . . . .	107
12.4	Summary of the particle identification criteria. . . . .	107
12.5	Offline selections for $\tau_{h3}$ in the $\mu\tau_{h3}$ channel, for the three analysis regimes. . . . .	108
12.6	Selections in common to all analysis regimes . . . . .	108
12.7	Selections specific for each analysis regime. . . . .	108
13.1	Di-tau branching fraction, acceptance, reconstruction efficiency, offline selection efficiencies, and purity factor used in the computation of eq. 13.1, shown in percentage. . . . .	110
13.2	Numbers of estimated $Z \rightarrow \mu\mu$ backgrounds. . . . .	110
13.3	Statistics of $Z \rightarrow ll$ background estimation in $\mu\tau_{h1}$ , $\mu\tau_e$ channel. The ‘‘Mean mis-id’’ gives the lepton misidentification averaged over the $p_T$ range of the selected di-lepton. The uncertainties from the same background source are correlated. . . . .	111
13.4	Results of the fit of the $\Delta p_T$ variable for same-sign $\mu\tau$ candidates. . . . .	111
13.6	Result of the $\chi^2$ test between the observed and expected $\mu\tau$ candidates using the equiprobable binning technique. . . . .	113
13.5	Expected number of background candidates, and the number of observed candidates. . . . .	114
15.1	Systematic uncertainties on the parameters for the cross-section calculation, given in percentages. When the uncertainty depends on more parameters (e.g., $m_H$ , selection regime), only the range is indicated. . . . .	123
15.2	Correlation across channels for each term in the cross-section computation. . . . .	123
15.3	Relative uncertainties on the number of expected backgrounds, shown in percentages. . . . .	124
15.4	Correlation factors between QCD and $Vj$ background uncertainties. . . . .	124
17.1	Approximate efficiencies of $\varepsilon_{\text{rec}}$ and $\varepsilon_{\text{sel}}$ used in the estimation of future prospect. . . . .	138

## List of Tables

---

17.2	Estimated Run-II signal yield using current selection. . . . .	138
17.3	Estimated Run-II signal yield using improved kinematic selection. . . . .	138
A.1	Signal retention from the mass window cut at the acceptance level (with all other cuts on $p_T$ and $\eta$ applied). . . . .	147
A.2	Muon-alley specification for trigger–stripping. . . . .	148
A.3	Electron-alley specification for trigger–stripping. . . . .	148
A.4	<code>StrippingZ02MuMuLine</code> from <code>StrippingZ02MuMu.py</code> , used as control sample for $\varepsilon_{\text{sel}}$ systematics. . . . .	149
A.5	<code>StrippingMuIDCalib_JpsiFromBNNoPIDNoMip</code> from <code>StrippingMuIDCalib.py</code> , used for low- $p_T$ muon tag-and-probe $\varepsilon_{\text{PID},\mu}$ . . . . .	149
A.6	<code>StrippingWMuLine</code> from <code>StrippingWMu.py</code> , used for high- $p_T$ muon tag-and-probe $\varepsilon_{\text{PID},\mu}$ , and for muon misidentification study. . . . .	149
A.7	<code>StrippingJpsi2eeForElectronIDBu2JpsiKLine</code> from <code>StrippingElectronID.py</code> , used for low- $p_T$ electron tag-and-probe $\varepsilon_{\text{PID},e}$ . . . . .	150
A.8	<code>StrippingWeLine</code> from <code>StrippingWe.py</code> , used for high- $p_T$ electron tag-and-probe $\varepsilon_{\text{PID},e}$ , and $\varepsilon_{\text{trig},e}$ . . . . .	150
A.9	<code>StrippingNoPIDstarWithD02RSKPiLine</code> from <code>StrippingNoPIDstarWithD02RSKPi.py</code> , used for charged hadron tag-and-probe $\varepsilon_{\text{PID},h}$ . . . . .	151
B.1	Muon misidentification tag-and-probe fitting results. . . . .	172
C.1	Numbers of expected opposite-sign di-lepton candidates in $\tau_\mu\tau_e$ channel, allowing the estimation of dominating processes in faking $Z \rightarrow ll$ background in $\tau_\mu\tau_{h1}$ , $\tau_e\tau_{h1}$ , $\tau_\mu\tau_e$ channels. . . . .	173
C.2	Number of observed candidates in data and projection factor $r$ for the calculation of QCD background. . . . .	175
C.3	Detailed result from the fitting of same-sign candidates to different compositions via <code>ROOT.TFractionFitter</code> class. . . . .	175
C.4	The number of expected opposite-sign di-tau candidates using QCD data-driven cuts. The values are normalized by the integrated luminosity, with cross-section and $\varepsilon_{\text{gen}}$ from Table 4.2. The number of selected candidates before normalization is in the bracket. . . . .	176
C.5	The number of expected same-sign di-tau candidates using QCD data-driven cuts. The values are normalized by the integrated luminosity, with cross-section and $\varepsilon_{\text{gen}}$ from Table 4.2. The number of selected candidates before normalization is in the bracket. . . . .	177
C.6	The number of expected di-tau candidates from simulation, using offline selection in the region of the $Z$ -peak (an invariant mass between $[80,100]$ $\text{GeV}/c^2$ for the $\tau_\mu\tau_\mu$ channel, and $[70,100]$ $\text{GeV}/c^2$ for the $\tau_e\tau_e$ channel). . . . .	178
C.7	Number of selected candidates from simulation and projection factor $r$ for the calculation of $Vj$ background. . . . .	179
C.8	Same-sign candidates fit results at different $Z \rightarrow \tau\tau$ fit constraints, where constraints are the multipliers applied to the $2\text{-}\sigma$ upper limit on same-sign $Z \rightarrow \tau\tau$ from simulation. . . . .	179
E.1	$\varepsilon_{\text{track},\mu}$ as a function of muon $\eta$ . . . . .	191
E.2	$\varepsilon_{\text{track},e}$ as a function of electron $\eta$ and event track multiplicity. . . . .	191



E.3	$\varepsilon_{\text{track},h}$ as a function of charged hadron $\eta$ and event track multiplicity, for $\tau_\mu\tau_{h1}$ channel. . . . .	191
E.4	$\varepsilon_{\text{track},h}$ as a function of charged hadron $\eta$ and event track multiplicity, for $\tau_e\tau_{h1}$ channel. . . . .	191
E.5	$\varepsilon_{\text{PID},\mu}$ as a function of muon $\eta$ , $p_T$ . . . . .	192
E.6	$\varepsilon_{\text{PID},e}$ as a function of electron $\eta$ , $p_T$ . . . . .	192
E.7	$\varepsilon_{\text{PID},h}$ as a function of charged hadron $\eta$ , $p_T$ . . . . .	193
E.8	$\varepsilon_{\text{trig},\mu}$ as a function of muon $\eta$ , $p_T$ . . . . .	194
E.9	$\varepsilon_{\text{trig},e}$ as a function of electron $\eta$ , $p_T$ . . . . .	194
E.10	Channel $\tau_\mu\tau_\mu$ . . . . .	195
E.11	Channel $\tau_\mu\tau_{h1}$ . . . . .	196
E.12	Channel $\tau_\mu\tau_{h3}$ . . . . .	196
E.13	Channel $\tau_e\tau_e$ . . . . .	196
E.14	Channel $\tau_e\tau_{h1}$ . . . . .	197
E.15	Channel $\tau_e\tau_{h3}$ . . . . .	197
E.16	Channel $\tau_\mu\tau_e$ . . . . .	198
F.1	Statistics for the calculation of the acceptance factor $\mathcal{A}$ . The migration into acceptance refers to the fraction of di-tau candidates found inside acceptance that are from outside the fiducial region. . . . .	199
F.2	Statistics for the calculation of the kinematic selection efficiency $\varepsilon_{\text{kine}}$ . The first five rows refers to the number of di-tau candidates from the simulated $Z \rightarrow \tau\tau$ sample after the given selection is applied: <b>acc</b> for the acceptance selection, <b>trk</b> for the track quality selection, and <b>kine</b> the kinematical selection. The migration into $\varepsilon_{\text{kine}}$ refers to the fraction of di-tau candidates passing the track and kinematic selections but are from outside the acceptance region. . . . .	199
G.1	Summary of correlation across channels for each term in the cross-section computation, and their contributions to combined cross-section uncertainties. . . . .	201
J.1	Opposite-sign low-mass selection . . . . .	219
J.2	Same-sign low-mass selection . . . . .	219
J.3	Opposite-sign central selection . . . . .	220
J.4	Same-sign central selection . . . . .	220
J.5	Opposite-sign high-mass selection . . . . .	221
J.6	Same-sign high-mass selection . . . . .	221
K.1	Signal acceptance from inclusive ( $4\pi$ ) production for different channel at different selection regimes, shown in percentage. . . . .	229
K.2	Signal acceptance from production inside LHCb fiducial volume for different channel at different selection regimes, shown in percentage. . . . .	229
K.3	Detail of $\varepsilon_{\text{rec}}$ in $\mu\tau_e$ channel. . . . .	230
K.4	Detail of $\varepsilon_{\text{rec}}$ in $\mu\tau_{h1}$ channel. . . . .	231
K.5	Detail of $\varepsilon_{\text{rec}}$ in $\mu\tau_{h3}$ channel. . . . .	232
K.6	Detail of $\varepsilon_{\text{rec}}$ in $\mu\tau_\mu$ channel. . . . .	233
K.7	Signal selection efficiencies for different channels at different selection regimes, shown in percentage. . . . .	235

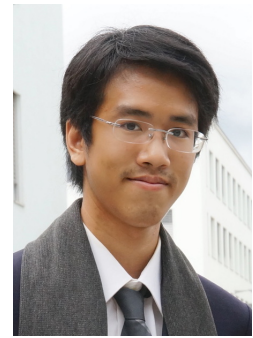
## List of Tables

---

L.1	Summary of construction degree of freedom of models. . . . .	237
M.1	Best fit signal yield using extended likelihood model for different channels at different selection regimes. . . . .	250
M.2	The best fit, expected, and observed upper limits of $\sigma_{gg \rightarrow H \rightarrow \mu\tau}$ from full solid angle. . . . .	251
M.3	The best fit, expected, and observed upper limits of $\sigma_{gg \rightarrow H \rightarrow \mu\tau}$ with $H \rightarrow \mu\tau$ inside LHCb geometrical acceptance. . . . .	251
M.4	The best fit, expected, and observed upper limits of $\mathcal{B}_{H \rightarrow \mu\tau}$ using the BSM Higgs production cross-section from LHCHSWG. . . . .	254

# Chitsanu Khurewathanakul

15 Aug 1989, Thai citizen  
Chemin du Coteau 11  
Pully, 1009. Switzerland  
+41 (76) 451-3839  
chitsanu.khurewathanakul@gmail.com



## EDUCATION

---

- 2013 – 2017: **Ph.D Thesis** at EPFL in the Laboratory of High Energy Physics, and CERN (LHCb collaboration), Switzerland  
*Search for lepton-flavour-violating Higgs-like boson decay to  $\mu\tau$  at LHCb*
- 2011 – 2013: **Master of Science in Physics** (EPFL, Switzerland)  
*Can a Higgs decay to four bottom quarks be observed at LHCb?*
- 2007 – 2011: **Bachelor of Science in Physics** (EPFL, Switzerland)

## EXPERIENCES

---

- 2011–2015 Co-founder, Committee, President (2015): Association of Thai Students in Switzerland.
  - Various events organized throughout the academic year in order to build a supportive network of Thai students for their well-integration in Switzerland.
- 2010-2016 Teaching Assistant at EPFL
  - Teaching duties at the Bachelor and Master levels, in both theoretical and experimental.
- 2009 July Laboratory assistance for master project.  
Synchrotron Light Research Institute (SLRI), *Thailand.*
  - Experiment on determination of the composition of ancient artifacts using X-ray Absorption Spectroscopy (XAS beamline).

## COMPETENCES

---

Languages	Thai (Mother-tongue), English (C1), French (A2/B1), German (A2/B1)
Computer Languages	Python, Go, C++, Java, R, SQL, VB, LaTeX, markdown, HTML
Framework	ROOT/TMVA/RooFit/RooStats, Pythia, Android, GoogleAppEngine, git, pytest, numpy-pandas, sphinx.

## MISCELLANEOUS

---

IB diploma, certified scuba diver, languages (human/computational) gourmet, movie immerser, multimedia director of school play, skiing, hiking, taekwondo, piano.

อดีตของโลก... คืออนาคตของเรา

อดีตของเรา... คืออนาคตของทุกคน

— คติพจน์นักไซอิต

